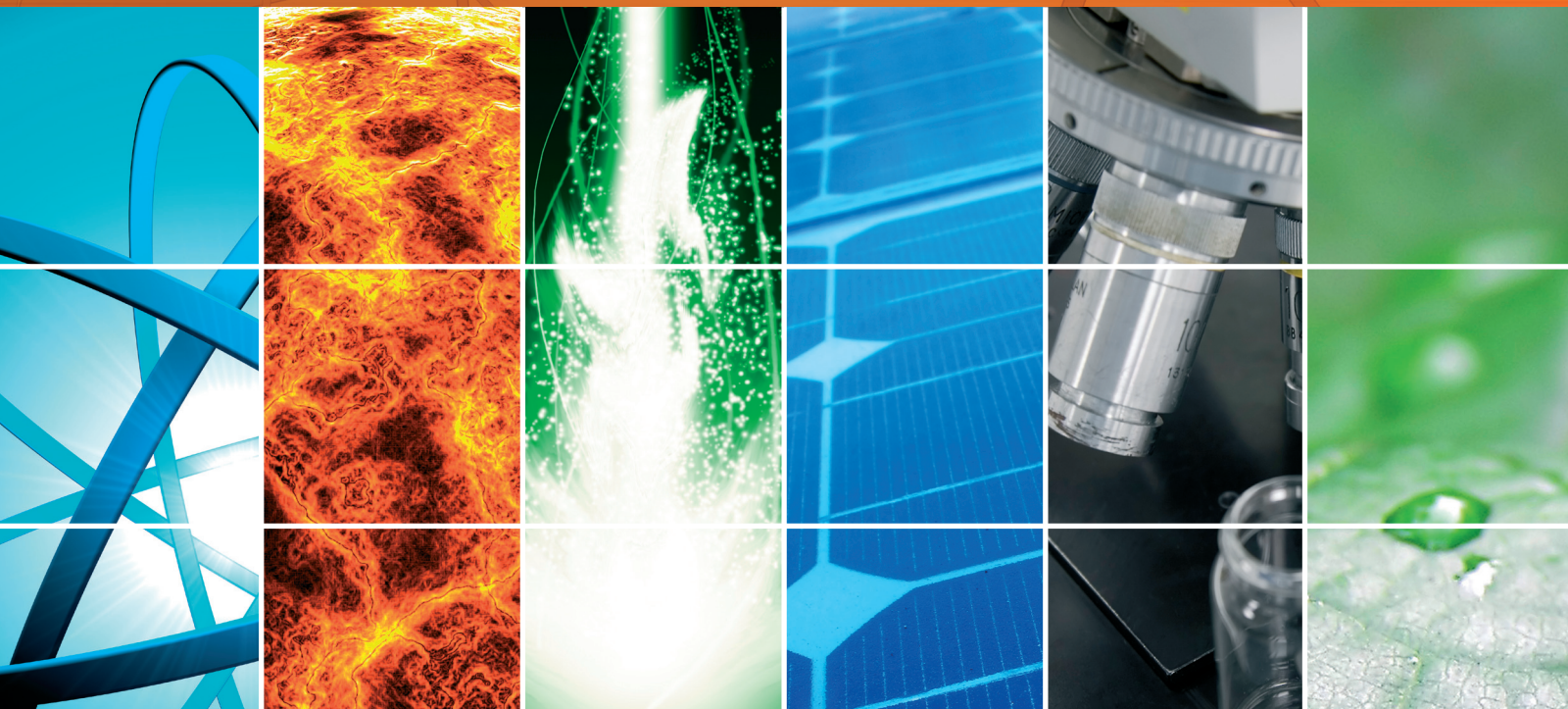


# Solar Energy and Nanomaterials for Clean Energy Development

Guest Editors: M. S. A. Abdel-Mottaleb, Frank Nüesch,  
and Mohamed M. S. A. Abdel-Mottaleb





---

# **Solar Energy and Nanomaterials for Clean Energy Development**

International Journal of Photoenergy

---

## **Solar Energy and Nanomaterials for Clean Energy Development**

Guest Editors: M. S. A. Abdel-Mottaleb, Frank Nüesch,  
and Mohamed M. S. A. Abdel-Mottaleb



Copyright © 2009 Hindawi Publishing Corporation. All rights reserved.

This is a special issue published in volume 2009 of “International Journal of Photoenergy.” All articles are open access articles distributed under the Creative Commons Attribution License, which permits unrestricted use, distribution, and reproduction in any medium, provided the original work is properly cited.

## Editorial Board

M. S. Abdel-Mottaleb, Egypt  
Nihal Ahmad, USA  
Nicolas Alonso-Vante, France  
Wayne A. Anderson, USA  
Vincenzo Augugliaro, Italy  
Eray Aydil, USA  
Detlef W. Bahnemann, Germany  
Ignazio Renato Bellobono, Italy  
Raghu N. Bhattacharya, USA  
Gion Calzaferri, Switzerland  
Sebastiano Campagna, Italy  
Vikram L. Dalal, USA  
D. (Dion) D. Dionysiou, USA  
Abderrazek Douhal, Spain  
Samy El-Shall, USA  
Beverley Glass, Australia

Shahed Khan, USA  
Cooper H. Langford, Canada  
Gianluca Li Puma, UK  
Panagiotis Lianos, Greece  
Stefan Lis, Poland  
Gilles Mailhot, France  
Ugo Mazzucato, Italy  
Jacek Miller, Poland  
Franca Morazzoni, Italy  
Leonardo Palmisano, Italy  
David Lee Phillips, Hong Kong  
Marie-Paule Pileni, France  
Xie Quan, China  
Tijana Rajh, USA  
Saffa Riffat, UK  
Peter Robertson, UK

Jean-Louis Scartezzini, Switzerland  
Pathiyamattom Joseph Sebastian, Mexico  
Panagiotis Smirniotis, USA  
Sam-Shajing Sun, USA  
Masanori Tachiya, Japan  
Gopal Nath Tiwari, India  
Veronica Vaida, USA  
Roel van De Krol, The Netherlands  
Mark van Der Auweraer, Belgium  
Han Vos, Ireland  
David Worrall, UK  
Fahrettin Yakuphanoglu, Turkey  
Jimmy C. Yu, Hong Kong  
Klaas Zachariasse, Germany  
Jincai H. Zhao, China

# Contents

**Solar Energy and Nanomaterials for Clean Energy Development**, M. S. A. Abdel-Mottaleb, Frank Nüesch, and Mohamed M. S. A. Abdel-Mottaleb  
Volume 2009, Article ID 525968, 2 pages

**Study of Dye-Sensitized Solar Cells by Scanning Electron Micrograph Observation and Thickness Optimization of Porous TiO<sub>2</sub> Electrodes**, Seigo Ito, Mohammad K. Nazeeruddin, Shaik M. Zakeeruddin, Peter Pěchy, Pascal Comte, Michael Grätzel, Takaki Mizuno, Atsushi Tanaka, and Tsuguo Koyanagi  
Volume 2009, Article ID 517609, 8 pages

**Prospects of Nanostructure-Based Solar Cells for Manufacturing Future Generations of Photovoltaic Modules**, N. Gupta, G. F. Alapatt, R. Podila, R. Singh, and K. F. Poole  
Volume 2009, Article ID 154059, 13 pages

**The Effect of UV-Irradiation (under Short-Circuit Condition) on Dye-Sensitized Solar Cells Sensitized with a Ru-Complex Dye Functionalized with a (diphenylamino)Styryl-Thiophen Group**, Kazuteru Nonomura, Yunhua Xu, Tannia Marinado, Daniel P. Hagberg, Rong Zhang, Gerrit Boschloo, Licheng Sun, and Anders Hagfeldt  
Volume 2009, Article ID 471828, 9 pages

**Computational Study of 3,4-Diphenyl-1,2,5-Thiadiazole 1-Oxide for Organic Photovoltaics**, Daniel Glossman-Mitnik  
Volume 2009, Article ID 806714, 8 pages

**Squaraine Planar-Heterojunction Solar Cells**, Bin Fan, Ylenia Maniglio, Marina Simeunovic, Simon Kuster, Thomas Geiger, Roland Hany, and Frank Nüesch  
Volume 2009, Article ID 581068, 7 pages

**Hydrothermal Preparation of Gd<sub>3</sub>+Doped Titanate Nanotubes: Magnetic Properties and Photovoltaic Performance**, Hoda S. Hafez, M. Saif, James T. McLeskey, Jr., M. S. A. Abdel-Mottaleb, I. S. Yahia, T. Story, and W. Knoff  
Volume 2009, Article ID 240402, 8 pages

**Improved Performances of a Fluidized Bed Photoreactor by a Microscale Illumination System**, Paolo Ciambelli, Diana Sannino, Vincenzo Palma, Vincenzo Vaiano, and Roberto S. Mazzei  
Volume 2009, Article ID 709365, 7 pages

**Photocatalytic Activity of TiO<sub>2</sub>-WO<sub>3</sub> Composites**, Beata Tryba, Michał Piszcz, and Antoni W. Morawski  
Volume 2009, Article ID 297319, 7 pages

**Removal of Organic Impurities from Water Using a Reactor with Photoactive Refill**, Joanna Grzechulska-Damszel  
Volume 2009, Article ID 304712, 6 pages

**Photoelectrocatalytic Degradation of Organic Pollutants in Aqueous Solution Using a Pt-TiO<sub>2</sub> Film**, Chun He, Mudar Abou Asi, Ya Xiong, Dong Shu, and Xiangzhong Li  
Volume 2009, Article ID 634369, 7 pages

**From Laboratory Studies to the Field Applications of Advanced Oxidation Processes: A Case Study of Technology Transfer from Switzerland to Burkina Faso on the Field of Photochemical Detoxification of Biorecalcitrant Chemical Pollutants in Water**, S. Kenfack, V. Sarria, J. Wéthé, G. Cissé,

A. H. Maïga, A. Klutse, and C. Pulgarin  
Volume 2009, Article ID 104281, 8 pages

**Generation of Useful Hydrocarbons and Hydrogen during Photocatalytic Decomposition of Acetic Acid on CuO/Rutile Photocatalysts**, Sylwia Mozia

Volume 2009, Article ID 469069, 8 pages

**Influence of MWCNTs Doping on the Structure and Properties of PEDOT:PSS Films**, Jiao Li,

Juncheng Liu, Congjie Gao, Jinling Zhang, and Hanbin Sun

Volume 2009, Article ID 650509, 5 pages

**Manipulation of Energy Transfer Processes in Nanochannels**, André Devaux and Gion Calzaferri

Volume 2009, Article ID 741834, 9 pages

**Acylation of 2-(N-arylamino)methylbenzo[b]thiophene-3(2H)-Ones: Molecular Switches with Varying Migrants and Substituents**, Alexander D. Dubonosov, Vladimir P. Rybalkin, Lydia L. Popova,

Alexey V. Tsukanov, Yurii V. Revinsky, Vladimir A. Bren, and Vladimir I. Minkin

Volume 2009, Article ID 694196, 6 pages

**Multifunctional Spirocyclic Systems**, Boris Lukyanov, Gennadii Vasilyuk, Eugene Mukhanov,

Leonid Ageev, Maria Lukyanova, Yury Alexeenko, Serguei Besugliy, and Valeri Tkachev

Volume 2009, Article ID 689450, 9 pages

**Synthesis of Novel Iono- and Photochromic Spiroprans Derived from**

**6,7-Dihydroxy-8-Formyl-4-Methyl-2H-Chromene-2-One**, Olga G. Nikolaeva, Alexey V. Tsukanov,

Evgenii N. Shepelenko, Boris S. Lukyanov, Anatoly V. Metelitsa, Olga Yu. Kostyrina,

Alexander D. Dubonosov, Vladimir A. Bren, and Vladimir I. Minkin

Volume 2009, Article ID 238615, 6 pages

**Optical Study on Poly(methyl methacrylate)/Poly(vinyl acetate) Blends**, R. M. Ahmed

Volume 2009, Article ID 150389, 7 pages

**Optical, XPS and XRD Studies of Semiconducting Copper Sulfide Layers on a Polyamide Film**,

Valentina Krylova and Mindaugas Andrulevičius

Volume 2009, Article ID 304308, 8 pages

**Photoluminescence Spectroscopy of CdTe/ZnTe Self-Assembled Quantum Dots**, Nebojša Romčević,

Maja Romčević, Radmila Kostić, Dušanka Stojanović, Aleksandra Milutinović, Jelena Trajić,

Grzegorz Karczewski, and Robert Galazka

Volume 2009, Article ID 358790, 4 pages

**Growth of GaN@InGaN Core-Shell and Au-GaN Hybrid Nanostructures for Energy Applications**,

Teveye Kuykendall, Shaul Aloni, Ilan Jen-La Plante, and Taleb Mokari

Volume 2009, Article ID 767951, 6 pages

## Editorial

# Solar Energy and Nanomaterials for Clean Energy Development

**M. S. A. Abdel-Mottaleb,<sup>1</sup> Frank Nüesch,<sup>2</sup> and Mohamed M. S. A. Abdel-Mottaleb<sup>3</sup>**

<sup>1</sup>*Nano-Photochemistry and Solarchemistry Laboratory, Department of Chemistry, Faculty of Science, Ain Shams University, Abbassia, Cairo 11566, Egypt*

<sup>2</sup>*Laboratory for Functional Polymers, EMPA, Überlandstrasse 129, CH-8600 Dübendorf, Switzerland*

<sup>3</sup>*Nanotechnology Program, Nile University, Smart Village-B71 K28, Cairo/Alex Desert Road, Cairo, Egypt*

Correspondence should be addressed to M. S. A. Abdel-Mottaleb, phochem08@photoenergy.org

Received 31 December 2009; Accepted 31 December 2009

Copyright © 2009 M. S. A. Abdel-Mottaleb et al. This is an open access article distributed under the Creative Commons Attribution License, which permits unrestricted use, distribution, and reproduction in any medium, provided the original work is properly cited.

This special issue on “Solar energy and nanomaterials for clean energy development” is composed of selected, full-length versions of papers presented during the international Solar’09 conference that was held in the fascinating historical city of Luxor. The conference gathered scientists from 26 countries, to discuss outstanding research on a multitude of topics and disciplines. As was pointed out by Professor Paul Barbara from the University of Texas in Austin at the opening session of the conference, this medium-sized conference offered the unique opportunity to learn and exchange scientific issues from distinct disciplines that have one main thing in common, solar photons. This exceptional opportunity to learn about other fields of research not only required particular didactic skills from the speakers, but also demanded special attention and openness from the audience.

Under the headline of “powering a greener future,” a total of 41 oral presentations were delivered and complemented by a similar number of posters. Photovoltaics, photocatalysis, solar irradiance, photodegradation, photo-induced electron transfer, photochemistry, photobatteries and photospectroscopy are just a flavour of the high diversity of discussed topics. There was even an enriching contribution on pellet fuels for future generation IV nuclear plants, reminding that continued progress is also necessary in already proven technologies. A strong emphasis was placed on organic-based photovoltaics. Dye-sensitized solar cells have now reached a high degree of maturity in theoretical and experimental understanding of the various microscopic

processes contributing to the overall working principle. The dye-sensitized (Grätzel) solar cell is the earliest solar cell directly utilizing nanoscale components for its performance. Here, light absorption takes place predominantly in dye molecules anchored to the surface of nanoparticles of a wide bandgap semiconductor, usually TiO<sub>2</sub>. Upon excitation with visible light, the dye injects electrons from its excited state into the TiO<sub>2</sub> conduction band, leading to a charge-separated state. To absorb enough light, the TiO<sub>2</sub> is made nanoporous, with a large surface area per unit volume and weight. The optimization of the dye/TiO<sub>2</sub> layer is heavily dependent on nanoscale fabrication and characterization; the TiO<sub>2</sub> layer must have a large surface area to incorporate enough dye, but a structure that is thin and open enough to allow for efficient charge transport with minimum losses. Above all, the quest for novel dyes in dye sensitized solar cells is clear, for efficient near-infrared absorbers that are still missing. Interfacial charge transfer complexes on TiO<sub>2</sub> showed a new way to achieve direct interfacial charge-transfer. Due to the important advances worldwide, this thin film photovoltaic technology is on the verge of large-scale commercialisation. In solid organic solar cells, higher efficiencies have still to be met. Fundamental studies are certainly required for this technology to be in accordance with dye-sensitized solar cells. As was shown in one contribution, single molecule fluorescence spectroscopy can reveal microscopic response of conjugated polymers to charging. Single-molecule probes were also shown to be new experimental tools to explore nanoporous

materials, in addition to examining light-harvesting systems. Classical photographic dyes have also been proposed as new material class for organic solar cells. Novel device concepts based on plasmon resonances in nanoparticles were proposed.

Besides photovoltaics, photocatalysis was another theme encompassing the four conference days. Photocatalyzed decomposition of pollutants at various titania surfaces is of great interest. Electron transfer reactions are at the base of these photoinduced processes and were also the subject of one of the theoretical contributions. Water purification, pollutant degradation, and hydrogen production were the most targeted applications. The principle of photocatalysis is to use the energy of photons in the visible to near-UV range (ca. 1.5–5 eV) to generate active chemical species driving a surface chemical reaction on a photocatalyst.

The typical scheme of photocatalysis involves harvesting of light photons in a semiconductor (most commonly  $\text{TiO}_2$ ), and subsequent conversion of these photons to electronic excitations, which then induce the desired chemical reaction on the semiconductor surface. One main bottleneck of this scheme is a high recombination rate of the excited electron-hole pairs, which is relatively slower in case of semiconductor particles of nanodimensions. The majority of charge carriers in nanoparticles will have the opportunity of diffusing into the nearby surface, and thus generating the reactive species leading to efficient surface reactions. It is, thus, obvious that nanostructures offer the opportunity for the charges to survive in order to induce a surface reaction, before recombination occurs.

As well as scientific research, engineered systems such as solar water pumping systems or solar dryers highlighted the benefit of solar powered applications that could be implemented already today.

The conference highlights were not only scientific, but also cultural and culinary. A full day was dedicated to visit the West Bank of Luxor, including memorable visits to the Valley of the Kings, the mortuary temple of pharaoh Hatshepsut, and Hapu Temple of Ramsis 3rd. Well preserved colour reliefs, built 4000 years ago, were simply breath-taking and demonstrated that they were built to last for eternity. Today we have lost the desire to build for eternity; instead, we are burning up so much fossil fuel that it is doubtful whether there will be anything left for future generations. Power from the sun can be harnessed to provide sustainable energy, and many solar-based technologies are ready to be implemented now.

The highly successful solar conference series, started in 1991, provide a place where researchers interested in fundamental and applied aspects of photochemistry can meet and inspire one another. The solar conferences recognize that successful photochemical applications go hand in hand with advancement of fundamental understanding of photoinduced processes and excited states.

The focus of this conference series is of great importance to the current global energy security situation. A coordinated action on a global level is urgently needed to avert the crisis. The developing world must take an active role in any such coordinated action.

Currently, nanotechnology is generating a lot of attention and it is generating great expectations not only in the academic community but also among investors, the governments, and industry. Its unique capability to fabricate new structures at atomic scale has already produced novel materials and devices with great potential applications in a wide number of fields. Among them, significant breakthroughs are especially required in the energy sector that will allow us to maintain our increasing demand for energy. Nanotechnology offers, for the first time, tools to develop new industries based on cost-effective and cost-efficient economies, thus seriously contributing to a sustainable economic growth.

This special issue covers some specific contributions from nanotechnology to various sustainable energies. As mentioned above, the issue's main focus is on three broad areas, namely, light harvesting, catalysis, and materials. Articles on PV chemical solar cells are the most significant examples of the contributions of nanotechnology in the energy sector. The aim of this issue is to present some significant contributions from different research groups working on different approaches, to find solutions to one of the great challenges of our time, that is, the production and use of greener energy from one of the most exciting and multidisciplinary fields, nanotechnology.

Focusing on the energy domain, nanotechnology has the potential to significantly reduce the impact of energy production, storage, and use. Even if we are still far from a truly sustainable energy system, the scientific community is looking at a further development of energy nanotechnologies. In fact, one of the 10 top-level themes of the VII Framework Program of the European Union (FP7) is energy. Accordingly, the research will be focused on accelerating the development of cost-effective technologies for a more sustainable energy economy.

According to the "Roadmap Report Concerning the use of Nanomaterials in the Energy Sector" from the 6th Framework Program, the most promising application fields for the energy conversion domain will be mainly focused on solar energy (mostly photovoltaic technology for local supply), hydrogen conversion, and thermoelectric devices.

It is hoped that this issue may provide an overview of the contribution of nanotechnology to the solar energy in a broad sense and to sustainable ways to store energy as a step forward a more sustainable use of energy.

*M. S. A. Abdel-Mottaleb*

*Frank Nüesch*

*Mohamed M. S. A. Abdel-Mottaleb*

## Research Article

# Study of Dye-Sensitized Solar Cells by Scanning Electron Micrograph Observation and Thickness Optimization of Porous TiO<sub>2</sub> Electrodes

Seigo Ito,<sup>1,2</sup> Mohammad K. Nazeeruddin,<sup>2</sup> Shaik M. Zakeeruddin,<sup>2</sup> Peter Péchy,<sup>2</sup> Pascal Comte,<sup>2</sup> Michael Grätzel,<sup>2</sup> Takaki Mizuno,<sup>3</sup> Atsushi Tanaka,<sup>3</sup> and Tsuguo Koyanagi<sup>3</sup>

<sup>1</sup> Department of Electrical Engineering and Computer Sciences, Graduate School of Engineering, University of Hyogo, 2167 Shosha, Himeji, Hyogo 671-2280, Japan

<sup>2</sup> Laboratoire de Photonique et Interfaces, Institut des Sciences et Ingénierie Chimiques, École Polytechnique Fédérale de Lausanne (EPFL), Station 6, CH-1015 Lausanne, Switzerland

<sup>3</sup> New Business Research Center, JGC Catalysts and Chemicals Ltd., 13-2 Kitaminato-Machi, Wakamatsu-Ku, Kitakyushu, Fukuoka 808-0027, Japan

Correspondence should be addressed to Seigo Ito, itou@eng.u-hyogo.ac.jp

Received 13 April 2009; Accepted 12 May 2009

Recommended by Mohamed Abdel-Mottaleb

In order to improve the photoenergy conversion efficiency of dye-sensitized solar cells (DSCs), it is important to optimize their porous TiO<sub>2</sub> electrodes. This paper examines the surface and cross-sectional views of the electrodes using scanning electron micrography. Two types of samples for cross-sectional viewing were prepared by mechanically breaking the substrate and by using an Ar-ion etching beam. The former displays the surface of the TiO<sub>2</sub> particles and the latter shows the cross-section of the TiO<sub>2</sub> particles. We found interesting surface and cross-sectional structures in the scattering layer containing the 400 nm diameter particles, which have an angular and horned shape. The influence of TiO<sub>2</sub> particle size and the thickness of the nanocrystalline-TiO<sub>2</sub> electrode in DSCs using four kinds of sensitizing dyes (D149, K19, N719 and Z907) and two kinds of electrolytes (acetonitrile-based and ionic-liquid electrolytes) are discussed in regards to conversion efficiency, which this paper aims to optimize.

Copyright © 2009 Seigo Ito et al. This is an open access article distributed under the Creative Commons Attribution License, which permits unrestricted use, distribution, and reproduction in any medium, provided the original work is properly cited.

## 1. Introduction

Dye-sensitized solar cells (DSCs) have recently been developed as a cost-effective photovoltaic system due to their low-cost materials and facile processing [1–4]. The production of DSCs involves chemical and thermal processes but no vacuum is involved. Therefore, DSCs can be fabricated without using expensive equipment. The use of dyes and nanocrystalline TiO<sub>2</sub> is one of the most promising approaches to realize both high performance and low cost. A high light-to-electricity conversion efficiency can be obtained from a large surface area of porous TiO<sub>2</sub> electrodes on which the dyes can be sufficiently adsorbed.

In order to fabricate DSC devices characterized by high efficiency (>10%) and/or long-term stability, further understanding and state-of-art techniques are necessary. The

key points of the DSC mechanism are as follows

- (1) Ultrafast electron injection from the dye to the TiO<sub>2</sub> electrode (<20 femtoseconds) [5].
- (2) Fast dye regeneration via reduction by I<sup>-</sup> (100 nanoseconds without voltage bias) [6].
- (3) The very long electron lifetime in the TiO<sub>2</sub> electrode to I<sub>3</sub><sup>-</sup> (>0.1 second below 0.7 V forward bias) [7].
- (4) The large roughness factor of the TiO<sub>2</sub> electrode (>1600) [8].
- (5) The diode effect of Ru dye on the TiO<sub>2</sub> electrode [8].
- (6) Photon adsorption controlled by the thickness of the TiO<sub>2</sub> layers (transparent layer,  $d = 20$  nm, 12–14  $\mu$ m thickness; scattering layer,  $d = 400$  nm, 4–5  $\mu$ m thickness) [9].

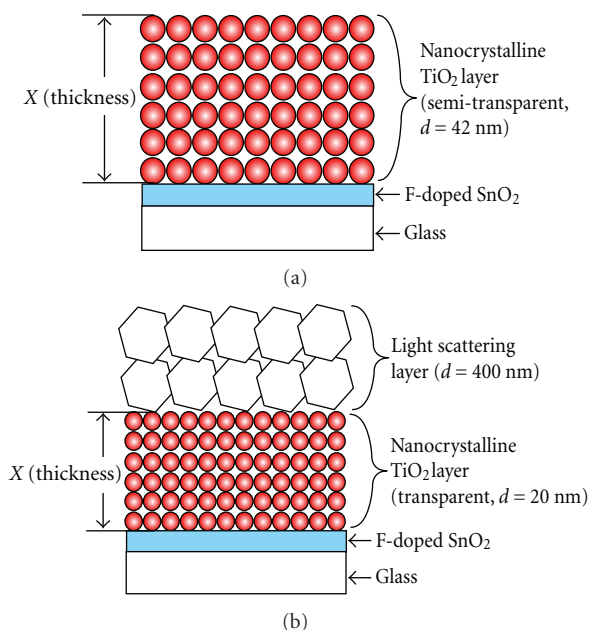
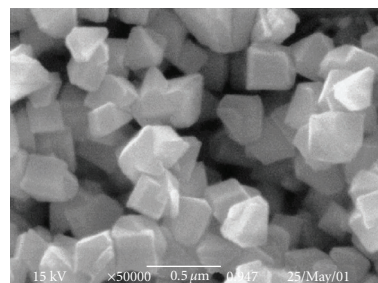


FIGURE 1: Structure of DSC with single-layer (a) and double-layer (b) structures of nanocrystalline-TiO<sub>2</sub> electrodes. X's in figures show the thickness of nanocrystalline-TiO<sub>2</sub> electrodes that was varied for the optimization of high-efficiency DSC (Figures 5, 6 and 7).

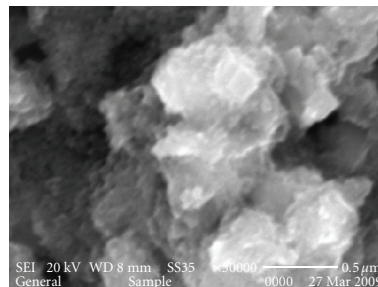
(7) A high-activity Pt counter electrode for  $I^-/I_3^-$  redox ( $<8 \Omega$ ) [10].

Each point listed above is necessary for high-efficiency DSCs. One of the key materials is the TiO<sub>2</sub> electrode, which has been fabricated by using sol-gel screen printing. With this method, the TiO<sub>2</sub> particle size and the thickness of the nanocrystalline-TiO<sub>2</sub> layer ("X" in Figure 1) can be varied, allowing for control of the photovoltage and photocurrent. Thus, we can optimize the design of the porous TiO<sub>2</sub> electrode, the sensitizing dye and the electrolyte.

In this paper, we study the surface and cross-sectional structure of double-layered porous TiO<sub>2</sub> electrodes by SEM observation. We found significant differences between the SEM images of the original structure composed of sub-micron particles and those of a structure composed of a mixture of sub-micron particles and nanoparticles. The two types of cross-sectional samples were prepared either by mechanically breaking the substrate or using an Ar-ion beam etching technique, resulting in confirmation of the significant difference in the appearance of the two samples and the observation of the interesting angular and horned structure of the 400 nm diameter particles in the cross-sectional view. Subsequently, the effect of the TiO<sub>2</sub> particle size ( $d = 20$  nm, 42 nm and 400 nm) and the thickness of the nanocrystalline-TiO<sub>2</sub> electrode on the photovoltaic properties of DSCs are evaluated with four kinds of sensitizing dyes (D149, K19, N719 and Z907) and two kinds of electrolytes (acetonitrile (AcCN) based and ionic-liquid (IL) electrolytes) in order to achieve high conversion efficiency.



(a)



(b)

FIGURE 2: SEM images of the surface of TiO<sub>2</sub> submicron particles (400C, JGC-CCIC) (a) and a mixture of TiO<sub>2</sub> submicron particles and nanoparticles (PST-400C, JGC-CCIC) (b). Magnification of each view is 50,000 times.

## 2. Experimental

**2.1. Materials.** Three kinds of screen-printing paste containing different TiO<sub>2</sub> (anatase) particles (20 nm [9], 42 nm [11] and 400 nm [9]) were prepared by previously reported procedures. For SEM observations, we used TiO<sub>2</sub> materials from JGC Catalysis and Chemicals Ltd. (JGC-CCIC, Japan). The syntheses of *cis*-Ru-di(thiocyanato)-N,N'-bis(2,2'-bipyridyl-4-carboxylic acid-4'-tetrabutylammonium carboxylate) (**N-719**) [12], *cis*-(SCN)<sub>2</sub> (4, 4'-dicarboxylic acid-2,2'-bipyridine) (4, 4'-dinonyl-2, 2'-bipyridine) (**Z907**) [13], Ru((4,4-dicarboxylic acid-2, 2'-bipyridine) (4, 4'-bis(p-hexyloxystyryl)-2,2 bipyridine) (NCS)2 (**K19**) [14] and indoline dye (**D149**) [15] have been reported in previous papers. The chromatographic purification of the Ru dyes was carried out on a column of Sephadex LH-20 using a previously reported procedure [9, 12].

**2.2. Porous TiO<sub>2</sub> Electrodes.** To prepare the working electrodes, the fluorine-doped tin oxide (FTO) glass that was used as the current collector (Nippon Sheet Glass, Solar, 4 mm thickness) was first cleaned in a detergent solution using an ultrasonic bath for 15 minutes and then rinsed with water and ethanol. After treatment in an UV-O<sub>3</sub> system for 18 minutes, the FTO glass plates were immersed in a 40 mM aqueous solution of TiCl<sub>4</sub> at 70°C for 30 minutes and washed with water and ethanol.

A layer of nanocrystalline-TiO<sub>2</sub> paste was coated onto the FTO glass plates by screen printing and kept in a clean box for 3 minutes so that the paste could settle to

reduce the irregularity of the surface and then dried for 6 minutes at 125°C. This screen-printing procedure with the paste (coating, storing and drying) was repeated to obtain a working electrode of appropriate thickness [9]. By adjusting the thickness of the TiO<sub>2</sub> pastes, the TiO<sub>2</sub> electrodes were designed as shown in Figure 1. The porous TiO<sub>2</sub> layers of 20 nm [9], 42 nm [11] and 400 nm [9] were transparent, semitransparent and scattering, respectively. For the scattering layer, two coatings of macrocrystalline-TiO<sub>2</sub> paste were deposited by screen printing, resulting in a light-scattering TiO<sub>2</sub> layer of 4–5 μm thickness containing 400 nm-sized anatase particles. The electrodes coated with the TiO<sub>2</sub> pastes were gradually heated under an air flow at 325°C for 5 minutes, at 375°C for 5 minutes, at 450°C for 15 minutes and 500°C for 15 minutes.

The sintered TiO<sub>2</sub> film was treated with 40 mM TiCl<sub>4</sub> solution as described above, rinsed with water and ethanol and sintered again at 500°C for 30 minutes. After cooling to 80°C, the TiO<sub>2</sub> electrode was immersed in a 0.5 mM dye solution in a mixture of acetonitrile and tert-butyl alcohol (v/v: 1:1) and kept at room temperature for 20–24 hours (Ru dyes) or 4 hours (D149 with 1.0 mM chenodeoxy cholic acid) to complete the sensitizer uptake.

**2.3. Pt Counter Electrodes.** To prepare the counter electrode, a hole was drilled in the FTO glass (LOF Industries, TEC 15 Ω/□, 2.2 mm thickness) by sand blasting. The perforated glass sheet was washed with H<sub>2</sub>O as well as with a 0.1 M HCl solution in ethanol and cleaned by ultrasound in an acetone bath for 10 minutes. After removing residual organic contaminants by heating in air for 15 minutes at 400°C, the Pt catalyst was deposited on the FTO glass by coating with a drop of H<sub>2</sub>PtCl<sub>6</sub> solution (3 mg Pt in 1 mL ethanol) and repeating the heat treatment at 400°C for 15 minutes.

**2.4. DSC Assembly.** The dye-covered TiO<sub>2</sub> electrode and Pt counter electrode were assembled into a sandwich-type cell and sealed with a hot-melt gasket of 25 μm thickness made of the ionomer Surlyn1702 or liner low density polyethylene Bynel4164 (DuPont) on a heating stage. A drop of the electrolyte was put on the hole in the back of the counter electrode. The acetonitrile (AcCN) based electrolyte for N719 was 0.60 M BMII, 0.03 M I<sub>2</sub>, 0.10 M guanidinium thiocyanate and 0.50 M 4-tert-butylpyridine in a mixture of acetonitrile and valeronitrile (v/v: 85 : 15) [8–10]. The ionic-liquid (IL) electrolyte for Z907 and K19 was 0.2 M I<sub>2</sub>, 0.5 M NMBI and 0.1 M GuNCS in a mixture of PMII/EMINCS (v/v: 13 : 7) [14]. The AcCN-based electrolyte for D149 was 0.10 M lithium iodide, 0.60 M butylmethylimidazolium iodide, 0.05 M I<sub>2</sub> and 0.05 M 4-tert-butylpyridine in AcCN:valeronitrile (v/v: 85 : 15) [16]. The IL electrolyte for D149 was 0.20 M I<sub>2</sub> in 1-methyl-3-propylimidazolium iodide, 1-ethyl-3-methylimidazolium bis((trifluoromethyl) sulfonyl) imide and 1-ethyl-3-methylimidazolium triflate (v/v/v: 2 : 1 : 1) [16].

The cell was placed in a small vacuum chamber for a few seconds to remove the inside air. Exposing it again to

ambient pressure caused the electrolyte to be driven into the cell. Finally, the hole was sealed using a hot-melt liner low density polyethylene film (Bynel 4164, 35 μm thickness, Du-Pont) and a cover glass (0.1 mm thickness). In order to have good electrical contact between the connections and the photovoltaic measurement equipment, the edge of the FTO outside of the cell was scraped slightly with sandpaper or a file. A solder (Cerasolza, Asahi Glass) was applied on each side of the FTO electrodes.

**2.5. Measurements.** Photovoltaic measurements employed an AM 1.5 solar simulator (100 mW cm<sup>-2</sup>). Masks made of black plastic tape were attached on the Arctop filter to reduce the scattering of light [17]. The intensity of the simulated light was calibrated by using a reference Si photodiode equipped with an IR cutoff filter (KG-3, Schott) in order to reduce the mismatch in the region of 350–750 nm between the simulated light and AM 1.5 to less than 2% [18]. I-V curves were obtained by applying an external bias voltage to the cell and measuring the generated photocurrent with a digital source meter (Keithley 2400, Keithley Instruments).

### 3. Results and Discussions

**3.1. SEM Observation of Nanocrystalline-TiO<sub>2</sub> Porous Electrodes.** Figure 2(a) shows the SEM images of submicron TiO<sub>2</sub> particles that were used in the light-scattering layer (Figure 1(b)). The particles were a pyramid-like angular shape. The light-scattering TiO<sub>2</sub> layer was a mixture of nano-sized and submicron TiO<sub>2</sub> particles [9]. In the SEM observations, the angular shape of the submicron TiO<sub>2</sub> particles could not be seen in the light-scattering layer (Figure 2(b)). The submicron TiO<sub>2</sub> particles were surrounded by nanoparticles. The outline of the angular shape can be seen through the surrounding nanoparticles.

Figure 3 shows cross-sectional SEM images of a porous TiO<sub>2</sub> electrode that was prepared by breaking the substrate with a glass cutter. It is noticeable that the electrode has a double-layered structure, as illustrated in Figure 1(b). The magnified view of the light-scattering layer (Figure 3(b)) is similar to Figure 2(b); the submicron particles were coated by nanoparticles in the cross-sectional view of a sample prepared by mechanically breaking the substrate.

Figure 4 shows the cross-sectional images of a nanocrystalline-TiO<sub>2</sub> porous electrode prepared by polishing with an Ar-ion beam (the preparation and observation of the samples were done by KOBELCO Research Institute, Inc., Japan). The observed nanocrystalline-TiO<sub>2</sub> porous electrode has a double-layered structure on a glass substrate similar to Figure 1(b). The nanocrystalline-TiO<sub>2</sub> layer is smooth and flat, while the submicroncrystalline-TiO<sub>2</sub> layer is rough due to the large particle size (Figure 4(a)). The nanocrystalline-TiO<sub>2</sub> layer appears very homogeneous at 5 000-times magnification (Figure 4(b)). At 50 000 times magnification (Figure 4(c)), small cracks can be seen in the layer due to shrinkage caused by the heating procedure. At 200 000 times magnification, the nanoparticles can be

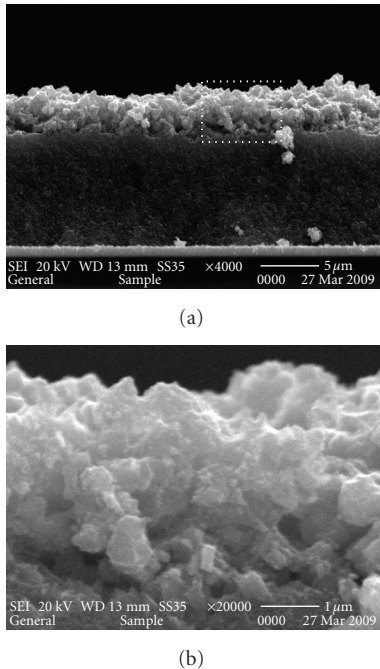


FIGURE 3: Cross-sectional views of a double-layer electrode prepared by mechanically breaking the substrate. The white dotted quadrangle in Figure 3(a) indicates the zoomed-in area shown in Figure 3(b).

observed (Figure 4(d)), but the image is not clear because no metal was deposited by sputtering in order to observe them. Figure 4(e) shows the cross-section of the light-scattering layer by submicroncrystalline-TiO<sub>2</sub> particles. The material of this layer is a mixture of 90% of submicroncrystalline-TiO<sub>2</sub> particles and 10% of nanocrystalline-TiO<sub>2</sub> particles [9]. We can see the exact cross-sectional view of the submicroncrystalline-TiO<sub>2</sub> particles (Figure 4(f)). The size of the cross-sectioned submicron crystals is between 100 nm and 500 nm. This size distribution is due to the Ar-ion beam etching, which cut the crystal at the center and/or the edge. It is surprising that the structure of the submicroncrystalline-TiO<sub>2</sub> particles is rather complicated (angular and horned) in the cross-sectional view, which cannot be observed in the SEM images of Figure 2(a).

**3.2. I-V Curves with Variation of TiO<sub>2</sub> Thickness.** Figure 5 shows the I-V curves of the DSCs with double-layer TiO<sub>2</sub> ( $d = 20$  nm and 400 nm) electrodes (Figure 1(b)). The thickness of the nanocrystalline-TiO<sub>2</sub> layer was adjusted between 2.8  $\mu\text{m}$  to 17.4  $\mu\text{m}$ . The sensitizing dye was a Ru dye (N719), and the electrolyte was an AcCN-based electrolyte. It was observed that the thicker layer gave higher photocurrent and lower photovoltage. On the other hand, the thinner layer gave lower photocurrent and higher photovoltage. This is a typical phenomenon in DSCs regardless of the kind of particles and dyes. In the next sections, we discuss the photovoltaic characteristics for two sizes of TiO<sub>2</sub> nanoparticles ( $d = 42$  nm and 20 nm).

**3.3. Single-Layer Electrodes.** Figure 6 shows the photovoltaic characteristics of single-layer electrodes with a semitransparent layer of 42 nm TiO<sub>2</sub> particles (Figure 1(a)). The combinations of sensitizing dyes and electrolytes were (Ru dye (N719)/AcCN-based electrolyte) and (Ru dye (Z907)/IL electrolyte).

For both combinations of dye and electrolyte, the open-circuit photovoltage ( $V_{oc}$ ) decreased linearly with increasing thickness of the nanocrystalline-TiO<sub>2</sub> electrode (Figure 6(a)).

However, the behavior of the short-circuit photocurrent density ( $J_{sc}$ ) (Figure 6(b)) was different for the electrolytes. For the AcCN-based electrolyte, the  $J_{sc}$  increased and became saturated with increasing thickness. On the other hand, the  $J_{sc}$  for the IL electrolyte reached a maximum around 14  $\mu\text{m}$ . At the thin TiO<sub>2</sub> electrode (4  $\mu\text{m}$  thickness), the values of  $J_{sc}$  for the AcCN-based (11.8 mA cm<sup>-2</sup>) and IL (10.5 mA cm<sup>-2</sup>) electrolytes were similar; the difference was only 12% (1.3 mA cm<sup>-2</sup>). Upon increasing the thickness, the difference increased to 42% for the 21  $\mu\text{m}$  thick films. This arises from the high viscosity and slow  $\text{I}^-/\text{I}_3^-$  diffusion in the IL electrolyte [16]. The redox couple ( $\text{I}^-/\text{I}_3^-$ ) can diffuse readily across the thin nanocrystalline-TiO<sub>2</sub> layer and sustain the low photocurrent. However, transport is impaired in thicker nanocrystalline electrode films where larger photocurrents must be sustained. By contrast, the viscosity of AcCN is so low that high photocurrent can be supported even for thick nanocrystalline-TiO<sub>2</sub> layers.

The fill factor (FF) was not affected by variations in the thickness of the nanocrystalline-TiO<sub>2</sub> layer (Figure 6(c)).

Consequently, the conversion efficiency reached a maximum (Figure 6(d)). Nevertheless, the viscosity and the diffusion coefficient of  $\text{I}^-/\text{I}_3^-$  differed by a factor of 100 [16], the AcCN-based and IL electrolytes gave peaks in the same position for the 14–16  $\mu\text{m}$  thickness.

**3.4. Double-Layer Electrodes.** Figure 7 shows the photovoltaic characteristics of the double-layer electrodes (Figure 1(b)). The particle sizes for the transparent and light-scattering layers were 20 nm and 400 nm, respectively. In this paper, the thickness of the transparent layer ( $d = 20$  nm; “X” in Figure 1(b)) was varied. Four combinations of sensitizing dyes and electrolytes were used: (Ru dye (N719)/AcCN-based electrolyte), (Ru dye (K19)/IL electrolyte), (organic dye (D149)/AcCN-based electrolyte) and (organic dye (D149)/IL electrolyte).

In all cases,  $V_{oc}$  decreased linearly with increasing the thickness of the nanocrystalline-TiO<sub>2</sub> electrode (Figure 7(a)). This phenomenon was the same as that of the single-layer system (Figure 6(a)). It was remarkable that the highest  $V_{oc}$  was over 900 mV for the nanocrystalline-TiO<sub>2</sub> electrode (3  $\mu\text{m}$ ) using Ru dye (N719) and AcCN-based electrolyte.

Figure 7(b) shows the differences in the behavior of  $J_{sc}$  in relation to the nanocrystalline-TiO<sub>2</sub> ( $d = 20$  nm) thickness (Figure 1(b)) between AcCN-based and IL electrolytes, which is similar to the phenomenon observed for the single-layer electrode ( $d = 42$  nm, Figure 6(b)). Using the AcCN-based electrolyte, the  $J_{sc}$  increased and became saturated

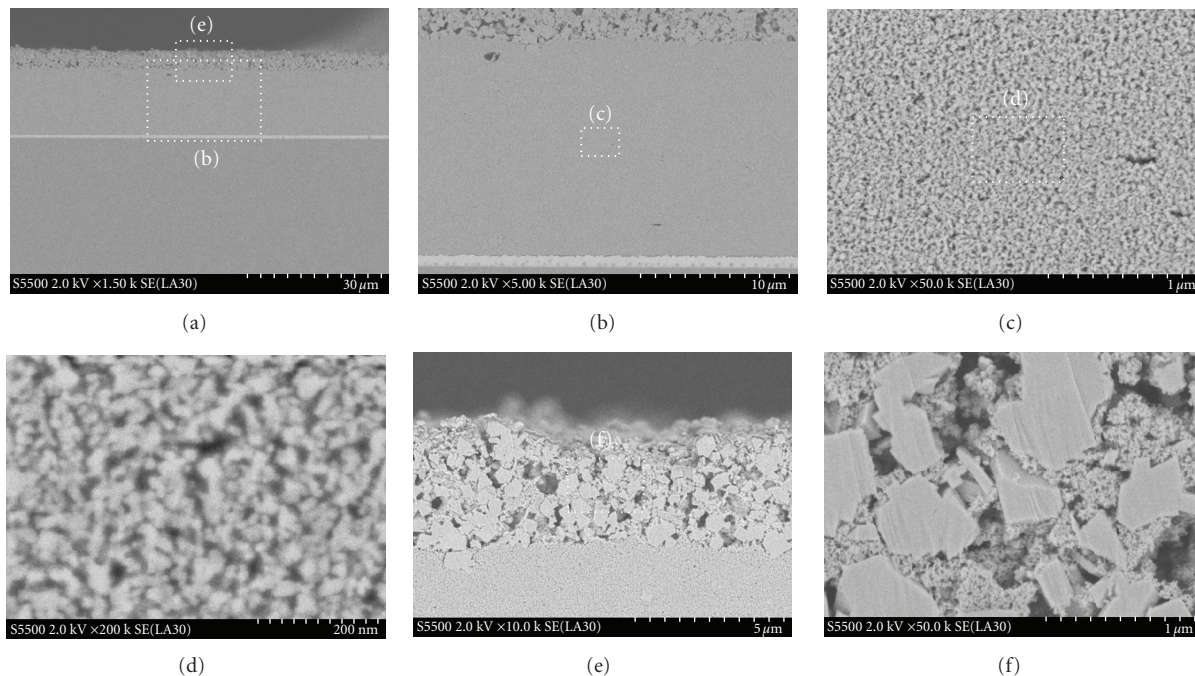


FIGURE 4: Cross-sectional SEM images of a porous double-layered  $\text{TiO}_2$  electrode polished with an Ar-ion beam (nanocrystalline- $\text{TiO}_2$  layer:  $14\ \mu\text{m}$  thick; submicron crystalline- $\text{TiO}_2$  layer:  $5\ \mu\text{m}$  thick). (a) is the most zoomed-out image. White dotted quadrangles show the zoomed-in area for the other images.

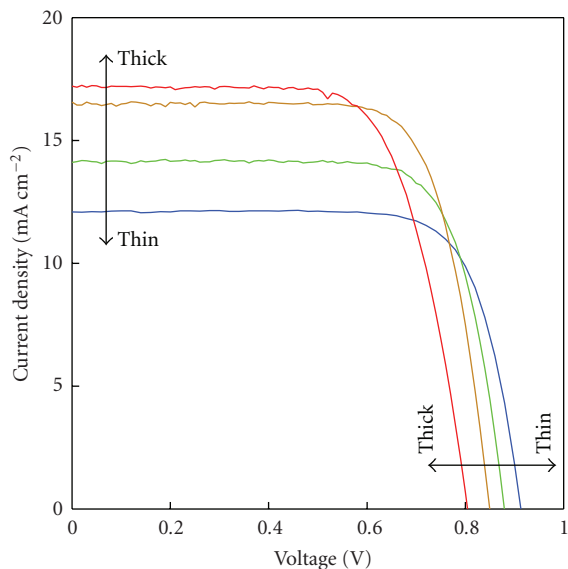


FIGURE 5: Photo I-V curves in relation to the thickness of double-layer nanocrystalline- $\text{TiO}_2$  electrodes (as shown in Figure 1(b)) with Ru dye (N719) and AcCN-based electrolyte.

with increasing thickness. On the other hand, using the IL electrolyte, the  $J_{sc}$  had a peak at a thickness of around  $6\ \mu\text{m}$ . The optimal thickness for the  $20\ \text{nm}$  particles (Figure 7(b)) was half that obtained for the  $42\ \text{nm}$  particles (Figure 6(b)). The larger particles ( $d = 42\ \text{nm}$ , Figure 6(b)) produced

larger pores into which the redox couple ( $\text{I}^-/\text{I}_3^-$ ) could diffuse more effectively than into the smaller pores created by the smaller particles ( $d = 20\ \text{nm}$ ). Therefore, the larger particles gave a  $J_{sc}$  peak at a larger thickness than the smaller particles.

The FF was not greatly affected by variations in the thickness of the nanocrystalline- $\text{TiO}_2$  layer (Figure 7(c)). In the case of the organic dye (D149) with IL electrolyte, however, the FF decreased as a result of the high photocurrent and the low diffusion coefficient of the redox couple.

Consequently, the conversion efficiency reached a maximum (Figure 7(d)). The AcCN-based and IL electrolytes gave peaks at  $14\ \mu\text{m}$  and  $6\ \mu\text{m}$  thickness, respectively. The important point is that the position of the peaks was unrelated to the nature of the Ru dye and the organic dye, in spite of the 4-fold difference between their absorption coefficients (N719:  $13,900\ \text{M}^{-1}\ \text{cm}^{-1}$ , K19:  $18,200\ \text{M}^{-1}\ \text{cm}^{-1}$ , D149:  $68,700\ \text{M}^{-1}\ \text{cm}^{-1}$ ). At first, we expected that the organic dye would yield the highest efficiency when the thickness of the nanocrystalline- $\text{TiO}_2$  layer was small; however, the peak of efficiency was determined by the electrolyte and the particle size, not by the type of sensitizer.

#### 4. Conclusions

The structure of the cross-section of the double-layered  $\text{TiO}_2$  electrode, which was prepared by Ar-ion beam etching, has been observed by SEM for the first time. We confirmed the difference between the cross-sectional structures prepared by mechanically breaking the substrate and Ar-ion beam

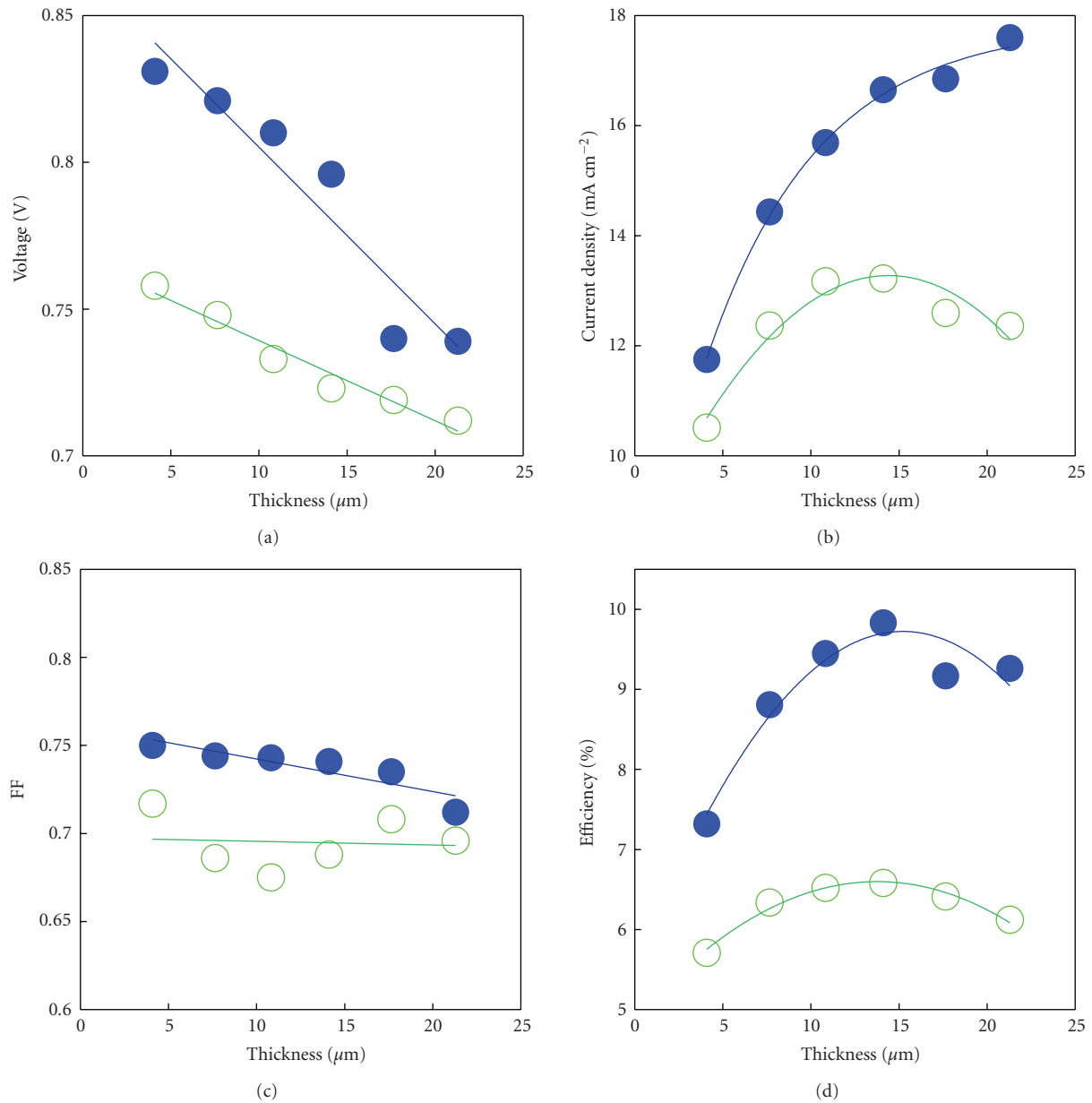


FIGURE 6: Photovoltaic characteristics related to the thickness of nanocrystalline- $\text{TiO}_2$  ( $d = 42 \text{ nm}$ ) layers of single-layer electrodes (as shown in Figure 1(a)): N719-sensitized solar cells using AcCN-based electrolytes (solid circles); Z907-sensitized solar cells using IL electrolytes (open circles).

etching and observed the unique structure of the 400 nm  $\text{TiO}_2$  particles with respect to the light-scattering effect.

In order to optimize the design of DSCs for maximal conversion efficiency, the  $\text{TiO}_2$  particle size and the thickness of the nanocrystalline- $\text{TiO}_2$  layer were varied and tested with several sensitizing dyes and electrolytes. For the single-layer electrodes (semitransparent,  $d = 42 \text{ nm}$ ), the maximal efficiencies were 6.6% at  $14 \mu\text{m}$  and 9.9% at  $16 \mu\text{m}$  with  $\langle \text{Z907/IL} \rangle$  and  $\langle \text{N719/AcCN} \rangle$ , respectively. For the double-layer electrodes (transparent layer:  $d = 20 \text{ nm}$ ; light-scattering layer:  $d = 400 \text{ nm}$ ), the maximal efficiencies were 7.0% at  $6 \mu\text{m}$ , 6.3% at  $6 \mu\text{m}$ , 10.2% at  $14 \mu\text{m}$  and

9.0% at  $14 \mu\text{m}$  with  $\langle \text{K19/IL} \rangle$ ,  $\langle \text{D149/IL} \rangle$ ,  $\langle \text{N719/AcCN} \rangle$  and  $\langle \text{D149/AcCN} \rangle$ , respectively. The optimal thickness of the nanocrystalline- $\text{TiO}_2$  layer depends on the electrolyte and  $\text{TiO}_2$  particle size but not on the absorption coefficient of the dye.

From these experimental results, we can estimate the conversion efficiency of a DSC for an ideal case where  $V_{oc}$ ,  $J_{sc}$  and FF attain their maximal values. The best values were a  $V_{oc}$  of 900 mV (Figure 7(a)), a  $J_{sc}$  of  $20 \text{ mA cm}^{-2}$  (Figure 7(b)) and an FF of 0.77 (Figure 7(c)). Using these values, the ideal conversion efficiency reaches 13.9%. In order to obtain this value, we need to use a dye with

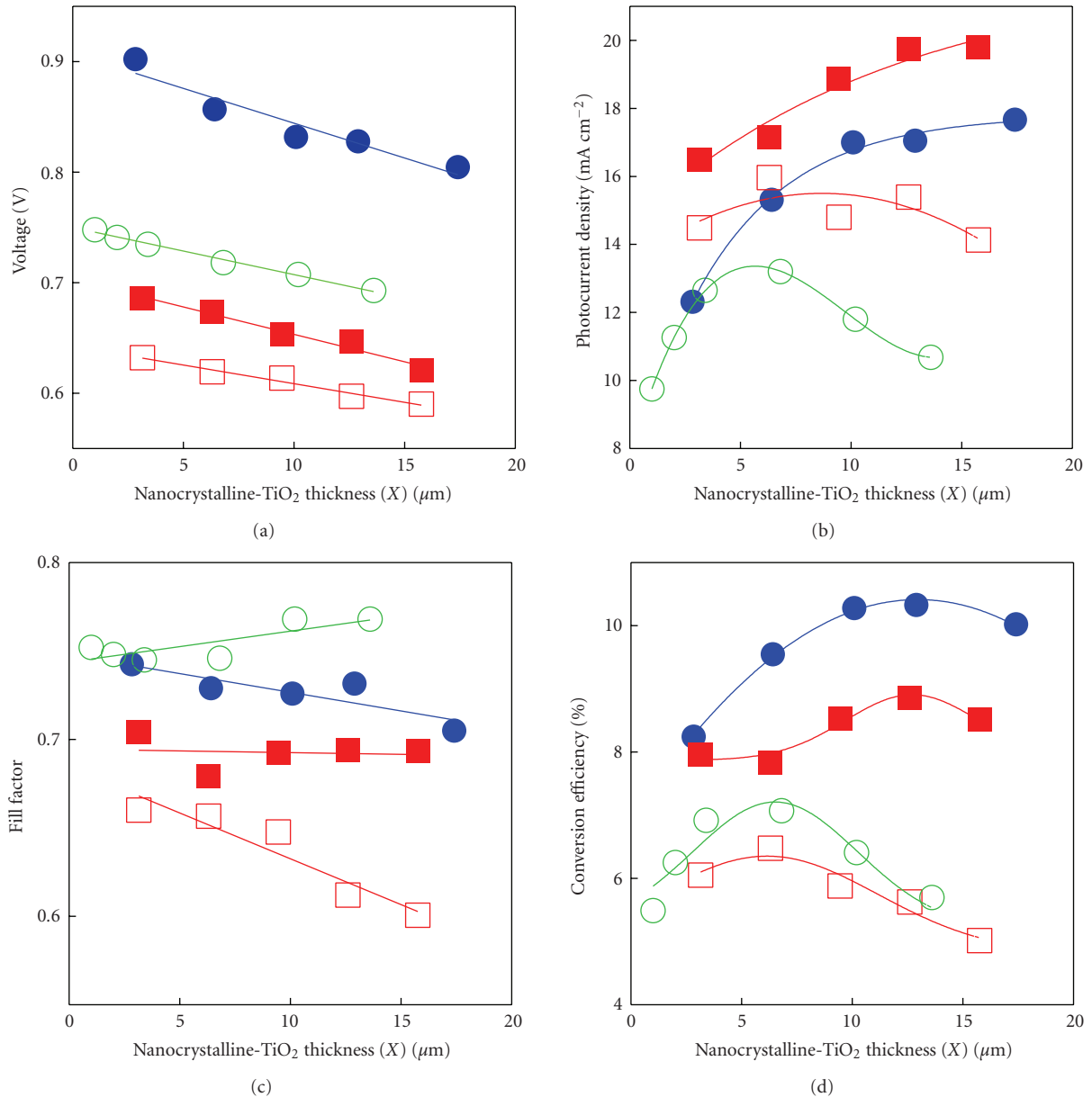


FIGURE 7: Photovoltaic characteristics in relation to the thickness of nanocrystalline-TiO<sub>2</sub> ( $d = 20$  nm) layers in double-layer electrodes (as shown in Figure 1(b)): N719-sensitized solar cells using AcCN-based electrolytes (solid circles); K19-sensitized solar cells using ionic-liquid-based electrolytes (open circles); D149-sensitized solar cells using AcCN-based (solid square) and ionic-liquid-based (open square) electrolytes.

a high absorption coefficient that displays a strong blocking effect against charge recombination. We hope that this report is helpful for the development of DSCs for practical applications.

### Acknowledgments

This work was supported by a grant from the Swiss Federal Energy Office (OFEN). The authors thank Mr. Tamotsu Horiuchi (Riko Co., Ltd., Japan) for assistance. The SEM cross-sectional views were obtained with the help of Dr. Mizuno (KOBELCO Co., Ltd., Japan).

### References

- [1] B. O'Regan and M. Grätzel, "A low-cost, high-efficiency solar cell based on dye-sensitized colloidal TiO<sub>2</sub> films," *Nature*, vol. 353, no. 6346, pp. 737–740, 1991.
- [2] M. Grätzel, "Photoelectrochemical cells," *Nature*, vol. 414, no. 6861, pp. 338–344, 2001.
- [3] Y. Bai, Y. Cao, J. Zhang, et al., "High-performance dye-sensitized solar cells based on solvent-free electrolytes produced from eutectic melts," *Nature Materials*, vol. 7, no. 8, pp. 626–630, 2008.
- [4] S. Ito, S. M. Zakeeruddin, P. Comte, P. Liska, D. Kuang, and M. Grätzel, "Bifacial dye-sensitized solar cells based on an ionic

- liquid electrolyte," *Nature Photonics*, vol. 2, no. 11, pp. 693–698, 2008.
- [5] B. Wenger, M. Grätzel, and J.-E. Moser, "Rationale for kinetic heterogeneity of ultrafast light-induced electron transfer from Ru(II) complex sensitizers to nanocrystalline TiO<sub>2</sub>," *Journal of the American Chemical Society*, vol. 127, no. 35, pp. 12150–12151, 2005.
- [6] S. A. Haque, Y. Tachibana, D. R. Klug, and J. R. Durrant, "Charge recombination kinetics in dye-sensitized nanocrystalline titanium dioxide films under externally applied bias," *Journal of Physical Chemistry B*, vol. 102, no. 10, pp. 1745–1749, 1998.
- [7] J. Bisquert, A. Zaban, M. Greenshtein, and I. Mora-Seró, "Determination of rate constants for charge transfer and the distribution of semiconductor and electrolyte electronic energy levels in dye-sensitized solar cells by open-circuit photovoltage decay method," *Journal of the American Chemical Society*, vol. 126, no. 41, pp. 13550–13559, 2004.
- [8] S. Ito, P. Liska, P. Comte, et al., "Control of dark current in photoelectrochemical (TiO<sub>2</sub>/I<sup>-</sup> - I<sub>3</sub><sup>-</sup>) and dye-sensitized solar cells," *Chemical Communications*, no. 34, pp. 4351–4353, 2005.
- [9] S. Ito, T. N. Murakami, P. Comte, et al., "Fabrication of thin film dye sensitized solar cells with solar to electric power conversion efficiency over 10%," *Thin Solid Films*, vol. 516, no. 14, pp. 4613–4619, 2008.
- [10] S. Ito, N.-L. C. Ha, G. Rothenberger, et al., "High-efficiency (7.2%) flexible dye-sensitized solar cells with Ti-metal substrate for nanocrystalline-TiO<sub>2</sub> photoanode," *Chemical Communications*, no. 38, pp. 4004–4006, 2006.
- [11] S. D. Burnside, V. Shklover, C. Barbé, et al., "Self-organization of TiO<sub>2</sub> nanoparticles in thin films," *Chemistry of Materials*, vol. 10, no. 9, pp. 2419–2425, 1998.
- [12] Md. K. Nazeeruddin, S. M. Zakeeruddin, R. Humphry-Baker, et al., "Acid-base equilibria of (2,2'-bipyridyl-4,4'-dicarboxylic acid)ruthenium(II) complexes and the effect of protonation on charge-transfer sensitization of nanocrystalline titania," *Inorganic Chemistry*, vol. 38, no. 26, pp. 6298–6305, 1999.
- [13] P. Wang, S. M. Zakeeruddin, J. E. Moser, Md. K. Nazeeruddin, T. Sekiguchi, and M. Grätzel, "A stable quasi-solid-state dye-sensitized solar cell with an amphiphilic ruthenium sensitizer and polymer gel electrolyte," *Nature Materials*, vol. 2, no. 6, pp. 402–407, 2003.
- [14] D. Kuang, S. Ito, B. Wenger, et al., "High molar extinction coefficient heteroleptic ruthenium complexes for thin film dye-sensitized solar cells," *Journal of the American Chemical Society*, vol. 128, no. 12, pp. 4146–4154, 2006.
- [15] T. Horiuchi, H. Miura, K. Sumioka, and S. Uchida, "High efficiency of dye-sensitized solar cells based on metal-free indoline dyes," *Journal of the American Chemical Society*, vol. 126, no. 39, pp. 12218–12219, 2004.
- [16] S. Ito, S. M. Zakeeruddin, R. Humphry-Baker, et al., "High-efficiency organic-dye-sensitized solar cells controlled by nanocrystalline-TiO<sub>2</sub> electrode thickness," *Advanced Materials*, vol. 18, no. 9, pp. 1202–1205, 2006.
- [17] S. Ito, Md. K. Nazeeruddin, P. Liska, et al., "Photovoltaic characterization of dye-sensitized solar cells: effect of device masking on conversion efficiency," *Progress in Photovoltaics*, vol. 14, no. 7, pp. 589–601, 2006.
- [18] S. Ito, H. Matsui, K.-I. Okada, et al., "Calibration of solar simulator for evaluation of dye-sensitized solar cells," *Solar Energy Materials and Solar Cells*, vol. 82, no. 3, pp. 421–429, 2004.

## Review Article

# Prospects of Nanostructure-Based Solar Cells for Manufacturing Future Generations of Photovoltaic Modules

N. Gupta,<sup>1</sup> G. F. Alapatt,<sup>1</sup> R. Podila,<sup>2</sup> R. Singh,<sup>1</sup> and K. F. Poole<sup>1</sup>

<sup>1</sup> Center for Silicon Nanoelectronics and Holcombe, Department of Electrical and Computer Engineering, Clemson University, Clemson, SC 29634-0915, USA

<sup>2</sup> Department of Physics and Astronomy, Clemson University, Clemson, SC 29634-0915, USA

Correspondence should be addressed to R. Singh, rajendra.singh@ces.clemson.edu

Received 22 April 2009; Revised 9 July 2009; Accepted 15 August 2009

Recommended by Mohamed Sabry Abdel-Mottaleb

We present a comprehensive review on prospects for one-, two-, or three-dimensional nanostructure-based solar cells for manufacturing the future generation of photovoltaic (PV) modules. Reducing heat dissipation and utilizing the unabsorbed part of the solar spectrum are the key driving forces for the development of nanostructure-based solar cells. Unrealistic assumptions involved in theoretical work and the tendency of stretching observed experimental results are the primary reasons why quantum phenomena-based nanostructures solar cells are unlikely to play a significant role in the manufacturing of future generations of PV modules. Similar to the invention of phase shift masks (to beat the conventional diffraction limit of optical lithography) clever design concepts need to be invented to take advantage of quantum-based nanostructures. Silicon-based PV manufacturing will continue to provide sustained growth of the PV industry.

Copyright © 2009 N. Gupta et al. This is an open access article distributed under the Creative Commons Attribution License, which permits unrestricted use, distribution, and reproduction in any medium, provided the original work is properly cited.

## 1. Introduction

Globally the photovoltaic (PV) market grew 110% last year and reached a record 5.95 GW in 2008 [1]. It is also predicted that by 2012 more than 20 GW PV systems will be installed. Gartner has predicted an increase in PV industry revenue to \$34 billion within the next five years from \$15.8 billion in 2008 [2]. Currently, wafer-based silicon (single crystal, poly crystalline, and multicrystalline) solar cells and thin film solar cells based on amorphous silicon, CdTe, CuInGaSe<sub>2</sub>, and III–V semiconductors dominate PV manufacturing [3]. For future generations of solar cells a number of approaches are being explored [4]. An examination of the current literature shows that most of these solar cells are based on one-, two-, or three-dimensional structures with nanodimensions (<100 nm). The R&D work related to the nanostructures falls under the buzz word of “nanotechnology” and there are questionable claims on the scientific facts [5]. As an example, the publication of a research paper on multiexciton generation in colloidal silicon nanocrystals [6] motivated the

author of [7] to claim that silicon nanocrystals-based solar cells can generate two electrons from one photon, and single junction solar cell efficiencies as high as 40% are possible. The fact is that multiple exciton generation phenomena observed in nanocrystals or quantum dots have no direct relevance to the operation of the solar cell. The incorrect assumption that multiple electron hole pairs (EHPs) generation will improve the solar cell efficiency ignores the fact that the collection of the carriers is a necessary part of the solar cell operation. This can impact the further direction of basic research that is generally funded by public money [8] as well as investment of private money for establishing new photovoltaic businesses. In the broader sense of green electricity generation our objective is to examine critically all the current PV approaches that are under investigation.

PV manufacturing has its origin in semiconductor manufacturing and most of the thin film PV manufacturing (use of large glass substrate) has its origin in liquid crystal display (LCD) manufacturing. Based on an examination of the fundamentals of materials, devices, and the experience

of semiconductor manufacturing, LCD manufacturing, and related manufacturing, it is possible to examine the prospects of incorporating nanostructure-based solar cells into PV manufacturing for next generation solar cells. Recently, a number of review papers on applications of nanostructures in solar cells have been published [3, 9–18]. However, none of these papers address the issues related to manufacturing of next generations of PV modules. The objective of this paper is to critically examine the published work and point out the suitability or unsuitability of the particular nanostructure for future generations of photovoltaic module manufacturing. In the following section, we provide the background material which is essentially required to make PV systems a significant source of electricity generation. In the third section, we examine the theoretical and experimental results associated with the materials and devices of nanostructure-based future generation of solar cells. The discussion of the paper is presented in Section 4. Finally, the paper is concluded in Section 5.

## 2. Background Material

In order to create huge PV markets, the following selection criterion must be used in the selection of appropriate technology: (i) no material supply constraint, (ii) low cost of ownership, (iii) low production cost, (iv) prospects of further cost reduction, and (v) green manufacturing with no environmental safety and health issues. In a previous publication [3], we have discussed these points in depth however for completeness key points are briefly discussed in this section.

**2.1. No Material Supply Constraints.** Just after oil embargo of 1973 [19], a number of semiconductor materials were proposed as the potential materials for manufacturing solar cells. In 1980, one of us published an article on the economic requirements for new materials for solar cells and predicted that silicon is the best material for large-scale PV manufacturing [20]. Over the last 29 years our prediction has been correct, since more than 90% solar cells manufactured in 2008 are made out of silicon. Thus it is quite relevant to go back to our 1980 paper and rewrite the rules for selecting photovoltaic materials. The key guidelines from 1980 publications [20] are given in the following paragraphs.

When one considers the availability of materials at reasonable cost, one has to establish the rate of production required for the application and compare it to the current world rate of production as well as to the possible total availability of the material in the earth's crust. As shown in Figure 1, a number of elements used in solar cell manufacturing have very low level of reserve [21]. In order that the use of the material in the photovoltaic application does not drive up the cost of the material, the additional uses for photovoltaic applications must be less than 10% of the world production (study of world production rates of minerals shows that historically the production rate of any mineral has rarely grown faster than 10% per year). For example, due to high demand of poly-silicon, price of poly-silicon

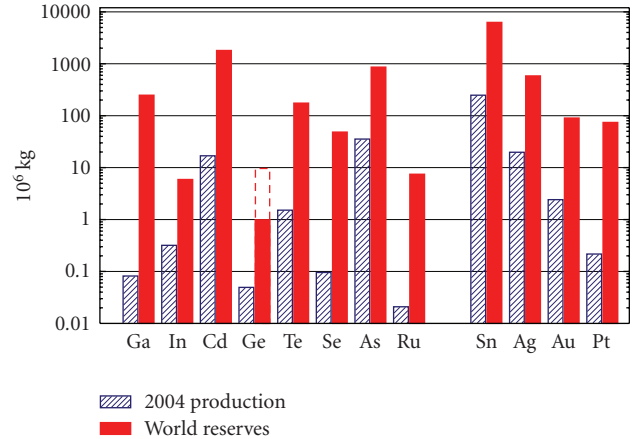


FIGURE 1: Estimated 2004 annual production levels and material reserves for various materials used in PV industry (from [21]).

went high in 2008 due to increased demand and poor supply. Fortunately, due to abundance of the raw material, the supply chain of poly-silicon has improved again. Recently, iSuppli has reported that due to an increase in production of poly-silicon by 112% in 2009, price will drop by half [22].

**2.2. Low Cost of Ownership (COO) for Manufacturing.** Similar to the semiconductor manufacturing and LCD manufacturing industry, photovoltaic manufacturing also needs huge capital investments. Ideally for a given technology, the capital expenditures should be as low as possible. However, capital expenditure is only one component in the cost of ownership. Since the manufacturing of a PV module consists of a number of processing steps, the underutilization of equipment adds extra cost. Over the life time of the manufacturing facility, the equipment reliability, utilization, and yield of the PV modules have a greater impact on cost of ownership than initial purchase cost. The cost of ownership can be expressed by following expression [23]:

$$\text{COO} = \frac{\text{CF} + \text{CV} + \text{CY}}{\text{TPT} * \text{Y} * \text{U}}, \quad (1)$$

where COO: cost of ownership, CF: fixed cost, CV: variable cost, CY: cost due to yield loss, TPT: throughput, Y: composite Yield, U: utilization.

The use of a roll-to-roll (RTR) process (similar to the way in which newspapers are printed) is a driving force to develop PV manufacturing processes with low capital expenditures. The success or failure of RTR and other similar processes depends on the yield of each process step and resulting PV module yield. The above expression can be used to judge the suitability or unsuitability of a low-cost capital expenditure manufacturing process versus alternate high-cost capital expenditure manufacturing.

In the selection of appropriate manufacturing process technology, process variability is one of the important issues. In other words the power out of each device in a module and the power output of each module in a system must be as

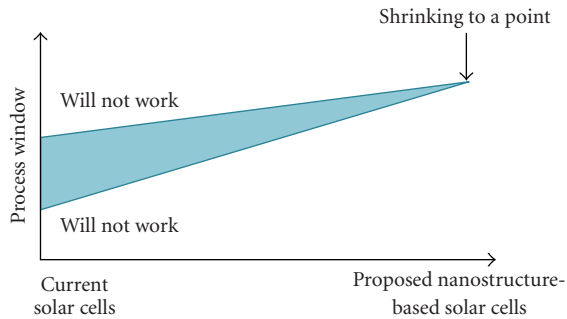


FIGURE 2: Shrinking process window for ultra-small structures.

identical as possible. Due to series and parallel connections (to get desired voltage and current) devices or modules with minimum voltage or current will dictate the power output of the system. A sophisticated and expensive advanced process control (APC) will provide lower cost of ownership than a low-cost statistical process control for a given process used in the PV module manufacturing. For one-dimensional nanostructure such as single-wall carbon nanotubes, we have demonstrated the need for a high level of control of the process variation which is far beyond that which is currently achievable through conventional methods [24]. Process variability is one of the most critical issues for nanostructure-based integrated circuit manufacturing. The same issues are also true for solar cells based on nanostructures. As shown in Figure 2, for nanostructures-based solar cells the process window is replaced by the process points. Relative to currently manufactured solar cells, the COO will be higher for nanostructure-based solar cells.

**2.3. Low Production Cost.** For reducing the production cost of PV modules, it is necessary to use larger silicon wafers or larger substrates rather than the smaller ones. For product cost reduction, this technique has been very successful for IC and display industry. Other than the efficiency of PV modules, energy consumed in the manufacturing process, materials, gases and substrates cost, automation and throughput, yield is a very important factor in the overall cost. Of course factors such as low labor cost and low cost of electricity also affect the cost of PV modules. The typical manufacturing cost relationship should be used to size the appropriate production capacity of the manufacturing process. An absolute control on the supply chain and ultra-large-scale volume manufacturing are the principal requirements to bring PV technology to a level where generation of electricity is cheaper than other energy sources.

**2.4. Prospects for Further Cost Reduction.** Other than increasing the efficiency of PV module, the manufacturing process should be capable of further cost reduction. For cost reduction of the PV modules, the change of substrate size with time by the IC and display industry is the perfect choice for PV industry. Currently some amorphous silicon manufacturers are using glass substrates of the size of 5.7 m<sup>2</sup>.

Similar to LCD industry these manufacturers can increase the glass size to Gen 10 substrates with the area equal to 8.7 m<sup>2</sup>. Without inventing any new process, the Gen 10 substrate size will provide cost reductions similar to LCD industry.

**2.5. Environmental Safety and Health (ESH) Issues and Green Manufacturing.** As compared to other method of electricity generation, PV technologies have distinct environmental advantages for generating electricity over conventional technologies. Electricity generation by PV systems does not produce any noise, toxic-gas emissions, or greenhouse gases. Photovoltaic energy not only can help meet the growing worldwide demand for electricity, but it can do so economically without any environmental concerns. Compared to burning coal, every gigawatt-hour of electricity generated by photovoltaics would prevent the emission of about 10 tons of sulfur dioxide, 4 tons of nitrogen oxides, 0.7 tons of particulates, and up to 1000 tons of carbon dioxide.

The techniques used in PV manufacturing are quite similar to \$350 billion semiconductor industry. During the last half century the semiconductor industry has evolved to the point that in spite of the use of a number hazardous chemicals, tools and processes exist for the safe handling of such chemicals, materials, and gases. The PV industry has adopted handling of materials chemicals, and gases in a way similar to the semiconductor industry. Thus from environmental, occupational health, and safety point, there is no concern. The only material that poses a real concern is the use of Cadmium (Cd) in CdTe-based solar cells. According to the Occupational Safety and Health Administration (OSHA) of USA, Cadmium is considered both toxic and a lung carcinogen. OSHA considers all Cd compounds (including CdTe) to be toxic. For further reading of health problems related to the use of Cd in solar cells interested reader is referred to our earlier publication [3].

### 3. Critical Examination of Proposed Nanostructures for Solar Cell Applications

The nanostructures involve length scale of approximately 1–100 nm range. In this paper we will not differentiate between the approaches used in the fabrication of these structures. The issue of “bottom up” (atom-by-atom approach to build the required <100 nm dimension) or “top down” (current lithography techniques used to reduce material dimension <100 nm) approach will be dictated by throughput and cost related manufacturing issues. It has been known for long time that the properties of ultra-thin films differ from the bulk values. The invention of scanning tunneling microscope in 1981 and the advancements in the silicon integrated circuits as well as other related semiconductor products (e.g., improved detectors with high signal-to-noise ratio) have helped the development of instruments that have the ability to manipulate and analyze material on the atomic scale. Research in the nanodimension material in the last decade has established that the properties of nano-dimension material differ from the corresponding thin film materials.

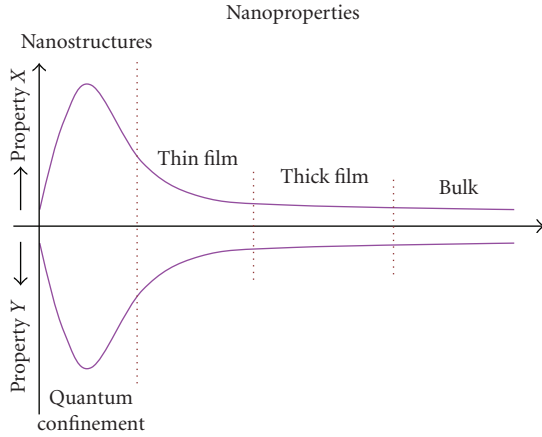


FIGURE 3: Change in properties of any material due to its physical size.

TABLE 1: Various solar energy losses in single junction silicon (1.1 eV energy band gap) solar cell under AM 1.5 solar spectra at 300° K temperature [13].

Photo-electro energy conversion	32.9%
Unabsorbed energy losses	18.7%
Heat loss	46.8%
Other losses	1.6%

As shown in Figure 3, at nanoscales the properties of material depend on the quantum confinements. The one- to three-dimensional nanomaterials provide unique opportunities to optimize a number of physical, chemical, biological, mechanical, electrical, optical, and thermal properties of interest for future photovoltaic devices. The challenge is to integrate these unique properties of nanostructures and enhance the performance, reliability, and yield of photovoltaic devices for manufacturing next generation of photovoltaic modules.

In 1961, Shockley and Queisser calculated thermodynamic limit of maximum efficiency for a p-n junction silicon (1.1 eV energy bandgap) solar cell to be around 33% under AM 1.5 solar illumination at 300° K [25]. The energy associated with photons greater than the energy band gap of silicon is converted into heat. As shown in Table 1, heat loss is mainly responsible for lower efficiency of silicon solar cells. The unabsorbed energy loss can be partially recovered by using the concept of tandem solar cells where higher and lower energy band gap solar cells are connected optically in series. The concept of tandem solar cells is already used for manufacturing amorphous silicon solar cells and III–V-based high efficiency concentrator solar cells. Since a major part of the incident solar energy is lost as heat, maximum efforts have been made to prevent incident solar energy getting converted to heat. These losses are the driving force to build new approaches to utilize the energy losses. As mentioned earlier, structures of size 1 nm to 100 nm are proposed to make solar cells more efficient. The use of nanostructures has been suggested to build new highly efficient solar cells considering the

following key points. (1) Hot carriers generated by absorbing photons of energy more than the energy band gap can be employed to generate additional current and or voltage, and (2) energy states in the energy band gap can be used to trap carriers generated from photon of energy lower than the energy band gap. Various approaches based on the one-, two-, and three-dimensional nanostructures (quantum dots and semiconductor nanocrystals) are currently being pursued to utilize the energy losses listed in Table 1. In the following subsections, we have examined the theoretical and experimental results of various nanostructures reported in the open literature.

*3.1. Proposed Use of Hot Carriers to Boost up Solar Cell Efficiency.* There have been numerous publications discussing the potential use of hot carriers for solar cell efficiency enhancement [6, 9, 10, 12, 26–31]. Hot carrier solar cells claim to convert excess photon energies into stable form before the excited states equilibrate with the environment. In semiconductors, excess energy appears as the kinetic energy of the carriers where as in molecules it becomes a phonon and is dissipated as heat. As shown in Figures 4(a)–4(b), when the incoming photon has excess energy ( $h\nu > E_g$ ), electrons are excited and the thermalization occurs through carrier-phonon scattering. Excess energy is delivered to the carriers of lesser effective mass. Thus for the highest efficiency of the solar cell, excess photon energies must be delivered to the bands capable of sustaining the hot carriers. The following are the proposed ways for extraction of the excess energy.

- (1) Remove the carrier from the device before it cools and obtain a higher energy electron and thus getting a higher output voltage (Figures 4(c)–4(d)). Theoretically for this to be feasible, the rate of cooling of hot electrons must be lower than the rate of hot carrier separation, transport, and collection at contacts [30].
- (2) Make the excited “hot” electron spend its extra energy to excite another electron from valence band and thus getting a higher output current (Figures 4(e)–4(f)). This is known as impact ionization and can occur only if the rate of impact ionization is more than the relaxation processes which include generation of phonon and Auger recombination. [30].

The photocurrent generation in semiconductor p-n junction of solar cell is shown in Figure 5. When a photon with energy more than band gap of absorber material hits p-n junction, it creates an electron hole pair and due to the inbuilt electric field, photoproduced carriers are transported to the electrodes. Thus for making a solar cell, the basic requirements are an absorber material and a junction with electric field that assists transport of the photogenerated carriers to the electrodes. There is also a probability that photogenerated carriers can recombine before reaching the electrodes. Therefore for crystalline and polycrystalline solar cells, the charge separation time of photo generated carriers must be smaller than the minority carrier lifetime.

For the bulk materials, rate of impact ionization or multiple carrier excitations (MCEs) is slower than the rate of

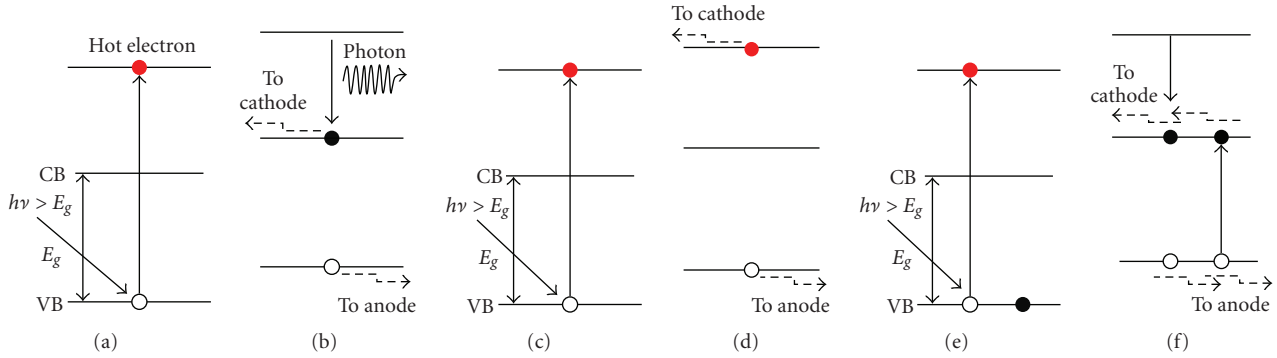


FIGURE 4: (a) A photon with energy ( $h\nu$ ) greater than band gap energy ( $E_g$ ) strikes on solar cell and excites an electron to Conduction Band (CB) from Valence Band (VB); (b) the extra energy ( $h\nu - E_g$ ) is released as phonon; (c) a photon with energy ( $h\nu$ ) greater than band gap energy ( $E_g$ ) strikes on solar cell and excites an electron to CB from VB; (d) the extra energy ( $h\nu - E_g$ ) is used to produce higher voltage by  $h\nu - E_g$ ; (e) a photon with energy ( $h\nu$ ) more than band gap energy ( $E_g$ ) strikes on solar cell and excites an electron; (f) extra energy ( $h\nu - E_g$ ) is used to excites one more electron from VB to CB.

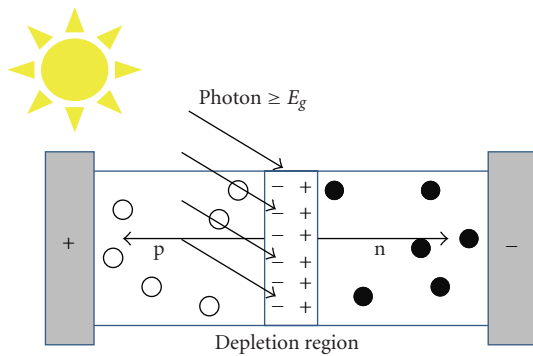


FIGURE 5: Basic p-n junction solar cell and charge transport phenomena.

thermal cooling of hot carriers through intraband relaxations processes [9]. Therefore various groups started to investigate the use of quantum dots for utilizing hot carrier effects [9, 29, 32]. However, to date no one has provided experimental data to prove that for quantum dots the rate of multiple carrier excitation is faster than the thermal cooling rate of hot carriers. Also, the Auger recombination rate and cooling rate depend on the surface area of the nanostructure as shown in Figure 6 [13]; for example, the Auger recombination is more in nanorods than nanodots [9]. Results shown in Figure 7 indicate that not only carrier relaxation time decreases, photo generated exciton life time also decreases with the size of nanocrystal [13].

In [32], authors have reported excitation of seven electrons from a photon in PbSe nanocrystal and have reported an internal quantum efficiency of 700%. Based on the type of measurements reported in [32], one is tempted to believe that for solar cells more than one EHP could be generated for each incoming photon, which in turn will improve the solar cell efficiency. In reality, for solar cell efficiency enhancement these multiple EHPs must be extracted from the device through electrodes. Fundamentally this is not possible, since all the reported internal quantum

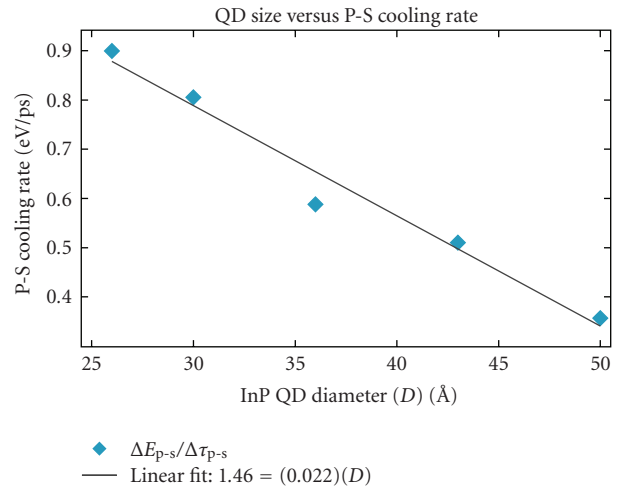


FIGURE 6: Carrier cooling rate increases as size of quantum dot decreases (from [13]).

efficiencies of above 100% are based on the measurement of Transient Absorption Spectra (TAS). In TAS, two ultrafast femtosecond LASER pulses are used. First, the high energy LASER beam is used to excite the electrons and the other LASER beam probes the excited states. The pumped power used for multiple exciton generation in [6] is  $1.126 \text{ mW/cm}^2$  which is roughly an order of magnitude more than the power available at 600 nm in AM1.5 solar spectrum. The TAS measurements may give information about the excited states [28], but these experimental conditions have nothing to do with the required conditions for solar cell applications.

As early as 1980 one of us [33] provided experimental data to refute the claim that one can observe short circuit current density greater than predicted by Shockley and Queisser limit [25]. An extensive search of the open literature beyond 1980 did not show any direct current-voltage measurements under illumination or enhancement in efficiency of solar cells by utilizing hot carriers or by any other mechanism including generation of multiple excitons.

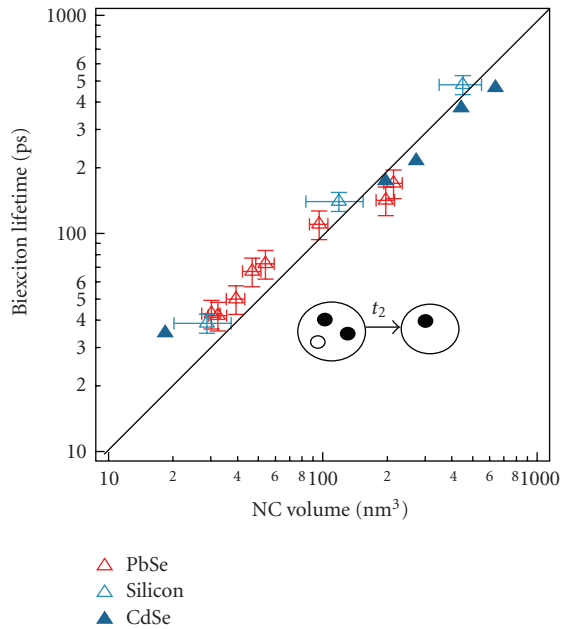


FIGURE 7: Biexciton lifetime as a function of volume of nanocrystal (from [13]).

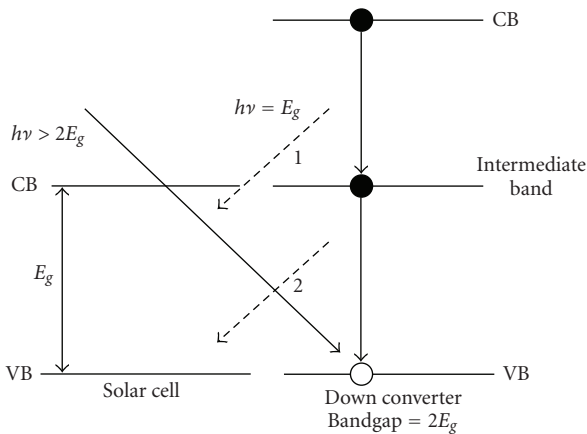


FIGURE 8: A photon with energy more than  $2E_g$  strikes on down converter and produces two photons with energy  $E_g$ .

**3.2. Up Conversion and Down Conversion.** Up/Down conversion involves altering the incident spectrum which is available to the solar cell. In down conversion, one high energy photon will be split in to two or more photons which can be converted into two or more electron hole pairs by the solar cell. In up conversion, two or more low energy photons are converted in to a single photon which can be converted by the solar cell to generate an electron hole pair.

Figure 8 shows the operating mechanism of proposed down converter solar cell. The solar cell is a regular silicon-based solar cell with energy band gap of  $E_g$ . It converts only photons of energy greater than  $E_g$  in to EHPs. According to proposed down conversion mechanism, if a photon with energy of  $2E_g$  strikes the solar cell and passes through it and further strikes the converter placed behind the solar cell

which has an energy band gap of  $2E_g$ . This results in exciting an electron from the valence band to the conduction band. This excited electron falls back into the valence band in two steps. In the first step, it falls to an intermediate state emitting a photon “1” of energy  $E_g$  and then in the second step, it falls down in to the valence band emitting another photon “2” as shown in Figure 8 of energy  $E_g$ . These two photons with energy  $E_g$  will go back to the solar cell and get converted in to two EHPs. Thus, the single high energy photon will result in two EHPs which is not possible in a conventional solar cell. Also, the solar cell is assumed to be very thin to pass photon with energy  $2E_g$  which could have a negative impact on the efficiency.

The theory of high efficiency down conversion process is proposed on the assumption that “no nonradiative recombination takes place anywhere in the device” [34]. For a photon of energy greater than  $2E_g$ , a band-to-band transition happens in the converter and these excited electrons recombine via intermediate bands in the converter. All the photons with energy between  $E_g$  and  $2E_g$  will be wasted if they cross the solar cell. Also, photons with energy more than  $2E_g$  will be absorbed by the converter and will result in thermalization which will further decrease the efficiency. If the down converter is placed above the solar cell, it will absorb all photons with energy greater than its band gap. Thus, the solar cell collects photons only generated by the down converter via photoluminescence. Also, only half of the photons can be expected to be radiated into the solar cell. The other half will be radiated outwards from the converter.

With the assumptions described above, the AM 1.5 efficiency limit for a down-conversion solar cell with  $E_g = 1.05$  eV is 39.6% [34] while the Shockley and Queisser limit is about 33% for single junction silicon solar cell [25]. The mathematical calculations about up conversion also have fundamental flaws and the efficiency limit for this process is calculated as 47.6% for nonconcentrated sunlight [35]. The authors of [36] have conducted a review on the existing materials to modify the solar spectrum and a few results on solar cell up/down conversion using nanostructures were also reported. Most of the results reported in [36] are nothing other than the explorations of the photoluminescence properties of materials.

Use of Si nanocrystals (NCs) as a down converter is reported in [37] which show no change in open circuit voltage and a little increase in short circuit current which results in net efficiency increase by only 0.4%. Also, it is worth mentioning here that in [37] the results of only one sample were reported for claiming the efficiency improvements. As reported in [37], the difference between the value of current density measured by spectral response and the value extracted from electrical measurement data is 40%. Thus the legitimacy of the claim by authors of [37] about the 0.4 % net efficiency improvement by the use the down converter based on silicon nanocrystals is questionable. The internal quantum efficiency results reported in [37] are shown in Figure 9. The reduction in internal quantum efficiency for cells annealed at  $200^\circ\text{C}$  and  $500^\circ\text{C}$  indicates device reliability problems. [37] was published in 2004 and in the last five years

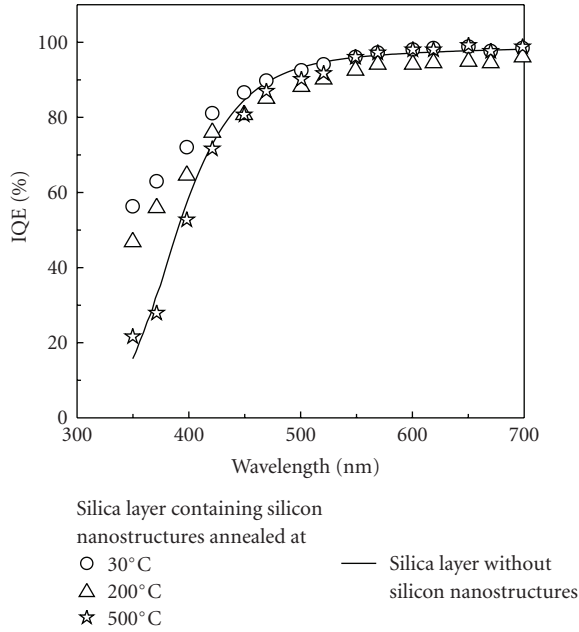


FIGURE 9: Measured internal quantum efficiency of solar cell with (symbols) and without a silica layer containing silicon nanocrystals. The reduction in internal quantum efficiency for cells annealed at 200°C and 500°C indicates reliability problem (from [36]).

no new results about improving the efficiency by up/down conversion have been reported.

In summary, no one has reported experimental results of the up/down conversion process with a meaningful efficiency enhancement to pursue these nanostructure-based solar cells for further research and development.

**3.3. Nanocrystals-Based Tandem Solar Cells.** As we stated earlier, the full solar spectrum cannot be efficiently absorbed by a solar cell using single energy band gap material. In 1955 for the first time, Jackson proposed to use layers of different energy band gap materials to enhance the solar cell efficiency [38]. III-V semiconductor and amorphous silicon-based tandem solar cells are already in production. A lot of research has been done in the search for a perfect combination of materials to absorb the entire solar spectrum. This motivated researchers to think for the application of low-dimensional structures such as quantum wells as an absorber layer in solar cells. The use of quantum wells in solar cells was first proposed by Burnham and Duggan in 1990 [39]. It is well-known fact that the energy band gap of quantum confined structures can be tuned by altering their size.

Very recently Cho et al. [40] have shown an efficiency of 10.6% by embedding 3 nm quantum dots in 2 nm SiO<sub>2</sub> layers. They used 15 layers of the phosphorous doped quantum dots embedded in SiO<sub>2</sub> on a p type crystalline silicon wafer. Also, they claimed that the current density of this cell is 29.8 mA cm<sup>-2</sup> and it is equivalent to the current density of single junction nontextured solar cell [40]. Table 2 summarizes their experimental results. It can be seen from

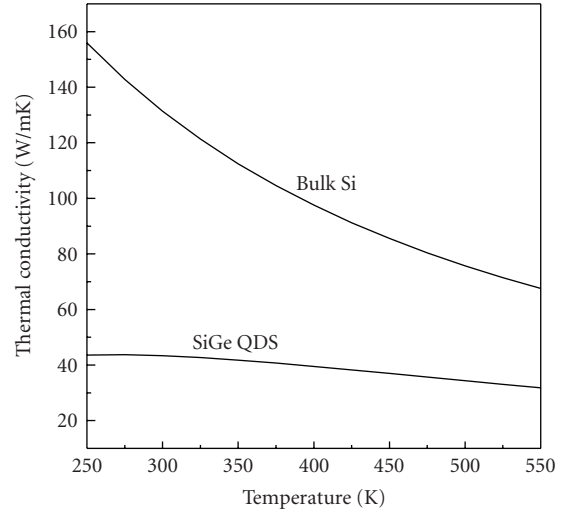


FIGURE 10: In plane lattice thermal conductivity of Si<sub>1- $\delta$</sub> Ge <sub>$\delta$</sub>  quantum dot superlattice and bulk silicon as a function of temperature. The value of  $x$  is 0.05 and size of quantum dot is 4 nm (from [43]).

Table 2 that there is not any significant difference in the efficiency of various sized quantum dots embedded in the oxide layers. However, the maximum efficiency reported efficiency from their work is far below the efficiency of commercially available single junction silicon solar cells. In case of quantum dots as well as other nanostructures-based semiconductor devices fundamental issues related to heat removal and reliability are very important [24]. Therefore thermal conductivity of quantum dots [41–44] must be considered for applications of quantum dots in solar cells. As shown in Figure 10 [43], the thermal conductivity of the Si<sub>1- $\delta$</sub> Ge <sub>$\delta$</sub>  quantum dot super lattice is much lower than that of bulk silicon. The scattering of acoustic phonons on quantum dots is key scattering mechanism for decrease in the thermal conductivity [43]. Figure 11 shows the in-plane lattice thermal conductivity as a function of dot volume fraction ( $\delta$ ) of Germanium in Si<sub>1- $\delta$</sub> Ge <sub>$\delta$</sub>  alloy with dot size as the variable parameter. Additional complexity in the applications of quantum dots in solar cells will arise from the fact that quantum dots in the order of quadrillion (10<sup>15</sup>) will be required for a silicon wafer of the size of 150 mm. Physics related to many body problems must be considered to understand the interactions among various quantum nanocrystals [45]. Control on the size distribution of nanocrystals is another challenge. The interaction between nanocrystals increases when size distribution of nanocrystals is large and results in reduced mobility and short circuit current. The reason for the mobility reduction is hopping of charge carriers between adjacent nanocrystals [17].

**3.4. Intermediate Band Solar Cells (IBSCs).** In 1960 Wolf described various loss factors in solar cells and discussed various mechanisms including multitransition solar cells (introducing energy levels in forbidden energy gap of active layer) to reduce energy losses [46]. Luque and Marti [47] introduced the concept of intermediate band solar cells in

TABLE 2: Electrical measurements of solar cell with different size silicon nanocrystals embedded in layers of silicon rich oxide (SRO)/Silicon Dioxide ( $\text{SiO}_2$ ) under standard condition (AM 1.5 spectrum,  $100 \text{ mW cm}^{-2}$ ,  $298^\circ \text{K}$ ) (from [40]).

SRO/ $\text{SiO}_2$ thickness, number of bilayers	Open circuit voltage $V_{oc}$ (mV)	Short circuit current density $J_{sc}$ ( $\text{mA cm}^{-2}$ )	Fill factor(%)	Efficiency(%)
3 nm/2 nm 15 BL	555.6	29.8	63.8	10.6
4 nm/2 nm 25 BL	540.3	25.0	76.8	10.4
5 nm/2 nm 25 BL	517.9	27.9	72.3	10.5
8 nm/1 nm 25 BL	470.8	18.6	65.1	5.7

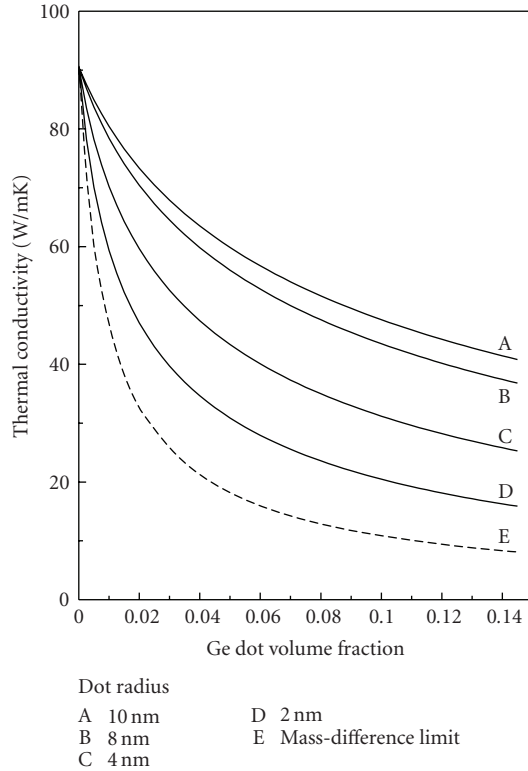


FIGURE 11: In-plane lattice thermal conductivity as a function of dot volume fraction ( $\delta$ ) of Germanium in  $\text{Si}_{1-\delta}\text{Ge}_\delta$  alloy. The value of dot size is 10.0 nm, 8.0 nm, 4.0 nm, and 2.0 nm for curve A, B, C, and D, respectively (from [43]).

1997 which is similar to the concept of multitransition solar cells. The basic concept of IBSC is to have an intermediate band to utilize low energy photons from the solar spectrum [47]. The formation of intermediate band is proposed by utilizing some impurities other than basic absorber material or alloy or quantum dots [48–50]. Fundamentally, the concept of IBSC is against the theory of recombination generation where energy levels near the mid-gap degrade the performance of all type of solar cells. This is indeed the case as has been confirmed by the experimental results [48]. The dark and light current density–voltage characteristics of GaAs reference cell, GaAs IBSC solar cells based on quantum dot with and without delta ( $\delta$ ) doping of quantum dot layers are shown in Figures 12 and 13, respectively. As expected the results of Figures 12 and 13 confirm that the introduction of

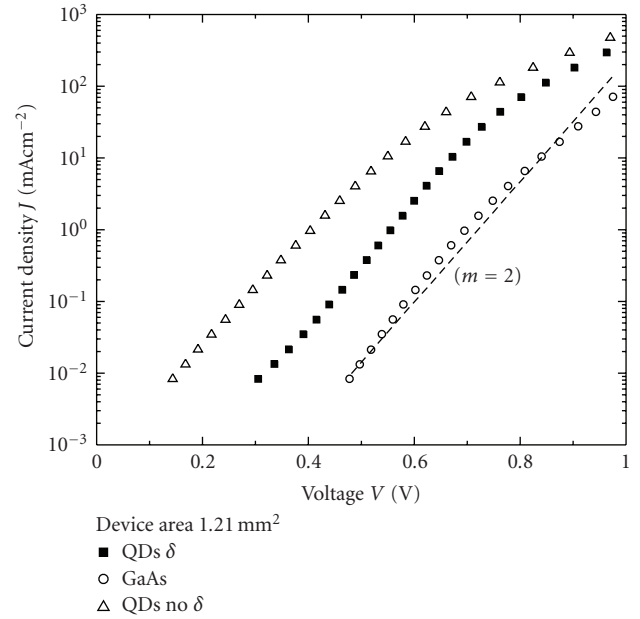


FIGURE 12: The dark current density–voltage characteristics of GaAs reference cell, GaAs IBSC solar cells based on quantum dot with and without delta ( $\delta$ ) doping of quantum dot layers (from [48]).

intermediate band layer degrades the solar cells performance. Similar negative results about IBSC solar cells results have been reported by others [51].

**3.5. Dye-Sensitized Solar Cells.** Dye-sensitized solar cells (DSCs) are currently being explored as ultra-low-cost solar cells. DSCs utilize three main components to perform photo-electro conversion which are metal oxide semiconductor nanostructures, dye, and electrolyte. A dye is used to create electron hole pairs and other two materials transport these photogenerated charge carriers to the electrodes. The most popular metal oxide semiconductor nanostructures are made of Titania ( $\text{TiO}_2$ ). Various researchers have proposed the use of nanotubes for DSCs and these results are discussed in the next paragraph. For a device of aperture area equal to  $0.219 \text{ cm}^2$  and platinum coated glass as the counter electrode, the best efficiency reported by researcher at Sharp for DSC is 11.18% [52]. Scaling to large area practical solar cells is a difficult challenge. A number of dyes including Ruthenium-based diketonato Ru (II) complex are used in

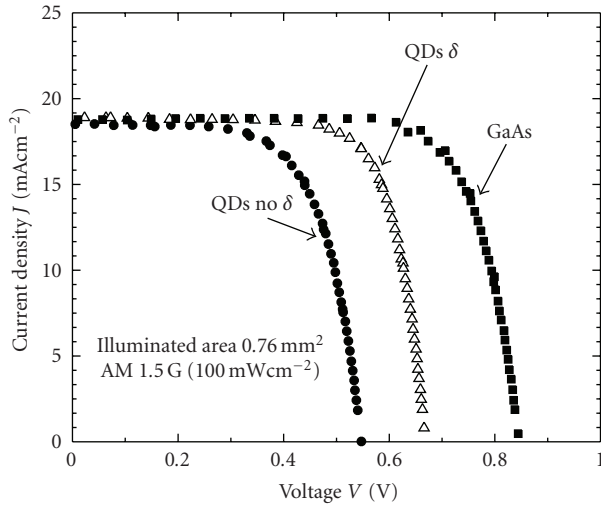


FIGURE 13: The light current density-voltage characteristics of GaAs reference cell, GaAs IBSC solar cells based on quantum dot with and without  $\delta$  doping of quantum dot layers (from [48]).

DSCs. Ruthenium is a very costly metal and it requires extra recycling fee [11]. The hole transport material in DSCs, that is, electrolyte, can be a room temperature ionic liquid, quasisolid state, or solid state material [11]. A liquid electrolyte can fill the pores of the metal oxide semiconductor nanoparticles but it is not possible with a quasi-solid state or solid state electrolyte [18]. As a result, the best efficiencies are achieved for DSCs with liquid electrolyte. The liquid electrolytes get evaporated under exposure of solar radiations for longtime and poses fundamental problem of reliability.

Other than nanoparticles, nanowire (NW) film that provides a large surface area for the incorporation of light harvesting molecules, is being investigated to improve the performance of DSCs. However, NW DSCs rely on trap-limited diffusion for electron transport, a slow mechanism that limits the device efficiency, especially at longer wavelengths. During operation, photons intercepted by the dye monolayer create excitons that are rapidly split at the NW surface, with electrons injected into the NW film and holes leaving the opposite side of the device by means of redox species in a liquid or solid-state electrolyte [53].

Another option for improving the absorption of red and near-infrared light is thickening the nanoparticle film to increase its optical density, which was unsuccessful because the film thickness comes to exceed the electron diffusion length through the nanoparticle network. Even incorporation of NW does not improve the efficiency. Solar cells constructed with ZnO NW arrays of various surface areas, at one full Sun intensity, have highest  $J_{sc} = 5.3\text{--}5.85\text{ mA cm}^{-2}$ ,  $V_{oc} = 0.61\text{--}0.71\text{ V}$ ,  $FF = 0.36\text{--}0.38$ , and efficiency  $\eta = 1.2\text{--}1.5\%$  [55]. Incorporation of NW (Figure 14) into the film halves the fill factors, limiting their potential efficiencies. Ideally,  $20\text{ }\mu\text{m}$  long NW with a dominating diameter of  $60\text{ nm}$ , a density of  $10^{10}\text{ cm}^{-2}$ , and surface area of  $1080\text{ cm}^2$  per unit area of the substrate are needed where as the best that can be achieved is only 10% of ideal density and 18% of ideal

surface area [54]. An effort to reduce the recombination rates through the use of core-sheath NW reduces the efficiencies to a maximum of 0.29% [56]. Titania shells  $10\text{--}25\text{ nm}$  in thickness cause an increase in  $V_{oc}$  and fill factor but only with a current fall off, resulting in a overall conversion efficiency, only up to 2.25% under  $100\text{ mW cm}^{-2}$  AM 1.5 simulated sunlight [57]. Raising the efficiency of NW DSCs above 2.5% depends on achieving higher dye loadings through an increase in NW array surface area, which is a non trivial challenge. Besides the lower efficiencies of these NW cells, we note that increasing the aspect ratio of the NW and achieving 90% higher densities are a daunting task.

In summary, the reliability of DSC is a fundamental problem. In addition to reliability, a number of manufacturing issues that relate to scaling, materials, defect density, and cost of ownership need to be addressed. Without solving these fundamental problems, DSC will not play any significant role in manufacturing of next generation of PV modules.

**3.6. Organic Solar Cells.** Organic solar cells are solution processed PV devices and are attractive due to low processing temperature and simple fabrication techniques. After nearly three decades, it is still a challenge for organic solar cells to enter in the commercial market. Poor electrical and structural properties and fast degradation under solar radiation are the fundamental problems for current organic solar cells. The major material problems with organic solar cells are charge generation, geminate recombination, electric and magnetic field effects on charge separation and recombination, carrier mobility, polaronic effects, charge collection efficiency, organic semiconductors with optical gap in the near IR spectral range to better match the solar energy spectrum, interpenetrating morphologies, exciton range, and its dependence on the film morphology [58].

To date, the best efficiency achieved for organic solar cells using a tandem cell structure for solar intensity of  $20\text{ mW cm}^{-2}$  and  $200\text{ mW cm}^{-2}$  is 6.7% and 6.1%, respectively [59]. The device area was not mentioned in [59] and there may be a number of issues related to manufacturing of these devices. However, the fundamental problem is reliability. After 100 hours of continuous exposure under one sun (AM 1.5), the solar cell efficiency is degraded by 40% [59].

In 2001 one of us [60] critically examined the prospects of manufacturing organic semiconductor-based integrated circuits and pointed that there is no appropriate technology that can be implemented for pilot-line production, eventually leading to mass-scale manufacturing. Fundamentally, the low thermal conductivity of polymer semiconductor is a serious problem. Low-cost polymer deposition techniques (e.g., coating, electrodeposition, etc.) have not provided the desired microstructure properties. With the present approaches under investigation, it is difficult to imagine the possibility of controlling the surface defects and voids which are detrimental to the performance device performance [60]. Similar arguments apply to organic solar cells. As we mentioned in Section 2.2 the low-cost film deposition techniques (e.g., roll to roll process) are quite attractive from

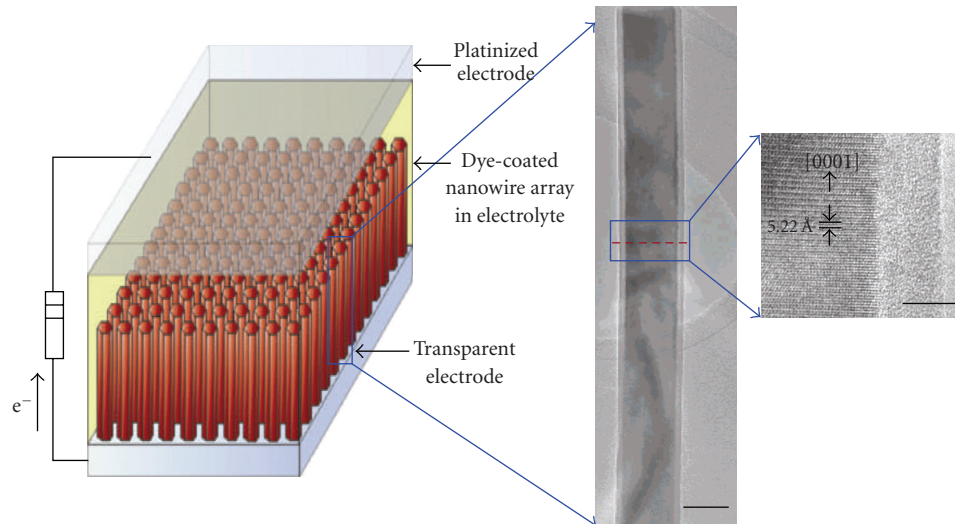


FIGURE 14: NW film-based DSC (from [54]).

capital expenditures. However due to high defect density, the cost of ownership of manufacturing for organic solar cells is high. Unless a new polymer is invented and manufacturing requirements discussed in Section 2 and reliability problems are solved, it is highly unlikely that organic solar cells will play any significant part in future manufacturing of photovoltaic modules.

#### 4. Discussions on Manufacturability of Nanostructure-Based Solar Cells

Figure 15 shows the evolution of a new concept leading to the mass-scale manufacturing of a new product. In case of nanostructure-based solar cells, currently we are in the very first block of Figure 15. The physics related to nanostructures mostly deals with quantum phenomena. There is nothing wrong with quantum physics or the associated quantum phenomena. The problem lies in stretching the results of observed phenomena beyond what is evident from the observed results. As an example in August 2007 Beard et al. [6] published a paper on multiple exciton generation in colloidal silicon nanocrystals and claimed that their findings are of particular importance for Si dominated photovoltaic solar cell industry. Based on the results of [6], Bullis published in Technology Review [7] that by generating multiple electrons from high-energy photons, solar cells made of silicon nanocrystals could theoretically convert more than 40 percent of the energy in light into electrical power. As we have discussed in Section 3.1, there is no direct correlation between the photoluminescence results reported in [6] and the operation of solar cells. This type of hype exists both in technical journals as well as financial publications. Based on our in depth review of the literature we do not see any evidence that nanostructure-based solar cells will be part of PV module manufacturing. The lack of thorough understanding of the physical phenomena and the tendency

of stretching observed experimental results is the fundamental reason that quantum phenomena-based nanostructures have a limited role to play in solar cells. Similar concerns about quantum phenomena-based nanostructures have been expressed for other semiconductor devices. According to Kelly [61], the new physics associated with one-dimensional and zero-dimensional structures, quantum interference, ballistic motion, or Coulomb blockade is unlikely to lead to practical devices until these effects can be exhibited, if ever they can, as robust phenomena.

Dye-sensitized solar cells (DSCs) and organic solar cells are currently being investigated by several companies. Other than manufacturing related issues, reliability is the main concern. It is worth mentioning here that the public and or private investment in a company does not mean that the investment will bring any product in the market and generate revenue. Due to lack of knowledge of manufacturing challenges, many times the investors think mass-scale manufacturing as a trivial exercise and the company is funded. Even for well-established companies, lack of necessary and sufficient data of defects, yield, and cost of ownership can result in failure. Based on the research work, Motorola formed a subsidiary called Thoughtbeam in November 2001 to develop, sell, and license its GaAs-on-silicon technology with applications to less-expensive optical communications, high-frequency radio devices, and high-speed microprocessor-based systems. Due to the fundamental nature of defects densities at the interface of GaAs and silicon and inability to deliver the desired device and circuit performance the subsidiary company was shut down in January 2003 [62]. Lack of manufacturing experience and not following the development and manufacturing cycle shown in Figure 15 can lead to wastage of millions of dollars. With an investment of at least \$322 million, Optisolar has to close operation due to manufacturing problems [63].

Based on the technical and business issues discussed in this section, it is obvious that none of the proposed



FIGURE 15: Basic product development and mass-scale manufacturing cycle.

nanostructure based solar cells that violates laws of physics, have any prospects of manufacturing PV modules. Due to the issues related to materials availability and toxicity of materials discussed in Section 2, CdTe, CuInGeSe<sub>2</sub>, and III-V semiconductor-based solar cells will not become a dominant player in multibillion dollar PV market. As one of us predicted in 1980 [20], silicon-based PV manufacturing will provide sustained growth of the PV industry and will emerge as a low-cost viable source of electricity generation for the 21st century. Following are the four silicon PV technology that are currently used in manufacturing, (i) ultra high efficiency single crystal technology, (ii) medium efficiency poly or multicrystalline technology, (iii) amorphous silicon thin film technology based on the use of larger glass substrates ( $\sim 5.2 \text{ m}^2$ ), and (iv) amorphous silicon technology based on flexible substrates. From the low-cost and multiterawatt PV power generation point of view, only amorphous silicon solar cells based on the use of large glass substrates have the potential to reach the goal of providing installed PV system cost of  $\$2.00/w_p$  in the next 3-4 years [64]. The ultra high efficiency single crystal PV modules may find a small niche market (where small area PV modules are warranted due to the area available for installation). The amorphous silicon technology based on flexible substrates may find a niche market for consumer products. The medium efficiency poly or multicrystalline silicon modules (limited size of silicon wafer) will not be able to be cost-effective compared to large area glass-based amorphous silicon thin film technology.

## 5. Conclusion

We have presented a comprehensive review on the subject of prospects of nanostructure-based solar cells for manufacturing future generation of photovoltaic modules. In search of reducing heat loss and utilizing the unabsorbed part of the spectrum, a number of solar cell concepts have been proposed. We have examined all proposed nanostructures for solar cell applications using the following five fundamental physics-based criterions.

- (1) Interactions between charge carriers (electrons and holes) and phonon cannot be neglected.
- (2) For all the known semiconductors, hot carriers (due to ultra short value of thermalization time) generated in one layer of the solar cell cannot be transported to the other side of the solar cell and collected at the other electrode.
- (3) The phenomenon of photoluminescence has no direct relationship with solar cell operation.

- (4) Intermediate band gap recombination center will reduce solar cell performance.
- (5) For nanostructures, the thermal conductivity is lower than the bulk values. For practical applications of nanostructures, the material must have high thermal conductivity to transport heat from the device.

Most of the work reported in the literature is based on assumptions which are not realistic. Infinite carrier mobility, optimal absorption, and lossless contacts are some examples of unrealistic assumptions used in the work reported in the literature. With current knowledge base, it is highly unlikely that the nanostructure-based solar cells employing Hot Carriers, Up/Down conversion, and Intermediate Band Solar Cells will be used in the manufacturing of PV modules. Similar to the invention of phase shift masks (to beat the conventional diffraction limit of optical lithography); clever design concepts need to be invented to take advantage of quantum-based nanostructures.

Both dye-sensitized solar cells and organic solar cells have fundamental problem of reliability. Silicon-based PV manufacturing will continue to provide sustained growth of the PV industry and will emerge as a low-cost viable source of electricity generation for the 21st century.

## Acknowledgments

The authors would like to thank Elsevier, Wiley-VCH Verlag GmbH & Co. KGaA, Institute of Physics and American Institute of Physics for granting us permission to republish some of the figures and tables used in this paper. The authors would also like to thank Dr. M. Green, Dr. M.C. Beard, Dr. A. Khitun, Dr. A. Freundlich, Dr. P. Yang, and Dr. A. Marti for their quick response for our e-mail requests.

## References

- [1] M. Osborne, "Worldwide photovoltaics installations grew 110% in 2008, says Solarbuzz," March 2009, <http://www.pv-tech.org/news/.a/worldwide-photovoltaics-installations-grew-stallations-grew-110-in-2008-says-solarbuzz>.
- [2] M. Osborne, "Gartner posts long-range forecast for photovoltaics industry," March 2009, <http://www.pv-tech.org/news/.a/gartner-posts-long-range-forecast-for-photovoltaics-industry>.
- [3] R. Singh, N. Gupta, and K. F. Poole, "Global energy conversion revolution in the 21st century through solid state devices," in *Proceedings of the 26th International Conference on Microelectronics (ICM '08)*, vol. 1, pp. 45–54, IEEE, Nis, Serbia, May 2008.

- [4] G. Conibeer, M. Green, R. Corkish, et al., "Silicon nanostructures for third generation photovoltaic solar cells," *Thin Solid Films*, vol. 511–512, pp. 654–662, 2006.
- [5] R. Singh, A. Venkateshan, K. F. Poole, D. Mohan, and P. Chatterjee, "Semiconductor manufacturing in the nanotechnology world of the 21st century," in *Proceedings of the 25th International Conference on Microelectronics (ICM '06)*, pp. 2–8, Belgrade, Serbia, May 2006.
- [6] M. C. Beard, K. P. Knutsen, P. Yu, et al., "Multiple exciton generation in colloidal silicon nanocrystals," *Nano Letters*, vol. 7, no. 8, pp. 2506–2512, 2007.
- [7] K. Bullis, "Nanocrystals for Superefficient Solar Cells," *Technology Review*, March 2007, <http://www.technologyreview.com/energy/19256>.
- [8] Department of Energy, Solar Energy Technologies Program, "Future Generation Photovoltaic Devices and Processes Selections," November 2007, <http://www.docstoc.com/docs/942337/Future-Generation-Photovoltaic-Devices-and-Processes-Selections>.
- [9] V. I. Klimov, "Mechanisms for photogeneration and recombination of multiexcitons in semiconductor nanocrystals: implications for lasing and solar energy conversion," *Journal of Physical Chemistry B*, vol. 110, no. 34, pp. 16827–16845, 2006.
- [10] A. Luque and A. Martí, "Ultra-high efficiency solar cells: the path for mass penetration of solar electricity," *Electronics Letters*, vol. 44, no. 16, pp. 943–945, 2008.
- [11] L. M. Goncalves, V. Z. Bermudez, H. A. Ribeiro, and A. M. Mendes, "Dye-sensitized solar cells: a safe bet for the future," *Energy and Environmental Science*, vol. 1, pp. 655–667, 2008.
- [12] A. J. Nozik, "Spectroscopy and hot electron relaxation dynamics in semiconductor quantum wells and quantum dots," *Annual Review of Physical Chemistry*, vol. 52, pp. 193–231, 2001.
- [13] M. C. Beard and R. J. Ellingson, "Multiple exciton generation in semiconductor nanocrystals: toward efficient solar energy conversion," *Laser and Photonics Reviews*, vol. 2, no. 5, pp. 377–399, 2008.
- [14] L. Tsakalakos, "Nanostructures for photovoltaics," *Materials Science and Engineering R*, vol. 62, no. 6, pp. 175–189, 2008.
- [15] A. Luque, A. Martí, and A. J. Nozik, "Solar cells based on quantum dots: multiple exciton generation and intermediate bands," *MRS Bulletin*, vol. 32, no. 3, pp. 236–241, 2007.
- [16] J.-F. Guillemoles and S. Kettemann, "Advanced concepts for photovoltaic conversion: bridging the gap from theory to real devices?" <http://www.physnet.uni-hamburg.de/hp/kettemann/ispra.pdf>.
- [17] V. V. Kislyuk and O. P. Dimitriev, "Nanorods and nanotubes for solar cells," *Journal of Nanoscience and Nanotechnology*, vol. 8, no. 1, pp. 131–148, 2008.
- [18] H. J. Snaith and L. Schmidt-Mende, "Advances in liquid-electrolyte and solid-state dye-sensitized solar cells," *Advanced Materials*, vol. 19, no. 20, pp. 3187–3200, 2007.
- [19] R. Licklider, "The power of oil: the Arab oil weapon and the Netherlands, the United Kingdom, Canada, Japan, and the United States," *International Studies Quarterly*, vol. 32, no. 2, pp. 205–226, 1988.
- [20] R. Singh and J. D. Leslie, "Economic requirements for new materials for solar photovoltaic cells," *Solar Energy*, vol. 24, no. 6, pp. 589–592, 1980.
- [21] A. Feltrin and A. Freundlich, "Material considerations for terawatt level deployment of photovoltaics," *Renewable Energy*, vol. 33, no. 2, pp. 180–185, 2008.
- [22] H. Wicht and S. deHaan, "Hann, Photovoltaics Raw Materials Tracker," 2008, <http://www.isuppli.com/Abstract/ABSTRACT%20-%20PV%20Raw%20Materials%20Market%20Tracker%202008.pdf>.
- [23] S. Y. Sohn and H. U. Moon, "Cost of ownership model for inspection of multiple quality attributes," *IEEE Transactions on Semiconductor Manufacturing*, vol. 16, no. 3, pp. 565–571, 2003.
- [24] R. Singh, P. Chandran, M. Grujicic, et al., "Dominance of silicon CMOS based semiconductor manufacturing beyond international technology roadmap and for many more decades to come," in *Semiconductor Fabtech*, pp. 104–113, 30th edition, 2006.
- [25] W. Shockley and H. J. Queisser, "Detailed balance limit of efficiency of p-n junction solar cells," *Journal of Applied Physics*, vol. 32, no. 3, pp. 510–519, 1961.
- [26] P. Würfel, A. S. Brown, T. E. Humphrey, and M. A. Green, "Particle conservation in the hot-carrier solar cell," *Progress in Photovoltaics: Research and Applications*, vol. 13, no. 4, pp. 277–285, 2005.
- [27] M. Wolf, R. Brendel, J. H. Werner, and H. J. Queisser, "Solar cell efficiency and carrier multiplication in  $\text{Si}_{1-x}\text{Ge}_x$  alloys," *Journal of Applied Physics*, vol. 83, no. 8, pp. 4213–4221, 1998.
- [28] Y. Takeda, T. Ito, R. Suzuki, T. Motohiro, S. Shrestha, and G. Conibeer, "Impact ionization and Auger recombination at high carrier temperature," *Solar Energy Materials and Solar Cells*, vol. 93, no. 6–7, pp. 797–802, 2009.
- [29] A. J. Nozik, "Multiple exciton generation in semiconductor quantum dots," *Chemical Physics Letters*, vol. 457, no. 1–3, pp. 3–11, 2008.
- [30] A. J. Nozik, "Quantum dot solar cells," *Physica E*, vol. 14, no. 1–2, pp. 115–120, 2002.
- [31] M. C. Hanna and A. J. Nozik, "Solar conversion efficiency of photovoltaic and photoelectrolysis cells with carrier multiplication absorbers," *Journal of Applied Physics*, vol. 100, no. 7, Article ID 074510, 2006.
- [32] R. D. Schaller, M. Sykora, J. M. Pietryga, and V. I. Klimov, "Seven excitons at a cost of one: redefining the limits for conversion efficiency of photons into charge carriers," *Nano Letters*, vol. 6, no. 3, pp. 424–429, 2006.
- [33] P. Smith, R. Singh, and J. Dubow, "Reverse current-voltage characteristics of indium tin oxide/silicon solar cells under illumination," *Journal of Applied Physics*, vol. 51, no. 4, pp. 2164–2166, 1980.
- [34] T. Trupke, M. A. Green, and P. Würfel, "Improving solar cell efficiencies by down-conversion of high-energy photons," *Journal of Applied Physics*, vol. 92, no. 3, pp. 1668–1674, 2002.
- [35] T. Trupke, M. A. Green, and P. Würfel, "Improving solar cell efficiencies by up-conversion of sub-band-gap light," *Journal of Applied Physics*, vol. 92, no. 7, pp. 4117–4122, 2002.
- [36] C. Strümpel, M. McCann, G. Beaucarne, et al., "Modifying the solar spectrum to enhance silicon solar cell efficiency—an overview of available materials," *Solar Energy Materials and Solar Cells*, vol. 91, no. 4, pp. 238–249, 2007.
- [37] V. Švrček, A. Slaoui, and J.-C. Muller, "Silicon nanocrystals as light converter for solar cells," *Thin Solid Films*, vol. 451–452, pp. 384–388, 2004.
- [38] E. D. Jackson, "Areas for improvement of the semiconductor solar energy converter," in *Transactions of the Conference on the Use of Solar Energy*, vol. 5, pp. 122–126, University of Arizona Press, Tucson, Ariz, USA, 1958.
- [39] K. W. J. Barnham and G. Duggan, "A new approach to high-efficiency multi-band-gap solar cells," *Journal of Applied Physics*, vol. 67, no. 7, pp. 3490–3493, 1990.

- [40] E.-C. Cho, S. Park, X. Hao, et al., "Silicon quantum dot/crystalline silicon solar cells," *Nanotechnology*, vol. 19, no. 24, Article ID 245201, 2008.
- [41] B. O. Dabbousi, M. G. Bawendi, O. Onitsuka, and M. F. Rubner, "Electroluminescence from CdSe quantum-dot/polymer composites," *Applied Physics Letters*, vol. 66, pp. 1316–1318, 1995.
- [42] M. J. Konstantinovic, S. Bersier, X. Wang, et al., "Raman scattering in cluster-deposited nanogranular silicon films," *Physical Review B*, vol. 66, no. 16, Article ID 161311, 4 pages, 2002.
- [43] A. Khitun, A. Balandin, J. L. Liu, and K. L. Wang, "In-plane lattice thermal conductivity of a quantum-dot superlattice," *Journal of Applied Physics*, vol. 88, no. 2, pp. 696–699, 2000.
- [44] W. L. Liu, T. Borca-Tasciuc, G. Chen, J. L. Liu, and K. L. Wang, "Anisotropic thermal conductivity of Ge quantum-dot and symmetrically strained Si/Ge superlattices," *Journal of Nanoscience and Nanotechnology*, vol. 1, no. 1, pp. 39–42, 2001.
- [45] V. A. Belyakov, V. A. Burdov, R. Lockwood, and A. Meldrum, "Silicon nanocrystals: fundamental theory and implications for stimulated emission," *Advances in Optical Technologies*, vol. 2008, Article ID 279502, 32 pages, 2008.
- [46] M. Wolf, "Limitations and possibilities for improvement of photovoltaic solar energy converters—part I: considerations for earth's surface operation," *Proceedings of the IRE*, vol. 48, pp. 1246–1262, 1960.
- [47] A. Luque and A. Martí, "Increasing the efficiency of ideal solar cells by photon induced transitions at intermediate levels," *Physical Review Letters*, vol. 78, no. 26, pp. 5014–5017, 1997.
- [48] A. Martí, N. López, E. Antolín, et al., "Novel semiconductor solar cell structures: the quantum dot intermediate band solar cell," *Thin Solid Films*, vol. 511–512, pp. 638–644, 2006.
- [49] K. M. Yu, W. Walukiewicz, J. Wu, et al., "Diluted II-VI oxide semiconductors with multiple band gaps," *Physical Review Letters*, vol. 91, no. 24, Article ID 246403, 4 pages, 2003.
- [50] E. Antolín, A. Martí, J. Olea, et al., "Lifetime recovery in ultra highly titanium-doped silicon for the implementation of an intermediate band material," *Applied Physics Letters*, vol. 94, Article ID 042115, 2009.
- [51] A. G. Norman, M. C. Hanna, P. Dippo, et al., "InGaAs/GaAs QD superlattices: MOVPE growth, structural and optical characterization, and application in intermediate-band solar cells," in *Proceedings of the 31st IEEE Photovoltaic Specialists Conference*, pp. 43–48, 2005.
- [52] Y. Chiba, A. Islam, Y. Watanabe, R. Komiya, N. Koide, and L. Han, "Dye-sensitized solar cells with conversion efficiency of 11.1%," *Japanese Journal of Applied Physics*, vol. 45, no. 24–28, pp. L638–L640, 2006.
- [53] J. Krüger, R. Plass, M. Grätzel, P. J. Cameron, and L. M. Peter, "Charge transport and back reaction in solid-state dye-sensitized solar cells: a study using intensity-modulated photovoltage and photocurrent spectroscopy," *Journal of Physical Chemistry B*, vol. 107, no. 31, pp. 7536–7539, 2003.
- [54] P. Yang, "Nanowire-based solar cell," in *Proceedings of the APS March Meeting*, 2006, Session G10.00001.
- [55] M. Law, L. E. Greene, J. C. Johnson, R. Saykally, and P. Yang, "Nanowire dye-sensitized solar cells," *Nature Materials*, vol. 4, no. 6, pp. 455–459, 2005.
- [56] L. E. Greene, M. Law, B. D. Yuhas, and P. Yang, "ZnO-TiO<sub>2</sub> core-sheath nanorod/P3HT solar cell," *Journal of Physical Chemistry C*, vol. 111, no. 50, pp. 18451–18456, 2007.
- [57] M. Law, L. E. Greene, A. Radenovic, T. Kuykendall, J. Liphardt, and P. Yang, "ZnO-Al<sub>2</sub>O<sub>3</sub> and ZnO-TiO<sub>2</sub> core-shell nanowire dye-sensitized solar cells," *Journal of Physical Chemistry B*, vol. 110, no. 45, pp. 22652–22663, 2006.
- [58] Z. V. Vardeny, A. J. Heeger, and A. Dodabalapur, "Fundamental research needs in organic electronic materials," *Synthetic Metals*, vol. 148, pp. 1–3, 2005.
- [59] Y. K. Jin, K. Lee, N. E. Coates, et al., "Efficient tandem polymer solar cells fabricated by all-solution processing," *Science*, vol. 317, no. 5835, pp. 222–225, 2007.
- [60] A. Lodha and R. Singh, "Prospects of manufacturing organic semiconductor-based integrated circuits," *IEEE Transactions on Semiconductor Manufacturing*, vol. 14, no. 3, pp. 281–296, 2001.
- [61] M. J. Kelly, "Are quantum semiconductor devices delivering?" *Materials Science and Engineering B*, vol. 35, no. 1–3, pp. 1–6, 1995.
- [62] M. LaPedus and P. Clarke, "Motorola closes GaAs-on-silicon wafer subsidiary," *EE Times*, January 2003, <http://www.eetimes.com/news/semi/showArticle.jhtml?articleID=10800321>.
- [63] M. Kanellos, "Inside OptiSolar's Grand Ambitions," April 2009, <http://www.greentechmedia.com/articles/read/inside-optisolars-grand-ambitions-6029/>.
- [64] R. Singh, unpublished results.

## Research Article

# The Effect of UV-Irradiation (under Short-Circuit Condition) on Dye-Sensitized Solar Cells Sensitized with a Ru-Complex Dye Functionalized with a (diphenylamino)Styryl-Thiophen Group

Kazuteru Nonomura,<sup>1</sup> Yunhua Xu,<sup>1</sup> Tannia Marinado,<sup>1</sup> Daniel P. Hagberg,<sup>1</sup> Rong Zhang,<sup>2</sup> Gerrit Boschloo,<sup>1,3</sup> Licheng Sun,<sup>1</sup> and Anders Hagfeldt<sup>1,3</sup>

<sup>1</sup> Department of Chemistry, Center of Molecular Devices, Royal Institute of Technology (KTH), Teknikringen 30, 100 44 Stockholm, Sweden

<sup>2</sup> State Key Laboratory of Fine Chemicals, DUT-KTH Joint Education and Research Center on Molecular Devices, Dalian University of Technology (DUT), Dalian 116012, China

<sup>3</sup> Department of Physical and Analytical Chemistry, Uppsala University, Box 259, 751 05 Uppsala, Sweden

Correspondence should be addressed to Kazuteru Nonomura, kazuteru@kth.se

Received 22 January 2009; Accepted 18 May 2009

Recommended by Mohamed Sabry Abdel-Mottaleb

A new ruthenium complex, *cis*-di(thiocyanato)(2,2'-bipyridine-4,4'-dicarboxylic acid)(4,4'-bis(2-(5-(2-(4-diphenylamino-phenyl)ethenyl)-thiophen-2-yl)ethenyl)-2,2'-bipyridine)ruthenium(II) (named E322) has been synthesized for use in dye-sensitized solar cells (DSCs). Higher extinction coefficient and a broader absorption compared to the standard Ru-dye, N719, were aimed. DSCs were fabricated with E322, and the efficiency was 0.12% initially. (4.06% for N719, as reference). The efficiency was enhanced to 1.83% by exposing the cell under simulated sunlight containing UV-irradiation at short-circuit condition. The reasons of this enhancement are (1) enhancing electron injection from sensitizer to TiO<sub>2</sub> following a shift toward positive potentials of the conduction band of TiO<sub>2</sub> by the adsorption of protons or cations from the sensitizer, or from the redox electrolyte and (2) improving the regeneration reaction of the oxidized dye by the redox electrolyte by the dissolution of aggregated dye from the surface of TiO<sub>2</sub> following the treatment.

Copyright © 2009 Kazuteru Nonomura et al. This is an open access article distributed under the Creative Commons Attribution License, which permits unrestricted use, distribution, and reproduction in any medium, provided the original work is properly cited.

## 1. Introduction

Dye-sensitized solar cells have been intensively investigated in the last decades after Graetzel and his coworkers showed more than 10% of sun light to electrical power conversion efficiency [1, 2]. Conventionally, a porous nanocrystalline TiO<sub>2</sub> thin film, Ru-complex dye molecules, and I<sup>-</sup>/I<sub>3</sub><sup>-</sup> redox couple are used. Ideal sensitizers for dye-sensitized solar cells should have a broad absorption spectrum to utilize the visible light, good charge separation property, and good energy matching with the conduction band of TiO<sub>2</sub> and the redox potential of electrolyte. A lot of Ru-complex dyes have been developed to achieve this goal [2–12]. For example, dyes such as N3, N719, and black dye are known as suitable dyes fulfilling the conditions mentioned above. However, it

is still a key issue to further develop sensitizers for dye-sensitized solar cells to improve the efficiency. A way to improve the efficiency is the development of a dye which has higher extinction coefficients. Such sensitizers allow the use of thinner TiO<sub>2</sub> nanocrystalline films, which is beneficial as it will reduce the recombination of electrons with redox electrolyte during electron transport to the external circuit. Considering solid states dye-sensitized solar cells, thinner semiconductor layer will also be required. Another way to improve the sensitizer is by improving the intramolecular charge separation. By attaching functional groups to Ru complex dyes, further charge separation of the HOMO and LUMO is aimed for. Such a structure is expected to promote electron injection into TiO<sub>2</sub> and delays subsequent recombination [13].

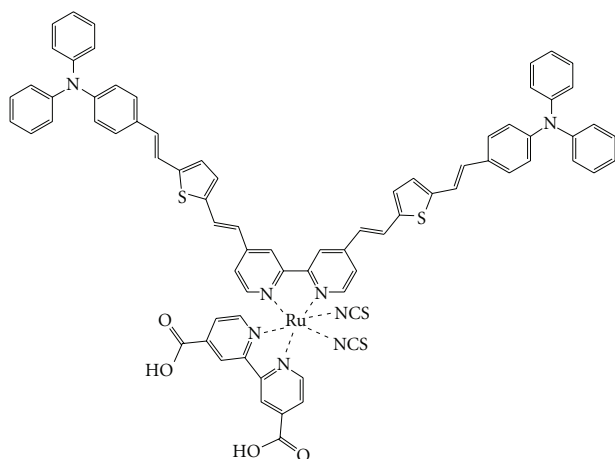


FIGURE 1: Molecular structure of **E322**.

We have recently reported a polyene-triphenylamine dye, named D5, which showed a good charge separation and almost the same light to electric conversion efficiency in dye-sensitized solar cell as N719 under comparable condition [14]. Quantum chemical calculations suggest that the dye has a clear intramolecular charge separation following the excitation. In this study, we attached polyene-triphenylamine to the bipyridine ligand of an Ru-complex dye to improve the extinction coefficient of the dye as well as to aim for a broad absorption in the visible-near infrared light region. The dye we have synthesized for this study is *cis*-di(thiocyanato)(2,2'-bipyridine-4,4'-dicarboxylic acid)(4,4'-bis(2-(5-(2-(4-diphenylaminophenyl)ethenyl)-thiophen-2-yl)ethenyl)-2,2'-bipyridine)ruthenium(II) (hereafter **E322**) (Figure 1).

Electrochemical characterization has been carried out to estimate the position of HOMO and LUMO potentials. The dye-modified TiO<sub>2</sub> nanoporous thin films were characterized by photoinduced absorption spectroscopy (PIA). Photoelectrochemical properties of the fabricated cells were characterized by current-voltage (I-V) measurement, incident photon to current conversion efficiency (IPCE), and measurement of the electron life time and accumulated charge. As reference, DSCs sensitized with N719 were also prepared, and their properties were compared.

## 2. Experimental

**2.1. Materials.** The synthesis of ligand **1** and complex **2** can be found in the Supporting Information.

**Complex 3.** Ligand **1** (316 mg, 0.347 mmol) and complex **2** (210 mg, 0.347 mmol) were reacted in DMF (30 mL) at 140°C for 8 hours. DMF was removed, and the residue was recrystallized from a mixture of CH<sub>2</sub>Cl<sub>2</sub> and acetone. The black precipitate formed was collected, washed with cold acetone, and dried, giving the product (410 mg, 85% yield). <sup>1</sup>H NMR (500 MHz, DMSO-d<sub>6</sub>): δ = 1.31 (t, *J* = 7.0 Hz, 3H), 1.44 (t, *J* = 7.0 Hz, 3H), 4.35 (q, *J* = 7.0 Hz, 2H), 4.50

(q, *J* = 7.0 Hz, 2H), 6.85 (d, *J* = 16.0 Hz, 1H), 6.92–6.97 (m, 5H), 7.00 (d, *J* = 16.0 Hz, 1H), 7.04–7.17 (m, 15H), 7.24 (d, *J* = 3.5 Hz, 1H), 7.27–7.40 (m, 13H), 7.48 (d, *J* = 8.5 Hz, 2H), 7.52–7.54 (m, 3H), 7.83 (d, *J* = 16.0 Hz, 1H), 7.91 (d, *J* = 6.0 Hz, 1H), 7.93 (s, 1H), 8.07 (d, *J* = 16.0 Hz, 1H), 8.19 (d, *J* = 6.0 Hz, 1H), 8.71 (s, 1H), 8.86 (s, 1H), 8.88 (s, 1H), 9.04 (s, 1H), 9.73 (d, *J* = 6.0 Hz, 1H), 10.22 ppm (d, *J* = 6.0 Hz, 1H). MALDI-TOF MS: *m/z* = 1365.719 (calcd for [M – Cl<sup>-</sup> + H<sub>2</sub>O]<sup>+</sup>: 1365.311).

**Complex 4.** A mixture of **3** (300 mg, 0.217 mmol) and NH<sub>4</sub>NCS (400 mg, 5.26 mmol) in DMF (50 mL) was heated at 130°C for 48 hours. Upon cooling, solvent was removed, and the residue was dissolved in CH<sub>2</sub>Cl<sub>2</sub> and washed with saturated aqueous solution of Na<sub>2</sub>CO<sub>3</sub>. The organic phase was dried over Na<sub>2</sub>SO<sub>4</sub>. After solvent removal, the crude product was purified by column chromatography on SiO<sub>2</sub> using 0.2% MeOH in CH<sub>2</sub>Cl<sub>2</sub> as eluent to give the desired product (190 mg, 61% yield). <sup>1</sup>H NMR (500 MHz, DMSO-d<sub>6</sub>): δ = 1.30 (t, *J* = 7.0 Hz, 3H), 1.42 (t, *J* = 6.5 Hz, 3H), 4.36 (q, *J* = 7.0 Hz, 2H), 4.47 (q, *J* = 7.0 Hz, 2H), 6.82 (d, *J* = 15.0 Hz, 1H), 6.92–7.01 (m, 5H), 7.04–7.12 (m, 13H), 7.16–7.28 (m, 5H), 7.31–7.37 (m, 10H), 7.40–7.43 (m, 2H), 7.49 (d, *J* = 8.5 Hz, 2H), 7.53 (d, *J* = 8.5 Hz, 2H), 7.65 (d, *J* = 6.0 Hz, 1H), 7.84 (d, *J* = 16.0 Hz, 1H), 7.89 (d, *J* = 6.0 Hz, 2H), 7.96–8.02 (m, 1H), 8.24 (s, br, 1H), 8.50–8.80 (m, 2H), 8.96 (s, 1H), 9.04 (d, *J* = 5.5 Hz, 1H), 9.11 (s, 1H), 9.49 ppm (d, *J* = 5.5 Hz, 1H). MALDI-TOF MS: *m/z* = 1370.279 (calcd for [M – NCS<sup>-</sup>]<sup>+</sup>: 1370.307).

**Complex E322.** A solution of complex **4** (94 mg, 0.066 mmol) in THF (20 mL) containing NaOH (excess, aqueous solution) was heated at 70°C for 12 hours. After cooling to room temperature, solvent was removed, and the residue was dissolved in a mixture of THF/H<sub>2</sub>O (1 : 1) and passed through a Sephadex LH-20 column. Main band was collected, and the pH was lowered to 2 by adding dilute aqueous HNO<sub>3</sub> solution. The precipitate was filtered and washed with water and methanol and dried, giving complex **E322** (114 mg, 85% yield). <sup>1</sup>H NMR (500 MHz, DMSO-d<sub>6</sub>): δ = 6.89 (d, *J* = 16.0 Hz, 1H), 6.92 (d, *J* = 8.5 Hz, 2H), 6.95 (d, *J* = 8.5 Hz, 2H), 7.01 (d, *J* = 16.0 Hz, 1H), 7.04–7.12 (m, 13H), 7.18 (d, *J* = 3.5 Hz, 1H), 7.25 (d, *J* = 3.5 Hz, 1H), 7.27–7.39 (m, 14H), 7.41 (d, *J* = 3.5 Hz, 1H), 7.49 (d, *J* = 9.0 Hz, 2H), 7.53 (d, *J* = 9.0 Hz, 2H), 7.65 (d, *J* = 6.0 Hz, 1H), 7.85 (s, 1H), 7.88 (d, *J* = 5.5 Hz, 1H), 8.03–8.10 (m, 2H), 8.29 (d, *J* = 5.5 Hz, 1H), 8.74 (s, br, 1H), 8.86–8.94 (m, 2H), 9.07 (s, 1H), 9.09 (d, *J* = 5.5 Hz, 1H), 9.45 ppm (d, *J* = 6.0 Hz, 1H). MALDI-TOF MS: *m/z* = 1314.609 (calcd for [M – H<sup>+</sup> + K<sup>+</sup> – NCS]<sup>+</sup>: 1314.248).

Absorption spectra of the dye solution and dye modified TiO<sub>2</sub> thin films were measured with HR-2000 Ocean Optics, fiber optics spectrophotometer. CH Instruments 660 Potentiostat was used for differential pulse voltammetry. Electrochemical analysis was carried out in 1 mM dye and 0.1 M of tetrabutylammonium hexafluorophosphate (TBAPF<sub>6</sub>, Tokyo kasei kogyo) in tetrahydrofuran (THF, Aldrich, 99.9%). A platinum electrode, a platinum wire, and

Ag/Ag<sup>+</sup> electrode were used as working electrode, counter electrode, and reference electrode, respectively. The obtained potentials were adjusted by comparing the redox potential of the Ferrocene/Ferrocenium redox couple.

For the preparation of TiO<sub>2</sub> films, conducting glass substrates (TEC8, Pilkington) were covered by Scotch-tape (3M) with a rectangular shaped hole (8 mm × 4 mm) at the center. TiO<sub>2</sub> nanocrystalline thin films were prepared by spreading a suspension onto the conducting glass substrates. A single deposition gave a 3 μm thick film. The data shown in Table 2 were obtained from a film which thickness was ca. 9 μm. To study the effect of UV irradiation, 3 μm thick films were used. The area of the TiO<sub>2</sub> film was 0.32 cm<sup>2</sup>. TiO<sub>2</sub> electrodes were sintered at 450°C for 30 minutes. The electrodes were put into the dye bath when the temperature cooled down to 80°C and kept for 24 hours at room temperature. The concentration of the dye was 0.5 mM. The solvent was ethanol (Kemetyl, 99.5%) and tetrahydrofuran for N719 purchased from solaronix S.A and E322, respectively.

The electrodes were assembled with a counter electrode (thermally platinized TEC8) using a thermoplastic frame. Redox electrolyte was introduced through a hole drilled in the counter electrode that was sealed afterward. The electrolyte was composed of 0.1 M LiI (Aldrich, 99.9%), 0.6 M TBAI (tetrabutyl ammonium iodide, Sigma-aldrich, 98%), 0.05 M I<sub>2</sub> (Aldrich, 99.999%), and 0.5 M 4-TBP (4-tert-butylpyridine, Aldrich, 99%) in Acetonitrile (Aldrich, 99.8%). Prepared solar cells were characterized by IV measurements and various “tool-box” techniques [15]. A xenon arc lamp (300 W Cermax, ILC Technology) with filter (Tempax 113, Schott) was used as light source for IV measurements. The light intensity was adjusted to 1000 W m<sup>-2</sup>. IPCE was measured by using a computerized setup consisting of a xenon arc lamp (300 W Cermax, ILC Technology), a 1/8 m monochromator (CVI Digikröm CM 110), and a Keithley 2400 source/meter. The amounts of charge, open circuit photovoltage, and electron lifetime in the dye-sensitized solar cells were measured in a system using a red-light-emitting diode (Luxeon Star 1 W, λ<sub>max</sub> = 640 nm) as the light source. The relation between potential and charge was investigated using a combined voltage decay/charge extraction method. The solar cell was illuminated for 5 seconds under open circuit conditions, and the voltage was left to decay for a certain period in the dark to a voltage V. Subsequently, the cell was short-circuited, and the current was measured and integrated over 10 seconds to obtain Q<sub>oc</sub> (V). Electron lifetimes were determined by monitoring the transient photovoltage response after a small change in light intensity. A square wave modulation (<10% intensity) was added to the base light intensity, and the step response was recorded using the DAQ (data acquisition) board. The current and voltage responses were fitted using first-order decay kinetics, and time constants were obtained accordingly.

Photoinduced absorption spectroscopy (PIA) was carried out for the prepared electrodes. PIA measurements were performed using white probe light (a tungsten-halogen lamp) and superimposed on/off modulated blue light (450 nm) from an LED (Luxeon 1 Watt Star, Royal Blue) for

excitation. The transmitted probe light was focused onto a monochromator (Acton Research Corporation SP-150) and detected by an UV enhanced silicon photodiode connected to a current amplifier and lock-in amplifier (Stanford Research Systems models SR570 and SR830, resp.). PIA measurements were performed slightly above room temperature (25–28°C). PIA measurements were also carried out in the presence of the electrolyte.

### 3. Results and Discussion

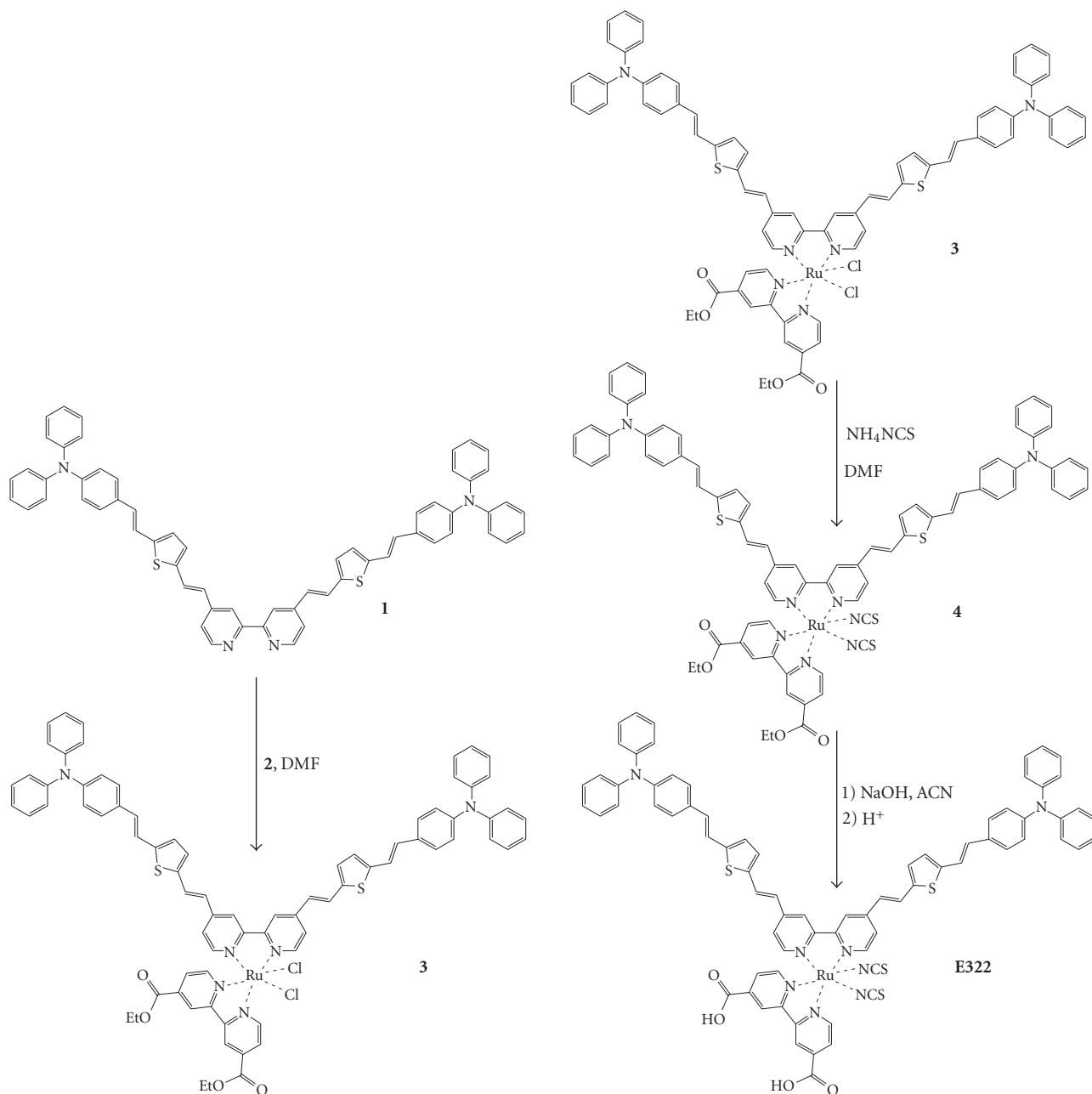
**3.1. Synthesis.** The synthesis of the dye started from the reaction of the ligand **1** with the ruthenium complex **2**, which afforded the dichloro ruthenium complex **3**. The two chlorides in complex **3** were replaced with thiocyanates by refluxing the mixture of **3** and excess NH<sub>4</sub>NCS in DMF, giving complex **4**. Ester groups in **4** were hydrolyzed in the presence of NaOH in acetonitrile followed by acidification to afford the final product **E322**. All the ruthenium complexes were characterized by <sup>1</sup>H and <sup>13</sup>C NMR and MS spectroscopy.

The absorption spectra of E322 and N719 in THF and ethanol, respectively, are shown in Figure 2. The extinction coefficient of E322 at the absorption maximum at 469 nm is 4.2 × 10<sup>4</sup> M<sup>-1</sup> cm<sup>-1</sup>. Compared to the extinction coefficient of N719 which is 1.3 × 10<sup>4</sup> M<sup>-1</sup> cm<sup>-1</sup> at 518 nm in ethanol solution [16], the obtained extinction coefficient for E322 is 3 times higher. The spectrum of E322 is very broad. Although the absorption peak of E322 is blue shifted compared to N719, the extinction coefficient of E322 exceeds that of N719 in the whole visible range and has an onset that is more than 100 nm red-shifted.

The oxidation potential and the reduction potential of the dye were measured by differential pulse voltammetry. The HOMO potential of the dyes was estimated from the oxidation potential. Obtained values are listed in Table 1. E<sub>0-0</sub> was estimated from the tail of the absorption spectrum in the longer wavelength region. From these two values, the LUMO potential was estimated. The obtained values fulfill the conditions required for dye-sensitized solar cells; the potential of the LUMO is higher than the conduction band of TiO<sub>2</sub>, and the potential of the HOMO is lower than the potential of the redox electrolyte [17].

Photocurrent action spectra were measured for E322 and N719 and are shown in Figure 3. It can be seen for all the dyes that photocurrents were generated from a rather wide range of the visible light. IPCE of 50% and 27% was obtained at 540 nm for N719 and E322, respectively. Comparing the shape of the action spectra, E322 has a broader spectral response than N719. However, the IPCE at 540 nm for E322 is lower than N719. It should be noted that an IPCE value of 27% for E322 was obtained after treating the cell with simulated sunlight containing UV under short-circuit condition. When no treatment was introduced, the value of IPCE at 540 nm is virtually zero, 0.45%. The details for this intriguing observation are discussed below.

The results of solar cell characterization are shown in Table 2.



SCHEME 1: Synthesis of E322.

Although E322 has a high extinction coefficient and the film is deeply colored by the dye, the photocurrent under short-circuit condition,  $I_{sc}$ , is lower than for N719. The open-circuit photovoltage,  $V_{oc}$ , of the cells with E322 was 0.54 V, while  $V_{oc}$  of N719 was 0.77 V. The fill factor, ff, showed a similar tendency as  $V_{oc}$ , relatively high for N719 and low for E322. Consequently, the cell with N719 showed a higher conversion efficiency of 4.1%, compared to 1.8% for the cells with E322. It should be noted that the optimizations of the cell, such as a blocking layer and scattering layers, to obtain higher efficiencies have not been introduced in this study. It should also be noted that the efficiency of 1.8% for E322 was

obtained after exposing the cell to the simulated solar light containing UV light at short circuit condition for 70 hours.

When the solar cell sensitized with E322 was irradiated with simulated solar light under short circuit condition, the photocurrent increased gradually and reached a plateau (Figure 4).

Before applying this treatment, the efficiency of the cell was 0.12% (Table 2). The efficiency was enhanced more than 10 times by employing the UV treatment. The time to reach the plateau depends on the amount of the adsorbed dye. The time to reach the plateau for lightly colored films was shorter than deeply colored films. This phenomenon only occurred

TABLE 1: Experimental data for electrochemical and spectral properties of the dyes.

Dye	$E_{D/D^+}$ [V] vs. NHE	$E_{red}$ [V] vs. NHE	$E_{(o-o)}^{(b)}$ [eV]	$E_{D^*/D^+}^{(c)}$ [V]	$\lambda_{max}$ [nm]	Extinction coefficient [ $M^{-1} cm^{-1}$ ]
E322	0.74 <sup>(a)</sup>	-0.93 <sup>(a)</sup>	1.55	-0.81	469	$4.2 \times 10^4$
N719	1.13 <sup>(d)</sup>	-1.16 <sup>(d)</sup>	1.88	-0.75	518	$1.3 \times 10^4$

<sup>(a)</sup> oxidation potential and reduction potential were measured from differential pulse voltammetry in 1 mM E322 and 0.1 M TBAPF<sub>6</sub> in THF, <sup>(b)</sup>  $E_{o-o}$  energy was estimated from the wavelength at the tail of the absorption in longer wavelength, <sup>(c)</sup>  $E_{D^*/D^+}$  was estimated from oxidation potential and  $E_{o-o}$  energy, <sup>(d)</sup> values were obtained by referring the value  $E_{ox} = 0.5$  V vs. Fc and  $E_{1/2} = -1.79$  V vs. Fc from [7] and indicated vs. NHE by using the redox potential of ferrocene (0.63 V vs. NHE).

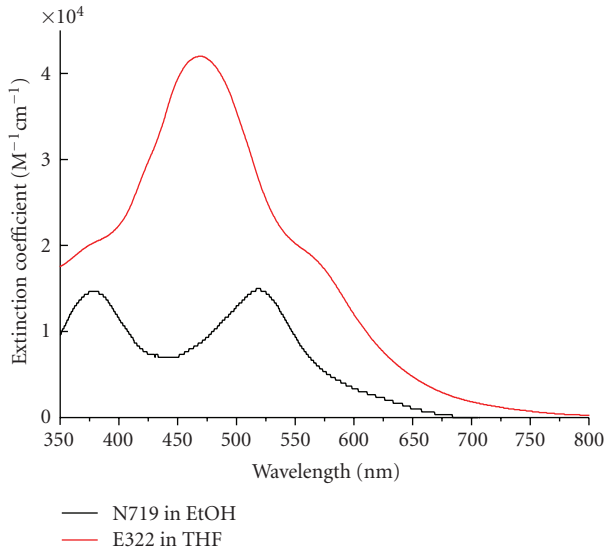


FIGURE 2: Absorption spectrum of the dye solution. THF and ethanol were used as solvent for E322 and N719, respectively.

TABLE 2: Photovoltaic performance of dye-sensitized solar cells with E322 and N719, respectively.

Dye	$J_{sc}/mA cm^{-2}$	$V_{oc}/V$	ff	Efficiency/%
E322 (after treatment)	5.41	0.538	0.630	1.83
E322 (before treatment)	0.55	0.414	0.534	0.12
N719	7.47	0.770	0.707	4.06

when the following conditions were fulfilled: UV light and short circuit condition.

To explain these phenomena, possible reasons are suggested: (1) dye degradation, (2) higher electron injection efficiency, (3) longer electron lifetime in TiO<sub>2</sub>, that is, due to reduced recombination of the electrons in the TiO<sub>2</sub> with oxidized dyes or species in the electrolyte, and (4) more efficient regeneration reaction. These reasons can be rationalized as follows. First, if dye molecules are degraded by UV irradiation and if the degraded dye molecules are more efficient as sensitizers, then the cell performance can be enhanced. Second, the electron injection efficiency can be low due to either dye aggregation or unmatched energy levels between the LUMO of the dye and the conduction band of TiO<sub>2</sub>. If these unsuitable conditions are altered by the UV

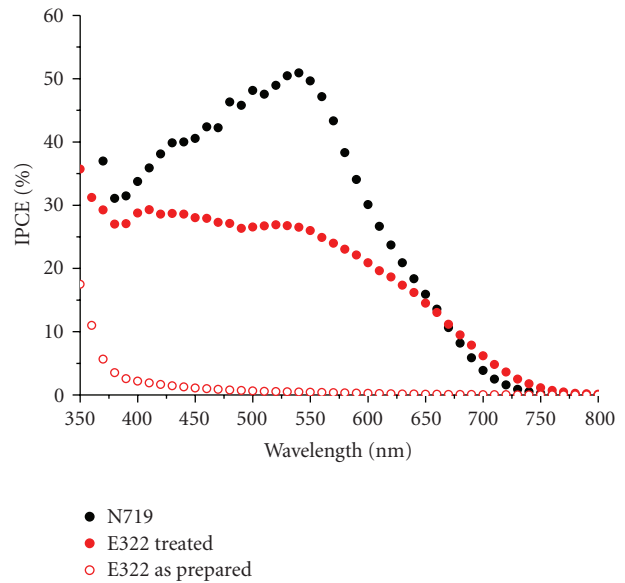


FIGURE 3: Action spectra of dye-sensitized solar cells with E322 and N719, respectively.

treatment, an enhanced efficiency can be obtained. Third, if the electron lifetime in TiO<sub>2</sub> is short due to unfavorable interactions among aggregated dyes and if the electron lifetime increases by decreasing these interactions, this can be another reason of the enhancement of the efficiency. Fourth, if the regeneration of the oxidized dye by the redox electrolyte was blocked by the aggregated dyes and if this blocking was reduced by UV treatment, the efficiency can be enhanced. Those possible reasons are examined in the following section.

A possible reason of the enhanced efficiency after the UV treatment under short-circuit condition can be the photodegradation of the E322 resulting in a better sensitizer for the dye-sensitized solar cell. The absorption spectra of the dye solution, the dissolved dye from the surface of TiO<sub>2</sub> after sensitization, and the dissolved dye from TiO<sub>2</sub> after UV treatment were compared (see supporting information). The shapes of the absorption spectra were different between the dye solution and the desorbed dye from the surface of TiO<sub>2</sub> after the sensitization. The peak wavelengths were, however, the same. The shapes of the absorption spectra between dissolved dye after sensitization and dissolved dye after UV treatment were very similar. The height of the absorption peak can, of course, vary by the amount of dye aggregation. Since the peak wavelengths are identical, it can be assumed that there is no degradation of the dye by introducing

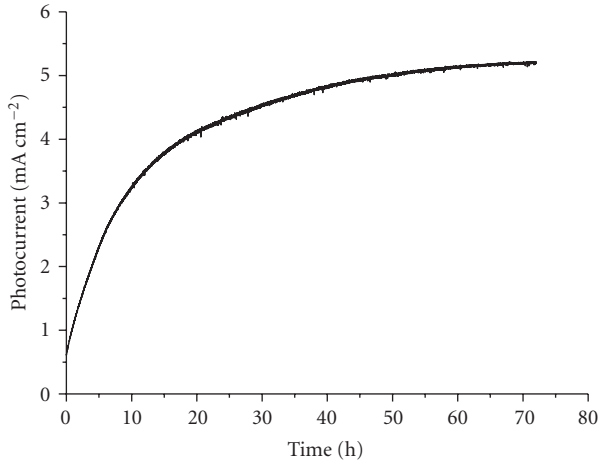


FIGURE 4: Time-current curve of the cell with E322. The short circuit photocurrent was recorded continuously at the light intensity of  $1000 \text{ W m}^{-2}$ .

the UV irradiation treatment. Furthermore, the IR spectra before and after the treatment were very similar, confirming that no dye decomposition had occurred (See supporting information).

As a second possible reason, the electron injection efficiency can be improved by dissolving aggregates of the dye resulting in a more favorable monolayer of the sensitizer, and/or by shifting the conduction band in  $\text{TiO}_2$  to more positive potentials. To check the dye adsorption after the UV treatment, a solar cell assembled with lightly dyed film with E322 was disassembled after the treatment. The absorption spectrum of the electrode was measured and compared with the spectrum measured before fabricating the solar cell (Figure 5).

It is clearly seen that the absorption in the visible light region decreased after the treatment. Thus, we conclude that the dye desorbed from the surface of  $\text{TiO}_2$  during this treatment. Since the photocurrent increased after the treatment, the dye molecules which desorbed from the surface of  $\text{TiO}_2$  were not effective as sensitizers in the dye-sensitized solar cells. These dyes acted as a filter for the incoming light. By comparing the absorption spectra of E322 and N719 on transparent  $\text{TiO}_2$  thin films, it was found that E322 is adsorbed at a 3 times higher concentration compared to N719 (see supporting information). A nearly monolayer adsorption can be expected in the case of N719 [18].

The conduction band shift of  $\text{TiO}_2$  was checked by charge extraction measurements. From these measurements, information of the relation between the accumulated charge in the film and open-circuit potential of the dye-sensitized solar cell can be obtained (Figure 6).

By comparing the voltage at the same amount of the accumulated charge in  $\text{TiO}_2$ , it can be seen that the voltage is ca. 0.2 V less after the UV treatment compared to the value before the treatment. Since the amount of charge is the same, the shift of the voltage can be explained by the positive shift of the conduction band of  $\text{TiO}_2$  after the UV treatment [19–21]. This will promote the charge injection from the

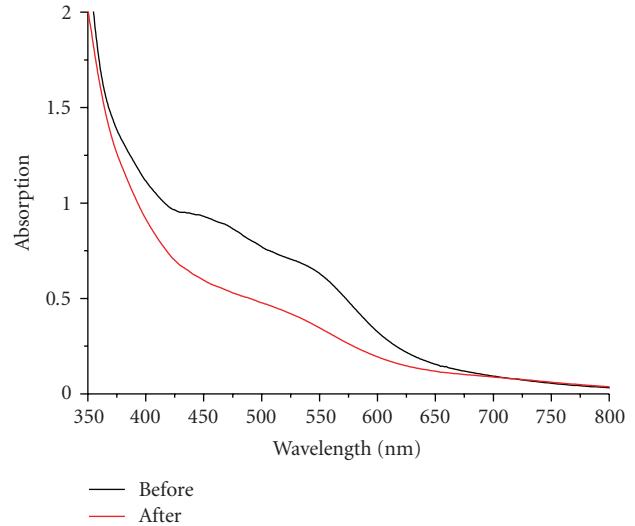


FIGURE 5: Absorption spectra of a  $\text{TiO}_2$  film ( $3 \times 10^{-6} \text{ m}$  thick) sensitized with E322 before and after employing the UV-light treatment.  $\text{SnO}_2$  glass substrate was used as reference.

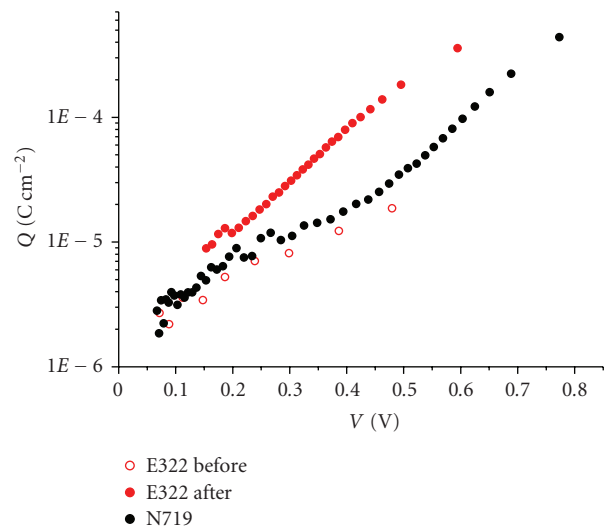


FIGURE 6: Extracted charge as a function of the open circuit photovoltage in dye-sensitized solar cell with E322 and N719. This measurement was carried out for the cell with E322 before and after employing the UV treatment.

excited dye to the conduction band of  $\text{TiO}_2$ . The cause of the positive bandedge shift is a more positive surface charge of  $\text{TiO}_2$ . This could be induced by the degradation of dye aggregates because of the treatment and/or the adsorption of protons or cations from the electrolyte. If these are the reasons for the enhanced efficiency, the efficiency should be initially high by the use of only  $\text{Li}^+$  in the electrolyte since  $\text{Li}^+$  is well known as a potential determining ion for  $\text{TiO}_2$  which shifts the conduction band to more positive potential [22–24]. When 0.1 M  $\text{LiI}$  and 0.05 M  $\text{I}_2$  was used as electrolyte, the short circuit photocurrent was ca.  $3 \text{ mA cm}^{-2}$  without any further treatment. This is ca. 5 times higher than the photocurrent with electrolyte containing the base

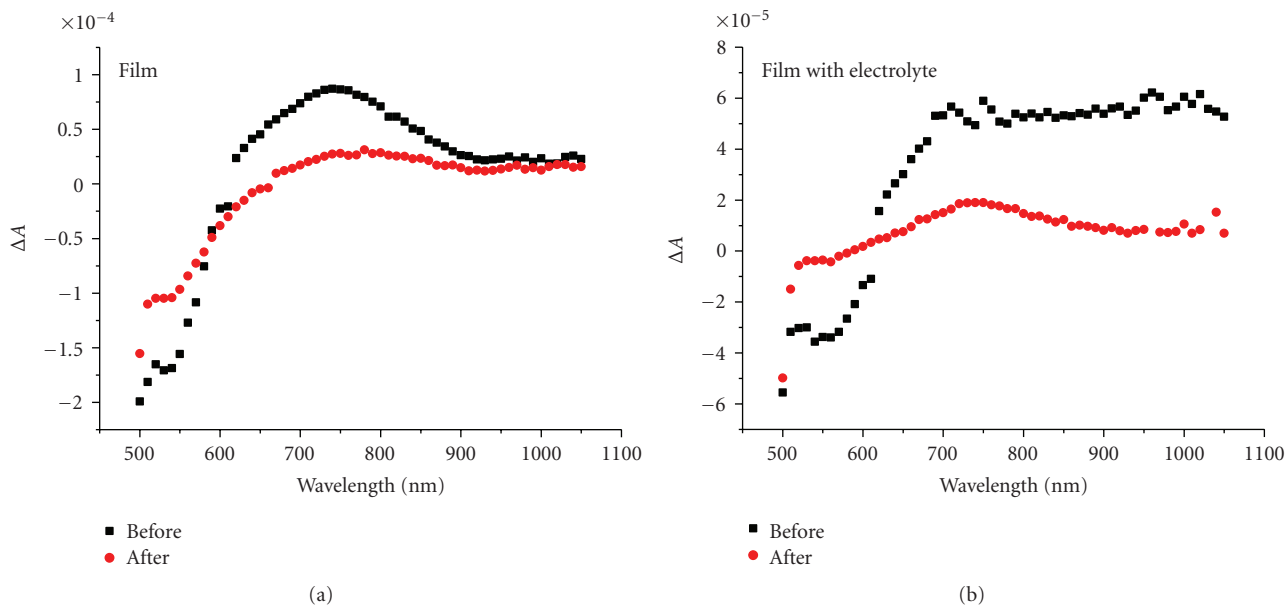


FIGURE 7: Photoinduced absorption spectra, excitation wavelength 450 nm with a frequency of 7 Hz, E322 sensitized TiO<sub>2</sub> thin film in the absent (a) and the present (b) of redox electrolyte. For both cases, the measurements were carried out before and after employing the UV treatment.

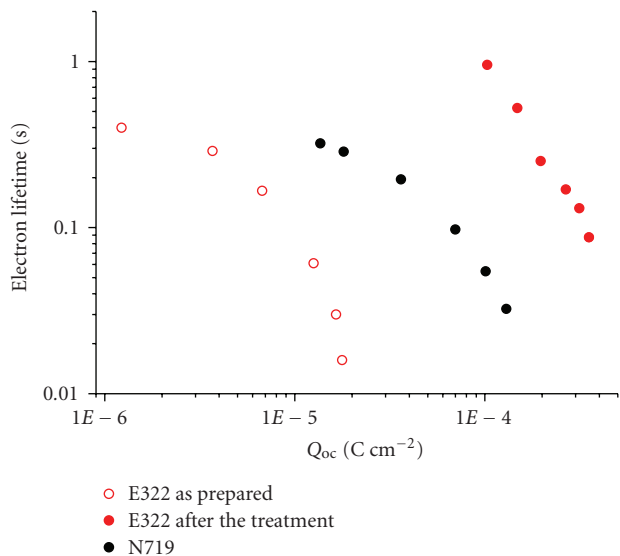


FIGURE 8: Electron lifetime as the function of the charge at open circuit condition, measured for the cell with E322 before/after the UV-treatment and the cell with N719.

additive, 4-tert-butylpyridine (4TBP). It indicates that an unmatched potential between the LUMO of the dye and the conduction band of TiO<sub>2</sub> is a main reason for the low initial efficiency. Nevertheless, by introducing the UV treatment, the photocurrent increased to ca. 5 mA cm<sup>-2</sup>. This means that the conduction band shift is not the only reason for the enhancement of the efficiency. Aggregation and/or multilayer adsorption of the sensitizer is also hindering the performance of the solar cell.

Aggregation and/or multilayer adsorption of the sensitizers leads to inefficient regeneration of the oxidized dye from the redox electrolyte. This can be demonstrated with PIA [25, 26].

In the PIA spectrum of E322 on TiO<sub>2</sub> (Figure 7(a)), a bleach can be observed at 545 nm. It indicates that the sensitizer is in the oxidized form, which means that the injection of the electron from the sensitizer to the conduction band of TiO<sub>2</sub> is occurring. In the presence of the redox electrolyte (Figure 7(b)), however, the bleach is still present. In highly efficient dye-sensitized solar cells, a bleach in PIA cannot be seen in the presence of redox electrolyte since the oxidized dyes are rapidly regenerated. In the case of N719 on TiO<sub>2</sub>, no bleach is seen in the presence of the redox electrolyte (not shown). These results indicate that the oxidized dye molecules are not fully regenerated by the redox electrolyte in the case of E322. After the UV treatment, on the other hand, the bleach disappears in PIA spectrum, suggesting that the oxidized dye is regenerated by the redox electrolyte. In addition to the favorable shift of the TiO<sub>2</sub> conduction band for the injection process, the desorption of nonactive dye molecules allows for injecting dye molecules to be regenerated by the redox electrolyte.

The electron lifetime and the amount of the charge in the electrode were measured for a lightly dyed electrode before and after UV treatment (Figure 8). Before the UV treatment, the electron lifetime in the cell with E322 is about one order of magnitude shorter compared to the cell with N719. The interaction between aggregates or multilayer adsorption of E322 and the injected electron in TiO<sub>2</sub> shortens apparently the electron lifetime. After the UV treatment, increase of the electron lifetime and more accumulated charge in the dye-modified TiO<sub>2</sub> thin film electrode were detected

compared to the results measured before the treatment. It is reasonable that the amount of charge in the dye-modified TiO<sub>2</sub> thin film increases since both the injection and the regeneration process improve after the treatment. An efficient regeneration process reduces the recombination reaction between the electrons in the TiO<sub>2</sub> and the oxidized dyes. The increased electron lifetime in the electrode seems to be caused by the decreased aggregation of the dye molecules. Moreover, the positive shift of the conduction band potential decreases the free energy difference between the TiO<sub>2</sub> and redox electrolyte. This also decreases the driving force of the reaction between electrons in TiO<sub>2</sub> and redox electrolyte.

Although the position of the TiO<sub>2</sub> conduction band shifts positive by the UV treatment, the open-circuit photovoltage was increased by the larger amount of accumulated charge in the TiO<sub>2</sub> film as implied by the increased amount of injected electrons and the longer electron lifetime.

It is peculiar that the desorption of the dye occurs only when UV light is irradiated to the electrode under the short circuit condition. The valence band hole created following the light absorption of TiO<sub>2</sub> seems to play some role to desorb the dye from the surface of the film. No desorption of the dye detected neither by dipping the dye-modified TiO<sub>2</sub> thin film into the electrolyte nor by the irradiation of visible light excluding the UV part nor by exposing the electrode under the simulated solar light containing UV at open-circuit condition. To explain this phenomenon, we propose the following as mechanism. When TiO<sub>2</sub> absorbs UV light, an electron is excited to the conduction band, and a hole is formed in the valence band. In the case of open circuit, the electron-hole pair recombines. But in the case of short circuit, the electron can move to external circuit before recombination, and the hole may react with species at the semiconductor surface or in the electrolyte. If oxidized dyes react with holes before the regeneration by redox electrolyte, they may be decomposed by the TiO<sub>2</sub> valence band hole. In short circuit condition with UV containing irradiation, such reaction can happen with dyes which have no contact with redox electrolyte. However, such reaction would end when the remaining dyes have contact with the redox electrolyte since such dyes are regenerated by the redox electrolyte before it reacts with the hole.

According to the absorption spectrum of the film after the treatment, the color of the film is very pale. It means that the light harvesting efficiency of the film is not sufficient to absorb the incident photons. Further optimization to establish the monolayer adsorption of the dye on TiO<sub>2</sub> is thus required.

#### 4. Conclusion

An Ru complex dye, E322, was synthesized and applied to dye-sensitized solar cells. Compared to N719, E322 has a broader absorption spectrum, and the extinction coefficient for E322 is about 3 times higher than N719. The cell with E322 showed very poor IPCE of 0.45% at 540 nm although it has a broader absorption and a higher extinction coefficient than N719. The reason of the low efficiency was caused by

unmatched energy levels between the LUMO potential of the dye and the conduction band of the TiO<sub>2</sub> and the aggregation and/or multilayer adsorption of the dye. Aggregated dye molecules block the contact between the active dye and the redox electrolyte, which leads to poor regeneration of the oxidized dye after the electron injection into the conduction band of TiO<sub>2</sub>. The efficiency increased dramatically, more than 10 times, after treating the cell with simulated solar light containing UV irradiation under short circuit condition. By this treatment, the aggregated dye molecules were removed from the surface of the electrode, and the conduction band of TiO<sub>2</sub> was shifted toward more positive potential (by the adsorption of cation from the degradation of either aggregated dye or protons or cations in the redox electrolyte). These two phenomena enhanced the electron injection from the sensitizer to TiO<sub>2</sub> and the regeneration reaction between the oxidized dye and redox electrolyte.

#### Acknowledgments

The authors thank the Swedish Energy Agency and the Knut and Alice Wallenberg foundation for financial support. K. Nonomura appreciates Professor Shogo Mori for fruitful discussion.

#### References

- [1] B. O'Regan and M. Grätzel, "A low-cost, high-efficiency solar cell based on dye-sensitized colloidal TiO<sub>2</sub> films," *Nature*, vol. 353, no. 6346, pp. 737–740, 1991.
- [2] Md. K. Nazeeruddin, A. Kay, I. Rodicio, et al., "Conversion of light to electricity by cis-X2bis(2,2'-bipyridyl-4,4'-dicarboxylate)ruthenium(II) charge-transfer sensitizers (X = Cl-, Br-, I-, CN-, and SCN-) on nanocrystalline TiO<sub>2</sub> electrodes," *Journal of the American Chemical Society*, vol. 115, no. 14, pp. 6382–6390, 1993.
- [3] K.-J. Jiang, N. Masaki, J.-B. Xia, S. Noda, and S. Yanagida, "A novel ruthenium sensitizer with a hydrophobic 2-thiophen-2-yl-vinyl- conjugated bipyridyl ligand for effective dye sensitized TiO<sub>2</sub> solar cells," *Chemical Communications*, no. 23, pp. 2460–2462, 2006.
- [4] D. Kuang, C. Klein, S. Ito, et al., "High-efficiency and stable mesoscopic dye-sensitized solar cells based on a high molar extinction coefficient ruthenium sensitizer and nonvolatile electrolyte," *Advanced Materials*, vol. 19, no. 8, pp. 1133–1137, 2007.
- [5] P. Wang, S. M. Zakeeruddin, J. E. Moser, Md. K. Nazeeruddin, T. Sekiguchi, and M. Grätzel, "A stable quasi-solid-state dye-sensitized solar cell with an amphiphilic ruthenium sensitizer and polymer gel electrolyte," *Nature Materials*, vol. 2, no. 6, pp. 402–407, 2003.
- [6] C. S. Karthikeyan, H. Wietasch, and M. Thelakkat, "Highly efficient solid-state dye-sensitized TiO<sub>2</sub> solar cells using donor-antenna dyes capable of multistep charge-transfer cascades," *Advanced Materials*, vol. 19, no. 8, pp. 1091–1095, 2007.
- [7] Md. K. Nazeeruddin, F. de Angelis, S. Fantacci, et al., "Combined experimental and DFT-TDDFT computational study of photoelectrochemical cell ruthenium sensitizers," *Journal of the American Chemical Society*, vol. 127, no. 48, pp. 16835–16847, 2005.

- [8] K.-J. Jiang, J. Xia, N. Masaki, S. Noda, and S. Yanagida, "Efficient sensitization of nanocrystalline TiO<sub>2</sub> films with high molar extinction coefficient ruthenium complex," *Inorganica Chimica Acta*, vol. 361, no. 3, pp. 783–785, 2008.
- [9] C.-Y. Chen, S.-J. Wu, C.-G. Wu, J.-G. Chen, and K.-C. Ho, "A ruthenium complex with superhigh light-harvesting capacity for dye-sensitized solar cells," *Angewandte Chemie International Edition*, vol. 45, no. 35, pp. 5822–5825, 2006.
- [10] D. Kuang, S. Ito, B. Wenger, et al., "High molar extinction coefficient heteroleptic ruthenium complexes for thin film dye-sensitized solar cells," *Journal of the American Chemical Society*, vol. 128, no. 12, pp. 4146–4154, 2006.
- [11] F. Gao, Y. Wang, D. Shi, et al., "Enhance the optical absorptivity of nanocrystalline TiO<sub>2</sub> film with high molar extinction coefficient ruthenium sensitizers for high performance dye-sensitized solar cells," *Journal of the American Chemical Society*, vol. 130, no. 32, pp. 10720–10728, 2008.
- [12] H. Choi, C. Baik, S. Kim, et al., "Molecular engineering of hybrid sensitizers incorporating an organic antenna into ruthenium complex and their application in solar cells," *New Journal of Chemistry*, vol. 32, no. 12, pp. 2233–2237, 2008.
- [13] S. A. Haque, S. Handa, K. Peter, E. Palomares, M. Thelakkat, and J. R. Durrant, "Supermolecular control of charge transfer in dye-sensitized nanocrystalline TiO<sub>2</sub> films: towards a quantitative structure-function relationship," *Angewandte Chemie International Edition*, vol. 44, no. 35, pp. 5740–5744, 2005.
- [14] D. P. Hagberg, T. Edvinsson, T. Marinado, G. Boschloo, A. Hagfeldt, and L. Sun, "A novel organic chromophore for dye-sensitized nanostructured solar cells," *Chemical Communications*, no. 21, pp. 2245–2247, 2006.
- [15] A. Hagfeldt, G. Boschloo, H. Lindström, et al., "A system approach to molecular solar cells," *Coordination Chemistry Reviews*, vol. 248, no. 13–14, pp. 1501–1509, 2004.
- [16] Md. K. Nazeeruddin, S. M. Zakeeruddin, R. Humphry-Baker, et al., "Acid-base equilibria of (2,2'-bipyridyl-4,4'-dicarboxylic acid)ruthenium(II) complexes and the effect of protonation on charge-transfer sensitization of nanocrystalline titania," *Inorganic Chemistry*, vol. 38, no. 26, pp. 6298–6305, 1999.
- [17] A. Hagfeldt and M. Grätzel, "Molecular photovoltaics," *Accounts of Chemical Research*, vol. 33, no. 5, pp. 269–277, 2000.
- [18] M. Grätzel, "Transition metal complexes as sensitizers for efficient mesoscopic solar cells," *Bulletin of Japan Society of Coordination Chemistry*, vol. 51, pp. 3–12, 2008.
- [19] A. Hagfeldt, U. Björkstén, and M. Grätzel, "Photocapacitance of nanocrystalline oxide semiconductor films: band-edge movement in mesoporous TiO<sub>2</sub> electrodes during UV illumination," *Journal of Physical Chemistry*, vol. 100, no. 20, pp. 8045–8048, 1996.
- [20] S. Ferrere and B. A. Gregg, "Large increases in photocurrents and solar conversion efficiencies by UV illumination of dye sensitized solar cells," *Journal of Physical Chemistry B*, vol. 105, no. 32, pp. 7602–7605, 2001.
- [21] B. A. Gregg, S.-G. Chen, and S. Ferrere, "Enhanced dye-sensitized photoconversion efficiency via reversible production of UV-induced surface states in nanoporous TiO<sub>2</sub>," *Journal of Physical Chemistry B*, vol. 107, no. 13, pp. 3019–3029, 2003.
- [22] Y. Liu, A. Hagfeldt, X.-R. Xiao, and S.-E. Lindquist, "Investigation of influence of redox species on the interfacial energetics of a dye-sensitized nanoporous TiO<sub>2</sub> solar cell," *Solar Energy Materials and Solar Cells*, vol. 55, no. 3, pp. 267–281, 1998.
- [23] N.-G. Park, S.-H. Chang, J. van de Lagemaat, K.-J. Kim, and A. J. Frank, "Effect of cations on the open-circuit photovoltage and the charge-injection efficiency of dye-sensitized nanocrystalline rutile TiO<sub>2</sub> films," *Bulletin of the Korean Chemical Society*, vol. 21, no. 10, pp. 985–988, 2000.
- [24] K. Fredin, J. Nissfolk, G. Boschloo, and A. Hagfeldt, "The influence of cations on charge accumulation in dye-sensitized solar cells," *Journal of Electroanalytical Chemistry*, vol. 609, no. 2, pp. 55–60, 2007.
- [25] G. Boschloo and A. Hagfeldt, "Photoinduced absorption spectroscopy of dye-sensitized nanostructured TiO<sub>2</sub>," *Chemical Physics Letters*, vol. 370, no. 3–4, pp. 381–386, 2003.
- [26] G. Boschloo and A. Hagfeldt, "Photoinduced absorption spectroscopy as a tool in the study of dye-sensitized solar cells," *Inorganica Chimica Acta*, vol. 361, no. 3, pp. 729–734, 2008.

## Research Article

# Computational Study of 3,4-Diphenyl-1,2,5-Thiadiazole 1-Oxide for Organic Photovoltaics

**Daniel Glossman-Mitnik**

*Grupo NANOCOSMOS, Centro de Investigación en Materiales Avanzados, SC, Miguel de Cervantes 120, Complejo Industrial Chihuahua, Chihuahua, Chih. 31109, Mexico*

Correspondence should be addressed to Daniel Glossman-Mitnik, daniel.glossman@cimav.edu.mx

Received 26 July 2009; Revised 28 October 2009; Accepted 31 October 2009

Recommended by Mohamed Sabry Abdel-Mottaleb

We make use of a model chemistry within Density Functional Theory (DFT) recently presented, which is called CHIH-DFT, to calculate the molecular structure of 3,4-diphenyl-1,2,5-thiadiazole 1-oxide (TSO), as well to predict its infrared (IR), ultraviolet (UV-Vis) and fluorescence (Fluo) spectra, the dipole moment and polarizability, the free energy of solvation in different solvents as an indication of solubility, and the chemical reactivity parameters that arise from Conceptual DFT. The calculated values are compared with the available experimental data for this molecule as a means of validation of our proposed model chemistry.

Copyright © 2009 Daniel Glossman-Mitnik. This is an open access article distributed under the Creative Commons Attribution License, which permits unrestricted use, distribution, and reproduction in any medium, provided the original work is properly cited.

## 1. Introduction

Since the dawn of history, man has been fascinated by the Sun, the provider of the light and warmth that sustains life on Earth. In preindustrial times, our major sources of energy wood, wind and water power derived from solar energy. The subsequent discovery and massive exploitation of fossil fuels laid down in the Earth's crust by early aeons of photosynthetic activity have conditioned the developed world to be dependent on convenient, readily available energy [1].

Despite much effort, semiconductor photovoltaic devices made with traditional inorganic semiconductors have remained sufficiently expensive that their uses are confined to a number of niches. Much effort is currently directed towards the use of thin-film semiconductors, in place of silicon wafers, since the direct fabrication of thin devices on substrates offers the prospect of lower manufacturing costs, particularly for larger area applications. An alternative approach is the use of organic, molecular semiconductors, which can be processed over large areas at relatively low temperatures, either by vacuum sublimation of molecular materials, or, preferably, by processing from solution of film-forming materials such as polymers [2].

The objective of this work is to perform a detailed calculation of the molecular structure of 3,4-diphenyl-1,2,5-thiadiazole 1-oxide (TSO), as well as to predict its infrared (IR), ultraviolet (UV-Vis), fluorescence (Fluo) spectra, some physical properties related to solubility and the chemical reactivity, by using a model chemistry within Density Functional Theory (DFT) [3] specially tailored to study heterocyclic systems [4] and to validate the calculated results by comparison with the available experimental data related to the molecular structure for this molecule. This compound has several desirable characteristics related to its use in Organic Photovoltaics and OLEDs: (i) it contains the 1,2,5-thiadiazole 1-oxide group, with molecular parameters similar to the thiophene 1-oxide derivatives that have been shown to be useful as nanostructured molecular materials; (ii) the  $\pi$ -conjugated derivatives are generally efficient fluorophores, and as such, useful for the fabrication of nanobiosensors; (iii) it can be used as an attractive building block for Organic Molecular Materials.

## 2. Theory and Computational Details

All computational studies were performed with the Gaussian 03W [5] series of programs with density functional methods

as implemented in the computational package. The equilibrium geometries of the molecules were determined by means of the gradient technique. The force constants and vibrational frequencies were determined by the FREQ calculations on the stationary points obtained after the optimization to check if there were true minima. Density functionals used in this study are a modification of those incorporated in the Gaussian 03W computational package [5]. To this end, we have defined a new model chemistry that we have found empirically that works well with heterocyclic molecules. The model was found by trial and error determination of the molecular structure of several heterocycles and a comparison with the experimental results. The implementation is a slight different version of the PBE0 hybrid density functional [6, 7]. In the PBE0 (or PBE1PBE one-parameter) functional, there is only one coefficient which is theoretically adjusted to 0.25, reflecting the mix of Hartree-Fock or exact exchange and the DFT exchange which is represented by the PBE density functional [8]. The correlation part is also represented by the PBE correlation functional [8] with coefficient equal to one. Our proposed density functional model, which we have called PBEg, is the same as PBE0, but with the mixing coefficient  $g$  which adopts different values depending on the number of heteroatoms in the studied molecule, or, in turn, of its molecular structure. The value of  $g$  can be calculated through the following empirical formula:  $g = 0.02 + 0.14 \times \text{FHA} \times \text{FV} + 0.03 \times \text{AHA}$ , where FHA is the first heteroatom chosen as the one less electronegative, FV is valence factor which represents the oxidation state of the FHA (i.e., 1 for the first oxidation state, two for the second, and so on), and AHA is the number of additional heteroatoms besides the FHA. FHA is always equal to one. This formula has been empirically found by studying a large number of heterocyclic compounds with different number of heteroatoms and oxidation states. For example, for the 1,2,5-thiadiazole molecule, the  $g$  coefficient will be  $g = 0.02 + 0.14 \times 1 + 0.03 \times 2 = 0.22$ , thus implying that 22% of HF exchange will be mixed with 78% of PBE exchange. Similarly, for 1,2,5-thiadiazole 1,1-dioxide, the  $g$  coefficient will be  $g = 0.02 + 0.14 \times 3 + 0.03 \times 2 = 0.50$ , reflecting 50% of HF exchange and 50% of PBE exchange. For those cases in which the molecule has several heterocyclic rings, we will calculate the coefficient  $g$  by averaging the coefficient for each heterocycle. As it is evident, the bounds to the empirical formula are 0 and 1 meaning no mixing of HF exchange in the first case and a purely HF model in the last case. The reasons for the dependence of the mix of HF and DFT exchange with the number of heteroatoms and their oxidation state are not apparent, but the validity of the empirical formula have been computationally assessed for several different molecular systems [4, 9–20]. Based on these results it is clear that our choice of this particular functional has been done because its performance is superior to other methods both in accuracy and computational cost.

A model chemistry is an unbiased, uniquely defined, and uniformly applicable theoretical model for predicting the properties of chemical systems. A model chemistry generally consists of the combination of a theoretical method with a basis set [21–30]. In order to define our model chemistry,

we have to couple the proposed density functional with one or more basis sets. In this way, the new model chemistry that we have called CHIH-DFT can be represented by the expression  $\text{CHIH} = \text{PBEg}/\text{basis sets}$ . There are three different CHIH-DFT model chemistries: CHIH(small) that uses the 3-21G\* basis set for geometry optimizations and frequency calculations, and the CBSB2\*\* basis set for the calculation of the electronic properties; CHIH(medium) that uses the CBSB2\*\* basis set for geometry optimizations and frequency calculations and the CBSB4 basis set for the electronic properties; and CHIH(large) which uses the CBSB7 basis set for geometry optimizations and frequency calculations and the CBSB1 basis set for the electronic properties. In this way, by considering a compromise between accuracy and CPU time, the CHIH(large) will be used for small heterocyclic molecules, the CHIH(medium) for medium-sized molecules and the CHIH(small) for large heterocyclic molecules. We understand that a molecule is small when the number of atoms within the cycle is five or six. When the number of atoms in the cycle is more than six, we considered it a medium-sized molecule. If there is more than one cycle, or if there are a large number of side-chain radical substituents, we say that the molecule is large. The CHIH-DFT model chemistry has been already validated for the case of antiparasitic drugs [9–11], flavonoids [12–14], organic corrosion inhibitors [15–17], alkaloids [18, 19] and antitubercular drugs [20]. Thus, in our case for the 3,4-diphenyl-1,2,5-thiadiazole 1-oxide molecule (TSO), the value of the mixing will be  $g = 0.36$ , implying that 36% of Hartree-Fock (HF) exchange is mixed with 64% of DFT exchange. The correlation part is taken as the PBE correlation functional with coefficient equal to one [8].

For the purpose of comparison, the molecular structure of the molecule has been computed using different model chemistries. Additional density functionals used in this study, are LSDA or SVWN [31, 32], BLYP [33, 34], B3LYP [34, 35], B3PW91 [35, 36], PBEPBE [8], PBE0 [7], TPSSPSS [37] and TPSSh [38]. A suitable description of these density functionals is provided in some of the most important Computational Chemistry recent books [25, 27, 39, 40].

The calculation of the ultraviolet (UV-Vis) and fluorescence (Fluo) spectra of 3,4-diphenyl-1,2,5-thiadiazole 1-oxide (TSO) has been performed by solving the time dependent Kohn-Sham equations according to the method implemented in Gaussian 03W [39, 41–43]. The equations have been solved for 10 excited states.

The infrared (IR), ultraviolet (UV-Vis), and fluorescence (Fluo) spectra were calculated and visualized using the Swizard program [44]. In all cases the displayed spectra show the calculated frequencies and absorption or emission wavelengths.

### 3. Results and Discussion

The results for the equilibrium conformation of the neutral molecule of 3,4-diphenyl-1,2,5-thiadiazole 1-oxide (or TSO, for short) calculated with the CHIH(small) model chemistry are presented in Figure 1 through a representation

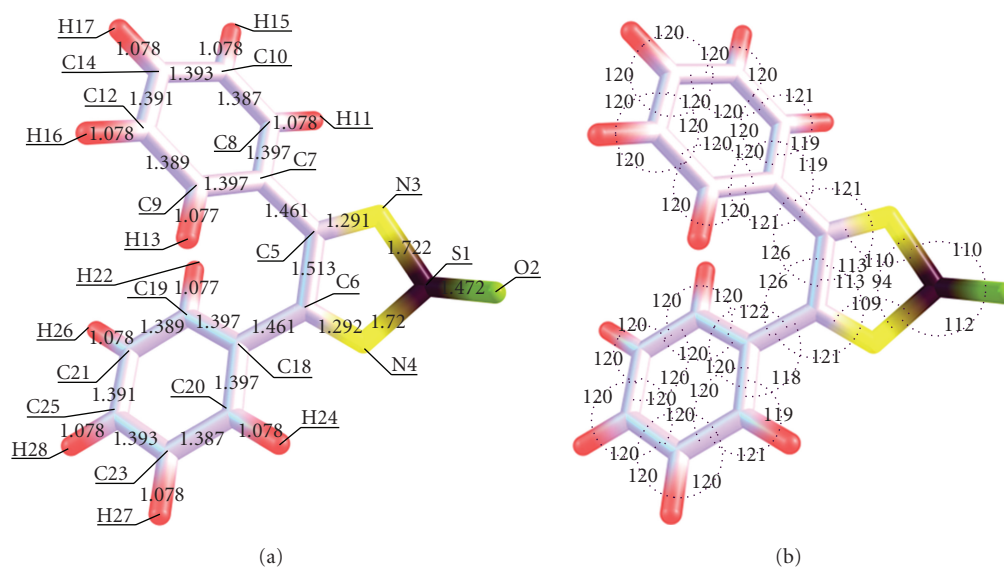


FIGURE 1: Interatomic bond distances (Å) and bond angles (deg) for 3,4-diphenyl-1,2,5-thiadiazole 1-oxide.

of the molecular structure showing the atomic labelling and numbering as well as the interatomic bond lengths and angles. The results have been compared with the experimental X-ray crystallography determination of the molecular structure of TSO [45]. The agreement is generally good: the standard error of the differences between the experimental and the calculated bond lengths and bond angles being very low. Although not shown in Figure 1, an analysis of the torsional angles reveals that the heterocycle is almost planar. The good agreement with the experimental data is more noticeable for the heterocyclic ring, because the model have been parameterized for this kind of systems [4].

As an additional comparison, we have calculated the optimized structure of the studied molecule, using several different common density functionals (local, nonlocal GGA, hybrid, meta-GGA and meta-GGA hybrid) coupled with the CBSB2\*\* basis set. The molecular structure obtained from each calculation was compared with the experimental results by aligning both structures and calculating the Root Mean-Square Deviation (RMSD). The results can be summarized as follows: CHIH(small) = 0.026, PBE0 = 0.033, TPSSH = 0.049, B3LYP = 0.054, LSDA = 0.066, TPSS = 0.053, PBEPBE = 0.053, BLYP = 0.087. It can be concluded that the CHIH(small) model chemistry performs better than other hybrids functionals and even better than a recently proposed hybrid meta-GGA functional. The behavior of CHIH(small) and is similar and better than local and nonhybrids functionals. This is remarkable if we consider that this model chemistry is more efficient from a computational point of view.

The molecular dipole moment is perhaps the simplest experimental measure of charge distribution in a molecule. The accuracy of the overall distribution of electrons in a molecule is hard to quantify, since it involves all the multipoles. From the present calculations, the total energy,

the total dipole moment and the isotropic polarizability of the ground state with the CHIH(small) model chemistry are  $-1121.415$  au,  $6.9576$  Debye, and  $66.94$  Bohr<sup>3</sup> for the TSO molecule. These results could be of interest as an indication of the solubility and chemical reactivity of the studied molecule, not only for its synthesis but for the potential polymerization as a step in its use in organic electronics and photovoltaics.

The infrared spectrum (IR) for the TSO molecule calculated with the CHIH(small) model chemistry is displayed in Figure 2. To the best of our knowledge, the experimental spectrum has not been reported in the literature. The vibrational band assignments have been done using the ChemCraft for Windows molecular visualization program. The symmetric vibration of the SO group has been found at  $1225$  cm<sup>-1</sup>. The symmetric stretching of the C=N double bonds is located at  $1595$  cm<sup>-1</sup>. At  $1319$  cm<sup>-1</sup> there is a signal belonging to heterocyclic C-C symmetric stretching, while at  $752$  cm<sup>-1</sup> there is a strong peak that corresponds to the vibrations of all the aromatic ring hydrogens. These are by far the most intense signals in the IR spectrum. There are two signals at  $549$  and  $599$  cm<sup>-1</sup> that belong to the asymmetric and symmetric stretching of the S-N bonds. At  $835$  cm<sup>-1</sup> there is a signal related to the vibrations of only three of the hydrogens of the benzenic rings. The asymmetric and symmetric out-of-plane vibrations of the aromatic ring carbons can be observed at  $1070$  and  $1136$  cm<sup>-1</sup>, respectively. The peak at  $999$  cm<sup>-1</sup> belongs to the vibrations of the C-N-S of the thiadiazole moiety. Finally, the symmetric and asymmetric in-plane vibrations of the aromatic ring carbons are observed at  $1549$  and  $1675$  cm<sup>-1</sup>.

As the experimental IR spectrum has not been reported, the scaling factor could not be calculated. However, from our experience based on previous calculations with similar molecules [4], it is possible to say that the scaling factor

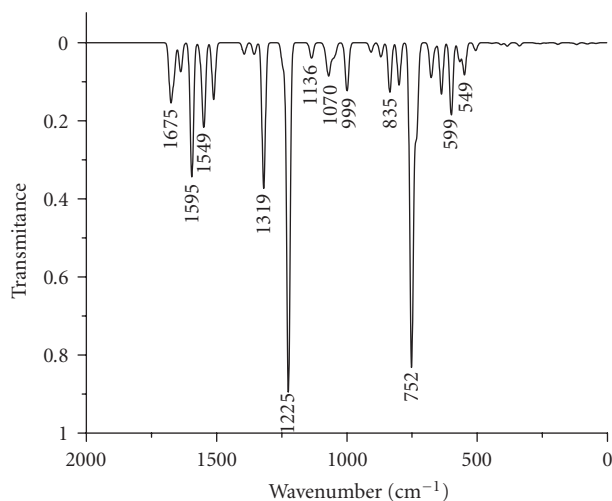


FIGURE 2: Infrared spectrum (IR) of the TSO molecule calculated with the CHIH-DFT(small) model chemistry.

will be between 0.97 and 1. Thus, it is expected that the model chemistry used in this work could reproduce the experimental spectrum of the TSO molecule with a certain degree of accuracy.

The ultraviolet spectrum (UV-Vis) of the TSO molecule calculated with the CHIH(small) model chemistry is displayed in Figure 3. The results for the energy of the excitations and the oscillator strengths computed for the ten low-lying singlet excited states are presented in Table 1. In order to characterize the excited state transitions presented in Table 1, we performed an analysis of all the molecular orbitals involved, taking into consideration that orbital 66 is the HOMO and orbital 67 is the LUMO. For example, in alpha molecular orbital 66 (occupied,  $E = -0.038439$ ) main atomic orbitals are: N22 (Px on atom O2) [0.462], N26 (Px on atom O2) [0.429]. In alpha molecular orbital 67 (unoccupied,  $E = 0.035442$ ) main atomic orbitals are: N24 (Pz on atom O2) [0.439], N28 (Pz on atom O2) [0.438]. This means that the HOMO has a  $\pi$  character, while the LUMO has a  $\pi^*$  character. On the basis of the above analysis of transitions and MOs, it can be said that the absorption bands of TSO in the visible and UV regions are typical  $\pi$ - $\pi^*$  transitions.

As the HOMO-LUMO transition takes place in the ultraviolet region, close to but out of the visible zone, it can be predicted that this molecule will be colorless or slightly colored. In order to calculate the fluorescence spectrum of the studied molecule, the first singlet excited state was optimized by using the CIS/3-21G(d) model chemistry. The results of a TDDFT calculation at the CHIH(small) model chemistry on the optimized singlet excited state are not shown but reported as the fluorescent spectrum, where the HOMO-LUMO transition takes place at 613 nm, being this signal very weak. This means that the studied molecule will present fluorescence in the visible region. Thus, it could be of potential application for the fabrication of OLEDs.

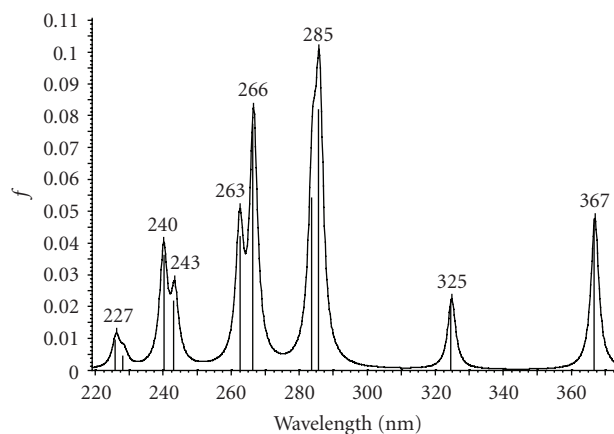


FIGURE 3: UV-Vis spectrum of the TSO molecule calculated with the CHIH-DFT(small) model chemistry.

The free energy of solvation  $\Delta G(\text{solv})$  of the molecule have been calculated for TSO by resorting to the CHIH(small) model chemistry coupled with the Integral-Equation-Formalism of the Polarized Continuum Model (IEF-PCM) for different solvents as implemented in Gaussian 03. The solubility of a molecule will depend on several kinetic and thermodynamic factors. However, it can be said that the magnitude and the sign of  $\Delta G(\text{solv})$  could be a good approximation as an index of solubility. In this way, a negative sign and a large magnitude will be an indication of increased solubility. The results of these calculations for the studied molecule can be summarized as follows: Chloroform =  $-4.56$  Kcal/mol, Cyclohexane =  $-2.75$  kcal/mol, Ethanol =  $-10.30$  Kcal/mol, THF =  $-5.18$  Kcal/mol, Toluene =  $-2.33$  Kcal/mol, and Water =  $-5.20$  Kcal/mol. These values could be an indication that the studied molecule will be mostly soluble in ethanol, and this can be related to the results obtained for the dipole moment and polarizability.

The HOMO and LUMO of TSO calculated with the CHIH(small) model chemistry are displayed in Figure 4. The HOMO density corresponds to the nitrogens, the oxygen and some carbon atoms of the nonheterocyclic rings, while the LUMO density is over the whole molecule. This can give us an idea of the reactivity of the molecule.

The reactive sites can be identified through an analysis of the total and orbital densities. The representation of the calculated HOMO and LUMO densities in Figure 4 show that the electrophilic attack would occur preferentially at the nitrogens and the nucleophilic attack at the heterocyclic ring carbons.

The condensed Fukui functions can also be employed to determine the reactivity of each atom in the molecule. The corresponding condensed functions are given by  $f_k^+ = q_k(N+1) - q_k(N)$  (for nucleophilic attack),  $f_k^- = q_k(N) - q_k(N-1)$  (for electrophilic attack), and  $f_k^0 = [q_k(N+1) - q_k(N-1)]/2$  (for radical attack), where  $q_k$  is the gross charge of atom  $k$  in the molecule.

It is possible to evaluate condensed Fukui functions from single-points calculations directly, without resorting to

TABLE 1: Excitation energies and oscillator strengths of 3,4-diphenyl-1,2,5-thiadiazole 1-oxide calculated by using TDDFT and the CHIH(small) model chemistry.

Excited State	1:	Singlet-A	3.3786 eV	366.97 nm	$f = 0.0477$
63 → 67		0.22354			
65 → 67		0.14980			
66 → 67		0.60774			
Excited State	2:	Singlet-A	3.8166 eV	324.85 nm	$f = 0.0222$
61 → 67		0.41771			
63 → 67		0.22445			
64 → 67		0.17251			
65 → 67		0.41396			
66 → 67		-0.11265			
Excited State	3:	Singlet-A	4.3360 eV	285.94 nm	$f = 0.0819$
63 → 67		-0.31629			
64 → 67		0.56550			
66 → 67		0.19535			
Excited State	4:	Singlet-A	4.3668 eV	283.93 nm	$f = 0.0543$
61 → 67		-0.12090			
63 → 67		-0.40626			
64 → 67		-0.24884			
65 → 67		0.45779			
Excited State	5:	Singlet-A	4.6504 eV	266.61 nm	$f = 0.0774$
60 → 67		0.11497			
61 → 67		0.34959			
62 → 67		0.40642			
63 → 67		-0.23124			
64 → 67		-0.18987			
65 → 67		-0.20023			
66 → 67		0.14139			
Excited State	6:	Singlet-A	4.7230 eV	262.51 nm	$f = 0.0422$
61 → 67		-0.31143			
62 → 67		0.52106			
63 → 67		0.19105			
64 → 67		0.11226			
64 → 68		-0.10636			
Excited State	7:	Singlet-A	5.0935 eV	243.41 nm	$f = 0.0219$
58 → 67		0.10081			
59 → 67		0.17992			
60 → 67		0.39836			
61 → 67		-0.15856			
66 → 68		0.45570			
Excited State	8:	Singlet-A	5.1635 eV	240.12 nm	$f = 0.0363$
58 → 67		0.12525			
60 → 67		0.47276			
66 → 68		-0.44998			
Excited State	9:	Singlet-A	5.4269 eV	228.46 nm	$f = 0.0046$
59 → 67		0.57372			
61 → 67		0.14968			
64 → 68		0.10981			
66 → 68		-0.18025			
Excited State	10:	Singlet-A	5.4817 eV	226.18 nm	$f = 0.0097$
59 → 67		-0.12433			
62 → 67		0.19734			
62 → 71		0.12404			
63 → 68		0.14583			
63 → 69		-0.16390			
63 → 70		-0.11249			
64 → 68		0.49784			
65 → 68		-0.14970			
65 → 70		0.11729			
66 → 69		0.25687			

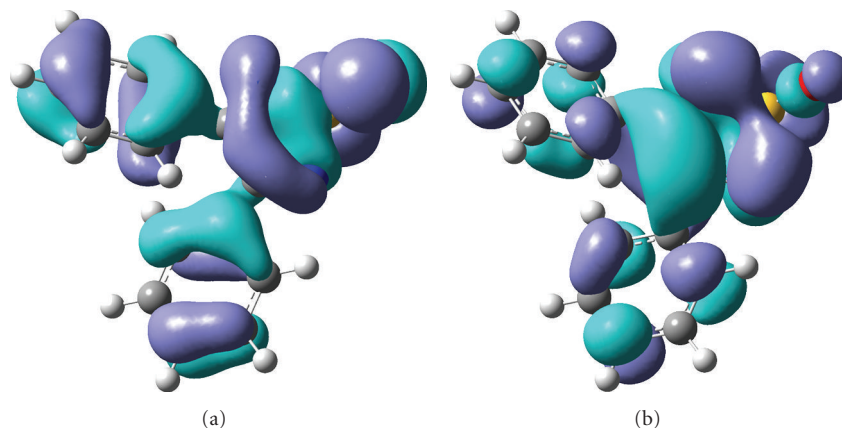


FIGURE 4: HOMO and LUMO of the TSO molecule calculated with the CHIH-DFT model chemistry.

additional calculations involving the systems with  $N - 1$  and  $N + 1$  electrons:

$$f_k^+ = \sum_{a \in k} \left[ c_{ai}^2 + c_{ai} \sum_{b \neq a} c_{bi} S_{ab} \right] \quad (\text{where } i = \text{LUMO}),$$

$$f_k^- = \sum_{a \in k} \left[ c_{ai}^2 + c_{ai} \sum_{b \neq a} c_{bi} S_{ab} \right] \quad (\text{where } i = \text{HOMO})$$
(1)

with  $c_{ai}$  being the LCAO coefficients and  $S_{ab}$  the overlap matrix. The condensed Fukui functions are normalized, thus  $\sum_k f_k = 1$  and  $f_k^0 = [f_k^+ + f_k^-]/2$ .

The results from the calculation of the condensed Fukui functions for nucleophilic, electrophilic, and radical attack have been obtained by resorting to the AOMix molecular analysis program [46] and are presented in Table 2.

The sites for electrophilic attack will be those atoms bearing a negative charge and where the Fukui function  $f_k^-$  is a maximum. These values confirm that the site for the electrophilic attack is the oxygen atom. The site for potential nucleophilic attack would depend on the values of  $f_k^+$  on the atoms with a positive charge density. The results from Table 1 show that the site for nucleophilic attack will be the nitrogen atoms and also the heterocyclic carbon atoms. Finally, the sites for radical attack, governed by the values of  $f_k^0$  will be the oxygen atom, and perhaps the sulfur atom. The benzenic rings are not very reactive in this context.

#### 4. Conclusions

In this work, our model chemistry within DFT (the CHIH-DFT chemistry model) has been presented and the methodology has been applied to the study of a molecule which is potentially useful for OLEDs and photovoltaic devices. The molecular structure for TSO has been determined by using the CHIH(small) model chemistry. A comparison has been made with the results from the experimental X-ray crystallography for this molecule. The agreement is generally very good. It is worth noting that the results obtained with the (faster) CHIH(small) model chemistry are very

TABLE 2: Condensed Fukui functions calculated by using the CHIH(small) model chemistry and through the AOMIX molecular analysis program.

Atom	$f_k^+$	$f_k^-$	$f_k^0$
1 S	0.0099	0.2253	0.1176
2 O	0.0022	0.2999	0.1511
3 N	0.1758	0.0071	0.0915
4 N	0.1794	0.0025	0.0910
5 C	0.1486	0.0023	0.0755
6 C	0.1533	0.0028	0.0781
7 C	0.0009	0.0070	0.0039
8 C	0.0028	0.0018	0.0023
9 C	0.0026	0.0028	0.0027
10 C	0.0012	0.0155	0.0083
11 H	0.0003	0.0001	0.0002
12 C	0.0046	0.0079	0.0062
13 H	0.0006	0.0006	0.0006
14 C	0.0318	0.0572	0.0445
15 H	0.0001	0.0003	0.0002
16 H	0.0002	0.0001	0.0002
17 H	0.0003	0.0004	0.0004
18 C	0.0011	0.0042	0.0026
19 C	0.0295	0.0269	0.0282
20 C	0.0333	0.0057	0.0195
21 C	0.0045	0.0015	0.0030
22 H	0.0008	0.0003	0.0005
23 C	0.0016	0.0177	0.0096
24 H	0.0004	0.0001	0.0003
25 C	0.0387	0.0345	0.0361
26 H	0.0001	0.0004	0.0002
27 H	0.0001	0.0001	0.0001
28 H	0.0004	0.0002	0.0003

similar to those obtained using the PBE0 functional with a CBSB7 basis set, thus implying that equally accurate results could be obtained in a reasonable time in the study of

heterocycles. A general comparison with the results from the optimization of the molecular structure using several different density functionals have also been performed and the conclusion is that the CHIH-DFT is a good alternative to other model chemistries based on hybrids GGA and meta-GGA functionals for the prediction of molecular structures.

The shape of the frontier orbitals of this molecule were displayed as well as some electronic parameters like the total energy, the dipole moment and the polarizability. Moreover, the calculation of the condensed Fukui functions can be useful to obtain an idea of the chemical reactivity of the studied molecule. This is of special importance if we consider that the studied molecule could be the starting point for a polymeric material of potential application in organic electronics and photovoltaics, and that the chemical reactivity indices could assist the experimentalists in planning and guiding the synthetic and polymerization processes.

The infrared (IR) and ultraviolet (UV-Vis) and fluorescence (Fluo) spectra for TSO have been predicted according to the CHIH(small) model chemistry, and an assignment of the principal peaks have been achieved. The shape of the UV-Vis spectra and the maximum absorption wavelength belonging to this molecule have been presented and this have been compared with the fluorescence spectra. The results showed that the studied molecule could be an useful starting point for the preparation of materials of use in organic electronic and photovoltaics.

The free energy of solvation  $\Delta G(\text{solv})$  of the molecule have been calculated for TSO by resorting to the CHIH(small) model chemistry coupled with the Integral-Equation-Formalism of the Polarized Continuum Model (IEF-PCM) for different solvents and the results gave an indication of ethanol as the solvent in which this molecule could be potentially soluble.

The CHIH-DFT model chemistry appears to be a useful tool for the study of the molecular structure and electronic properties of heterocycles, and further applications to several molecular systems are being pursued in our laboratory.

## Acknowledgments

This work has been partially supported by Consejo Nacional de Ciencia y Tecnología (CONACYT, Mexico) and by Fondo Mixto del Estado de Baja California (FOMIX-BC) through Project 69363. The author is a researcher of CONACYT and CIMAV.

## References

- [1] M. D. Archer and R. Hill, *Clean Electricity from Photovoltaics*, Imperial College Press, London, UK, 2001.
- [2] J. J. M. Halls and R. H. Friend, "Organic photovoltaic devices," in *Clean Electricity from Photovoltaics*, M. D. Archer and R. Hill, Eds., Imperial College Press, London, UK, 2001.
- [3] R. G. Parr and W. Yang, *Density Functional Theory of Atoms and Molecules*, Oxford University Press, New York, NY, USA, 1989.
- [4] D. Glossman-Mitnik, "CHIH-DFT determination of the molecular structure and infrared and ultraviolet spectra of azathiophenes," *Theoretical Chemistry Accounts*, vol. 117, no. 1, pp. 57–68, 2007.
- [5] M. J. Frisch, G. W. Trucks, H. B. Schlegel, et al., *Gaussian 03, Revision E.01*, Gaussian, Inc., Wallingford, Conn, USA, 2004.
- [6] M. Ernzerhof and G. E. Scuseria, "Assessment of the Perdew-Burke-Ernzerhof exchange-correlation functional," *Journal of Chemical Physics*, vol. 110, no. 11, pp. 5029–5036, 1999.
- [7] C. Adamo, "Toward reliable density functional methods without adjustable parameters: the PBE0 model," *Journal of Chemical Physics*, vol. 110, no. 13, pp. 6158–6170, 1999.
- [8] J. P. Perdew, K. Burke, and M. Ernzerhof, "Generalized gradient approximation made simple," *Physical Review Letters*, vol. 77, no. 18, pp. 3865–3868, 1996.
- [9] N. Flores-Holguín and D. Glossman-Mitnik, "CHIH-DFT determination of the molecular structure, infrared and ultraviolet spectra of the antiparasitic drug megalol," *Journal of Molecular Structure: THEOCHEM*, vol. 681, no. 1–3, pp. 77–82, 2004.
- [10] N. Flores-Holguín and D. Glossman-Mitnik, "CHIH-DFT determination of the electrical, optical, and magnetic properties and NICS aromaticity of megalol," *Journal of Molecular Structure: THEOCHEM*, vol. 717, no. 1–3, pp. 1–3, 2005.
- [11] N. Flores-Holguín and D. Glossman-Mitnik, "CHIH-DFT determination of the reactivity sites of the antiparasitic drug megalol," *Journal of Molecular Structure: THEOCHEM*, vol. 723, no. 1–3, pp. 231–234, 2005.
- [12] A. M. Mendoza-Wilson and D. Glossman-Mitnik, "CHIH-DFT determination of the molecular structure, infrared and ultraviolet spectra of the flavonoid quercetin," *Journal of Molecular Structure: THEOCHEM*, vol. 681, no. 1–3, pp. 71–76, 2004.
- [13] A. M. Mendoza-Wilson and D. Glossman-Mitnik, "CHIH-DFT study of the electronic properties and chemical reactivity of quercetin," *Journal of Molecular Structure: THEOCHEM*, vol. 716, no. 1–3, pp. 67–72, 2005.
- [14] A.M. Mendoza-Wilson and D. Glossman-Mitnik, "Theoretical study of the molecular properties and chemical reactivity of (+)-catechin and (–)-epicatechin related to their antioxidant ability," *Journal of Molecular Structure: THEOCHEM*, vol. 761, no. 1–3, pp. 97–106, 2006.
- [15] L. M. Rodríguez-Valdez, A. Martínez-Villafañe, and D. Glossman-Mitnik, "CHIH-DFT determination of the molecular structure, infrared and ultraviolet spectra of potentially organic corrosion inhibitors," *Journal of Molecular Structure: THEOCHEM*, vol. 681, no. 1–3, pp. 83–88, 2004.
- [16] L. M. Rodríguez-Valdez, A. Martínez-Villafañe, and D. Glossman-Mitnik, "CHIH-DFT theoretical study of isomeric thiazoles and their potential activity as corrosion inhibitors," *Journal of Molecular Structure: THEOCHEM*, vol. 716, no. 1–3, pp. 61–65, 2005.
- [17] L. M. Rodríguez-Valdez, W. Villamizar, M. Casales, et al., "Computational simulations of the molecular structure and corrosion properties of amidoethyl, aminoethyl and hydroxyethyl imidazoles inhibitors," *Corrosion Science*, vol. 48, no. 12, pp. 4053–4064, 2006.
- [18] D. Glossman-Mitnik, "CHIH-DFT determination of the molecular structure and IR and UV spectra of solanidine," *Journal of Molecular Modeling*, vol. 13, no. 1, pp. 43–46, 2007.
- [19] D. Glossman-Mitnik, "CHIH-DFT determination of the molecular structure and infrared and ultraviolet spectra of  $\gamma$ -solanine," *Spectrochimica Acta Part A*, vol. 66, no. 1, pp. 208–211, 2007.
- [20] A. Favila, M. Gallo, and D. Glossman-Mitnik, "CHIH-DFT determination of the molecular structure infrared spectra,

- UV spectra and chemical reactivity of three antitubercular compounds: rifampicin, isoniazid and pyrazinamide,” *Journal of Molecular Modeling*, vol. 13, no. 4, pp. 505–518, 2007.
- [21] W. J. Hehre, L. Radom, P. V. Schleyer, and J. Pople, *Ab Initio Molecular Orbital Theory*, Wiley-Interscience, New York, NY, USA, 1986.
- [22] J. B. Foresmand and A. Frisch, *Exploring Chemistry with Electronic Structure Methods*, chapter 4, Gaussian, Inc., Wallingford, Conn, USA, 2nd edition, 1996.
- [23] P. R. Westmoreland, P. A. Kollman, A. M. Chaka, et al., Eds., *Applications of Molecular and Materials Modeling*, Springer, Berlin, Germany, 2002.
- [24] A. Hinchliffe, Ed., *Chemical Modelling: Applications and Theory*, vol. 5, The Royal Society of Chemistry, London, UK, 2008.
- [25] D. Young, *Computational Chemistry: A Practical Guide for Applying Techniques to Real-World Problems*, John Wiley & Sons, New York, NY, USA, 2001.
- [26] S. M. Bachrach, *Computational Organic Chemistry*, John Wiley & Sons, New York, NY, USA, 2007.
- [27] C. J. Cramer, *Essentials of Computational Chemistry: Theories and Models*, John Wiley & Sons, Chichester, UK, 2002.
- [28] J. M. Seminario and P. Politzer, Eds., *Modern Density Functional Theory: A Tool for Chemistry*, Elsevier, Amsterdam, The Netherlands, 1995.
- [29] A. Hinchliffe, *Molecular Modelling for Beginners*, John Wiley & Sons, New York, NY, USA, 2nd edition, 2008.
- [30] C. E. Dykstra, G. Frenking, K. S. Kim, and G. E. Scuseria, *Theory and Applications of Computational Chemistry: The First Forty Years*, Elsevier, Amsterdam, The Netherlands, 2005.
- [31] J. C. Slater, *Quantum Theory of Molecular and Solids, Vol. 4: The Self-Consistent Field for Molecular and Solids*, McGraw-Hill, New York, NY, USA, 1974.
- [32] S. H. Vosko, L. Wilk, and M. Nusair, “Accurate spin-dependent electron liquid correlation energies for local spin density calculations: a critical analysis,” *Canadian Journal of Physics*, vol. 58, no. 8, pp. 1200–1211, 1980.
- [33] A. D. Becke, “Density-functional exchange-energy approximation with correct asymptotic behavior,” *Physical Review A*, vol. 38, no. 6, pp. 3098–3100, 1988.
- [34] C. Lee, W. Yang, and R. G. Parr, “Development of the Colle-Salvetti correlation-energy formula into a functional of the electron density,” *Physical Review B*, vol. 37, no. 2, pp. 785–789, 1988.
- [35] A. D. Becke, “Density-functional thermochemistry—part III: the role of exact exchange,” *The Journal of Chemical Physics*, vol. 98, no. 7, pp. 5648–5652, 1993.
- [36] J. P. Perdew, J. A. Chevary, S. H. Vosko, K. A. Jackson, M. R. Pederson, D. J. Singh, and C. Fiolhais, “Atoms, molecules, solids, and surfaces: applications of the generalized gradient approximation for exchange and correlation,” *Physical Review B*, vol. 46, no. 11, pp. 6671–6687, 1992.
- [37] J. Tao, J. P. Perdew, V. N. Staroverov, and G. E. Scuseria, “Climbing the density functional ladder: nonempirical meta-generalized gradient approximation designed for molecules and solids,” *Physical Review Letters*, vol. 91, no. 14, Article ID 146401, 4 pages, 2003.
- [38] V. N. Staroverov, G. E. Scuseria, J. Tao, and J. P. Perdew, “Comparative assessment of a new nonempirical density functional: molecules and hydrogen-bonded complexes,” *Journal of Chemical Physics*, vol. 119, no. 23, pp. 12129–12137, 2003.
- [39] E. Lewars, *Computational Chemistry: Introduction to the Theory and Applications of Molecular and Quantum Mechanics*, Kluwer Academic Publishers, Norwell, Mass, USA, 2003.
- [40] F. Jensen, *Introduction to Computational Chemistry*, John Wiley & Sons, Chichester, UK, 2007.
- [41] R. E. Stratmann, G. E. Scuseria, and M. J. Frisch, “An efficient implementation of time-dependent density-functional theory for the calculation of excitation energies of large molecules,” *Journal of Chemical Physics*, vol. 109, no. 19, pp. 8218–8224, 1998.
- [42] R. Bauernschmitt and R. Ahlrichs, “Treatment of electronic excitations within the adiabatic approximation of time dependent density functional theory,” *Chemical Physics Letters*, vol. 256, no. 4-5, pp. 454–464, 1996.
- [43] M. E. Casida, C. Jamorski, K. C. Casida, and D. R. Salahub, “Molecular excitation energies to high-lying bound states from time-dependent density-functional response theory: characterization and correction of the time-dependent local density approximation ionization threshold,” *Journal of Chemical Physics*, vol. 108, no. 11, pp. 4439–4449, 1998.
- [44] S. I. Gorelsky, “SWizard program,” <http://www.sg-chem.net/>.
- [45] E. E. Castellano, O. E. Piro, J. A. Caram, et al., “Crystallographic study and molecular orbital calculations of thiadiazole derivatives. 2. 3,4-diphenyl-1,2,5-thiadiazole 1-monoxide,” *Journal of Molecular Structure*, vol. 604, no. 2-3, pp. 195–203, 2002.
- [46] S. I. Gorelsky, “AOMix program,” <http://www.sg-chem.net/>.

## Research Article

# Squaraine Planar-Heterojunction Solar Cells

**Bin Fan, Ylenia Maniglio, Marina Simeunovic, Simon Kuster, Thomas Geiger, Roland Hany, and Frank Nüesch**

*Swiss Federal Laboratories for Materials Testing and Research, EMPA, Ueberlandstrasse 129, 8600 Dübendorf, Switzerland*

Correspondence should be addressed to Bin Fan, bin.fan@empa.ch

Received 10 April 2009; Accepted 2 June 2009

Recommended by Mohamed Sabry Abdel-Mottaleb

The photovoltaic performance of squaraine-based organic solar cells is investigated. Two squaraine derivatives with extraordinarily high extinction coefficients are used as electron donors in bilayer heterojunctions with fullerene C<sub>60</sub> as electron acceptor. Due to the very strong squaraine absorption band in the red spectral domain, antibatic behavior due to light filtering is observed in the photocurrent spectrum for film thicknesses of 35 nm to 40 nm. At reduced film thicknesses of 20 nm, this filtering effect at maximum absorption can be alleviated and power conversion efficiencies under simulated AM 1.5 full sun irradiation of 0.59% and 1.01% are obtained for the two squaraine derivatives, respectively. The photovoltaic properties of these cells are investigated with respect to electrode materials and chemical doping.

Copyright © 2009 Bin Fan et al. This is an open access article distributed under the Creative Commons Attribution License, which permits unrestricted use, distribution, and reproduction in any medium, provided the original work is properly cited.

## 1. Introduction

The developments in organic semiconductors provide efficient and inexpensive solutions for solar energy conversion. Continuous optimization of organic solar cells has resulted in power conversion efficiencies (PCEs) from 4% to 5% for single junction cells based on spin-coated polymers [1] and thermally evaporated small molecules [2]. Compared to polymeric materials, small molecular semiconductors benefit from well-controlled synthesis and characterization along with easier purification [3–5]. Soluble small molecules are even more advantageous due to their low cost processability [6]. Several works have now demonstrated efficiencies above 1% in planar heterojunction cells [7], bulk-heterojunction cells, [8] and Schottky-type cells [9].

Among these soluble small molecular semiconductors, squaraine dyes are attracting a lot of attention due to their unique photophysical and photochemical properties. They are characterized by an aromatic four-membered ring system derived from squaric acid [10]. Their extinction coefficients are extraordinarily high and absorption in the far red and infrared domain has been demonstrated. Squaraine dyes that are solution-processible have already been applied in laser printers, photocopier, and optical disks as photoconductive materials [11, 12]. Their application in nonlinear optical

devices has also been investigated [13]. The exceptional optical properties of squaraines are of particular interest to solar cells. First of all, strong absorption coefficients open the possibility to use thinner active films, which may facilitate charge transport in the devices. Furthermore, there are only few organic materials absorbing so strongly in the far red and near infrared domain. Indeed, squaraines have already been employed quite early in organic Schottky-type solar cells, though with rather poor efficiency [14]. In recent years, squaraines have been extensively investigated in dye-sensitized solar cells (DSSCs) [15–20]. The best power conversion efficiency so far has reached 4.5% [21]. There are only few works that report on solid organic solar cells based on squaraines. Recently, a power conversion efficiency of 1.2% has been obtained in bulk-heterojunction solar cells using a blend of a squaraine derivative and (6,6)-phenyl C<sub>61</sub> butyric acid methylester (PCBM) [22].

To our best knowledge, bilayer heterojunction photovoltaic devices based on squaraines have not been reported so far. In this work, we report on planar-heterojunction solar cells based on two soluble squaraine derivatives, respectively, that we use as electron donors in combination with vacuum-deposited electron acceptor C<sub>60</sub>. In particular, we investigate the influence of squaraine film thickness on the photovoltaic performance. We further improve device performance by

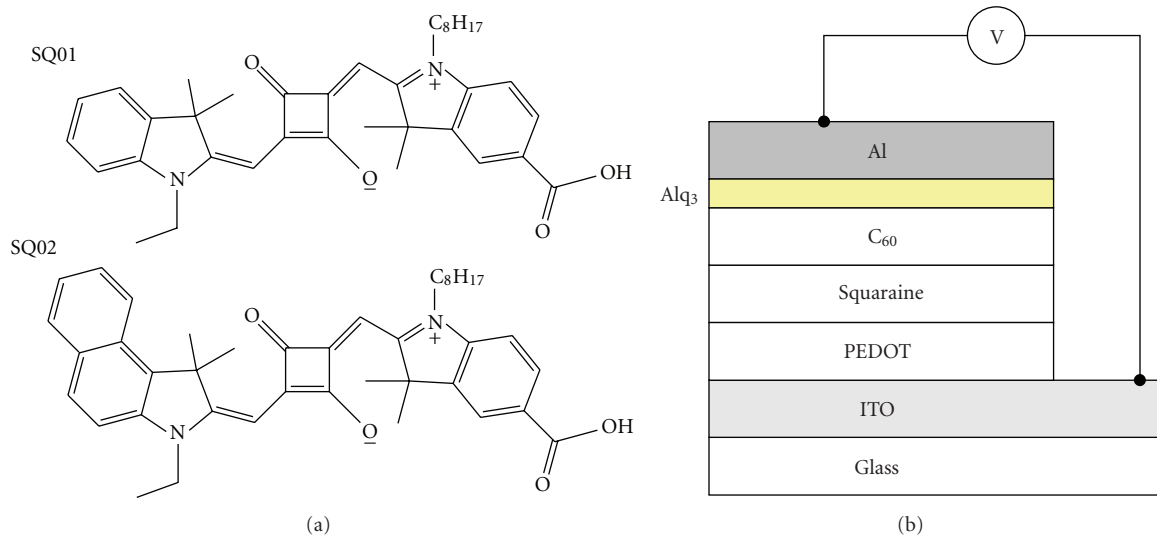


FIGURE 1: (a) Molecular structure of SQ01 and SQ02. (b) Solar cell architecture.

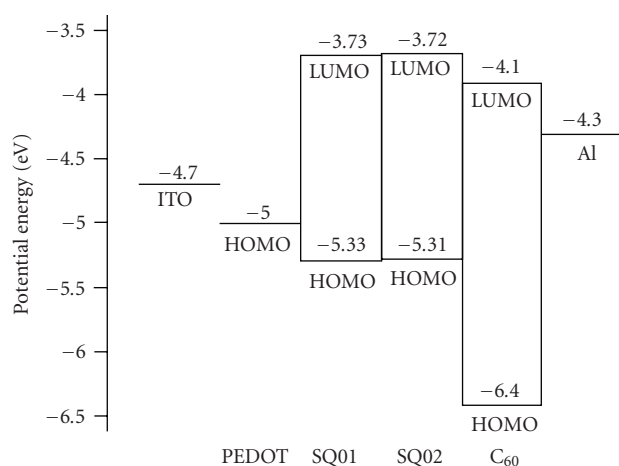


FIGURE 2: Energy level diagram of the organic materials and electrodes. The work function of Ca of  $-2.9$  eV is not shown in this diagram.

choosing an appropriate cathode material. The effect of chemical doping of the squaraine layer is also investigated.

## 2. Experimental

The molecular structures of squaraine dyes SQ01 and SQ02 used in this work are shown in Figure 1(a). Both dyes were synthesized in our laboratory according to a previously published procedure [21] and exhibit extinction coefficients of approximately  $300\,000\text{ L mol}^{-1}\text{ cm}^{-1}$  [23]. The architecture of our organic solar cells is shown in Figure 1(b). The indium tin oxide glass substrate (ITO, from AFC) was first cleaned in ozone plasma, then placed subsequently in acetone, ethanol, and soap ultrasonic baths, and finally dried in a nitrogen flow. A 50 nm thick layer of hole-transporting poly(styrene sulfonate) doped

poly (3,4-ethylenedioxythiophene) (PEDOT:PSS) (Sigma-Aldrich) was spin-coated on top of the ITO substrate from a water solution, then heated to  $120^\circ\text{C}$  for 15 minutes in order to remove residual water. The coated substrates were transferred into an  $\text{N}_2$  glovebox to avoid exposure to oxygen and humidity. The squaraine dyes were spin-coated on top of the PEDOT:PSS layer from 5 mg/mL solutions in chloroform, resulting in layer thickness of 40 nm and 35 nm for SQ01 and SQ02, respectively. Thinner films of 20 nm were achieved by diluting the chloroform solutions accordingly. The  $\text{C}_{60}$  layer (40 nm) was vapor-deposited on top of the squaraine layer. Aluminum or calcium (60 nm) were used as top cathode to define an active device area of  $7.1\text{ mm}^2$ . Note that when applying aluminum as the cathode, an ultra-thin layer (2.5 nm) of tris(8-hydroxyquinoline)aluminum ( $\text{Alq}_3$ ) was always inserted between Al and  $\text{C}_{60}$  as to protect the organic layers during aluminum deposition [24].  $\text{Alq}_3$  was not applied when calcium was used as cathode. To increase the conductivity of one of the squaraine films, SQ02 was doped with nitrosonium tetrafluoroborate ( $\text{NO}^+\text{BF}_4^-$ ). Doping was first achieved in solution before coating the SQ02 solution to form a film. For that purpose, precise amounts of  $\text{NO}^+\text{BF}_4^-$  from a 0.01 mol/L  $\text{NO}^+\text{BF}_4^-$  master solution in  $\text{CH}_3\text{CN}$  were added to the SQ02 solutions in chloroform.

The energy level diagram of the organic materials and electrodes applied is shown in Figure 2. The levels of the highest occupied molecular orbitals (HOMOs) and lowest unoccupied molecular orbitals (LUMOs) of the squaraine dyes were determined by cyclic-voltammetry in dilute N,N-dimethylformamide (DMF) solutions using  $\text{Fc}/\text{Fc}^+$  as an internal reference. The vacuum-referenced energy values were determined by adopting the potential of  $+0.72\text{ V}$  versus NHE for  $\text{Fc}/\text{Fc}^+$  in DMF and setting NHE at 4.5 eV below the zero vacuum energy level. The energy levels of the other materials are taken from our previous work [25].

The photovoltaic performances of the solar cells were measured under simulated AM 1.5 solar irradiation, with an

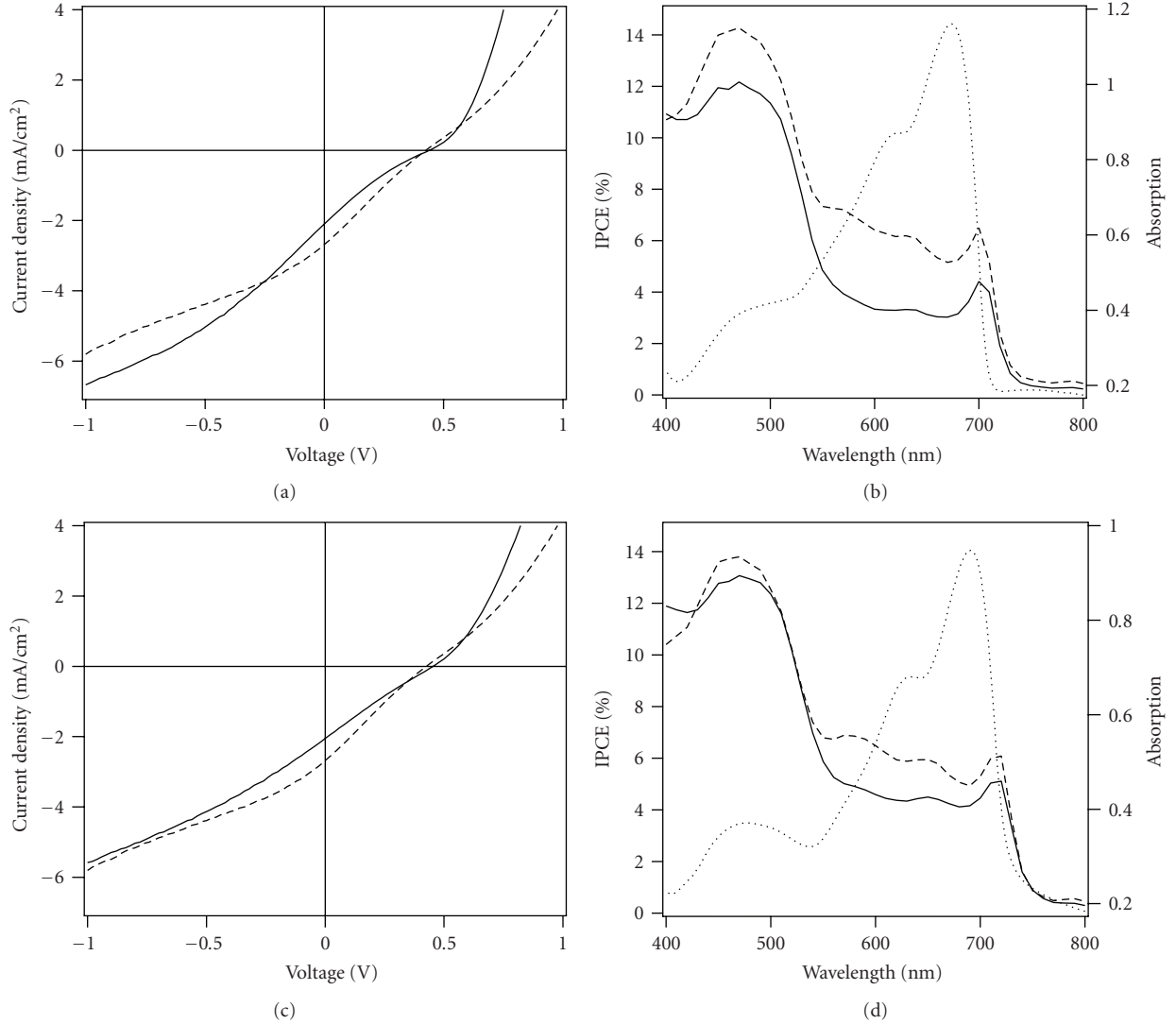


FIGURE 3: Current-voltage characteristics and IPCE curves of solar cells based on SQ01 ((a) and (b)) and SQ02 ((c) and (d)). The solid curves represent the cells using an Al/Alq<sub>3</sub> cathode, the dashed curves represent the cells using a Ca cathode. The dotted line in (b) and (d) represents the cell absorption. The thickness for SQ01 and SQ02 is 40 nm and 35 nm, respectively.

incident light intensity of  $P_{in} = 100 \text{ mW/cm}^2$ . The open-circuit voltage ( $V_{OC}$ ) and short-circuit current ( $J_{SC}$ ) were obtained directly from the current density-voltage ( $J$ - $V$ ) characteristics of the solar cells. The PCE is calculated as

$$\text{PCE}(\%) = \frac{\text{FF} \cdot V_{OC} \cdot J_{SC}}{P_{in}} \times 100\%, \quad (1)$$

with fill factor

$$\text{FF} = \frac{(J \cdot V)_{\max}}{V_{OC} \cdot J_{SC}}. \quad (2)$$

However,  $(J \cdot V)_{\max}$  is the maximum power point and FF is the fill factor. The incident photon-to-current conversion efficiency (IPCE) is defined as the number of electrons

collected in the external circuit divided by the number of incident photons per second and is calculated according to

$$\text{IPCE}(\%) = \frac{hcJ_{SC}}{e\lambda P_{in}}, \quad (3)$$

where  $h$  is Planck's constant,  $c$  is the speed of light,  $e$  is the elementary charge, and  $\lambda$  is the monochromatic irradiation wavelength.

### 3. Results and Discussion

The  $J$ - $V$  characteristics of solar cells using 40 nm thick SQ01 film or a 35 nm thick SQ02 film under AM 1.5 white light irradiation are shown in Figures 3(a) and 3(c), respectively. The photovoltaic parameters of these cells are summarized in Table 1. Comparing the photovoltaic performance of the two squaraines, we see that despite the structural difference

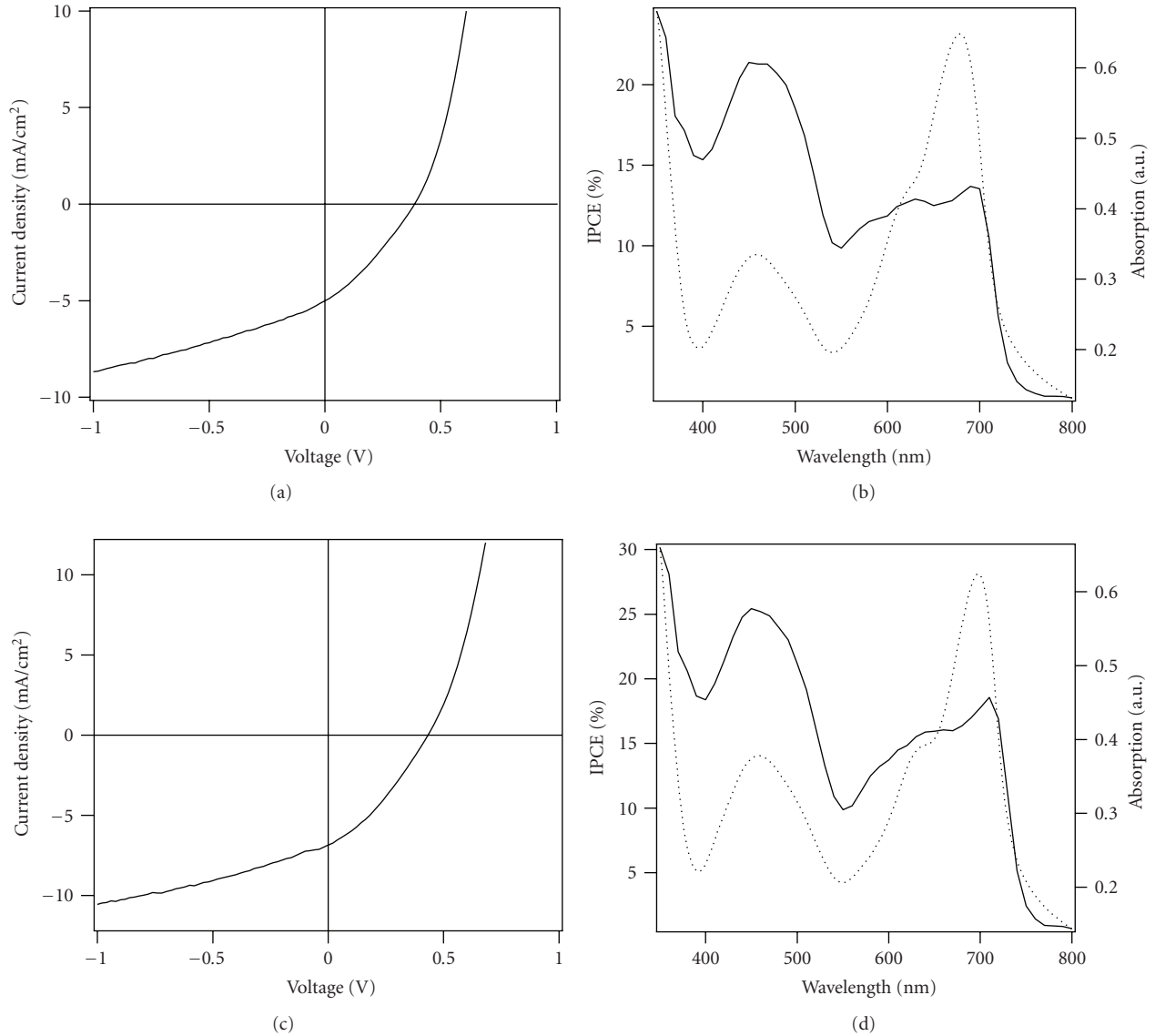


FIGURE 4: Current-voltage characteristics and IPCE curves for solar cells based on 20 nm thick SQ01 ((a) and (b)) and SQ02 ((c) and (d)) films. The dotted lines in (b) and (d) represent the absorption of SQ01 and SQ02 based cells, respectively.

of the dyes, the photovoltaic performance of SQ01 and SQ02 are rather similar. Both *J-V* curves show a typical S-shape behavior, which is somewhat dependent on the choice of the cathode. This feature could be induced by poor charge carrier transport in the squaraine layers. We do not exclude the possibility that a contact barrier at the anode interface could also lead to the S-shape feature. For both devices, the Ca cathode provides higher  $J_{SC}$ , FF, and slightly lower  $V_{OC}$ . We have attributed the better device performance to Ohmic contact formation between Ca and C<sub>60</sub>. Al-C<sub>60</sub> contact generally introduces an energy barrier that hinders the electron extraction by the cathode. This barrier can be reduced significantly by introducing a thin buffer layer of Alq<sub>3</sub> [24]. In our devices, the charge extraction ability of the Ca cathode turns out to be still better than the Al cathode with Alq<sub>3</sub> buffer layer. The lowered  $V_{OC}$  could be explained

by the higher workfunction of the aluminum electrode as compared to the low workfunction of Ca [26–28].

The corresponding IPCE curves are shown in Figures 3(b) and 3(d) together with the absorption spectra of the cells. The IPCE of the cells using Ca cathodes are significantly higher than those using Al cathodes, indicating better charge extraction. The latter may also result from a higher built-in field produced in the devices using Ca cathodes. Strikingly, in the absorption region from 600 nm to 700 nm, the IPCE does not match the absorbance of the dye films. On the contrary, the minimum IPCE occurs at the maximum absorbance, which is also termed as antibatic behavior. Light irradiation penetrating through the ITO and PDOT:PSS layer is strongly absorbed when entering the dye layer, where excited states (excitons) are formed [29]. It appears that a large part of the excitons is not able to reach the charge separating

TABLE 1: Photovoltaic performance of SQ01- and SQ02-based solar cells using  $C_{60}$  as electron acceptor. Film thicknesses of 40 nm and 35 nm were used for SQ01 and SQ02, respectively. When ultrathin films were used, the thickness corresponds to 20 nm for both squaraine derivatives. The type of cathode utilized in the devices is also indicated.

	$J_{SC}$ (mA/cm <sup>2</sup> )	$V_{OC}$ (V)	FF	$\eta_p$ (%)
SQ01				
Al cathode	1.7	0.42	0.218	0.16
Ca cathode	2.6	0.38	0.229	0.23
Thin SQ film	5.0	0.38	0.312	0.59
SQ02				
Al cathode	2.0	0.46	0.228	0.21
Ca cathode	2.7	0.42	0.241	0.27
Thin SQ film	6.8	0.44	0.328	1.01

organic heterointerface, indicating that the exciton diffusion length is certainly smaller than the film thickness of SQ01 and SQ02. Even though fairly thin squaraine films were used, a substantial portion of the incoming light is merely filtered and cannot contribute to charge generation. As a consequence, the IPCE values in the absorption region of the squaraines are below 6%. The maximum IPCE locates between 450 nm and 500 nm, a spectral region where  $C_{60}$  is known to have a photocurrent peak [30]. As a matter of fact, the incident photons with wavelengths in the  $C_{60}$  absorption region are not filtered by the squaraine layer but are transmitted to the  $C_{60}$  layer where absorption occurs. In this process, the excited  $C_{60}$  molecule provides the possibility of electron transfer from the HOMO of the squaraine to the HOMO of  $C_{60}$ , resulting in the IPCE peak around 450 nm.

In order to improve device performance in squaraine-based bilayer devices, one possibility is to reduce the squaraine film thickness. Although less photons are being absorbed by the thinner film, a much larger proportion of excitons would be able to reach the organic heterointerface, resulting in a higher number of generated charges. In Figure 4, the performance of devices using 20nm thick squaraine dye films is shown. It has to be noted that decent diode characteristics were obtained despite the extremely small thickness of the dye films. Apparently, the squaraine derivatives used here own excellent film forming properties. In these devices, the IPCE in the absorption region of SQ01 and SQ02 reaches 12.8% and 18.5%, respectively. Moreover, the IPCE spectrum now resembles the absorption spectrum of the dye films. Again, this corroborates the fact that light filtering without charge generation is occurring for the thicker squaraine films. Additionally to improved charge generation, the reduced film thickness also leads to a better hole-transport through the squaraine film, and hence a smaller series resistance. Importantly, the S-shape, which is observed for the thicker squaraine layers, has been largely reduced when thin layers are employed. As demonstrated by  $J$ - $V$  curves (Figures 4(a) and 4(c)), the  $J_{SC}$  and FF increase for both devices results in much better PCE of 0.59% for SQ01 and 1.01% for SQ02.

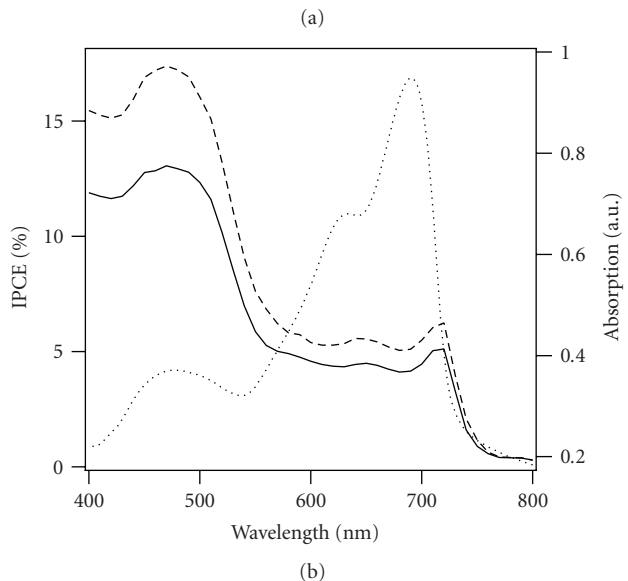
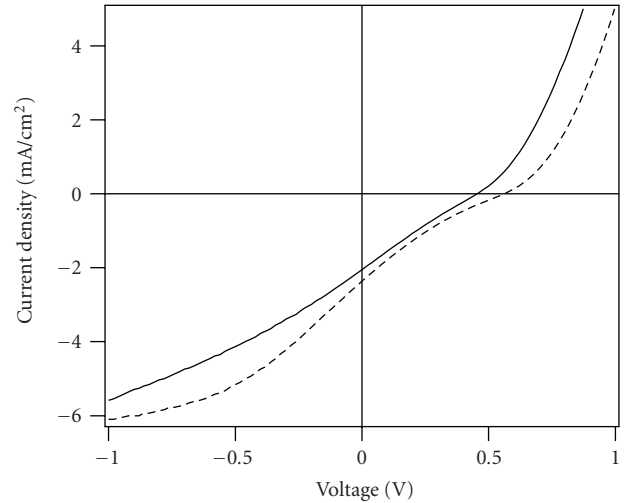


FIGURE 5: Current-voltage characteristics (a) and IPCE curves (b) of pristine (full line) and doped (dashed line) solar cells based on SQ02. The absorbance of the cell is also indicated (dotted line).

Charge transport in squaraine films has been investigated very scarcely in literature. In the crystalline state, a field effect hole mobility of  $1 \times 10^{-3} \text{ cm}^2 \text{ V}^{-1} \text{ s}^{-1}$  was reported for a particular squaraine derivative [31]. As demonstrated by the authors, the mobility was strongly dependent on the morphology of the thin electroactive film. In the present work, we use asymmetric squaraine dyes that moreover possess octyl chains. This particular chemical structure provides good solubility and is probably also responsible for good film forming properties. However, the particular structure of SQ01 and SQ02 may be unfavorable for charge transport and may be responsible for low charge carrier mobility.

In our previous work, we were able to increase the hole transport by doping the electron-donor film [25]. By introducing oxidative dopants, the film conductivity rises,

and hence more photogenerated charges can be extracted. We applied the same strategy in the case of SQ02-based devices. In order to evaluate the effect of doping, we focussed on the thicker SQ02 film of 35 nm, since the effect of conductivity is expected to be higher in this case. SQ02 was first doped in solution using  $\text{NO}^+\text{BF}_4^-$  as oxidizing agent before being coated on the PEDOT:PSS layer. We found that doping was not substantially enhancing device performance. The optimum doping concentration was obtained for an  $\text{NO}^+\text{BF}_4^-/\text{SQ02}$  ratio of 0.005 (mol/mol). At higher concentration, doping has a deteriorating effect, probably due to defect formation in the organic layer. As shown in Figure 5, doping increases the current output ( $J_{\text{SC}}$ , IPCE) and open-circuit voltage (see Table 1). Similarly to our previous work, we believe that the increased  $V_{\text{OC}}$  is due to the formation of a Schottky barrier at the PEDOT:PSS/SQ02 interface upon equilibration of the respective Fermi levels.

#### 4. Conclusion

In summary, we have fabricated a series of organic solar cells with squaraine dyes SQ01 and SQ02. The active organic layers form planar heterojunctions, where charge separation takes place between the squaraine electron donor and the  $\text{C}_{60}$  acceptor. Due to the extremely high extinction coefficients and the limited exciton diffusion length in squaraines, these devices show strong light filtering effects even at small film thicknesses of 35 nm to 40 nm. Only if the film thickness is reduced to 20 nm, power conversion efficiencies of 1% can be achieved. The photovoltaic performance is a result of both the photoactivity of  $\text{C}_{60}$  in the blue-to-green spectral domain and the photogeneration in the far red domain, where the squaraine dyes absorb. Further optimization of the devices would imply an increase of the hole carrier transport in the squaraine films. This conclusion is corroborated by the fact that oxidative doping of the dye film leads to increased  $J_{\text{SC}}$  and  $V_{\text{OC}}$ .

#### Acknowledgments

The Swiss Competence Center for Energy and Mobility CCEM-CH and "Swisselectric Research" are gratefully acknowledged for their financial support.

#### References

- [1] W. Ma, C. Yang, X. Gong, K. Lee, and A. J. Heeger, "Thermally stable, efficient polymer solar cells with nanoscale control of the interpenetrating network morphology," *Advanced Functional Materials*, vol. 15, no. 10, pp. 1617–1622, 2005.
- [2] J. Xue, B. P. Rand, S. Uchida, and S. R. Forrest, "A hybrid planar-mixed molecular heterojunction photovoltaic cell," *Advanced Materials*, vol. 17, no. 1, pp. 66–71, 2005.
- [3] P. Peumans, A. Yakimov, and S. R. Forrest, "Small molecular weight organic thin-film photodetectors and solar cells," *Journal of Applied Physics*, vol. 93, no. 7, pp. 3693–3723, 2003.
- [4] M. Riede, T. Müller, W. Tress, R. Schüppel, and K. Leo, "Small-molecule solar cells—status and perspectives," *Nanotechnology*, vol. 19, no. 42, Article ID 424001, 12 pages, 2008.
- [5] B. P. Rand, J. Genoe, P. Heremans, and J. Poortmans, "Solar cells utilizing small molecular weight organic semiconductors," *Progress in Photovoltaics: Research and Applications*, vol. 15, no. 8, pp. 659–676, 2007.
- [6] M. T. Lloyd, J. E. Anthony, and G. G. Malliaras, "Photovoltaics from soluble small molecules," *Materials Today*, vol. 10, no. 11, pp. 34–41, 2007.
- [7] F. Meng, K. Chen, H. Tian, L. Zuppiroli, and F. Nüesch, "Cyanine dye acting both as donor and acceptor in heterojunction photovoltaic devices," *Applied Physics Letters*, vol. 82, no. 21, pp. 3788–3790, 2003.
- [8] M. T. Lloyd, A. C. Mayer, A. S. Tayi, et al., "Photovoltaic cells from a soluble pentacene derivative," *Organic Electronics*, vol. 7, no. 5, pp. 243–248, 2006.
- [9] G. A. Chamberlain, "Organic solar cells: a review," *Solar Cells*, vol. 8, no. 1, pp. 47–83, 1983.
- [10] H. E. Sprenger and W. Ziegenbein, "Cyclobutenediylum dyes," *Angewandte Chemie International Edition*, vol. 7, pp. 530–535, 1968 (English).
- [11] K.-Y. Law, "Organic photoconductive materials: recent trends and developments," *Chemical Reviews*, vol. 93, no. 1, pp. 449–486, 1993.
- [12] K.-Y. Law and F. C. Bailey, "Squaraine chemistry. Synthesis, characterization, and optical properties of a class of novel unsymmetrical squaraines: [4-(dimethylamino)phenyl](4'-methoxyphenyl)squaraine and its derivatives," *Journal of Organic Chemistry*, vol. 57, no. 12, pp. 3278–3286, 1992.
- [13] C.-T. Chen, S. R. Marder, and L.-T. Cheng, "Syntheses and linear and nonlinear optical properties of unsymmetrical squaraines with extended conjugation," *The Journal of the American Chemical Society*, vol. 116, no. 7, pp. 3117–3118, 1994.
- [14] D. L. Morel, "Some aspects of the role of solid state chemistry in the performance of organic solar cells," *Molecular Crystals and Liquid Crystals*, vol. 50, no. 1–4, pp. 127–137, 1979.
- [15] A. Burke, L. Schmidt-Mende, S. Ito, and M. Grätzel, "A novel blue dye for near-IR 'dye-sensitized' solar cell applications," *Chemical Communications*, no. 3, pp. 234–236, 2007.
- [16] Md. K. Nazeeruddin, R. Humphry-Baker, M. Grätzel, et al., "Efficient near-IR sensitization of nanocrystalline  $\text{TiO}_2$  films by zinc and aluminum phthalocyanines," *Journal of Porphyrins and Phthalocyanines*, vol. 3, no. 3, pp. 230–237, 1999.
- [17] S. Alex, U. Santhosh, and S. Das, "Dye sensitization of nanocrystalline  $\text{TiO}_2$ : enhanced efficiency of unsymmetrical versus symmetrical squaraine dyes," *Journal of Photochemistry and Photobiology A*, vol. 172, no. 1, pp. 63–71, 2005.
- [18] C. Li, W. Wang, X. Wang, B. Zhang, and Y. Cao, "Molecular design of squaraine dyes for efficient far-red and near-IR sensitization of solar cells," *Chemistry Letters*, vol. 34, no. 4, pp. 554–555, 2005.
- [19] A. Otsuka, K. Funabiki, N. Sugiyama, T. Yoshida, H. Minoura, and M. Matsui, "Dye sensitization of ZnO by unsymmetrical squaraine dyes suppressing aggregation," *Chemistry Letters*, vol. 35, no. 6, pp. 666–667, 2006.
- [20] S. Hotchandani, S. Das, K. G. Thomas, M. V. George, and P. V. Kamat, "Interaction of semiconductor colloids with J-aggregates of a squaraine dye and its role in sensitizing nanocrystalline semiconductor films," *Research on Chemical Intermediates*, vol. 20, no. 9, pp. 927–938, 1994.
- [21] J.-H. Yum, P. Walter, S. Huber, et al., "Efficient far red sensitization of nanocrystalline  $\text{TiO}_2$  films by an unsymmetrical squaraine dye," *Journal of the American Chemical Society*, vol. 129, no. 34, pp. 10320–10321, 2007.

- [22] F. Silvestri, M. D. Irwin, L. Beverina, A. Facchetti, G. A. Pagani, and T. J. Marks, "Efficient squaraine-based solution processable bulk-heterojunction solar cells," *Journal of the American Chemical Society*, vol. 130, no. 52, pp. 17640–17641, 2008.
- [23] T. Geiger, S. Kuster, J. H. Yum, et al., "Molecular design of unsymmetrical squaraine dyes for high efficiency conversion of low energy photon on TiO<sub>2</sub> nanocrystalline films," *Advanced Functional Materials*, vol. 19, pp. 734–738, 2007.
- [24] Q. L. Song, F. Y. Li, H. Yang, et al., "Small-molecule organic solar cells with improved stability," *Chemical Physics Letters*, vol. 416, no. 1–3, pp. 42–46, 2005.
- [25] B. Fan, R. Hany, J.-E. Moser, and F. Nüesch, "Enhanced cyanine solar cell performance upon oxygen doping," *Organic Electronics*, vol. 9, no. 1, pp. 85–94, 2008.
- [26] V. D. Mihailetschi, P. W. M. Blom, J. C. Hummelen, and M. T. Rispens, "Cathode dependence of the open-circuit voltage of polymer:fullerene bulk heterojunction solar cells," *Journal of Applied Physics*, vol. 94, no. 10, pp. 6849–6854, 2003.
- [27] D. Cheyns, J. Poortmans, P. Heremans, et al., "Analytical model for the open-circuit voltage and its associated resistance in organic planar heterojunction solar cells," *Physical Review B*, vol. 77, no. 16, Article ID 165332, 10 pages, 2008.
- [28] C. Uhrich, D. Wynands, S. Olthof, et al., "Origin of open circuit voltage in planar and bulk heterojunction organic thin-film photovoltaics depending on doped transport layers," *Journal of Applied Physics*, vol. 104, no. 4, Article ID 043107, 2008.
- [29] B. A. Gregg, S.-G. Chen, and R. A. Cormier, "Coulomb forces and doping in organic semiconductors," *Chemistry of Materials*, vol. 16, no. 23, pp. 4586–4599, 2004.
- [30] A. Geiser, B. Fan, H. Benmansour, et al., "Poly(3-hexylthiophene)/C<sub>60</sub> heterojunction solar cells: implication of morphology on performance and ambipolar charge collection," *Solar Energy Materials and Solar Cells*, vol. 92, no. 4, pp. 464–473, 2008.
- [31] E. C. P. Smits, S. Setayesh, T. D. Anthopoulos, et al., "Near-infrared light-emitting ambipolar organic field-effect transistors," *Advanced Materials*, vol. 19, no. 5, pp. 734–738, 2007.

## Research Article

# Hydrothermal Preparation of $Gd^{3+}$ -Doped Titanate Nanotubes: Magnetic Properties and Photovoltaic Performance

Hoda S. Hafez,<sup>1,2</sup> M. Saif,<sup>2,3</sup> James T. McLeskey, Jr.,<sup>4</sup> M. S. A. Abdel-Mottaleb,<sup>2</sup>  
I. S. Yahia,<sup>5</sup> T. Story,<sup>6</sup> and W. Knoff<sup>6</sup>

<sup>1</sup> Environmental Studies and Research Institute (ESRI), Minoufiya University, Sadat Branch, 32897 Sadat City, Egypt

<sup>2</sup> Nano-Photochemistry and Solarchemistry Laboratories, Department of Chemistry, Faculty of Science, Ain Shams University, Abbassia, 11566 Cairo, Egypt

<sup>3</sup> Department of Chemistry, Faculty of Education, Ain Shams University, Roxy, 32897 Cairo, Egypt

<sup>4</sup> Energy Conversion Systems Laboratory, Department of Mechanical Engineering, Virginia Commonwealth University, Richmond, VA 23284, USA

<sup>5</sup> Semi-Conductor Laboratory, Physics Department, Faculty of Education, Ain Shams University, Roxy, 32897 Cairo, Egypt

<sup>6</sup> Institute of Physics, Polish Academy of Sciences, Al. Lotnikow 32/46, 02-668 Warszawa, Poland

Correspondence should be addressed to M. S. A. Abdel-Mottaleb, phochem08@photoenergy.org

Received 9 September 2009; Accepted 6 November 2009

Recommended by Frank Nüesch

Pure and  $Gd^{3+}$ -doped titanate nanotubes (TNTs) materials were synthesized by a hydrothermal method. Their morphology, optical properties, thermal stability, and magnetic properties were characterized by X-ray diffraction (XRD), transmission electron microscope (TEM), UV-Vis spectroscopy, thermal analysis, and magnetic measurements. It was found that doping renders  $Gd^{3+}$ -TNT visible light active and results in smaller crystallite size and larger surface area as well as higher thermal stability compared to pure titanate nanotubes. The estimated magnetic moments point to presence of weak antiferromagnetic interaction. Application of the prepared  $Gd^{3+}$ -TNT for modifying conventional photoanodes in polymer solar cells was attempted. Preliminary results show slightly improved photovoltaic energy conversion efficiency in the devices containing the newly designed  $Gd^{3+}$ -doped nanotubes.

Copyright © 2009 Hoda S. Hafez et al. This is an open access article distributed under the Creative Commons Attribution License, which permits unrestricted use, distribution, and reproduction in any medium, provided the original work is properly cited.

## 1. Introduction

After the innovative work of Kasuga et al. [1], titanium dioxide and titanate nanotubes (TNTs) with large specific surface area and pore volume have gained promising and important prospect due to their fascinating microstructures and excellent properties [2].  $TiO_2$ -derived nanotubes such as sodium titanate ( $Na_xH_{1-x}Ti_3O_7$ ,  $x \sim 0.75$ ) and hydrogen titanate ( $H_2Ti_3O_7$  or  $H_3Ti_5O_{11}$ ) prepared by a simple hydrothermal method are particularly interesting partly due to their one-dimensional nanostructures, uniform nanochannel, electronic conductivity, and larger specific surface area [3]. This showed promise for applications such as photocatalysis, sensing, adsorbents, mesoporous catalyst, and a good candidate material for dye-sensitized solar cells [4]. Nanotubes have a large specific surface area available for the absorption of photons compared to the bulk material while also providing channels for enhanced electron transfer,

thereby helping to increase the efficiencies for photovoltaic energy conversion [5].

Rare earth ions have been widely used in high-performance luminescence devices, catalysts, and other functional materials because of the electronic, optical, and chemical characteristics originating from their 4f electrons [6]. Rare earth titanates have interesting dielectric, piezoelectric, and ferroelectric properties [7–9]. These materials usually possess a pyrochlore structure [10–13], which find numerous applications.

In this study, the titanate nanotubes doped with  $Gd^{3+}$  ions, with different concentrations of metal levels, were synthesized by hydrothermal treatment of pure anatase  $Gd^{3+}$ -doped  $TiO_2$  powders in concentrated NaOH solution. It is the first time to obtain titanate nanotubes doped with paramagnetic  $Gd^{3+}$  ions in the view of their possible promising application in inorganic/polymer hybrid solar cell devices. Moreover,  $Gd^{3+}$  materials could be manipulated

with an external magnetic field for better alignment on different surfaces. The morphology, structure, thermal stability, and the magnetic properties of these titanate nanotubes doped with  $Gd^{3+}$  were described and discussed.

## 2. Experimental

**2.1. Chemicals.** Titanium(IV) isopropoxide,  $Ti[O(C_3H_7)]_4$  (TTIP) 98.9%, Fluka, Gadolinium(III) nitrate pentahydrate  $Gd(NO_3)_3 \cdot 5H_2O$  (99.9% pure grade), Aldrich, Sodium poly [2-(3-thienyl)-ethoxy-4-butylsulfonate], or PTEBS is a water-soluble thiophene polymer, American Dye Source. All other chemicals were of analytic purity grades and were used as received from Sigma-Aldrich Inc.

Conducting glass plates (FTO glass, Fluorine-doped tin oxide overlayer, and sheet resistance  $25 \pm 5 \Omega$ , purchased from Hartford Glass Co., USA) were used as a substrate for precipitating titania porous film and were cut into  $25 \times 25 \times 2.3$  mm sheets.

**2.2. Synthesis of  $Gd^{3+}$ -Doped Titanate Nanotubes.** The anatase  $Gd^{3+}$ -doped  $TiO_2$  powders were first prepared by a conventional sol-gel process. 4.6 mL of TTIP is dissolved in 30 mL of methanol under stirring. This is followed by the addition of a mixture of 0.2 mL of concentrated HCl (catalyst), and 1.6 mL of water for hydrolysis. The hydrolysis of TTIP is allowed to proceed for 15–30 minutes. Then 0, 2, 5, 7 mol% of gadolinium nitrate dissolved in 20 mL of methanol is added to the above mixture under stirring. The resulting transparent colloidal suspension is stirred for 2 hours and aged for 24 hours until the formation of a gel. The resulting gel is dried at  $80^\circ C$  and then ground into a powder which is then calcinated at  $450^\circ C$  for 2 hours.

$Gd^{3+}$ -doped titanate nanotubes ( $Gd^{3+}$ -TNTs) are prepared as described in Reference [14]. In a typical procedure, 100 mg of the pure anatase  $Gd^{3+}$ -doped  $TiO_2$  nanoparticles are transferred into a Teflon-lined autoclave, which contained 20 mL of 10 M NaOH. The autoclave is then placed in an oven at  $130^\circ C$  for 48 hours. The contents of the autoclave are filtered and the resulting powders are washed with dilute HCl then deionized water until  $pH = 7$  and dried at  $80^\circ C$  for 5 hours in a vacuum oven.

**2.3. Material Characterizations.** The nanotubes are characterized in a number of ways. Transmission Electron Microscopy (TEM) is done using a Jeol model JEM-1230 TEM operated at 100 kV. X-ray diffraction (XRD) analysis is made using a D/max  $\gamma A$ . X-ray diffractometer ( $X'$  Pert Pro, Japan) with  $Cu K_\alpha$  radiation ( $K_\alpha = 0.15418$  nm) at 45 kV and 40 mA. Raman scattering spectra are recorded with a Horiba Jobin Yvon Raman spectrometer, using the 632.817 nm He-Ne laser for excitation. The light beam is focused through a standard Olympus Microscope with a 100x lens down to 5–10  $\mu m$  in diameter. Differential scanning calorimetry (DSC) and thermogravimetric analyses (TGA) are performed using a Perkin-Elmer PYRIS TGA, under  $N_2$  gas, at a heating rate of  $10^\circ C/min$ . The temperature ranged from room temperature to  $800^\circ C$  in order to obtain crystallization and phase-transformation data. The optical properties of the

samples are characterized by using a Jasco V550 UV-Vis spectrophotometer.

The dc magnetic susceptibility is carried out using superconducting SQUID magnetometry in the temperature range of 5–100 K with an excitation field  $H_{ac} = 400$  Oe. On the basis that the magnetic susceptibility can be related to atomic properties, we converted mass magnetic susceptibility to the molar magnetic susceptibility  $\chi_M$  using  $\chi_M = \chi_g \cdot M_w$ , where  $M_w$  is the molecular weight of the investigated samples.

For the characterization of the photovoltaic devices, current–voltage IV characteristics in the dark and under illumination were measured using a Keithley 236 source measurement unit with an AM 1.5 solar simulator (Spectra-Physics model 96000). The intensity of about  $80$  mW/cm<sup>2</sup> was measured with a Spectra-Physics optical power meter (model 407A).

**2.4. Solar Cell Fabrication.** The hybrid inorganic/polymer solar cell devices were fabricated as described in the literature [15] but with the addition of a  $TiO_2$  hole blocking layer (HBL) [16]. Twelve devices were fabricated per substrate to check the reproducibility. Each device (area =  $0.15$  cm<sup>2</sup>) consists of four layers on top of the FTO-coated glass substrate, namely, a dense  $TiO_2$  HBL, a porous nanocrystalline TNT layer, the PTEBS polymer layer (approximately  $8 \mu m$  thick) prepared by dropcasting, and Au layer deposited by sputter-coating.

The porous titanate layer was prepared by mixing 1 g titanate powder with 30 mL ethanol containing 1 mL acetic acid and five drops of triton X-100. The mixture was sonicated for 15 minutes and spin coated on top of the HBL at 2000 rpm for 30 s. The coating process was repeated to obtain thick films. The resulting films was sintered at  $450^\circ C$  for 2 hours in air.

## 3. Results and Discussion

**3.1. Morphology and Crystal Properties.** The TEM images of the precursor  $TiO_2$  nanoparticles and the obtained undoped and  $Gd^{3+}$ -doped TNT after the hydrothermal treatment are shown in Figure 1. The pure titania precursor for the preparation of the titanate nanotubes were nanoparticles of pure anatase titania with an average diameter of about 15 nm as shown in Figure 1(a). The TEM morphologies of the undoped and  $Gd^{3+}$ -doped titanate nanotubes were shown in Figures 1(b) and 1(c). It is clear from these figures a well-identified multiwalled nanotubular structure with an average outer (inner) diameter of approximately 11 nm (5 nm) and a length of few hundreds of nanometers.

The mechanism for forming the nanotubes via the hydrothermal reaction was proposed by Viriya-Empikul et al. [17]. The process begins when the  $TiO_2$  and doped  $TiO_2$  powders are dissolved completely in the NaOH solution. These powders then form octahedrally configured  $[Ti(OH)_6]^{2-}$  and  $[M(OH)_6]^{n-}$  anions in the solution. The anions connect by sharing edges to form  $Ti_5O_{11}^-$  nanosheets, which are a few thick atomic layers and they may roll themselves into nanotubes to minimize the surface energy.

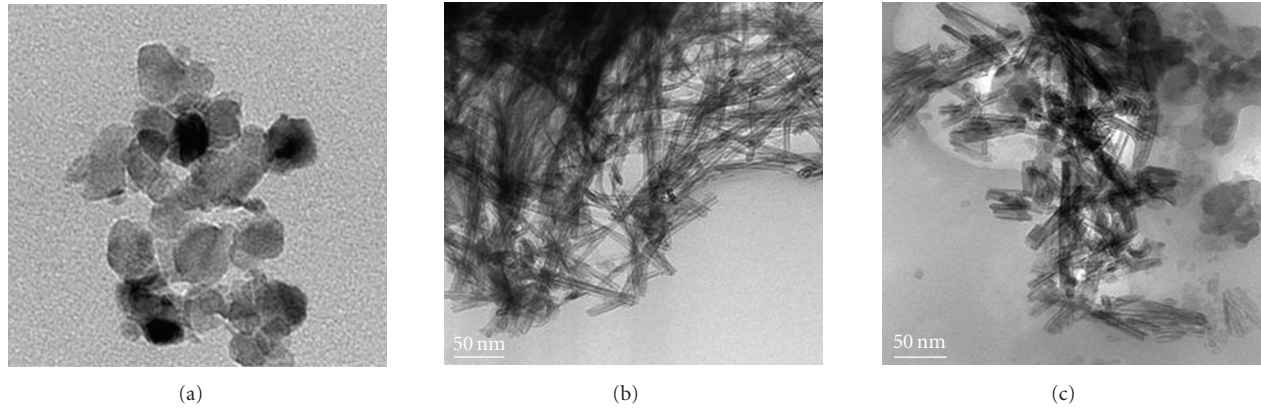


FIGURE 1: TEM micrographs of (a)  $\text{TiO}_2$  nanoparticles, (b) pure TNT (c) 5%  $\text{Gd}^{3+}$ -TNT.

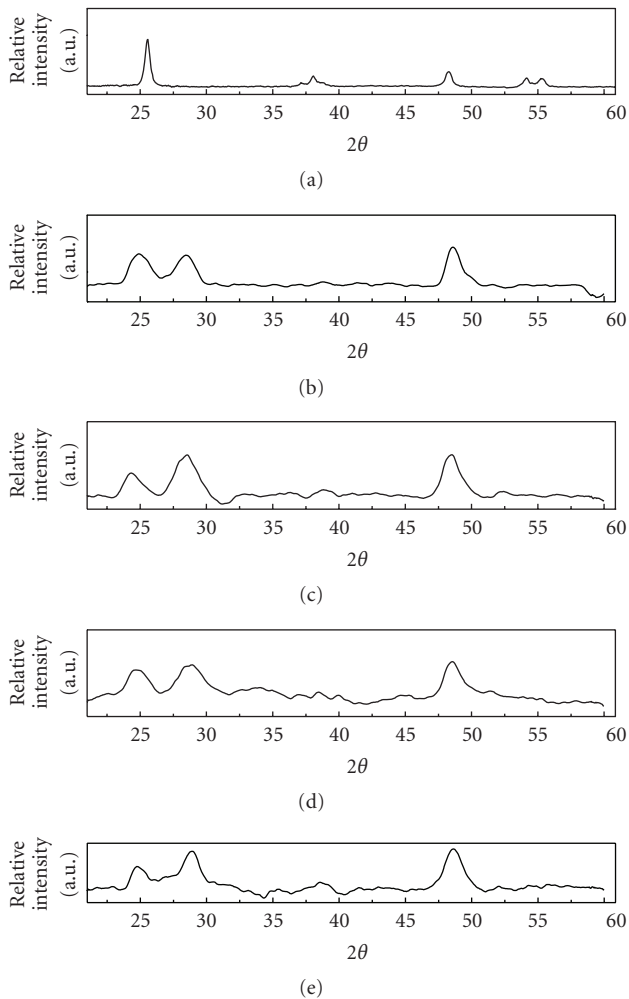


FIGURE 2: XRD patterns of: (a) Pure  $\text{TiO}_2$ ; (b) pure TNT, and (c) 2%  $\text{Gd}^{3+}$ -TNT; (d) 5%  $\text{Gd}^{3+}$ -TNT; (e) and 7%  $\text{Gd}^{3+}$ -TNT.

XRD patterns of the starting precursor titania nanoparticles and hydrothermally synthesized  $\text{Gd}^{3+}$ -titanate nanotubes with different  $\text{Gd}^{3+}$ -doping level (from 2%–7% molar ratio) are presented in Figure 2. For the starting

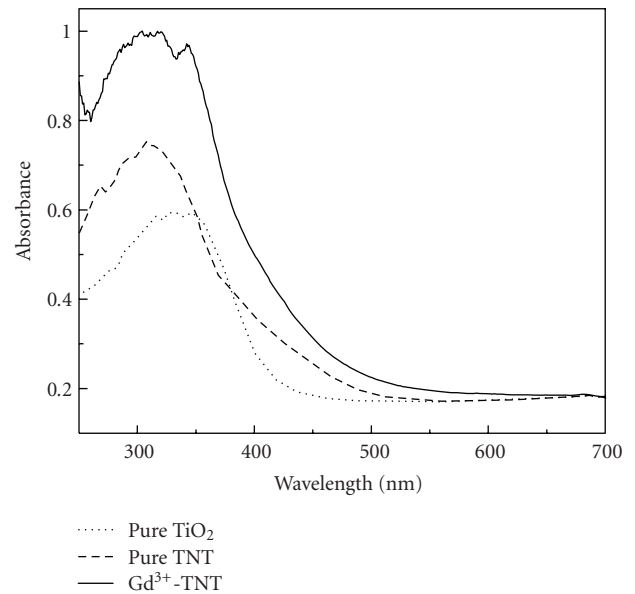


FIGURE 3: UV-Vis absorption spectra obtained from (1) pure  $\text{TiO}_2$ ; (2) Pure TNT; (3) 5%  $\text{Gd}^{3+}$ -TNT.

material (Figure 2(a)), only the peaks corresponding to the pure anatase  $\text{TiO}_2$  phase (JCPDS 21-1272) were observed. However, the titanate nanotubes have a new crystalline structure which is different from the well-defined anatase and rutile phase, but compatible with the reported phase of known titanate (see Figure 2(b)) [18]. The peak positions of the pure and the  $\text{Gd}^{3+}$ -doped titanate nanotubes are almost the same and the obtained diffraction peaks are identified to be those of  $\text{H}_3\text{Ti}_7\text{O}_{11}$  (JCPDS 44-0131) [19]. With enhancing the  $\text{Gd}^{3+}$ -doping level, it was found that there is no peak ascribed to gadolinia (Figures 2(c)–2(e)). It means that  $\text{Gd}^{3+}$  ions are indeed doped into the structure of titanate nanotubes and the doping of paramagnetic  $\text{Gd}^{3+}$  ions did not change the structure of nanotubes obviously [20].

**3.2. Optical Properties.** Figure 3 shows UV-Vis absorption spectra of the pure and  $\text{Gd}^{3+}$ -doped TNT compared with

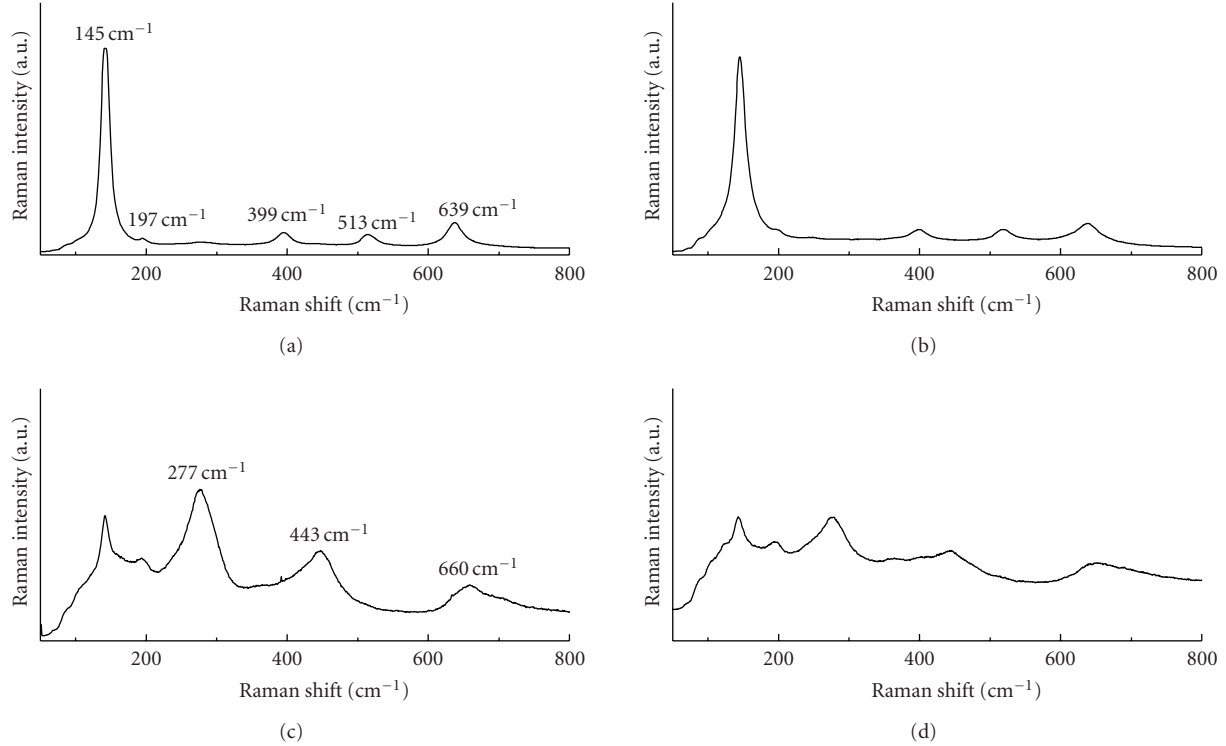


FIGURE 4: Raman spectra of: (a) Pure  $\text{TiO}_2$ ; (b) 5%  $\text{Gd}^{3+}$ - $\text{TiO}_2$ ; (c) Pure TNT; (d) 5%  $\text{Gd}^{3+}$ -TNT.

pure titania nanoparticles. A red shift of the absorption onset is observed for the doped TNT relative to the bulk anatase  $\text{TiO}_2$ . The observed visible light activity could be attributed to the charge-transfer transition between the f electrons of  $\text{Gd}^{3+}$  with the conduction or valence band of titanate [21].

The  $\text{Gd}^{3+}$ -doped titanate nanotubes were further characterized by Raman spectra, which are shown in Figure 4. The pure  $\text{TiO}_2$  anatase (Figure 4(a)) belongs to the symmetry space group  $D_{4h}^{19}$ . Group theory predicts six Raman active modes for the anatase phase: three  $E_g$  modes centered around 145, 197, and 639  $\text{cm}^{-1}$ ; two  $B_{1g}$  modes at 399 and 519  $\text{cm}^{-1}$ ; and an  $A_{1g}$  mode at 513  $\text{cm}^{-1}$  [22]. In the Raman spectrum of 5%  $\text{Gd}^{3+}$ -doped anatase nanoparticles (see Figure 4(b)), all the observed Raman peaks were also identified from the tetragonal anatase phase. After forming nanotube structures, their Raman spectrum is apparently different from its precursor anatase phase. In Figures 4(c) and 4(d), there are three new peaks located at 277, 443 and 660  $\text{cm}^{-1}$  in the Raman spectrum of the pure and  $\text{Gd}^{3+}$ -doped titanate nanotubes. The peak at 277  $\text{cm}^{-1}$  is assigned to the characteristic phonon mode of titanate nanotubes [23]. The peak at 443  $\text{cm}^{-1}$ , according to the study of Ma et al. [24], is assigned to the Ti–O bending vibration involving six-coordinated titanium atoms and three coordinated oxygen atoms. Based on the studies of Kasuga et al. [14], and Sun et al. [25], the peak at 660  $\text{cm}^{-1}$  is due to the H–O–Ti vibration in titanate nanotubes [2]. From the Raman spectrum of  $\text{Gd}^{3+}$ -doped titanate nanotubes, the presence of any other vibration modes from secondary phases (e.g., Gadolinium oxides or various  $\text{Gd}^{3+}$ -Ti oxide species) was not detected for any of these spectra.

**3.3. Thermal Analysis.** Differential scanning calorimetry (DSC) and thermogravimetric analysis (TGA) of the as synthesized  $\text{Gd}^{3+}$ -TNT are performed to study the thermal stability of the obtained nanotubes over a high range of temperature with a heating rate of 10°C/min in nitrogen atmosphere from room temperature to 800°C. The TGA/DSC data of 5%  $\text{Gd}^{3+}$ -doped TNT are shown in Figure 5. There are three weight loss peaks at 110, 180 and 300°C, which is inconsistent with three peaks in DSC spectrum of the doped-titanate nanotubes. The different weight loss peaks corresponded to water of different states in titanate nanotubes, including dissociated  $\text{H}_2\text{O}$  molecular; physisorbed  $\text{H}_2\text{O}$  molecular; chemisorbed  $\text{H}_2\text{O}$  molecular and Ti–OH bonds within tubular structure [23]. No obvious exothermal or endothermal peaks were observed over the temperature range 300 to 600°C, suggesting that the nanotubes have good thermal stability. The TGA/DSC data of the other  $x\%$   $\text{Gd}^{3+}$ -doped TNT (not shown here) are identical to that of 5%  $\text{Gd}^{3+}$ -TNT.

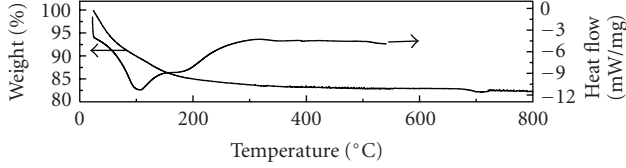
**3.4. Magnetic Properties.** Temperature dependence of the magnetic susceptibility  $\chi$  of the paramagnetic materials shows a Curie Weiss type behavior which can be expressed as follows [26, 27]:

$$\chi_M = \chi_{\text{diam.}} + \frac{C_M}{T - \theta_p}, \quad (1)$$

where  $\chi_{\text{diam}}$  is the diamagnetic susceptibility of the host matrix,  $C_M$  is the molar Curie constant,  $\theta_p$  is the paramagnetic Curie temperature, and  $T$  is the absolute temperature

TABLE 1: Magnetic parameters of  $x\text{Gd}-(100-x)\text{H}_2\text{Ti}_5\text{O}_{11}$  ( $x\%$   $\text{Gd}^{3+}$ -TNTs) where ( $x = 2, 5, 7$ ).

$X$ (mole % Gd)	$\theta_p$ , K, $\pm 0.04381$	$C_M$ , emu/mol, $\pm 0.17645$	$\chi_{\text{dia.}}$ , $\pm 0.00463$	$J$ , $\times 10^{-3}$	$\mu_{\text{eff.}}$ , $\mu_B$
2	-0.238	9.594	0.00054	24.86	6.19
5	-0.476	22.127	0.00467	21.53	6.16
7	-0.522	26.413	0.00026	19.77	5.49

FIGURE 5: DSC and DTG data for the 5%  $\text{Gd}^{3+}$ -TNT.

in kelvins. The dc magnetic susceptibility results for  $x\text{Gd}^{3+}-(100-x)\text{H}_3\text{Ti}_7\text{O}_{11}$ , where  $x = 0, 2, 5$  and  $7$  nanotube are displayed in Figure 6(a) as a function of the temperature  $T$ . It is clear from this figure that with the increase of  $\text{Gd}^{3+}$  ions content, the magnetic susceptibility is increased. The pure  $\text{TiO}_2$  shows the diamagnetic properties at the temperature higher than  $20\text{ K}$  while  $x\text{Gd}^{3+}-(100-x)\text{H}_3\text{Ti}_7\text{O}_{11}$  that is, ( $x\text{Gd}^{3+}-(100-x)$  TNTs) where ( $x = 2, 5$  and  $7$ ) showed a paramagnetic behavior. The data appear to follow a Curie–Weiss type behavior over the most of temperature range. All the measured curves are fitted according to the modified Curie Weiss law in the temperature range  $5\text{--}100\text{ K}$  with a correlation coefficient around  $0.9998$ . Values of the paramagnetic Curie temperature  $\theta_p$ , are determined for the investigated samples and tabulated in Table 1. The magnitude of the paramagnetic Curie temperature  $\theta_p$  increases with increasing the  $\text{Gd}^{3+}$  ions in the TNT matrix. Since the paramagnetic Curie temperature  $\theta_p$ , is a rough measure of the strength of the interaction between the magnetic ions in the samples, the higher value implies stronger interaction and/or more ions participating in the interaction. The negative small value for the paramagnetic Curie temperatures indicates that the magnetic interaction is predominately antiferromagnetic in  $\text{Gd}^{3+}$ -doped TNT.

Figure 6(b) shows the magnetization versus the applied field curves ( $M$  versus  $H$ ) of  $2\%$   $\text{Gd}^{3+}$ -98 TNT (as a representative example) at  $10\text{ K}$ . The almost linear field dependence of magnetization in this applied field range is a common feature of the paramagnetic compounds. Their fitting lines pass through the origin point indicating that  $\text{Gd}^{3+}$ -doped TNT is paramagnetic materials.

The experimental magnetic moment for the gadolinium ions  $\mu_{\text{Gd}^{3+}}$  was calculated according to the following relation [28]:

$$\mu_{\text{Gd}^{3+}}(\text{exp.}) = 2.827\sqrt{\frac{C_M}{x}}, \quad (2)$$

where  $x$  represents the molar fraction of  $\text{Gd}^{3+}$  inside the host matrix. The calculated values of the magnetic moment are given in Table 1. It is clear that the values of  $\mu_{\text{eff.}}$  is less

than the reported value of the atomic magnetic moment of  $\text{Gd}^{3+}$  ions in free ion state:  $\mu_{\text{Gd}^{3+}} = 7.98\mu_B$  [29–31]. The small negative values of  $\theta_p$ ,  $\theta_p < -2\text{ K}$  suggest the presence of weak antiferromagnetic interaction. The assumption of the antiferromagnetic nature of the interaction between the  $\text{Gd}^{3+}$  ions is also supported by the fact that the effective magnetic moment per gadolinium ion, is less than the magnetic moment of the free gadolinium ion  $\mu_{\text{Gd}^{3+}}$ .

Based on the experimental data, one can also determine the molecular field constant  $J$  as follows [32]:

$$J = \left| \frac{\theta_p}{C_M} \right| = \frac{2zJ_{ij}}{N \cdot g^2 \cdot \mu_B^2}, \quad (3)$$

where  $N$  and  $Z$  are the total and exchange-coupled number of magnetic ions,  $J_{ij}$  is the magnetic exchange integral,  $g$  is their spectroscopic splitting factor and  $\mu_B$  is the Bohr magnetron. The calculated values of  $J = \theta_p/C_M$  from the experimental data are given in Table 1. It is clear that the molecular field theory is approximately constant with increasing the  $\text{Gd}^{3+}$  ions content. This behavior assumes that the ratio  $z/N$  is constant, the number of exchange-coupled  $\text{Gd}^{3+}$  ions being proportional to the total number of magnetic ions in the samples. The data above are consistent with a random distribution of  $\text{Gd}^{3+}$  ions. The magnetic properties of the materials are due to both isolated and exchange-coupled  $\text{Gd}^{3+}$  ions, their relative number being dependent on composition [30].

When a magnetic field is applied to a magnetic material, its magnetic moments tend to align themselves in the magnetic field direction and a more ordered state is achieved, so the magnetic entropy of the system decreases. In an isothermal process of magnetization, the magnetic entropy change of the system due to the application of a magnetic field,  $\Delta S_M$ , can be derived from Maxwell relations in [27, 33]:

$$\Delta S_M(T, H) = \int_{H_{\min}}^{H_{\max}} \left( \frac{\partial M}{\partial T} \right)_H \cdot dH, \quad (4)$$

where  $H_{\min}$  and  $H_{\max}$  represent the initial and final values of the magnetic field. It seems clear that a high magneto-caloric effect will be observed when the temperature dependence of the magnetization (i.e.,  $\partial M/\partial T$ ) is large. This occurs, for example, at the Curie temperature for ferromagnetic-paramagnetic transitions, at which the maximum absolute value of the entropy change is expected, and at low temperatures for paramagnetic materials. Measurements of magnetic entropy variation when a fixed magnetic field change is applied allow one to determine whether a magnetic material may be considered to be a good magnetic refrigerant. Thus,

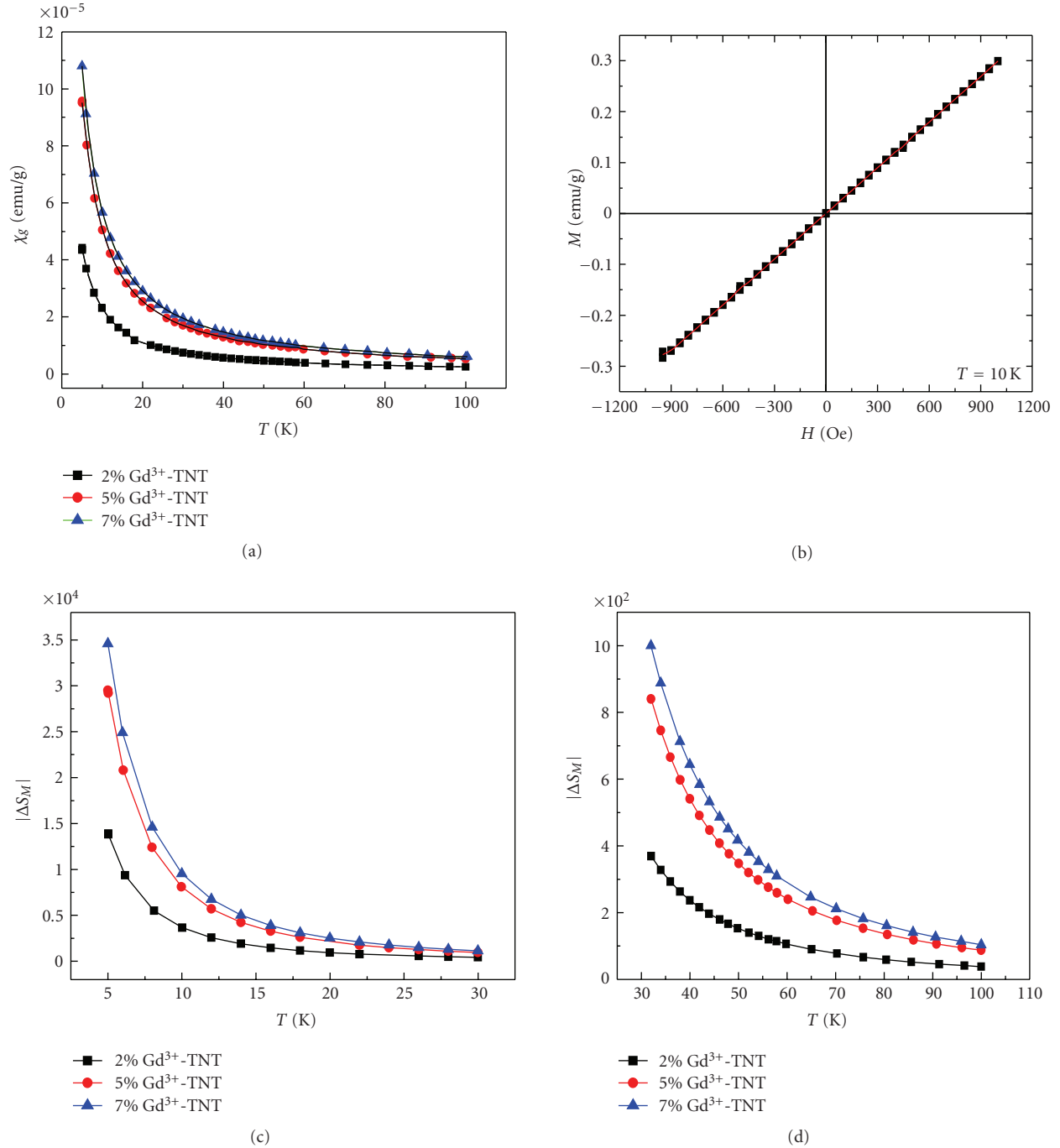


FIGURE 6: (a) dc magnetic susceptibility versus temperature for  $x$  Gd<sup>3+</sup>-(100- $x$ ) TNT, where ( $x = 2, 5, 7$ ); (b) The magnetization versus the applied field curves ( $M$  versus  $H$ ) of 2% Gd<sup>3+</sup>-98 TNT at 10 K (as a representative example); as well as (c) and (d) Temperature dependence of the entropy change for different mole percent of Gd<sup>3+</sup>-TNT under an external magnetic field equal to 400 Oe.

for paramagnetic materials, the entropy change  $\Delta S_M$  will be (5):

$$\Delta S_M = -\frac{C_M}{2} \frac{(\Delta H)^2}{(T - \theta_p)^2}, \quad (5)$$

where on has  $C_M$  in emu/mole,  $T$  and  $\theta$  in K and  $\Delta H$  in Oe. Figures 6(c) and 6(d) show the temperature dependence

of the entropy change obtained for different mole percent of Gd<sup>3+</sup> inside the host matrix TNT. It is clear that the entropy change decreases with increasing of the temperature and increased with increasing of the mole percent of Gd<sup>3+</sup> ions added to the host materials. This behavior is expected for paramagnetic materials because their magnetization increases quickly when the temperature decreases at a low temperature range. Because of their paramagnetic behavior

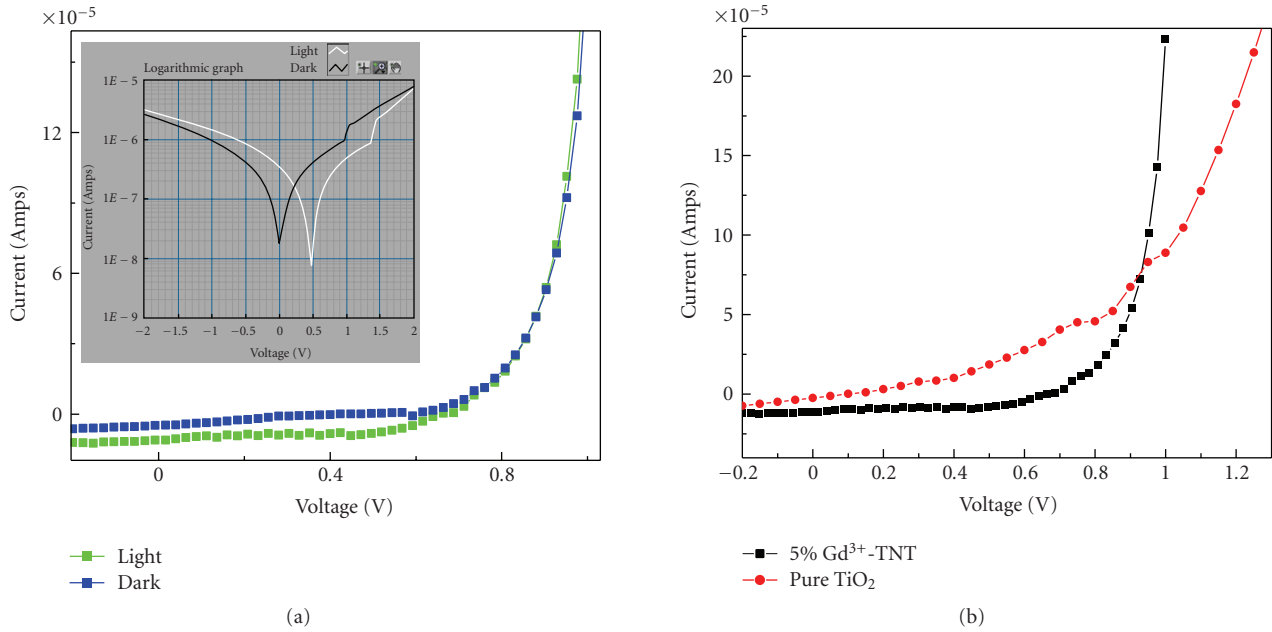


FIGURE 7: (a) Dark and Light IV curves of 5%  $Gd^{3+}$ -TNT/PTEBS hybrid polymer solar cell; (b) IV curves of pure  $TiO_2$  and 5%  $Gd^{3+}$ -TNT hybrid solar cells.

at low temperatures, these materials have an entropy change that increases its absolute value when the temperature decreases. This implies the possibility of using these materials as active magnetic refrigerants in a wide range of temperature (5–100k).

**3.5. Photovoltaic Efficiency of the Hybrid Polymer Solar Cells Based on  $Gd^{3+}$ -TNT.** The hybrid polymer solar cells were fabricated by spin coating of the 5%  $Gd^{3+}$ -titanate nanotube layer onto the conductive FTO-glass which is repeated several times to obtain a thick film with approximately  $8\ \mu m$ . The titanate film was then sintered at  $450^\circ C$  for 30 minutes. The PTEBS polymer is then drop cast on top of the resulting nanotube layer. The photocurrent-voltage IV characterization of the obtained device is shown in Figure 7. Dark and light IV characteristics of the device were tested under AM1.5 illumination with an intensity of approximately  $80\ mW/cm^2$  through the FTO electrode as shown in Figure 7(a). The PTEBS  $Gd^{3+}$ -doped TNT hybrid solar cell exhibits a short circuit current density ( $J_{sc}$ ) of  $84\ \mu A/cm^2$ , an open circuit voltage ( $V_{oc}$ ) of 0.66 V, and a fill factor (FF) of 0.49, resulting in a power conversion efficiency ( $\eta$ ) of 0.034%. Comparing with the PTEBS pure titania devices ( $\eta = 0.01\%$ ), a slightly higher photovoltaic performance of  $Gd^{3+}$ -TNT polymer solar cell was observed as illustrated in Figure 7(b). This could be attributed to a better polymer loading and light harvesting of the applied titanate nanotube film.

These preliminary results demonstrate promising application of gadolinium doped titanate nanotubes for efficient hybrid polymer solar cells. Better alignment of the paramagnetic  $Gd^{3+}$ -TNT in polymer solar cell by applying external

magnetic field is expected to enhance electron transport properties leading to more efficient light to electricity conversion. Further studies in this direction are in progress.

## 4. Conclusions

The aim has been to identify promising design for the future development of new multifunctional nanomaterials. We have successfully synthesized  $Gd^{3+}$ -TNT nanotubes through a simple hydrothermal procedure, and comprehensively characterized its properties. The structural and optical analyses indicate that doping of the TNT by  $Gd^{3+}$  enhances its thermal stability, hinders the growth of its crystallite size, and increases its surface area. Doped materials exhibit visible light absorption efficiency. Moreover,  $Gd^{3+}$ -TNT samples exhibit paramagnetic character and weak antiferromagnetic interaction. Testing the prepared hybrid polymer solar cells using doped 5%  $Gd^{3+}$ -TNT showed an improvement of light to electricity conversion efficiencies. There is still a need to optimize their alignment by external magnetic field manipulation to further improvement of the solar cells efficiency to a profitable exploitation extent.

## Acknowledgments

This work is primarily funded by a grant from the US-Egypt Joint Science and Technology Board. Dr. Mona M. Saif and Dr. I.S. Yahia were supported under the Partnership and Ownership initiative (PAROWN) from the Egyptian Ministry of Higher Education. TEM microscopy was performed at VCU Department of Neurobiology & Anatomy microscopy facility. XRD measurements were made in the VCU Department of Chemistry.

## References

- [1] T. Kasuga, M. Hiramatsu, A. Hoson, T. Sekino, and K. Niihara, "Formation of titanium oxide nanotube," *Langmuir*, vol. 14, no. 12, pp. 3160–3163, 1998.
- [2] Z. Tang, L. Zhou, L. Yang, and F. Wang, "A study on the structure transformation and luminescence of Eu(III) titanate nanotubes synthesized at various hydrothermal temperatures," *Journal of Alloys and Compounds*, vol. 481, no. 1–2, pp. 704–709, 2009.
- [3] W. Wang, J. Zhang, H. Huang, Z. Wu, and Z. Zhang, "Surface-modification and characterization of H-titanate nanotube," *Colloids and Surfaces A*, vol. 317, no. 1–3, pp. 270–276, 2008.
- [4] M. Adachi, Y. Murata, I. Okada, and S. Yoshikawa, "Formation of titania nanotubes and applications for dye-sensitized solar cells," *Journal of the Electrochemical Society*, vol. 150, no. 8, pp. G488–G493, 2003.
- [5] K. Uchiyama, M. Yoshida, Y. Hayashi, and K. Narasaka, "Synthesis of dihydropyrroles and tetrahydropyridines by the intramolecular cyclization of O-methylsulfonyloximes having an active methine group," *Chemistry Letters*, no. 7, pp. 607–608, 1998.
- [6] L. Fu, Z. Liu, Y. Liu, et al., "Coating carbon nanotubes with rare earth oxide multiwalled nanotubes," *Advanced Materials*, vol. 16, no. 4, pp. 350–352, 2004.
- [7] I. Burn and S. Neirman, "Dielectric properties of donor-doped polycrystalline SrTiO<sub>3</sub>," *Journal of Materials Science*, vol. 17, no. 12, pp. 3510–3524, 1982.
- [8] D. W. Hwang, J. S. Lee, W. Li, and S. H. Oh, "Electronic band structure and photocatalytic activity of Ln<sub>2</sub>Ti<sub>2</sub>O<sub>7</sub> (Ln = La, Pr, Nd)," *Journal of Physical Chemistry B*, vol. 107, no. 21, pp. 4963–4970, 2003.
- [9] M. A. Subramanian, G. Aravamudan, and G. V. Subba Rao, "Oxide pyrochlores—a review," *Progress in Solid State Chemistry*, vol. 15, no. 2, pp. 55–143, 1983.
- [10] K. B. Helean, S. V. Ushakov, C. E. Brown, et al., "Formation enthalpies of rare earth titanate pyrochlores," *Journal of Solid State Chemistry*, vol. 177, no. 6, pp. 1858–1866, 2004.
- [11] F. X. Zhang and S. K. Saxena, "Structural changes and pressure-induced amorphization in rare earth titanates RE<sub>2</sub>Ti<sub>2</sub>O<sub>7</sub> (RE: Gd, Sm) with pyrochlore structure," *Chemical Physics Letters*, vol. 413, no. 1–3, pp. 248–251, 2005.
- [12] N. Zhong, P. H. Xiang, D. Z. Sun, and X. L. Dong, "Effect of rare earth additives on the microstructure and dielectric properties of 0.67Pb(Mg<sub>1/3</sub>Nb<sub>2/3</sub>)O<sub>3</sub> – 0.33PbTiO<sub>3</sub> ceramics," *Materials Science and Engineering B*, vol. 116, no. 2, pp. 140–145, 2005.
- [13] S. T. Bramwell, M. N. Field, M. J. Harris, and I. P. Parkin, "Bulk magnetization of the heavy rare earth titanate pyrochlores—a series of model frustrated magnets," *Journal of Physics: Condensed Matter*, vol. 12, no. 4, pp. 483–495, 2000.
- [14] T. Kasuga, M. Hiramatsu, A. Hoson, T. Sekino, and K. Niihara, "Titania nanotubes prepared by chemical processing," *Advanced Materials*, vol. 11, no. 15, pp. 1307–1311, 1999.
- [15] Q. Qiao and J. T. McLeskey Jr., "Water-soluble polythiophene-nanocrystalline TiO<sub>2</sub> solar cells," *Applied Physics Letters*, vol. 86, no. 15, Article ID 153501, 3 pages, 2005.
- [16] P. Ravirajan, D. D. C. Bradley, J. Nelson, et al., "Efficient charge collection in hybrid polymer/ TiO<sub>2</sub> solar cells using poly(ethylenedioxythiophene)/polystyrene sulphonate as hole collector," *Applied Physics Letters*, vol. 86, no. 14, Article ID 143101, 3 pages, 2005.
- [17] N. Viriya-Empikul, N. Sano, T. Charinpanitkul, T. Kikuchi, and W. Tanthapanichakoon, "A step towards length control of titanate nanotubes using hydrothermal reaction with sonication pretreatment," *Nanotechnology*, vol. 19, no. 3, Article ID 035601, 6 pages, 2008.
- [18] Q. Chen, W. Zhou, G. H. Du, and L.-M. Peng, "Trititanate nanotubes made via a single alkali treatment," *Advanced Materials*, vol. 14, no. 17, pp. 1208–1211, 2002.
- [19] *JCPDS PDF-2 Release 2001*, ICDD, Newtown Square, Pa, USA, 2001.
- [20] M. Wang, G. Song, J. Li, L. Miao, and B. Zhang, "Direct hydrothermal synthesis and magnetic property of titanate nanotubes doped magnetic metal ions," *Journal of University of Science and Technology Beijing: Mineral Metallurgy Materials*, vol. 15, no. 5, pp. 644–648, 2008.
- [21] W. Zhou, Y. Zhou, and S. Tang, "Formation of TiO<sub>2</sub> nano-fiber doped with Gd<sup>3+</sup> and its photocatalytic activity," *Materials Letters*, vol. 59, no. 24–25, pp. 3115–3118, 2005.
- [22] M. Mikami, S. Nakamura, O. Kitao, and H. Arakawa, "Lattice dynamics and dielectric properties of TiO<sub>2</sub> anatase: a first-principles study," *Physical Review B*, vol. 66, no. 15, Article ID 10.1103/PhysRevB.66.155213, 6 pages, 2002.
- [23] L. Qian, Z.-L. Du, S.-Y. Yang, and Z.-S. Jin, "Raman study of titania nanotube by soft chemical process," *Journal of Molecular Structure*, vol. 749, no. 1–3, pp. 103–107, 2005.
- [24] R. Ma, K. Fukuda, T. Sasaki, M. Osada, and Y. Bando, "Structural features of titanate nanotubes/nanobelts revealed by raman, X-ray absorption fine structure and electron diffraction characterizations," *Journal of Physical Chemistry B*, vol. 109, no. 13, pp. 6210–6214, 2005.
- [25] X. Sun and Y. Li, "Synthesis and characterization of ion-exchangeable titanate nanotubes," *Chemistry: A European Journal*, vol. 9, no. 10, pp. 2229–2238, 2003.
- [26] M. A. Salim, G. D. Khattak, P. S. Fodor, and L. E. Wenger, "X-ray photoelectron spectroscopy (XPS) and magnetization studies of iron-vanadium phosphate glasses," *Journal of Non-Crystalline Solids*, vol. 289, no. 1–3, pp. 185–195, 2001.
- [27] A. Fernández, X. Bohigas, J. Tejada, E. A. Sulyanova, I. I. Buchinskaya, and B. P. Sobolev, "The magnetocaloric effect in high-spin paramagnetic rare-earth fluorites," *Materials Chemistry and Physics*, vol. 105, no. 1, pp. 62–66, 2007.
- [28] S. Simon, I. Ardelean, S. Filip, I. Bratu, and I. Cosma, "Structure and magnetic properties of Bi<sub>2</sub>O<sub>3</sub>-Gd<sub>2</sub>O<sub>3</sub>-Gd<sub>2</sub>O<sub>3</sub> glasses," *Solid State Communications*, vol. 116, no. 2, pp. 83–86, 2000.
- [29] I. Coroiu, E. Culea, I. Vida Simiti, and A. Darabont, "Magnetic properties of some gadolinium silica glass ceramics," *Journal of Optoelectronics and Advanced Materials*, vol. 8, no. 2, pp. 526–528, 2006.
- [30] I. Ardelean and L. Griguta, "EPR and magnetic susceptibility studies of B<sub>2</sub>O<sub>3</sub>-Bi<sub>2</sub>O<sub>3</sub>-Gd<sub>2</sub>O<sub>3</sub> glasses," *Journal of Non-Crystalline Solids*, vol. 353, no. 24–25, pp. 2363–2366, 2007.
- [31] Y. B. Saddeek, I. S. Yahia, W. Dobrowolski, L. Kilanski, N. Romčević, and M. Arciszewska, "Infrared, raman spectroscopy and ac magnetic susceptibility of Gd<sub>2</sub>O<sub>3</sub>-TeO<sub>2</sub>-V<sub>2</sub>O<sub>5</sub> glasses," *Optoelectronics and Advanced Materials-Rapid Communications*, vol. 3, pp. 559–564, 2009.
- [32] L. F. Bates, *Modern Magnetism*, Cambridge University, London, UK, 1962.
- [33] A. M. Tishin and Y. I. Spichkin, *The Magnetocaloric Effect and Its Applications*, chapter 1, Institute of Physics Publishing, Bristol, UK, 2003.

## Research Article

# Improved Performances of a Fluidized Bed Photoreactor by a Microscale Illumination System

Paolo Ciambelli,<sup>1,2</sup> Diana Sannino,<sup>1,2</sup> Vincenzo Palma,<sup>1</sup> Vincenzo Vaiano,<sup>1</sup>  
and Roberto S. Mazzei<sup>1</sup>

<sup>1</sup>Department of Chemical and Food Engineering, University of Salerno, Via Ponte Don Melillo, 84084 Fisciano (Salerno), Italy

<sup>2</sup>NANO\_MATES, Research Centre for Nanomaterials and Nanotechnology at Salerno University, University of Salerno, Via Ponte Don Melillo, 84084 Fisciano (Salerno), Italy

Correspondence should be addressed to Diana Sannino, dsannino@unisa.it

Received 31 March 2009; Revised 17 July 2009; Accepted 2 September 2009

Recommended by Mohamed Sabry Abdel-Mottaleb

The performances of a gas-solid two-dimensional fluidized bed reactor in photocatalytic selective oxidation reactions, irradiated with traditional UV lamps or with a microscale illumination system based on UV emitting diodes (UVA-LEDs), have been compared. In the photocatalytic oxidative dehydrogenation of cyclohexane to benzene on  $\text{MoO}_x/\text{TiO}_2\text{-Al}_2\text{O}_3$  catalyst the use of UVA-LEDs modules allowed to achieve a cyclohexane conversion and benzene yield higher than those obtained with traditional UV lamps. The better performances with UVA-LEDs are due to the UVA-LEDs small dimensions and small-angle emittance, which allow photons beam be directed towards the photoreactor windows, reducing the dispersion outside of photoreactor or the optical path length. As a consequence, the effectively illuminated mass of catalyst is greater. We have found that this illumination system is efficient for photo-oxidative dehydrogenation of cyclohexane to cyclohexene on sulphated  $\text{MoO}_x/\gamma\text{-Al}_2\text{O}_3$  and ethanol to acetaldehyde on  $\text{VO}_x/\text{TiO}_2$ .

Copyright © 2009 Paolo Ciambelli et al. This is an open access article distributed under the Creative Commons Attribution License, which permits unrestricted use, distribution, and reproduction in any medium, provided the original work is properly cited.

## 1. Introduction

Heterogeneous photocatalysis is the subject of an increasing interest during the last twenty years. A challenging research topic is the synthesis and production of chemicals by partial photo-oxidation reactions by molecular oxygen under mild conditions [1]. In this context photocatalysis can lead to more sustainable processes by increasing both reactivity and selectivity towards the desired products because of mild operating conditions, that are, low temperature and pressure [2]. However, a competitive full-scale photocatalytic oxidation process in industrial application requires overcoming photons and mass transfer limitations in the photocatalytic reactors [2]. With reference to mass transfer limitations a large number of novel solutions have been developed for the photoreactors, including spinning disc reactors [3, 4], monolith photoreactors [5], and microreactors [6]. Fluidized bed photoreactors are well known in enhancing mass transfer kinetics. Moreover, they provide easy temperature control

and good contacting between reactants and photocatalysts with respect to fixed bed photoreactors [7–11].

Regarding photons transfer, microscale illumination systems are a promising solution [2]. This type of illumination is realized mainly by irradiating the photoreactor with UV emitting diodes (UVA-LEDs) device [12–14]. LEDs are replacing traditional UV lamps in many applications, owing to the much higher efficiency in light-electricity conversion, since the light emission by LEDs is induced by the recombination of electrons and holes excess [15]. Further advantages of LEDs derive from the small dimensions, robustness, and the long lasting (hundred thousands of hours compared to thousands of hours in the case of classical lamps) [2].

The use of microscale illumination in photoreactors can provide both a large catalyst surface area per unit of reactor volume and high illumination efficiency, also profiting of the small angle of emittance of the LEDs [2].

In this work, the performances of a gas-solid two-dimensional fluidized bed reactor with traditional UV lamps

TABLE 1: List of the photocatalysts and their characteristics

Catalyst	Support	V <sub>2</sub> O <sub>5</sub> wt%	MoO <sub>3</sub> wt%	SO <sub>4</sub> wt%	SSA m <sup>2</sup> /g	Band gap energy eV
8Mo2S	γ-Al <sub>2</sub> O <sub>3</sub>	0	8	2.6	147	3.4
5V	TiO <sub>2</sub>	5	0	0.2	74	2.5
10MoPCAl	TiO <sub>2</sub> -Al <sub>2</sub> O <sub>3</sub>	0	10	0.8	148	3.3

and with a microscale illumination system based on UV emitting diodes (UVA-LEDs) have been compared for the oxidative dehydrogenation of cyclohexane to benzene as probe reaction. The effectiveness of the device in photocatalytic oxidative dehydrogenation both in cyclohexane to cyclohexene and in ethanol to acetaldehyde was also evaluated.

## 2. Experimental

**2.1. Catalysts Preparation.** The photocatalysts formulation investigated in this work (Table 1) is the result of previous optimization studies on photo-oxidative dehydrogenation of cyclohexane to benzene [16] or cyclohexene [9, 10], and of ethanol to acetaldehyde [17].

The 8Mo2S photocatalyst was prepared by wet impregnation of Al<sub>2</sub>O<sub>3</sub> (Puralox SBA 150, SASOL, 144 m<sup>2</sup>/g) with aqueous solution of ammonium heptamolybdate (NH<sub>4</sub>)<sub>6</sub> Mo<sub>7</sub>O<sub>24</sub> · 4H<sub>2</sub>O. Powder samples were dried at 120°C for 12 hours and calcined in air at 500°C for 3 hours. A successive wet impregnation with aqueous solution of ammonium sulphate was performed to obtain sulphated catalyst samples [9, 10].

The TiO<sub>2</sub>-Al<sub>2</sub>O<sub>3</sub> formed support was prepared by dispersing the parent titania (PC100, 87 m<sup>2</sup>/g, 20 nm crystallites average size, provided by Millenium Inorganic Chemicals) powder in a boehmite sol (10 wt% of Condea Pural in bydistilled water, pH < 2 by HNO<sub>3</sub>). The sol was gelled by slight heating until it was too viscous to stir. The gel was thus dried at 120°C for 3 hours and calcined at 500°C for 2 hours. After calcination the solid was crushed and sieved to 50–90 μm size. Finally, the solid (30 wt% Al<sub>2</sub>O<sub>3</sub>) was impregnated with (NH<sub>4</sub>)<sub>6</sub>Mo<sub>7</sub>O<sub>24</sub> solution, dried and calcined at 400°C [16] to have 10MoPCAl sample.

The 5V catalyst was prepared by wet impregnation method. Anatase titania sample (PC105, 86 m<sup>2</sup>/g, 23 nm crystallites average size, provided by Millenium Inorganic Chemicals) was added to an aqueous solution of NH<sub>4</sub>VO<sub>3</sub> and dried at 120°C until achieving a dense paste. The paste was calcined in static air heating up to 400°C at 10°C/min heating rate, then kept isotherm for 3 hours to get the final catalyst [17].

The specific surface area of calcined samples was evaluated by N<sub>2</sub> adsorption isotherm at –196°C with a Costech Sorptometer 1040, after pretreatment at 180°C for 2 hours in He flow (99.9990%).

UV-Vis reflectance spectra of powder bare catalysts were recorded by a Perkin Elmer spectrophotometer Lambda 35 with an RSA-PE-20 reflectance spectroscopy accessory (Labsphere Inc., North Sutton, NH). An 8° sample positioning holder was used to obtain total reflectance spectra with

reference to a calibrated standard SRS-010-99 (Labsphere Inc., North Sutton, NH). The reflectance data were reported as the F(R<sub>∞</sub>) value from Kubelka-Munk theory versus the wavelength. Band gap determinations were made by plotting [F(R<sub>∞</sub>) \* hν]<sup>2</sup> versus hν (eV) as reported in [9, 10].

**2.2. Photoreactor and Photocatalytic Tests.** A two-dimensional fluidized bed photoreactor was designed in order to improve both exposure of the catalysts to light irradiation and contact between reactants and catalysts [18]. The reactor is a two-dimensional fluidized bed system with 40 mm × 10 mm cross section, 230 mm height, pyrex-glass walls (2 mm thickness), and a bronze filter (mean pores size 5 μm) to provide uniform distribution of fed gas [9, 18]. In the first configuration the reactor was illuminated by two UV lamps (EYE MERCURY LAMP, 125 W) with spectrum emission centred at 365 nm, in a dark box (Figure 1(a)). The light intensity entering at the reactor walls, measured by an UVA meter, was 30 mW/cm<sup>2</sup>. The reaction temperature was controlled by a PID temperature controller connected to a heating system positioned at the external of the reactor, into the dark box surrounding it (Figure 1(b)). In the second configuration the same fluidized bed reactor was irradiated by two or four UVA-LEDs modules positioned in front of the Pyrex windows.

In Figure 2 an overall view and a schematic picture of the fluidized bed photoreactor equipped with UVA-LEDs device are shown. The reactor is also equipped with an internal electrical heater, immersed within the catalytic bed to control the reaction temperature (Figure 2(a)), avoiding the use of external screens.

Each UVA-LED module consists of 20 pieces of UVA-LEDs, emitting at 365 nm with a band width of about 38 nm. The modules (Figure 3(a)) were assembled and adapted to the fluidized bed photoreactor windows in the best way to obtain the maximum reactor surface illumination.

A cooling system (Figure 3(b)) was designed with CAD software and manufactured by using a rapid prototyping technique. In front of the cooling box, a perforated grid, designed to contain one UVA-LED in each hole of the grid, was inserted. The cooling fluid was compressed air injected at a pressure of about 5 bars. This device (Figure 3(b)) ensures a perfect cooling of each UVA-LEDs module, whose operating temperature should not exceed 75–80°C.

The use of four UVA-LEDs modules resulted in a larger irradiated window allowing to load a catalysts weight doubled with respect to two UVA-LEDs modules. An electrical control system connected to UVA-LEDs allows to control the light intensity incident to the external walls of the photoreactor. The light intensity was varied in the range 30–124 mW/cm<sup>2</sup>.

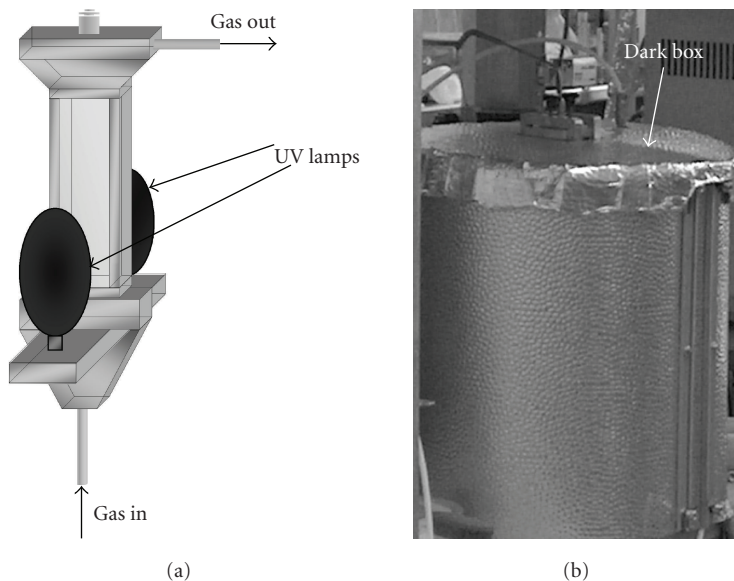


FIGURE 1: (a) Schematic picture of the fluidized bed photoreactor with UV lamps and (b) surrounded by dark box.

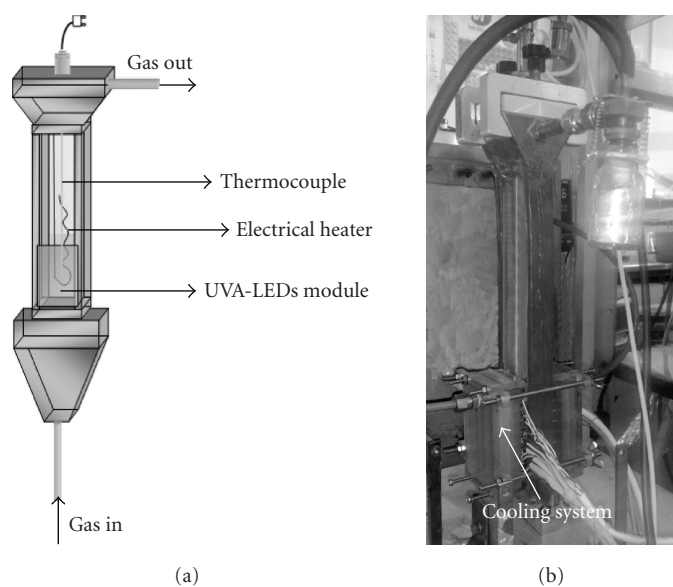


FIGURE 2: Fluidized bed photoreactor with UVA-LEDs device.

Photocatalytic activity tests were performed with the laboratory apparatus shown in Figure 4. Hydrocarbons and water were vaporized by two temperature controlled saturators. The gas flow rates were measured and regulated by mass flow controllers (Brooks Instrument). Concentrations of inlet reactants and outlet products were measured by an online quadrupole mass detector (Trace MS, ThermoElectron) and a continuous CO-CO<sub>2</sub> NDIR analyzer (Uras 10, Hartmann & Braun).

### 3. Results and Discussion

Typical photocatalytic test started feeding the gas reacting mixture to the photoreactor at reaction temperature in dark.

After complete adsorption of reactant on the catalyst surface corresponding to the restoring of initial inlet concentration, UV sources were switched on. Without UV irradiation no reaction products were observed either during the hydrocarbon dark adsorption or after hydrocarbon adsorption equilibrium was reached.

*3.1. Photocatalytic Oxidative Dehydrogenation of Cyclohexane to Benzene.* Photocatalytic oxidative dehydrogenation of cyclohexane to benzene was carried out on 10MoPCAl catalyst feeding 830 (stp) cm<sup>3</sup>/min nitrogen stream containing 0.1 vol. % cyclohexane, with oxygen/cyclohexane and water/cyclohexane ratio equal to 1.5 and 1.6, respectively. The reaction temperature was set at 120°C. In Figure 5

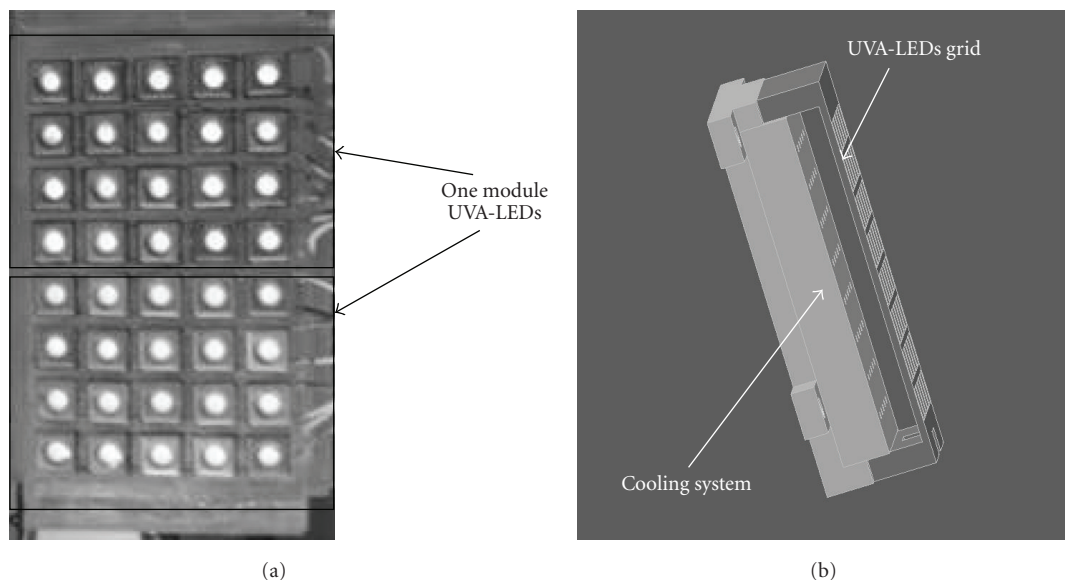


FIGURE 3: (a) UVA LEDs modules, inside the black rectangles, and (b) UVA-LEDs cooling system.

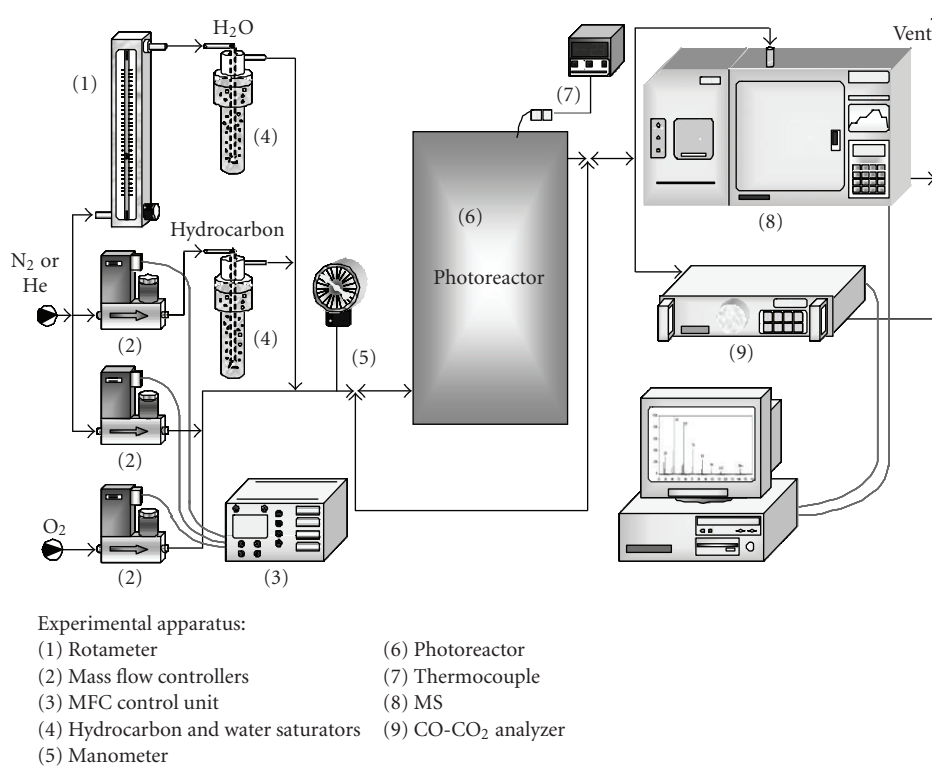


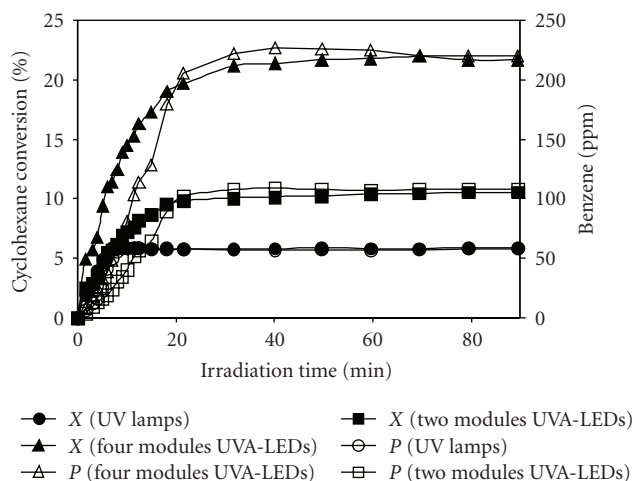
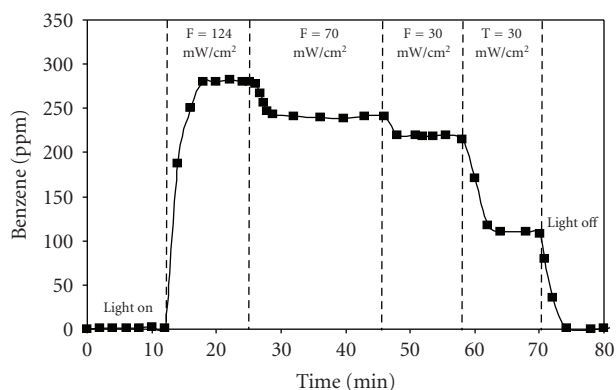
FIGURE 4: Laboratory apparatus for photocatalytic tests.

cyclohexane conversion ( $X$ ) and benzene production ( $P$ ) are compared by using UVA-LEDs or UV lamps. It is observed that by using two UVA-LEDs modules (catalyst weight: 14 g), the cyclohexane conversion and benzene concentration were, respectively, 11% and 108 ppm, while by using UV lamps (catalyst weight: 14 g) the values were 6% and 58 ppm. This result indicates that UVA-LEDs have better performances in

terms of catalyst illumination due to the special geometry that hinders photons dispersion. As a consequence, the effectively illuminated mass of catalyst is larger. With four UVA-LEDs modules (catalyst weight: 28 g) the benzene concentration was higher (217 ppm), the cyclohexane conversion reaching 22%. In all cases the selectivity to benzene was higher than 99%.

TABLE 2: Apparent quantum yield for different illumination systems; T: two UVA-LEDs modules; F: four UVA-LEDs modules.

UV source	Cyclohexane conversion %	Catalyst weight g	Incident light intensity $\text{mW}/\text{cm}^2$	Irradiated window $\text{cm}^2$	Apparent quantum yield %
UV lamps	6	14	30	92	0.44
T	11	14	30	40	1.86
F	22	28	30	80	1.86

FIGURE 5: Cyclohexane conversion ( $X$ ) and benzene concentration ( $P$ ) as a function of irradiation time; reaction temperature:  $120^\circ\text{C}$ ; light intensity:  $30\text{ mW}/\text{cm}^2$ ; catalyst:  $10\text{ MoPCAL}$ .FIGURE 6: Benzene concentration as function of run time and light intensity; catalyst:  $10\text{ MoPCAL}$ ; catalyst weight:  $28\text{ g}$ ; reaction temperature:  $120^\circ\text{C}$ ; T: two UVA-LEDs modules; F: four UVA-LEDs modules.

The apparent quantum yield, calculated as the ratio between the number of cyclohexane molecules reacted per second and the number of photons entering the reactor per second, is reported in Table 2.

It is evident that the apparent quantum yield with UVA-LEDs is fourfold that obtained with UV lamps, clearly indicating that process limitations are due to photon transfer. The apparent quantum yield is similar by using two and four UVA-LEDs modules, as expected since the amount of

incident photons per gram of photocatalyst is the same. This comparison evidences the better performances of UVA-LEDs, due to their small dimensions and small-angle emittance, which allow photons beam be directed towards the photoreactor windows, limiting their dispersion outside of photoreactor or the length of the optical path.

To assess the effect of light intensity the experiments were performed ranging between 0 and  $124\text{ mW}/\text{cm}^2$  and with different number of UVA-LEDs modules. The cyclohexane consumption rate grows with light intensity (not reported). The results are plotted in Figure 6 in terms of benzene concentration.

It is worthwhile to note that benzene did not form in the absence of light, while its outlet concentration grew up to  $280\text{ ppm}$  with a light intensity of  $124\text{ mW}/\text{cm}^2$  and catalyst weight of  $28\text{ g}$ . It is evident that the benzene concentration decreases by decreasing the light intensity and that, at the same light intensity value ( $30\text{ mW}/\text{cm}^2$ ), it was two times higher with four modules of UVA-LEDs compared to two UVA-LEDs modules illumination.

**3.2. Photocatalytic Oxidative Dehydrogenation of Cyclohexane to Cyclohexene.** In photocatalytic oxidative dehydrogenation of cyclohexane to cyclohexene the best condition for catalyst fluidization was obtained mixing  $7$  or  $14\text{ g}$  of  $8\text{ Mo}_2\text{S}$  catalyst with  $16$  or  $32\text{ g}$  of  $\alpha\text{-Al}_2\text{O}_3$ , respectively. The operating conditions for photocatalytic oxidative dehydrogenation of cyclohexane to cyclohexene were the same as those used for cyclohexane oxidative dehydrogenation to benzene. The incident light intensity was  $90\text{ mW}/\text{cm}^2$ . The photocatalyst allowed  $100\%$  conversion of cyclohexane to cyclohexene, without formation of benzene and  $\text{CO}_2$  as by-products [9, 10].

Cyclohexene was the only product detected in the gas phase; it was formed simultaneously to cyclohexane conversion after the UV irradiation was switched on (Figure 7). Cyclohexene outlet concentration reached the highest value ( $110\text{ ppm}$  after  $40$  minutes) with four UVA-LEDs modules and  $14\text{ g}$  catalyst weight, while by using two UVA-LEDs modules and  $7\text{ g}$  catalyst weight it was smaller (about  $70\text{ ppm}$ ) (Figure 7).

**3.3. Photocatalytic Oxidative Dehydrogenation of Ethanol to Acetaldehyde.** Photocatalytic oxidative dehydrogenation of ethanol to acetaldehyde was carried out on  $5\text{ V}$  catalyst [17], feeding  $830\text{ (stp) cm}^3/\text{min}$  He stream containing  $0.2$  or  $1\text{ vol. \%}$  ethanol with oxygen/ethanol ratio equal to  $2$ ; reaction temperature and pressure were, respectively,  $100^\circ\text{C}$  and  $1\text{ atm}$ . The incident light intensity was  $90\text{ mW}/\text{cm}^2$ .

TABLE 3: Influence of inlet ethanol concentration and UVA-LEDs modules number on ethanol conversion, acetaldehyde concentration, and apparent quantum yield.

UVA-LEDs modules number	Inlet ethanol concentration vol. %	Ethanol conversion %	Acetaldehyde concentration ppm	Incident light intensity mW/cm <sup>2</sup>	Irradiated window cm <sup>2</sup>	Apparent quantum yield %
2	0.2	73	1416	90	40	8.2
2	1	27	2592	90	40	15.2
4	0.2	100	1940	90	80	5.6
4	1	57	5472	90	80	16.1

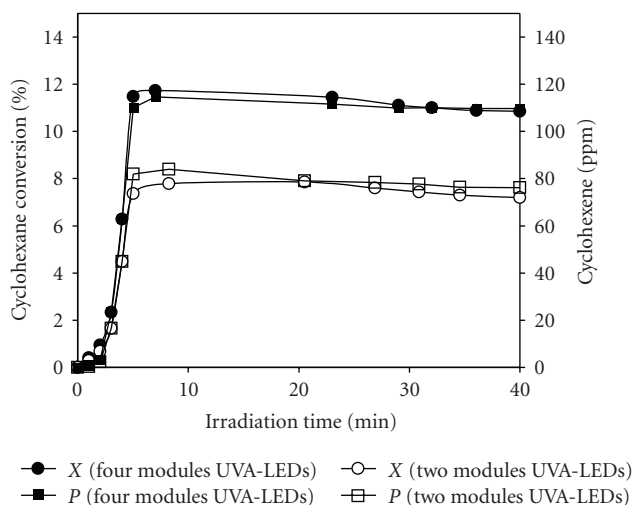


FIGURE 7: Cyclohexane conversion ( $X$ ) and cyclohexene concentration ( $P$ ) as a function of irradiation time; temperature: 120°C; light intensity: 90 mW/cm<sup>2</sup>; catalyst: 8Mo2S.

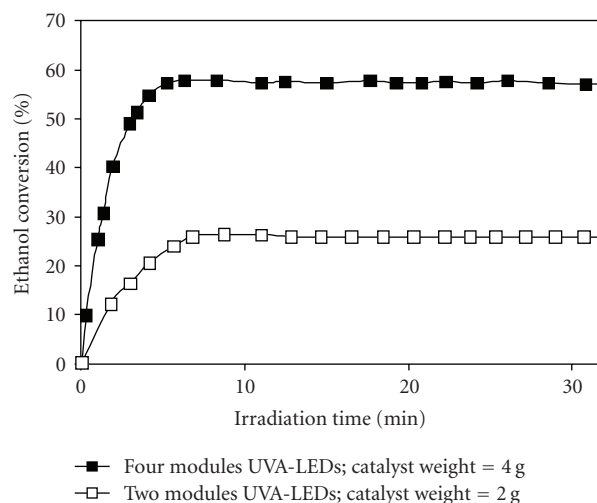


FIGURE 9: Ethanol conversion as function of irradiation time; initial ethanol concentration: 1 vol. %; reaction temperature: 100°C; light intensity: 90 mW/cm<sup>2</sup>; catalyst: 5V.

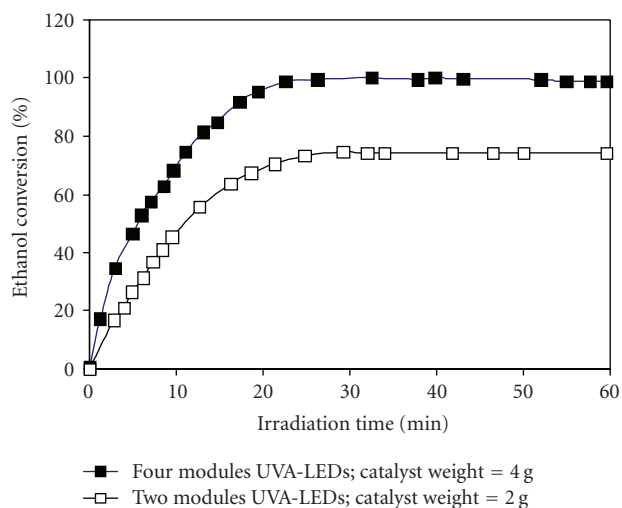


FIGURE 8: Ethanol conversion as function of irradiation time; initial ethanol concentration: 0.2 vol. %; reaction temperature: 100°C; light intensity: 90 mW/cm<sup>2</sup>; catalyst: 5V.

Similar selectivity values to acetaldehyde (96%-97%) were obtained for both values of ethanol concentration and

only CO<sub>2</sub> and ethylene were detected as by-products. Both ethanol conversion and products concentrations (Figures 8 and 9) remained unchanged during the irradiation time (~60 minutes). The dependence of ethanol conversion from catalyst weight and irradiation configuration at 0.2 and 1 vol. % inlet concentration are shown in Figures 8 and 9, respectively.

The comparison of the photocatalytic performances with two modules of UVA-LEDs and 2 g catalyst weight shows that ethanol conversion decreases from 73% to 27% by increasing ethanol initial concentration from 0.2 to 1 vol. %, with small differences in products selectivity.

However, this corresponds to an increase of acetaldehyde concentration from 1416 to 2592 ppm (Table 3). Similarly, with four modules of UVA-LEDs and 4 g catalyst weight ethanol conversion was complete with 0.2 vol. % alcohol initial concentration and reached about 57% with 1 vol. %, giving up to 5472 ppm of acetaldehyde outlet concentration without variation in products selectivity. Apparent quantum yield increased by increasing ethanol inlet concentration (Table 3) reaching higher values than usually reported [19, 20]. At high ethanol initial concentration quite similar values of apparent quantum yield were found with two and four UVA-LEDs modules.

## 4. Conclusions

In this work the photocatalytic performances of a two-dimensional fluidized bed reactor illuminated by traditional UV lamps and by a microscale illumination system based on UVA-LEDs have been compared for the oxidative dehydrogenation of cyclohexane to benzene as probe reaction.

By irradiating the fluidized bed reactor by UVA-LEDs higher photoactivity was achieved with  $\text{MoO}_x/\text{TiO}_2\text{-Al}_2\text{O}_3$  catalyst in similar operating conditions than with UV lamps. The microscale illumination system based on UVA-LEDs allowed overcoming photon transfer limitations. Better performances in terms of catalyst illumination were likely due to the special geometry of UV-LEDs that avoids photons dispersion and long optical paths. Moreover, the UV-LEDs-fluidized bed photoreactor has smaller dimension and higher safety and does not need any deflectors. Microscale illumination is very effective also in different synthesis reactions such as photocatalytic oxidative dehydrogenation of cyclohexane to cyclohexene on fluidizable sulphated  $\text{MoO}_x/\gamma\text{-Al}_2\text{O}_3$  and ethanol to acetaldehyde on  $\text{VO}_x/\text{TiO}_2$ .

## Acknowledgment

The authors thank Millenium Inorganic Chemicals for providing titania samples used in this work.

## References

- [1] C. B. Almquist and P. Biswas, "The photo-oxidation of cyclohexane on titanium dioxide: an investigation of competitive adsorption and its effects on product formation and selectivity," *Applied Catalysis A*, vol. 214, no. 2, pp. 259–271, 2001.
- [2] T. Van Gerven, G. Mul, J. Moulijn, and A. Stankiewicz, "A review of intensification of photocatalytic processes," *Chemical Engineering and Processing*, vol. 46, no. 9, pp. 781–789, 2007.
- [3] D. D. Dionysiou, G. Balasubramanian, M. T. Suidan, A. P. Khodadoust, I. Baudin, and J.-M. Lainé, "Rotating disk photocatalytic reactor: development, characterization, and evaluation for the destruction of organic pollutants in water," *Water Research*, vol. 34, no. 11, pp. 2927–2940, 2000.
- [4] H. C. Yatmaz, C. Wallis, and C. R. Howarth, "The spinning disc reactor—studies on a novel  $\text{TiO}_2$  photocatalytic reactor," *Chemosphere*, vol. 42, no. 4, pp. 397–403, 2001.
- [5] H. Lin and K. T. Valsaraj, "Development of an optical fiber monolith reactor for photocatalytic wastewater treatment," *Journal of Applied Electrochemistry*, vol. 35, no. 7-8, pp. 699–708, 2005.
- [6] H. Lu, M. A. Schmidt, and K. F. Jensen, "Photochemical reactions and on-line UV detection in microfabricated reactors," *Lab on a Chip*, vol. 1, no. 1, pp. 22–28, 2001.
- [7] T. H. Lim, S. M. Jeong, S. D. Kim, and J. Gyenis, "Photocatalytic decomposition of NO by  $\text{TiO}_2$  particles," *Journal of Photochemistry and Photobiology A*, vol. 134, no. 3, pp. 209–217, 2000.
- [8] P. Ciambelli, V. Palma, D. Sannino, S. Vaccaro, and V. Vaiano, "Selective oxidation of cyclohexane to benzene on molybdena-titania catalysts in fluidized bed photocatalytic reactor," *Studies in Surface Science and Catalysis*, vol. 172, p. 453, 2007.
- [9] P. Ciambelli, D. Sannino, V. Palma, et al., "Tuning the selectivity of  $\text{MoO}_x$  supported catalysts for cyclohexane photo-oxidation," *Catalysis Today*, vol. 128, no. 3-4, pp. 251–257, 2007.
- [10] P. Ciambelli, D. Sannino, V. Palma, et al., "Photocatalytic cyclohexane photo-oxidation on sulphated  $\text{MoO}_x/\gamma\text{-Al}_2\text{O}_3$  catalysts," *Catalysis Today*, vol. 141, no. 3-4, pp. 367–373, 2009.
- [11] P. Ciambelli, D. Sannino, V. Palma, and V. Vaiano, "The effect of sulphate doping on nanosized  $\text{TiO}_2$  and  $\text{MoO}_x/\text{TiO}_2$  catalysts in cyclohexane photo-oxidation," *International Journal of Photoenergy*, vol. 2008, Article ID 258631, 8 pages, 2008.
- [12] R. Gorges, S. Meyer, and G. Kreisel, "Photocatalysis in microreactors," *Journal of Photochemistry and Photobiology A*, vol. 167, no. 2-3, pp. 95–99, 2004.
- [13] D. H. Chen, X. Ye, and K. Li, "Oxidation of PCE with a UV LED photocatalytic reactor," *Chemical Engineering and Technology*, vol. 28, no. 1, pp. 95–97, 2005.
- [14] P. Ciambelli, D. Sannino, V. Palma, and V. Vaiano, "Fotoreattore catalitico ad alta efficienza di illuminazione per processi intensificati di fotocatalisi," Italian patent pending SAA2008000012.
- [15] H.-W. Chen, Y. Ku, and A. Irawan, "Photodecomposition of o-cresol by UV-LED/ $\text{TiO}_2$  process with controlled periodic illumination," *Chemosphere*, vol. 69, no. 2, pp. 184–190, 2007.
- [16] P. Ciambelli, D. Sannino, V. Palma, and V. Vaiano, "Improved photocatalytic synthesis of benzene by oxidative dehydrogenation of cyclohexane on  $\text{MoO}_x/\text{TiO}_2\text{-Al}_2\text{O}_3$  catalysts," *Chemical Engineering Transactions*, vol. 11, p. 971, 2007.
- [17] P. Ciambelli, D. Sannino, V. Palma, V. Vaiano, and R. S. Mazzei, "A step forwards in ethanol selective photo-oxidation," *Photochemical and Photobiological Sciences*, vol. 8, no. 5, pp. 699–704, 2009.
- [18] V. Vaiano, "Heterogeneous photocatalytic selective oxidation of cyclohexane," Ph.D. thesis, University of Salerno, Salerno, Italy, March 2006.
- [19] A. V. Vorontsov, E. N. Savinov, G. B. Barannik, V. N. Troitsky, and V. N. Parmon, "Quantitative studies on the heterogeneous gas-phase photo-oxidation of CO and simple VOCs by air over  $\text{TiO}_2$ ," *Catalysis Today*, vol. 39, no. 3, pp. 207–218, 1997.
- [20] P. Du, J. A. Moulijn, and G. Mul, "Selective photo(catalytic)-oxidation of cyclohexane: effect of wavelength and  $\text{TiO}_2$  structure on product yields," *Journal of Catalysis*, vol. 238, no. 2, pp. 342–352, 2006.

## Research Article

# Photocatalytic Activity of TiO<sub>2</sub>-WO<sub>3</sub> Composites

Beata Tryba, Michał Piszcz, and Antoni W. Morawski

*Department of Chemical Technology and Engineering, Institute of Chemical Technology and Environmental Engineering, West Pomeranian University of Technology, ul. Pulaskiego 10, 70-322 Szczecin, Poland*

Correspondence should be addressed to Beata Tryba, beata.tryba@ps.pl

Received 11 March 2009; Revised 17 April 2009; Accepted 22 May 2009

Recommended by Mohamed Sabry Abdel-Mottaleb

TiO<sub>2</sub>-WO<sub>3</sub> photocatalysts were prepared in a vacuum evaporator by impregnation of TiO<sub>2</sub> with WO<sub>3</sub> dissolved in an H<sub>2</sub>O<sub>2</sub> solution (30%) and followed by calcination at 400 and 600 °C. XRD analyses showed that at 400 °C monoclinic phase of WO<sub>3</sub> was dominated whereas at 600 °C both monoclinic and regular phases of WO<sub>3</sub> were present. Modification of TiO<sub>2</sub> by WO<sub>3</sub> caused increasing in the absorption of light to the visible range. TiO<sub>2</sub> and photocatalysts modified with low amount of WO<sub>3</sub> (1–5 wt.%) showed high adsorption of Acid Red (AR) on their surface and enhanced photocatalytic activity under UV irradiation. Under visible light irradiation, TiO<sub>2</sub>-WO<sub>3</sub> photocatalysts prepared at 400 °C were more active for AR decomposition than those prepared at 600 °C suggesting that monoclinic phase of WO<sub>3</sub> is more active under visible light than regular WO<sub>3</sub>. Although TiO<sub>2</sub>-WO<sub>3</sub> photocatalysts appeared to be active under visible light for decomposition of AR, the UV irradiation was more efficient.

Copyright © 2009 Beata Tryba et al. This is an open access article distributed under the Creative Commons Attribution License, which permits unrestricted use, distribution, and reproduction in any medium, provided the original work is properly cited.

## 1. Introduction

The photocatalytic process using TiO<sub>2</sub> photocatalyst is very promising for application in the water purification, because many organic compounds can be decomposed and mineralized by the proceeding oxidation and reduction processes on TiO<sub>2</sub> surface. The most commonly tested compounds for decomposition through the photocatalysis are phenols, chlorophenols, pesticides, herbicides, benzenes, alcohols, dyes, pharmaceuticals, humic acids, organic acids, and others [1–3].

TiO<sub>2</sub> is the most commonly used photocatalyst, because it is nontoxic, chemically stable, cheap, and very efficient. However it has some disadvantages, from which one of the most important is a relatively high value of the band gap, around 3.2 eV, which limits its using to the UV light. Therefore nowadays a lot of research work is focused on the preparation of visible light active photocatalysts in order to utilize the solar light more efficiently and stop using UV lamps as a driving force of photocatalytic process, because it consumes a lot of energy.

A lot of works have been done in preparation of anion-doped TiO<sub>2</sub> photocatalysts, such as nitrogen, carbon, and sulphur-doped TiO<sub>2</sub>, which showed the photocatalytic

activity under visible light [4–6]. The other solution is coupling of TiO<sub>2</sub> with semiconductor, which has sensitivity to the visible light. Such semiconductor can be WO<sub>3</sub>, which has a band gap of 2.8 eV and can absorb the light in the visible range. However it also shows high speed of recombination process between generated free carriers. It was reported that by coupling of these two semiconductors, TiO<sub>2</sub> and WO<sub>3</sub>, an efficient charge separation can be achieved which results in enhanced photocatalytic activity of TiO<sub>2</sub> photocatalyst [7–9].

Different methods of preparation of TiO<sub>2</sub>/WO<sub>3</sub> photocatalysts were applied, such as sol-gel, ball milling, hydrothermal, sol-precipitation, and impregnation [9–14].

In presented results the preparation of TiO<sub>2</sub>-WO<sub>3</sub> photocatalysts was performed by dissolving of WO<sub>3</sub> in hydrogen peroxide, wet impregnation on the anatase particles, and calcination at 400 and 600 °C. The impregnation method was selected for preparation to get well dispersion of tungsten oxide particles on the used TiO<sub>2</sub> material, which as original exhibits high BET surface area, around 300 m<sup>2</sup>/g. Addition of tungsten oxide before calcination can also retard the phase transformation of anatase to less active rutile. The influence of doping WO<sub>3</sub> to TiO<sub>2</sub> on its photocatalytic activity under UV and visible light irradiations was tested.

## 2. Preparation of WO<sub>3</sub>-TiO<sub>2</sub> Photocatalysts

As a source of TiO<sub>2</sub>, a raw material of white TiO<sub>2</sub> was used, which was supported by the Police S.A. Company in Poland. This TiO<sub>2</sub> has BET surface area of 300 m<sup>2</sup>/g and contains poorly crystallized anatase phase and some nuclei of rutile. WO<sub>3</sub>-TiO<sub>2</sub> composites were prepared by mixing of TiO<sub>2</sub> with WO<sub>2</sub> dissolved in an H<sub>2</sub>O<sub>2</sub> solution (30%) in a vacuum evaporator at 70 °C for 1 hour. Then the solution was heated up to 100 °C to evaporate the water. The obtained powder was dried in a dryer overnight and then was subjected to calcination at 400 and 600 °C. The amount of WO<sub>3</sub> in the prepared WO<sub>3</sub>-TiO<sub>2</sub> samples ranged from 1 to 90 wt. %.

## 3. Analytical Methods

The phase composition of TiO<sub>2</sub> and WO<sub>3</sub>-TiO<sub>2</sub> composites was measured by XRD in X'Pert PRO diffractometer of Philips Company, with CuK $\alpha$  lamp (35 kW, 30 mA). The obtained XRD patterns were compared with (JCPDSs Joint Committee on Powder Diffraction Standards) cards. The morphology of the photocatalysts surface and content of WO<sub>3</sub> in WO<sub>3</sub>-TiO<sub>2</sub> composites were evaluated by SEM measurements with EDS analysis. The particle size was measured in Zetasizer Nano ZS of Malvern Company by (DLS Dynamic Light Scattering) method. For measurements photocatalyst samples were suspended in ultra pure water solution with dispersant and were treated with ultrasonic vibrations.

UV-Vis spectra of TiO<sub>2</sub> and WO<sub>3</sub>-TiO<sub>2</sub> powders were taken in UV-Vis spectrometer Jasco V-540. These spectra were transformed to Kubelka-Munk equation for indirect semiconductor, and the band gap was calculated.

Hydroxyl radicals were detected by using fluorescence technique. Coumarine can easily react with hydroxyl radicals to form highly fluorescence compound, 7-hydroxycoumarin, which is determined in the Fluorescence Spectrometer Hitachi F-2500. For these measurements the photocatalyst samples were irradiated under UV in the coumarin solution (10<sup>-3</sup> M), and then the solution after separation from a photocatalyst was taken to analysis. The fluorescence measurements were performed at the excitation wavelength of 332 nm and the emission of 335–600 nm with maximum peak at 460 nm. The detailed procedure has been described elsewhere [15].

For photocatalytic test, azo dye, Acid Red (AR) was decomposed, 30 mg/L AR in 500 mL solution and catalyst loading 0.2 g/L under UV irradiation with UV intensity 154 W/m<sup>2</sup> and Vis 100 W/m<sup>2</sup>. Experiments of AR decomposition were also performed under fluorescence light irradiation with intensity of Vis = 715 W/m<sup>2</sup>, for that photocatalytic test lower concentration of AR solution was used, 10 mg/L. Fading of AR solution was monitored by UV-Vis spectroscopy.

## 4. Photocatalytic Activity Test

The photoactivities of prepared samples were tested for decomposition of azo dye Acid Red under irradiation of two different sources: UV and fluorescence lamps. UV was

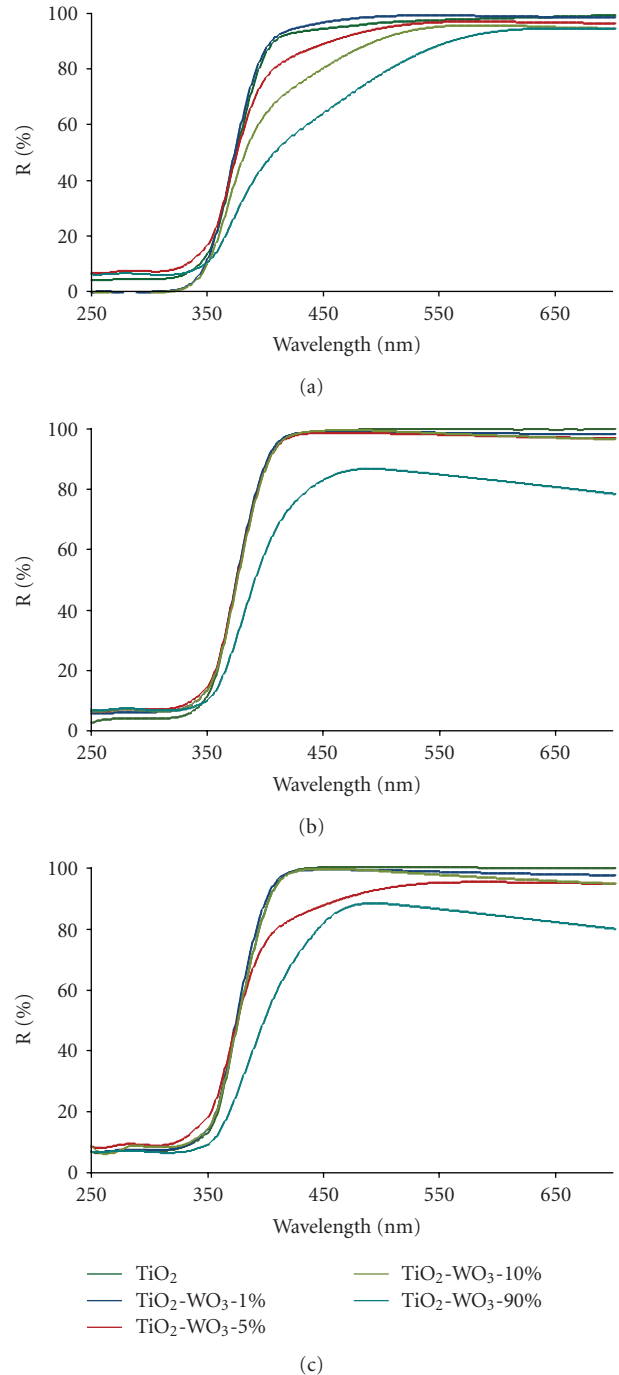


FIGURE 1: Diffuse reflectance spectra of TiO<sub>2</sub> and WO<sub>3</sub>-TiO<sub>2</sub> photocatalysts, (a) as received, (b) calcined at 400 °C, and (c) calcined at 600 °C.

emitted from UV six lamps of Philips Company with power of 20 W each. These lamps emit the radiation at UV range of 154 W/m<sup>2</sup> and at the visible region of about 100 W/m<sup>2</sup> in the range of 312–553 nm with a maximum at around 350 nm. The fluorescence lamps used as a source of visible light (4 × 18 W) emit light in the visible region with intensity of 715 W/m<sup>2</sup> and insignificant amount of UV with intensity of 0.22 W/m<sup>2</sup>.

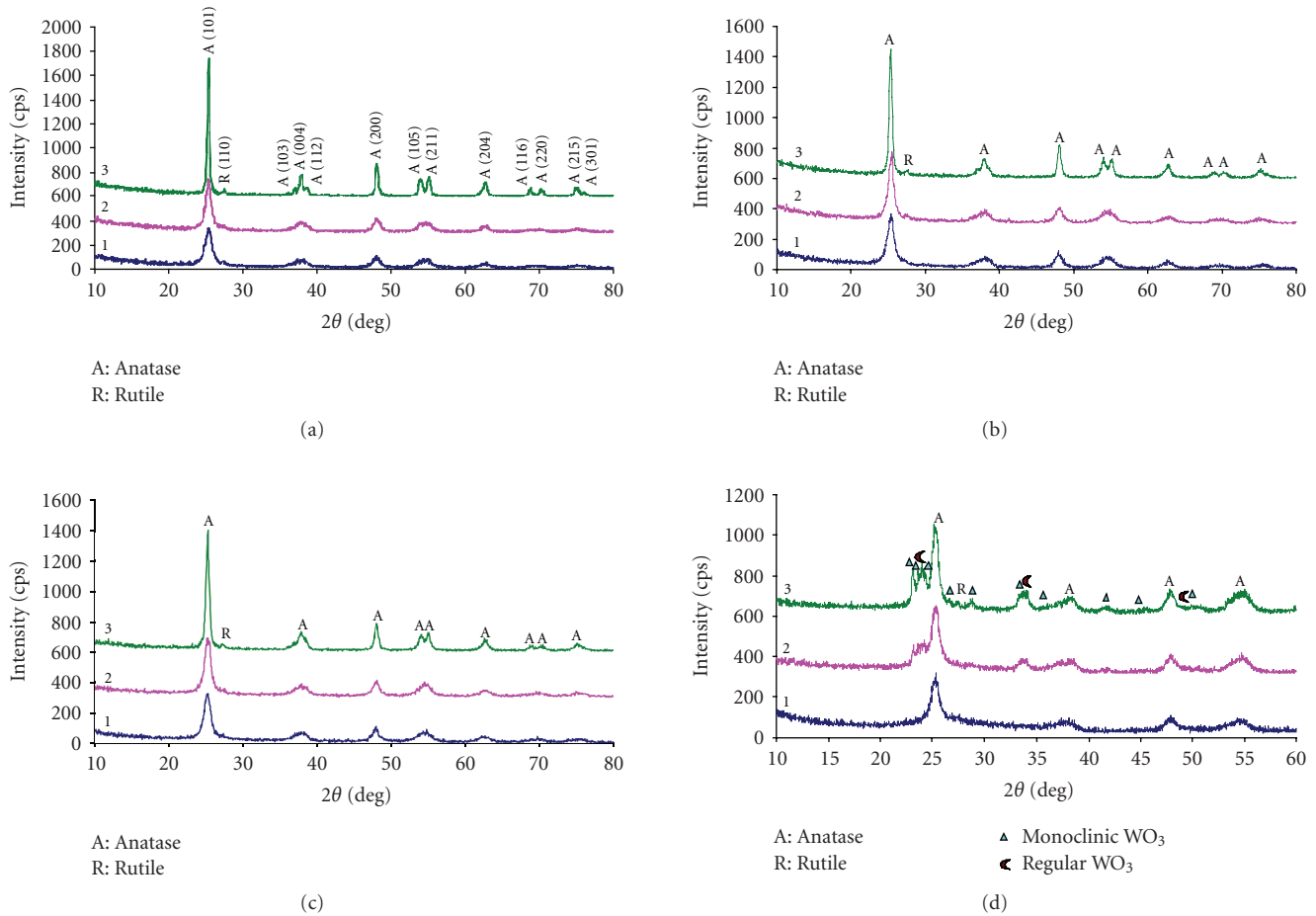


FIGURE 2: XRD patterns of (a)  $\text{TiO}_2$ , (b)  $\text{TiO}_2\text{-WO}_3\text{-3\%}$ , (c)  $\text{TiO}_2\text{-WO}_3\text{-10\%}$ , and (d)  $\text{TiO}_2\text{-WO}_3\text{-90\%}$  photocatalysts: (1) as received, (2)  $400^\circ\text{C}$ -treated, (3)  $600^\circ\text{C}$ -treated.

Each time, for the photocatalytic test, the beaker with 500 mL of a dye solution of concentrations around 0.03 g/L under UV, and 0.01 g/L under visible light and 0.1 g of photocatalyst was used. The solutions were first magnetically stirred in a dark for 30 minutes in order to estimate the adsorption of dye on the photocatalyst surface and then were irradiated under UV or visible lights from the top of the beaker. The concentration of a dye solution was analyzed in UV-Vis spectrophotometer,

## 5. Results and Discussion

UV-Vis spectra of measured  $\text{TiO}_2$  and  $\text{WO}_3\text{-TiO}_2$  photocatalysts are shown in Figures 1(a)–1(c).

In general modification of  $\text{TiO}_2$  by  $\text{WO}_3$  caused increasing the absorption of light to the visible range; however heat treatment caused almost complete reduction of absorption in the range of 400–700 nm, and only a few percentage of light absorption in the range of 500–700 nm could be noticed for modified samples; the exception is  $\text{WO}_3\text{-TiO}_2$  with doped amount of 5 and 90 wt.%, which exhibited higher absorption of visible light even after heat treatment.

XRD measurements of  $\text{TiO}_2$  and  $\text{WO}_3\text{-TiO}_2$  photocatalysts were performed. Phase  $\text{WO}_3$  was difficult to observe in the prepared samples with doping  $\text{WO}_3$  less than 50%. In Figure 2 XRD patterns of  $\text{TiO}_2$  and  $\text{TiO}_2$  with different amounts of doped  $\text{WO}_3$  photocatalysts as received and calcined at different temperatures are presented.

Original  $\text{TiO}_2$  consists of poorly crystallized anatase phase with insignificant amount of rutile. Heating of anatase- $\text{TiO}_2$  caused narrowing of the diffraction peaks of anatase phase due to the growing of its crystals. The additional reflexes from anatase phase such as 103, 112, 116, 220, 215, and 301 were clearly observed for well crystallized anatase. In case of  $\text{TiO}_2\text{-WO}_3\text{-90\%}$  photocatalyst monoclinic phase of  $\text{WO}_3$  appeared at  $400^\circ\text{C}$  whereas at  $600^\circ\text{C}$  additionally regular  $\text{WO}_3$  phase was present.

Doping  $\text{WO}_3$  to  $\text{TiO}_2$  caused inhibition of growing anatase crystals during heat treatment, and narrowing of the anatase reflex (101) was insignificant, mostly for the samples with doped  $\text{WO}_3$  amount up to 3%. Above 3% of doped  $\text{WO}_3$  the anatase reflexes 103 and 112 were not observed, and some reflexes as 105 and 211 were not distinguished due to the presence of broad peaks, even after heated at  $600^\circ\text{C}$ .

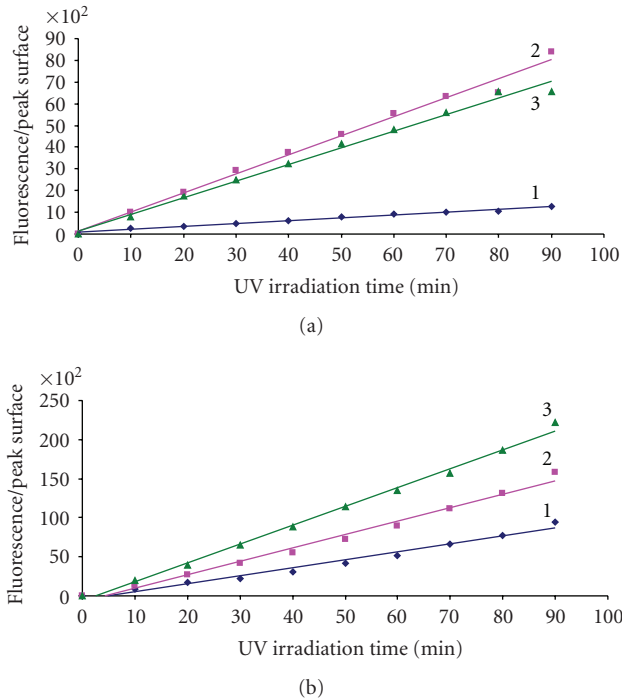


FIGURE 3: OH radicals formation on the photocatalyst surface by the fluorescence measurements of 7-hydroxycoumarin for (a)  $\text{TiO}_2$  and (b)  $\text{TiO}_2\text{-WO}_3\text{-3\%}$ ; (1) as received, (2)  $400^\circ\text{C}$ -treated, and (3)  $600^\circ\text{C}$ -treated.

The exception is  $\text{TiO}_2$  with doped amount of  $\text{WO}_3$  10%, in which narrowing of anatase 101 reflex was significant, and reflexes 105 and 211 were clearly identified. In this sample probably distribution of  $\text{WO}_3$  particles on  $\text{TiO}_2$  was not homogeneous.

Photoactivity of  $\text{TiO}_2$  and prepared photocatalysts in direction of OH radicals formation was tested by the fluorescence technique. In Figure 3 there are presented results from OH radicals measurements on  $\text{TiO}_2$  and  $\text{TiO}_2\text{-WO}_3$  photocatalysts during UV irradiation.

The linear correlation of OH radicals formation from the irradiation time can be noticed. Doping  $\text{WO}_3$  to  $\text{TiO}_2$  and higher calcination temperature caused increasing in the amount of OH radicals formation. This tendency was observed for modified samples with doping  $\text{WO}_3$  up to 3%; for higher amount of doped  $\text{WO}_3$  the photocatalysts heat treated at  $400^\circ\text{C}$  showed higher amount of OH radicals formation than those as received and calcined at  $600^\circ\text{C}$ . The highest photoactivity toward OH radicals formation was noted for  $\text{TiO}_2\text{-WO}_3\text{-3\%}$  heat treated at  $600^\circ\text{C}$ . In Figure 4 OH radicals formation on the photocatalysts under visible light are presented.

OH radicals formation under visible light was much lower than under UV, when we compare Figures 3 and 4, but again  $\text{TiO}_2$  doped with  $\text{WO}_3$  showed higher amount of OH radicals formation than  $\text{TiO}_2$ . From Figure 4 it can be seen that  $\text{TiO}_2\text{-WO}_3\text{-10\%}$  heat treated at  $400^\circ\text{C}$  was much more photoactive than heat treated at  $600^\circ\text{C}$  and no calcinated one. The same tendency was kept for the other photocatalysts

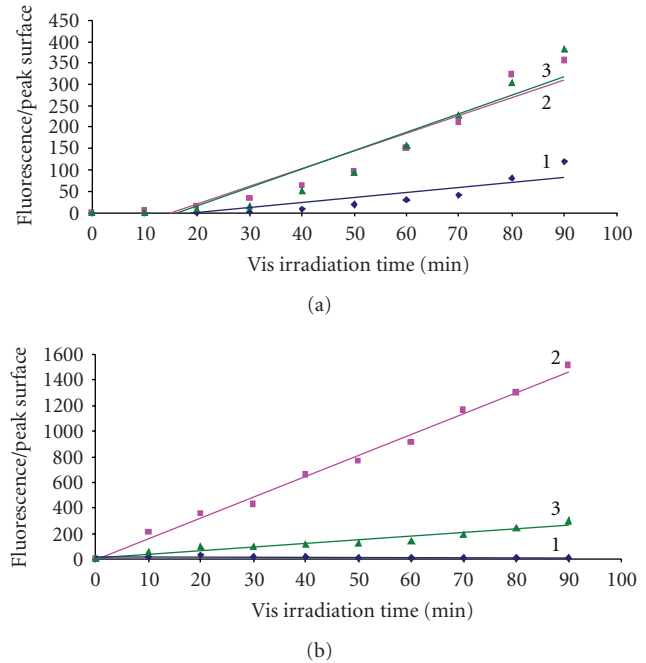


FIGURE 4: OH radicals formation on the photocatalyst surface by the fluorescence measurements of 7-hydroxycoumarin for (a)  $\text{TiO}_2$ , (b)  $\text{TiO}_2\text{-WO}_3\text{-10\%}$ ; (1) as received, (2)  $400^\circ\text{C}$ -treated, (3)  $600^\circ\text{C}$ -treated.

with doping  $\text{WO}_3$  from 5%–90%. The highest OH radicals formation under visible light was obtained on the  $\text{TiO}_2\text{-WO}_3$  photocatalyst with doping amount of 10% heat treated at  $400^\circ\text{C}$ . However this sample did not show significant absorption of light in the visible range; coupling of  $\text{WO}_3$  and  $\text{TiO}_2$  could occur at small amount of visible light absorption by  $\text{WO}_3$  and absorption of UV light by  $\text{TiO}_2$ , even although the energy of UV light was insignificant.  $\text{TiO}_2$  with 90% of doped  $\text{WO}_3$  showed much higher absorption of visible light than the other samples with lower content of  $\text{WO}_3$  but had low activity under visible light. It is concluded that  $\text{TiO}_2$  activity is much more powerful than  $\text{WO}_3$  in generation of OH radicals, and  $\text{WO}_3$  can serve as a support in OH radicals formation by transfer electrons to the conductive band of  $\text{TiO}_2$  under visible light or can retard the recombination reaction occurring in  $\text{TiO}_2$ .

The influence of doping  $\text{WO}_3$  to  $\text{TiO}_2$  on the particles size of photocatalysts was measured. The results from the measurements of particles size of  $\text{TiO}_2$  and  $\text{TiO}_2\text{-WO}_3$  samples are listed in Table 1.

In general particles size of  $\text{WO}_3$  doped  $\text{TiO}_2$  photocatalysts were lower than  $\text{TiO}_2$ . Calcination caused growing of crystals, and so some heat-treated samples exhibited higher size of particles than those as received ones.

The structure of photocatalysts and particles size were observed on SEM photos. For comparison SEM of not modified  $\text{TiO}_2$  and  $\text{TiO}_2\text{-WO}_3\text{-3\%}$  calcinated at  $600^\circ\text{C}$  are presented in Figure 5.

Some agglomerates of primary particles of  $\text{TiO}_2$  can be seen with size over  $1\ \mu\text{m}$  in Figure 5(a) whereas  $\text{TiO}_2$  doped with  $\text{WO}_3$  comprises of much smaller particles.

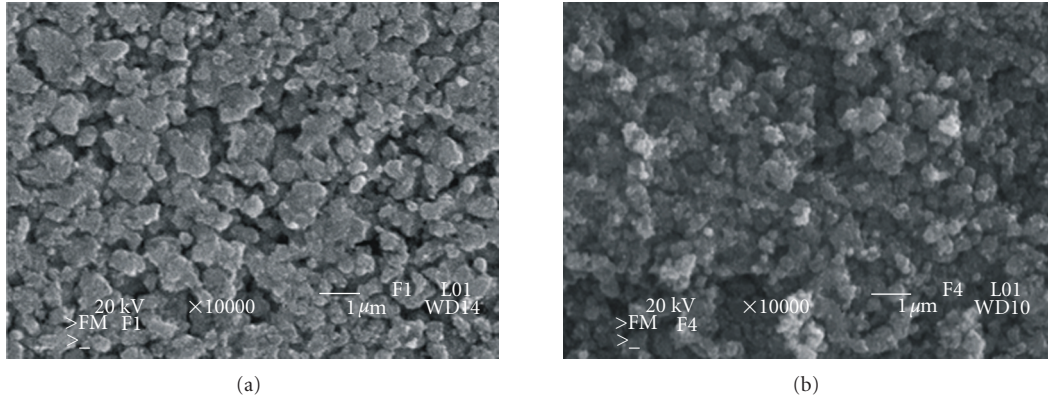


FIGURE 5: SEM of (a)  $\text{TiO}_2$  and (b)  $\text{TiO}_2\text{-WO}_3\text{-3\%}$  heat treated at  $600^\circ\text{C}$ .

TABLE 1: Particles size of photocatalysts measured by DLS method.

Sample	Particles size [nm]							
	0	1	3	5	10	30	50	90
As received	365	444	355	365	172	190	174	185
$400^\circ\text{C}$ -treated	369	380	367	373	222	178	199	175
$600^\circ\text{C}$ -treated	402	369	400	415	201	207	205	192

TABLE 2: Adsorption of AR on the photocatalysts surface.

Photocatalyst	Adsorption of acid red/%					
	Heat treatment temperature/ $^\circ\text{C}$					
	30		10		400	
mg/L	mg/L	mg/L	mg/L	mg/L	mg/L	
$\text{TiO}_2$	19.8	21.5	14.8	26.9	2.0	14.1
$\text{TiO}_2\text{-WO}_3\text{-1\%}$	28	36.5	16.8	32.5	3.7	14.6
$\text{TiO}_2\text{-WO}_3\text{-3\%}$	15.8	38.4	7.8	16.7	—	—
$\text{TiO}_2\text{-WO}_3\text{-5\%}$	14.1	12.6	15.2	20.5	15.9	21.3
$\text{TiO}_2\text{-WO}_3\text{-10\%}$	0	1	2.8	5.8	0	0
$\text{TiO}_2\text{-WO}_3\text{-30\%}$	0	0	0	0	0	0.5
$\text{TiO}_2\text{-WO}_3\text{-50\%}$	0	0	0	0	0	0
$\text{TiO}_2\text{-WO}_3\text{-90\%}$	0	0	0	0	0	0

Both measurements, DLS and SEM, showed that doping  $\text{WO}_3$  to  $\text{TiO}_2$  cause, reduction of its particles size, mostly because of reducing tendency of  $\text{TiO}_2$  particles to form agglomerates. Smaller particle size of  $\text{TiO}_2\text{-WO}_3$  composites in comparison to  $\text{TiO}_2$  prepared by the sol-gel method was also reported by Li et al. [7].

From EDS analysis the measured amount of Ti was 93 wt.%, W – 6 wt.%, and S – 1 wt.%. Sulphur came from the production process of  $\text{TiO}_2$ .

Photocatalytic activity of prepared samples was tested for Acid Red decomposition under UV and visible light irradiations. Preliminary adsorption of this dye on the photocatalysts surface was performed. The results from the adsorption measurements are presented in Table 2. The

initial concentrations of AR used in case of UV and Vis radiations were 30 and 10 mg/L, respectively.

Noncalcined samples of  $\text{TiO}_2$  and  $\text{TiO}_2$  doped with low amount of  $\text{WO}_3$  up to 5% showed quantitatively adsorption of AR on their surface, which generally was decreasing with heat treatment temperature; only  $\text{TiO}_2\text{-WO}_3$  photocatalyst with doping amount of 5% showed opposite tendency, that is increased adsorption of AR after heat treatment.

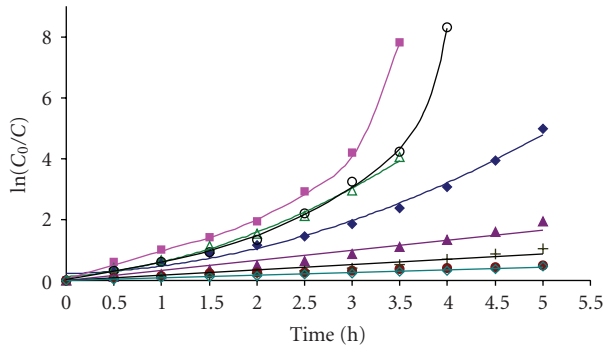
After adsorption, these photocatalysts were submitted to UV and Vis radiations. The results from the measurements are presented in Figures 6 and 7.

Photocatalysts which exhibited high adsorption of AR on their surface showed no linear correlation of  $\ln(C_0/C)$  from time of irradiation during AR decomposition. The high acceleration of AR decomposition with time of irradiation on these photocatalysts could be caused by occurring sensitized photocatalysis. Therefore doping  $\text{WO}_3$  to  $\text{TiO}_2$ , which caused their increased absorption of light to the visible range and high adsorption of AR, appeared to be beneficial for decomposition of AR, as it can be seen especially in case of noncalcined samples used under UV irradiation and  $\text{TiO}_2\text{-WO}_3\text{-5\%}$  heat treated at  $600^\circ\text{C}$  used under visible light. Although both  $\text{TiO}_2$  and  $\text{TiO}_2\text{-WO}_3$  photocatalysts were active under visible light irradiation, UV light was more powerful in AR degradation.

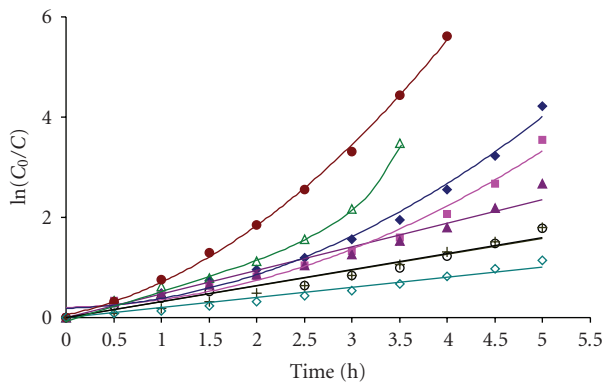
Under visible light irradiation  $\text{WO}_3\text{-TiO}_2$  photocatalysts prepared at  $400^\circ\text{C}$  were more active for AR decomposition than those prepared at  $600^\circ\text{C}$  and noncalcined one.

## 6. Conclusions

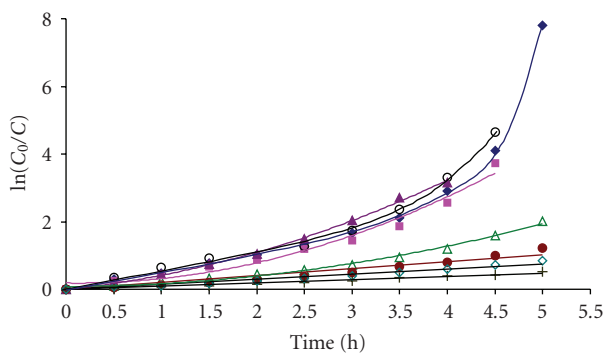
Doping  $\text{WO}_3$  to  $\text{TiO}_2$  caused increasing its absorption of light to the visible range; however it was observed mostly for noncalcined samples. Although OH radicals formation on prepared  $\text{TiO}_2\text{-WO}_3$  photocatalysts was higher than on  $\text{TiO}_2$  it was not a key factor affecting the rate of AR decomposition. Both high adsorption of AR on the photocatalyst surface and their ability to absorption of visible light were responsible for the photocatalytic properties of photocatalysts, and therefore the  $\text{TiO}_2\text{-WO}_3$  photocatalysts with low amount of  $\text{WO}_3$  (1–5 wt.%) were more active than the others. Doping  $\text{WO}_3$  to



(a)



(b)

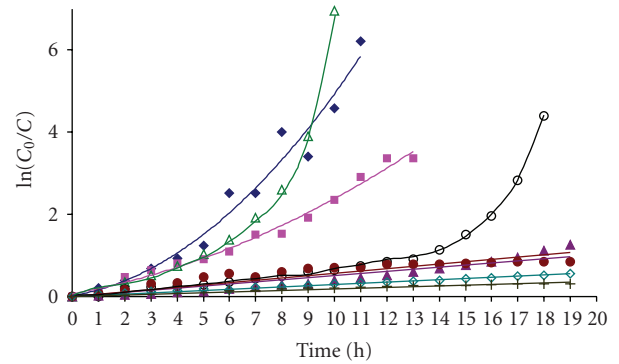


(c)

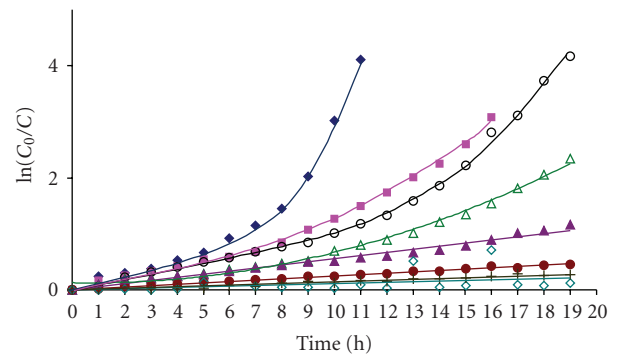


FIGURE 6: AR decomposition under UV irradiation on TiO<sub>2</sub> and TiO<sub>2</sub>-WO<sub>3</sub> photocatalysts, (a) as received, (b) 400 °C-treated, and (c) 600 °C-treated.

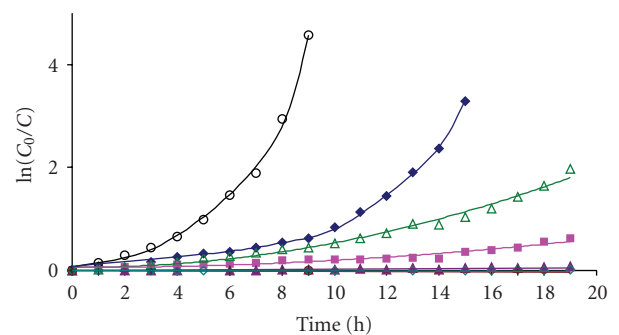
TiO<sub>2</sub> caused also reduction of its particles size, which could improve ability of TiO<sub>2</sub> for dispersion in water and increase the accessible surface for adsorbates. Under visible light irradiation WO<sub>3</sub>-TiO<sub>2</sub> photocatalysts prepared at 400 °C were more active for AR decomposition than those prepared at 600 °C suggesting that monoclinic phase of WO<sub>3</sub> is more active under visible light than regular WO<sub>3</sub>. Although the photocatalysts were active under both UV and visible light



(a)



(b)



(c)



FIGURE 7: AR decomposition under Vis irradiation on TiO<sub>2</sub> and TiO<sub>2</sub>-WO<sub>3</sub> photocatalysts, (a) as received, (b) 400 °C-treated, and (c) 600 °C-treated.

irradiations, UV light was more powerful for decomposition of AR than visible light, but the latter had important meaning during occurring sensitized photocatalysis.

### Acknowledgment

This work was supported by the research project from the Ministry of Science and Higher Education no.COST/299/2006 for 2007-2010.

## References

- [1] A. Fujishima, K. Hashimoto, and T. Watanabe, *TiO<sub>2</sub> Photocatalysis Fundamentals and Applications*, BKC, Tokyo, Japan, 1999.
- [2] A. Sobczykński and A. Dobosz, “Water purification by photocatalysis on semiconductors,” *Polish Journal of Environmental Studies*, vol. 10, no. 4, pp. 195–205, 2001.
- [3] S. Malato, J. Blanco, A. Vidal, and C. Richter, “Photocatalysis with solar energy at a pilot-plant scale: an overview,” *Applied Catalysis B*, vol. 37, no. 1, pp. 1–15, 2002.
- [4] H. Shen, L. Mi, P. Xu, W. Shen, and P.-N. Wang, “Visible-light photocatalysis of nitrogen-doped TiO<sub>2</sub> nanoparticulate films prepared by low-energy ion implantation,” *Applied Surface Science*, vol. 253, no. 17, pp. 7024–7028, 2007.
- [5] M. Shen, Z. Wu, H. Huang, Y. Du, Z. Zou, and P. Yang, “Carbon-doped anatase TiO<sub>2</sub> obtained from TiC for photocatalysis under visible light irradiation,” *Materials Letters*, vol. 60, no. 5, pp. 693–697, 2006.
- [6] K. M. Reddy, B. Baruwati, M. Jayalakshmi, M. M. Rao, and S. V. Manorama, “S-, N- and C-doped titanium dioxide nanoparticles: synthesis, characterization and redox charge transfer study,” *Journal of Solid State Chemistry*, vol. 178, no. 11, pp. 3352–3358, 2005.
- [7] X. Z. Li, F. B. Li, C. L. Yang, and W. K. Ge, “Photocatalytic activity of WO<sub>x</sub>-TiO<sub>2</sub> under visible light irradiation,” *Journal of Photochemistry and Photobiology A*, vol. 141, no. 2-3, pp. 209–217, 2001.
- [8] H. Yang, R. Shi, K. Zhang, Y. Hu, A. Tang, and X. Li, “Synthesis of WO<sub>3</sub>/TiO<sub>2</sub> nanocomposites via sol-gel method,” *Journal of Alloys and Compounds*, vol. 398, no. 1-2, pp. 200–202, 2005.
- [9] D. Ke, H. Liu, T. Peng, X. Liu, and K. Dai, “Preparation and photocatalytic activity of WO<sub>3</sub>/TiO<sub>2</sub> nanocomposite particles,” *Materials Letters*, vol. 62, no. 3, pp. 447–450, 2008.
- [10] H. Yang, D. Zhang, and L. Wang, “Synthesis and characterization of tungsten oxide-doped titania nanocrystallites,” *Materials Letters*, vol. 57, no. 3, pp. 674–678, 2002.
- [11] H. Song, H. Jiang, X. Liu, and G. Meng, “Efficient degradation of organic pollutant with WO<sub>x</sub> modified nano TiO<sub>2</sub> under visible irradiation,” *Journal of Photochemistry and Photobiology A*, vol. 181, no. 2-3, pp. 421–428, 2006.
- [12] C. Su, B.-Y. Hong, and C.-M. Tseng, “Sol-gel preparation and photocatalysis of titanium dioxide,” *Catalysis Today*, vol. 96, no. 3, pp. 119–126, 2004.
- [13] C. Shifu, C. Lei, G. Shen, and C. Gengyu, “The preparation of coupled WO<sub>3</sub>/TiO<sub>2</sub> photocatalyst by ball milling,” *Powder Technology*, vol. 160, no. 3, pp. 198–202, 2005.
- [14] T. Kim, A. Burrows, C. J. Kiely, and I. E. Wachs, “Molecular/electronic structure—surface acidity relationships of model—supported tungsten oxide catalysts,” *Journal of Catalysis*, vol. 246, no. 2, pp. 370–381, 2007.
- [15] K.-I. Ishibashi, A. Fujishima, T. Watanabe, and K. Hashimoto, “Detection of active oxidative species in TiO<sub>2</sub> photocatalysis using the fluorescence technique,” *Electrochemistry Communications*, vol. 2, no. 3, pp. 207–210, 2000.

## Research Article

# Removal of Organic Impurities from Water Using a Reactor with Photoactive Refill

**Joanna Grzechulska-Damszel**

*Institute of Chemical and Environment Engineering, West Pomeranian University of Technology in Szczecin, Pułaskiego 10, 70-322 Szczecin, Poland*

Correspondence should be addressed to Joanna Grzechulska-Damszel, joanna.grzechulska@zut.edu.pl

Received 17 March 2009; Accepted 20 April 2009

Recommended by Mohamed Sabry Abdel-Mottaleb

The aim of the presented work was the removal of phenol from water using a reactor with photoactive refill. Titanium dioxide (Chemical Factory "Police" Poland) was immobilized on the base material as a thin layer from the alcoholic suspension followed by thermal stabilization. The glass fabric was applied as a support for the titania coating. The results of studies revealed that the titania coatings show a high photocatalytic activity toward the phenol decomposition in water. The complete removal of phenol was achieved in the relatively short time of 23 hours. The prepared coatings exhibit high stability in repeated cycles of water treatment. The proposed reactor with photoactive refill solves the problem of necessity of replacement of the reactor or the parts of the reactor when the photocatalysts activity decreases. In the case of activity drop of the photocatalyst, only the photoactive refill can be easily replaced.

Copyright © 2009 Joanna Grzechulska-Damszel. This is an open access article distributed under the Creative Commons Attribution License, which permits unrestricted use, distribution, and reproduction in any medium, provided the original work is properly cited.

## 1. Introduction

Advance Oxidation Processes (AOPs) have been reported to be useful for photooxidation of organic pollutants in wastewater [1–9]. Among the various Advanced Oxidation Processes employed in water treatment, heterogeneous semiconductor photocatalysis shows great importance due to its ability to destroy a wide range of organic pollutants at ambient temperature and pressure, without generation of harmful byproducts [10–24]. The most commonly used photocatalyst is  $\text{TiO}_2$ . Titanium dioxide has essentially proved itself to be the best material for environmental purification because of its many desirable properties.  $\text{TiO}_2$  is a cheap, readily available material capable of oxidation of a wide range of organic pollutants into harmless compounds, often leading to complete mineralization of organics.

The use of photocatalysis has been proved to be a good choice to achieve an effective elimination of phenolic compounds from waters [25–42]. Also, phenol is usually taken as a model compound for advanced wastewater treatment studies [43–45].

The photocatalytic processes can operate using catalyst suspended in the solution or immobilized on various supports. Photocatalytic reactors with suspended catalyst give much better contact between the photocatalyst and dissolved impurities comparing to reactors with immobilized catalyst. However, in this case the step of separation of the catalyst is necessary, which increases the overall costs of the process. Different researchers have tried to minimize these problems by immobilizing  $\text{TiO}_2$  on various solid supports or on the reactor walls, which eliminates arduous step of separation [46–56]. Titanium dioxide was immobilized on various supports and using various methods. Immobilization of the photocatalyst on the reactor walls or other parts of the reactor shows disadvantages when the activity of the catalyst decreases, and it has to be replaced. Thus, the better solution is to immobilize the photocatalyst on the replaceable elements that can be easily removed and placed again in the reactor. The other advantage of such supports is to provide a good contact of the treated medium with the photocatalyst surface and also a good penetration of light in the reactor. A flexible textiles seemed to be adequate support for the photoactive titania coatings. However, textiles are an

organic materials and can itself undergo the photocatalytic degradation.

The aim of the presented work was the removal of organic impurities from water using a reactor with photoactive refill. Titanium dioxide (Chemical Factory "Police" Poland) was immobilized on the base material as a thin layer from the alcoholic suspension followed by thermal stabilization. In case of activity drop of the photocatalyst, only the photoactive refill can be easily replaced.

## 2. Experimental

The commercial anatase form of titanium dioxide produced by Chemical Factory "Police" (Poland) was used as a photocatalyst. Phenol (POCh S.A., Poland) was used as a model organic compound. Titanium dioxide was immobilized on the base material from the alcoholic solution followed by thermal stabilization. The support for titania photoactive coating was a glass fabric produced by "Pabiantex" factory (Poland). The glass fabric with titania coating was a replaceable photoactive refill placed in the reactor where the process of water purification was conducted.

The process of photocatalytic oxidation of phenol was conducted using a laboratory installation (Figure 1) where the main component of the system was the flow reactor (Trojan Technologies, Canada). This is a cylindrical reactor with length of approximately 29.5 cm and the diameter of 6.8 cm. The mercury lamp emitting UV radiation in the range of 250–800 nm, with high maximum at 254, 436, and 546 nm, was placed inside the reactor, in the center. The photoactive refill was also placed inside the reactor in a way to stick the inner walls of the reactor.

The photocatalyst was fixed to the glass fabric according to the following procedure. The suspension of  $\text{TiO}_2$  in ethanol was sonicated for 1 hour with a frequency of 40 kHz. The glass fabric (size  $19 \times 24$  cm) was immersed in such prepared suspension and then dried for at  $105^\circ\text{C}$ . The procedure was repeated twice. After that the coating was stabilized by thermal treatment at the temperature of  $150^\circ\text{C}$  overnight. The excess of the immobilized photocatalyst was rinsed by flowing water through the reactor before the photocatalytic process.

The solution of phenol, with the initial concentration of  $20\text{ mg/dm}^3$ , was pumped to the reactor by peristaltic pump from the container and was circulated through the reactor with the flow rate of  $36\text{ dm}^3/\text{h}$ . The volume of the reaction solution was  $2.5\text{ dm}^3$ . The amount of the solution inside the reactor was approximately  $1\text{ dm}^3$ . The changes of phenol concentration in the solution were determined by absorbance measurement at maximal absorption wavelength  $270\text{ nm}$  (Jasco V-530 spectrometer, Japan). Total organic carbon (TOC) concentration was measured by "multi N/C 2000" analyzer (Analytik Jena, Germany). Total dissolved solids (TDS) content, conductivity, and pH of the solution (Ultrameter 6P, Myron L Company, USA) were also monitored during the process. The reaction solution circulated in the reactor for 15 minutes without illumination to obtain the adsorption equilibrium. The adsorption of phenol onto photocatalyst surface was low, only about 1% (by weight).

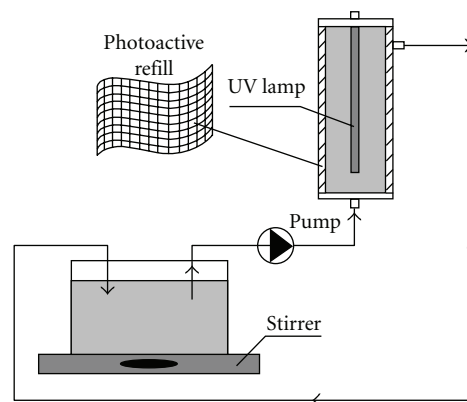


FIGURE 1: The scheme of installation for the process of photocatalytic oxidation of phenol.

## 3. Results and Discussion

The experiments of the photocatalytic degradation of phenol were conducted for the initial concentration of  $20\text{ mg/dm}^3$ . The volume of the treated solution was  $2.5\text{ dm}^3$ . The first test reaction of photocatalytic decomposition of phenol was conducted until the complete decay of phenol in the reaction solution (phenol presence was not detected by UV/Vis analysis). The next tests were conducted for 10 hours.

At the beginning of studies blank experiments were performed. No decomposition occurred when an aqueous solution of phenol flowed through the reactor in the dark, and the direct photolysis was also negligible. Decomposition of phenol in the solution could only be observed with the simultaneous presence of  $\text{TiO}_2$  and of UV light. Therefore, it can be stated that in the presence of  $\text{TiO}_2$  a true heterogeneous catalytic regime takes place.

Figure 2 presents the changes in phenol concentration during the photocatalytic process for four tests performed with the same photoactive refill. The concentration of phenol decreases with the time of the process. As can be seen from Figure 2, the decrease in phenol concentration is the highest during the first hours of the process. After that, the rate of decrease of concentration of phenol decelerates; however, the complete removal of phenol from the treated solution was obtained. During the first test the complete removal of phenol was observed after 23 hours of the process. In the second tests, the concentration of phenol in the solution after 10 hours of illumination was a little higher comparing to the first one; however, the third and the fourth tests showed comparable time of decomposition as the second one.

The reaction of photocatalytic phenol decomposition followed the first-order reaction kinetics concerning to phenol concentration. A plot of  $\ln(C_0/C)$  versus time represents a straight line (Figure 2), the slope of which upon the linear regression equals the apparent first-order rate constant  $k'$  according to the equation of the Langmuir-Hinshelwood model:

$$r = -\frac{dC}{dt} = \frac{k_r k_a C}{1 + k_a C}, \quad (1)$$

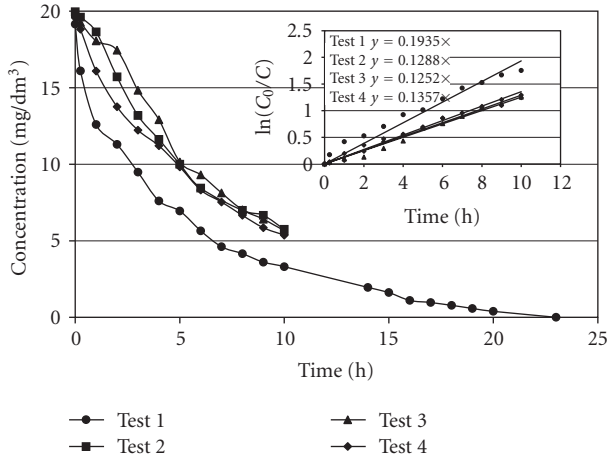


FIGURE 2: The changes in phenol concentration during the photocatalytic process.

TABLE 1: Apparent first-order rate constants ( $k'$ ) and linear regression coefficients ( $R^2$ ) of phenol photodecomposition reactions.

Test no.	$k'$	$R^2$
1	0.1935	0.9821
2	0.1288	0.9896
3	0.1252	0.9864
4	0.1357	0.9905

which can be simplified to a apparent first-order equation:

$$\ln\left(\frac{C_0}{C}\right) = k_r k_{at} = k' t. \quad (2)$$

Table 1 lists the values of  $k'$  and the linear regression coefficients of photodegradation of phenol for each test performed. According to the values in the table, the appropriate linear relationship appears well.

The changes in phenol concentration were monitored by UV/Vis spectroscopy. Figure 3 presents an example UV/Vis spectra recorded during the photocatalytic process of phenol decomposition. The progressive fading of the absorption peak at the wavelength of 270 nm is observed indicating the decrease of phenol concentration in the consecutive samples taken for the analysis during the process.

Together with the decrease of the concentration of phenol in the reaction solution with the time of the process, the decrease of TOC concentration was observed (Figure 4). Total disappearance of the reactant was obtained after 23 hours of the process while the organic carbon was still present in the solution after this time of the photocatalytic process. TOC concentration in the starting solution was equal to 14.4 mg/dm<sup>3</sup> for the first test. After the photocatalytic process was completed, the TOC concentration decreased to 6.56 mg/dm<sup>3</sup>, which gives over 54% of removal of organic carbon from the solution. The decrease of TOC concentration was the result of the aromatic ring opening and subsequent decomposition of intermediate products formed; however, the complete mineralization of phenol was not achieved. The time of photocatalytic process should be

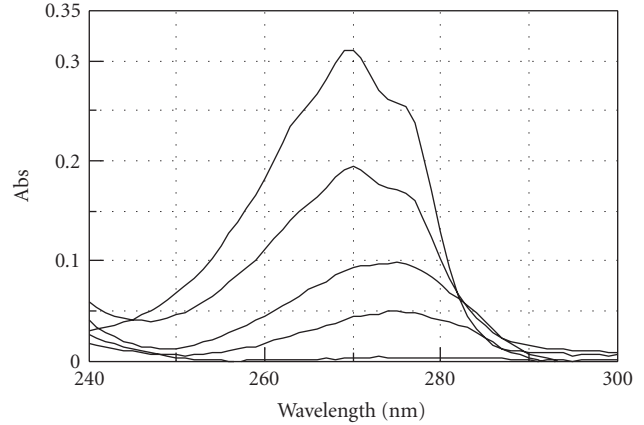


FIGURE 3: The example spectra of the reaction solution recorded during the photocatalytic process. From top: starting solution, after 1 hour of the process, after 5 hours of the process, after 10 hours of the process, and after 23 hours of the process.

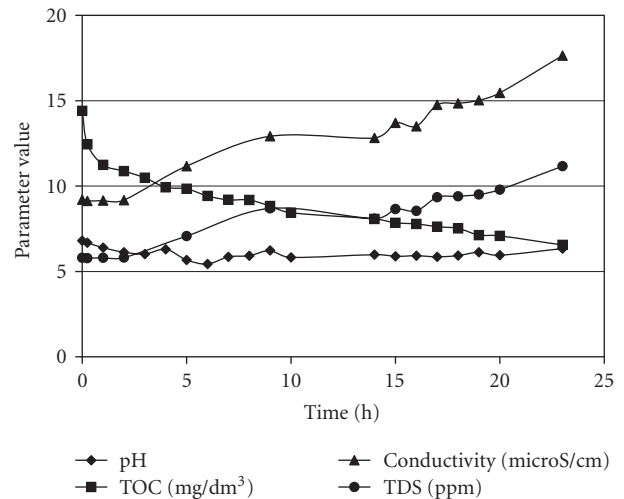


FIGURE 4: The changes of parameters monitored during the photocatalytic process.

elongated to obtain the oxidation of phenol to the final products: CO<sub>2</sub> and H<sub>2</sub>O.

The values of TDS, conductivity, and pH measured during the process give a better view to the degradation reaction. The changes of these parameters are presented in Figure 4. The data presented on Figure 4 refer to the first test of decomposition of phenol. For the other three tests the tendency of changes was similar. The conductivity and TDS values tend to increase with the time of the process. This indicates the mineralization of organic molecules and increase of dissolved species present in the solution. However, this also indicates that the decomposition process was not complete; this is to say it did not lead to full mineralization of the reactant, since in such a case the values of TDS and conductivity would settle at the some value and remained constant. The analysis of organic carbon in the reaction solution confirms the above statement.

## 4. Conclusions

Conclusions are listed as follows.

- (i) The process of the photocatalytic removal of phenol can be successfully conducted in the reactor with photoactive refill presented in these studies.
- (ii) The photoactive refill applied in the studies is prepared using a very simple method and in the case of decrease of photoactivity can be easily replaced.
- (iii) The titania coating shows a high photocatalytic activity toward the model organic compound (phenol) decomposition in water.
- (iv) The prepared coating exhibits high stability in repeated cycles of water treatment.
- (v) The proposed reactor with photoactive refill solves the problem of necessity of replacement of the reactor or the parts of the reactor when the photocatalyst activity decreases.
- (vi) Application of glass fabric is advantageous since it is resistant to UV light and does not undergo the photocatalytic decomposition on the contrary to the natural fabrics.

## Acknowledgment

This work was financed by the Polish Government in the framework of a Grant (2006–2009).

## References

- [1] Handbook, "Advanced photochemical oxidation processes," Tech. Rep. EPA/625/1R-98/1004, United States Environmental Protection Agency, Washington, DC, USA, 1998.
- [2] R. Munter, "Advanced oxidation processes—current status and prospects," *Proceedings of the Estonian Academy of Sciences. Chemistry*, vol. 50, no. 2, pp. 59–80, 2001.
- [3] R. Munter, S. Preis, J. Kallas, M. Trapido, and Y. Veressinina, "Advanced oxidation processes (AOPs): water treatment technology for the twenty-first century," *Finnish Chemical Journal*, vol. 28, no. 5, pp. 354–362, 2001.
- [4] A. Mills and S.-K. Lee, "A web-based overview of semiconductor photochemistry-based current commercial applications," *Journal of Photochemistry and Photobiology A*, vol. 152, no. 1–3, pp. 233–247, 2002.
- [5] S. Esplugas, J. Giménez, S. Contreras, E. Pascual, and M. Rodríguez, "Comparison of different advanced oxidation processes for phenol degradation," *Water Research*, vol. 36, no. 4, pp. 1034–1042, 2002.
- [6] M. Rodríguez, "Fenton and UV-vis based advanced oxidation processes in wastewater treatment: degradation, mineralization and biodegradability enhancement," Universitat de Barcelona, Facultat de Química, Departament d'Enginyeria Química i Metallúrgia, Programa de Doctorado de Ingeniería Química Ambiental, Biennio 1998–2000, Barcelona, Spain 2003.
- [7] P. R. Gogate and A. B. Pandit, "A review of imperative technologies for wastewater treatment—I: oxidation technologies at ambient conditions," *Advances in Environmental Research*, vol. 8, no. 3-4, pp. 501–551, 2004.
- [8] P. R. Gogate and A. B. Pandit, "A review of imperative technologies for wastewater treatment—II: hybrid methods," *Advances in Environmental Research*, vol. 8, no. 3-4, pp. 553–597, 2004.
- [9] M. I. Maldonado, P. C. Passarinho, I. Oller, et al., "Photocatalytic degradation of EU priority substances: a comparison between TiO<sub>2</sub> and fenton plus photo-fenton in a solar pilot plant," *Journal of Photochemistry and Photobiology A*, vol. 185, no. 2-3, pp. 354–363, 2007.
- [10] M. R. Hoffmann, S. T. Martin, W. Choi, and D. W. Bahnemann, "Environmental applications of semiconductor photocatalysis," *Chemical Reviews*, vol. 95, no. 1, pp. 69–96, 1995.
- [11] A. L. Linsebigler, G. Lu, and J. T. Yates Jr., "Photocatalysis on TiO<sub>2</sub> surfaces: principles, mechanisms, and selected results," *Chemical Reviews*, vol. 95, no. 3, pp. 735–758, 1995.
- [12] M. Schiavello, *Heterogeneous Photocatalysis*, John Wiley & Sons, New York, NY, USA, 1997.
- [13] A. Mills and S. LeHunte, "An overview of semiconductor photocatalysis," *Journal of Photochemistry and Photobiology A*, vol. 108, no. 1, pp. 1–35, 1997.
- [14] J.-M. Herrmann, "Heterogeneous photocatalysis: fundamentals and applications to the removal of various types of aqueous pollutants," *Catalysis Today*, vol. 53, no. 1, pp. 115–129, 1999.
- [15] A. Fujishima, T. N. Rao, and D. A. Tryk, "Titanium dioxide photocatalysis," *Journal of Photochemistry and Photobiology C*, vol. 1, no. 1, pp. 1–21, 2000.
- [16] D. S. Bhatkhande, V. G. Pangarkar, and A. A. C. M. Beenackers, "Photocatalytic degradation for environmental applications—a review," *Journal of Chemical Technology and Biotechnology*, vol. 77, no. 1, pp. 102–116, 2002.
- [17] M. Kaneko and I. Okura, *Photocatalysis. Science and Technology*, Kodansha, Tokyo, Japan; Springer, Berlin, Germany, 2002.
- [18] D. Bahnemann, "Photocatalytic water treatment: solar energy applications," *Solar Energy*, vol. 77, no. 5, pp. 445–459, 2004.
- [19] K. Hashimoto, H. Irie, and A. Fujishima, "TiO<sub>2</sub> photocatalysis: a historical overview and future prospects," *Japanese Journal of Applied Physics*, vol. 44, no. 12, pp. 8269–8285, 2005.
- [20] A. Mills and M. McFarlane, "Current and possible future methods of assessing the activities of photocatalyst films," *Catalysis Today*, vol. 129, no. 1-2, pp. 22–28, 2007.
- [21] J.-M. Herrmann, C. Duchamp, M. Karkmaz, et al., "Environmental green chemistry as defined by photocatalysis," *Journal of Hazardous Materials*, vol. 146, no. 3, pp. 624–629, 2007.
- [22] A. Fujishima, X. Zhang, and D. A. Tryk, "Heterogeneous photocatalysis: from water photolysis to applications in environmental cleanup," *International Journal of Hydrogen Energy*, vol. 32, no. 14, pp. 2664–2672, 2007.
- [23] U. I. Gaya and A. H. Abdullah, "Heterogeneous photocatalytic degradation of organic contaminants over titanium dioxide: a review of fundamentals, progress and problems," *Journal of Photochemistry and Photobiology C*, vol. 9, no. 1, pp. 1–12, 2008.
- [24] N. S. Allen, M. Edge, J. Verran, J. Stratton, J. Maltby, and C. Bygott, "Photocatalytic titania based surfaces: environmental benefits," *Polymer Degradation and Stability*, vol. 93, no. 9, pp. 1632–1646, 2008.
- [25] K. Okamoto, Y. Yamamoto, H. Tanaka, M. Tanaka, and A. Itaya, "Heterogeneous photocatalytic decomposition of phenol over TiO<sub>2</sub> powder," *Bulletin of the Chemical Society of Japan*, vol. 58, pp. 2015–2022, 1985.

- [26] K. Okamoto, Y. Yamamoto, H. Tanaka, and A. Itaya, "Kinetics of heterogeneous photocatalytic decomposition of phenol over anatase TiO<sub>2</sub> powder," *Bulletin of the Chemical Society of Japan*, vol. 58, pp. 2023–2027, 1985.
- [27] S. Cheng, S.-J. Tsai, and Y.-F. Lee, "Photocatalytic decomposition of phenol over titanium oxide of various structures," *Catalysis Today*, vol. 26, no. 1, pp. 87–96, 1995.
- [28] A. W. Morawski, J. Grzechulska, and K. Kałucki, "A new method for preparation of potassium-pillared layered titanate applied in photocatalysis," *Journal of Physics and Chemistry of Solids*, vol. 57, no. 6–8, pp. 1011–1017, 1996.
- [29] Z. Ding, G. Q. Lu, and P. F. Greenfield, "Role of the crystallite phase of TiO<sub>2</sub> in heterogeneous photocatalysis for phenol oxidation in water," *The Journal of Physical Chemistry B*, vol. 104, no. 19, pp. 4815–4820, 2000.
- [30] A. M. Peiró, J. A. Ayllón, J. Peral, and X. Doménech, "TiO<sub>2</sub>-photocatalyzed degradation of phenol and ortho-substituted phenolic compounds," *Applied Catalysis B*, vol. 30, no. 3–4, pp. 359–373, 2001.
- [31] B. Tryba, A. W. Morawski, and M. Inagaki, "Application of TiO<sub>2</sub>-mounted activated carbon to the removal of phenol from water," *Applied Catalysis B*, vol. 41, no. 4, pp. 427–433, 2003.
- [32] J. Grzechulska and A. W. Morawski, "Photocatalytic labyrinth flow reactor with immobilized P25 TiO<sub>2</sub> bed for removal of phenol from water," *Applied Catalysis B*, vol. 46, no. 2, pp. 415–419, 2003.
- [33] A. Sobczykński, L. Duczmal, and W. Żmudziński, "Phenol destruction by photocatalysis on TiO<sub>2</sub>: an attempt to solve the reaction mechanism," *Journal of Molecular Catalysis A*, vol. 213, no. 2, pp. 225–230, 2004.
- [34] S. Lathasree, A. N. Rao, B. SivaSankar, V. Sadasivam, and K. Rengaraj, "Heterogeneous photocatalytic mineralisation of phenols in aqueous solutions," *Journal of Molecular Catalysis A*, vol. 223, pp. 101–105, 2004.
- [35] D. Vione, C. Minero, V. Maurino, M. E. Carlotti, T. Picatonotto, and E. Pelizzetti, "Degradation of phenol and benzoic acid in the presence of a TiO<sub>2</sub>-based heterogeneous photocatalyst," *Applied Catalysis B*, vol. 58, no. 1–2, pp. 79–88, 2005.
- [36] Z. Guo, R. Ma, and G. Li, "Degradation of phenol by nanomaterial TiO<sub>2</sub> in wastewater," *Chemical Engineering Journal*, vol. 119, no. 1, pp. 55–59, 2006.
- [37] M. H. Priya and G. Madras, "Kinetics of photocatalytic degradation of phenols with multiple substituent groups," *Journal of Photochemistry and Photobiology A*, vol. 179, no. 3, pp. 256–262, 2006.
- [38] C. Karunakaran and R. Dhanalakshmi, "Semiconductor-catalyzed degradation of phenols with sunlight," *Solar Energy Materials & Solar Cells*, vol. 92, no. 11, pp. 1315–1321, 2008.
- [39] S. Liu, N. Jaffrezic, and C. Guillard, "Size effects in liquid-phase photo-oxidation of phenol using nanometer-sized TiO<sub>2</sub> catalysts," *Applied Surface Science*, vol. 255, no. 5, part 2, pp. 2704–2709, 2008.
- [40] G. Busca, S. Berardinelli, C. Resini, and L. Arrighi, "Technologies for the removal of phenol from fluid streams: a short review of recent developments," *Journal of Hazardous Materials*, vol. 160, no. 2–3, pp. 265–288, 2008.
- [41] B. Tryba, "Immobilization of TiO<sub>2</sub> and Fe-C-TiO<sub>2</sub> photocatalysts on the cotton material for application in a flow photocatalytic reactor for decomposition of phenol in water," *Journal of Hazardous Materials*, vol. 151, no. 2–3, pp. 623–627, 2008.
- [42] C.-H. Chiou, C.-Y. Wu, and R.-S. Juang, "Influence of operating parameters on photocatalytic degradation of phenol in UV/TiO<sub>2</sub> process," *Chemical Engineering Journal*, vol. 139, no. 2, pp. 322–329, 2008.
- [43] N. Serpone, G. Sauve, R. Koch, et al., "Standardization protocol of process efficiencies and activation parameters in heterogeneous photocatalysis: relative photonic efficiencies," *Journal of Photochemistry and Photobiology A*, vol. 94, no. 2–3, pp. 191–203, 1996.
- [44] N. Serpone, "Relative photonic efficiencies and quantum yields in heterogeneous photocatalysis," *Journal of Photochemistry and Photobiology A*, vol. 104, no. 1–3, pp. 1–12, 1997.
- [45] N. Serpone and A. Salinaro, "Terminology, relative photonic efficiencies and quantum yields in heterogeneous photocatalysis—part I: suggested protocol," *Pure and Applied Chemistry*, vol. 71, no. 2, pp. 303–320, 1999.
- [46] A. Fernández, G. Lassaletta, V. M. Jiménez, A. Justo, A. R. González-Elipe, and J.-M. Herrmann, "Preparation and characterization of TiO<sub>2</sub> photocatalysts supported on various rigid supports (glass, quartz and stainless steel). Comparative studies of photocatalytic activity in water purification," *Applied Catalysis B*, vol. 7, no. 1–2, pp. 49–63, 1995.
- [47] M. F. J. Dijkstra, A. Michorius, H. Buwalda, H. J. Panneman, J. G. M. Winkelman, and A. A. C. M. Beenackers, "Comparison of the efficiency of immobilized and suspended systems in photocatalytic degradation," *Catalysis Today*, vol. 66, no. 2–4, pp. 487–494, 2001.
- [48] S. Gelover, P. Mondragón, and A. Jiménez, "Titanium dioxide sol-gel deposited over glass and its application as a photocatalyst for water decontamination," *Journal of Photochemistry and Photobiology A*, vol. 165, no. 1–3, pp. 241–246, 2004.
- [49] S. Parra, S. E. Stanca, I. Guasaquillo, and K. R. Thampi, "Photocatalytic degradation of atrazine using suspended and supported TiO<sub>2</sub>," *Applied Catalysis B*, vol. 51, no. 2, pp. 107–116, 2004.
- [50] G. Balasubramanian, D. D. Dionysiou, M. T. Suidan, I. Baudin, and J.-M. Lainé, "Evaluating the activities of immobilized TiO<sub>2</sub> powder films for the photocatalytic degradation of organic contaminants in water," *Applied Catalysis B*, vol. 47, no. 2, pp. 73–84, 2004.
- [51] S. Mozia, M. Tomaszewska, and A. W. Morawski, "Decomposition of nonionic surfactant in a labyrinth flow photoreactor with immobilized TiO<sub>2</sub> bed," *Applied Catalysis B*, vol. 59, no. 3–4, pp. 155–160, 2005.
- [52] J. Gunlazuardi and W. A. Lindu, "Photocatalytic degradation of pentachlorophenol in aqueous solution employing immobilized TiO<sub>2</sub> supported on titanium metal," *Journal of Photochemistry and Photobiology A*, vol. 173, no. 1, pp. 51–55, 2005.
- [53] M. F. J. Dijkstra, A. Michorius, H. Buwalda, H. J. Panneman, J. G. M. Winkelman, and A. A. C. M. Beenackers, "Comparison of the efficiency of immobilized and suspended systems in photocatalytic degradation," *Catalysis Today*, vol. 66, no. 2–4, pp. 487–494, 2001.
- [54] H. D. Mansilla, C. Bravo, R. Ferreyra, et al., "Photocatalytic EDTA degradation on suspended and immobilized TiO<sub>2</sub>," *Journal of Photochemistry and Photobiology A*, vol. 181, no. 2–3, pp. 188–194, 2006.

- [55] J. Krýsa, G. Waldner, H. Měšťánková, J. Jirkovský, and G. Grabner, "Photocatalytic degradation of model organic pollutants on an immobilized particulate TiO<sub>2</sub> layer. Roles of adsorption processes and mechanistic complexity," *Applied Catalysis B*, vol. 64, no. 3-4, pp. 290–301, 2006.
- [56] V. Goetz, J. P. Cambon, D. Sacco, and G. Plantard, "Modeling aqueous heterogeneous photocatalytic degradation of organic pollutants with immobilized TiO<sub>2</sub>," *Chemical Engineering and Processing*, vol. 48, no. 1, pp. 532–537, 2008.

## Research Article

# Photoelectrocatalytic Degradation of Organic Pollutants in Aqueous Solution Using a Pt-TiO<sub>2</sub> Film

Chun He,<sup>1</sup> Mudar Abou Asi,<sup>1</sup> Ya Xiong,<sup>1</sup> Dong Shu,<sup>2</sup> and Xiangzhong Li<sup>3</sup>

<sup>1</sup> School of Environmental Science and Engineering, Sun Yat-sen University, Guangzhou 510275, China

<sup>2</sup> Key Lab of Electrochemical Technology on Energy Storage and Power Generation in Guangdong Universities, School of Chemistry and Environment, South China Normal University, Guangzhou 510006, China

<sup>3</sup> Department of Civil and Structural Engineering, The Hong Kong Polytechnic University, Hong Kong, China

Correspondence should be addressed to Chun He, hechun@mail.sysu.edu.cn

Received 1 April 2009; Accepted 27 June 2009

Recommended by Mohamed Sabry Abdel-Mottaleb

A series of Pt-TiO<sub>2</sub> films with nanocrystalline structure was prepared by a procedure of photodeposition and subsequent dip-coating. The Pt-TiO<sub>2</sub> films were characterized by X-ray diffraction, scanning electronic microscope, electrochemical characterization to examine the surface structure, chemical composition, and the photoelectrochemical properties. The photocatalytic activity of the Pt-TiO<sub>2</sub> films was evaluated in the photocatalytic (PC) and photoelectrocatalytic (PEC) degradation of formic acid in aqueous solution. Compared with a TiO<sub>2</sub> film, the efficiency of formic acid degradation using the Pt-TiO<sub>2</sub> films was significantly higher in both the PC and PEC processes. The enhancement is attributed to the action of Pt deposits on the TiO<sub>2</sub> surface, which play a key role by attracting conduction band photoelectrons. In the PEC process, the anodic bias externally applied on the illuminated Pt-TiO<sub>2</sub> films can further drive away the accumulated photoelectrons from the metal deposits and promote a process of interfacial charge transfer.

Copyright © 2009 Chun He et al. This is an open access article distributed under the Creative Commons Attribution License, which permits unrestricted use, distribution, and reproduction in any medium, provided the original work is properly cited.

## 1. Introduction

The widespread pollution of drinking water or effluents from industries and household with hazards and biorecalcitrant organic compounds demands an increasing effort towards the development of technologies for the cleanup of such wastewater [1, 2]. In past decades heterogeneous photocatalysis using TiO<sub>2</sub> has been attracted much attention in the field of environmental research for the degradation of undesirable organics in aqueous solution [3, 4]. The appeal of this technology is the prospect of complete mineralization of the pollutants into harmless compounds to environment in addition to the abundance, relatively low cost, chemical stability, and nontoxic nature of the catalyst. However, the PC efficiency is limited by the high degree of electron-hole recombination [5, 6].

Recently many studies have been devoted to improving PC activity by modifying TiO<sub>2</sub> using the deposition of noble metals [7–10]. In these cases, a Schottky barrier between the metal and TiO<sub>2</sub> is formed, while both metal and TiO<sub>2</sub>

Fermi levels equilibrate. Upon irradiation, the conduction band electrons flow from TiO<sub>2</sub> to the deposited metal that can act as a sink for the photogenerated electrons. This migration of the generated electrons to metal particles, on the one hand, can increase the lifetime of holes and suppress the electron-hole recombination, thus favoring PC oxidation of organic pollutants [7, 8, 10]; on the other hand, the migration can also enhance the PC reductive activity of TiO<sub>2</sub> [11, 12]. The reduction of organic pollutant is a process of increasing COD, generally unbeneficial to environmental protect. Moreover, the positive-charged holes, negative-charged metal particles, and organic pollutants are in a same reaction system; as a result, the system possibly suffers from a disadvantage that the intermediates of oxidized organic pollutants are re-reduced, leading to the formation of short-circuit similar to the mechanism of TiO<sub>2</sub> deactivation by chlorine ions [13] because any species with a reduction potential more positive than the flat band potential of TiO<sub>2</sub> (~ -0.7 V versus SCE, at pH 7), in theory, can be reduced [14]. In fact, recently many authors have demonstrated

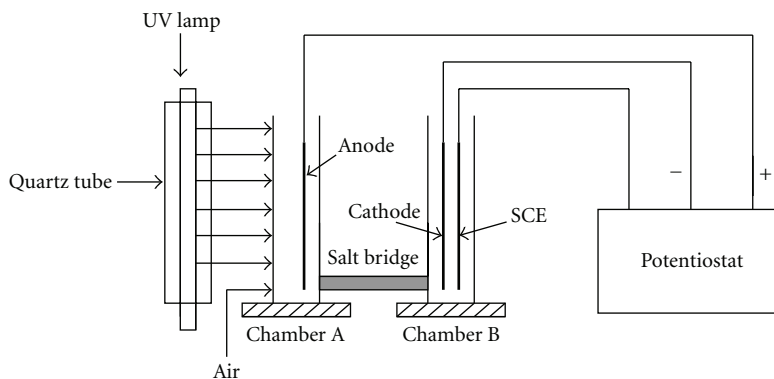


FIGURE 1: Schematic diagram of PC and PEC photoreactor systems.

that the PC oxidation activity of the metallized  $\text{TiO}_2$  is comparable to, and what is more, less than that of native  $\text{TiO}_2$  [15–17].

Based on the above considerations, it is significant for the oxidation of organic pollutants to further transfer the migrated electrons on the metal particles out of the reaction system by the alternatively externally applied anodic bias; the process is addressed as PEC one [18]. The externally anodic bias potential on the illuminated metal-loaded  $\text{TiO}_2$  film cannot only spatially separate the capture of conduction band electrons from the oxidation process but also drive away the accumulated photogenerated electrons on metal particles to another compartment of cell. Although many efforts have been directed to the PEC degradation of organic pollutants on  $\text{TiO}_2$  film [19–23], to date, rare information is available on the PEC oxidation of organic pollutants on metal-loaded  $\text{TiO}_2$  film except our recent reported examples [24, 25]. The above-mentioned situation aroused us to make attempts to prepare a novel platinum-deposited titanium dioxide film, Pt- $\text{TiO}_2$  film, and to investigate photoelectrochemical performance of Pt- $\text{TiO}_2$  film electrode and PEC activity towards the oxidation of organic pollutants on Pt- $\text{TiO}_2$  film electrode.

## 2. Experimental

**2.1. Materials.** Photocatalyst was  $\text{TiO}_2$  (Degussa P25). Formic acid solution was  $15 \text{ mmol}^{-1}$  (COD:  $239 \text{ mg l}^{-1}$ ). ITO (indium-tin oxide) conductive glass plates were used as a support of platinised  $\text{TiO}_2$  film to conveniently perform photoelectrochemical measurements.

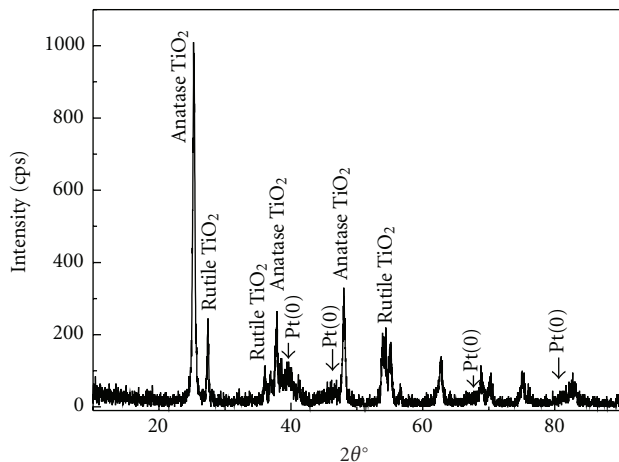
**2.2. Preparation of  $\text{TiO}_2$  and Pt- $\text{TiO}_2$  Film.** A  $\text{TiO}_2$ /ITO film was first prepared according to the procedure described in literature [23], in which, 40 g of  $\text{TiO}_2$  powder was added into 500 mL of distilled water. The  $\text{TiO}_2$  slurry was sonicated for 30 minutes to break the loosely-attached aggregates up and then vigorously agitated to form fine  $\text{TiO}_2$  suspension. Then the  $\text{TiO}_2$  in the suspension was loaded on the ITO glass plate ( $1.0 \text{ cm} \times 5.0 \text{ cm}$ ) by a procedure of dip-coating, drying, and sintering. The  $\text{TiO}_2$ -coated ITO film was dried for 15 minutes on a hot plate at  $100^\circ\text{C}$  and subsequently

sintered in a muffle furnace at  $400^\circ\text{C}$  for 2 hours to obtain the  $\text{TiO}_2$ /ITO film. The quantity of  $\text{TiO}_2$  loading was about  $1.07\text{--}1.10 \text{ mg cm}^{-2}$ .

Pt- $\text{TiO}_2$  film was prepared using a dip-coating procedure followed by Pt photodeposition. An aqueous suspension of  $\text{TiO}_2$  ( $80.0 \text{ g l}^{-1}$ ) was sonicated 30 minutes before coating. The suspension was loaded on an ITO glass ( $12 \text{ cm} \times 4.8 \text{ cm}$ ), dried 15 minutes on a hot plate at  $100^\circ\text{C}$  and then sintered 2 hours at  $400^\circ\text{C}$ . The loading, drying, and sintering was repeated three times. The quantity of  $\text{TiO}_2$  was about  $0.94\text{--}1.00 \text{ mg cm}^{-2}$  by weighing. The resulting  $\text{TiO}_2$  plate was immersed in a 40-mL aqueous solution containing  $\text{H}_2\text{PtCl}_6$  ( $2.2 \text{ mmol}^{-1}$ ) and  $\text{HCOOH}$  ( $1 \text{ mol}^{-1}$ ) and then subjected to photodeposition of Pt. The deposited Pt content was controlled under the different illumination time of 0.5, 1.0, 5.0, 10.0, and 20.0 minutes. An EDS analysis was carried out to confirm the amount of Pt content in the  $\text{TiO}_2$  films, which were 0.7%, 1.8%, 2.7%, 3.5%, and 4.2% (Wt. Pt/ Wt.  $\text{TiO}_2$ ), respectively.

**2.3. Characterization of  $\text{TiO}_2$ /ITO and Metal-Deposited  $\text{TiO}_2$  Films.** X-ray reflection diffraction (XRD) was performed using D/Max-III A Diffractometer (Rigaku Corporation, Japan) with Radiation of Cu target ( $K\alpha 1, \lambda = 1.54056 \text{ nm}$ ). Scanning electron microscope (SEM) images were obtained on a JSM-6330F-mode Field Emission Scanning Electron Microscope (JEOL, Japan). A UV-PC3101PC spectrophotometer (SHIMASZU, Japan) was used for recording the UV absorption spectra of solution. Photoelectrochemical measurement was performed with a Model CH650 Potentiostat.

**2.4. Experiments of PC and PEC Oxidation.** Formic acid chemical with analytical grade was supplied by Guangzhou Chemical Co. and used as a model chemical in this study. 15 mM formic acid solution was first prepared with an initial COD concentration of  $239 \text{ mg L}^{-1}$  and pH 2.73. About 35.0 mL of the 15 mM formic acid solution was used in both the PC and PEC reactions. Both of PC and PEC oxidation reactions were carried out in a photoreactor system as shown in Figure 1, consisting of two chambers (A and B,  $2.0 \text{ cm} \times 1.1 \text{ cm} \times 8.0 \text{ cm}$ ) connected via a salt bridge. When the PC reaction was conducted using the chamber

FIGURE 2: XRD spectra of Pt-TiO<sub>2</sub>.

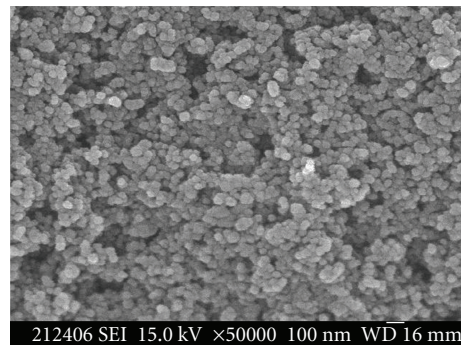
A only, the PEC reaction was performed using both the chambers. In the meantime, a 500-W UV lamp with main emission at 365 nm was used as a UV source, and air bubbling was continuously provided during reaction. Either the TiO<sub>2</sub> or Pt-TiO<sub>2</sub> plate was placed in the chamber A and used as an anodic electrode, while a Pt electrode and a saturated calomel electrode (SCE) were positioned in the chamber B and used as counter and reference electrodes, respectively. The photoelectrochemical measurement was performed with a potentiostat (Model CH 650, Shanghai).

**2.5. Analysis.** Chemical oxygen demand (COD) was measured with potassium dichromate after the sample was digested with a WMX COD microwave digestion system [26].

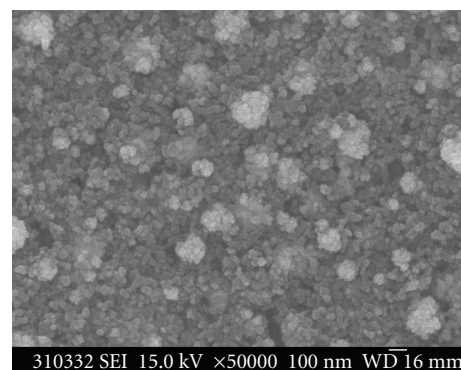
### 3. Results and Discussion

**3.1. Preparation and Characterization of Pt-TiO<sub>2</sub> Film.** In our previous work, nano-Ag and Cu were successfully deposited on TiO<sub>2</sub> film by photoreduction [24, 25]. Herein, we also try to directly deposit Pt on the film surface by the same method, using H<sub>2</sub>PtCl<sub>6</sub> as a Pt precursor and HCOOH as a hole scavenger, in order to prepare Pt-TiO<sub>2</sub> film. Upon illuminating TiO<sub>2</sub> film inserted in the H<sub>2</sub>PtCl<sub>6</sub>-HCOOH solution, a layer of black deposits on the surface of TiO<sub>2</sub> film was observed. The XRD pattern of the black deposits mixed with TiO<sub>2</sub> was shown in Figure 2. Four weak and broad XRD peaks were observed at 2θ angles of 39.74, 46.16, 67.56, and 80.98. The 2θ angles are corresponding to that of metallic Pt, and the breadth of these peaks is characteristic of Pt nanocrystals [9, 27]. Their average crystal size was calculated as 8 nm by using the Scherrer equation.

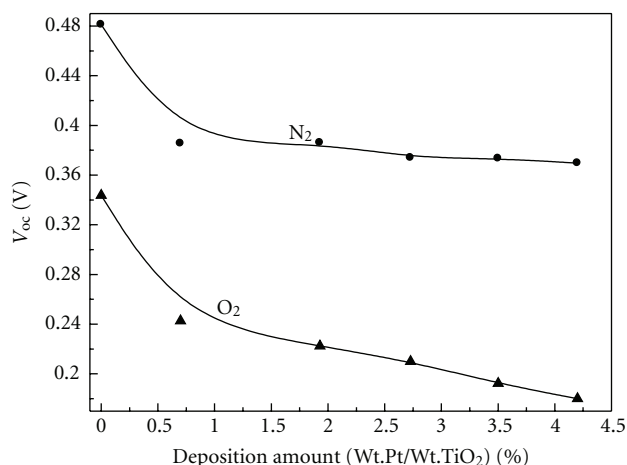
Figure 3 represents the SEM micrographs of the TiO<sub>2</sub> and platinumised films. The morphologies are noticeably dependent on the composition of films. TiO<sub>2</sub> film was of highly porous and particulate surface (Figure 3(a)). The particulate size is estimated to be approximate 50 nm, greater than that of the original P25 TiO<sub>2</sub> powder (30 nm). The fact indicates that



(a)



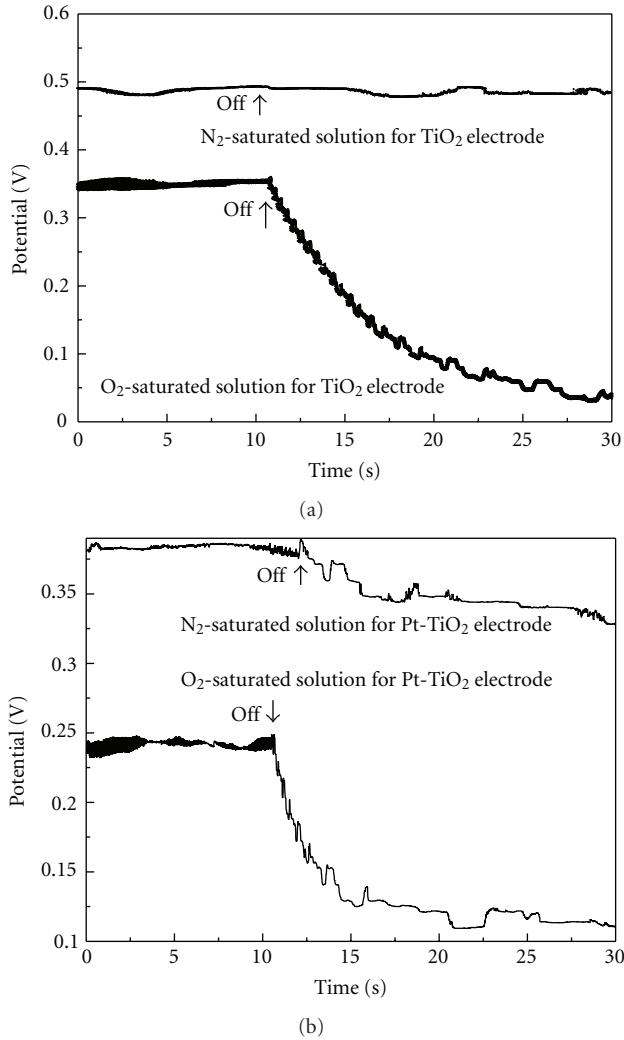
(b)

FIGURE 3: SEM images of TiO<sub>2</sub> and Pt-TiO<sub>2</sub> films (a) TiO<sub>2</sub> film and (b) Pt-TiO<sub>2</sub> with 1.8 wt.% Pt.FIGURE 4: Change of  $V_{oc}$  of Pt-TiO<sub>2</sub> with deposited Pt amount ( $V_{oc}$  (N<sub>2</sub>) for N<sub>2</sub>-saturated solution and  $V_{oc}$  (O<sub>2</sub>) for O<sub>2</sub>-saturated solution).

the TiO<sub>2</sub> particles were slightly aggregated during sintering. The surface of Pt-TiO<sub>2</sub> film is similar to that of TiO<sub>2</sub> film (Figure 3(b)). It characterized a porous and particulate appearance, but the particulate size was smoother than that of the particulates on TiO<sub>2</sub> film according to the resolution used; therefore, it means that the supported film contains smaller grains in the Pt-TiO<sub>2</sub> than in pure TiO<sub>2</sub>.

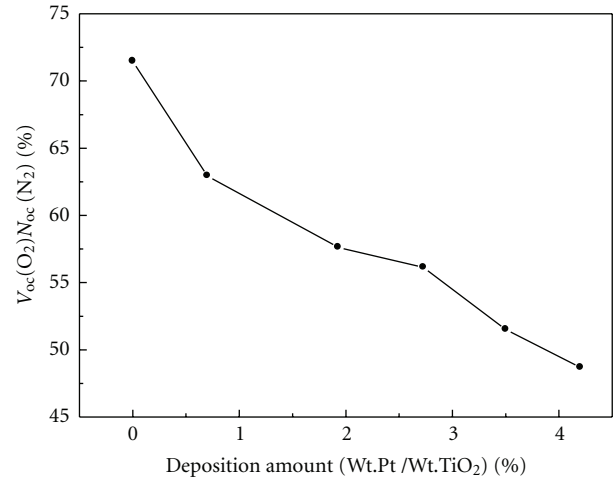
TABLE 1: The values of kinetic coefficient  $k$  in four experiments with application of the first-order kinetic model.

ID	Catalyst	Process	Rate constant ( $\text{min}^{-1}$ )	$k$ Correlation coefficient (R)
A	TiO <sub>2</sub>	PC	0.007	0.9600
B	TiO <sub>2</sub> electrode	PEC	0.011	0.9914
C	Pt-TiO <sub>2</sub>	PC	0.028	0.9901
D	Pt-TiO <sub>2</sub> electrode	PEC	0.038	0.9726

FIGURE 5: Decay curves of open circuit voltage after light was turned off (a) TiO<sub>2</sub> film and (b) Pt-TiO<sub>2</sub>.

### 3.2. Photoelectrochemical Characterization of Pt-TiO<sub>2</sub> Film.

The dependence of photovoltage of Pt-TiO<sub>2</sub> film on Pt content in N<sub>2</sub>- or O<sub>2</sub>-saturated solution is shown in Figure 4. In the dark, the Fermi level of a semiconductor film equilibrates with the redox couple in solution; upon excitation of TiO<sub>2</sub> film, the photogenerated electrons accumulate in the TiO<sub>2</sub> particulate film, leading to a rise in the photovoltage. As a result, any accumulation of electrons in the film will present a rise in  $V_{oc}$ . The observation that  $V_{oc}(O_2)$  of Pt-TiO<sub>2</sub> film in O<sub>2</sub>-saturation solution is lower than that in N<sub>2</sub>-saturated

FIGURE 6: Dependence of  $[V_{oc}(O_2)/V_{oc}(N_2)]$  on deposited Pt amount.

solution confirms the fact, due to the surface-adsorbed O<sub>2</sub> scavenging the photogenerated electrons in the O<sub>2</sub>-saturated solution. In addition to the above evidence, it is noting that in either N<sub>2</sub>- or O<sub>2</sub>-saturated solution for Pt-TiO<sub>2</sub> film,  $V_{oc}$  decreases with increase of Pt content. Generally, TiO<sub>2</sub> electrode deposited metallic nanoparticles shifts the photovoltage to more positive value, ascribing to the fact that the metallic nanoparticles improve the accumulation of electrons within the particulate film by facilitating the hole transfer at the electrolyte interface [7, 24]. An alternative explanation for the above-observed decrease of  $V_{oc}$  was based on the consideration while metal nanoparticles are surrounded by electron donors, and these deposited Pt can diminish the accumulation of photogenerated electrons. We attribute decrease of  $V_{oc}$  to the two tentative factors. Firstly, the deposited Pt can facilitate the reactions of scavenging photogenerated electrons, such as, O<sub>2</sub> reduction (1) and H<sub>2</sub> evolution (2):

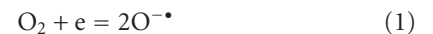


Figure 5 clearly shows that, after UV light turns off, the  $V_{oc}$  of Pt-TiO<sub>2</sub> film decreases more rapidly than that of TiO<sub>2</sub> film, either for N<sub>2</sub>-saturated solution or for O<sub>2</sub>-saturated solution, suggesting that deposited Pt can facilitate the reactions of scavenging photogenerated electrons for Pt-TiO<sub>2</sub> film via the reactions (1) and (2).

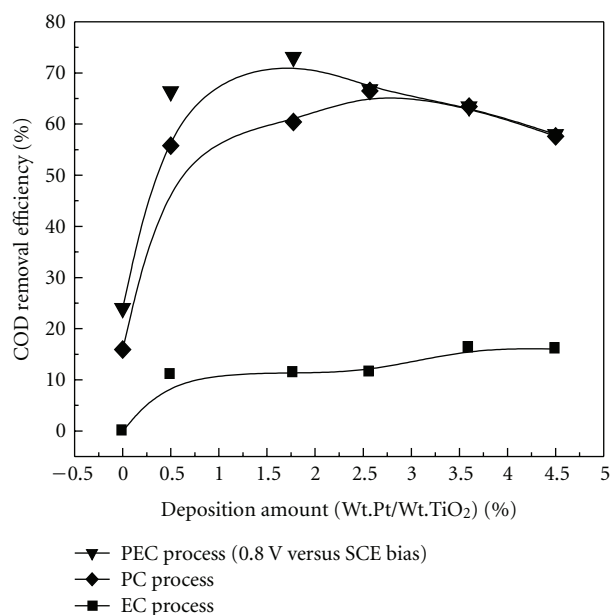


FIGURE 7: Dependence of COD removal efficiency on deposited Pt amount.

At the same time, it is also seen from Figure 5 that, compared with O<sub>2</sub>-saturated solution, all the  $V_{oc}$  for N<sub>2</sub>-saturated solution merely decreases slightly, indicating that the capture of electrons is mainly by the reaction (1), not (2). Therefore, the fraction of the remained photogenerated electrons on the platinised film can be approximately estimated by  $V_{oc}(O_2)/V_{oc}(N_2)$  [28]. The estimated results (Figure 6) suggested that there are still rather remained accumulated electrons on Pt-TiO<sub>2</sub> film in the experimental range although Pt deposition can increase the efficiency of the charge separation. For example, for Pt-TiO<sub>2</sub> film with 0.7% Pt content, the fraction of the remained electrons is 63%. Therefore, it is reasonable to employ an anodic bias to drive away the remained accumulation electrons in order to increase PC efficiency.

**3.3. PC and PEC Oxidation of Pt-TiO<sub>2</sub> Film.** The PC and PEC oxidation activities of Pt-TiO<sub>2</sub> films towards formic acid were evaluated in the term of COD removal efficiency in the present investigation. Presently, the influence of Pt content concentration on COD removal efficiencies is studied in a range from 0 to 4.5% not only for PC process but also for electrochemical and PEC processes. As shown in Figure 7, respectively, the COD removal efficiency is dependent on the amount of the Pt content for both PC and PEC processes, while the COD removal efficiency of electrochemical (EC) process changes slightly with Pt content. For PC processes, the COD removal efficiencies increase with the Pt content in the range of 0% ~ 2.7%. The enhancement effect further shows that Pt serves as an electron trapper and reduces the recombination of hole-electron pairs. However, over-deposited Pt resulted in a decrease in PC activity due to the reason that the cluster or aggregation of metal deposits on the surface changes the function

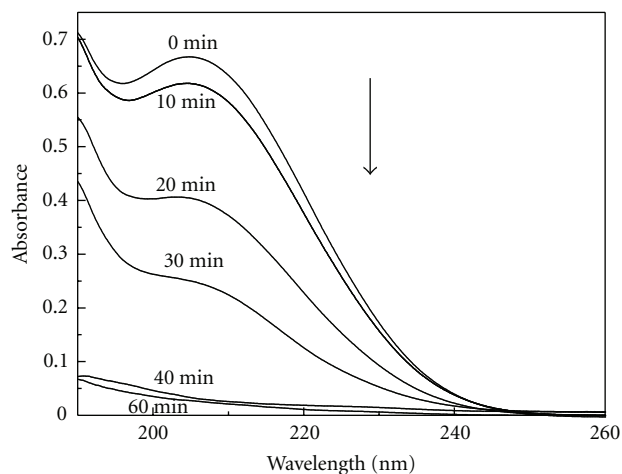


FIGURE 8: Change of UV spectra of formic acid at various reaction intervals for PEC process in the presence of 0.8 V versus SCE anodic bias.

from an electron separation center to an electron recombination center and consequently reduced the PC activity [29].

For PEC process, a similar change tendency was observed. However, it was also found that the COD removal efficiency for PEC process is considerably higher than that of PC process. For example, in the absence of Pt, the COD removal efficiency of PEC process is 24.0% while that of PC process is only 15.9%. For TiO<sub>2</sub> film with a Pt content of 1.7%, the COD removal efficiency of the PEC process is 73.4% while that of PC process is 60.4%, higher than the sum the COD removal efficiency for individual PC process (60.4%) and electrochemical process (11%). The observations denote that there is a significant synergistic effect existing in the PEC process.

In addition, the difference between PEC and PC processes on Pt-TiO<sub>2</sub> films with a Pt content of 1.7% is 13%, higher than that for neat TiO<sub>2</sub> film (8%), indicating that the enhancement effect of the external electric field in the presence of Pt is more obvious than in the absence of Pt. The more obvious enhancement effect can be explained by the fact that the Pt can not only trap the photogenerated electrons but also assist the external electric field to migrate them from the TiO<sub>2</sub> film to counter electrode in another compartment of the cell by improving electric conductivity of TiO<sub>2</sub> film as well as decrease the recombination. For either PEC or PC process, the Pt-TiO<sub>2</sub> films with Pt content of 1.7% possess a relative good performance of COD removal, all the rest of our experiments was conducted using the Pt-TiO<sub>2</sub> films with Pt content of 1.7%.

**3.4. Comparison of Rate Constants for PC or PEC Processes.** The UV spectra of formic acid in the PEC process at various reaction intervals are presented in Figure 8. It can be observed from the figure that formic acid decreased dramatically. And the COD removal efficiencies, at any tested time, are much higher than that for either PC process on Pt-TiO<sub>2</sub> film or PEC process on TiO<sub>2</sub> film as shown in Figure 9.

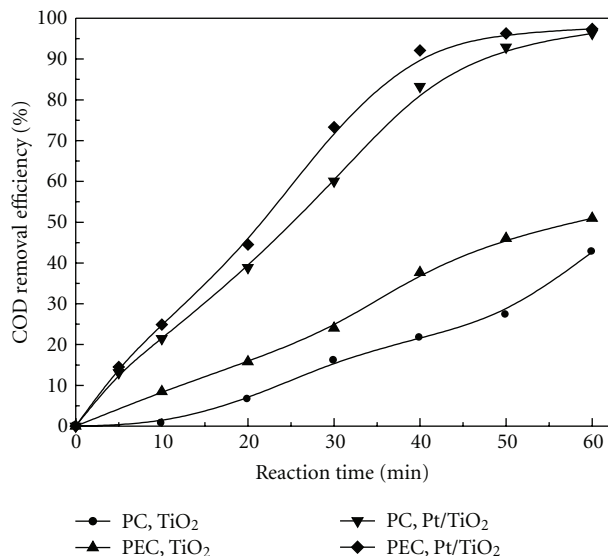


FIGURE 9: Dependence of COD removal efficiency on treatment time for various processes.

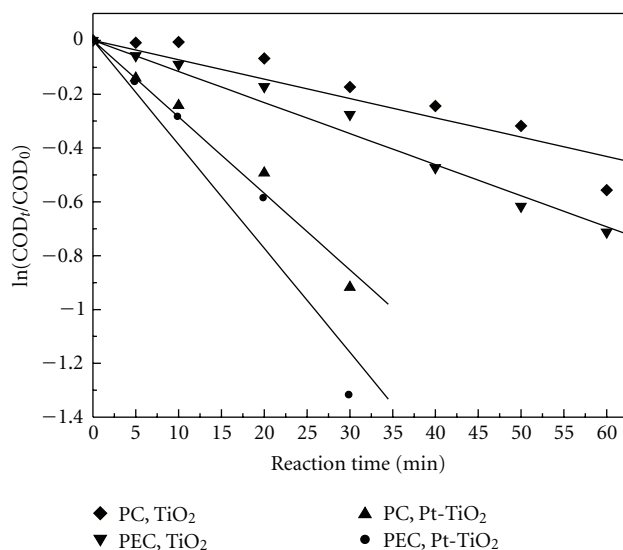


FIGURE 10: Logarithm of formic acid normalized COD concentration as a function of treatment time for the four processes.

It is also well recognized that PC degradation of organic pollutants accords with the first-order kinetics [30–32]. In this work, the first-order kinetics were also confirmed not only in the PC but also in the PEC process by the linear transforms  $\ln(\text{COD}_t/\text{COD}_0) = -kt$  of Figure 9 as shown in Figure 10. The kinetic regression equations and parameters were listed in Table 1; the rates for the PC oxidation or the PEC oxidation on Pt-TiO<sub>2</sub> film electrode are more than 4 times or 5.4 times of the PC oxidation on TiO<sub>2</sub> film, respectively. The observation further confirms that the combination of Pt deposition and the application of external electric field had a beneficial effect on enhancing the efficiency of the PC oxidation of formic acid.

## 4. Conclusion

The feasibility of improving the PC activity of TiO<sub>2</sub> film towards the oxidation of organic pollutant by combining the modification of Pt nanoparticles with the application of anodic bias was investigated. In this experiment Pt-TiO<sub>2</sub> films were used as photoanodes in a two-compartment photoelectrochemical cell to investigate its photoelectrochemical performance and the PEC activity towards the oxidation of formic acid. The experimental results showed that the deposited Pt has an apparent enhancement effect with respect to suppressing the recombination between the photogenerated charge carriers and enhancing the PC oxidation of formic acid, and the PC and PEC activities of Pt-TiO<sub>2</sub> film towards the oxidation of formic acid were considerably dependent on the amount of deposited Pt. Compared with a TiO<sub>2</sub> film, the degradation efficiency of formic acid on the Pt-TiO<sub>2</sub> films increased markedly in both the PC and PEC oxidation processes.

## Acknowledgments

The authors wish to thank for the financial support to this work from the National Natural Science Foundation of China (no. 20877025), the Specialized Research Fund for the Doctoral Program of Higher Education of China Education Ministry (no. 200805611015), and the Scientific Research Foundation for the Returned Overseas Chinese Scholars, State Education Ministry.

## References

- [1] G. Ceñti, P. Ciambelli, S. Perathoner, and P. Russo, "Preface: outlooks for environmental catalysis," *Catalysis Today*, vol. 75, no. 1–4, pp. 1–2, 2002.
- [2] D. Simonsson, "Electrochemistry for a cleaner environment," *Chemical Society Reviews*, vol. 26, no. 3, pp. 181–189, 1997.
- [3] A. Fujishima, T. N. Rao, and D. A. Tryk, "TiO<sub>2</sub> photocatalysts and diamond electrodes," *Electrochimica Acta*, vol. 45, no. 28, pp. 4683–4690, 2000.
- [4] D. A. Tryk, A. Fujishima, and K. Honda, "Recent topics in photoelectrochemistry: achievements and future prospects," *Electrochimica Acta*, vol. 45, no. 15–16, pp. 2363–2376, 2000.
- [5] J. C. Yu, J. Lin, and R. W. M. Kwok, "Enhanced photocatalytic activity of Ti<sub>1-x</sub>V<sub>x</sub>O<sub>2</sub> solid solution on the degradation of acetone," *Journal of Photochemistry and Photobiology A*, vol. 111, no. 1–3, pp. 199–203, 1997.
- [6] S. Li, G. Ye, and G. Chen, "Low-temperature preparation and characterization of nanocrystalline anatase TiO<sub>2</sub>," *Journal of Physical Chemistry C*, vol. 113, no. 10, pp. 4031–4037, 2009.
- [7] V. Subramanian, E. Wolf, and P. V. Kamat, "Semiconductor-metal composite nanostructures. To what extent do metal nanoparticles improve the photocatalytic activity of TiO<sub>2</sub> films?" *Journal of Physical Chemistry B*, vol. 105, no. 46, pp. 11439–11446, 2001.
- [8] D. Hufschmidt, D. Bahnemann, J. J. Testa, C. A. Emilio, and M. I. Litter, "Enhancement of the photocatalytic activity of various TiO<sub>2</sub> materials by platinumisation," *Journal of Photochemistry and Photobiology A*, vol. 148, no. 1–3, pp. 223–231, 2002.
- [9] Z. Luo, K. Katayama-Hirayama, K. Hirayama, T. Akitsu, and H. Kaneko, "Photocatalytic degradation of pyrene in

- porous Pt/TiO<sub>2</sub>-SiO<sub>2</sub> photocatalyst suspension under UV irradiation," *Nano*, vol. 3, no. 5, pp. 317–322, 2008.
- [10] A. Sclafani and J.-M. Herrmann, "Influence of metallic silver and of platinum-silver bimetallic deposits on the photocatalytic activity of titania (anatase and rutile) in organic and aqueous media," *Journal of Photochemistry and Photobiology A*, vol. 113, no. 2, pp. 181–188, 1998.
- [11] F. Boccuzzi, A. Chiorino, M. Manzoli, and D. Andreeva, "Gold, silver and copper catalysts supported on TiO<sub>2</sub> for pure hydrogen production," *Catalysis Today*, vol. 75, no. 1–4, pp. 169–175, 2002.
- [12] R. M. Lahtinen, D. J. Fermín, H. Jensen, K. Kontturi, and H. H. Girault, "Two-phase photocatalysis mediated by electrochemically generated Pd nanoparticles," *Electrochemistry Communications*, vol. 2, no. 4, pp. 230–234, 2000.
- [13] F. Sunada and A. Heller, "Effects of water, salt water, and silicone overcoating of the TiO<sub>2</sub> photocatalyst on the rates and products of photocatalytic oxidation of liquid 3-octanol and 3-octanone," *Environmental Science and Technology*, vol. 32, no. 2, pp. 282–286, 1998.
- [14] P. S. M. Dunlop, J. A. Byrne, N. Manga, and B. R. Eggins, "The photocatalytic removal of bacterial pollutants from drinking water," *Journal of Photochemistry and Photobiology A*, vol. 148, no. 1–3, pp. 355–363, 2002.
- [15] U. Siemon, D. Bahnemann, J. J. Testa, D. Rodríguez, M. I. Litter, and N. Bruno, "Heterogeneous photocatalytic reactions comparing TiO<sub>2</sub> and Pt/TiO<sub>2</sub>," *Journal of Photochemistry and Photobiology A*, vol. 148, no. 1–3, pp. 247–255, 2002.
- [16] J. Chen, D. F. Ollis, W. H. Rulkens, and H. Bruning, "Photocatalyzed oxidation of alcohols and organochlorides in the presence of native TiO<sub>2</sub> and metallized TiO<sub>2</sub> suspensions. Part (I): photocatalytic activity and pH influence," *Water Research*, vol. 33, no. 3, pp. 661–668, 1999.
- [17] V. Vamathavan, R. Amal, D. Beydoun, G. Low, and S. McEvoy, "Photocatalytic oxidation of organics in water using pure and silver-modified titanium dioxide particles," *Journal of Photochemistry and Photobiology A*, vol. 148, no. 1–3, pp. 233–245, 2002.
- [18] K. Vinodgopal and P. V. Kamat, "Enhanced rates of photocatalytic degradation of an azo dye using SnO<sub>2</sub>/TiO<sub>2</sub> coupled semiconductor thin films," *Environmental Science and Technology*, vol. 29, no. 3, pp. 841–845, 1995.
- [19] R. Pelegrini, P. Peralta-Zamora, A. R. De Andrade, and J. Reyes, "Electrochemically assisted photocatalytic degradation of reactive dyes," *Applied Catalysis B*, vol. 22, no. 2, pp. 83–90, 1999.
- [20] X. Z. Li, H. L. Liu, P. T. Yue, and Y. P. Sun, "Photoelectrocatalytic oxidation of rose Bengal in aqueous solution using a Ti/TiO<sub>2</sub> mesh electrode," *Environmental Science and Technology*, vol. 34, no. 20, pp. 4401–4406, 2000.
- [21] D. H. Kim and M. A. Anderson, "Solution factors affecting the photocatalytic and photoelectrocatalytic degradation of formic acid using supported TiO<sub>2</sub> thin films," *Journal of Photochemistry and Photobiology A*, vol. 94, no. 2–3, pp. 221–229, 1994.
- [22] M. V. B. Zanoni, J. J. Sene, and M. A. Anderson, "Photoelectrocatalytic degradation of Remazol Brilliant Orange 3R on titanium dioxide thin-film electrodes," *Journal of Photochemistry and Photobiology A*, vol. 157, no. 1, pp. 55–63, 2003.
- [23] J. Rodriguez, M. Gomez, S. E. Lindquist, and C. G. Granqvist, "Photo-electrocatalytic degradation of 4-chlorophenol over sputter deposited Ti oxide films," *Thin Solid Films*, vol. 360, no. 1–2, pp. 250–255, 2000.
- [24] C. He, Y. Xiong, D. Shu, and X. H. Zhu, "Enhanced photocatalytic efficiency of TiO<sub>2</sub> by combining the modification of Ag nanoparticles with the application of anodic bias," *Chinese Chemical Letters*, vol. 14, no. 5, pp. 539–542, 2003.
- [25] C. He, Y. Xiong, and X. Zhu, "Improving photocatalytic activity of Cu-loaded TiO<sub>2</sub> film using a pulse anodic bias," *Catalysis Communications*, vol. 4, no. 4, pp. 183–187, 2003.
- [26] Y. Xiong, P. J. Strunk, H. Xia, X. Zhu, and H. T. Karlsson, "Treatment of dye wastewater containing acid orange II using a cell with three-phase three-dimensional electrode," *Water Research*, vol. 35, no. 17, pp. 4226–4230, 2001.
- [27] D. K. Lee and D. S. Kim, "Catalytic wet air oxidation of carboxylic acids at atmospheric pressure," *Catalysis Today*, vol. 63, no. 2–4, pp. 249–255, 2000.
- [28] N. Chandrasekharan and P. V. Kamat, "Improving the photoelectrochemical performance of nanostructured TiO<sub>2</sub> films by adsorption of gold nanoparticles," *Journal of Physical Chemistry B*, vol. 104, no. 46, pp. 10851–10857, 2000.
- [29] A. Sclafani and J. M. Herrmann, "Influence of metallic silver and of platinum-silver bimetallic deposits on the photocatalytic activity of titania (anatase and rutile) in organic and aqueous media," *Journal of Photochemistry and Photobiology A*, vol. 113, no. 2, pp. 181–188, 1998.
- [30] J. Matos, J. Laine, and J. M. Herrmann, "Synergy effect in the photocatalytic degradation of phenol on a suspended mixture of titania and activated carbon," *Applied Catalysis B*, vol. 18, no. 3–4, pp. 281–291, 1998.
- [31] T. C. An, X. H. Zhu, and Y. Xiong, "Synergic degradation of reactive brilliant red X-3B using three dimension electrode-photocatalytic reactor," *Journal of Environmental Science and Health A*, vol. 36, no. 10, pp. 2068–2082, 2001.
- [32] T. C. An, X. H. Zhu, and Y. Xiong, "Feasibility study of photoelectrochemical degradation of methylene blue with three-dimensional electrode-photocatalytic reactor," *Chemosphere*, vol. 46, no. 6, pp. 897–903, 2002.

## Research Article

# From Laboratory Studies to the Field Applications of Advanced Oxidation Processes: A Case Study of Technology Transfer from Switzerland to Burkina Faso on the Field of Photochemical Detoxification of Biorecalcitrant Chemical Pollutants in Water

S. Kenfack,<sup>1</sup> V. Sarria,<sup>2</sup> J. Wéthé,<sup>3</sup> G. Cissé,<sup>4</sup> A. H. Maïga,<sup>3</sup> A. Klutse,<sup>1</sup> and C. Pulgarin<sup>5</sup>

<sup>1</sup> *Département de Recherche et Projets de Démonstration (REPRODEM), Centre Régional pour l'Eau potable et l'Assainissement (CREPA), 03BP 7112 Ouagadougou 03, Burkina Faso*

<sup>2</sup> *Departamento de Química, Universidad de los Andes, Cra 1 No 18A-10, Bogota, Colombia*

<sup>3</sup> *Unité Thématique d'Enseignement et de Recherche en Gestion et Valorisation de l'Eau et de l'Assainissement (UTER-GVEA), Institut International d'Ingénierie de l'Eau et de l'Environnement, 01 BP 594 Ouagadougou 01, Burkina Faso*

<sup>4</sup> *Centre Suisse de Recherche Scientifique de Côte d'Ivoire (CSRS), 01 BP 1301 Abidjan 01, Cote d'Ivoire*

<sup>5</sup> *Ecole Polytechnique Fédérale de Lausanne, Institute of Chemical Sciences and Engineering, GGEC, Station 6, CH, 1015 Lausanne, Switzerland*

Correspondence should be addressed to S. Kenfack, skenfack@yahoo.fr

Received 26 February 2009; Accepted 4 May 2009

Recommended by Mohamed Sabry Abdel-Mottaleb

The Fenton and photo-Fenton detoxification of non-biodegradable chemical pollution in water was investigated under simulated UV light in the laboratory and under direct sunlight in Ouagadougou, Burkina Faso. The laboratory experiments enable one to make a systematic diagnosis among three types of wastewaters, identifying a biorecalcitrant wastewater containing the Chloro-hydroxy-Pyridine (CHYPR). The application of the photo-Fenton process on effluent containing the CHYPR showed not to stimulate the generation of biodegradable by-products. Optimal conditions for detoxification of effluent containing the CHYPR were found at pH = 2.8,  $[\text{Fe}^{2+}] = 5.2 \text{ mM}$ , initial  $[\text{H}_2\text{O}_2] = 768 \text{ mM}$ , for an effluent concentrated at 2.2 mM of CHYPR. The application of the photochemical process on a field pilot solar photoreactor for the detoxification of water polluted with a pesticide made with Endosulfan showed very promising results, with potential biodegradable effluents obtained at the end of the photochemical treatment. Optimal conditions of the applied study were found at pH = 3,  $[\text{H}_2\text{O}_2] = 8 \text{ mM}$  and  $[\text{Fe}^{2+}] = 0.18 \text{ mM}$  for an initial concentration of 0.36 mM of Endosulfan.

Copyright © 2009 S. Kenfack et al. This is an open access article distributed under the Creative Commons Attribution License, which permits unrestricted use, distribution, and reproduction in any medium, provided the original work is properly cited.

## 1. Introduction

An estimation of the global world water pollution reveals that 60%–70% of the total pollution is due to the agricultural activities, 25% to 30% by industries, and the remaining 5% to 10% due to the domestic uses [1]. The report showed that, in the most optimistic cases, the water pollution from agricultural origin is mostly consisted of the residues of pesticide and contributes to at least 50% on the deterioration of the quality of natural waters (surface and subsoil waters). This is closely followed by the pollution of chemical industrial origin. In fact, more than 1000 new substances

are marketed each year in the world whereas up to now the toxicological information on only 1000 to 2000 of these products is accessible [2].

Most of these substances are xenobiotic (c.a. foreign to life), and very often they are synthetic products. Indeed, xenobiotic substances are in general not easily biodegradable, and they cross the biological water treatment systems without being completely degraded or even sometimes not degraded at all.

Some of these substances such as the pesticides are recognized as cause of carcinogenic, mutagen effects, or of hormonal disruptions to the fauna, wild life, and human beings.

To face these problems, waste treatment techniques such as incineration, wet oxidation, and activated carbon adsorption are often used. Unfortunately, these techniques are very expensive, and the environmental virtues of some of them are discussed.

However, biological processes remain the most economical and environmentally compatible alternative for wastewater treatment. Thus, it would be important to confirm the biorecalcitrancy of a wastewater before the application of a photocatalytic treatment. Moreover, biorecalcitrant wastewater could only be photocatalytically treated up to the point where its biodegradability is enough to let the phototreated water follows a biological treatment. Two case studies are reported in this paper to illustrate the strategy of enhancing the biodegradability of biorecalcitrant wastewaters throughout a photocatalytic process. These studies are representative of two problem solving approaches: one in an industrial developed country (Switzerland) and the other in a tropical developing country (Burkina Faso).

### 1.1. The Laboratory Solving Problem Approach in Switzerland versus the Field Applied Approach in Burkina Faso

**1.1.1. Case Study 1: The Chemical Pollution in Wastewater in a Swiss Manufacture.** In June 2004, a Swiss chemical company started the manufacture of a new significant chemical, following a three-step process. Three types of effluent of a specific composition were generated at each step, and all the three effluents were mixed to other effluents of the manufacture and treated in an activated sludge wastewater treatment plant. Before the new production, the yield of the wastewater treatment plant was efficient, and it could respect the legal rejection norms. But since the production of the new chemical has started, the yield has fallen down and the plant could not any more respect the standards, even when the hydraulic capacity overshooting of the treatment plant was still very low. The laboratory study aimed at making a diagnosis identifying the biorecalcitrant effluent and studied its degradation using the photoFenton treatment process.

**1.1.2. Case Study 2 The Problem of Persistent Organic Pollutants and Obsolete Pesticides in Burkina Faso.** In order to implement the national plan of the Stockholm's Convention on the persistent organic pollutants (POPs), the government of Burkina Faso carried out in 2001 and 2004 two inventories of stocks of POPs pesticides available on the extent territory of Burkina Faso. Table 1 reports the results of these inventories.

It was noticed that 90% of these pesticides were formulated with Cypermethrin (67%) and Endosulfan (3%) which are classified in the categories II and III (from the toxic to very toxic) by the WHO. The same report revealed that 13 contaminated sites of major importance are available in Burkina Faso. Since there is neither incinerator in Burkina Faso nor a specialized hazardous waste treatment plant, the experimental approach developed at the EPFL, Switzerland, was tested for the degradation of a pesticide containing Endosulfan, one of the chemicals which is known to generate toxic metabolites after a first step biological degradation [4].

## 2. Experimental

**2.1. Materials and Apparatus.** At the LBE-EPFL, the photocatalytic studies were performed using a 50 mL Pyrex flask with a cut-off at  $\lambda = 290$  nm placed into a Hanau Suntest (Figure 1).

The radiation source was a Xenon lamp where the radiant flux ( $80 \text{ mW} \cdot \text{cm}^{-2}$ ) was measured with a power meter of YSI Corporation. The lamp had a regular distribution of wavelengths with about 0.5% of the emitted photons at wavelengths shorter than 300 nm (UV-C range) and about 7% between 300 and 400 nm (UV-B range). The profile of the photons emitted between 400 and 800 nm (UV-A range) followed the solar spectrum.

Experiments were done at the light intensity of  $560 \text{ W} \cdot \text{m}^{-2}$ , which corresponds to a relative UVA (300–400 nm) intensity of  $\text{W} \cdot \text{m}^{-2}$ . All the chemicals ( $\text{FeSO}_4$ ,  $7\text{H}_2\text{O}$ ), HCl and  $\text{H}_2\text{O}_2$  (30% w/w) were bought from Fluka (Switzerland), and all were analytical grade (p.a.).

Three types of wastewaters (see Table 1) containing pyridine compounds were received from DLK Technology S.A, a Swiss company specialized in the developing specific technical plants for water and wastewater treatment.

The pilot plant, a SOLARDETOX ACADUS-2003 device model delivered by Ecosystem SA, Barcelona, Spain, is a one plate Compound Parabolic Concentrator (CPC) module (collector useful surface:  $2.12 \text{ m}^2$ , photoreactor active volume 15.1 L within a total volume of 16.07 L) made of sixteen borosilicate cylindrical glass tubes. Each tube lies on a CPC aluminum mirror with one sun of concentration.

The reactor is mounted on a two-position fixed platform inclinable at  $10^\circ$  and  $35^\circ$  allowing operating at the approximate local latitude of Ouagadougou-Burkina Faso ( $12.2^\circ \text{ N}$ ), at  $10^\circ$  angle position most of the time. A picture and the technical design of the CPC photoreactor used are shown in Figure 2.

From the operational point of view, the plant behaves a plug-flow reactor in the collector zone, connected to a 50 L polypropylene stirred tank (recirculating tank or buffer tank) for wastewater preparation: pH adjustments, catalyst, and oxidant feeding. The ensemble constituted by a plug-flow reactor in the collector zone plus a tank and a recirculation system is equivalent to a batch photoreactor.

**2.2. Procedures.** In the laboratory, a systematic diagnosis including the characterization of each of the three effluents received was first made, followed by the photoassisted studies on the effluent containing chloro-2-pyridin. 2 liters of the raw effluent were first acidified at  $\text{pH} = 3$ . For the photodegradation processing, 50 mL of this preparation was put into a 60 mL of a Pyrex flask glass, and reactants (iron and peroxide) were added. The flask glass was placed into the Suntest photoreactor for a determined time of illumination. Samplings were made every 10 minutes for TOC, HPLC, and spectrophotometric analyses, and during the Zahn Wellens tests sampling were made daily.

The field application took place at the International Institute of Water and Environmental Engineering (2iE), Ouagadougou, Burkina Faso ( $12^\circ 21' \text{ N}$ ,  $1^\circ 31' \text{ W}$ ). It is an

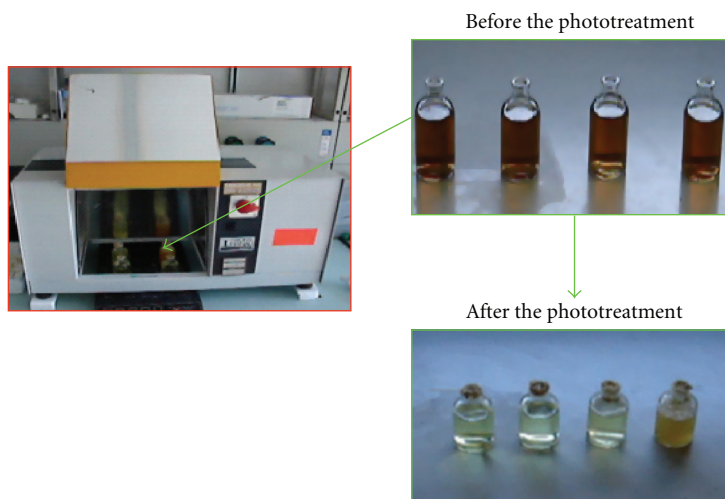


FIGURE 1: A Hanau Suntest Simulator containing 04 Pyrex flask samples during a laboratory processing at the BE-EPFL, Lausanne, Switzerland.

TABLE 1: Results of the surveys of POPs and obsolete pesticides in Burkina Faso (2001 and 2004) [3].

Form	Quantity		Nature of the pesticide in 2004	
	2001	2004		
Contaminated empty containers (—)	1450000	120'000		
Powder (kg)	26000	3000	Cypermethrin	Endosulfan
Liquid (Liters)	250000	130000	85700	4000

ideal place where solar applied researches can be carried out with more than 300 days—2500 sunny hours per year (e.g., in Almería, Spain, it is estimated up to 3000 sunny hours per year) [3].

At the beginning of an experiment, the mixture is homogenized to achieve a fixed concentration in the system, by circulating the preparation in a closed loop circuit (Tank-pump-photoreactor-tank). A desired stock of pesticide solution was first dissolved in 2 liters of tap water and stirred for at least 2 hours in the laboratory. Afterward, the solution was poured into the conditioning tank of the photoreactor in which 20 liters of tap water were previously added. Three more liters of tap water were used to rinse the predissolved Pyrex flask and added to the conditioning tank. The pH of the solution was adjusted to 3 with HCl, and the catalyst ( $\text{FeCl}_3$ ) was added. The entire system was homogenized by closing the valves (1) and (3) and circulating the polluted water in a closed loop circuit for 15 minutes (see Figure 2).

Once the solution is ready, the required amount of hydrogen peroxide was added, and the feeding valve (1) was opened according to the water circulation speed needed for the operation. The water flow was varied by regulating the valve (1) to: 0.3, 0.4, and  $0.5 \text{ m} \cdot \text{s}^{-1}$ .

The solar ultraviolet radiation was determined during the experiments through a UVA radiometer ACADUS 85 UV mounted on the reactor, at the same angle ( $10^\circ$ ) as its plate part. It provides data in terms of incident UVA radiation per

area unit ( $\text{W} \cdot \text{m}^{-2}$ ) and the accumulated energy  $E_{(t)}$  on the  $2.12 \text{ m}^2$  surface of the photoreactor (in Wh).  $E_{(t)}$  is linked to the instantaneous irradiance flux ( $\overline{UV}$ ), the reactor total active area ( $A$ ), the water volume ( $V$ ), and the experiment duration ( $t$ ) by the following relation:

$$E_{(t)} = E_{(t_0)} + \Delta t \times \overline{UV} \times \frac{A}{V}. \quad (1)$$

**2.3. Analytical Methods.** At the LBE, HPLC analyses were carried out in a Varian 9065 unit provided with a Varian 9012 solvent delivery system, an automatic injector 9100 and a Varian Pro Star Variable (200–400 nm) diode array detector: 9065 Polychromic. All modules were piloted with a computer on which the Varian Star 5.3 software is installed for liquid chromatography data delivery. A reverse phase spherisorb silica column ODS-2 and a (70/30) (v/v) mixture of acetonitrile/water mobile phase were used to run the chromatography in isocratic mode at a flow rate of  $1 \text{ mL} \cdot \text{min}^{-1}$ . This technique allows the measuring of the main pollutant concentration in the solution and to follow the overall formation and decay of the aromatic and aliphatic by-products during the process.

A Hitachi UV-vis U-3010 and a Biomate 3 model spectrophotometers were used, respectively, at the LBE and at the 2iE, with a 1.0 cm quartz cell. The Hitachi UV-vis U-3010 spectrophotometer allowed generating the

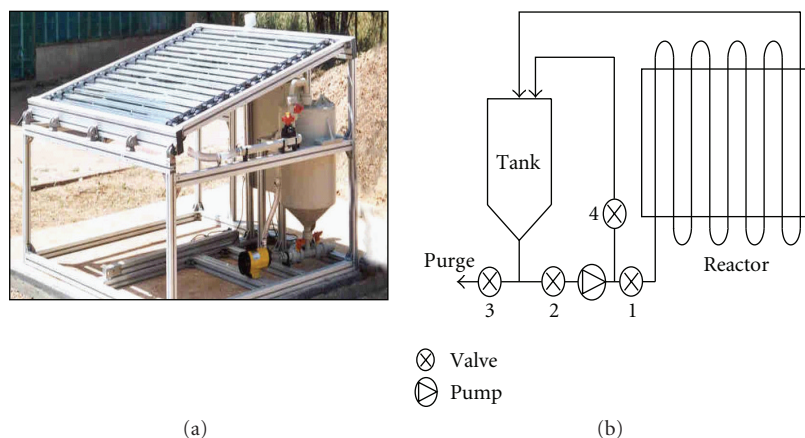
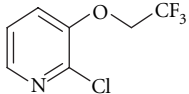
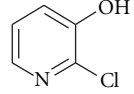


FIGURE 2: A Picture and the technical design of the CPC photoreactor.

TABLE 2: Synthesis of the characteristics of the three effluents.

Type of effluent	Main pollutant	Molecular structure	pH	TOC ( $\text{g} \cdot \text{L}^{-1}$ )
WW <sub>1</sub>	CTFEP		8.3	45
WW <sub>2</sub>	LQV	Confidential	6	43.5
WW <sub>3</sub>	CHPYR		5.8	6.5

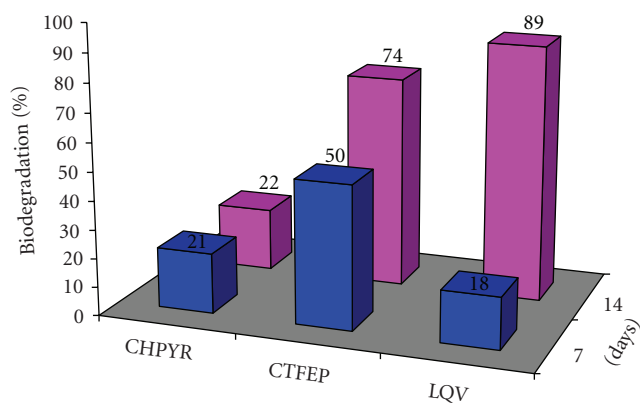


FIGURE 3: Percentage of biodegradation respectively 07 (■) and 14 days (■).

characteristic spectra of phototreated samples in the wavelength range of 200–600 nm, so that all the chemicals and/or complexes in the solutions can be signalled at their maximum absorption wavelength. Once we identified the specific absorption wavelengths through the spectra, we chose these particular wavelengths for the analyses on the multiwavelengths *Biomate 3* spectrophotometer during the field's application at the 2iE at Ouagadougou, Burkina Faso.

The biological Zahn Wellens tests were carried out on the phototreated samples after 60% degradation of the TOC, following the OCDE standard method [5].

The Chemical Oxygen Demand (COD) analyses were carried out via a Hach-2000 spectrophotometer using the dichromate solution as the oxidant in a strong acid medium. 2 mL of the samples were put into the low range kits ( $0\text{--}150 \text{ mg} \cdot \text{L}^{-1}$ ) and digested at  $150^\circ\text{C}$  for two hours. Once the digested samples were cooled, their optical density was determined at  $\lambda = 430 \text{ nm}$ , in comparison to a blank, prepared with 2 mL of distilled water. The Biological Oxygen Demand for five days ( $\text{BOD}_5$ ) was measured by means of an Hg-free WTW 2000 Oxytop unit thermostated at  $20^\circ\text{C}$  according to the standard method.

### 3. Results

#### 3.1. A Systematic Study of the Photocatalytic Removal of the Chemical Pollution of the Industrial Wastewater in Switzerland

3.1.1. *Diagnosis: Physicochemical and Biological Characterization of Different Types of Effluents Resulting from the Processing of LQV.* Table 2 presents the characteristics of three effluents ( $\text{WW}_i$ ) from the production of the LQV (its molecular

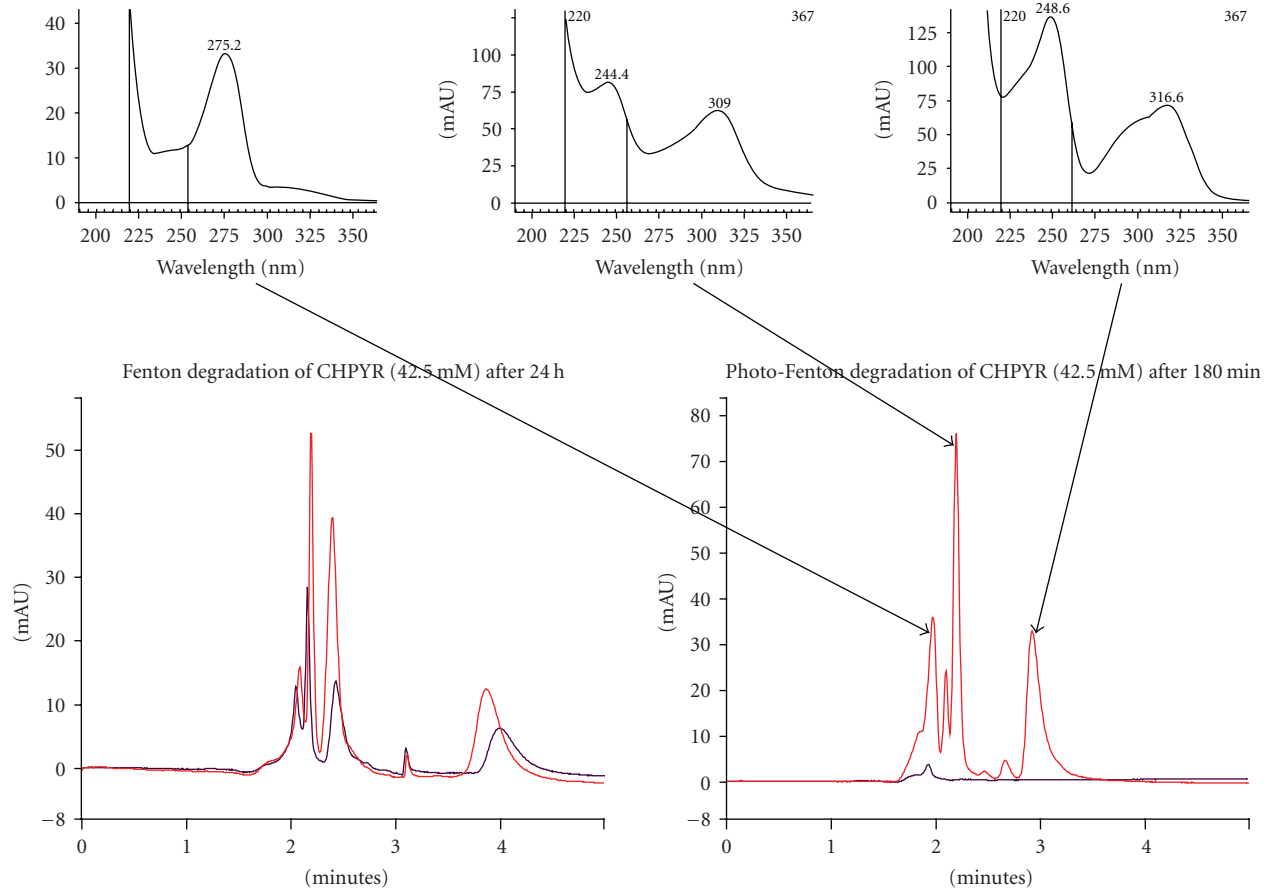


FIGURE 4: HPLC chromatograms of the CHPYR effluent before and after the Fenton (a) and the photoFenton (b) processes.

formula is confidential), and Figure 3 shows the results of the Zahn wellens tests carried out on the three effluents.

From these results, one can conclude the following.

- (i) The wastewater mainly containing CTFEP is easily biodegradable and that with LQV is biodegradable after a certain period for bacteria adaptation.
- (ii) The wastewater mainly containing CHPYR is biorecalcitrant. No change in the degradation rate was observed at the 7th, 14th, and up to the 28th day. The Fenton and photoFenton processes were applied to WW<sub>3</sub>, and the experimental conditions were optimized for the catalyst ( $\text{Fe}^{2+}$ ) and the electron acceptor ( $\text{H}_2\text{O}_2$ ).

**3.1.2. Fenton and PhotoFenton Treatment of the CHPYR Polluted Wastewater.** Figure 4 shows the chromatograms of the CHPYR effluent carried out at the beginning and after 24 hours of Fenton treatment on 50% diluted effluent on the one hand compared to the photoFenton treatment on the same effluent for 1 h30. The UV spectra of three significant peaks are observed on the raw effluent (nontreated). The two most important peaks of the chromatograms completely disappeared in case of the photoFenton treatment, and the one

at 275.2 nm is 90% degraded; all the other peaks regressed relatively for 50% in case of the Fenton process after 24 hours.

**3.1.3. Optimization of the  $\text{H}_2\text{O}_2$  and  $\text{Fe}^{2+}$  Concentrations.** Figure 5 shows that the optimal conditions for the photoFenton treatment of the CHPYR effluent are obtained in 2 hours with an initial concentration of the solution of  $\text{TOC} = 2200 \text{ mg} \cdot \text{L}^{-1}$ ,  $\text{Fe}^{2+} = 5.2 \text{ mM}$ ,  $\text{H}_2\text{O}_2 = 768 \text{ mM}$ . Under these conditions, 60% of the organic pollutants (main pollutants and their degradation intermediates) are mineralized when the CHPYR is completely exhausted in the solution within the two hours of photoFenton treatment.

**3.1.4. Biodegradability of the PhotoTreated Effluent.** Figure 6 shows the results of the OECD's Zahn Wellens test carried out on the phototreated CHPYR effluent under the optimal photoFenton degradation conditions ( $\text{Fe}^{2+} = 5.2 \text{ mM}$ ;  $\text{H}_2\text{O}_2 = 768 \text{ mM}$ ;  $\text{pH} = 2.8$ ), with a decrease of 60% of total organic carbon. This shows that, relatively less than 15% to 18% of biological degradation is reached at the end of the first weeks followed by a fold down to 12% and stagnation until the 28th day. It is assumed that the photogenerated intermediates of degradation of the CHPYR are also biorecalcitrant or toxic. Hence a total mineralization following the Fenton or photoFenton process is necessary.

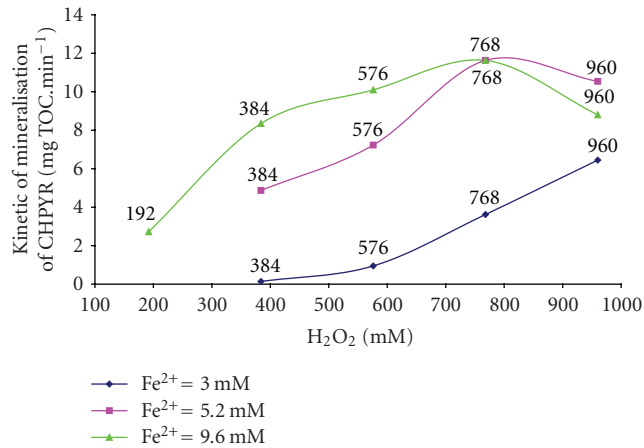


FIGURE 5: Kinetic of mineralisation of the CHPYR at various H<sub>2</sub>O<sub>2</sub> concentration: (■) for 3mM; (▲) for 5.2 mM and (●) for 9.6 mM, as a function of the H<sub>2</sub>O<sub>2</sub> concentration during the PhotoFenton process in a 50% diluted effluent (42.5 mM).

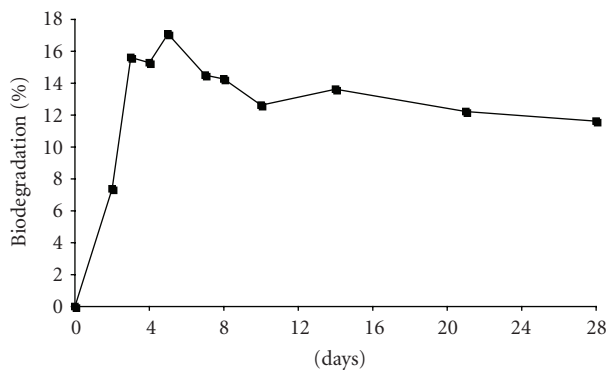


FIGURE 6: Evolution of the biodegradability following the Zahn Wellens process carried out on the CHPYR phototreated effluent.

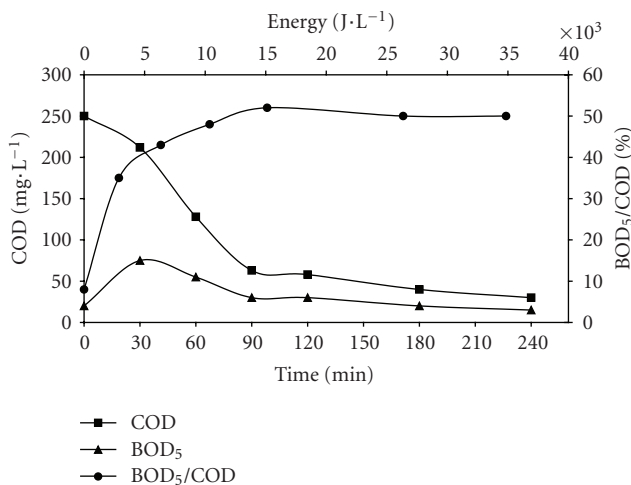


FIGURE 7: Evolution of biochemical parameter of the Endosulfan polluted water during the helio-photoFenton treatment, (■) for the COD, (▲) for BOD<sub>5</sub>, and (●) for the BOD<sub>5</sub>/COD ratio.

3.2. *Application of the Helio-PhotoFenton Process for the Degradation Wastewater Polluted with Endosulfan.* The monitoring of the biodegradability of the solar-treated effluent was conducted on 30 minutes sampled effluents. The results in Figure 7 show that the BOD<sub>5</sub> increases during the first 30 minutes of the treatment and decreases during the next hour; after that it remains constant. At the same time, the COD is continuously decreasing during one and half hour after which it remains constant. As a consequence of the evolution of these two parameters, the intrinsic biodegradability defined as the ratio BOD<sub>5</sub>/COD is continuously increasing up to 50% where it became constant when the energetic treatment factor of the process is  $15 \times 10^3 \text{ J} \cdot \text{L}^{-1}$ .

## 4. Discussions

4.1. *Study of the Management of the Chemical Industry Effluents.* Figure 4 confirmed the presence of biorecalcitrant pollutant (CHPYR) with maximum UV absorption at 309 nm. The studies carried out on the three types of effluents also showed that the effluents mainly containing LQV and of the CTFEP were biodegradable and only that of CHPYR was biorecalcitrant. However, the CHPYR effluent can be degraded through the Fenton and photoFenton processes, within the optimal conditions:  $[\text{Fe}^{2+}] = 5.2 \text{ mM}$ ;  $[\text{H}_2\text{O}_2] = 768 \text{ mM}$  for effluent concentrated at  $2.2 \text{ g} \cdot \text{L}^{-1}$  of CHPYR. However, the Fenton process was not timely efficient.

The Zahn Wellens tests carried out on the phototreated effluent up to 60% TOC reduction did not show any significant biodegradability meaning that the remaining carbonic components in the treated effluent still were biorecalcitrant. It would be preferable to phototreat the effluent totally (i.e., up to more than 90% mineralization).

For a better management of the effluents resulting from that manufacture, the following diagram in Figure 8 would be recommendable.

4.2. *The Scaling up Approach from Laboratory Studies to the Field Application.* Studies in the laboratory and within very high-tech experimental device potential, made it possible to highlight the applicability of the Fenton and photoFenton processes for the detoxification of non biodegradable pollution in water. However, since the aim of this research is to undertake this process for solving real problems, its scaling up applicability (on more significant volumes) still to be evaluated, particularly when operating using the sunlight and not the lamps which of course, are cost expensive. The example of the artificial contamination of water by Endosulfan in Burkina Faso approaches more the reality since cases of contamination of water of the ground water by the pesticides had been reported in Burkina [6].

It's possible that, by submitting the commercial pesticide which composed of the active component: the endosulfan (water solubility  $0.325 \text{ mg} \cdot \text{L}^{-1}$ ) and other additives such as emulsifiers and adhering agents (which stabilizes the product on the plant once it is pulverized) to the Fenton and photoFenton processes, some of these additives would

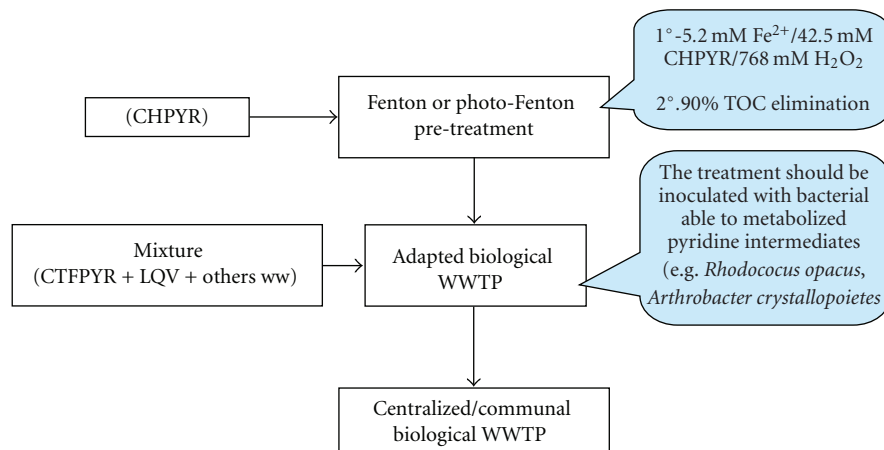


FIGURE 8: A proposed scheme of a diagram for the management of the studied effluents.

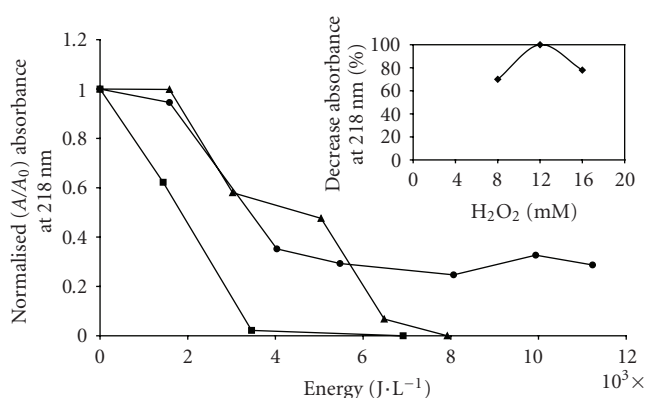


FIGURE 9: Relative absorbance of the phototreated Endosulfan contaminated water as a function of the specific energy. The  $\text{H}_2\text{O}_2$  is varied from: (●) 8 mM, (■) 12 mM to (▲) 16 mM. The insert is percentage of relative degradation of the Endosulfan (monitored at 218 nm) when  $6 \times 10^3 \text{ J} \cdot \text{L}^{-1}$  energy is accumulated in the photoreactor for the three  $\text{H}_2\text{O}_2$  values tested.

be destroyed by photolysis and/or oxidation with oxygen from air [7]. The decrease of 40% of the absorbance at 218 nm as observed in Figure 9, does not inevitably mean that the Endosulfan is degraded, since it was shown that the molecule of Endosulfan is stable when exposed to solar radiation and the tests of stabilization for the commercial formulation of pesticides, taking into account the sunlight exposition aspects [8]. The effect of photolysis and aeration on the Endosulfan solution could be put into account of the degradation of the additives (emulsifiers and adherents).

Since the photocatalytic treatment is not considered as a cost effective process when compared to biological treatment [9–12], when taken into account the cost of hydrogen peroxide on the one hand, the technical choice of a treatment, total photochemical mineralization or coupling photochemical-biological processes, on the other hand, it is necessary to make a compromise over the optimal concentration of  $\text{H}_2\text{O}_2$  and the duration of the treatment, by

considering the biodegradability of the phototreated effluent. In the case of this study, the choice was made on the lowest concentration of the peroxide (8 mM) with 0.18  $\text{Fe}^{2+}$  mM for an initial concentration of 0.36 mM of Endosulfan, conditions within which, is that 50% of the biodegradability of the phototreated effluent is reached after 1 h30.

Assuming the relatively high value of the  $\text{BOD}_5/\text{COD}$  ratio noticed in Figure 7, one can conclude that the phototreated pesticide effluent containing Endosulfan can become biodegradable in the natural environment. However, it would be necessary to send such effluents into a biological wastewater treatment plant before they could be reused for any purpose or be rejected in the natural media (river, dam, or lake) following the scheme proposed in Figure 8. Otherwise, more studies need to be carried out, that is, by coupling photochemical and a biological process to oversee the complete degradation of endosulfan polluted water.

## 5. Conclusion

The difficulty and the complexity of treating real biorecalcitrant wastewaters were observed within the two studied cases. The increase of the biodegradability was observed after the photoFenton treatment of the effluent contaminated with Endosulfan but not with the CHPYR effluent. Thus, a total mineralization process is recommendable in the second case and rather an improvement of the biodegradability of the Endosulfan effluent.

The study on the pesticide effluent enables one to notice that the photolysis could lower by 30% the COD of the effluent (Figure 9) by contrast to the absence of COD decrease for a simple aeration.

In the two case studies, the helio-photoFenton process is effective proportionally to the amount of hydrogen peroxide added; but for economic reasons, a compromise should be made between the highest kinetics of the treatment process of the Endosulfan effluent and the overall objective (or strategy)

of the treatment, namely, the coupling of photochemical and biological processes which is a cost minimization option in the treatment strategies of biorecalcitrant wastewaters.

Is the high DBO<sub>5</sub>/DCO ratio in the case of the photodegradation of Endosulfan effluent necessarily a good indicator to confirm the biotreatability of the phototreated effluent? Such a request could be looked out through very concise chemical analyses of the components of the effluents.

Eventually, this study shows a soft approach of transferring a laboratory high-tech context study to a field applied context within a North-South cooperation.

## Acknowledgments

This work was supported by the Swiss Federal Department for the Cooperation throughout the fifth EPFL-2iE-DDC convention (2002–2006), the NCCR-NS research programme- IP 4-JACS-WA, the EPFL student association “Ingénieurs du Monde”, and the EPFL-Colombia Environment Programme. The authors are very gratefully to MM. Cesar Lador, former student at the EPFL, and Amadou Zakari Yeou from the International Institute of Water and Environmental Engineering (2iE) who jointly did an internship works training in this project during the Easter 2005. Beside them, MM Bernard Zongo and Jules Ouédraogo are also thanked for their help during the field work at the 2iE experimental water treatment platform in Ouagadougou, Burkina Faso.

## References

- [1] Population.Information.Program, “Solutions for a water-short world,” 1–31, 1998.
- [2] K. Toepfer, “Statement on the occasion of the Stockholm Convention on Persistent Organic Pollutants Coming into Force,” UNEP, 2004.
- [3] J. Blanco and S. R. Malato, “Solar detoxification,” Alméria, UNESCO/PSA, 2001.
- [4] G. S. Kwon, H. Y. Sohn, K. S. Shin, E. Kim, and B. I. Seo, “Biodegradation of the organochlorine insecticide, endosulfan, and the toxic metabolite, endosulfan sulfate, by *Klebsiella oxytoca* KE-8,” *Applied Microbiology and Biotechnology*, vol. 67, pp. 845–850, 2005.
- [5] OECD, “Guidelines for testing of chemicals,” test 302 B, 1996.
- [6] H. K. Tapsoba and Y. L. Bonzi-Coulibaly, “Production cotonnière et pollution des eaux par les pesticides au Burkina Faso,” *Journal de la Société Ouest-Africaine de Chimie*, no. 21, pp. 87–93, 2006.
- [7] N. Sethunathan, M. Megharaj, Z. Chen, N. Singh, R. S. Kookana, and R. Naidu, “Persistence of endosulfan and endosulfan sulfate in soil as affected by moisture regime and organic matter addition,” *Bulletin of Environmental Contamination and Toxicology*, vol. 68, no. 5, pp. 725–731, 2002.
- [8] K. P. Bentson, “Fate of xenobiotics in foliar pesticide deposits; reviews of environmental contamination and toxicology,” *CODEN RCTOE4*, vol. 114, pp. 125–161, 1990.
- [9] D. F. Ollis, “Process economics for water purification: a comparative assessment,” in *Photocatalysis and Environment*, pp. 663–677, Kluwer Academic Publishers, Boston, Mass, USA, 1988.
- [10] C. Pulgarin, M. Invernizzi, S. Parra, V. Sarria, R. Polania, and P. Péringier, “Strategy for the coupling of photochemical and biological flow reactors useful in mineralization of biorecalcitrant industrial pollutants,” *Catalysis Today*, vol. 54, no. 2-3, pp. 341–352, 1999.
- [11] J. Blanco and S. R. Malato, “Solar detoxification,” Alméria, UNESCO/PSA, 2003.
- [12] V. Sarria, S. Kenfack, O. Guillod, and C. Pulgarin, “An innovative coupled solar-biological system at field pilot scale for the treatment of biorecalcitrant pollutants,” *Journal of Photochemistry and Photobiology A*, vol. 159, no. 1, pp. 89–99, 2003.

## Research Article

# Generation of Useful Hydrocarbons and Hydrogen during Photocatalytic Decomposition of Acetic Acid on CuO/Rutile Photocatalysts

Sylwia Mozia

*Institute of Chemical and Environment Engineering, West Pomeranian University of Technology, ul. Pułaskiego 10, 70-322 Szczecin, Poland*

Correspondence should be addressed to Sylwia Mozia, sylwiam@ps.pl

Received 14 May 2009; Accepted 14 May 2009

Recommended by Mohamed Sabry Abdel-Mottaleb

The presented studies have focused on a photocatalytic generation of useful hydrocarbons, mainly methane and ethane, from acetic acid under  $N_2$  atmosphere. CuO-loaded rutile, as well as unmodified rutile and anatase-phase  $TiO_2$  photocatalysts were applied in the experiments. The efficiency of the catalysts towards methane generation changed in the following order: Cu- $TiO_2$  (10% Cu) > crude  $TiO_2$   $\approx$  Cu- $TiO_2$  (20% Cu) > Cu- $TiO_2$  (5% Cu) > rutile. The amount of  $CH_4$  produced in the presence of the catalyst containing 10 wt% of Cu was higher for ca. 33% than in case of pure rutile. The concentration of ethane was 14–16 times lower than the amount of methane, regardless of the catalyst used. Low concentrations of hydrogen were also detected in the gaseous mixtures. After 5 hours of the process conducted with the catalyst containing 5–20 wt% of Cu the concentration of hydrogen amounted to 0.06–0.14 vol.%, respectively.

Copyright © 2009 Sylwia Mozia. This is an open access article distributed under the Creative Commons Attribution License, which permits unrestricted use, distribution, and reproduction in any medium, provided the original work is properly cited.

## 1. Introduction

Energy has progressively become a major global concern due to the depletion of natural resources and the global warming problem. Moreover, although the oil prices, compared to the prices in summer last year, have recently decreased due to the global recession, it is impossible to predict what oil prices will be next year. In view of this, the development of renewable energy sources is very important. Among numerous alternative energy sources, bioenergy, especially biogas, seems to be the most environmentally friendly and economically viable one. Moreover, except from being the source of energy, the biogas could be an effective solution to the wastes and wastewaters problem.

Biogas typically refers to a mixture of gases, mainly methane and carbon dioxide, produced by the anaerobic digestion or fermentation of organic matter under anaerobic conditions. Other compounds present in the biogas could be  $N_2$ ,  $H_2$ ,  $H_2S$ ,  $O_2$ ,  $CO$ ,  $H_2O$ , and  $NH_3$ . The composition of biogas varies depending on the origin of wastes used in the anaerobic digestion process as well as the process conditions.

The traditional production of biogas based on anaerobic digestion technology requires the presence of particular kinds of bacteria. The methanogenic bacteria are highly sensitive to the  $O_2$  concentration in the system and their activities depend on the concentrations of fatty and acetic acids, and the pH value [1]. In addition, bacteria are not able to treat substances which are biorecalcitrant (e.g., herbicides) or bactericide. This reduces the number of possible sources for biogas generation to those which do not contain substances dangerous to the bacteria [2].

In view of this, it seems to be beneficial to find another solution for conversion of wastewaters into useful energy (biogas). In our opinion, such a solution could be development of biogas production via photocatalytic decomposition of organic compounds. Photocatalysis is not specific (or almost not) for particular substrates what means that could be applied for any type of wastewaters, regardless of its toxicity. Therefore, different biogas sources could be utilized for photocatalytic generation of biogas, or “photo-biogas”.

Most of the already published papers [3–11] on photocatalytic production of methane concern reduction of  $CO_2$

under UV light in the presence of pure or modified TiO<sub>2</sub>. The reactions were carried out either in liquid or in gaseous phase. The efficient photoreduction of carbon dioxide in aqueous medium was found to be difficult since the solubility of carbon dioxide is rather low (ca. 0.03 mol/dm<sup>3</sup> at ambient conditions) [11]. Therefore, attempts to conduct the process in gaseous phase were made [12–14]. Generation of methane from CO<sub>2</sub> is often proposed as a method of solving the global warming problem. Another very important environmental problem is treatment of wastewaters. As was mentioned earlier, the photocatalytic production of methane from sewage is supposed to be helpful in solving this problem.

Literature data concerning photocatalytic generation of methane from organic compounds in liquid phase are very limited. All of them concern production of CH<sub>4</sub> from aliphatic acids [15–18] and alcohols [19]. In 1970's Kraeutler and Bard [15–17] published a series of papers concerning photocatalytic decarboxylation of acetic acid in the presence of Pt/TiO<sub>2</sub> catalyst. The main products of the reaction were methane and carbon dioxide. Similarly, Sakata et al. [18] observed formation of methane and ethane during photodecomposition of acetic and propionic acids in the presence of TiO<sub>2</sub> and Pt/TiO<sub>2</sub>.

One of the crucial points in the photocatalytic generation of methane from organic compounds is development of an effective photocatalyst. Most of literature data on the photocatalytic production of methane in aqueous phase show application of TiO<sub>2</sub> or Pt/TiO<sub>2</sub> photocatalysts [15–18]. In the presented studies we have focused on preparation of CuO-modified rutile photocatalysts and their application in photocatalytic generation of methane in N<sub>2</sub> atmosphere. CuO was selected on a basis of literature data [3, 20–23]. For example, Slamet et al. [3] found that CuO was very effective modifying agent in photoreduction of CO<sub>2</sub>. The authors investigated the effect of modification of TiO<sub>2</sub> with CuO, Cu<sub>2</sub>O and Cu and found that CuO was the most active modifier compared to the other species. Sreethawong and Yoshikawa [23] reported that CuO/TiO<sub>2</sub> photocatalysts exhibited significant activity in photocatalytic hydrogen evolution. Taking into consideration these data, CuO was selected as a modifying agent in the presented experiments. Acetic acid was used as a source of the “photobiogas”. Application of acetic acid as a model compound seems to be reasonable since amongst the final by-products of photocatalytic degradation of most organic compounds in water different aliphatic acids, including CH<sub>3</sub>COOH, are present.

## 2. Experimental

The catalysts used in this study were prepared from crude TiO<sub>2</sub> obtained directly from the Chemical Factory “Police” (Poland). The crude TiO<sub>2</sub> was modified with CuCl<sub>2</sub> · 2H<sub>2</sub>O as follows. A defined amount of TiO<sub>2</sub> was introduced into a beaker containing aqueous solution of modifying agent and stirred for 22 hours. After that water was evaporated and the samples were dried at 105°C for 24 hours in an oven. Such prepared samples were calcinated at 700°C in Ar atmosphere (5 dm<sup>3</sup>/h) for 1 hour. The amount of Cu introduced to the

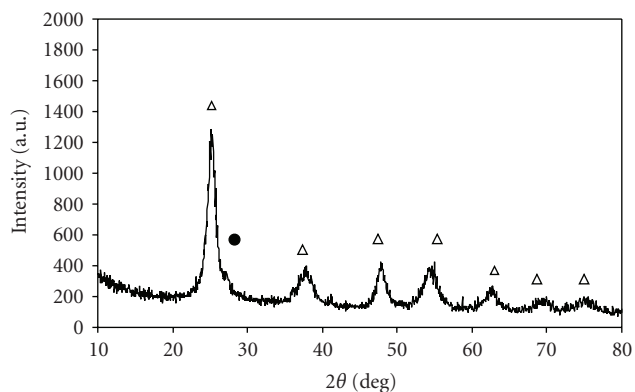
samples was 5, 10 or 20 wt%. In order to compare the results, a sample containing rutile phase without CuO was prepared by annealing of crude TiO<sub>2</sub> at 800°C for 1 hour in air. At the temperature of 700°C, which was applied for preparation of CuO/rutile catalysts, the anatase phase, not rutile, was obtained. Therefore, the temperature of 800°C was selected for preparation of pure rutile without CuO.

X-ray diffraction (XRD) analyses were performed on a powder diffractometer Philips X'Pert PRO (CuK<sub>α</sub>, 35 kV, 30 mA). UV-VIS/DR spectra were recorded using Jasco V 530 spectrometer (Japan) equipped with the integrating sphere accessory for diffuse reflectance spectra. BaSO<sub>4</sub> was used as a reference.

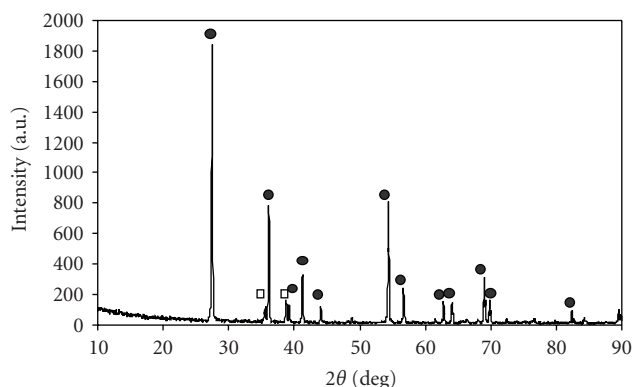
The photocatalytic reaction was conducted in a cylindrical glass reactor containing 0.35 dm<sup>3</sup> of CH<sub>3</sub>COOH (1 mol/dm<sup>3</sup>) and 0.35 g of a catalyst. At the beginning of the experiment N<sub>2</sub> was bubbled through the reactor for at least 3 hours to ensure that the dissolved oxygen was eliminated. Then, the UV lamp (λ<sub>max</sub> = 365 nm), positioned in the center of the reactor, was turned on to start the photoreaction. Gaseous products were analyzed using GC SRI 8610C equipped with TCD and HID detectors, and Shincarbon (carbon molecular sieve; 4 m, 1 mm, 10–120 mesh) and molecular sieve 5A (2 m, 2 mm, 80–100 mesh) columns. Helium was used as a carrier gas.

## 3. Results and Discussion

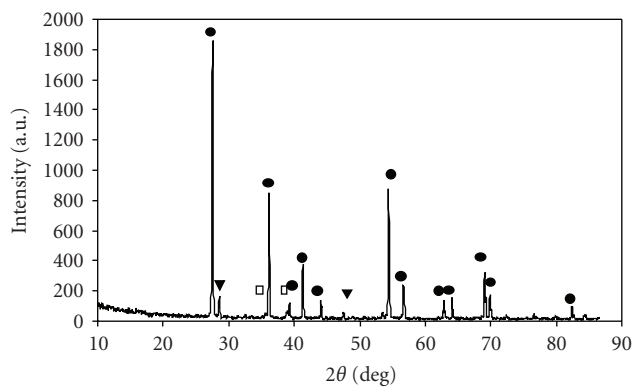
Figure 1 presents XRD patterns of crude TiO<sub>2</sub> and photocatalysts modified with CuO. It can be observed that crude TiO<sub>2</sub> contained almost pure (97%) anatase phase. The diffraction lines were weak and broad suggesting poor crystallinity of the sample. The crystallite size of anatase in the crude TiO<sub>2</sub> was 9 nm. The catalysts containing 5 and 10 wt% Cu were composed of rutile and CuO only. In case of the sample containing 20 wt% of Cu, except from rutile and CuO phases, CuCl was also identified. The presence of CuCl suggests that the amount of CuCl<sub>2</sub> used was too high and the transformation of CuCl<sub>2</sub> to CuO was not complete under the conditions applied. Some amount of copper (II) was reduced to copper (I) forming CuCl. The sample prepared by calcination of crude TiO<sub>2</sub> at 800°C and denoted later as rutile consisted of 97% of rutile and 3% of anatase [24]. As was mentioned earlier (see Section 2), the temperature of 800°C was selected because application of calcination temperature of 700°C resulted not in rutile, but anatase phase. These data clearly show that the presence of CuO strongly affects the temperature of phase transformation from anatase to rutile. Such a phenomenon was already reported in literature [25]. Francisco and Mastelaro [25] explained it by catalyzing properties of copper oxide. CuO probably catalyzes the mass transport to the nucleation region of rutile phase, promoting rutile nuclei growth, thus favoring the phase transition. CuO is responsible for a higher number of defects inside the anatase phase, in such a way that formation and growth of a higher number of rutile nuclei into TiO<sub>2</sub> anatase take place faster. The mechanism responsible for such a modification is an excess of oxygen vacancies that accelerates the transition and the crystallite growth [25].



(a)



(b)



(c)

FIGURE 1: XRD patterns of crude TiO<sub>2</sub> and Cu-modified photocatalysts: (a) crude TiO<sub>2</sub>; (b) photocatalyst containing 10 wt% Cu; (c) photocatalyst containing 20 wt% Cu. ●-rutile; Δ-anatase; □-CuO; ▼-CuCl.

The crystallite size of rutile calculated on a basis of the Scherrer equation was similar for pure rutile and CuO/rutile catalysts and ranged from 300 to 320 nm, respectively. However, since 100 nm is generally considered the upper limit for XRD crystal size measurements, these data cannot be interpreted as accurate dimensions of the rutile crystals. The only conclusion could be that crystallite sizes of rutile in all of the samples (i.e., pure rutile and CuO/TiO<sub>2</sub>) were similar. This might lead to the conclusion that the crystallite size of rutile, being almost the same for all the samples,

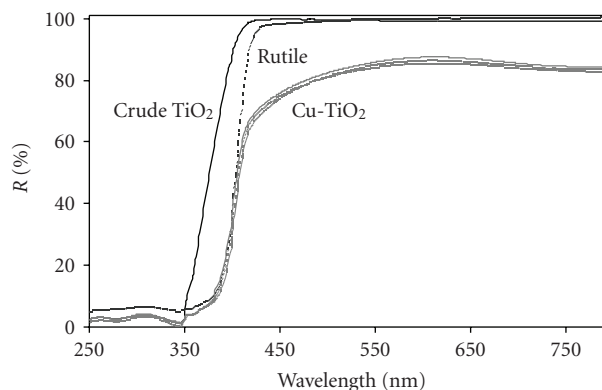


FIGURE 2: UV/Vis-DR spectra of crude TiO<sub>2</sub>, rutile and Cu-rutile photocatalysts.

should not affect the photocatalytic behavior of the CuO-modified rutile.

Figure 2 shows UV-Vis/DR spectra of crude TiO<sub>2</sub>, rutile and Cu-modified catalysts. It can be observed that all the spectra of CuO-rutile photocatalysts exhibit a similar course and are red shifted for over 30 nm relative to crude TiO<sub>2</sub>, what indicates a decrease of the band gap energy. This decrease was associated with phase transformation from anatase to rutile. A similar red shift relative to crude TiO<sub>2</sub> can be observed in case of pure rutile. To determine the band gap energy ( $E_g$ ) of the samples, the Kubelka-Munk method was used. The  $E_g$  values were calculated from the  $(F(R)h\nu)^{1/2}$  versus  $h\nu$  plots, where  $F(R) = (1 - R)/2R$  [26]. The absorption edge for crude TiO<sub>2</sub> was found to be 378 nm, which value corresponded to the band gap energy of  $E_g = 3.28$  eV. The absorption edges determined for pure rutile and CuO-rutile samples were 412 and 414 nm, what corresponded to  $E_g$  of 3.01 and 2.99 eV, respectively. From Figure 2 it can be also found that CuO-rutile catalysts absorbed more visible light than pure TiO<sub>2</sub>. The increased absorption in the Vis region was due to grey color of the CuO-modified photocatalysts.

The TiO<sub>2</sub> and Cu-TiO<sub>2</sub> photocatalysts were applied for the photocatalytic decomposition of acetic acid under N<sub>2</sub> atmosphere. The reaction was conducted for 5 hours. Figure 3 presents changes of concentration of methane in gaseous mixtures versus time of irradiation.

For the initial 2 hours of the process, no significant difference in the amount of methane generated on different catalysts was observed. The concentration of CH<sub>4</sub> was in the range of 0.24–0.28 vol.% what corresponded to 0.12–0.14 mmolCH<sub>4</sub>/molCH<sub>3</sub>COOH. However, with increasing time of irradiation the differences between the amounts of methane formed with application of different catalysts were becoming more significant. After 5 hours of irradiation the pure rutile was found to be the least efficient catalyst. The amount of methane formed in the presence of rutile was ca. 0.6 vol.%, what corresponded to 0.29 mmolCH<sub>4</sub>/molCH<sub>3</sub>COOH. The highest amount of methane was generated in case of the catalyst containing 10 wt% of Cu. After 5 hours of irradiation the

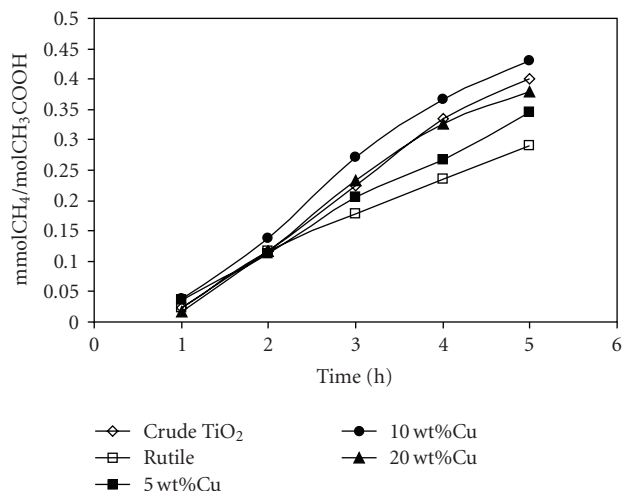


FIGURE 3: Photocatalytic generation of methane on different photocatalysts.

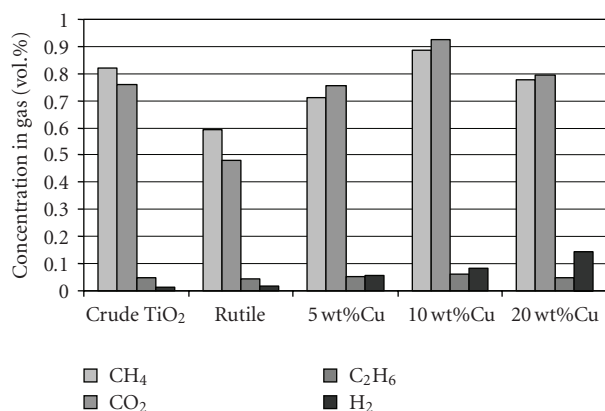


FIGURE 4: A comparison of the amount of products obtained after 5 hours of reaction conducted with different photocatalysts.

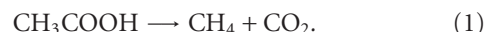
concentration of CH<sub>4</sub> in gaseous mixture was 0.88 vol.% (0.43 mmolCH<sub>4</sub>/molCH<sub>3</sub>COOH). On the basis of the results presented in Figure 3, the efficiency of the catalysts toward methane generation can be put in the following order: Cu-TiO<sub>2</sub> (10% Cu) > crude TiO<sub>2</sub> ≈ Cu-TiO<sub>2</sub> (20% Cu) > Cu-TiO<sub>2</sub> (5% Cu) > rutile. It should be noticed here that all the rutile catalysts containing CuO were more active than pure rutile. The amount of methane generated on Cu-rutile photocatalyst was higher than that obtained in case of pure rutile for ca. 16, 33 and 24%, for catalysts containing 5–20 wt% of Cu, respectively.

Taking into consideration the above results, the catalyst containing 10 wt% of Cu was further applied in a long term process. Irradiation was conducted for 28 hours. It was found that the amount of methane generated was continuously increasing with increasing time of irradiation. After 5 hours of the process the concentration of methane in gas amounted to 0.88 vol.%, whereas after 28 hours the amount of methane increased up to 3.66 vol.%.

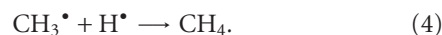
Another gaseous products which were identified in the reaction mixture were carbon dioxide and ethane. Figure 4

shows a comparison of the amount of these compounds generated after 5 hours of irradiation. From the obtained data it was found that the main products of acetic acid decomposition were methane and carbon dioxide. The lowest concentrations of CH<sub>4</sub> and CO<sub>2</sub> in the gaseous mixture were obtained in case of pure rutile, whereas the highest—in case of rutile containing 10 wt% of Cu. The ratio of CH<sub>4</sub>/CO<sub>2</sub> formation was found to be in the range of 0.94–0.98 in case of CuO-modified TiO<sub>2</sub>, ca. 1.1 in case of crude TiO<sub>2</sub> and about 1.2 for rutile. These data clearly show that for pure TiO<sub>2</sub> the amount of methane was higher than the amount of CO<sub>2</sub>. On the contrary in case of the CuO-rutile catalysts the concentration of CO<sub>2</sub> was higher than concentration of CH<sub>4</sub>. In Figure 4 it can be also observed that the amount of ethane was significantly lower than the amount of methane and carbon dioxide, regardless of the catalyst used. The lowest concentration of ethane after 5 hours of irradiation was observed for rutile (0.043 vol.%) and the highest for CuO/rutile catalyst containing 10 wt% of Cu (0.062 vol.%). The ratio of CH<sub>4</sub>/C<sub>2</sub>H<sub>6</sub> was found to be about 14–16.

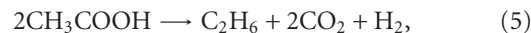
Taking into consideration that the main gaseous products identified were methane and carbon dioxide and that the CH<sub>4</sub>/CO<sub>2</sub> ratio was about 1, it might be concluded that the photodecomposition of acetic acid followed the so-called “photo-Kolbe” reaction pathway [15–17]:



Reaction (1) represents the photocatalytic decarboxylation of acetic acid under anaerobic conditions. The reaction is initiated by photogenerated holes and can be also written as follows [27]:



The reaction of the formation of ethane from acetic acid can be presented as follows [18]:



or, taking into consideration the recombination of methyl radicals [27]:



Reactions (5) and (6) in the discussed system are minor ones, what can be concluded on a basis of the obtained data (Figure 4) showing that the amount of ethane was significantly lower than that of methane.

From Figure 4 it can be also found that amongst the gaseous products of the reaction hydrogen was present. Changes of H<sub>2</sub> concentration in time of the experiment are presented in Figure 5. It can be observed that in case of crude TiO<sub>2</sub> and pure rutile the amount of hydrogen was significantly lower than of the Cu-modified photocatalysts. In case of the catalysts containing CuO the H<sub>2</sub> concentration

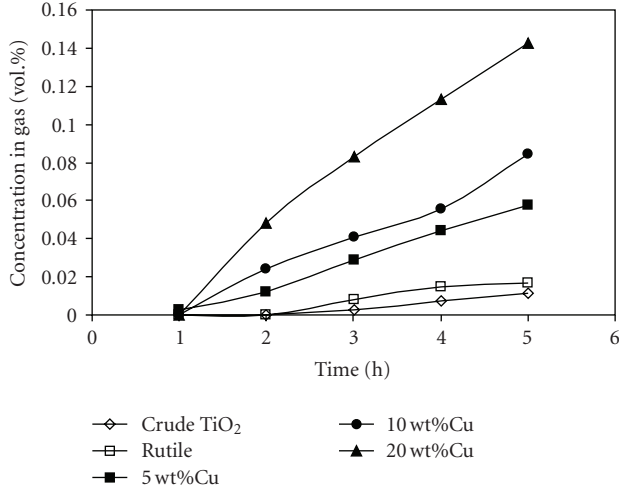
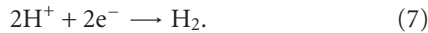


FIGURE 5: Photocatalytic generation of hydrogen on different photocatalysts.

was increasing with increasing Cu loading. After 5 hours of irradiation about 0.06–0.14 vol.% of H<sub>2</sub> was obtained for photocatalysts containing 5–20 wt% of Cu, respectively.

The photocatalytic evolution of hydrogen in the presence of sacrificial agents has been already described in the literature [18, 20–22, 26–34]. In general, when the reducing agent, or hole scavenger, such as alcohol [20, 23, 26–29], organic acid [18, 30, 31] or sulfide ion [32, 33], is present in the solution, the photogenerated holes react with the reducing agent. As a result the photocatalyst is enriched with electrons and H<sub>2</sub> evolution reaction is enhanced [34]:

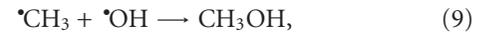
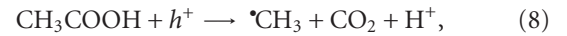


According to Kudo and Miseki [34] the hydrogen evolution in the presence of sacrificial agent does not mean the “water splitting”. Water splitting means to split water into H<sub>2</sub> and O<sub>2</sub> in a stoichiometric amount in the absence of sacrificial reagents [34].

The photocatalytic hydrogen evolution can be enhanced by modification of TiO<sub>2</sub>. Literature data [20–23] show that CuO/TiO<sub>2</sub> photocatalysts are very effective in H<sub>2</sub> generation. The TiO<sub>2</sub> acts as the primary catalyst and CuO acts as a cocatalyst, helping charge separation [20]. After absorption of a photon ( $h\nu$ ) with sufficient energy, that is, equal or higher than the band gap energy ( $E_g$ ) of TiO<sub>2</sub>, the electrons and holes are generated. The hole scavenger consumes holes in the valence band rapidly leaving electrons in the conduction band of TiO<sub>2</sub>. The conduction band (CB) of CuO is positioned below the CB of TiO<sub>2</sub> which allows transfer of electrons from the CB of TiO<sub>2</sub> to the CB of CuO. These results in a more negative CB potential of CuO and, as a result, enhanced hydrogen evolution. The yield of H<sub>2</sub> evolution greatly relies on the competition between the trapping of the excited electrons by cocatalyst active sites followed by reduction reaction and the electron-hole recombination [23]. As was mentioned earlier, the amount of hydrogen in case of the Cu-modified photocatalysts was significantly higher than in case of pure TiO<sub>2</sub>. This might

lead to a conclusion that the limited hydrogen evolution in case of crude TiO<sub>2</sub> and rutile resulted from rapid recombination of holes and electrons, since the separation of electron-hole pairs in case of pure TiO<sub>2</sub> is not as efficient as in the presence of CuO.

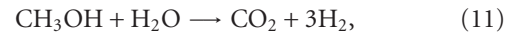
The source of hydrogen in case of the photocatalytic reactions conducted in the presence of sacrificial agents is still under debate. Bandara et al. [20] have argued that H<sub>2</sub> is produced from water. They have drawn such a conclusion on a basis of the experiment performed with application of absolute methanol. During this process no H<sub>2</sub> evolution was observed. On the other hand, Sakata et al. [18] proposed that H<sub>2</sub> formation is due to photocatalytic decomposition of acetic acid:



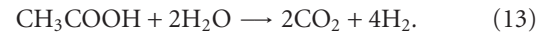
or



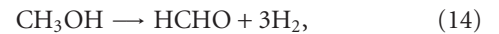
In the next step, CH<sub>3</sub>OH and HOCH<sub>2</sub>COOH are decomposed into carbon dioxide and hydrogen:



The overall reaction summarizing (8)–(12) can be written as follows:



The photocatalytic decomposition of methanol was also presented as follows [29]:



From the mechanism proposed by Sakata et al. [18] it can be found that H<sub>2</sub> is produced from methanol and glycolic acid, which are formed from acetic acid ((9) and (10)). These two reactions are possible when hydroxyl radicals are present in the solution. However, in the low pH region the amount of OH<sup>•</sup> radicals formed is not high due to low concentration of OH<sup>-</sup>. Therefore, the amount of methanol and glycolic acid which might be produced in the reactions (9) and (10) should be rather low. This leads to a conclusion that in the low pH region the reaction (13) is of minor importance [18]. In view of this, it is more probable that the hydrogen ions come mainly from decomposition of acetic acid presented by (8), rather than from decomposition of methanol or glycolic acid (reactions (11) and (12)). Water could be also involved in H<sub>2</sub> generation through the reaction (7), however, according to Jang et al. [33] its effect should be insignificant due to the low concentration of protons in neutral water. Summing up, the photocatalytic evolution of H<sub>2</sub> in the

presence of acetic acid as a sacrificial agent was probably mainly due to reduction of protons ( $H^+$ ) generated during decomposition of  $CH_3COOH$  (8). Moreover, it can be also supposed that some amount of hydrogen was generated from by-products of acetic acid decomposition, such as methanol and glycolic acid, as well as from water molecules. However, the  $H_2$  evolution during the latter two processes compared to the overall hydrogen evolution is supposed to be of minor importance.

An evidence for the supposition that the source of hydrogen is acetic acid, not water, might be also the ratio of methane to carbon dioxide concentrations (Figure 4). As was mentioned earlier, in case of crude  $TiO_2$  and rutile the amount of methane was higher than the amount of  $CO_2$ , whereas for  $CuO-TiO_2$  catalysts the concentration of  $CH_4$  was lower than  $CO_2$ . This might suggest that in case of these two types of photocatalysts some other reactions, despite of those described by (1)–(6) took place. One explanation might be generation of hydrogen from acetic acid. Assuming that both, methane and at least part of the hydrogen were produced from acetic acid, the amounts of these compounds should depend on the efficiency of the reactions of their formation. Thus, the higher amount of  $H_2$ , the lower amount of  $CH_4$  should be generated, since  $H^+$  would take part in reaction (7) instead of (1)–(4). In case of pure  $TiO_2$  the amount of  $H_2$  was very low and therefore the  $CH_4/CO_2$  ratio was above 1. For the  $CuO-TiO_2$  catalysts higher amount of hydrogen was generated, what might be supposed to be a reason of a decrease of  $CH_4$  concentration. Moreover, the effect of  $C_2H_6$  and possibly higher hydrocarbons formation on methane concentration in the reaction mixture should be also taken into consideration. However, taking into account that the amount of  $C_2H_6$  was comparable for all the catalysts used (0.02–0.03 mmol $C_2H_6$ /mol $CH_3COOH$  after 5 hours of irradiation) the effect of ethane generation on  $CH_4/CO_2$  ratio seems to be of lower importance. Besides, it might be also supposed that a certain amount of carbon dioxide was reduced to  $CH_4$ , what might be concluded from the fact that the concentration of  $CO_2$  in case of crude  $TiO_2$  and rutile was lower than that of methane. Literature data [3, 8, 9, 35] show that the reduction of carbon dioxide in the presence of various types of modified  $TiO_2$  is possible. However, in order to state unequivocally what affects the  $CH_4/CO_2$  ratio in the presence of pure  $TiO_2$  and  $CuO/TiO_2$  catalysts, further investigations are necessary.

Summing up, from the presented data (Figures 3 and 4) it can be clearly seen that the most active photocatalyst towards hydrocarbons (i.e., methane and ethane) generation was  $Cu-TiO_2$  containing 10 wt% Cu. Since the crystallite size of rutile in all of the  $Cu$ -modified photocatalysts as well as in pure rutile could be assumed to be comparable, it might be supposed that the highest photoactivity of  $Cu-TiO_2$  (10% Cu) was associated with the amount of  $CuO$  present in this sample. The photocatalytic activity of rutile-type samples increased as follows: pure rutile <  $Cu-TiO_2$  (5% Cu) <  $Cu-TiO_2$  (10% Cu), what suggests that 5 wt% of Cu was below the optimum value. Taking into consideration that in case of the  $Cu-TiO_2$  containing 20 wt% Cu the yield of  $CH_4$  formation decreased, one might draw a conclusion

that this sample was overloaded with  $CuO$ . This overloading might have led to a “shading effect” of  $CuO$  [3], which means that particles of copper oxide covered most of active sites of titania. As a result, the  $TiO_2$  surface accessible to acetic acid molecules decreased and the yield of the “photo-Kolbe” reaction also decreased. However, the efficiency of photocatalysts toward hydrogen evolution (Figures 4 and 5) was as follows:  $Cu-TiO_2$  (20% Cu) >  $Cu-TiO_2$  (10% Cu) >  $Cu-TiO_2$  (5% Cu) > rutile  $\approx$  crude  $TiO_2$ . These results show that the catalyst which was the most effective in methane production (i.e., containing 10 wt% Cu) was the second one in case of hydrogen generation. Therefore, the explanation about “shading effect” of  $CuO$  in case of the catalyst containing 20 wt% Cu seems to be unsatisfactory. In view of these, more probable explanation is that at higher  $CuO$  content, higher amount of acetic acid molecules took place in the reaction of  $H_2$  formation rather than  $CH_4$  generation. Therefore, since the amount of substrate, that is,  $CH_3COOH$ , was always the same, the increased production of hydrogen should lead to a decreased production of methane, what was observed in the discussed experiments.

#### 4. Conclusions

It was found that it is possible to generate useful hydrocarbons, such as  $CH_4$  and  $C_2H_6$ , from acetic acid in the presence of  $Cu$ -modified rutile under UV irradiation. The efficiency of the catalysts toward methane generation changed in the following order:  $Cu-TiO_2$  (10% Cu) > crude  $TiO_2 \approx Cu-TiO_2$  (20% Cu) >  $Cu-TiO_2$  (5% Cu) > rutile. The amount of  $CH_4$  produced in the presence of the catalyst containing 10 wt% of Cu was higher for ca. 7% than in case of crude anatase-phase  $TiO_2$  and for ca. 33% than in case of pure rutile. The concentration of ethane was 14–16 times lower than the amount of methane. The lowest concentration of  $C_2H_6$  after 5 hours of irradiation was observed for rutile (0.043 vol.%) and the highest for  $CuO$ /rutile catalyst containing 10 wt% of Cu (0.062 vol.%). The mechanism of methane generation from acetic acid followed the photo-Kolbe reaction pathway, what was concluded on a basis of  $CH_4/CO_2$  ratio, which was found to be  $\sim 1$ . Low concentrations of hydrogen were also detected in the gaseous mixtures. The amount of  $H_2$  was increasing with increasing  $Cu$  loading. After 5 hours of irradiation about 0.06–0.14 vol.% of  $H_2$  was obtained for photocatalysts containing 5–20 wt% of Cu, respectively. On the basis of the experimental data it is supposed that the source of hydrogen was acetic acid, not water.

Further investigations on the effectiveness of methane generation in the presence of  $CuO/TiO_2$  photocatalyst are in progress.

#### Acknowledgments

This work has been supported by the Polish Ministry of Science and Higher Education as a scientific project no. N523 413435 (2008–2011). The author wish to thank Professor A. W. Morawski, Head of the Institute of Chemical and Environment Engineering for precious advices and creative discussion during preparation of this article.

## References

- [1] G. Lastella, C. Testa, G. Cornacchia, M. Notornicola, F. Voltasio, and V. K. Sharma, "Anaerobic digestion of semi-solid organic waste: biogas production and its purification," *Energy Conversion and Management*, vol. 43, no. 1, pp. 63–75, 2002.
- [2] V. Augugliaro, M. Litter, L. Palmisano, and J. Soria, "The combination of heterogeneous photocatalysis with chemical and physical operations: a tool for improving the photoprocess performance scale for the treatment of biorecalcitrant pollutants," *Journal of Photochemistry and Photobiology C*, vol. 7, no. 4, pp. 127–144, 2006.
- [3] Slamet, H. W. Nasution, E. Purnama, S. Kosela, and J. Gunlazuardi, "Photocatalytic reduction of CO<sub>2</sub> on copper-doped Titania catalysts prepared by improved-impregnation method," *Catalysis Communications*, vol. 6, no. 5, pp. 313–319, 2005.
- [4] K. Kočí, L. Obalová, and Z. Lacný, "Photocatalytic reduction of CO<sub>2</sub> over TiO<sub>2</sub> based catalysts," *Chemical Papers*, vol. 62, no. 1, pp. 1–9, 2008.
- [5] S. S. Tan, L. Zou, and E. Hu, "Photosynthesis of hydrogen and methane as key components for clean energy system," *Science and Technology of Advanced Materials*, vol. 8, no. 1-2, pp. 89–92, 2007.
- [6] C.-C. Lo, C.-H. Hung, C.-S. Yuan, and J.-F. Wu, "Photoreduction of carbon dioxide with H<sub>2</sub> and H<sub>2</sub>O over TiO<sub>2</sub> and ZrO<sub>2</sub> in a circulated photocatalytic reactor," *Solar Energy Materials and Solar Cells*, vol. 91, no. 19, pp. 1765–1774, 2007.
- [7] Y. Shiraishi and T. Hirai, "Selective organic transformations on titanium oxide-based photocatalysts," *Journal of Photochemistry and Photobiology C*, vol. 9, no. 4, pp. 157–170, 2008.
- [8] I.-H. Tseng, J. C. S. Wu, and H.-Y. Chou, "Effects of sol-gel procedures on the photocatalysis of Cu/TiO<sub>2</sub> in CO<sub>2</sub> photoreduction," *Journal of Catalysis*, vol. 221, no. 2, pp. 432–440, 2004.
- [9] I.-H. Tseng, W.-C. Chang, and J. C. S. Wu, "Photoreduction of CO<sub>2</sub> using sol-gel derived titania and titania-supported copper catalysts," *Applied Catalysis B*, vol. 37, no. 1, pp. 37–48, 2002.
- [10] G. Guan, T. Kida, and A. Yoshida, "Reduction of carbon dioxide with water under concentrated sunlight using photocatalyst combined with Fe-based catalyst," *Applied Catalysis B*, vol. 41, no. 4, pp. 387–396, 2003.
- [11] N. Sasirekha, S. J. S. Basha, and K. Shanthi, "Photocatalytic performance of Ru doped anatase mounted on silica for reduction of carbon dioxide," *Applied Catalysis B*, vol. 62, no. 1-2, pp. 169–180, 2006.
- [12] S. S. Tan, L. Zou, and E. Hu, "Photocatalytic reduction of carbon dioxide into gaseous hydrocarbon using TiO<sub>2</sub> pellets," *Catalysis Today*, vol. 115, no. 1–4, pp. 269–273, 2006.
- [13] H. Yamashita, Y. Fujii, Y. Ichihashi, et al., "Selective formation of CH<sub>3</sub>OH in the photocatalytic reduction of CO<sub>2</sub> with H<sub>2</sub>O on titanium oxides highly dispersed within zeolites and mesoporous molecular sieves," *Catalysis Today*, vol. 45, no. 1–4, pp. 221–227, 1998.
- [14] O. Ozcan, F. Yukruk, E. U. Akkaya, and D. Uner, "Dye sensitized artificial photosynthesis in the gas phase over thin and thick TiO<sub>2</sub> films under UV and visible light irradiation," *Applied Catalysis B*, vol. 71, no. 3-4, pp. 291–297, 2007.
- [15] B. Kraeutler and A. J. Bard, "Photoelectrosynthesis of ethane from acetate ion at an n-type TiO<sub>2</sub> electrode. The photo-Kolbe reaction," *Journal of the American Chemical Society*, vol. 99, no. 23, pp. 7729–7731, 1977.
- [16] B. Kraeutler and A. J. Bard, "Heterogenous photocatalytic synthesis of methane from acetic acid—new Kolbe reaction pathway," *Journal of the American Chemical Society*, vol. 100, no. 7, pp. 2239–2240, 1978.
- [17] B. Kraeutler, C. D. Jaeger, and A. J. Bard, "Direct observation of radical intermediates in the photo-Kolbe reaction—heterogenous photocatalytic radical formation by electron spin resonance," *Journal of the American Chemical Society*, vol. 100, no. 15, pp. 4903–4905, 1978.
- [18] T. Sakata, T. Kawai, and K. Hashimoto, "Heterogeneous photocatalytic reactions of organic acids and water. New reaction paths besides the photo-Kolbe reaction," *Journal of Physical Chemistry*, vol. 88, no. 11, pp. 2344–2350, 1984.
- [19] G. R. Dey and K. K. Pushpa, "Methane generated during photocatalytic redox reaction of alcohols on TiO<sub>2</sub> suspension in aqueous solutions," *Research on Chemical Intermediates*, vol. 32, no. 8, pp. 725–736, 2006.
- [20] J. Bandara, C. P. K. Udawatta, and C. S. K. Rajapakse, "Highly stable CuO incorporated TiO<sub>2</sub> catalyst for photocatalytic hydrogen production from H<sub>2</sub>O," *Photochemical and Photobiological Sciences*, vol. 4, no. 11, pp. 857–861, 2005.
- [21] Z. Jin, X. Zhang, Y. Li, S. Li, and G. Lu, "5.1% apparent quantum efficiency for stable hydrogen generation over eosin-sensitized CuO/TiO<sub>2</sub> photocatalyst under visible light irradiation," *Catalysis Communications*, vol. 8, no. 8, pp. 1267–1273, 2007.
- [22] H.-J. Choi and M. Kang, "Hydrogen production from methanol/water photodecomposition over the Cu loaded TiO<sub>2</sub>," *Applied Chemistry*, vol. 10, no. 2, pp. 453–456, 2006.
- [23] T. Sreethawong and S. Yoshikawa, "Comparative investigation on photocatalytic hydrogen evolution over Cu-, Pd-, and Au-loaded mesoporous TiO<sub>2</sub> photocatalysts," *Catalysis Communications*, vol. 6, no. 10, pp. 661–668, 2005.
- [24] S. Mozia, "Effect of calcination temperature on photocatalytic activity of TiO<sub>2</sub>. Photodecomposition of mono- and polyazo dyes in water," *Polish Journal of Chemical Technology*, vol. 10, no. 3, pp. 42–49, 2008.
- [25] M. S. P. Francisco and V. R. Mastelaro, "Inhibition of the anatase-rutile phase transformation with addition of CeO<sub>2</sub> to CuO-TiO<sub>2</sub> system: Raman spectroscopy, X-ray diffraction, and textural studies," *Chemistry of Materials*, vol. 14, no. 6, pp. 2514–2518, 2002.
- [26] N. Todorova, T. Giannakopoulou, G. Romanos, T. Vaimakis, J. Yu, and C. Trapalis, "Preparation of fluorine-doped TiO<sub>2</sub> photocatalysts with controlled crystalline structure," *International Journal of Photoenergy*, vol. 2008, Article ID 534038, 9 pages, 2008.
- [27] M. Subrahmanyam, S. Kaneco, and N. Alonso-Vante, "A screening for the photo reduction of carbon dioxide supported on metal oxide catalysts for C<sub>1</sub>–C<sub>3</sub> selectivity," *Applied Catalysis B*, vol. 23, no. 2-3, pp. 169–174, 1999.
- [28] M.-K. Jeon, J.-W. Park, and M. Kang, "Hydrogen production from methanol/water decomposition in a liquid photosystem using the anatase and rutile forms of Cu-TiO<sub>2</sub>," *Journal of Industrial and Engineering Chemistry*, vol. 13, no. 1, pp. 84–91, 2007.
- [29] T. Kawai and T. Sakata, "Photocatalytic hydrogen production from liquid methanol and water," *Journal of the Chemical Society, Chemical Communications*, no. 15, pp. 694–695, 1980.
- [30] B. Zielińska, J. Sreńscek-Nazzal, and R. J. Kaleńczuk, "Photocatalytic hydrogen generation over alkali niobates in the presence of organic compounds," *Polish Journal of Chemical Technology*, vol. 10, no. 4, pp. 1–3, 2008.

- [31] B. Zielińska, E. Borowiak-Paleń, and R. J. Kaleńczuk, "Photocatalytic hydrogen generation over alkaline-earth titanates in the presence of electron donors," *International Journal of Hydrogen Energy*, vol. 33, no. 7, pp. 1797–1802, 2008.
- [32] K. G. Kanade, B. B. Kale, J.-O. Baeg, et al., "Self-assembled aligned Cdoped ZnO nanoparticles for photocatalytic hydrogen production under visible light irradiation," *Materials Chemistry and Physics*, vol. 102, no. 1, pp. 98–104, 2007.
- [33] J. S. Jang, H. G. Kim, P. H. Borse, and J. S. Lee, "Simultaneous hydrogen production and decomposition of H<sub>2</sub>S dissolved in alkaline water over CdS.TiO<sub>2</sub> composite photocatalysts under visible light irradiation," *International Journal of Hydrogen Energy*, vol. 32, no. 18, pp. 4786–4791, 2007.
- [34] A. Kudo and Y. Miseki, "Heterogeneous photocatalyst materials for water splitting," *Chemical Society Reviews*, vol. 38, no. 1, pp. 253–278, 2009.
- [35] M. Anpo, H. Yamashita, Y. Ichihashi, and S. Ehara, "Photocatalytic reduction of CO<sub>2</sub> with H<sub>2</sub>O on various titanium oxide catalysts," *Journal of Electroanalytical Chemistry*, vol. 396, no. 1-2, pp. 21–26, 1995.

## Research Article

# Influence of MWCNTs Doping on the Structure and Properties of PEDOT:PSS Films

Jiao Li,<sup>1,2</sup> Juncheng Liu,<sup>2</sup> Congjie Gao,<sup>1</sup> Jinling Zhang,<sup>2</sup> and Hanbin Sun<sup>2</sup>

<sup>1</sup> College of Chemistry and Chemical Engineering, Ocean University of China, Qingdao 266003, China

<sup>2</sup> School of Materials Science and Engineering, Shandong University of Technology, Zibo 255049, China

Correspondence should be addressed to Congjie Gao, gaocjie@mail.hz.zj.cn

Received 26 March 2009; Revised 6 August 2009; Accepted 7 September 2009

Recommended by Mohamed Sabry Abdel-Mottaleb

Poly(3,4-ethylenedioxythiophene):poly(4-styrenesulfonate) (PEDOT:PSS) doped with multi-walled carbon nanotubes (MWCNTs) films is fabricated on quartz substrates by spin coating method. The effects of MWCNTs on the structure and properties of PEDOT:PSS film have been investigated. X-ray diffractometer (XRD) and Fourier transform Raman spectroscopy (FTRM) show that the crystallization behavior and the main chain of PEDOT:PSS are not changed. Atomic force microscopy (AFM) shows that individual nanotubes are well dispersed in the PEDOT:PSS matrix. Moreover, some nanotubes overlap into a net-like structure, forming new conductive channels, which can enhance efficiently the film conductivity. The conductivity of PEDOT:PSS film doped with a lower percentage of MWCNTs (0.2 wt%) is 9.16 S/cm, higher than that of pure PEDOT:PSS film (0.28 S/cm), although the optical transmission of PEDOT:PSS decreases a little after the addition of MWCNTs. The interaction between MWCNTs and PEDOT:PSS during melt mixing is also given a possible explanation.

Copyright © 2009 Jiao Li et al. This is an open access article distributed under the Creative Commons Attribution License, which permits unrestricted use, distribution, and reproduction in any medium, provided the original work is properly cited.

## 1. Introduction

In the recent years, films fabricated from commercially available poly(3,4-ethylenedioxythiophene):poly(4-styrenesulfonate) (PEDOT:PSS) aqueous dispersions have attracted a lot of attention mainly due to their exceptional advantages of high transparency in the visible range, excellent thermal stability, and aqueous solution processibility [1, 2]. With all these properties, PEDOT:PSS is now widely used in optoelectronic devices. For example, it can be used as a hole transporter layer in organic light-emitting diodes (OLED) [3–5], or as a buffer layer between the ITO and active layers in organic solar cells (OSC) [6–8]. However, the film also suffers low conductivity with about 0.05 ~ 0.8 S/cm [9, 10], which directly affects the performance of the device [11, 12]. Therefore, the improvement of the film conductivity has been considered to be an urgent work.

Recently, several strategies have been applied to increase the conductivity of PEDOT:PSS [10, 13–15]. Kim et al. [10] reported that the enhancement of the PEDOT:PSS conductivity could be achieved by adding organic solvent

dimethyl sulfoxide or N,N-dimethylformamide. Ouyang et al. [13, 14] reported that the addition of ethylene glycol to the aqueous PEDOT:PSS dispersion could induce the change of conductivity, and they proposed that the conductivity enhancement results from the conversion of the PEDOT molecular conformation from “ben structure” to “quoid structure”.

Nanotubes can serve as a good filler for conducting polymer. It has been reported that incorporating of nanotubes into conventional conducting polymers improves the conductivity of nanotubes/polymer composites by many orders of magnitude [15–20], which could be attributed to nanotubes' large contact area, high dimensional aspect ratio, and exceptional electrical conductivity [21].

In this work, the PEDOT:PSS doped with multiwalled carbon nanotubes (MWCNTs) transparent conducting film was fabricated on quartz substrates by spin coating method. The pristine and doped PEDOT:PSS films were characterized by XRD, FTRM, AFM, UV-Vis spectroscopy, and four-point measurement. The effects of MWCNTs on the structure and properties of the PEDOT:PSS film were also investigated.

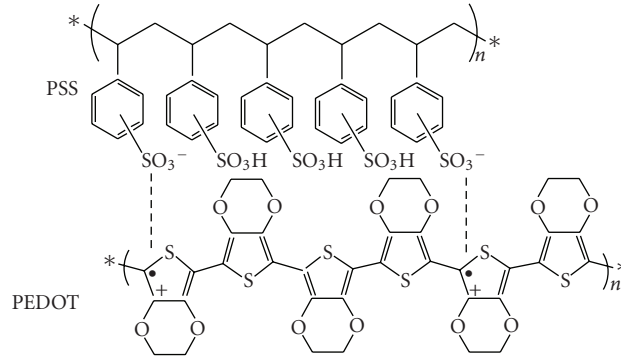


FIGURE 1: Chemical structure of PEDOT:PSS. The “dot” and “plus” represent the unpaired electron and positive charge on the PEDOT chain, respectively.

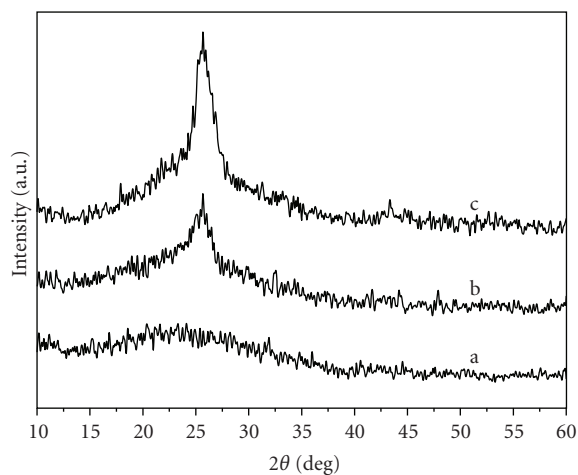


FIGURE 2: XRD patterns of (a) pure PEDOT:PSS, (b) M-PEDOT:PSS (0.1 wt%), and (c) MWCNTs films.

## 2. Experimental

Multiwalled carbon nanotubes (diameter: 10 ~ 30 nm, length: 5 ~ 15  $\mu\text{m}$ , purity: >95%) were purchased from Beijing Nachen Nanotech Co., Ltd and were further acid-treated by the previously established methods [22, 23]. The MWCNTs after acid-treatment can be dispersed into aqueous PEDOT:PSS solution and no precipitation is observed in the solution after several weeks. PEDOT:PSS aqueous solution (1.3 wt% dispersed in  $\text{H}_2\text{O}$ ) was from Aldrich. Other reagents and solvents were of analytical grade.

The chemical structure of PEDOT:PSS is shown in Figure 1. In the PEDOT:PSS dispersion, PEDOT is the charge transporting species [9, 10]. PSS acts as a charge-compensating counterion to stabilize the p-doped conducting polymer, and forms a processable water-borne dispersion of negatively charged swollen colloidal particles consisting of PEDOT and excess PSS [24, 25].

All the quartz substrates (20 mm  $\times$  20 mm) were ultrasonically cleaned with a series of organic solvents (ethanol, methanol, and acetone), then rinsed in ultrasonic bath with deionized water, and dried in a vacuum oven. Residual

organic contaminations were subsequently removed by exposing to a UV-ozone lamp for 30 min. Prior to spin coating, the precursor solution of PEDOT:PSS with appropriate mass of MWCNTs was prepared. Some amount of acid treated-MWCNTs were added to the PEDOT:PSS aqueous dispersion in ultrasonic bath for about 12 hours. The PEDOT:PSS and acid treated-MWCNTs-doped PEDOT:PSS films (PEDOT:PSS and M-PEDOT:PSS, separately) with a thickness of 95–100 nm, as determined with scanning electron microscopy, were fabricated on transparent quartz substrates by spin coating method. The spin coating procedure included 20 seconds of 2000 rpm followed by 30 seconds of 5000 rpm. Then these films were dried at 110° for 60 minutes in the vacuum oven before any further characterization.

The molecular structure analysis of all the samples was carried out with Fourier transform Raman spectroscopy, which was recorded with a RFS 100 Bruker spectrometer (excitation wavelength 1064 nm). Sample structures were analyzed with D8 Advance Bruker AXS X-ray diffractometer, with  $\text{Cu K}\alpha_1$  radiation. The dispersion of acid-treated MWCNTs in PEDOT:PSS matrix was investigated with atomic force microscopy, which was performed with Digital Instruments Nanoscope III operating in tapping mode. The optical properties were characterized with a TU-1901 Dual-beam UV-Visible spectrophotometer. The conductivity of the films was measured by the four-point probe technique with a Keithley 2400 Source Meter. All the measurements were performed at room temperature.

## 3. Results and Discussion

The XRD patterns of pure MWCNTs, PEDOT:PSS, and M-PEDOT:PSS films are shown in Figure 2. There are not any sharp peaks in the pristine PEDOT:PSS profile (Figure 2(a)), which indicates substantial amorphous nature of the PEDOT:PSS film. Similar results were also obtained by different research groups [26, 27]. The pure MWCNTs film shows a sharp peak centered on  $2\theta$  value of 25.6° corresponding to the (0 0 2) planes of MWCNTs (Figure 2(c)). The composite film (Figure 2(b)) shows the characteristic peaks of both MWCNTs and PEDOT:PSS without any additional

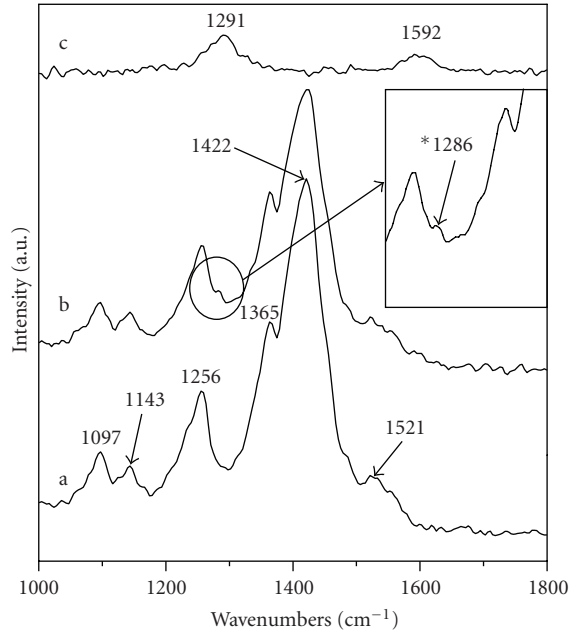


FIGURE 3: Raman spectra of (a) pure PEDOT:PSS, (b) M-PEDOT:PSS (0.1 wt%), and (c) MWCNTs films. \*The inset curve shows clearly the peak of  $1286\text{ cm}^{-1}$ .

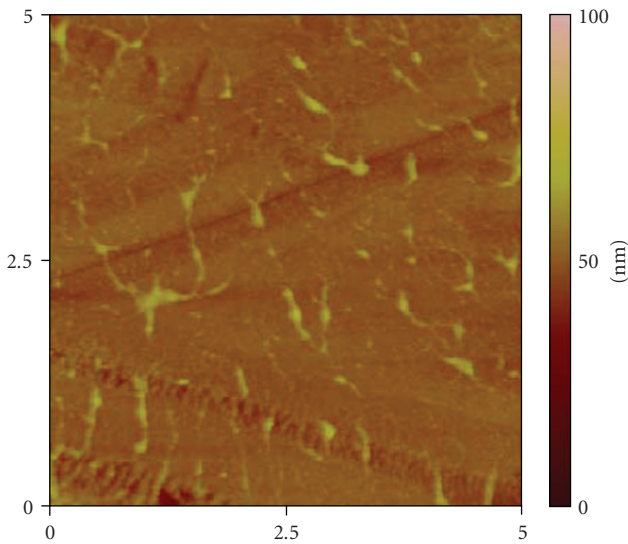


FIGURE 4: AFM image ( $5 \times 5\ \mu\text{m}$ ) of M-PEDOT:PSS (0.1 wt%) film.

bands, which represents the absence of covalent interactions between the phases. Moreover, the crystallization behavior of the PEDOT:PSS film is not changed.

The Raman spectrum of pure PEDOT:PSS film is identified in [28–30] (Figure 3(a)). Raman spectrum shows six dominant principal peaks of PEDOT. The peak at  $1521\text{ cm}^{-1}$  represents  $C_{\alpha}=C_{\beta}$  asymmetric vibrations;  $1421\text{ cm}^{-1}$  can be assigned to  $C_{\alpha}=C_{\beta}$  symmetric vibrations,  $1365\text{ cm}^{-1}$  to C–C stretching deformations,  $1256\text{ cm}^{-1}$  to C–C in-plane symmetric stretching, and  $1143\text{ cm}^{-1}$  and  $1097\text{ cm}^{-1}$  to C–C in-plane bending. As shown in Figure 3(c), there are

mainly two optically active phonon modes in the first-order Raman spectrum of MWCNTs film, and two peaks at  $1592\text{ cm}^{-1}$  and  $1291\text{ cm}^{-1}$  represent a graphite  $E_{2g}$  mode and an MWCNTs disordered  $A_{1g}$  mode, respectively. The disordered  $A_{1g}$  mode indicates the imperfection of the  $sp^2$  hybridization of MWCNTs, which may occur during the production process or the acid-treated process [31]. Raman spectrum of the M-PEDOT:PSS film is essentially the same as that of PEDOT:PSS film except one additional peak centered at  $1286\text{ cm}^{-1}$  (Figure 3(b)).

Chemical and physical interactions between some materials and MWCNTs often occur during melt mixing, and these interactions can affect the Raman spectrum of MWCNTs. These phenomena have been confirmed by both theoretical and experimental researches [32, 33]. Combining with the results of XRD, we speculate that there may be some noncovalent interactions, which might stem from the  $\pi$ - $\pi$  interaction between the delocalized  $\pi$  bond network of MWCNTs and the thiophene rings of PEDOT backbone. This conjugated interaction would affect the electronic density among MWCNTs. Therefore, the peak of MWCNTs at  $1291\text{ cm}^{-1}$ , which shifts red from  $1291\text{ cm}^{-1}$  to  $1286\text{ cm}^{-1}$ , may result from the change of electronic density of MWCNTs. While the peak of MWCNTs at  $1592\text{ cm}^{-1}$  is so weak that it cannot be observed (Figure 3(b)). However, the mechanism of the interactions between MWCNTs and PEDOT:PSS during melt mixing is still an assumption and needs to be further studied.

AFM image ( $5 \times 5\ \mu\text{m}$ ) in Figure 4 shows that individual nanotubes are well dispersed in the PEDOT:PSS matrix. Some nanotubes overlap into a net-like structure, which implies that some continuous channels are embedded in the PEDOT:PSS matrix.

When PEDOT:PSS is applied in OLED or OSC devices, it is always important to keep its transmittance high. Figure 5 shows the wavelength dependence of the optical transparency of PEDOT:PSS and M-PEDOT:PSS thin films on the wavelength range from 550 nm to 950 nm, which corresponds to the power density of ambient sunlight on the Earth's surface [34]. The PEDOT:PSS film gives a good optical transmittance in the above wavelength range (93.2% average) (Figure 5(a)). Moreover, The transmittance increases from 950 nm to 550 nm, which is mainly because of more absorptions in the infrared region for the PEDOT:PSS film [5, 35], as shown in Figure 5(b). Transmittance curve of M-PEDOT:PSS film is about 88.5% average, about 5% less than that of pure PEDOT:PSS film. This may result from the formation of the conductive network of MWCNTs and some absorptions of MWCNTs in the above wavelength range [24, 36].

As shown in Figure 6, the conductivity of pure PEDOT:PSS film is 0.28 S/cm. While the conductivity increases drastically when MWCNTs doping concentration increases from 0.04 wt% to 0.12 wt%, and then increases moderately at loading levels in excess of 0.12 wt%. When MWCNTs content reaches about 0.2 wt%, the conductivity of composite film is 9.16 S/cm. These indicate that the percolation threshold of the nanocomposite films resides between 0.04 wt% and 0.12 wt%, where some conductive

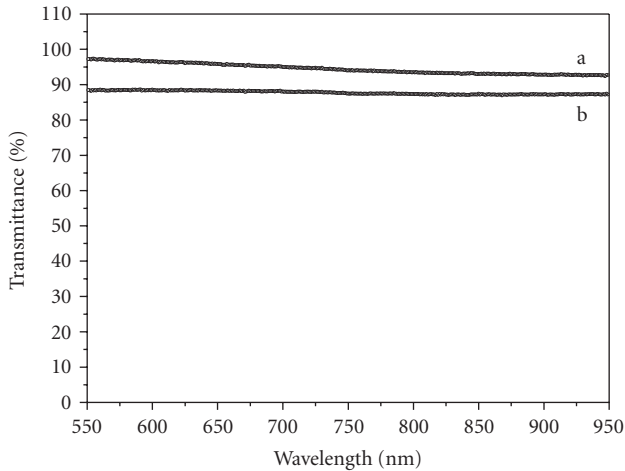


FIGURE 5: Transmittance of (a) pure PEDOT:PSS and (b) M-PEDOT:PSS (0.1 wt%) films.

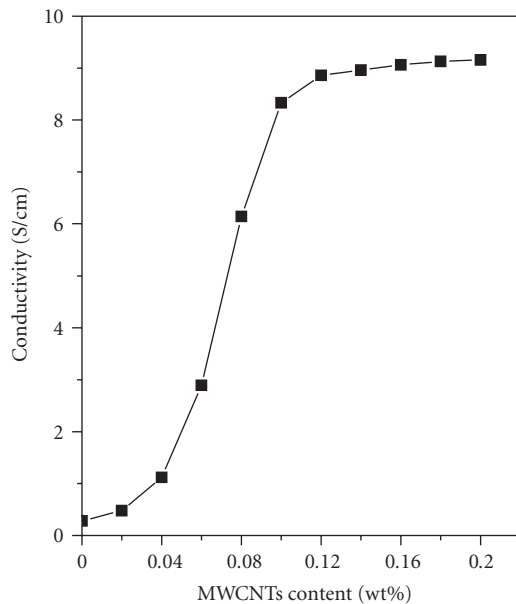


FIGURE 6: The electrical conductivity of composite films as a function of weight fraction of MWCNTs.

MWCNT channels in the PEDOT:PSS matrix might form, as shown in AFM (Figure 4), which can help charge transport and enhance the conductivity of films [37, 38].

#### 4. Conclusion

In summary, influences of MWCNTs doping on the structure and properties of PEDOT:PSS films have been investigated. XRD and FTRM show that the crystallization behavior and the main chain of PEDOT:PSS are not changed. AFM shows that individual nanotubes are well dispersed in the PEDOT:PSS matrix. Moreover, some nanotubes overlap into a net-like structure, forming new conductive channels, which can enhance efficiently the film conductivity.

The conductivity of PEDOT:PSS film doped with a lower percentage of MWCNTs (0.2 wt%) is 9.16 S/cm, higher than that of pure PEDOT:PSS film (0.28 S/cm), although the optical transmission of PEDOT:PSS decreases a little after the addition of MWCNTs. The interaction between MWCNTs and PEDOT:PSS during melt mixing is also given a possible explanation. However, this explanation is still an assumption and needs to be further studied.

#### Acknowledgment

Financial support from the program for New Century Excellent Talents in University (NCET, Grant no. NCET-04-0648) is gratefully acknowledged.

#### References

- [1] G. Heywang and F. Jonas, "Poly(alkylenedioxythiophene)-new, very stable conducting polymers," *Advanced Materials*, vol. 4, no. 2, pp. 116–118, 1992.
- [2] L. Groenendaal, F. Jonas, D. Freitag, H. Pielartzik, and J. R. Reynolds, "Poly(3,4-ethylenedioxythiophene) and its derivatives: past, present, and future," *Advanced Materials*, vol. 12, no. 7, pp. 481–494, 2000.
- [3] Y.-F. Zhou, Y.-B. Yuan, L.-F. Cao, et al., "Improved stability of OLEDs with mild oxygen plasma treated PEDOT:PSS," *Journal of Luminescence*, vol. 122-123, pp. 602–604, 2007.
- [4] T.-C. Tsai, W.-Y. Hung, L.-C. Chi, K.-T. Wong, C.-C. Hsieh, and P.-T. Chou, "A new ambipolar blue emitter for NTSC standard blue organic light-emitting device," *Organic Electronics*, vol. 10, no. 1, pp. 158–162, 2009.
- [5] P. Vacca, M. Petrosino, R. Miscioscia, et al., "Poly(3,4-ethylenedioxythiophene):poly(4-styrenesulfonate)ratio: structural, physical and hole injection properties in organic light emitting diodes," *Thin Solid Films*, vol. 516, no. 12, pp. 4232–4237, 2008.
- [6] C.-J. Ko, Y.-K. Lin, F.-C. Chen, and C.-W. Chu, "Modified buffer layers for polymer photovoltaic devices," *Applied Physics Letters*, vol. 90, no. 6, Article ID 063509, 3 pages, 2007.
- [7] J. Bouclé, S. Chyla, M. S. P. Shaffer, J. R. Durrant, D. D. C. Bradley, and J. Nelson, "Hybrid solar cells from a blend of poly(3-hexylthiophene) and ligand-capped TiO<sub>2</sub> nanorods," *Advanced Functional Materials*, vol. 18, no. 4, pp. 622–633, 2008.
- [8] K. X. Steirer, M. O. Reese, B. L. Rupert, et al., "Ultrasonic spray deposition for production of organic solar cells," *Solar Energy Materials & Solar Cells*, vol. 93, no. 4, pp. 447–453, 2009.
- [9] S. K. M. Jönsson, J. Birgersson, X. Crispin, et al., "The effects of solvents on the morphology and sheet resistance in poly(3,4-ethylenedioxythiophene)-polystyrenesulfonic acid (PEDOT-PSS) films," *Synthetic Metals*, vol. 139, no. 1, pp. 1–10, 2003.
- [10] J. Y. Kim, J. H. Jung, D. E. Lee, and J. Joo, "Enhancement of electrical conductivity of poly(3,4-ethylenedioxythiophene)/poly(4-styrenesulfonate) by a change of solvents," *Synthetic Metals*, vol. 126, no. 2-3, pp. 311–316, 2002.
- [11] C. C. Oey, A. B. Djurišić, C. Y. Kwong, et al., "Nanocomposite hole injection layer for organic device applications," *Thin Solid Films*, vol. 492, no. 1-2, pp. 253–258, 2005.
- [12] J. Huang, P. F. Miller, J. S. Wilson, A. J. de Mello, J. C. de Mello, and D. D. C. Bradley, "Investigation of the effects of doping and post-deposition treatments on the conductivity,

- morphology, and work function of poly(3,4-ethylenedioxythiophene)/poly(styrene sulfonate) films,” *Advanced Functional Materials*, vol. 15, no. 2, pp. 290–296, 2005.
- [13] J. Ouyang, Q. Xu, C.-W. Chu, Y. Yang, G. Li, and J. Shinar, “On the mechanism of conductivity enhancement in poly(3,4-ethylenedioxythiophene):poly(styrene sulfonate) film through solvent treatment,” *Polymer*, vol. 45, no. 25, pp. 8443–8450, 2004.
- [14] J. Ouyang, C.-W. Chu, F.-C. Chen, Q. Xu, and Y. Yang, “Polymer optoelectronic devices with high-conductivity poly(3,4-ethylenedioxythiophene) anodes,” *Journal of Macromolecular Science Part A*, vol. 41, no. 12, pp. 1497–1511, 2004.
- [15] H. Peng and X. Sun, “Highly aligned carbon nanotube/polymer composites with much improved electrical conductivities,” *Chemical Physics Letters*, vol. 471, no. 1–3, pp. 103–105, 2009.
- [16] Z. Yang, H. Pu, J. Yuan, D. Wan, and Y. Liu, “Phthalocyanines-MWCNT hybrid materials: fabrication, aggregation and photoconductivity properties improvement,” *Chemical Physics Letters*, vol. 465, no. 1–3, pp. 73–77, 2008.
- [17] M.-C. Wu, Y.-Y. Lin, S. Chen, et al., “Enhancing light absorption and carrier transport of P3HT by doping multi-wall carbon nanotubes,” *Chemical Physics Letters*, vol. 468, no. 1–3, pp. 64–68, 2009.
- [18] K. R. Reddy, B. C. Sin, K. S. Ryu, J.-C. Kim, H. Chung, and Y. Lee, “Conducting polymer functionalized multi-walled carbon nanotubes with noble metal nanoparticles: synthesis, morphological characteristics and electrical properties,” *Synthetic Metals*, vol. 159, no. 7–8, pp. 595–603, 2009.
- [19] T.-M. Wu, H.-L. Chang, and Y.-W. Lin, “Synthesis and characterization of conductive polypyrrole/multi-walled carbon nanotubes composites with improved solubility and conductivity,” *Composites Science and Technology*, vol. 69, no. 5, pp. 639–644, 2009.
- [20] Y. Ma, S. R. Ali, A. S. Doodoo, and H. He, “Enhanced sensitivity for biosensors: multiple functions of DNA-wrapped single-walled carbon nanotubes in self-doped polyaniline nanocomposites,” *Journal of Physical Chemistry B*, vol. 110, no. 33, pp. 16359–16365, 2006.
- [21] R. H. Baughman, A. A. Zakhidov, and W. A. de Heer, “Carbon nanotubes: the route toward applications,” *Science*, vol. 297, no. 5582, pp. 787–792, 2002.
- [22] G.-F. Wang, X.-M. Tao, and R.-X. Wang, “Fabrication and characterization of OLEDs using PEDOT:PSS and MWCNT nanocomposites,” *Composites Science and Technology*, vol. 68, no. 14, pp. 2837–2841, 2008.
- [23] R. A. Hatton, N. P. Blanchard, L. W. Tan, G. Latini, F. Cacialli, and S. R. P. Silva, “Oxidised carbon nanotubes as solution processable, high work function hole-extraction layers for organic solar cells,” *Organic Electronics*, vol. 10, no. 3, pp. 388–395, 2009.
- [24] S. Ghosh and O. Inganäs, “Self-assembly of a conducting polymer nanostructure by physical crosslinking: applications to conducting blends and modified electrodes,” *Synthetic Metals*, vol. 101, no. 1–3, pp. 413–416, 1999.
- [25] F. Jonas and G. Heywang, “Technical applications for conductive polymers,” *Electrochimica Acta*, vol. 39, no. 8–9, pp. 1345–1347, 1994.
- [26] L. Zhan, Z. Song, J. Zhang, et al., “PEDOT: cathode active material with high specific capacity in novel electrolyte system,” *Electrochimica Acta*, vol. 53, no. 28, pp. 8319–8323, 2008.
- [27] C. Zhou, S. Wang, Q. Zhuang, and Z. Han, “Enhanced conductivity in polybenzoxazoles doped with carboxylated multi-walled carbon nanotubes,” *Carbon*, vol. 46, no. 9, pp. 1232–1240, 2008.
- [28] M. Łapkowski and A. Proń, “Electrochemical oxidation of poly(3,4-ethylenedioxythiophene)—“in situ” conductivity and spectroscopic investigations,” *Synthetic Metals*, vol. 110, no. 1, pp. 79–83, 2000.
- [29] B.-H. Wang, Y.-H. Deng, J. Ge, X. Zhou, X.-G. Wang, and B.-Z. Yang, “Chemical synthesis of poly(3,4-ethylenedioxythiophene) in three different solvents,” *Journal of Functional Materials*, vol. 36, no. 10, pp. 1610–1612, 2005 (Chinese).
- [30] S. Garreau, G. Louarn, J. P. Buisson, G. Froyer, and S. Lefrant, “In situ spectroelectrochemical Raman studies of poly(3,4-ethylenedioxythiophene) (PEDT),” *Macromolecules*, vol. 32, no. 20, pp. 6807–6812, 1999.
- [31] W. Jarernboon, S. Pimanpang, S. Maensiri, E. Swatsitang, and V. Amornkitbamrung, “Effects of multiwall carbon nanotubes in reducing microcrack formation on electrophoretically deposited TiO<sub>2</sub> film,” *Journal of Alloys and Compounds*, vol. 476, no. 1–2, pp. 840–846, 2009.
- [32] G. Q. Tang, H. M. Wang, S. S. Jin, et al., “Interaction between multi-walled carbon nanotubes and bromine and conducting mechanism,” *Acta Chimica Sinica*, vol. 66, no. 6, pp. 675–679, 2008.
- [33] H.-X. Wu, R. Tong, X.-Q. Qiu, et al., “Functionalization of multiwalled carbon nanotubes with polystyrene under atom transfer radical polymerization conditions,” *Carbon*, vol. 45, no. 1, pp. 152–159, 2007.
- [34] B. R. Saunders and M. L. Turner, “Nanoparticle-polymer photovoltaic cells,” *Advances in Colloid and Interface Science*, vol. 138, no. 1, pp. 1–23, 2008.
- [35] L. A. A. Pettersson, S. Ghosh, and O. Inganäs, “Optical anisotropy in thin films of poly(3,4-ethylenedioxythiophene)-poly(4-styrenesulfonate),” *Organic Electronics*, vol. 3, no. 3–4, pp. 143–148, 2002.
- [36] J. K. W. Sandler, J. E. Kirk, I. A. Kinloch, M. S. P. Shaffer, and A. H. Windle, “Ultra-low electrical percolation threshold in carbon-nanotube-epoxy composites,” *Polymer*, vol. 44, no. 19, pp. 5893–5899, 2003.
- [37] S. Kumar, T. D. Dang, F. E. Arnold, et al., “Synthesis, structure, and properties of PBO/SWNT composites,” *Macromolecules*, vol. 35, no. 24, pp. 9039–9043, 2002.
- [38] J. Zhang, M. Mine, D. Zhu, and M. Matsuo, “Electrical and dielectric behaviors and their origins in the three-dimensional polyvinyl alcohol/MWCNT composites with low percolation threshold,” *Carbon*, vol. 47, no. 5, pp. 1311–1320, 2009.

## Review Article

# Manipulation of Energy Transfer Processes in Nanochannels

André Devaux<sup>1</sup> and Gion Calzaferri<sup>2</sup>

<sup>1</sup>Physikalisches Institut, Westfälische Wilhelms-Universität, 48149 Münster, Germany

<sup>2</sup>Department of Chemistry and Biochemistry, University of Bern, 3012 Bern, Switzerland

Correspondence should be addressed to André Devaux, andre.devaux@gmx.ch

Received 26 March 2009; Accepted 27 December 2009

Recommended by Mohamed Sabry Abdel-Mottaleb

The realisation of molecular assemblies featuring specific macroscopic properties is a prime example for the versatility of supramolecular organisation. Microporous materials such as zeolite L are well suited for the preparation of host-guest composites containing dyes, complexes, or clusters. This short tutorial focuses on the possibilities offered by zeolite L to study and influence Förster resonance energy transfer inside of its nanochannels. The highly organised host-guest materials can in turn be structured on a larger scale to form macroscopic patterns, making it possible to create large-scale structures from small, highly organised building blocks for novel optical applications.

Copyright © 2009 A. Devaux and G. Calzaferri. This is an open access article distributed under the Creative Commons Attribution License, which permits unrestricted use, distribution, and reproduction in any medium, provided the original work is properly cited.

## 1. Introduction

Supramolecular organisation is a fruitful concept for the design of systems exhibiting specific macroscopic properties. Molecular sieves, such as zeolites, have been shown to be ideal host materials for the supramolecular organisation of dye molecules, complexes, or clusters. The inserted species usually exhibit an increased chemical and photochemical stability in the host matrix. Constraints imposed by the well-defined geometry of the host channels or cavities lead to a preferred spatial arrangement of the guests, thereby generating highly organised materials. Further functionalities can be added by assembling host-guest objects into well-defined macroscopic structures on various supports [1–18] and by promoting communication between guests and external species or devices [17–19]. The large variety in pore structure and morphologies provided by different types of molecular sieves offers many possibilities for the design of host-guest materials with specific properties [20]. Readers are referred to [21–23] for reviews on chromophores in porous silica and minerals. This tutorial will be focused on zeolite L, as it has proven to be an excellent host material for the organization of highly luminescent guest molecules [24–27]. The reasoning and methods presented here are, however, also valid for other host materials with similar properties. The tutorial will start with a description of the host material

and how guests are arranged inside of it. We will follow with a short theoretical background on Förster resonance energy transfer, for which we use the abbreviation FRET, illustrated with a case study. The last section will be devoted to an overview on how dye-zeolite materials can be arranged into larger patterns to form highly organized materials for novel optical applications.

## 2. Discussion

*2.1. Supramolecular Organization of Guests inside of Zeolite L.* Zeolite L crystals can be synthesised with different morphologies and sizes varying from of 30 nm up to about 10 000 nm, meaning that about 7 orders of magnitude in terms of volume can be covered [28–34]. Figure 1 depicts the structure and morphology of zeolite L. The primary building unit of the framework consists of TO<sub>4</sub> tetrahedrons where T represents either Al or Si. The secondary building unit, the cancrinite cage, is made up by 18 corner-sharing tetrahedrons. These cages are stacked into columns, which are then connected by means of oxygen bridges in the *a,b* plane to form a one-dimensional channel system running parallel to the crystals *c*-axis, exhibiting a hexagonal symmetry. The molar composition of zeolite L is (M<sup>+</sup>)<sub>9</sub>[(AlO<sub>2</sub>)<sub>9</sub>(SiO<sub>2</sub>)<sub>27</sub>] × *n*H<sub>2</sub>O, where M<sup>+</sup> are monovalent cations, compensating

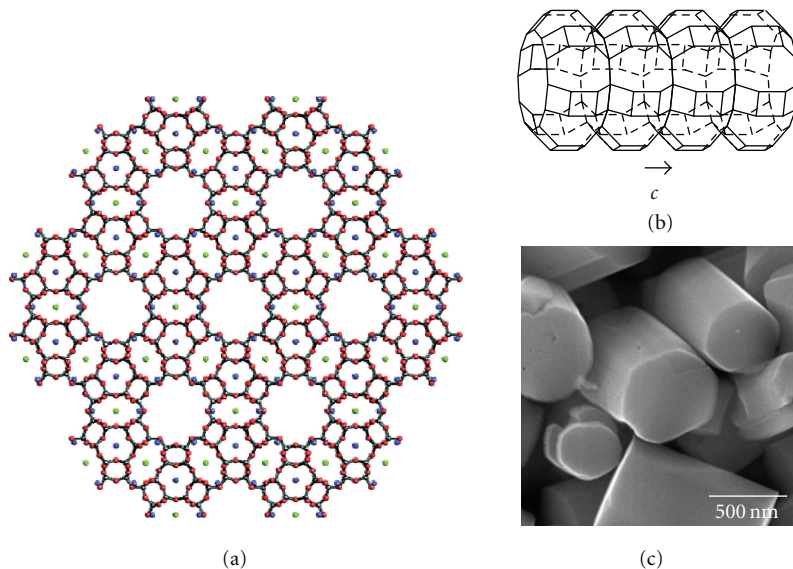


FIGURE 1: Zeolite L. (a) Top view of the structure of zeolite L illustrating its hexagonal framework. It shows a channel surrounded by six neighbouring channels. The centre-to-centre distance between two channels is 1.84 nm. (b) Side view of a channel that consists of 0.75 nm long unit cells with a Van der Waals opening of 0.71 nm at the smallest and 1.26 nm at the widest place. (c) SEM image of zeolite L crystals.

the negative charge resulting from the aluminium atoms.  $n$  is equal to 21 in fully hydrated materials, and to 16 for crystals equilibrated at about 22% relative humidity [35–38].

Zeolite L can be considered as consisting of a bunch of strictly parallel channels [19, 24–27, 39]. The channels have the smallest free diameter of about 0.71 nm, while the largest diameter inside is 1.26 nm. The centre-to-centre distance between two channels is 1.84 nm. Each zeolite L crystal consists of a large number of channels ( $n_{\text{ch}}$ ) which can be estimated by

$$n_{\text{ch}} = 0.267(d_z)^2, \quad (1)$$

where  $d_z$  represents the diameter of the crystal in nm. For example, a crystal with a diameter of 600 nm features nearly 100 000 strictly parallel channels. The ratio of void space available in the channels with respect to the total crystal volume is about 0.26. An important consequence is that zeolite L allows through geometrical constraints the realization of extremely high concentrations of well-oriented molecules. Depending on their shape and size, the guests usually behave as monomers. A 30 nm by 30 nm crystal can take up to nearly 5000 dye molecules that occupy 2 unit cells; while a 60 nm by 60 nm crystal can host nearly 40 000 of the same guest type. The dye concentration of a dye-zeolite material  $c(p)$  can be expressed as a function of the loading  $p$  as follows:

$$c(p) = 0.752 \frac{p}{n_s} \left( \frac{\text{mol}}{\text{L}} \right), \quad (2)$$

where  $n_s$  indicates the number of unit cells which form a site and can be occupied by one guest. The value of  $n_s$  is usually

an integer, but this must not necessarily be so. The loading, or occupation probability,  $p$ , is defined as follows:

$$p = \frac{\text{number of occupied sites}}{\text{total amount of sites}}. \quad (3)$$

Zeolite L is a versatile host material allowing for the design and preparation of a respectable variety of highly organized host-guest systems, as illustrated in Figure 2. It is the only currently available microporous material allowing the realization of the full range of organizational patterns presented here. The “cornerstones” in the development of these composite materials were the finding that dye-loaded crystals with different well defined domains can be prepared [40, 41], the invention of the stopcock principle [42, 43], the discovery of quasi 1D energy transfer [44], the preparation of unidirectional energy transfer material [17, 18, 45–47], and finding ways to create hybrid materials fully transparent in the visible range [48, 49]. The latter is important for spectroscopic investigations and some applications, since the small zeolite crystals exhibit considerable light scattering due to their size and refractive index between 1.4 and 1.5.

Guest species can be inserted into the channels of zeolite L either by ion exchange or by adsorption from the gas phase, depending on whether they are a charged or neutral species, respectively. The geometrical constraint imposed by the host leads to a highly ordered and well-defined arrangement of the guests inside the channels. Molecules that can pass the 0.71 nm pore openings of zeolite L are usually too large to overtake or stack with molecules already present in the channels. Thus one can create, by sequential insertion, materials with two or more defined domains, each containing only one type of guests. The geometrical confinement makes it also possible to reach very high concentrations of essentially monomeric dyes. Very small

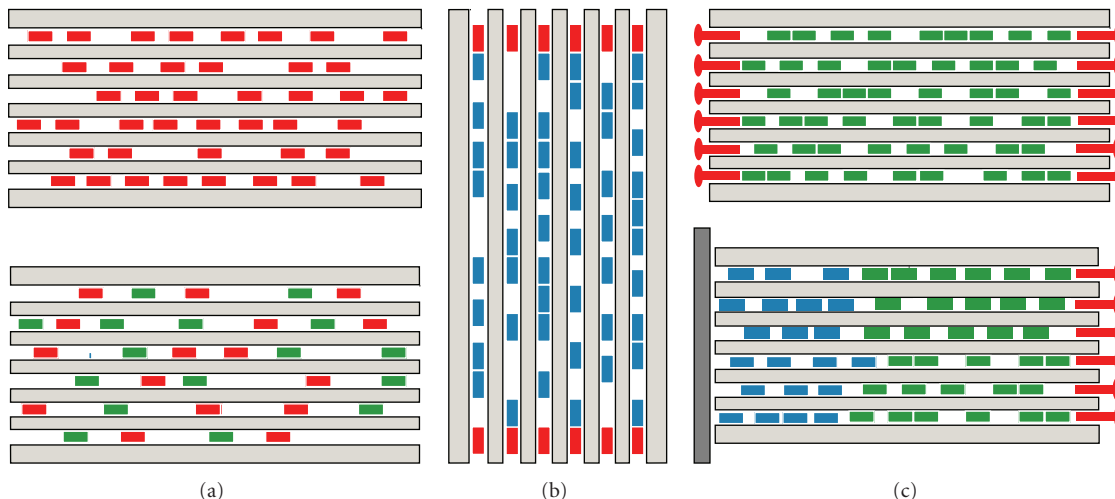


FIGURE 2: Schematic representations of supramolecularly organized dye-zeolite L systems. (a) *Single and mixed dye materials* are obtained by either loading zeolite crystals with one kind of dye (top) or by simultaneous insertion of different dye molecules (bottom). (b) *Antenna materials* can be prepared by the sequential insertion of different dyes. (c) *Stopcock-plugged antenna material* is obtained by modifying either bidirectional (top) or mono directional (bottom) antenna materials with specific closure molecules, called stopcocks.

molecules such as naphthalene can, however, form dimers inside of the channel system [50]. The structural formulae of dyes discussed in this work are summarised in Table 1.

Larger complexes can be prepared inside of the channel systems by means of a “ship-in-a-bottle” synthesis, a principle that was first developed by DeWild et al. in the early 80s of last century [51]. In a first step, the metal centres are introduced by means of ion exchange. The potential ligands can then diffuse into the channels where they will complex the metal centres. The reaction is easiest close to the channel entrances, as the access to the deeper lying metal ions is more difficult due to spatial restrictions. This principle has been successfully applied for the preparation of many different materials [52–56].

The channel ends of zeolite L can be modified by specific closure molecules, consisting typically of a head and a tail. Due to spatial restrictions, only the tail can pass the channel openings, while the head group is too bulky to fit through [42, 43]. Depending on their nature, these so-called *stopcock molecules* can be bound to the pore openings by either physisorption, electrostatical interaction, or by covalent bonding. As these molecules are only partially located inside the channels, they can be envisaged as mediators for interactions of species inside the crystals with outside entities or objects. Fluorescent stopcocks can be used to extract or inject electronic excitation energy into or from the zeolite L crystals by FRET [24–27, 42, 43, 57, 58]. Stopcock molecules can also prevent penetration of small molecules such as oxygen and water or hinder encapsulated dye molecules from leaving the channels [59].

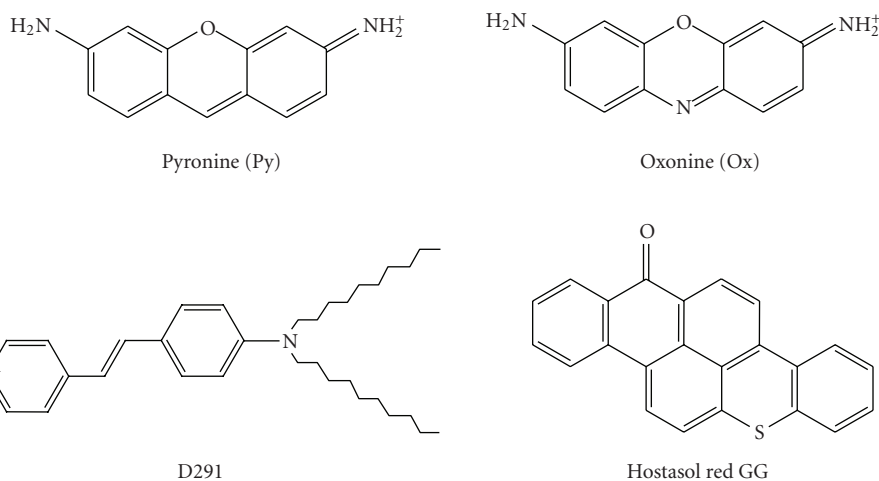
**2.2. FRET Processes inside of Host-Guest Materials.** This section will give a short overview on the theoretical background of FRET, followed by an experimental case study. Due to the geometrical properties outlined above, dye-zeolite L

composites are well suited for the study of FRET processes. The understanding of the FRET process is very advanced and goes back to the pioneering work of Förster [60–62]. A chromophore can be considered to consist of a backbone of positively charged nuclei surrounded by an electron cloud. When a photon is absorbed by the molecule, its energy is transformed into kinetic energy of one of these electrons. The oscillating electromagnetic field caused by the electrons rapid movement can interact with a neighbouring acceptor molecule *A*, as long as it bears states being in resonance with the excited state of the donor  $D^*$ . This radiationless electronic excitation energy transfer is solely due to the very weak near field interaction between excited configurations of the initial state ( $D^* \cdots A_i$ ) and of the final state ( $D \cdots A_i^*$ ). The Förster mechanism requires no orbital overlap between the donor and acceptor molecules. It should also be noted that this process involves no electron transfer from one species to the other. The donor *D* and the acceptor *A* can be either of the same type or they can be of different species. The rate constant  $k_{\text{EnT}}$  for the transfer from one electronic configuration to the other can be expressed as follows:

$$k_{\text{EnT}} = \text{TF} \frac{\kappa_{D^*A}^2 \phi_{D^*}}{n^4 R_{DA}^6 \tau_{D^*}} J_{D^*A}, \quad (4)$$

where  $\kappa_{D^*A}^2$  describes the relative orientation between the electronic transition dipole moments (ETDM) of donor and acceptor. This term can take values ranging from 0 to 4 for perpendicular or colinear arrangement of the ETDM, respectively. The centre-to-centre distance between the transition dipole moments is given by  $R_{DA}$ . Since the efficiency of the FRET process depends on the inverse sixth power of the intermolecular separation, it is useful over distances in the range of 1.5 nm to 10 nm. The terms  $\phi_{D^*}$  and  $\tau_{D^*}$  specify the quantum yield and lifetime of the donor in absence of acceptors.  $J_{D^*A}$  represents the overlap integral

TABLE 1: Summary of the structural formulae of dyes presented in this work.



between the acceptors absorption and the donors emission bands, thus taking into account the resonance condition. The environment of the donor-acceptor pair comes into play by the refractive index  $n$ .  $TF$  is a term that has been introduced to collect all constant terms from Theodor Försters original equation and has therefore the value [26, 27]

$$TF = \frac{9000 \ln(10)}{128\pi^5 N_L} \quad \text{or} \quad TF = 8.785 \cdot 10^{-25} \text{ mol.} \quad (5)$$

A nice case study of a FRET process is the mixed Py,Ox-zeolite L system [63]. The insertion kinetics of the strongly fluorescent dyes Py and Ox into zeolite L are very similar, providing a statistically homogeneous distribution of both dyes over the whole crystal. These dyes form an excellent donor acceptor pair, due to the large overlap ( $J_{Py/Ox}$ ) between the Py fluorescence and the Ox absorption spectra as can be seen in Figure 3(a). The energy transfer process is illustrated by the photographic images seven fluorescent samples in Figure 3(b). Zeolite L crystals with an average length of 300 nm were used for preparation of all samples. The two references Py and Ox were loaded with a concentration of  $5 \times 10^{-3}$  M of Py or Ox, while the samples A to E were filled with a 1:1 mixture of both dyes. The concentrations for samples shown in Figure 3(a) are: A,  $p = .0028$ ; B,  $p = .0070$ ; C,  $p = .0140$ ; D,  $p = .0280$ ; E,  $p = .0560$ . The increasing dye concentration from A to E leads in turn to a decrease in the mean donor-acceptor distance. All samples were excited at 485 nm, where Py has a strong absorbance and Ox absorbs next to no light. Sample A exhibits mainly the green fluorescence of Py, indicating that energy transfer is insignificant. This is schematically shown by the donor-acceptor configuration on the left of the photograph. The low dye loading leads to large donor-acceptor distances. After selective excitation of the donor, its fluorescence intensity is dominant (green light). The energy transfer process to an acceptor is insignificant, and thus acceptor fluorescence (red light) is very weak. The yellow colour of sample B is due to a mixture of green and red fluorescence, meaning that energy transfer becomes significant in this case. The process becomes more and more important with increasing

concentration so that from sample C on, the red fluorescence stemming from Ox is dominant. The donor-acceptor scheme on the right of the photograph illustrates this for the case E. The high dye loading results in a short donor-acceptor distance, increasing the efficiency of the energy transfer process. As a result, the donor fluorescence is significantly quenched, while fluorescence from the acceptors is strong.

The same effect can be observed on the single crystal scale, by following the diffusion of the random dye mixture as a function of time [64]. The fluorescence microscopy images of a mixed Py,Ox-zeolite L sample given in Figure 3(c) illustrate this very nicely. The images were taken after loading the crystals for 20 minutes (1), 60 minutes (2), 470 minutes (3a, 3b), and 162 hours (4), respectively. For all images, Py was specifically excited, with the exception of 3b where Ox<sup>+</sup> was specifically excited. The samples with short equilibrium times exhibit an orange to yellow luminescence, due to the overlap of the green Py and red Ox emission, an indication for efficient FRET. After a diffusion time of 162 hours, the dyes are so far apart from each other that upon selective excitation of Py only green emission can be observed.

**2.3. Organizing Host-Guest Materials on Larger Scale.** A higher degree of supramolecular organization can be reached by arranging the dye-zeolite composites into larger structure. Such hierarchically organized structures, presenting successive ordering from the molecular up to macroscopic scale, are of great interest for nanotechnology due to the relationship between molecular arrangements and macroscopic properties [65, 66]. The organization of quantum sized particles, nanotubes, and microporous materials on different surfaces has been studied and used in science, technology, diagnostics, and medicine [67–76]. Size, shape, and surface composition of the objects but also the properties of the surface on which they should be organized play a decisive role and in some cases determine not only the quality of the self-assembly but also its macroscopic properties. Self-assembly strategies in the organization of matter make hierarchical ordering attractive by avoiding expansive techniques such

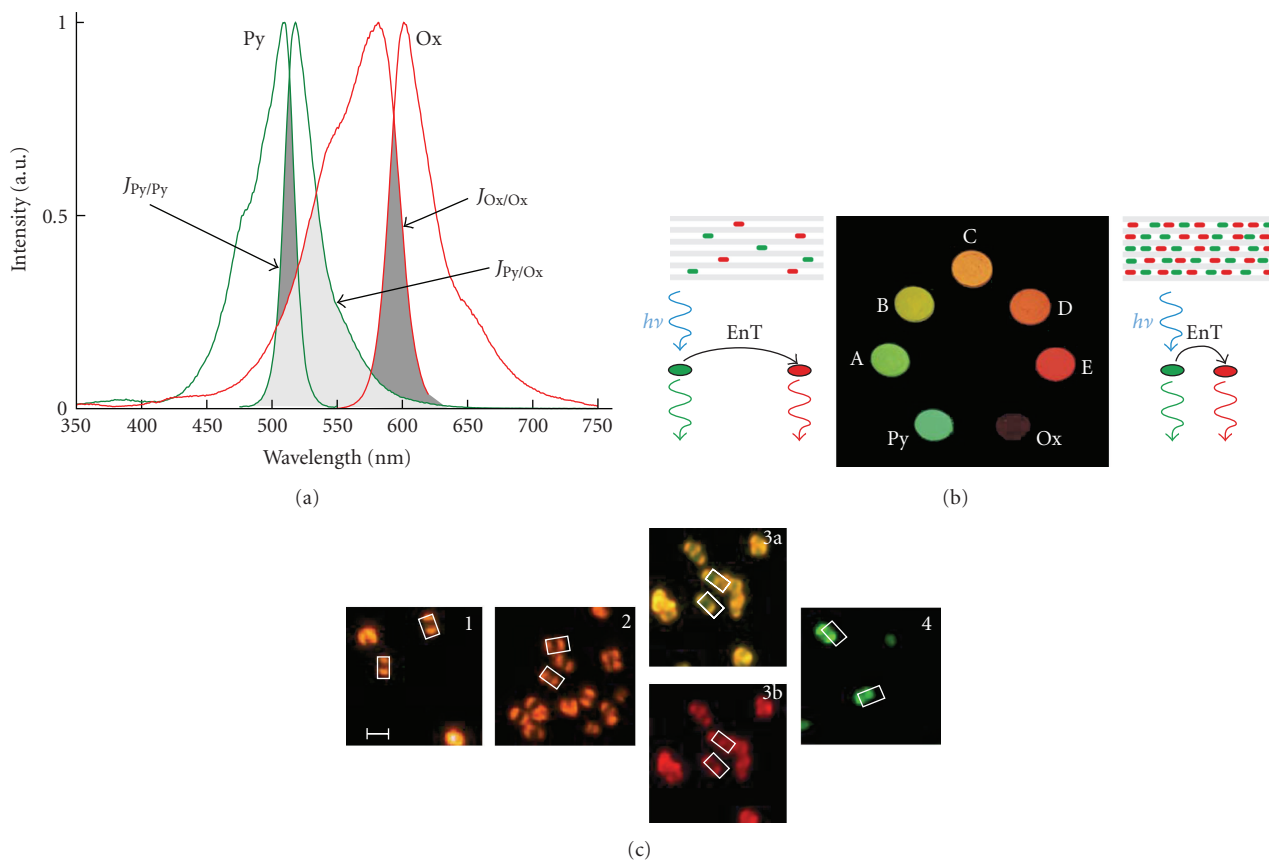


FIGURE 3: FRET case study on a mixed Py,Ox-zeolite L composite. (a) Excitation and fluorescence spectra of both dyes in zeolite L scaled to the same height at the maximum. The different overlap areas are indicated by grey shading. (b) Middle: photographic image of dye-loaded zeolite L layers upon monochromatic irradiation at 485 nm and observation through a 500 nm cut-off filter. The two samples indicated as P and Ox are references loaded with pure Py and Ox, respectively. Samples A to E contain a 1:1 mixture of Py and Ox with the following loading for each dye: A,  $p_{1/2} = .0014$ ; B,  $p_{1/2} = .0035$ ; C,  $p_{1/2} = .007$ ; D,  $p_{1/2} = .014$ ; E,  $p_{1/2} = .028$ . Left: Crystal and donor-acceptor pair describing the situation in sample A. Right: Crystal and donor-acceptor pair describing the situation in sample E [63]. (c) Fluorescence microscopy pictures, visualizing the diffusion of Ox to Py in zeolite L, taken after 20 minutes (1), 60 minutes (2), 470 minutes (3a, 3b), and 162 hours (4), respectively. Py was specifically excited, with the exception of 3b, where Ox was specifically excited. Two crystals of each image are framed. The scale given in 1 corresponds to a length of  $1.5 \mu\text{m}$  [64].

as photolithography. An overview of hierarchically ordered materials that were created by self-assembly from dye-zeolite composites is given in Figure 4 [26, 27].

Hybrid polymer/dye-zeolite L materials with randomly oriented crystals, as shown in Figure 4(a), are obtained by dispersing surface modified zeolites in the precursor monomer followed by a specific polymerization procedure [48, 49]. Surface modification with alkoxysilane derivatives improves the miscibility of the crystals with the organic monomers and even enabling copolymerization when an appropriate organic substituent is used. In this type of material, the usually strong light scattering of zeolite L can be suppressed by refractive index matching and avoidance of microphase separation.

Materials containing crystals oriented in a nematic phase, as shown in the sketch of Figure 4(b), can be obtained by using elastic polymers as substrate. After appropriate treatment of the polymer substrate such as stretching it with or without gentle heating, the crystals form the desired

nematic phase. The mechanical stretching force influences the zeolites and most will align along the pulling direction. The SEM and fluorescence microscopy images of Py-zeolite L embedded into a PVC polymer film shown in Figure 4(b) illustrate this well [48, 49].

Strategies based on the minimization of interfacial free energy for self-assembly have been applied to position small objects at the micrometric scale [81]. A novel approach towards micropatterning employing a surface tension was realized by Yunus et al. [78]. It was shown that dye-zeolite L crystals can be organized into hexagonal arrangement on a patterned polydimethylsiloxane (PDMS) surface as illustrated by the SEM and fluorescence microscopy images in Figure 4(c). The assembly process here is driven by surface tension interactions. This principle is a powerful tool for manipulations at the micrometer scale, allowing us to hierarchically organize molecular dyes on a macroscopic level.

Zeolite L crystals, with diameter around  $700 \text{ nm}$  and length in the range of  $1 \mu\text{m}$ , have been successfully embedded

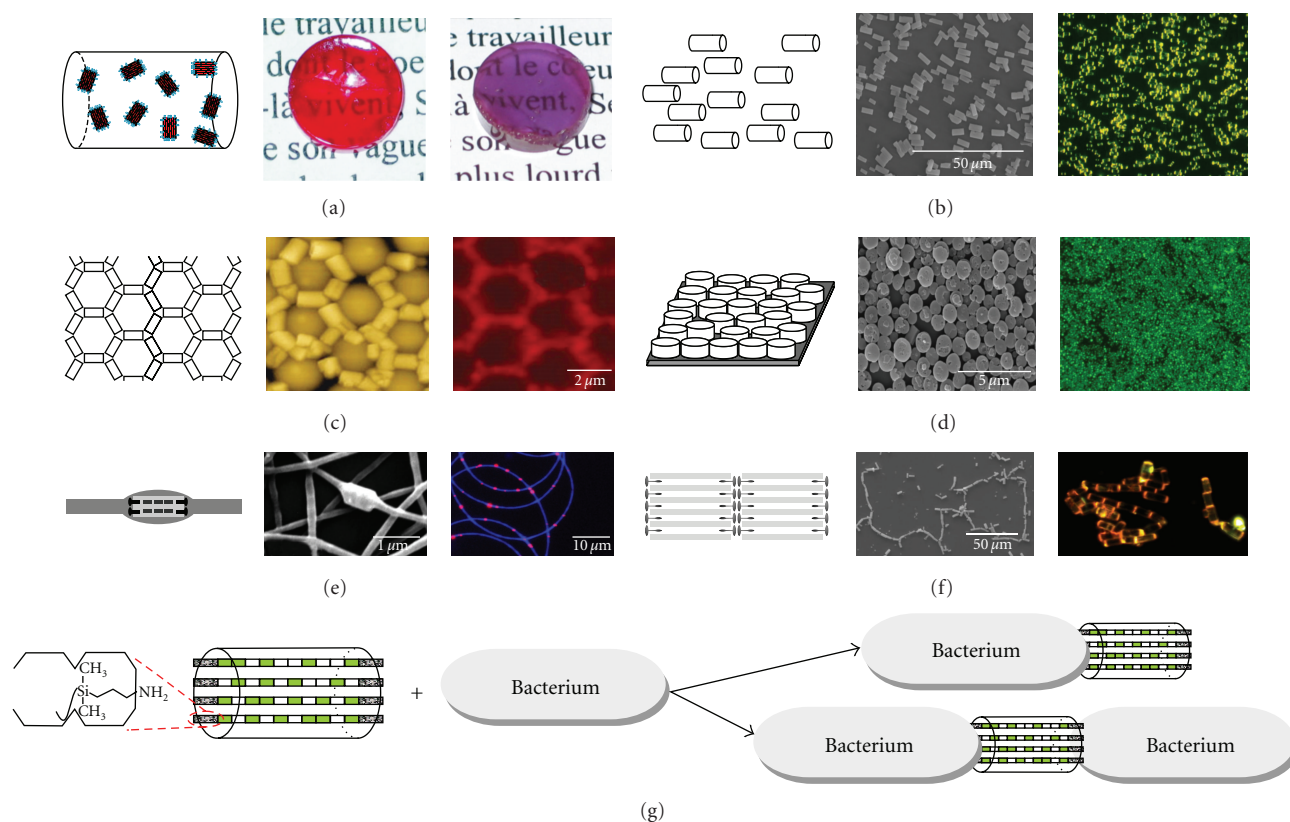


FIGURE 4: Summary of materials obtained by supramolecular organizations of zeolite L crystals. (a) Randomly oriented zeolite L crystals in a polymer. Photographic images of zeolite L-polymer hybrid materials prepared from crystals loaded with either red or violet dyes (Hostasol Red GG or Ox<sup>+</sup>, resp.) [48, 49]. (b) Nematic phase arrangement. Left: SEM and fluorescence microscopy image of Py<sup>+</sup>-zeolite L crystals aligned in a stretched PVC plastic film [77]. (c) Hexagonal arrangement. The dye-zeolite L crystals are organized by a surface-tension-driven self-assembly process on a PDMS/PS film (SEM and fluorescence microscopy image are shown) [78]. (d) Monolayers of standing zeolite L crystals. Left: SEM image of a monolayer. Right: fluorescence microscopy image of a monolayer loaded with Py [45–47]. (e) Nanofibers with embedded zeolite L. Left: SEM image of nanofiber with embedded zeolite L crystals. The crystals are oriented along the fiber axis. Right: Fluorescence image of a PEO/DDT nanofiber (blue emission) with embedded Ox-zeolite crystals (red sparks) [79]. (f) Chain-like assemblies of zeolite L crystals. Right: SEM image of zeolite crystals linked together by modifying the channel entrances with a cationic stopcock (D291) and corresponding fluorescence microscopy image [77]. (g) Assembly of zeolite L/bacterium in PBS buffer solution and self-assembly of two bacteria with functionalized 1-μm zeolite L as the junction [80].

into electrospun polymer fibers [79]. Electrospinning is a very efficient process for preparation of fibers with diameters ranging from the nano- to the micrometer scale [82, 83]. Polymer wires as thin as 150 nm are still able to enclose zeolites [84]. The crystals are aligned parallel to the fiber axis, as can be seen from the SEM image in Figure 4(e). Nanowires prepared by incorporating dye-loaded zeolites act as very bright, polarized light sources (Figure 4(e), left part) and are currently investigated for advanced nanophotonic applications.

Stopcock-plugged zeolite L crystals can be arranged into chain-like one-dimensional assemblies by exploiting coordinative interactions between the head groups of the stopper molecules, as illustrated in the scheme of Figure 4(f). The reversible nature of such coordinative bonds makes it possible to maximize the base-to-base interaction between crystals [85]. The chain-like arrangement of zeolite L crystals seen in the SEM image of Figure 4(f) is due to Van der Waals interactions between the long alkyl tails

of the stopcocks. The fluorescence microscopy image on the right part of Figure 4(f) shows a similar assembly of stopcock-plugged crystals. The luminescence concentration at the zeolite basal surfaces indicates the presence of the stopper molecules. Such microbarcode structures may be of interest for tagging or bio-imaging purposes [86, 87].

A recent breakthrough was realized by the attachment of dye-zeolite composites with amino-functionalized surfaces to living entities such as nonpathogenic *Escherichia coli* (*E. coli*) bacteria [80]. The situation schematically depicted in Figure 4(g) was investigated by means of optical and scanning electron microscopy. An interesting observation was that the crystals seem to always bind to one of the poles of *E. coli*. It was also possible to connect two bacteria together via a bridging, surface modified zeolite L crystal. The self-assembly of living systems with functional materials through chemically programmed construction opens up fascinating research fields.

### 3. Conclusion

The supramolecular organisation of molecules, complexes, or clusters inside the channels of zeolite L leads to host-guest composites with fascinating properties, a prime example being their use as artificial antenna materials. Further functionalities can be added by assembling such host-guest systems into well-defined macroscopic structures on various supports and by promoting communication between guests and external species or devices. The stopcock principle offers an elegant way to interface dye-loaded zeolite L crystals to other devices such as solar cells or even biological systems. Such materials are of interest in the development of novel optical devices such as luminescent probes, lenses, special mirrors, filters, polarisers, grids, optical storage devices, windows, and luminescent concentrators [26, 27, 88–90].

### Acknowledgment

Dr. A. Devaux wishes to acknowledge the Swiss National Science Foundation for funding (Grant PBBE2-121054).

### References

- [1] Y. Yan and T. Bein, "Molecular recognition on acoustic wave devices: sorption in chemically anchored zeolite monolayers," *Journal of Physical Chemistry*, vol. 96, no. 23, pp. 9387–9393, 1992.
- [2] T. Bein, "Synthesis and applications of molecular sieve layers and membranes," *Chemistry of Materials*, vol. 8, no. 8, pp. 1636–1653, 1996.
- [3] A. R. Pradhan, M. A. Macnaughtan, and D. Raftery, "Zeolite-coated optical microfibers for intrazeolite photocatalysis studied by in situ solid-state NMR," *Journal of the American Chemical Society*, vol. 122, no. 2, pp. 404–405, 2000.
- [4] P. Lainé, R. Seifert, R. Giovanoli, and G. Calzaferri, "Convenient preparation of close-packed monograin layers of pure zeolite A microcrystals," *New Journal of Chemistry*, vol. 21, no. 4, pp. 453–460, 1997.
- [5] S. Y. Choi, Y.-J. Lee, Y. S. Park, K. Ha, and K. B. Yoon, "Monolayer assembly of zeolite crystals on glass with fullerene as the covalent linker," *Journal of the American Chemical Society*, vol. 122, no. 21, pp. 5201–5209, 2000.
- [6] K. Ha, Y.-J. Lee, H. J. Lee, and K. B. Yoon, "Facile assembly of zeolite monolayers on glass, silica, alumina, and other zeolites using 3-halopropylsilyl reagents as covalent linkers," *Advanced Materials*, vol. 12, no. 15, pp. 1114–1117, 2000.
- [7] A. Kulak, Y.-J. Lee, Y. S. Park, and K. B. Yoon, "Orientation-controlled monolayer assembly of zeolite crystals on glass and mica by covalent linkage of surface-bound epoxide and amine groups," *Angewandte Chemie International Edition*, vol. 39, no. 5, pp. 950–953, 2000.
- [8] A. Kulak, Y. S. Park, Y.-J. Lee, Y. S. Chun, K. Ha, and K. B. Yoon, "Polyamines as strong molecular linkers for monolayer assembly of zeolite crystals on flat and curved glass," *Journal of the American Chemical Society*, vol. 122, no. 38, pp. 9308–9309, 2000.
- [9] G. S. Lee, Y.-J. Lee, K. Ha, and K. B. Yoon, "Orientation-controlled monolayer assembly of zeolite crystals on glass using terephthaldicarboxaldehyde as a covalent linker," *Tetrahedron*, vol. 56, no. 36, pp. 6965–6968, 2000.
- [10] Y. S. Chun, K. Ha, Y.-J. Lee, et al., "Diisocyanates as novel molecular binders for monolayer assembly of zeolite crystals on glass," *Chemical Communications*, vol. 8, no. 17, pp. 1846–1847, 2002.
- [11] K. Ha, Y.-J. Lee, D.-Y. Jung, J. H. Lee, and K. B. Yoon, "Micropatterning of oriented zeolite monolayers on glass by covalent linkage," *Advanced Materials*, vol. 12, no. 21, pp. 1614–1617, 2000.
- [12] K. Ha, Y.-J. Lee, Y. S. Chun, Y. S. Park, G. S. Lee, and K. B. Yoon, "Photochemical pattern transfer and patterning of continuous zeolite films on glass by direct dipping in synthesis gel," *Advanced Materials*, vol. 13, no. 8, pp. 594–596, 2001.
- [13] J. Choi, S. Ghosh, Z. Lai, and M. Tsapatsis, "Uniformly a-oriented MFI zeolite films by secondary growth," *Angewandte Chemie International Edition*, vol. 45, no. 7, pp. 1154–1158, 2006.
- [14] S. Hashimoto, K. Samata, T. Shoji, N. Taira, T. Tomita, and S. Matsuo, "Preparation of large-scale 2D zeolite crystal array structures to achieve optical functionality," *Microporous and Mesoporous Materials*, vol. 117, no. 1-2, pp. 220–227, 2009.
- [15] J. S. Lee, K. Ha, Y.-J. Lee, and K. B. Yoon, "Effect of method on monolayer assembly of zeolite microcrystals on glass with molecular linkages," *Topics in Catalysis*, vol. 52, no. 1-2, pp. 119–139, 2009.
- [16] F. Cucinotta, Z. Popović, E. A. Weiss, G. M. Whitesides, and L. De Cola, "Microcontact transfer printing of zeolite monolayers," *Advanced Materials*, vol. 21, no. 10-11, pp. 1142–1145, 2009.
- [17] A. Zabala Ruiz, H. Li, and G. Calzaferri, "Organizing supramolecular functional dye-zeolite crystals," *Angewandte Chemie International Edition*, vol. 45, no. 32, pp. 5282–5287, 2006.
- [18] G. Calzaferri, A. Zabala Ruiz, H. Li, and S. Huber, "Latest bibliographic data on file with the International Bureau," patent WO 2007/012216.
- [19] G. Calzaferri, M. Pauchard, H. Maas, S. Huber, A. Khatyr, and T. Schaafsma, "Photonic antenna system for light harvesting, transport and trapping," *Journal of Materials Chemistry*, vol. 12, no. 1, pp. 1–13, 2002.
- [20] Ch. Baerlocher, W. M. Meier, and D. H. Olson, *Atlas of Zeolite Framework Types*, Elsevier, Amsterdam, The Netherlands, 5th edition, 2001.
- [21] G. Schulz-Ekloff, D. Wöhrle, B. van Duffel, and R. A. Schoonheydt, "Chromophores in porous silicas and minerals: preparation and optical properties," *Microporous and Mesoporous Materials*, vol. 51, no. 2, pp. 91–138, 2002.
- [22] A. Corma and H. García, "Supramolecular host-guest systems in zeolites prepared by ship-in-a-bottle synthesis," *European Journal of Inorganic Chemistry*, no. 6, pp. 1143–1164, 2004.
- [23] V. Ramamurthy, *Photochemistry in Organized and Constrained Media*, VCH, New York, NY, USA, 1991.
- [24] G. Calzaferri, S. Huber, H. Maas, and C. Minkowski, "Host-guest antenna materials," *Angewandte Chemie International Edition*, vol. 42, no. 32, pp. 3732–3758, 2003.
- [25] G. Calzaferri, H. Maas, M. Pauchard, M. Pfenniger, S. Megelski, and A. Devaux, "Supramolecularly organized luminescent dye molecules in the channels of zeolite L," in *Advances in Photochemistry*, D. C. Neckers, G. von Bunau, and W. S. Jenks, Eds., vol. 27, pp. 1–50, John Wiley & Sons, New York, NY, USA, 2002.
- [26] G. Calzaferri and K. Lutkouskaya, "Mimicking the antenna system of green plants," *Photochemical and Photobiological Sciences*, vol. 7, no. 8, pp. 879–910, 2008.

- [27] G. Calzaferri and A. Devaux, "Manipulation of energy transfer processes within the channels of L-zeolite," in *Supramolecular Effects in Photochemical and Photophysical Processes*, V. Ramamurthy and Y. Inoue, Eds., John Wiley & Sons, Hoboken, NJ, USA, 2010.
- [28] S. Megelski and G. Calzaferri, "Tuning the size and shape of zeolite L-based inorganic-organic host-guest composites for optical antenna systems," *Advanced Functional Materials*, vol. 11, no. 4, pp. 277–286, 2001.
- [29] A. Zabala Ruiz, D. Brühwiler, T. Ban, and G. Calzaferri, "Synthesis of zeolite L. Tuning size and morphology," *Monatshefte für Chemie*, vol. 136, no. 1, pp. 77–89, 2005.
- [30] A. Zabala Ruiz, D. Bruhwiler, L.-Q. Dieu, and G. Calzaferri, "Controlling size and morphology of zeolite L," in *Materials Syntheses: A practical Guide*, U. Schubert, N. Hüsing, and R. Laine, Eds., pp. 1–7, Springer, Wien, Germany, 2008.
- [31] S. Ernst and J. Weitkamp, "Synthesis of large pore aluminosilicates," *Catalysis Today*, vol. 19, no. 1, pp. 27–60, 1994.
- [32] Y.-J. Lee, J. S. Lee, and K. B. Yoon, "Synthesis of long zeolite-L crystals with flat facets," *Microporous and Mesoporous Materials*, vol. 80, no. 1–3, pp. 237–246, 2005.
- [33] T. Ban, H. Saito, M. Naito, Y. Ohya, and Y. Takahashi, "Synthesis of zeolite L crystals with different shapes," *Journal of Porous Materials*, vol. 14, no. 2, pp. 119–126, 2007.
- [34] R. Brent and M. W. Anderson, "Fundamental crystal growth mechanism in zeolite L revealed by atomic force microscopy," *Angewandte Chemie International Edition*, vol. 47, no. 29, pp. 5327–5330, 2008.
- [35] W. Breck, *Zeolite Molecular Sieves*, John Wiley & Sons, New York, NY, USA, 1974.
- [36] Ch. Baerlocher, W. M. Meier, and D. H. Olson, *Atlas of Zeolite Framework Types*, Elsevier, Amsterdam, The Netherlands, 5th edition, 2001.
- [37] T. Ohsuna, B. Slater, F. Gao, et al., "Fine structures of zeolite-linde-L (LTL): surface structures, growth unit and defects," *Chemistry: A European Journal*, vol. 10, no. 20, pp. 5031–5040, 2004.
- [38] O. Larlus and V. P. Valtchev, "Crystal morphology control of LTL-type zeolite crystals," *Chemistry of Materials*, vol. 16, no. 17, pp. 3381–3389, 2004.
- [39] D. Brühwiler and G. Calzaferri, "Molecular sieves as host materials for supramolecular organization," *Microporous and Mesoporous Materials*, vol. 72, no. 1–3, pp. 1–23, 2004.
- [40] N. Gfeller, S. Megelski, and G. Calzaferri, "Transfer of electronic excitation energy between dye molecules in the channels of zeolite L," *Journal of Physical Chemistry B*, vol. 102, no. 14, pp. 2433–2436, 1998.
- [41] M. Pauchard, A. Devaux, and G. Calzaferri, "Dye-loaded zeolite L sandwiches as artificial antenna systems for light transport," *Chemistry: A European Journal*, vol. 6, no. 18, pp. 3456–3470, 2000.
- [42] G. Calzaferri, "Dye loaded zeolite material," patents EP 1335879, US 6932919, US 7327012.
- [43] H. Maas and G. Calzaferri, "Trapping energy from and injecting energy into dye-zeolite nanoantennae," *Angewandte Chemie International Edition*, vol. 41, no. 13, pp. 2284–2288, 2002.
- [44] C. Minkowski and G. Calzaferri, "Förster-type energy transfer along a specified axis," *Angewandte Chemie International Edition*, vol. 117, no. 33, pp. 5459–5463, 2005.
- [45] H. Li, Y. Wang, W. Zhang, B. Liu, and G. Calzaferri, "Fabrication of oriented zeolite L monolayers employing luminescent perylene diimide-bridged silsesquioxane precursor as the covalent linker," *Chemical Communications*, no. 27, pp. 2853–2854, 2007.
- [46] Y. Wang, H. Li, B. Liu, et al., "Fabrication of oriented zeolite L monolayer via covalent molecular linkers," *Journal of Solid State Chemistry*, vol. 181, no. 9, pp. 2469–2472, 2008.
- [47] G. Calzaferri, S. Huber, A. Devaux, et al., "Light-harvesting host-guest antenna materials for photonic devices," in *Organic Optoelectronics and Photonics II*, vol. 6192 of *Proceedings of SPIE*, Strasbourg, France, April 2006.
- [48] S. Suárez, A. Devaux, J. Buñuelos, O. Bossart, A. Kunzmann, and G. Calzaferri, "Transparent zeolite-polymer hybrid materials with adaptable properties," *Advanced Functional Materials*, vol. 17, no. 14, pp. 2298–2306, 2007.
- [49] H. J. Metz, G. Calzaferri, S. Suarez, A. Devaux, and A. Kunzmann, "Transparent zeolite-polymer hybrid material with tunable properties," patent EP 18732002.
- [50] S. Hashimoto, M. Hagiri, N. Matsubara, and S. Tobita, "Photophysical studies of neutral aromatic species confined in zeolite L: comparison with cationic dyes," *Physical Chemistry Chemical Physics*, vol. 3, no. 22, pp. 5043–5051, 2001.
- [51] W. DeWilde, G. Peeters, and J. H. Lunsford, "Synthesis and spectroscopic properties of tris(2,2'-bipyridine)ruthenium(II) in zeolite Y," *Journal of Physical Chemistry*, vol. 84, no. 18, pp. 2306–2310, 1980.
- [52] A. Corma and H. García, "Supramolecular host-guest systems in zeolites prepared by ship-in-a-bottle synthesis," *European Journal of Inorganic Chemistry*, no. 6, pp. 1143–1164, 2004.
- [53] Y. G. Wang, Z. Guo, and H. R. Li, "Highly luminescent host-guest systems based on zeolite L and lanthanide complexes," *Journal of Rare Earths*, vol. 25, pp. 283–285, 2007.
- [54] A. Monguzzi, G. MacChi, F. Meinardi, R. Tubino, M. Burger, and G. Calzaferri, "Sensitized near infrared emission from lanthanide-exchanged zeolites," *Applied Physics Letters*, vol. 92, no. 12, Article ID 123301, 3 pages, 2008.
- [55] Y. Wang, H. Li, Y. Feng, H. Zhang, G. Calzaferri, and T. Ren, "Orienting zeolite L microcrystals with a functional linker," *Angewandte Chemie International Edition*, vol. 49, no. 8, pp. 1434–1438, 2010.
- [56] Y. Wang, H. Li, L. Gu, Q. Gan, Y. Li, and G. Calzaferri, "Thermally stable luminescent lanthanide complexes in zeolite L," *Microporous and Mesoporous Materials*, vol. 121, no. 1–3, pp. 1–6, 2009.
- [57] S. Huber and G. Calzaferri, "Energy transfer from dye-zeolite L antenna crystals to bulk silicon," *ChemPhysChem*, vol. 5, no. 2, pp. 239–242, 2004.
- [58] G. Calzaferri, "Energy transfer in nanochannels," *Nuovo Cimento della Societa Italiana di Fisica B*, vol. 123, no. 10–11, pp. 1337–1367, 2008.
- [59] R. Q. Albuquerque and G. Calzaferri, "Proton activity inside the channels of zeolite L," *Chemistry: A European Journal*, vol. 13, no. 32, pp. 8939–8952, 2007.
- [60] Th. Förster, "Zwischenmolekulare Energiewanderung und Fluoreszenz," *Annalen der Physik*, vol. 437, no. 1–2, pp. 55–75, 1948.
- [61] Th. Förster, *Fluoreszenz Organischer Verbindungen*, Vandenhoeck & Ruprecht, Göttingen, Germany, 1951.
- [62] Th. Förster, "Excitation transfer," in *Comparative Effects of Radiation*, M. Barton, et al., Ed., pp. 300–319, John Wiley & Sons, New York, NY, USA, 1960.
- [63] K. Lutkouskaya and G. Calzaferri, "Transfer of electronic excitation energy between randomly mixed dye molecules in the channels of zeolite L," *Journal of Physical Chemistry B*, vol. 110, no. 11, pp. 5633–5638, 2006.

- [64] M. Pfenniger and G. Calzaferri, "Intrazeolite diffusion kinetics of dye molecules in the nanochannels of zeolite L, monitored by energy transfer," *ChemPhysChem*, vol. 1, no. 4, pp. 211–217, 2000.
- [65] D. R. Walt, "Nanomaterials: top-to-bottom functional design," *Nature Materials*, vol. 1, no. 1, pp. 17–18, 2002.
- [66] A. Böker, Y. Lin, K. Chiapperini, et al., "Hierarchical nanoparticle assemblies formed by decorating breath figures," *Nature Materials*, vol. 3, no. 5, pp. 302–306, 2004.
- [67] M. Bashouti, W. Salalha, M. Brumer, E. Zussman, and E. Lifshitz, "Alignment of colloidal CdS nanowires embedded in polymer nanofibers by electrospinning," *ChemPhysChem*, vol. 7, no. 1, pp. 102–106, 2006.
- [68] S.-J. Huo, X.-K. Xue, Q.-X. Li, S.-F. Xu, and W.-B. Cai, "Seeded-growth approach to fabrication of silver nanoparticle films on silicon for electrochemical ATR surface-enhanced IR absorption spectroscopy," *Journal of Physical Chemistry B*, vol. 110, no. 51, pp. 25721–25728, 2006.
- [69] L. Dai, A. Patil, X. Gong, et al., "Aligned Nanotubes," *ChemPhysChem*, vol. 4, no. 11, pp. 1150–1169, 2003.
- [70] G. A. Ozin and A. C. Arsenault, *Nanochemistry: A Chemical Approach to Nanomaterials*, Royal Society of Chemistry, Cambridge, UK, 2005.
- [71] S. J. Hurst, E. K. Payne, L. Qin, and C. A. Mirkin, "Multisegmented one-dimensional nanorods prepared by hard-template synthetic methods," *Angewandte Chemie International Edition*, vol. 45, no. 17, pp. 2672–2692, 2006.
- [72] T. Bein, "Zeolitic host-guest interactions and building blocks for the self-assembly of complex materials," *MRS Bulletin*, vol. 30, no. 10, pp. 713–720, 2005.
- [73] T. Bein, "Host-guest interactions in zeolites and periodic mesoporous materials," in *Studies in Surface Science and Catalysis*, J. Cejka, H. van Bekkum, A. Corma, and F. Schüth, Eds., vol. 168 of *Introduction to Zeolite Science and Practice*, pp. 611–657, Elsevier, Amsterdam, The Netherlands, 3rd revised edition, 2007.
- [74] A. Gouzinis and M. Tsapatsis, "On the preferred orientation and microstructural manipulation of molecular sieve films prepared by secondary growth," *Chemistry of Materials*, vol. 10, no. 9, pp. 2497–2504, 1998.
- [75] K. B. Yoon, "Organization of zeolite microcrystals for production of functional materials," *Accounts of Chemical Research*, vol. 40, no. 1, pp. 29–40, 2007.
- [76] J. S. Lee, H. Lim, K. Ha, H. Cheong, and K. B. Yoon, "Facile monolayer assembly of fluorophore-containing zeolite rods in uniform orientations for anisotropic photoluminescence," *Angewandte Chemie International Edition*, vol. 45, no. 32, pp. 5288–5292, 2006.
- [77] O. Bossart and G. Calzaferri, "Organisation and solubilisation of zeolite L crystals," *Chimia*, vol. 60, no. 4, pp. 179–181, 2006.
- [78] S. Yunus, F. Spano, G. Patrinoiu, et al., "Hexagonal network organization of dye-loaded zeolite L crystals by surface-tension-driven autoassembly," *Advanced Functional Materials*, vol. 16, no. 17, pp. 2213–2217, 2006.
- [79] I. Cucchi, F. Spano, U. Giovanella, et al., "Fluorescent electrospun nanofibers embedding dye-loaded zeolite crystals," *Small*, vol. 3, no. 2, pp. 305–309, 2007.
- [80] Z. Popović, M. Otter, G. Calzaferri, and L. De Cola, "Self-assembling living systems with functional nanomaterials," *Angewandte Chemie International Edition*, vol. 46, no. 32, pp. 6188–6191, 2007.
- [81] N. Bowden, A. Terfort, J. Carbeck, and G. M. Whitesides, "Assembly of mesoscale objects into ordered two-dimensional arrays," *Science*, vol. 276, no. 5310, pp. 233–235, 1997.
- [82] Z.-M. Huang, Y.-Z. Zhang, M. Kotaki, and S. Ramakrishna, "A review on polymer nanofibers by electrospinning and their applications in nanocomposites," *Composites Science and Technology*, vol. 63, no. 15, pp. 2223–2253, 2003.
- [83] H. J. Yu, S. V. Fridrikh, and G. C. Rutledge, "Production of submicrometer diameter fibers by two-fluid electrospinning," *Advanced Materials*, vol. 16, no. 17, pp. 1562–1566, 2004.
- [84] V. Vohra, A. Devaux, L.-Q. Dieu, et al., "Energy transfer in fluorescent nanofibers embedding dye-loaded zeolite L crystals," *Advanced Materials*, vol. 21, no. 10–11, pp. 1146–1150, 2009.
- [85] Z. Popović, M. Busby, S. Huber, G. Calzaferri, and L. De Cola, "Assembling micro crystals through cooperative coordinative interactions," *Angewandte Chemie International Edition*, vol. 46, no. 46, pp. 8898–8902, 2007.
- [86] M. Han, X. Gao, J. Z. Su, and S. Nie, "Quantum-dot-tagged microbeads for multiplexed optical coding of biomolecules," *Nature Biotechnology*, vol. 19, no. 7, pp. 631–635, 2001.
- [87] C. A. Strassert, M. Otter, R. Q. Albuquerque, et al., "Photoactive hybrid nanomaterial for targeting, labeling, and killing antibiotic-resistant bacteria," *Angewandte Chemie International Edition*, vol. 48, no. 42, pp. 7928–7931, 2009.
- [88] G. Calzaferri, H. Li, and D. Brühwiler, "Dye-modified nanochannel materials for photoelectronic and optical devices," *Chemistry: A European Journal*, vol. 14, no. 25, pp. 7442–7449, 2008.
- [89] D. Brühwiler, G. Calzaferri, T. Torres, et al., "Nanochannels for supramolecular organization of luminescent guests," *Journal of Materials Chemistry*, vol. 19, no. 43, pp. 8040–8067, 2009.
- [90] V. Vohra, G. Calzaferri, S. Destri, M. Pasini, W. Porzio, and Ch. Botta, "Toward White Light Emission through Efficient Two-Step Energy Transfer in Hybrid Nanofibers," *ACS Nano*. In press.

## Research Article

# Acylated 2-(N-arylaminomethylene)benzo[b]thiophene-3(2H)-Ones: Molecular Switches with Varying Migrants and Substituents

Alexander D. Dubonosov,<sup>1</sup> Vladimir P. Rybalkin,<sup>1</sup> Lydia L. Popova,<sup>2</sup> Alexey V. Tsukanov,<sup>1</sup> Yurii V. Revinsky,<sup>2</sup> Vladimir A. Bren,<sup>2</sup> and Vladimir I. Minkin<sup>1,2</sup>

<sup>1</sup> Southern Scientific Center of Russian Academy of Sciences, 344006 Rostov on Don, Russia

<sup>2</sup> Institute of Physical and Organic Chemistry, Southern Federal University, 344090 Rostov on Don, Russia

Correspondence should be addressed to Alexander D. Dubonosov, aled@ipoc.rsu.ru

Received 9 February 2009; Revised 7 May 2009; Accepted 22 May 2009

Recommended by Mohamed Sabry Abdel-Mottaleb

Synthesis and properties of photochromic acylated 2-(N-arylaminomethylene)benzo[b]thiophene-3(2H)-ones are described. Their structure largely depends on the nature of acyl migrant and in a less degree on N-aryl substituent.

Copyright © 2009 Alexander D. Dubonosov et al. This is an open access article distributed under the Creative Commons Attribution License, which permits unrestricted use, distribution, and reproduction in any medium, provided the original work is properly cited.

## 1. Introduction

2-(N-Acyl-N-arylaminomethylene)benzo[b]thiophene-3(2H)-ones represent a new family of photochromic molecular switches with fluorescent signalling [1], chiroptical [2], and chemosensor activity [3–5]. They may also serve as pH-sensors [6] and solar energy storage systems [7]. However the influence of the size and electronic properties of migrants and substituents in these compounds on their spectral, luminescent, and photochromic properties were insufficiently studied. To get a deeper insight into this problem we synthesized a series of novel N(O)-acylated compounds (2)–(8) and studied their structure, spectral properties, and quantum yields of the N→O acyl rearrangements.

## 2. Experimental

<sup>1</sup>H NMR spectra were recorded on a Varian Unity 300 spectrometer;  $\delta$  values were measured within 0.01 ppm. IR spectra in Nujol were measured using a Specord 75IR spectrometer. UV-Vis absorption spectra in toluene were obtained with a Specord M-40 spectrophotometer. Fluorescence emission and excitation spectra were recorded on a Hitachi 650–60 spectrofluorimeter. Irradiation of solutions

( $V = 2 \cdot 10^{-3}$  L) was carried out by filtered light of a high-pressure mercury lamp DRSh (250 W) supplied with a set of glass filters ( $\lambda_{\text{irr}} = 436$  nm). The intensity of light used for irradiation of the solutions was  $3 \cdot 10^{16}$  photons  $\cdot$  s<sup>-1</sup> for the spectral line 436 nm. Potassium ferrioxalate was used as the actinometer for the determination of quantum yields ( $\varphi$ ) of the photoreactions [8]. The samples had absorbance of 0.95 at  $\lambda_{\text{irr}} = 436$  nm ( $l = 1$  cm,  $V = 2 \cdot 10^{-3}$  L, rate of conversion of A→B  $\leq 5\%$ , the experimental error in  $\varphi$  is  $\pm 5\%$ ).

## 3. Results and Discussion

**3.1. Synthesis.** Compounds (2), (3a), (3b), (4a), (4b), (5), and (6) were synthesized according to the previously described procedure [9] (Scheme 1). Compound (4c) was synthesized according to procedure [7].

All the compounds obtained were divided into four groups according to the electronic and steric properties of acyl migrants and N-aryl substituents. The first group of acylated 2-(N-arylaminomethylene)benzo[b]thiophene-3(2H)-ones consists of the compounds with the gradually increased bulkiness of the migrant: R<sup>1</sup> = H (2), Me (3a), Et (3b), Pr<sup>i</sup> (4a), Bu<sup>t</sup> (5). The second one includes acylated ketoenamines possessing migrants with increasing

electron-donating properties of  $\alpha$ -C substituents: R<sup>1</sup> = H (2), Ph (4c), Me (3a), OMe (4b), NMe<sub>2</sub> (6).

The third series represents compounds with varying 4-substituents in the aroyl migrant: R<sup>3</sup> = H (4c), 4-MeO (7a), 4-Cl (7b), 4-NO<sub>2</sub> (7c). In the fourth group we united molecules with varying 4-substituent in N-Ar part of the molecule: R<sup>2</sup> = NMe<sub>2</sub> (8a), OMe (8b), Me (8c), I (8d), Br (8e), Cl (8f), F (8g), CN (8h), COMe (8i), NO<sub>2</sub> (8j). Their synthesis is shown on Scheme 2.

2-(*N*-aroyl-*N*-phenylaminomethylene)benzo[*b*]thiophene-3(2*H*)-ones (7a)–(7c) (general procedure). 2-(*N*-phenylaminomethylene)benzo[*b*]thiophene-3(2*H*)-one (1a) (1 mmol) was dissolved in 3 mL of acetonitrile in the presence of triethylamine and a solution of 1.2 mmol of corresponding aroyl chloride in 2 mL of acetonitrile was added at room temperature. The mixture was refluxed for 3–5 minutes. The precipitate was filtered and crystallized from toluene.

(i) 2-(*N*-4-methoxybenzoyl-*N*-phenylaminomethylene)benzo[*b*]thiophene-3(2*H*)-one (7a). (31%); mp 177–179°C; IR ( $\nu_{\max}/\text{cm}^{-1}$ , nujol): 1660, 1640, 1590, 1580, 1550; <sup>1</sup>H NMR (300 MHz, CDCl<sub>3</sub>):  $\delta$ 3.81 (3H, s, CH<sub>3</sub>), 6.80–7.84 (13H, m, Ar-H), 8.67 (1H, s, =CH); Anal. Calcd for C<sub>23</sub>H<sub>17</sub>NO<sub>3</sub>S: C, 71.30; H, 4.42; N, 3.61; Found: C, 71.19; H, 4.52; N, 3.73.

(ii) 2-(*N*-4-chlorobenzoyl-*N*-phenylaminomethylene)benzo[*b*]thiophene-3(2*H*)-one (7b). (64%); mp 215–216°C; IR ( $\nu_{\max}/\text{cm}^{-1}$ , nujol): 1640, 1580, 1560; <sup>1</sup>H NMR (300 MHz, CDCl<sub>3</sub>):  $\delta$ 7.16–7.85 (13H, m, Ar-H), 8.67 (1H, s, =CH); Anal. Calcd for C<sub>22</sub>H<sub>14</sub>ClNO<sub>2</sub>S: C, 67.43; H, 3.60; N, 3.57; Found: C, 67.50; H, 6.73; N, 3.41.

(iii) 2-(*N*-4-nitrobenzoyl-*N*-phenylaminomethylene)benzo[*b*]thiophene-3(2*H*)-one (7c). (57%); mp 211–212°C; IR ( $\nu_{\max}/\text{cm}^{-1}$ , nujol): 1690, 1680, 1600, 1580, 1560, 1520; <sup>1</sup>H NMR (300 MHz, CDCl<sub>3</sub>):  $\delta$ 7.18–8.17 (13H, m, Ar-H), 8.74 (1H, s, =CH); Anal. Calcd for C<sub>22</sub>H<sub>14</sub>N<sub>2</sub>O<sub>4</sub>S: C, 65.66; H, 3.51; N, 6.96; Found: C, 65.60; H, 3.66; N, 6.84.

(iv) 2-(*N*-acetyl-*N*-arylaminomethylene)benzo[*b*]thiophene-3(2*H*)-ones (8a)–(8j) (general procedure). Corresponding 2-(*N*-arylaminomethylene)benzo[*b*]thiophene-3(2*H*)-ones (1b)–(1n) [10] (1 mmol) were dissolved in acetic anhydride (2 mL) in the presence of triethylamine and refluxed for 5–10 minutes. The precipitate was filtered and crystallized from toluene.

(v) 2-{*N*-acetyl-*N*-(4-*N,N*-dimethylaminophenyl)aminomethylene}benzo[*b*]thiophene-3(2*H*)-one (8a). (77%); mp 245–246°C; IR ( $\nu_{\max}/\text{cm}^{-1}$ , nujol): 1690, 1640, 1590, 1550, 1510; <sup>1</sup>H NMR (300 MHz, CDCl<sub>3</sub>):  $\delta$ 2.03 (3H, s, CH<sub>3</sub>), 3.08 (6H, s, N(CH<sub>3</sub>)<sub>2</sub>), 6.77–7.82 (8H, m, Ar-H), 8.98 (1H, s, =CH); Anal. Calcd for C<sub>19</sub>H<sub>18</sub>N<sub>2</sub>O<sub>2</sub>S: C, 67.43; H, 5.36; N, 8.28; Found: C, 67.56; H, 5.28; N, 8.20.

(vi) 2-{*N*-acetyl-*N*-(4-methoxyphenyl)aminomethylene}benzo[*b*]thiophene-3(2*H*)-one (8b). (43%); mp 193–194°C; IR ( $\nu_{\max}/\text{cm}^{-1}$ , nujol): 1690, 1660, 1570, 1540; <sup>1</sup>H NMR (300 MHz, CDCl<sub>3</sub>):  $\delta$ 2.08 (3H, s, CH<sub>3</sub>), 3.94 (3H, s, OCH<sub>3</sub>), 7.02–7.83 (8H, m, Ar-H), 8.92 (1H, s, =CH); Anal. Calcd for C<sub>18</sub>H<sub>15</sub>NO<sub>3</sub>S: C, 66.44; H, 4.65; N, 4.30; Found: C, 66.59; H, 4.66; N, 4.18.

(vii) 2-{*N*-acetyl-*N*-(4-methylphenyl)aminomethylene}benzo[*b*]thiophene-3(2*H*)-one (8c). (83%); mp 210–212°C; IR ( $\nu_{\max}/\text{cm}^{-1}$ , nujol): 1700, 1650, 1580, 1550; <sup>1</sup>H NMR (300 MHz, CDCl<sub>3</sub>):  $\delta$ 2.05 (3H, s, COCH<sub>3</sub>), 2.52 (3H, s, CH<sub>3</sub>), 7.15–7.82 (8H, m, Ar-H), 8.95 (1H, s, =CH); Anal. Calcd for C<sub>18</sub>H<sub>15</sub>NO<sub>2</sub>S: C, 69.88; H, 4.89; N, 4.53; Found: C, 69.87; H, 4.74; N, 4.65.

(viii) 2-{*N*-acetyl-*N*-(4-iodophenyl)aminomethylene}benzo[*b*]thiophene-3(2*H*)-one (8d). (73%); mp 241–243°C; IR ( $\nu_{\max}/\text{cm}^{-1}$ , nujol): 1700, 1660, 1590, 1550; <sup>1</sup>H NMR (300 MHz, CDCl<sub>3</sub>):  $\delta$ 2.11 (3H, s, CH<sub>3</sub>), 7.03–7.94 (8H, m, Ar-H), 8.82 (1H, s, =CH); Anal. Calcd for C<sub>17</sub>H<sub>12</sub>INO<sub>2</sub>S: C, 48.47; H, 2.87; N, 3.32; Found: C, 48.38; H, 2.90; N, 3.32.

(ix) 2-{*N*-acetyl-*N*-(4-bromophenyl)aminomethylene}benzo[*b*]thiophene-3(2*H*)-one (8e). (85%); mp 218–219°C; IR ( $\nu_{\max}/\text{cm}^{-1}$ , nujol): 1700, 1660, 1590, 1560, 1550; <sup>1</sup>H NMR (300 MHz, CDCl<sub>3</sub>):  $\delta$ 2.12 (3H, s, CH<sub>3</sub>), 7.19–7.83 (8H, m, Ar-H), 8.82 (1H, s, =CH); Anal. Calcd for C<sub>17</sub>H<sub>12</sub>BrNO<sub>2</sub>S: C, 54.56; H, 3.23; N, 3.74; Found: C, 54.68; H, 3.17; N, 3.63.

(x) 2-{*N*-acetyl-*N*-(4-chlorophenyl)aminomethylene}benzo[*b*]thiophene-3(2*H*)-one (8f). (70%); mp 186–187°C; IR ( $\nu_{\max}/\text{cm}^{-1}$ , nujol): 1700, 1660, 1590, 1550; <sup>1</sup>H NMR (300 MHz, CDCl<sub>3</sub>):  $\delta$ 2.10 (3H, s, CH<sub>3</sub>), 7.19–7.84 (8H, m, Ar-H), 8.83 (1H, s, =CH); Anal. Calcd for C<sub>17</sub>H<sub>12</sub>ClNO<sub>2</sub>S: C, 61.91; H, 3.67; N, 4.25; Found: C, 62.03; H, 3.60; N, 4.27.

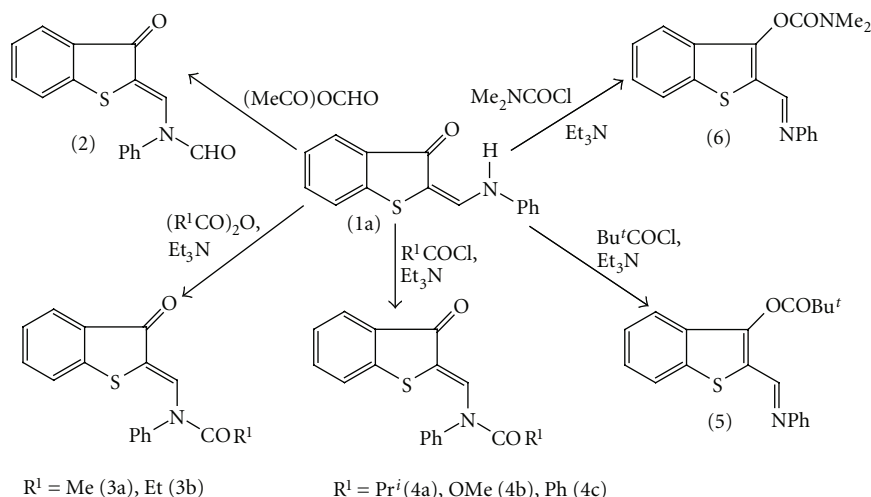
(xi) 2-{*N*-acetyl-*N*-(4-fluorophenyl)aminomethylene}benzo[*b*]thiophene-3(2*H*)-one (8g). (69%); mp 213–214°C; IR ( $\nu_{\max}/\text{cm}^{-1}$ , nujol): 1700, 1660, 1590, 1580, 1540; <sup>1</sup>H NMR (300 MHz, CDCl<sub>3</sub>):  $\delta$ 2.10 (3H, s, CH<sub>3</sub>), 7.20–7.84 (8H, m, Ar-H), 8.84 (1H, s, =CH); Anal. Calcd for C<sub>17</sub>H<sub>12</sub>FNO<sub>2</sub>S: C, 65.16; H, 3.86; N, 4.47; Found: C, 65.15; H, 3.95; N, 4.40.

(xii) 2-{*N*-acetyl-*N*-(4-cyanophenyl)aminomethylene}benzo[*b*]thiophene-3(2*H*)-one (8h). (57%); mp 215–216°C; IR ( $\nu_{\max}/\text{cm}^{-1}$ , nujol): 1690, 1670, 1580, 1560; <sup>1</sup>H NMR (300 MHz, CDCl<sub>3</sub>):  $\delta$ 2.21 (3H, s, CH<sub>3</sub>), 7.20–7.90 (8H, m, Ar-H), 8.73 (1H, s, =CH); Anal. Calcd for C<sub>18</sub>H<sub>12</sub>N<sub>2</sub>O<sub>2</sub>S: C, 67.48; H, 3.78; N, 8.74; Found: C, 67.54; H, 3.87; N, 8.62.

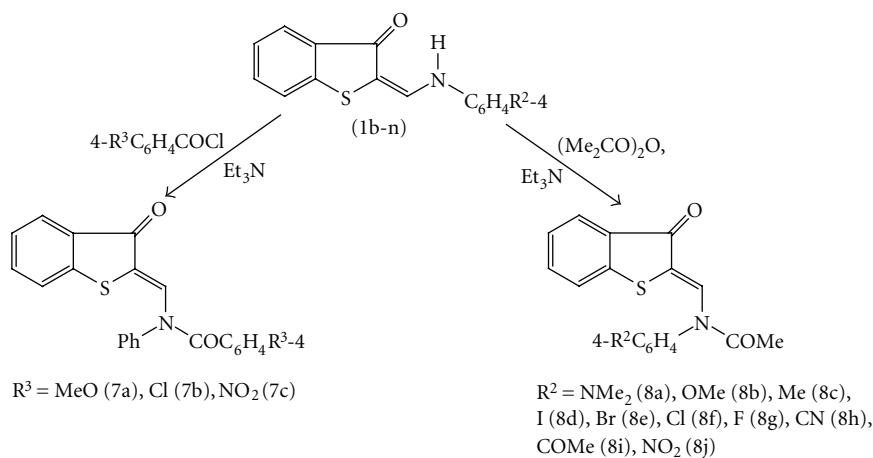
(xiii) 2-{*N*-acetyl-*N*-(4-acetylphenyl)aminomethylene}benzo[*b*]thiophene-3(2*H*)-one (8i). (48%); mp 186–187°C; IR ( $\nu_{\max}/\text{cm}^{-1}$ , nujol): 1695, 1670, 1660, 1595, 1570, 1550; <sup>1</sup>H NMR (300 MHz, CDCl<sub>3</sub>):  $\delta$ 2.16 (3H, s, NCOCH<sub>3</sub>), 2.74 (3H, s, COCH<sub>3</sub>), 7.15–8.18 (8H, m, Ar-H), 8.82 (1H, s, =CH); Anal. Calcd for C<sub>19</sub>H<sub>15</sub>NO<sub>3</sub>S: C, 67.64; H, 4.48; N, 4.15; Found: C, 67.69; H, 4.38; N, 4.22.

(xiv) 2-{*N*-acetyl-*N*-(4-nitrophenyl)aminomethylene}benzo[*b*]thiophene-3(2*H*)-one (8j). (37%); mp 199–200°C; IR ( $\nu_{\max}/\text{cm}^{-1}$ , nujol): 1700, 1670, 1600, 1580, 1560, 1530; <sup>1</sup>H NMR (300 MHz, CDCl<sub>3</sub>):  $\delta$ 2.22 (3H, s, CH<sub>3</sub>), 7.19–8.47 (8H, m, Ar-H), 8.74 (1H, s, =CH); Anal. Calcd for C<sub>17</sub>H<sub>12</sub>N<sub>2</sub>O<sub>4</sub>S: C, 59.99; H, 3.55; N, 8.23; Found: C, 59.86; H, 3.63; N, 8.23.

**3.2. Photochromic Properties.** According to the performed IR and NMR spectral study compounds (2)–(4), (7), and (8) exist in solutions as the *N*-acylated isomers. Their IR-spectra contain absorption bands of the amide (1660–1730 cm<sup>-1</sup>)



SCHEME 1



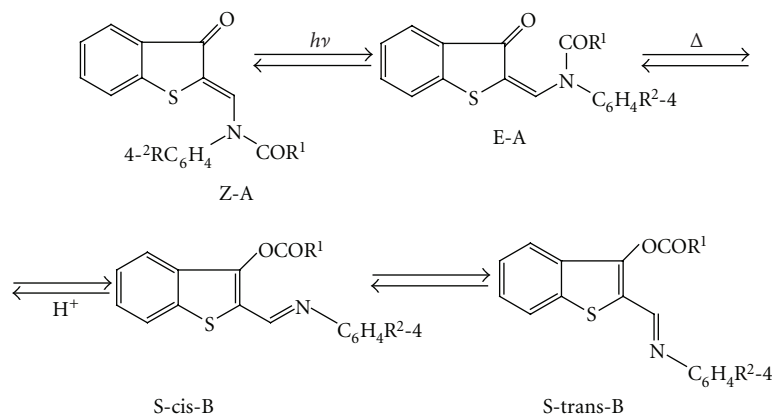
SCHEME 2

and exocyclic carbonyl groups ( $1660\text{--}1680\text{ cm}^{-1}$ ).  $^1\text{H}$  NMR spectra consist of characteristic signals of methine protons at  $8.70\text{--}9.00\text{ ppm}$  which correspond to the initial *Z*-configuration [3]. *N*-Acyated ketoenamines (2)–(4), (7), and (8) absorb in  $420\text{--}430\text{ nm}$  spectral region (Table 1). On the contrary, compounds (5), (6) correspond to *O*-acyl derivatives. They possess typical absorption in the UV spectral region ( $338\text{--}342\text{ nm}$ ) [9] and their IR spectra contain ester carbonyl group signals ( $1720\text{--}1750\text{ cm}^{-1}$ ).

For the majority of *N*-acylated forms A of compounds (3), (4), (7), (8) irradiation ( $\lambda_{\text{irr}} = 436\text{ nm}$ ) of toluene solutions results in *Z*→*E*-photoisomerization around the C=C bond followed by a fast thermal *N*→*O* acyl migration and *S-cis*→*S-trans* isomerization of *O*-acyl compounds B (Scheme 3, Figure 1). Quantum yields ( $\phi$ ) of the *A*→*B* photorearrangement include all stages shown on Scheme 3 from *Z*-A to *S-trans*-B though we consider all thermal rearrangements to be very rapid [7]. These summarized quantum yields are given in Table 1.

In the series of compounds with varying migrant volume, the smallest migrant CHO (2) inhibits *A*→*B* photorearrangement and restricts it by the thermally reversible *Z*→*E*-photoisomerization. The specific feature of this process is the formation of photostationary state depending on the wavelength of irradiation light (Figure 2). *N*-Acy derivatives (3a), (3b), and (4a) reveal typical photochromic behavior (Scheme 3). The compound with the most bulky  $\text{Bu}^t$  (5) substituent exists in the thermodynamically stable *O*-form B. Its photoinitiated reactions are limited by thermally reversible *anti-syn* isomerization around C=N bond.

The representatives of second group (2), (3a), (4b), (4c) with varying electronic migrant exist in *N*-acyl form A and demonstrate *N*→*O* acyl rearrangement in accordance with Scheme 3 (except above described ketoenamine 2). The compound with the strong electron-donating  $\alpha\text{-C}$  substituent  $\text{NMe}_2$  (6) occurs in the form of *O*-acyl isomer B and shows only *anti-syn* isomerization around the C=N bond, similar to (5).



SCHEME 3

TABLE 1: Spectral characteristics (long-wave length maxima) of (2)–(8) in acetonitrile solutions and quantum yields ( $\varphi$ ) of the A→B rearrangement.

Comp.	Absorption of (Z-A), $\lambda_{\max}$ (nm), ( $\epsilon \times 10^{-4}$ , $\text{dm}^3 \text{mol}^{-1} \text{cm}^{-1}$ )	$\varphi_{\text{A} \rightarrow \text{B}}$	Absorption of (S-trans-B), $\lambda_{\max}$ (nm), ( $\epsilon \times 10^{-4}$ , $\text{dm}^3 \text{mol}^{-1} \text{cm}^{-1}$ )
2*	424 (1.10)	—	—
3a*	427 (1.04)	0.60	338 (2.32)
3b	425 (1.24)	0.63	339 (2.27)
4a	427 (1.28)	0.62	342 (2.24)
4b*	422 (1.17)	0.41	333 (0.81)
4c*	423 (1.36)	0.52	340 (2.14)
7a	430 (1.42)	0.48	342 (2.19)
7b	430 (1.32)	0.40	343 (2.09)
7c	431 (1.34)	0.002	—
8a	430 (1.41)	—	—
8b	425 (1.22)	0.50	353 (2.20)
8c	425 (1.26)	0.50	345 (2.25)
8d	425 (1.23)	0.47	350 (2.56)
8e	424 (1.22)	0.51	347 (2.51)
8f	424 (1.23)	0.49	347 (2.51)
8g	424 (1.19)	0.41	342 (2.30)
8h	424 (1.13)	0.48	346 (2.52)
8i	424 (1.29)	0.45	350 (2.74)
8j	424 (1.14)	0.29	356 (2.65)
5	—	—	338 (2.36)
6	—	—	342 (2.14)

\* See [9].

Varying of 4-substituent in aroyl group (7a)–(7c) results in decrease of quantum yield A→B rearrangement almost up to zero (Table 1) as correlated with the increase of electron-withdrawing properties of  $\text{R}^3$ .

In the fourth series the substituents in the position 4 of the N-Ar moiety of the compounds (8b)–(8j) only slightly affect the character of the photochromic A→B photorearrangement (Table 1). The photochemical transformations of (8a) with  $\text{NMe}_2$  substituent lead to formation of a mixture

of O- and N-isomers with predominance of the last one due to overlap of long-wavelength absorption bands of initial compound and photoproduct.

In toluene solutions, at 293 K, N-acylated compounds (2)–(4), (7), and (8) exhibit weak fluorescence with maxima at 460–470 nm which extinguishes after the rearrangement into the O-acetyl isomers B due to the fast intersystem crossing processes (“on-off” process) [9]. The B→A back reaction occurring when passing dried hydrogen chloride

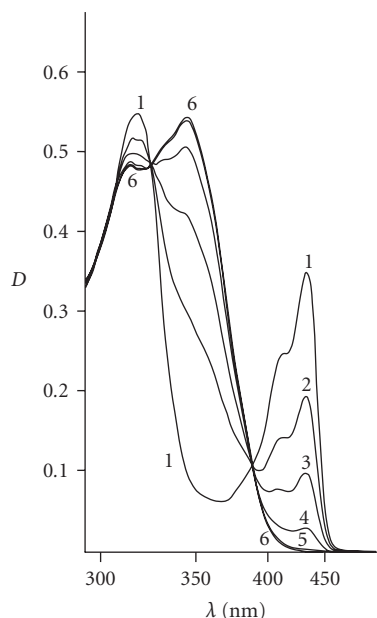


FIGURE 1: Absorption spectra of (8b) in toluene solution before irradiation (1); after 5 seconds (2); 10 seconds (3); 20 seconds (4); 40 seconds (5); 120 seconds (6) of irradiation ( $\lambda_{\text{irr}} = 436 \text{ nm}$ ,  $C = 2.5 \cdot 10^{-5} \text{ M}$ ).

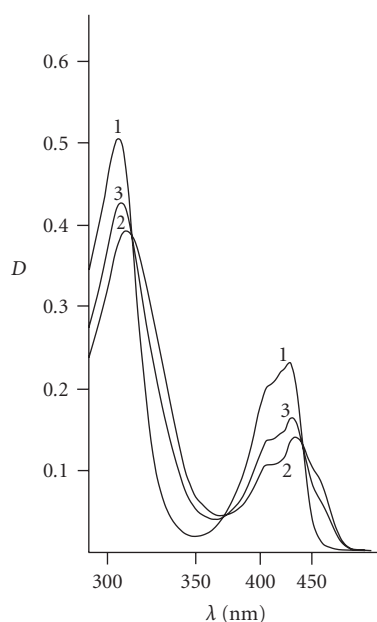


FIGURE 2: Absorption spectra of (1a) in toluene solution before irradiation (1); after 120 seconds (2) of irradiation ( $\lambda_{\text{irr}} = 365 \text{ nm}$ ) and after 120 seconds (3) of irradiation ( $\lambda_{\text{irr}} = 436 \text{ nm}$ );  $C = 2.5 \cdot 10^{-5} \text{ M}$ .

through a toluene solution of form B results in complete restoration of the initial absorption and emission spectra of form A (“off-on” process).

## 4. Conclusions

Series of N(O)-acylated 2-(N-arylamino)methylene)benzo[*b*]thiophene-3(2*H*)-ones with varying electronic and steric properties of substituents in the acyl migrants and N-aryl groups were prepared. By means of electronic absorption, vibrational, and  $^1\text{H}$  NMR spectroscopy, it was shown that ketoenamine with the smallest formyl substituent undergoes only reversible *Z*→*E* photoisomerization. The compounds containing the strongest electron-donating ( $\text{NMe}_2$ ) and the most bulky ( $\text{Bu}^t$ ) substituents in acyl migrants represent the thermodynamically stable O-isomers. Their irradiation results only in the thermally reversible *anti-syn* isomerization around the C=N bond. The other compounds exhibit negative photochromism ( $\lambda_{\text{max B}} < \lambda_{\text{max A}}$ ) based on photoinduced *Z*→*E* photoisomerization followed by the thermal N→O transfer of the acyl group.

## Acknowledgments

This work was supported by Russian Foundation for Basic Research (Grants N 06-03-32561, 09-03-00052), RF Ministry of Education and Science (Grants RNP.16012 and RNP.2348) and President’s of RF Grant (NSh-363.2008.3).

## References

- [1] V. A. Bren, A. D. Dubonosov, O. G. Karamov, et al., “2-[N-acetyl-N-(2-fluorenyl)aminomethylene]benzo[*b*]thiophen-3(2*H*)-one, a molecular fluorescent switch,” *Russian Journal of Organic Chemistry*, vol. 38, no. 11, pp. 1698–1699, 2002.
- [2] V. P. Rybalkin, J. Y. Vorob’eva, G. S. Borodkin, et al., “Synthesis and properties of photoacylotropic (2*Z*)-2-(N-acyl-N-arylamino)methylidene)benzo[*b*]thiophen-3(2*H*)-ones with a chiral migrating group,” *Russian Chemical Bulletin*, vol. 54, no. 12, pp. 2783–2789, 2005.
- [3] V. A. Bren, A. D. Dubonosov, V. I. Minkin, et al., “Photochromic crown-containing molecular switches of chemosensor activity,” *Journal of Physical Organic Chemistry*, vol. 20, no. 11, pp. 917–928, 2007.
- [4] V. A. Bren, A. D. Dubonosov, V. I. Minkin, et al., “Photochromic cation sensors,” *Molecular Crystals and Liquid Crystals*, vol. 431, pp. 417–422, 2005.
- [5] A. D. Dubonosov, V. I. Minkin, V. A. Bren, et al., “Photochromic 2-(N-acyl-N-arylamino)methylene)benzo[*b*]thiophene-3(2*H*)-ones with fluorescent labels and/or crown-ether receptors,” *Archive for Organic Chemistry*, vol. 2003, no. 13, pp. 12–20, 2003.
- [6] V. A. Bren, A. D. Dubonosov, V. I. Minkin, et al., “Molecular switching and PET effect in the molecules of 2-(9-anthrylmethylaminomethylene)benzo[*b*]thiophene and its N-acetyl derivative,” *Russian Journal of Organic Chemistry*, vol. 38, no. 12, pp. 1813–1814, 2002.
- [7] V. I. Minkin, V. A. Bren, and A. E. Lyubarskaya, *Organic Photochromes*, Consultants Bureau, New York, NY, USA, 1990.
- [8] C. A. Parker, *Photoluminescence of Solutions*, Elsevier, Amsterdam, The Netherlands, 1968.

- [9] V. P. Rybalkin, L. L. Popova, A. V. Tsukanov, A. D. Dubonosov, V. A. Bren, and V. I. Minkin, "*N(O)*-acylated 2-(*N*-phenylaminomethylene)benzo[*b*]thiophene-3(2*H*)-ones as molecular switches with a variable migrant," *High Energy Chemistry*, vol. 42, no. 7, pp. 606–609, 2008.
- [10] V. A. Bren, V. I. Usacheva, and V. I. Minkin, "Benzenoid—quinonoid tautomerism of azomethines and their structural analogs," *Chemistry of Heterocyclic Compounds*, vol. 8, no. 7, pp. 836–840, 1974.

## Research Article

# Multifunctional Spirocyclic Systems

**Boris Lukyanov,<sup>1</sup> Gennadii Vasilyuk,<sup>2</sup> Eugene Mukhanov,<sup>1</sup> Leonid Ageev,<sup>3</sup>  
Maria Lukyanova,<sup>1</sup> Yury Alexeenko,<sup>4</sup> Serguei Besugliy,<sup>4</sup> and Valeri Tkachev<sup>5</sup>**

<sup>1</sup>Institute of Physical and Organic Chemistry, Southern Federal University, Rostov-on-Don 344090, Russia

<sup>2</sup>Physical engineering department, Yanka Kupala State University, Grodno, 230023 Belorussia, Belarus

<sup>3</sup>Physical department, V. Karazin Kharkiv National University, Kharkiv 61077, Ukraine

<sup>4</sup>Southern Scientific Center, Russian Academy of Sciences, Rostov-on-Don 344006, Russia

<sup>5</sup>Institute of Problems of Chemical Physics, Russian Academy of Science, Chernogolovka 142432, Russia

Correspondence should be addressed to Boris Lukyanov, bluk@ipoc.rsu.ru

Received 26 March 2009; Revised 17 August 2009; Accepted 18 October 2009

Recommended by Mohamed Sabry Abdel-Mottaleb

New spiropyrans with different substituents in the benzopyran fragment have been synthesized and investigated. It was shown that introduction of aldehyde group in the structure of spiropyrans gives a possibility to obtain new functionalized compounds. Effects of the substituents on the photochromic behavior were studied.

Copyright © 2009 Boris Lukyanov et al. This is an open access article distributed under the Creative Commons Attribution License, which permits unrestricted use, distribution, and reproduction in any medium, provided the original work is properly cited.

## 1. Introduction

Photochromic compounds based on spiropyrans as well as [2H]-chromenes are perspective photosensitive materials for molecular switches, optical filters with modulated transmission, and hybrid multifunctional materials. Conceptual aspects of a spiropyran practical application are based on photo-, thermo-, solvate-, and electrochromic properties [1].

Spiropyrans are applicable for using in molecular logic devices, photochromic and electrooptical devices [2], and multifunctional artificial receptors [3]. Photochromic spiropyrans can be used for creation of various types of optical memory [4] in quantum computers.

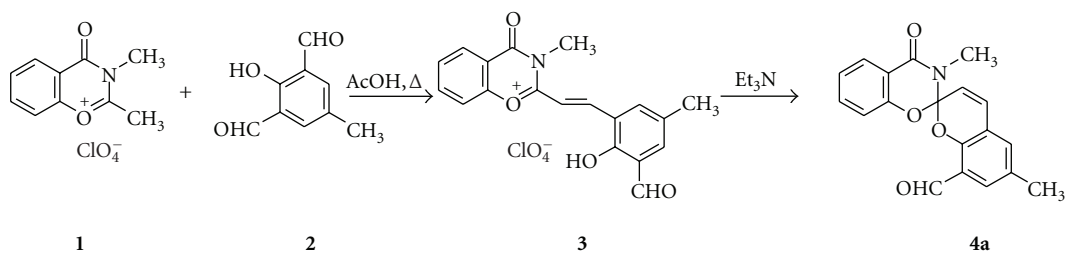
Reactions of different functional groups give an opportunity to obtain compounds with a variety of untraditional  $\pi$ -acceptor substituents, which can dramatically change

spiropyran properties. Synthesis of the differently substituted spiropyrans and results of these structural modifications will be discussed in this work.

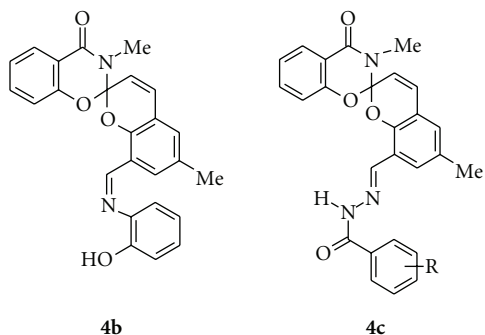
## 2. Results and Discussion

Previously we synthesized and studied number of spiropyrans of benzoxazinone and indoline series [5]. We decided to continue our research of aldehyde-substituted spirocompounds.

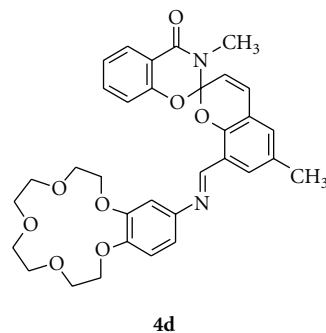
8'-Formyl-3,6'-dimethyl-4-oxo-3,4-dihydrospiro-2H-1,3-benzoxazine-2,2'-[2H]chromene **4a** was synthesized by the reaction of benzoxazinonium perchlorate **1** with 2,6-diformyl-4-methyl-phenol **2** followed by cyclization of obtained merocyanine salt **3**.



Reactivity of the aldehyde group in the benzopyran part allows to obtain derivatives figures **4b**, **c** containing azomethine and hydrazine fragment as a result of the reaction with amines and hydrazines correspondingly [6]. Multifunctional spirocyclic compounds and derivatives of spiropyrans possessing the ability to form mono- and binuclear complexes with transition metals could attract great interest due to their potential application as active light-sensitive components of the organic and composite nanostructures.

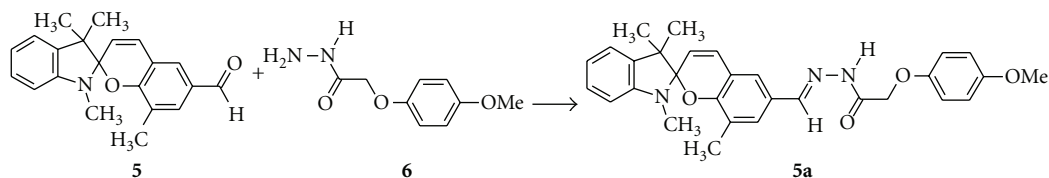


Spirocompound **4d** with the benzocrown-5 fragment was synthesized [7]. The benzocrown-5 fragment in **4d** was connected to the [2H]-chromene part through a conjugated  $\pi$ -electron-withdrawing C=N bond to prolong the conjugation



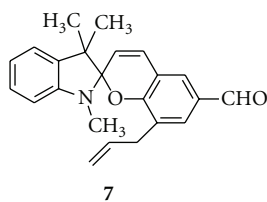
The complex formed by capture of metal ion in the crown-ether cavity could be an original  $\pi$ -acceptor substituent. Additional  $\pi$ -acceptor nitrosubstituent could turn on the photochromic properties in spiropyrans containing azomethyne substituents [8].

Spiropyran **5** was synthesized by condensation of the 1,2,3,3-tetramethylindolenilium salt with the 2,4-diformyl-6-methyl phenol. New compound **5a** was obtained after condensation with the *para*-methoxy-phenoxyacetic acid hydrazide **6**.



Presence of the chelating hydrazide fragment in the structure **5a** allowed to expect a complex compound formation with metal ions. It was shown that methoxy- and methyl- substituents in the benzopyran part of compound **5a** increase solubility and permit to carry out a detailed study of the obtained complex properties. In addition, the unshared electronic pairs of the methoxy group oxygen atom could expand the possibilities of complexation.

Also new aldehyde-substituted spiropyran **7** was synthesized by condensation of the 1, 2, 3, 3-tetramethylindolenilium salt with corresponding aldehyde.



### 3. Photochromic Properties

Spiropyran **4a** containing  $\pi$ -acceptor substituent possesses photochromic properties in solid state as well as in solution [9]. Thin films of spiropyran **4a**, which were prepared by thermal vacuum deposition on glass and quartz supports, turned colored under UV irradiation at  $\lambda_{\max} = 365$  nm. The resulting colored form is characterized by absorption in the visible region with  $\lambda_{\max} = 605$  nm and the lifetime of 1 hour (Figure 1).

Spiropyrans **4b**, **c** do not exhibit photochromic properties. Such behavior could be explained by the fact that modification of the 8'-aldehyde group substantially reduced the electron-accepting effect of this group. Consequently it reduces the polarity of the C<sub>spiro</sub>-O bond and negatively affects on photochromic properties of the compounds.

It was shown that obtaining of the colored merocyanine products **4d** does not occur under irradiation with UV-light (365 nm). Only reversible E-Z isomerization was observed under the experimental condition. The complex formed

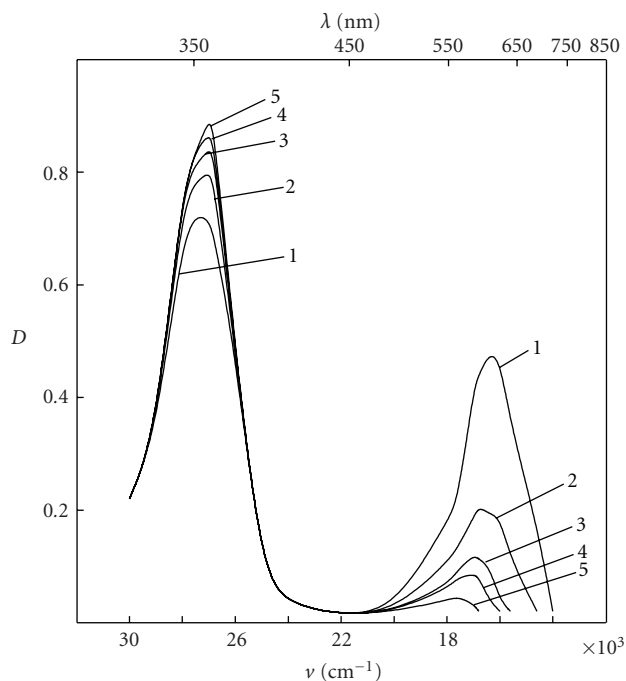


FIGURE 1: Electronic absorption spectra of the irradiated film of spiropyran **4a**: 1, the irradiated form (reverse dark reaction). Time after irradiation/min: 2, 5; 3, 15; 4, 30; 5, 60.

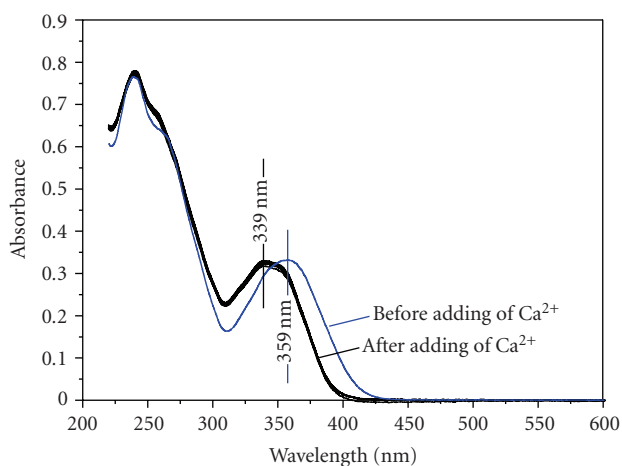


FIGURE 2: Changes in the absorption spectra of **4d** solution after adding of calcium ions.

by possible capture of a metal ion by the crown ether cavity may be a unique additional electron-withdrawing substituent, which activates photochromic properties in spiropyran containing an azomethine substituent. Adding of the lithium ions to the solution of **4d** does not lead to the breaking of  $C_{\text{spiro}}-O$  bond in contrast to the spiropyran of indoline series. However, hypsochromic shift of the absorption maxima (20 nm) was observed after adding of the calcium ions to the solution of **4d**. This fact was explained by the interaction between cyclic spiroform **4d** and  $Ca^{2+}$  ions (Figure 2).

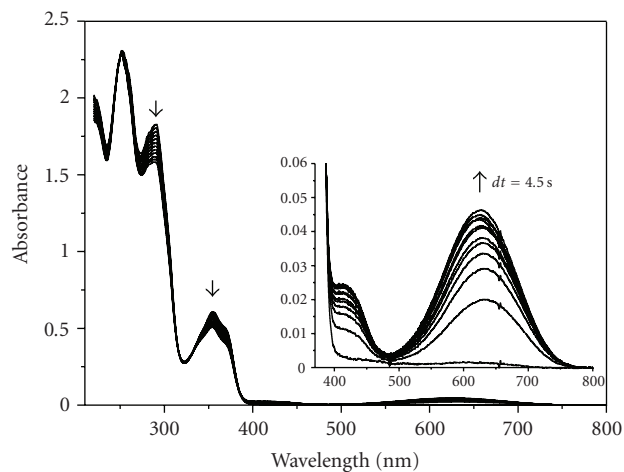
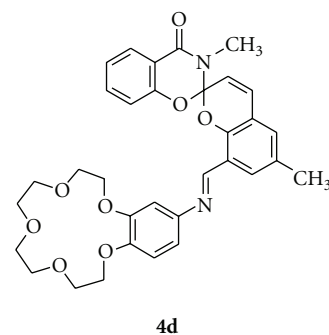


FIGURE 3: Absorption spectra of the compound **5a** in acetonitrile ( $C = 6,43 \times 10^{-5} M$ ,  $T = 30^\circ C$ ) under irradiation in stationary conditions by light  $\lambda_{\text{max}} 365 \text{ nm}$ .



Spiropyran **5a** undergoes reversible photochromic transformations and new long-wave maxima appears at the 630 nm under irradiation of the UV-light with the  $\lambda = 365 \text{ nm}$  in stationary conditions.

The system behavior in UV spectral region is essentially different for photo- (Figure 3) and back thermal reaction (Figure 4). Effective route for irreversible process could be the reason of such properties. Changing of the long-wave absorption band form is observed during back thermal reaction that could be explained by obtaining of several cis-trans merocyanine isomers.

This compound is a potential chemosensor due to its possibility to capture metal ions by chelating hydrazone fragment. This process could be interesting for using in active light-sensitive element of nanostructural materials.

Addition of the zinc salt to the compound **5a** acetonitrile solution results in strong coloration and change of the spectrum (Figure 5). Irradiation of the solution with the light 546/365 nm does not lead to any changes in the absorption spectra. This photochromic behavior could be the evidence of the  $C_{\text{spiro}}-O$  bond breaking and consequent involving of the oxygen atom into complex formation with metal ion that dramatically stabilizes merocyanine isomer. Obtained spectrum is probably the superposition of the different complex compound spectra.

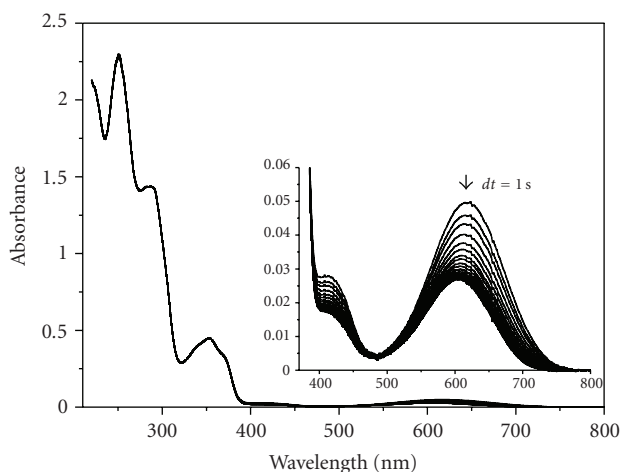


FIGURE 4: Change in the absorbance spectra of the compound **5a** in acetonitrile ( $C = 6,43 \times 10^{-5}$  M,  $T = 30^\circ\text{C}$ ) after irradiation (back thermal reaction).

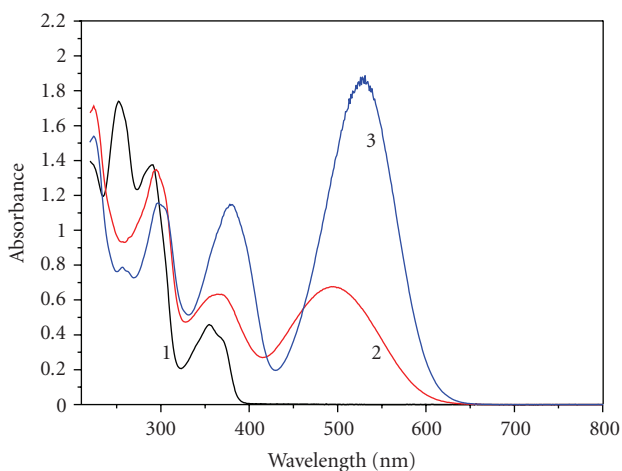
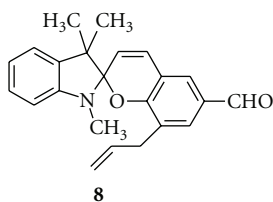


FIGURE 5: Absorption spectra of the compound **5a** in acetonitrile ( $C = 4,82 \times 10^{-5}$  M,  $T = 30^\circ\text{C}$ ) before (1), immediately after (2) and 20 seconds after (3) addition of zinc salt ( $[\text{Zn}^{++}] = 1,12 \times 10^{-3}$ ).

Photochromic properties of compound **7** implanted at the oligocarbonatedimethylacrylate film were investigated. Absorption spectrum of the spirocyanine **7** in the stationary conditions is represented on Figure 6. Open merocyanine isomer is produced under irradiation of the polymer film of compound **7** that leads to the appearance of absorption maxima at the 585 nm.



It is proposed to use photochromic compounds containing polymerized substituent in the structure as

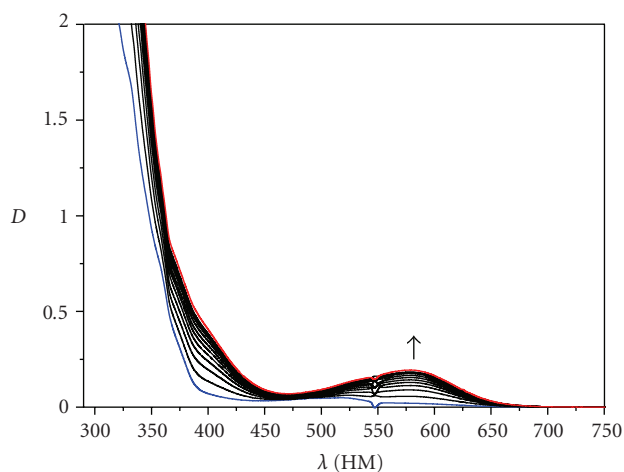


FIGURE 6: Absorption spectra of the spirocyanine **7** in the oligocarbonatedimethylacrylate film during the photocoloration process ( $\lambda_{\text{irr}} = 365$  nm;  $dt = 10$  s;  $T = 20^\circ\text{C}$ ).

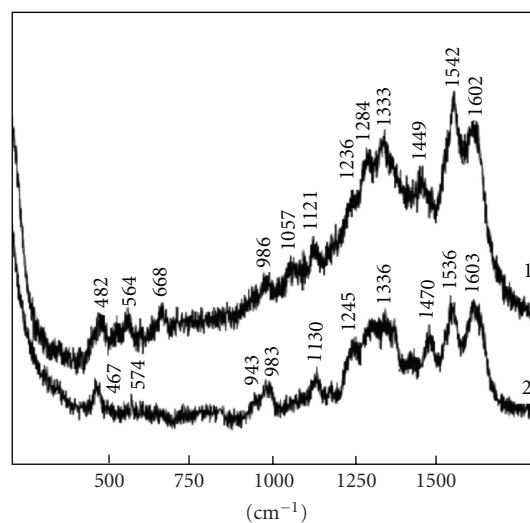


FIGURE 7: The SERS spectra ( $\lambda_{\text{exc}} = 514.5$  nm) of compound **5a** adsorbed on the annealed (1) and unannealed (2) silver films.

photochromic component in development of the next-generation intraocular lenses. These devices are very important due to the physiologically proved strategy of the retina protection and essential reduction of quantity of the short wave light reaching a retina and pigmentary epithelium.

#### 4. SERS and AFM Investigations

Study of the structure and photophysical properties of photochromes in an adsorbed state is of great importance for practical applications. One of the most efficient methods applied to investigate adsorbates is the spectroscopy of surface enhanced Raman scattering (SERS) [10]. Structure of the compound **5a** adsorbed on the annealed and unannealed silver films was investigated (Figure 7).

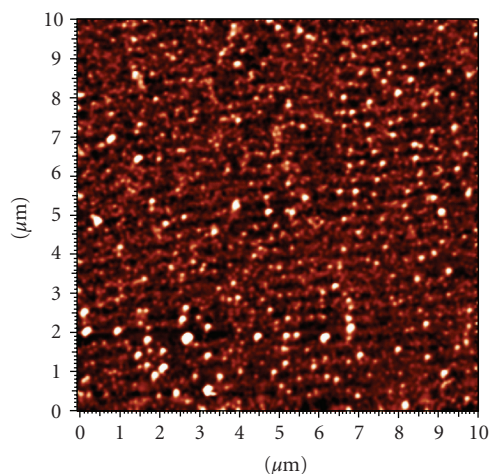


FIGURE 8: AFM-images of the photosensitive layer based on the optically attained (3 minutes) nanostructured AgCl-Ag.

In the SERS spectra the typical band of the colorless spiropyran form at about  $1640\text{ cm}^{-1}$  is absent [11]. Consequently, in our experiments with application of the SERS spectroscopy only the colored (with an open pyran cycle) form of the spiropyran molecules is detected. The equilibrium between the colorless and colored forms is shifted to the merocyanine on the silver surface. The photochromism in investigated solutions is manifested only with apparently low quantum yields and very small concentration of the open form. The dissociation of the adsorbed molecules, that is, the opening of the pyran ring at the adsorbed state can be associated with the fact that the energy of  $C_{\text{spiro}}\text{-O}$  bond decreases because of the spiro-oxygen interaction with the sorbent surface.

Using of the light-sensitive layers containing nanostructured colloid argentums (like AgCl-Ag) in the capacity of SERS-active substrates could give additional amplification of the SERS signal. Thin photosensitive layers of AgCl-Ag had been produced by the thermal vacuum deposition on the glass and quartz surfaces. Absorption spectra and AFM-images of the thin films were taken. The aggregate of the Ag granules with vertical dimensions  $5 \cdot \cdot \cdot 40\text{ nm}$  and horizontal dimensions  $50 \cdot \cdot \cdot 100\text{ nm}$  (Figure 8) acts like colloid and determines resonant absorption of the light in the AgCl-Ag films. Maximum of the colloidal absorption band for the AgCl-Ag films is located at the  $530\text{ nm}$  (Figure 9).

## 5. Experimental

The electronic spectra of the investigated compounds were recorded at room temperature on a Varian Carry spectrometer. The absorption spectra before and after irradiation were recorded on a Specord UV-Vis spectrometer fitted with a special cryostat for low-temperature measurements. The excitation source was a DRSh-250 mercury lamp with light filters isolating light with  $\lambda_{\text{max}}$  313 and 365 nm.

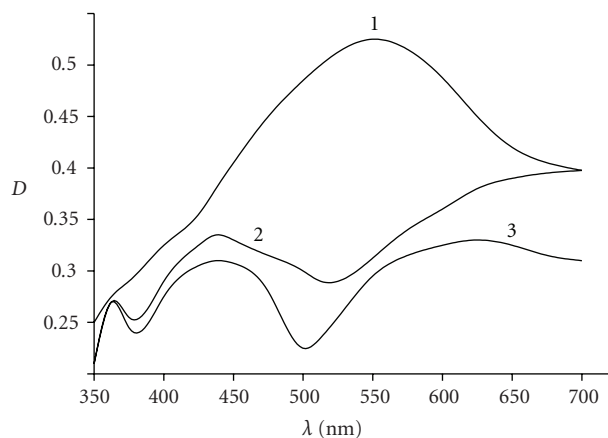


FIGURE 9: Absorption spectra of the the optically attained nanostructured AgCl-Ag: 1 minute before exposition; 2-3 minutes of exposition; 3-5 minutes of exposition by laser 514 nm, 30 mW.

5.1. *8'-Formyl-3,6-dimethyl-4-oxo-3,4-dihydrospiro-2H-1,3-benzoxazine-2,2'-[2H]chromene 4a*. Compound **4a** was prepared from benzoxazinonium perchlorate **1** with 2,6-diformyl-4-methyl-phenol **2** by a procedure described previously [12]. Yield—22 %. M.p.  $146^{\circ}\text{C}$  (EtOH). Found (%): C, 71.07; H, 4.64; N, 4.54.  $\text{C}_{19}\text{H}_{15}\text{NO}_3$ . Calculated (%): C, 71.02; H, 4.70; N, 4.36. IR,  $\nu/\text{cm}^{-1}$ : 1670 (C=O); 1638, 1610, 1582 (C=C); 958, 936 (C—O).  $^1\text{H NMR}$  ( $\text{CDCl}_3$ ),  $\delta$ : 2.33 (s, /3 H, 6'-Me); 3.04 (s, 3 H, N—Me); 6.00 (d, 1 H, 3'-H,  $J = 12.5\text{ Hz}$ ); 6.30–8.13 (m, 7 H); 9.75 (s, 1 H, 8'-CHO).

5.2. *8'-(3-Iminobenzo-15-crown-5)-3,6'-dimethyl-4-oxo-3,4-dihydrospiro(2H-1,3-benzoxazine-2,2'-[2H]-chromene) 4d*. 4-Aminobenzo-15-crown-5 (0.09 g, 0.031 mmol) was added to a solution of 8'-formyl-3,6'-dimethyl-4-oxo-3,4-dihydrospiro(2H-1,3-benzoxazine-2,2'-[2H]-chromene) **4a** (0.1 g, 0.3 mmol) in ethanol (3 ml) at reflux. The solution was heated at reflux for 30 minutes. The solvent was distilled off in vacuum and the residue obtained was recrystallized from ethanol to give 0.15 g (81%) **4d**. M.p.  $153\text{--}154^{\circ}\text{C}$ . Found, %: C 67.42; H 5.93; N 4.65.  $\text{C}_{33}\text{H}_{34}\text{N}_2\text{O}_6$ . Calculated, %: C 67.56; H 5.84; N 4.78. IR,  $\nu/\text{cm}^{-1}$ : 1680 (C=N), 1642 (C=O), 1617, 1578 (C=C), 1264 (C—N), 1148, 974, 952 (C—O).  $^1\text{H NMR}$  ( $\text{CDCl}_3$ ),  $\delta$ , ppm ( $J, \text{ Hz}$ ): 2.35 (1 H, s,  $\text{CH}_3$ ); 3.19 (1 H, s, N— $\text{CH}_3$ ); 3.64–4.18 (16 H, m, O— $\text{CH}_2\text{—CH}_2\text{—O}$ ); 6.12 (1 H, d,  $J = 9.7$ , H-3'); 6.39 (1 H, dd,  $J = 8.5, J = 2.3$ , H-5''); 6.54 (1 H, d,  $J = 2.3$ , H-3''); 6.74 (1 H, d,  $J = 8.5$ , H-6''); 6.84 (1 H, d,  $J = 8.0$ , H-8); 7.00 (1 H, d,  $J = 9.7$ , H-4'); 7.10–7.20 (2H, m, H-6, H-5'); 7.43 (1 H, m, H-7); 7.86 (1 H, m, H-7'); 8.04 (1 H, d,  $J = 7.8$ , H-5); 8.26 (1 H, s, N=CH).

5.3. *Spiropyran 5a*. To *para*-methoxy-phenoxyacetic acid hydrazide **6** (1.96 g, 0.01 mol) in benzene (10 ml) we added an equivalent amount of the spiropyran **5** (3.19 g, 0.01 mol). The mixture was refluxed for 1 hour and allowed to stand until a precipitate had separated. The precipitate was filtered off, dried, and recrystallized from ethanol. Yield 2.8 g (56%). M.p.  $194\text{--}196^{\circ}\text{C}$ .

Found, %: C 72.51; H 6.22; N 8.40.  $C_{30}H_{31}N_3O_4$ . Calculated, %: C 72.43; H 6.24; N 8.45. IR,  $\nu/cm^{-1}$ : 1673 (C=N), 1639 (C=O), 1610, 1583, 1572 (C=C), 1259 (C-N), 1135, 961, 952 (C-O).

$^1H$  NMR ( $CDCl_3$ ),  $\delta$ , ppm. ( $J$ , Hz): 1.19, 1.30 (6 H, 2-s, gem. ( $CH_3$ )<sub>2</sub>); 2.25 (3 H, s, 8'- $CH_3$ ); 2.78 (3 H, s, N- $CH_3$ ); 3.8 (3 H, s, O- $CH_3$ ); 4.58 (2 H, c, - $CH_2$ -); 5.7 (1 H, d,  $J$  = 8.5); 6.52–7.8 (11 H, m, aromatic H); 8.06 (1 H, s, N=CH); 9.4 (1 H, s, -NH-).

5.4. 6'-Formyl-8'-allyl-1,3,3-trimethylspiroindoline-2,2'-[2H]chromene 7. Piperidine (0.1 ml, 1.1 mmol) was added dropwise with heating to a solution of 2,4-diformyl-6-allylphenol (189 mg, 1 mmol) and 1,2,3,3-tetramethylindolenium perchlorate (274 mg, 1 mmol) in 2-propanol (5 ml). The reaction mixture was refluxed for 10 minutes and cooled. The precipitate was filtered off and recrystallized. M.p. 84°C. Found, %: C 79.99; H 6.62; N 4.11.  $C_{23}H_{23}NO_2$ . Calculated, %: C 80.00; H 6.67; N 4.06. IR,  $\nu/cm^{-1}$ : 1675 (C=O), 1630, 1590 (C=C), 1010, 920 (C-O).  $^1H$  NMR ( $CDCl_3$ ),  $\delta$ , ppm ( $J$ , Hz): 1.21, 1.32 (6 H, 2-s, gem. ( $CH_3$ )<sub>2</sub>); 2.66 (3 H, s, N- $CH_3$ ); 3.07–3.20 (2 H, m, = $CH_2$ ); 4.70–4.91 (2 H, m, - $CH_2$ -); 5.64–5.82 (1 H, m, =CH-); 5.77 (1 H, d,  $J$  = 9, 6, 3'-H); 6.53 (1 H, d,  $J$  = 7, 7, 4'-H); 6.84–7.57 (6 H, m, aromatic H); 9.81 (1 H, s, CHO).

## 6. Conclusion

New differently substituted spirocompounds were synthesized on the basis of formyl-containing spiropyran of benzoxazine and indoline series. Structure and photochromic properties of obtained compounds were investigated in solution and in thin solid films.

## Acknowledgments

This work was financial supported by Russian Foundation for Basic Research (Grants 07-03-00234, 08-03-90029-Bel), Belarusian Republic Foundation for Basic Research (Grant F08R-228) as well as the Grant of the Russian Federation President NSh-363.2008.3., Russian-American program BRHE, and the Ministry of Education and Science of Russian Federation (project RNP.2.2.2.3.16011, RNP 2.2.2.3.3915, BP3C04, BP4M04).

## References

- [1] V. I. Minkin, "Photo-, thermo-, solvato-, and electrochromic spiroheterocyclic compounds," *Chemical Reviews*, vol. 104, no. 5, pp. 2751–2776, 2004.
- [2] G. Favaro, G. Chidichimo, P. Formoso, S. Manfredi, U. Mazzucato, and A. Romani, "Chromatic and dynamic characteristics of some photochromes in the components of bifunctional photochromic and electro-optical devices," *Journal of Photochemistry and Photobiology A*, vol. 140, no. 3, pp. 229–236, 2001.
- [3] M. Inouye, "Molecular crystals and liquid crystals science and technology. Section A: molecular crystals and liquid crystals,"

*Molecular Crystals and Liquid Crystals*, vol. 246, pp. 169–172, 1994.

- [4] M. A. Suzuki, T. Hashida, J. Hibino, and Y. Kishimoto, "Multiple optical memory using photochromic spiropyran aggregates," *Molecular Crystals and Liquid Crystals*, vol. 246, pp. 389–396, 1994.
- [5] Yu. S. Alekseenko, B. S. Lukyanov, A. N. Utenyshev, et al., "Photo- and thermochromic spiranes. 24. Novel photochromic spiropyranes from 2,4-dihydroxyisophthalaldehyde," *Chemistry of Heterocyclic Compounds*, vol. 42, no. 6, pp. 803–812, 2006.
- [6] A. O. Bulanov, B. B. Safoklov, B. S. Luk'yanov, et al., "Photochromic and thermochromic spiropyranes. 22. Spiropyranes of the 4-Oxo-3,4-dihydro-3H-1,3-benzoxazine series containing  $\pi$ -accepting substituents at position 8'," *Chemistry of Heterocyclic Compounds*, vol. 39, no. 3, pp. 315–317, 2003.
- [7] M. B. Lukyanova, V. A. Kogan, and B. S. Lukyanov, "A new spiropyran with a cation receptor," *Chemistry of Heterocyclic Compounds*, vol. 43, no. 11, pp. 1477–1478, 2007.
- [8] B. S. Luk'yanov, L. E. Nivorozhkin, and V. I. Minkin, "Photo- and thermochromic spiranes," *Chemistry of Heterocyclic Compounds*, vol. 29, no. 2, pp. 152–154, 1993.
- [9] B. B. Safoklov, B. S. Luk'yanov, A. O. Bulanov, et al., "Photo... [2H]chromene) possessing photochromic properties in the solid phase," *Russian Chemical Bulletin*, vol. 51, no. 3, pp. 462–466, 2002.
- [10] R. K. Chang and T. E. Furtak, Eds., *Surface Enhanced Raman Scattering*, Moscow, Russia, 1984, [Russian translation].
- [11] K. Yoda, T. Ohzeki, T. Yuzawa, and H. Takahashi, "Resonance Raman studies of the solvatochromism and acid-base equilibria of 1', 3', 3'-trimethylspiro-[2H-1-benzopyran-2,2'-indoline]," *Spectrochimica Acta*, vol. 45A, no. 8, pp. 855–862, 1989.
- [12] B. S. Luk'yanov, Yu. I. Ryabukhin, G. N. Dorofeenko, L. E. Nivorozhkin, and V. I. Minkin, "Photochromic and thermochromic spiranes," *Chemistry of Heterocyclic Compounds*, vol. 14, no. 2, pp. 122–127, 1978.

## Research Article

# Synthesis of Novel Iono- and Photochromic Spiropyrans Derived from 6,7-Dihydroxy-8-Formyl-4-Methyl-2H-Chromene-2-One

Olga G. Nikolaeva,<sup>1</sup> Alexey V. Tsukanov,<sup>2</sup> Evgenii N. Shepelenko,<sup>2</sup> Boris S. Lukyanov,<sup>1</sup> Anatoly V. Metelitsa,<sup>1</sup> Olga Yu. Kostyrina,<sup>1</sup> Alexander D. Dubonosov,<sup>2</sup> Vladimir A. Bren,<sup>1</sup> and Vladimir I. Minkin<sup>1,2</sup>

<sup>1</sup>Institute of Physical and Organic Chemistry, Southern Federal University, 344090 Rostov on Don, Russia

<sup>2</sup>Southern Scientific Center of Russian Academy of Sciences, 344006 Rostov on Don, Russia

Correspondence should be addressed to Olga G. Nikolaeva, dubon@ipoc.rsu.ru

Received 31 March 2009; Accepted 29 May 2009

Recommended by Mohamed Sabry Abdel-Mottaleb

Novel photochromic spiropyrans (SPPs) containing 6'-hydroxy group were synthesized and their spectral properties as well as abilities for complexation with metal ions studied. In solutions they exist as equilibrium mixture of spirocyclic (A) and merocyanine (B) isomers. The largest content of merocyanine form was found for the derivative with an electron-donating methyl group in position 5 of hetaryl fragment. The irradiation of SPPs in acetonitrile shifts the equilibrium to the B form. Similar effect causes the addition of metal cations due to formation of colored complexes with merocyanine isomers.

Copyright © 2009 Olga G. Nikolaeva et al. This is an open access article distributed under the Creative Commons Attribution License, which permits unrestricted use, distribution, and reproduction in any medium, provided the original work is properly cited.

## 1. Introduction

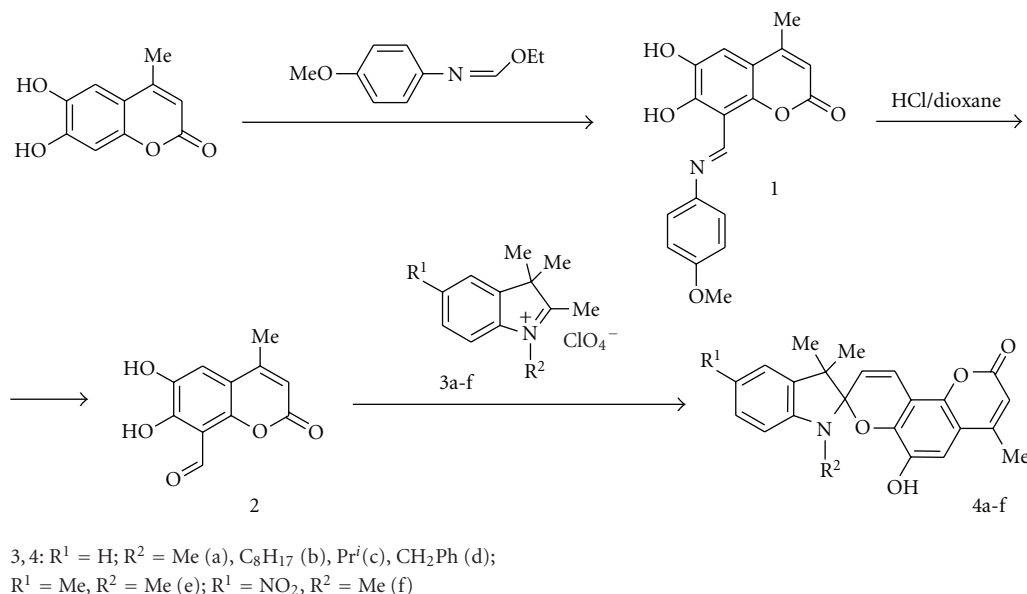
Design and synthesis of novel photochromic spiropyrans and spirooxazines (SPOs) displaying ionochromic properties are of significant interest due to their application as magnetic [1, 2], in devices of molecular electronics [3] and as effective photoswitchable chemosensors for metal cations [4–6]. The structure of the latter type compounds usually contains chelate [7–14], calixarene [15], or crown-ether ionophore groups [16, 17]. The coordination of metal cations occurring via interaction with ligating centers located in the chromene part of a spiropyran (or spirooxazine) can lead to thermally or photochemically driven cleavage of the C<sub>spiro</sub>–O bond of the cyclic isomer followed by Z/E-isomerization to give the metastable colored merocyanine form. By contrast, the complexation with ionophore conjugated with the hetaryl fragment of a spiropyran (or spirooxazine) results in destabilization of the merocyanine form caused by electrostatic repulsion between a metal cation and the positively charged nitrogen atom in the hetaryl moiety [18, 19]. We synthesized a series of novel SPPs containing 6'-hydroxy group in order to study their structure in solutions, photochromic properties, and ionochromic ability towards the alkali-earth and d-metal cations.

## 2. Experimental

<sup>1</sup>H NMR spectra were recorded on Bruker WM-250 (300 MHz) spectrometer using CDCl<sub>3</sub> as solvent. The <sup>1</sup>H chemical shifts were calibrated using the signals of solvent residual protons ( $\delta$  7.25 ppm). IR spectra were measured in Nujol using a Specord 75IR spectrometer. UV-Vis absorption spectra were obtained in acetonitrile with a Cary-100 spectrophotometer. Irradiation of solutions was carried out by filtered light of a high-pressure mercury lamp DRSh (250 W) supplied with glass filter ( $\lambda_{irr} = 365$  nm).

## 3. Results and Discussion

**3.1. Synthesis.** The compound 6,7-Dihydroxy-8-formyl-4-methyl-2H-chromene-2-one (2) was prepared by coupling 6,7-dihydroxy-4-methyl-2H-chromene-2-one with ethyl N-p-methoxyphenylformimidate formed in situ from 4-methoxyphenylamine and triethyl orthoformate followed by the hydrolysis of Schiff base (1) with diluted hydrochloric acid (Scheme 1). The spiropyrans (4) were synthesized by condensation of aldehyde (2) with corresponding 3H-indolium perchlorates (3) in presence of triethylamine.



SCHEME 1

(i) *6,7-dihydroxy-8-[(4-methoxyphenylimino)methyl]-4-methylchromen-2-one (1)*. A mixture of 10 g (45 mmol) 6,7-dihydroxy-4-methyl-2H-chromene-2-one, 11 g (90 mmol) 4-methoxyphenylamine, and 14 mL triethyl orthoformate was kept for 5 hours at 170°C. The precipitate obtained after cooling was filtered and washed with ethanol. The crude product was purified by recrystallization from DMFA. Yield 25%, mp 257–258°C. <sup>1</sup>H NMR (CDCl<sub>3</sub>): δ 2.35 (3H, s, CH<sub>3</sub>), 3.88 (3H, s, OMe), 6.06–7.43 (7H, m, Ar-H + OH), 9.02 (1H, s, CH=), 15.70 (1H, s, OH). Anal. Calcd for C<sub>18</sub>H<sub>15</sub>NO<sub>5</sub>: C, 66.46; H, 4.65; N, 4.31. Found: C, 66.36; H, 4.60; N, 4.41.

(ii) *6,7-dihydroxy-8-formyl-4-methyl-2H-chromene-2-one (2)*. 6,7-Dihydroxy-8-[(4-methoxyphenylimino)methyl]-4-methylchromen-2-one (1) (2.5 g, 7.7 mmol) was dissolved under heating in dioxane (300 mL) and 18% HCl (150 mL) was added. The solution obtained was allowed to stand 10–15 minutes at 60–70°C and the reaction mixture was poured into the water (500 mL). The crude product was filtered, dried, and purified by recrystallization from 2-propanol. Yield 32%, mp 234–235°C. <sup>1</sup>H NMR (CDCl<sub>3</sub>): δ 2.40 (3H, s, CH<sub>3</sub>), 5.64–7.35 (3H, m, Ar-H + OH), 10.59 (1H, s, CHO), 12.42 (1H, s, OH). Anal. Calcd for C<sub>11</sub>H<sub>8</sub>O<sub>5</sub>: C, 60.01; H, 3.66. Found: C, 60.15; H, 3.58.

(iii) *spiopyrans (4a–f) (general procedure)*. A mixture of corresponding perchlorate (3) (1 mmol), aldehyde (2) (1.1 mmol) and 0.1 mL (0.7 mmol) triethylamine was refluxed in 2-propanol (20 mL) for 5 hours. The solvent was removed, the residue was purified by column chromatography on SiO<sub>2</sub> with chloroform as an eluent and recrystallized from 2-propanol.

(iv) *6'-hydroxy-1,3,3,4'-tetramethylspiro[indoline-2,8'-pyrano[2,3-f]benzopyran]-2'-(7'H)-one (4a)*. Yield 24%, mp 208–209°C; IR (ν<sub>max</sub>/cm<sup>-1</sup>, nujol): 3120, 1685, 1580, 1560, 920. <sup>1</sup>H NMR (CDCl<sub>3</sub>): δ isomer A 1.20, 1.30 (6H, s + s, 2 gem-(CH<sub>3</sub>)<sub>2</sub>), 2.34 (3H, s, CH<sub>3</sub>), 2.77 (3H, s, NCH<sub>3</sub>), 5.35

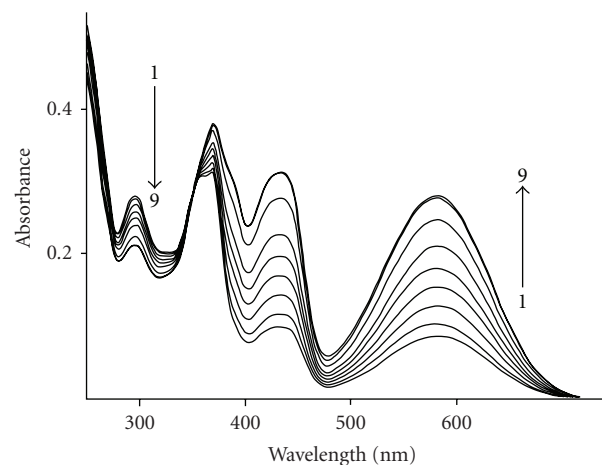
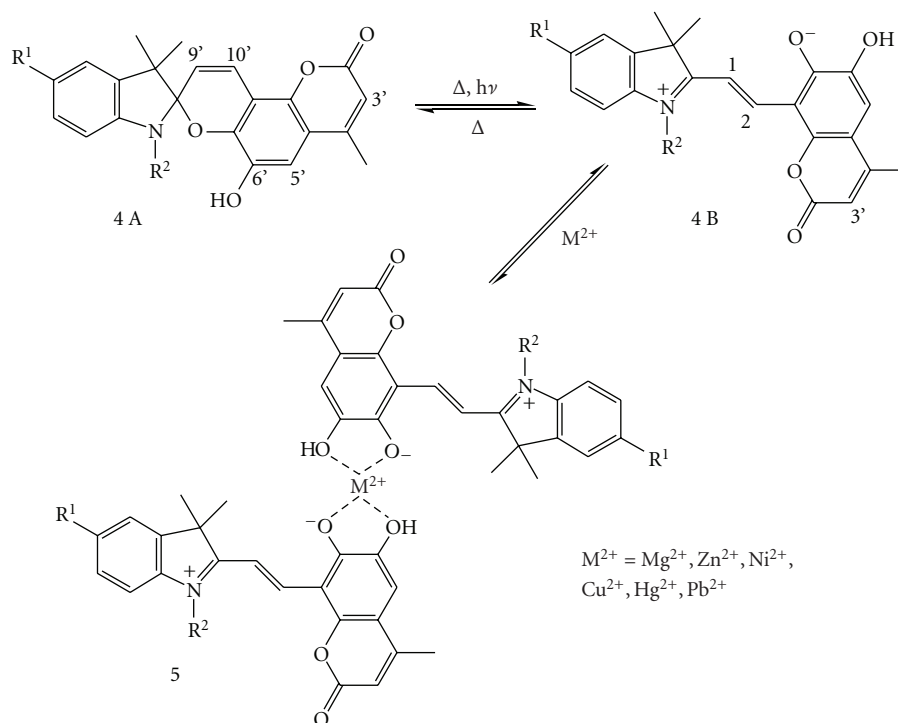


FIGURE 1: Absorption spectra of (4a) in acetonitrile solution before irradiation (1); after 15 seconds (2); 45 seconds (3); 90 seconds (4); 150 seconds (5); 180 seconds (6); 8 minutes (7); 16 minutes (8); 26 minutes (9) of irradiation ( $\lambda_{\text{irr}} = 365 \text{ nm}$ ,  $C = 2.5 \cdot 10^{-5} \text{ M}$ ).

(1H, br. s, OH), 5.84 (1H, d, H<sup>9'</sup>,  $J$  10.5), 6.16 (1H, s, H<sup>3'</sup>), 6.58–7.22 (5H, m, Ar-H), 7.47 (1H, d, H<sup>10'</sup>,  $J$  10.5). Isomer B: 1.84 (6H, s, 2 gem-(CH<sub>3</sub>)<sub>2</sub>), 2.31 (3H, s, CH<sub>3</sub>), 3.78 (3H, s, NCH<sub>3</sub>), 5.98 (1H, s, H<sup>3'</sup>), 6.16–7.22 (5H, m, Ar-H), 8.47 (1H, d, CH=,  $J$  14.8), 8.92 (1H, d, CH=,  $J$  14.8). Ratio of isomers A : B (see Table 1). Anal. Calcd for C<sub>23</sub>H<sub>21</sub>NO<sub>4</sub>: C, 73.58; H, 5.64; N, 3.73. Found: C, 73.41; H, 5.65; N, 3.82.

(v) *6'-hydroxy-1-octyl-3,3,4'-trimethylspiro[indoline-2,8'-pyrano[2,3-f]benzopyran]-2'-(7'H)-one (4b)*. Yield 27%, mp 145–146°C; IR (ν<sub>max</sub>/cm<sup>-1</sup>, nujol): 3180, 1685, 1610, 1560, 920. <sup>1</sup>H NMR (CDCl<sub>3</sub>): δ isomer A: 1.19–1.93 (21H, m, 3CH<sub>3</sub> + 6CH<sub>2</sub>), 2.34 (3H, s, Me), 3.17 (2H, m, NCH<sub>2</sub>), 5.30 (1H, br. s, OH), 5.81 (1H, d, H<sup>9'</sup>,  $J$  10.5), 6.17 (1H, s,



SCHEME 2

$H^{3'}$ ), 6.58–7.45 (6H, m, Ar-H +  $H^{10'}$ ). Isomer B: 1.19–1.93 (21H, m, 3CH<sub>3</sub> + 6CH<sub>2</sub>), 2.30 (3H, s, Me), 4.18 (2H, t, NCH<sub>2</sub>), 5.96 (1H, s,  $H^{3'}$ ), 6.58–7.45 (5H, m, Ar-H), 8.70 (1H, br. s, CH=), 8.92 (1H, d, CH=,  $J$  15.3). Ratio of isomers A : B is (see Table 1). Anal. Calcd for C<sub>30</sub>H<sub>35</sub>NO<sub>4</sub>: C, 76.08; H, 7.45; N, 2.96. Found: C, 76.18; H, 7.48; N, 2.87.

(vi) 6'-hydroxy-1-isopropyl-3,3,4'-trimethylspiro[indoline-2,8'-pyrano[2,3-f]benzopyran]-2' (7'H)-one (4c). Yield 68%, mp 214–215°C; IR ( $\nu_{max}/cm^{-1}$ , nujol): 3160, 1685, 1660, 1615, 1580, 920. <sup>1</sup>H NMR (CDCl<sub>3</sub>):  $\delta$  isomer A: 1.18–1.83 (12H, m, 4Me), 2.34 (3H, s, CH<sub>3</sub>), 3.84 (1H, m, CH), 5.42 (1H, br. s, OH), 5.81 (1H, d,  $H^{9'}$ ,  $J$  10.6), 6.16 (1H, s,  $H^{3'}$ ), 6.77–7.41 (5H, m, Ar-H), 7.44 (1H, d,  $H^{10'}$ ,  $J$  10.6). Isomer B: 1.18–1.83 (12H, m, 4CH<sub>3</sub>), 2.31 (3H, s, Me), 4.02 (1H, m, CH), 5.01 (1H, br. s, OH), 5.96 (1H, s,  $H^{3'}$ ), 6.77–7.41 (5H, m, Ar-H), 8.80 (1H, br. s, CH=), 8.92 (1H, d, CH=,  $J$  14.3). Ratio of isomers A : B (see Table 1). Anal. Calcd for C<sub>25</sub>H<sub>25</sub>NO<sub>4</sub>: C, 74.42; H, 6.25; N, 3.47. Found: C, 74.35; H, 6.39; N, 3.40.

(vii) 6'-hydroxy-1-benzyl-3,3,4'-trimethylspiro[indoline-2,8'-pyrano[2,3-f]benzopyran]-2' (7'H)-one (4d). Yield 31%, mp 216–217°C; IR ( $\nu_{max}/cm^{-1}$ , nujol): 3150, 1670, 1630, 1570, 928. <sup>1</sup>H NMR (CDCl<sub>3</sub>):  $\delta$  isomer A: 1.31, 1.34 (6H, s + s, 2 gem-(CH<sub>3</sub>)<sub>2</sub>), 2.35 (3H, s, CH<sub>3</sub>), 4.21 (1H, d, CH<sub>2</sub>,  $J$  16.7), 4.63 (1H, d, CH<sub>2</sub>,  $J$  16.7), 5.40 (1H, br. s, OH), 5.89 (1H, d,  $H^{9'}$ ,  $J$  10.7), 6.16 (1H, s,  $H^{3'}$ ), 6.37–7.55 (11H, m, Ar-H +  $H^{10'}$ ). Isomer B: 1.25 (6H, s, 2 gem-(CH<sub>3</sub>)<sub>2</sub>), 1.89 (2H, s, NCH<sub>2</sub>), 5.53 (1H, br. s, OH), 6.16 (1H, s,  $H^{3'}$ ), 6.37–7.55 (10H, m, Ar-H), 8.49 (1H, br. s, CH=), 8.93 (1H, d, CH=,  $J$  15.3). Ratio of isomers A : B (see Table 1). Anal. Calcd for C<sub>29</sub>H<sub>25</sub>NO<sub>4</sub>: C, 77.14; H, 5.58; N, 3.10. Found: C, 77.07; H, 5.52; N, 3.19.

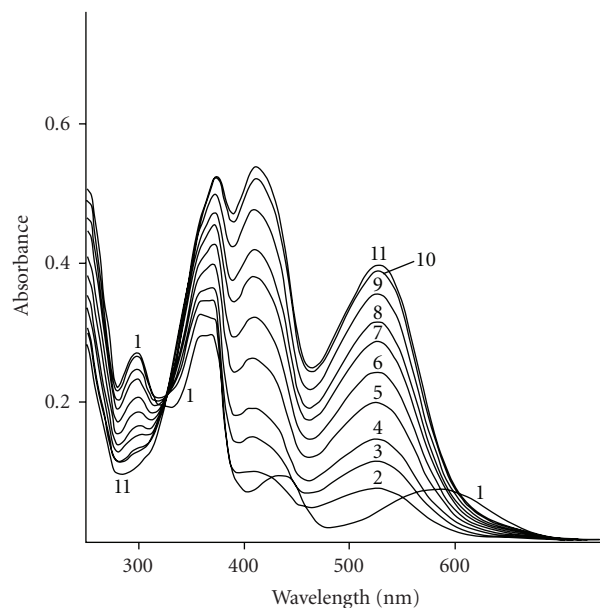


FIGURE 2: Absorption spectra of (4a) in dark conditions in acetonitrile solution before (1) and after addition of Mg(ClO<sub>4</sub>)<sub>2</sub> (2); after 5 minutes (3); 10 minutes (4); 20 minutes (5); 30 minutes (6); 45 minutes (7); 60 minutes (8); 90 minutes (9); 120 minutes (10); 180 minutes (11) ([4a] = 2.5 × 10<sup>-5</sup> M, [Mg<sup>2+</sup>] = 5 × 10<sup>-4</sup> M).

(viii) 6'-hydroxy-1,3,3,5,4'-pentamethylspiro[indoline-2,8'-pyrano[2,3-f]benzopyran]-2' (7'H)-one (4e). Yield 29%, mp 276–277°C; IR ( $\nu_{max}/cm^{-1}$ , nujol): 3170, 1685, 1610, 1570, 920. <sup>1</sup>H NMR (CDCl<sub>3</sub>):  $\delta$  isomer A: 1.20, 1.28 (6H,

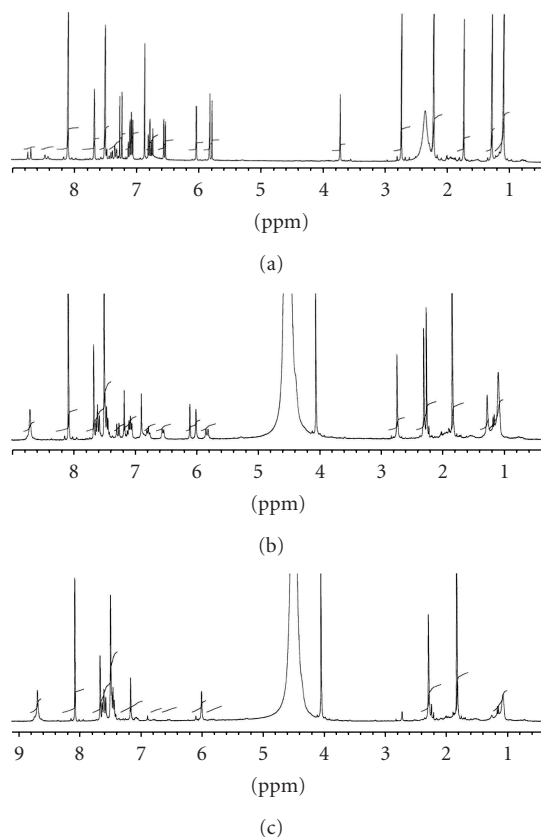


FIGURE 3: (a)  $^1\text{H}$  NMR spectra of (4a) in dark conditions in  $\text{CD}_3\text{CN}$ -nitrobenzene- $d_6$  (1 : 1 v/v) and (b) in presence of  $\text{Mg}(\text{ClO}_4)_2 \cdot 3\text{H}_2\text{O}$  after 10 minutes; (c) 1 hour ( $\nu_{\text{Mg}^{2+}}/\nu_{(4a)} = 5$ ).

s + s, 2 *gem*-( $\text{CH}_3$ ) $_2$ ), 2.35 (3H, s,  $\text{CH}_3$ ), 2.48 (3H, s,  $\text{CH}_3$ ), 2.73 (3H, s,  $\text{NCH}_3$ ), 5.38 (1H, br. s, OH), 5.84 (1H, d,  $\text{H}^{9'}$ ,  $J$  10.7), 6.15 (1H, s,  $\text{H}^{3'}$ ), 6.44–7.31 (4H, m, Ar-H), 7.46 (1H, d,  $\text{H}^{10'}$ ,  $J$  10.7). Isomer B: 1.25 (6H, s, 2 *gem* ( $\text{CH}_3$ ) $_2$ ), 1.83 (6H, s, Me), 2.33 (3H, s, Me), 3.85 (3H, s, NMe), 5.99 (1H, s,  $\text{H}^{3'}$ ), 6.44–7.31 (4H, m, Ar-H), 8.43 (1H, d,  $\text{CH}=\text{C}$ ,  $J$  15.1), 8.85 (1H, d,  $\text{CH}=\text{C}$ ,  $J$  15.1). Ratio of isomers A : B (see Table 1). Anal.Calcd for  $\text{C}_{24}\text{H}_{23}\text{NO}_4$ : C, 74.02; H, 5.95; N, 3.60. Found: C, 74.19; H, 5.91; N, 3.55.

(ix) 6'-hydroxy-5-nitro-1,3,3,4'-tetramethylspiro[indoline-2,8'-pyrano[2,3-f]benzopyran]-2'-(7'H)-one (4f). Yield 25%, mp 281–282°C; IR ( $\nu_{\text{max}}/\text{cm}^{-1}$ , nujol): 3170, 1700, 1600, 1560, 970.  $^1\text{H}$  NMR ( $\text{CDCl}_3$ ):  $\delta$  isomer A: 1.24, 1.37 (6H, s + s, 2 *gem*-( $\text{CH}_3$ ) $_2$ ), 2.36 (3H, s,  $\text{CH}_3$ ), 2.90 (3H, s,  $\text{NCH}_3$ ), 5.36 (1H, s, OH), 5.82 (1H, d,  $\text{H}^{9'}$ ,  $J$  10.5), 6.19 (1H, s,  $\text{H}^{3'}$ ), 6.55–8.18 (6H, m, Ar-H +  $\text{H}^{10'}$ ). Anal.Calcd for  $\text{C}_{23}\text{H}_{20}\text{N}_2\text{O}_6$ : C, 65.71; H, 4.79; N, 6.66. Found: C, 65.70; H, 4.68; N, 6.78.

### 3.2. Spectral Properties and Complexation with Metal Ions.

Electronic absorption spectra of SPP (4f) in toluene, chloroform, and acetonitrile show broad absorption bands at 295 and 365 nm. For compounds (4a–e), the spectra contain also additional long-wavelength bands with maxima centered around 430 and 580 nm (Tables 1 and 2, Figure 1). For

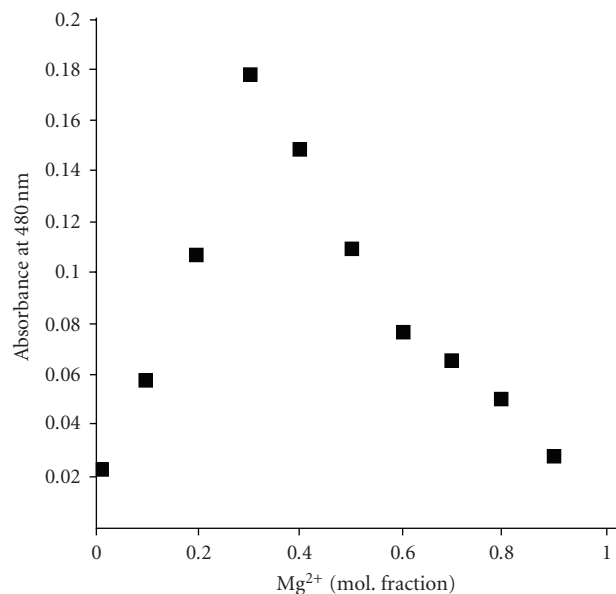


FIGURE 4: Continuous variation plot of the (4a)/ $\text{Mg}^{2+}$  ( $[\text{4a}] + [\text{Mg}^{2+}] = 5 \times 10^{-5}$  M) in acetonitrile.

SPPs (4a–e), the appearance of long-wavelength bands is accompanied by the additional proton signals of merocyanine isomers B in the  $^1\text{H}$  NMR spectra. The long-wavelength bands in absorption spectra of cyclic ( $\lambda_{\text{max}}^{\text{abs}} = 370\text{--}371$  nm) and merocyanine ( $\lambda_{\text{max}}^{\text{abs}} = 580\text{--}650$  nm) forms correspond to  $\text{S}_0 \rightarrow \text{S}_1$  transitions while the absorption bands of the cyclic form ( $\lambda_{\text{max}}^{\text{abs}} = 294\text{--}299$  nm) and merocyanine form ( $\lambda_{\text{max}}^{\text{abs}} = 456\text{--}471$  nm) correspond to  $\text{S}_0 \rightarrow \text{S}_2$  transitions (Table 2). According to  $^1\text{H}$  NMR and absorption spectroscopy data only SPP (4f) with an electron-withdrawing  $\text{NO}_2$ -group exists in solution of chloroform entirely as the cyclic form A, while the solutions of (4a–e) contain both spirocyclic A and merocyanine B isomers (Scheme 2). The percentage of the merocyanine form in the equilibrium mixture was estimated using  $^1\text{H}$  NMR data (Table 1). The largest content of form B is observed for the derivative (4e) with an electron-donating methyl group in position 5.

The irradiation of SPPs (4a–f) in acetonitrile ( $\lambda_{\text{irr}} = 365$  nm) leads to increase in intensity of the long-wavelength absorption band in the regions of 430–471 and 580–653 nm due to the formation of merocyanine form which is thermally converted to the ring-closed isomer A (Figure 1).

Lifetimes of the photoinduced absorption bands of forms B allow to evaluate their thermal stability because content of merocyanine isomers in the equilibrium state in low-polarity solvent is substantially less than that of the cyclic isomers. Therefore, relaxation process rate constant is determined by the rate constant for the  $\text{B} \rightarrow \text{A}$  reaction. The lowest lifetime of the photoinduced absorption was observed for compound (4f) with an electron-withdrawing group in 5th position and the highest lifetime for the compound (4e) with an electron donating group (Table 2). Analogous results were previously obtained for the spirooxazines [20].

TABLE 1: Long-wavelength maxima of (4) and parameters of (4A)-(4B) equilibrium in chloroform at 293 K.

Comp.	Absorption of (4), $\lambda_{\max}$ , (nm), ( $\epsilon \times 10^{-4}$ , $1 \text{ mol}^{-1} \text{ cm}^{-1}$ )	Content of form B, %	$K^{\circ} = [B]/[A]$
4a	448 (2.31), 595 (1.72)	28.6	0.401
4b	447 (2.35), 595 (1.78)	56.5	1.299
4c	447 (2.40), 596 (1.82)	23.5	0.307
4d	452 (3.07), 605 (2.04)	9.0	0.099
4e	448 (1.85), 593 (1.63)	63.0	1.702
4f	—	0	—

TABLE 2: Spectral characteristics of isomers A, B for (4a–f) and lifetimes for photoinduced absorption in toluene at 293 K.

Comp.	$^A \lambda_{\max}^{\text{abs}}$ , (nm)	$^B \lambda_{\max}^{\text{abs}}$ , (nm)	$\tau$ , s
4a	295, 354, 370	458, 614	161
4b	298, 355, 371	459, 617	205.7
4c	294, 354sh, 370	456, 619	170.9
4d	295, 354, 370	461, 617	44.1
4e	299, 356, 370	459, 614	257.7
4f	299, 355sh, 371	471, 653	6.5

Under dark conditions, addition of metal cations:  $\text{Mg}^{2+}$  (as perchlorate),  $\text{Zn}^{2+}$ ,  $\text{Ni}^{2+}$ ,  $\text{Cu}^{2+}$ ,  $\text{Hg}^{2+}$ ,  $\text{Pd}^{2+}$  (as acetates) shifts the equilibrium to the open form B with increase in the maximum of absorption band in the visible region due to the formation of complexes (5) (Figure 2). Position of the absorption maxima of these bands depends on the nature of the metal ion. For example, complex (4a) with  $\text{Mg}^{2+}$  is characterized by absorption bands at 369, 406, and 524 nm; with  $\text{Zn}^{2+}$  at 387, 440, and 550 nm; with  $\text{Hg}^{2+}$  at (372, 455, and 586 nm). The maxima of these absorption bands are hypsochromically shifted with respect to the free merocyanine absorption. The content of the complexes (5) is greatly raised under exposure of the solution to UV light ( $\lambda_{\text{irr}} = 365 \text{ nm}$ ).

The structure of complexes (5) was estimated by IR spectroscopy. The IR-spectra of initial compounds contain broad absorption band of the hydroxyl group at  $3100\text{--}3200 \text{ cm}^{-1}$  which slightly changes after complex formation, so the substitution of hydroxyl group protons was excluded.

$^1\text{H}$  NMR, IR spectrometry and the spectrophotometric titration method were employed for the analysis of the complexation processes. The  $^1\text{H}$  NMR spectral changes for (4a) upon the addition of  $\text{Mg}^{2+}$  ions in  $\text{CD}_3\text{CN}/\text{nitrobenzene-}d_6$  (1 : 1 v/v) solution are shown in Figure 3.

In a metal-free solution, signals of both spiro- and merocyanine forms are present in the spectrum. This spectrum is characterized by a doublet centered at  $\delta$  5.80 ppm for the proton (4A)- $\text{H}^{9'}$ , singlet at  $\delta$  6.1 ppm for the proton (4A)- $\text{H}^{3'}$  and two doublets at  $\delta$  8.4 ppm and 8.7 ppm for the protons (4B)- $\text{H}^1$ , (4B)- $\text{H}^2$ . The content of merocyanine isomer B was estimated as  $\sim 16\%$ . In the presence of metal salt chemical shifts of protons did not change significantly. After addition of  $\text{Mg}(\text{ClO}_4)_2 \cdot 3\text{H}_2\text{O}$  in darkness the appearance of a resonance signal at 6.00 ppm for the proton (4B)- $\text{H}^{3'}$  and substantial increase in the intensity of multiplet at  $\delta$  8.70 ppm for the protons (4B)- $\text{H}^1$ , (4B)- $\text{H}^2$

was observed (Figure 3). At the same time the intensity of the doublet at  $\delta$  5.80 ppm of the proton (4A)- $\text{H}^{9'}$  and singlet at  $\delta$  6.1 ppm for the proton (4A)- $\text{H}^{3'}$  was decreased. The data obtained indicate that the equilibrium is shifted to the merocyanine form due to the formation of complex (5) (Scheme 2). The content of the merocyanine form involved into the complexation with  $\text{Mg}^{2+}$  ion was estimated as  $\sim 83\%$  (1 hour after salt addition).

The absorption at 480 nm (Figure 4) was chosen to determine the composition of the complex by the method of molar ratios [21]. The molar ratios plot shown in Figure 4 makes it evident that the composition of the (4a)- $\text{Mg}^{2+}$  complex is 2 : 1.

## 4. Conclusions

Novel photochromic spiropyrans containing 6'-hydroxy group in solutions exist as equilibrium mixture of spirocyclic and merocyanine isomers. The addition of metal salts leads to formation of complexes with merocyanine isomers and shifts the equilibrium to the ring-opened forms. The results obtained indicate that binding of cations is an important factor affecting position of the spiropyran-merocyanine equilibrium. These ionochromic compounds can be used as the basis for design of chemosensors for metal ions.

## Acknowledgments

This work was supported by Russian Foundation for Basic Research (grants N 09-03-00052, 07-03-00234, and 09-03-00813), Ministry of Education and Science of Russian Federation (grant N RNP2348), "Russian Science Support Foundation" and and President's of RF grant (NSH-363.2008.3).

## References

- [1] A. O. Bulanov, L. D. Popov, G. I. Bondarenko, and V. A. Kogan, "New binuclear copper(II) complexes with bishydrazones derived from spiropyran of the benzoxazinonium series," *Russian Journal of General Chemistry*, vol. 76, no. 8, pp. 1272–1274, 2006.
- [2] A. O. Bulanov, B. S. Luk'yanov, V. A. Kogan, and V. V. Lukov, "Binuclear copper(II) complexes with hydrazones containing spiropyran fragment," *Russian Journal of Coordination Chemistry*, vol. 29, no. 9, pp. 658–659, 2003.
- [3] X. Guo, D. Zhang, and D. Zhu, "Photocontrolled electron transfer reaction between a new dyad, tetrathiafulvalene-photochromic spiropyran, and ferric ion," *Journal of Physical Chemistry B*, vol. 108, no. 1, pp. 212–217, 2004.
- [4] M. V. Alfimov, O. A. Fedorova, and S. P. Gromov, "Photo-switchable molecular receptors," *Journal of Photochemistry and Photobiology A*, vol. 158, no. 2-3, pp. 183–198, 2003.
- [5] K. Kimura, H. Sakamoto, and M. Nakamura, "Molecular design and applications of photochromic crown compounds—how can we manipulate metal ions photochemically?" *Bulletin of the Chemical Society of Japan*, vol. 76, no. 2, pp. 225–245, 2003.
- [6] A. M. A. Salhin, M. Tanaka, K. Kamada, et al., "Decisive factors in the photoisomerization behavior of crowned spirobenzopyrans: metal ion interaction with crown ether and phenolate anion moieties," *European Journal of Organic Chemistry*, no. 4, pp. 655–662, 2002.
- [7] N. Shao, Y. Zhang, S. Cheung, et al., "Copper ion-selective fluorescent sensor based on the inner filter effect using a spiropyran derivative," *Analytical Chemistry*, vol. 77, no. 22, pp. 7294–7303, 2005.
- [8] B. G. Jeliakova, S. Minkovska, and T. Deligeorgiev, "Effect of complexation on the photochromism of 5'-(benzothiazol-2-yl)spiroindolinonaphthooxazines in polar solvents," *Journal of Photochemistry and Photobiology A*, vol. 171, no. 2, pp. 153–160, 2005.
- [9] A. V. Chernyshev, N. A. Voloshin, I. M. Raskita, A. V. Metelitsa, and V. I. Minkin, "Photo- and ionochromism of 5'-(4,5-diphenyl-1,3-oxazol-2-yl) substituted spiro[indoline-naphthopyrans]," *Journal of Photochemistry and Photobiology A*, vol. 184, no. 3, pp. 289–297, 2006.
- [10] N. A. Voloshin, A. V. Chernyshev, A. V. Metelitsa, I. M. Raskita, E. N. Voloshina, and V. I. Minkin, "Synthesis of photochromic 5'-(4,5-diphenyl-1,3-oxazol-2-yl)-spiro[indoline-2,3'-naphtho[2,3-b]pyran]," *Russian Chemical Bulletin*, vol. 54, no. 3, pp. 705–710, 2005.
- [11] R. A. Kopelman, S. M. Snyder, and N. L. Frank, "Tunable photochromism of spirooxazines via metal coordination," *Journal of the American Chemical Society*, vol. 125, no. 45, pp. 13684–13685, 2003.
- [12] J. D. Winkler, C. M. Bowen, and V. Michelet, "Photodynamic fluorescent metal ion sensors with parts per billion sensitivity," *Journal of the American Chemical Society*, vol. 120, no. 13, pp. 3237–3242, 1998.
- [13] N. A. Voloshin, A. V. Chernyshev, A. V. Metelitsa, et al., "Photochromic spiro[indoline-pyridobenzopyrans]: fluorescent metal-ion sensors," *Archive for Organic Chemistry*, vol. 11, pp. 16–24, 2004.
- [14] M. S. Attia, M. M. H. Khalil, M. S. A. Abdel-Mottaleb, M. B. Lukyanova, Yu. A. Alekseenko, and B. Lukyanov, "Effect of complexation with lanthanide metal ions on the photochromism of (1,3,3-trimethyl-5'-hydroxy-6'-formyl-indoline-spiro2,2'-[2h] chromene) in different media," *International Journal of Photoenergy*, vol. 2006, Article ID 42846, 9 pages, 2006.
- [15] Z. Liu, L. Jiang, Z. Liang, and Y. Gao, "Photo-switchable molecular devices based on metal-ionic recognition," *Tetrahedron Letters*, vol. 46, no. 5, pp. 885–887, 2005.
- [16] A. Abdullah, C. J. Roxburgh, and P. G. Sammes, "Photochromic crowned spirobenzopyrans: quantitative metal-ion chelation by UV, competitive selective ion-extraction and metal-ion transportation demonstration studies," *Dyes and Pigments*, vol. 76, no. 2, pp. 319–326, 2008.
- [17] M. Tanaka, K. Kamada, H. Ando, T. Kitagaki, Y. Shibutani, and K. Kimura, "Synthesis and photochromism of crowned spirobenzothiaopyran: facilitated photoisomerization by cooperative complexation of crown ether and thiophenolate moieties with metal ions," *Journal of Organic Chemistry*, vol. 65, no. 14, pp. 4342–4347, 2000.
- [18] R. T. F. Jukes, B. Bozic, F. Hartl, P. Belser, and L. de Cola, "Synthesis, photophysical, photochemical, and redox properties of nitrospiropyrans substituted with Ru or Os tris(bipyridine) complexes," *Inorganic Chemistry*, vol. 45, no. 20, pp. 8326–8341, 2006.
- [19] V. V. Korolev, D. Yu. Vorobyev, E. M. Glebov, et al., "Spiro-naphthoxazines produced from crown-containing dihydroisoquinolines: synthesis and spectroscopic study of cation-dependent photochromism," *Journal of Photochemistry and Photobiology A*, vol. 192, no. 2-3, pp. 75–83, 2007.
- [20] V. Lokshin, A. Samat, and A. V. Metelitsa, "Spirooxazines: synthesis, structure, spectral and photochromic properties," *Russian Chemical Reviews*, vol. 71, no. 11, pp. 893–916, 2002.
- [21] M. Beck and I. Nagypal, *Chemistry of Complex Equilibria*, Akademiai Kiado, Budapest, Hungary, 1989.

## Research Article

# Optical Study on Poly(methyl methacrylate)/Poly(vinyl acetate) Blends

**R. M. Ahmed**

*Physics Department, Faculty of Science, Zagazig University, Zagazig 44519, Egypt*

Correspondence should be addressed to R. M. Ahmed, rania8.7@hotmail.com

Received 31 March 2009; Revised 26 July 2009; Accepted 26 August 2009

Recommended by Mohamed Sabry Abdel-Mottaleb

Transparent films of poly(methyl methacrylate)/poly(vinyl acetate) blend with different concentrations were prepared by using solution-cast technique. FT-IR transmission spectra were carried for the samples to detect the influence of UV radiation. In addition, optical absorption measurements were carried out for the samples at room temperature across the 190–900 nm wavelength regions before and after exposure to UV and filtered radiation using xenon arc lamp. The study has been also extended to include the changes in the optical parameters including the band tail width and band gap energies for the samples. Moreover, the refractive index was calculated for the samples from specular reflection and absorption spectrum before and after exposure to UV and filtered radiation.

Copyright © 2009 R. M. Ahmed. This is an open access article distributed under the Creative Commons Attribution License, which permits unrestricted use, distribution, and reproduction in any medium, provided the original work is properly cited.

## 1. Introduction

The popular and economic method of polymer modification is blending two or more components with different properties [1]. Polymer blending is an attractive route for producing new polymeric materials with tailored properties without having to synthesize totally new materials. Other advantages for polymer blending are versatility and simplicity [2]. Poly(methyl methacrylate) is one of the best organic optical materials and has been widely used to make a variety of optical devices, such as optical lenses. It is known that its refractive index changes upon UV irradiation, either in the pure [3, 4] or doped state [5], which provides a means to fabricate structures, such as gratings or waveguides. On the other hand, poly(vinyl acetate) had the ability to improve poly(vinyl chloride) photodegradation, photocross linking and photo-oxidation by making a blend of them [1]. Also, Kaminska et al. [6] studied the thermal and photochemical stability of poly(methyl methacrylate)/poly(vinyl acetate) blends and revealed that poly(vinyl acetate) acts as a stabilizer with respect to thermal and photochemical degradation when the processes take place in air. Indeed, poly(methyl methacrylate) and poly(vinyl acetate) form an important pair of polymers.

In the present study, a trail will be carried out to produce the best product of poly(methyl methacrylate)/poly(vinyl acetate) blend and also to overcome the defects of the individual homopolymers. Furthermore, the change in the optical absorption and the optical parameters will be determined for the samples after exposure to UV (unfiltered light) and filtered radiation. In addition, the refractive index ( $n$ ) will be calculated for the samples.

## 2. Materials and Methods

**2.1. Materials.** Both PMMA (poly methyl methacrylate) and PVAc (poly vinyl acetate) used in this study were obtained from Sigma, Aldrich (Germany) and were reported to have molecular weights of 996000 and 167000 g.mol<sup>-1</sup>, respectively. Chloroform has purity 99.8% (HPLC) and was used as a common solvent for both PMMA and PVAc.

**2.2. Preparation of the Samples.** Films (thickness 30–40 μm) of (PMMA/PVAc) blends were prepared by using solution-cast technique. Pure PMMA and PVAc were dissolved separately in chloroform for 48 hours at room temperature. The solutions of the two homopolymers were then mixed

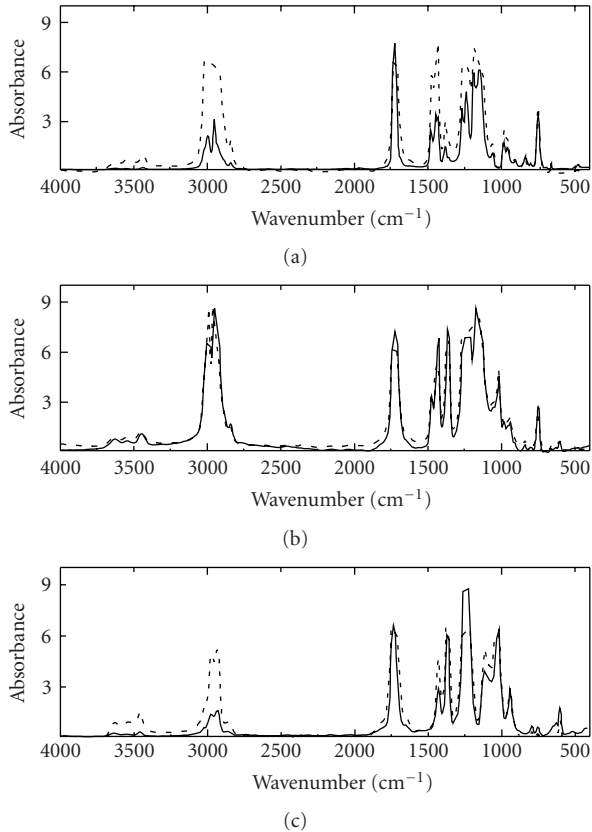


FIGURE 1: FT-IR spectra of (a) pure PMMA, (b) a blend of (50/50 PMMA/PVAc), and (c) pure PVAc before (—) and after exposure to UV radiation (- - -) for 24 hours.

with different concentrations and subsequently cast onto glass dishes and left in an oven at 40°C for 24 hours to form transparent films. After curing, the samples of the pure PMMA and PVAc and their blends were removed and then cut as desired. The concentrations of the prepared (PMMA/PVAc) blends are (0/100, 25/75, 50/50, 75/25, 100/0) by weight.

**2.3. Absorption Spectra.** The absorption spectra were recorded using Perkin Elmer Lambda 4B spectrophotometer (190–900) nm.

**2.4. UV Radiation.** The films were exposed to UV and filtered radiation from a 200 W xenon arc lamp.

**2.5. Reflection Measurements.** Specular reflection spectra were recorded with UV-Vis-NIR spectrometer (UV-3101 PC) shimadzu (200–600) nm.

**2.6. FT-IR Analysis.** FT-IR spectra were measured with a Fourier Transform Infrared Spectrometer (FT/IR – 460 plus) in the wave number range (400–4000  $\text{cm}^{-1}$ ).

### 3. Results and Discussion

**3.1. Characterization of PMMA/PVAc Blend.** FT-IR spectroscopy has long been recognized as a powerful tool for

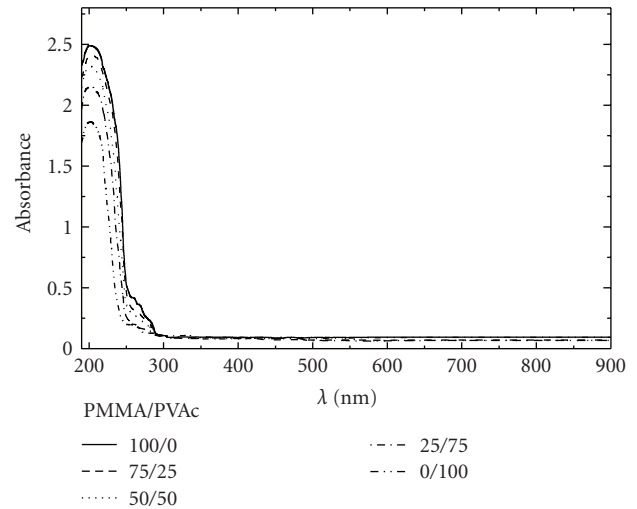


FIGURE 2: Absorption spectra of different concentrations of PMMA/PVAc blend before exposure to radiation.

elucidation of structural information. The position, intensity, and shape of vibrational bands are useful in clarifying conformational and environmental changes of polymers at the molecular level [7]. FT-IR transmission spectra as shown in Figure 1 have been studied to PMMA, PVAc, and their (50/50 PMMA/PVAc) blend before and after exposure to UV radiation for 24 hours.

It can be observed that a band at  $1435.3\text{ cm}^{-1}$  corresponds to asymmetrical bending vibration ( $\text{CH}_3$ ) of methyl group of PMMA. Besides, the vibrational bands observed at  $2855$  and  $1370.7\text{ cm}^{-1}$  are ascribed to  $\text{CH}_3$  symmetric stretching and symmetric bending vibrations of pure PVAc, respectively. In addition, a strong band at  $1718.3$  and  $1726.9\text{ cm}^{-1}$  can be attributed to the carbonyl group of PMMA and PVAc segments, respectively [6]. Also, the frequency shift of the peak due to C–O band of PMMA around  $1149.9\text{ cm}^{-1}$  for the sample of the blend implies that there is a specific interaction between PMMA and PVAc [7]. On the other hand, it can be illustrated that the appearance of the C–Cl peak characterizing chloroform [8] at  $755\text{ cm}^{-1}$  indicated the presence of solvents molecules.

Moreover, the band around  $1063.6\text{ cm}^{-1}$ , due to a stretching vibration of C–O–C group of PMMA, has shifted to a higher value ( $1066.9\text{ cm}^{-1}$ ) after exposure to UV radiation as well as the methoxy carbon ( $\text{O}-\text{CH}_3$ ) which appeared at  $2841.6\text{ cm}^{-1}$ . Similarly, the wave numbers corresponding to the characteristic transmission peaks of PVAc as acetates group at  $1370.7\text{ cm}^{-1}$  have been affected by UV radiation. Also, the decrease in the intensity of carbonyl band for PMMA sample (which is more pronounced than the intensity decrease of the blend) is an evidence of side group elimination from PMMA chains upon UV exposure. The broadening of the whole carbonyl band for the homopolymers indicates that new oxidized groups are formed resulting of photochemical reactions [1, 9]. Besides, the development of the band from  $3425$  to  $3666\text{ cm}^{-1}$  assigned to OH was observed for pure PMMA and PVAc

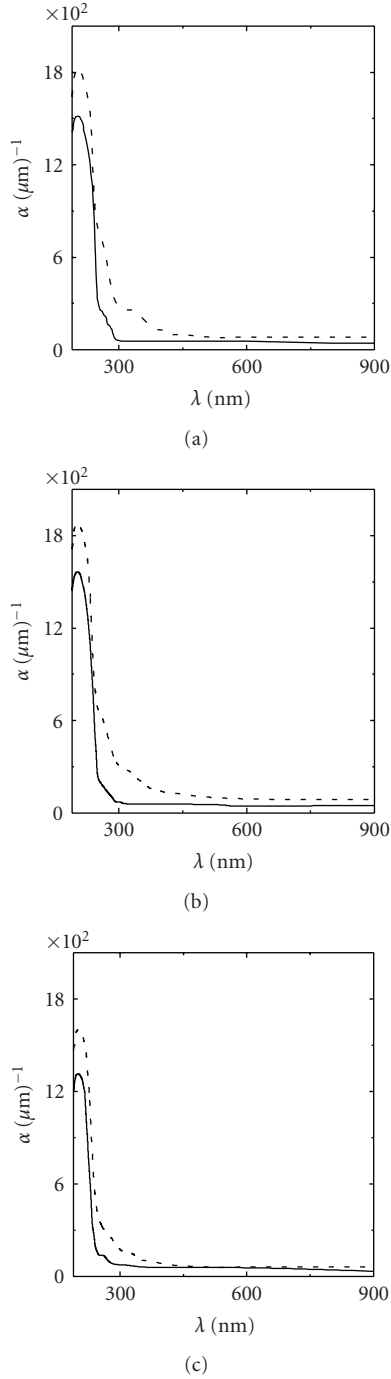


FIGURE 3: Absorption spectrum of (a) pure PMMA, (b) blend of (50/50 PMMA/PVAc), and (c) pure PVAc before (—) and after (---) exposure to UV radiation for 24 hours.

more pronounced than their blend after UV irradiation. This change is an obvious evidence of polymer photooxidation [1]. Consequently, (50/50 PMMA/PVAc) blend has improved the degradation of its homopolymer.

Furthermore, the observed decrease of the intensity of IR spectra can be explained on the bases that most synthetic polymers degrade after exposure to solar ultraviolet (UV)

radiation due to the presence of photosensitive impurities and/or abnormal structural moieties which are introduced during polymerization. The presence of groups such as ketones and aldehydes is implicated in polymer degradation [10].

**3.2. Optical Absorption Spectroscopy.** The study of the optical absorption spectra is one of the most productive methods in developing and understanding the structure and energy gap of amorphous nonmetallic materials. Figure 2 shows the absorption spectra of different concentrations of (PMMA/PVAc) blend before exposure to radiation. It can be observed that the intensity of absorption peak has increased by increasing the concentration of PMMA in the blend. Moreover, the absorption coefficient ( $\alpha$ ) has been estimated for all samples from (1):

$$\alpha(v) = \frac{2.3 \log(I_i/I_t)}{d} = \frac{2.3A}{d}, \quad (1)$$

where  $I_i$  and  $I_t$  are the intensity of the incident and transmitted light, respectively,  $A$  is the absorbance, and  $d$  is the film thickness. Figure 3 shows the absorption coefficient of PMMA, PVAc, and their (50/50 PMMA/PVAc) blend before exposure and after exposure to UV radiation. The observed wideness of the absorption spectrum of PMMA after exposure to UV radiation can be attributed to the existence of more transitions from higher vibration levels of the ground state to higher sublevels of the first excited singlet state [11]. In addition, the same behavior observed for PVAc can be interpreted as the existence of ketones and aldehydes due to the degradation by UV radiation as mentioned before.

**3.3. Interband Transitions.** When a quantum of radiation is absorbed by a material, the absorption coefficient, as a function of photon energy for simple parabolic band, can be expressed by Davis and Mott formula [12], as in (2)

$$\alpha E = B(E - E_g)^r, \quad (2)$$

where  $B$  is a constant,  $E_g$  is the optical band gap of the specimen, and  $r$  is an index having the values of 2, 3, 1/2, and 3/2, depending on the nature of electronic transition responsible for the absorption. Figure 4(a) illustrates the dependence of  $(\alpha E)^2$  on the photon energy  $E$  (eV) for the samples before exposure to light, which brought in to view a linear behavior that can be considered as an evidence of the direct transition (i.e., for  $r = 1/2$ ) [13]. The optical gap was estimated from the intercept on the energy axis of the linear fit of the large energy data of the plot [14]. The absorption spectra [15] clarify an extending tail for lower photon energies below the band edge, which can be described by (3)

$$\alpha = \alpha_o \exp\left(\frac{E}{E_u}\right), \quad (3)$$

where  $E_u$  is the energy of Urbach corresponding to the width of the band tails of localized states in the band gap. The values

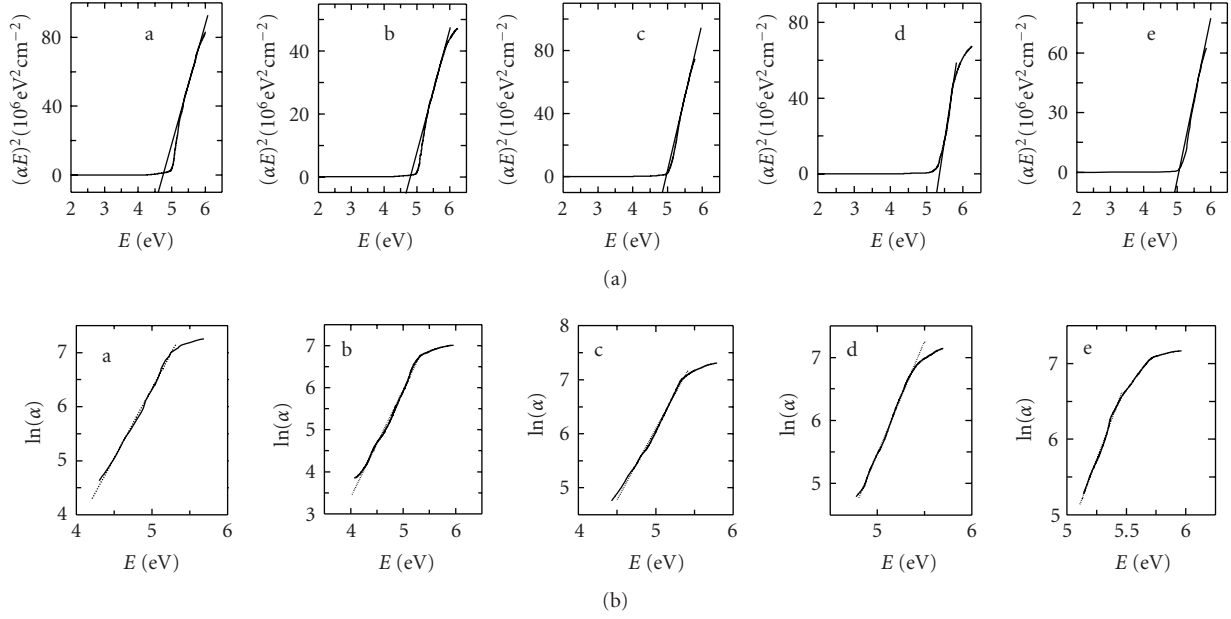


FIGURE 4: (a) The dependence of  $(\alpha E)^2$  on photon energy  $E$  (eV) for (a) pure PMMA, (b) blend of (75/25 PMMA/PVAc), (c) blend of (50/50 PMMA/PVAc), (d) blend of (25/75 PMMA/PVAc), and (e) pure PVAc without exposure to radiation.

(b) The dependence of  $\ln(\alpha)$  on photon energy  $E$  (eV) for (a) pure PMMA, (b) blend of (75/25 PMMA/PVAc), (c) blend of (50/50 PMMA/PVAc), (d) blend of (25/75 PMMA/PVAc), and (e) pure PVAc without exposure to light.

TABLE 1: The energy gap  $E_g$  (eV) for different concentrations of (PMMA/PVAc) blend after exposure to UV and filtered radiation at different exposure times.

PMMA/PVAc	Exposure radiation	Exposure time (hour)					Percentage of decrease of $E_g$ % (eV)
		0	4	12	20	24	
(100/0)	filter	4.60	4.57	4.56	4.52	4.48	2.61
	UV	<b>4.60</b>	<b>4.50</b>	<b>4.41</b>	<b>4.32</b>	<b>4.23</b>	<b>8.04</b>
(75/25)	filter	4.67	4.66	4.64	4.60	4.59	1.71
	UV	<b>4.67</b>	<b>4.54</b>	<b>4.47</b>	<b>4.36</b>	<b>4.30</b>	<b>7.92</b>
(50/50)	filter	4.85	4.84	4.83	4.80	4.77	1.65
	UV	<b>4.85</b>	<b>4.68</b>	<b>4.57</b>	<b>4.56</b>	<b>4.53</b>	<b>6.29</b>
(25/75)	filter	4.92	4.92	4.89	4.88	4.88	0.81
	UV	<b>4.92</b>	<b>4.83</b>	<b>4.77</b>	<b>4.73</b>	<b>4.70</b>	<b>4.47</b>
(0/100)	filter	5.28	5.28	5.27	5.24	5.24	0.76
	UV	<b>5.28</b>	<b>4.25</b>	<b>5.19</b>	<b>5.11</b>	<b>5.07</b>	<b>3.98</b>

of  $E_u$  were calculated as the reciprocal gradient of the linear portion of the plot. Moreover, Figure 4(b) shows the plot of  $\ln(\alpha)$  versus photon energy  $E$  (eV) samples before exposure to light.

Tables 1 and 2 summarize the values of optical parameters ( $E_g$  and  $E_u$ ), respectively, for different concentrations of (PMMA/PVAc) blend before and after exposure to filtered and UV radiation for 24 hours. It can be deduced that by increasing the concentration of PMMA in the blend, the values of  $E_g$  decreased and the values of  $E_u$  increased. Furthermore, Table 1 has illustrated that the decrease of  $E_g$  values by increasing the exposure time of UV radiation was

more obvious than that after exposure to filtered radiation because UV radiation has an energy higher than the energy of any bond molecules [16]. Moreover, the blend of (50/50 PMMA/PVAc) modified the wideness of PMMA spectra after exposure to UV radiation.

Also, the values of  $E_u$  have increased by increasing the exposure time as indicated in [17]. The increase of  $E_u$  values by increasing the concentration of PMMA in (PMMA/PVAc) blend can be attributed to the effect of internal potential fluctuation associated with the structural disorder [11]. In addition, the values of constant ( $B$ ) in (2) were determined from the slope of the linear part of Figure 4(a) for the

TABLE 2: The band tail width  $E_u$  (eV) for different concentrations of (PMMA/PVAc) blends after exposure to UV and filtered radiation at different exposure times.

PMMA/PVAc	Exposure radiation	Exposure Time (Hour)				
		0	4	12	20	24
(100/0)	filter	0.40	0.41	0.43	0.45	0.46
	UV	<b>0.40</b>	<b>0.42</b>	<b>0.46</b>	<b>0.49</b>	<b>0.53</b>
(75/25)	filter	0.39	0.39	0.43	0.43	0.43
	UV	<b>0.39</b>	<b>0.39</b>	<b>0.43</b>	<b>0.45</b>	<b>0.48</b>
(50/50)	filter	0.38	0.38	0.41	0.42	0.42
	UV	<b>0.38</b>	<b>0.38</b>	<b>0.43</b>	<b>0.45</b>	<b>0.47</b>
(25/75)	filter	0.28	0.28	0.30	0.30	0.32
	UV	<b>0.28</b>	<b>0.31</b>	<b>0.35</b>	<b>0.38</b>	<b>0.38</b>
(0/100)	filter	0.24	0.28	0.30	0.32	0.32
	UV	<b>0.24</b>	<b>0.34</b>	<b>0.37</b>	<b>0.37</b>	<b>0.38</b>

TABLE 3: Values of the constant  $B$  ( $\text{cm}^{-1} \text{eV}^{1/2}$ ) for different concentrations of PMMA/PVAc blend before and after exposure to UV and filtered radiation for 24 hours.

PMMA/PVAc	Before exposure to radiation	After exposure to filtered radiation	After exposure to UV radiation
(100/0)	67.5	58.5	78.8
(75/25)	39.7	78.4	45.5
(50/50)	91.6	78.7	102.6
(25/75)	85.8	69.5	63.2
(0/100)	127.3	123.2	138.5

samples before exposure to light and also after exposure to UV and filtered radiation which are summarized in Table 3. The unit may be given [18] as  $\text{cm}^{-1} \text{eV}^{(1-r)}$ .

**3.4. Optical Constants.** The absorption coefficient ( $\alpha$ ) of the medium provides valuable optical information for material identification. The attenuation coefficient ( $k$ ) [19] is directly proportional to the absorption coefficient ( $\alpha$ ) as seen in (4)

$$\alpha = \frac{4\pi k}{\lambda}, \quad (4)$$

where  $\lambda$  is the free space wavelength of light. For normal incidence, the reflection coefficient ( $R$ ) [19] is given by (5)

$$R = \frac{[(n-1)^2 + k^2]}{[(n+1)^2 + k^2]}. \quad (5)$$

The measurements of specular reflection and the absorbance are used to calculate the optical constants ( $n$ ,  $k$ ) by the two previous equations. Figure 5 illustrates the refractive index values for the blend of (PMMA/PVAc) with variant concentrations at wavelength of 200 nm. It has been found that the value of ( $n$ ) increases with increasing the concentration of PMMA in (PMMA/PVAc) blend which is a result of increasing the number of atomic refractions due

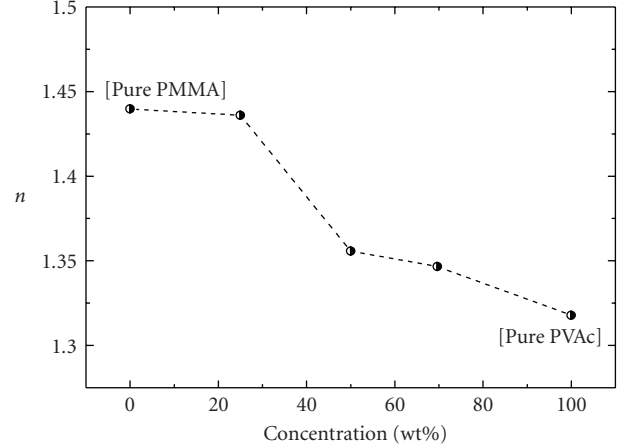


FIGURE 5: The variation of refractive index ( $n$ ) versus different concentrations of PVAc in (PMMA/PVAc) blends without exposure to radiation at wavelength of 200 nm.

to the increase of the linear polarizability in agreement with Lorentz formula [20], as in (6)

$$\frac{n^2 - 1}{n^2 + 2} = \frac{4}{3}\pi N\alpha_p, \quad (6)$$

where  $n$ ,  $N$ , and  $\alpha_p$  are refractive index, the number density of molecules, and linear polarizability, respectively. On the other hand, Figure 6 shows that there is a minimum peak in the wavelength range of the absorption band followed by an increase of the values of ( $n$ ), for PMMA, PVAc, and their (50/50 PMMA/PVAc) blend, which clarifies the presence of normal dispersion according to Cauchy's dispersion formula [16], as in (7):

$$\frac{dn}{d\lambda} = -\frac{2B_1}{\lambda^3}. \quad (7)$$

Also, the curves of refractive index ( $n$ ) show no minimum caused by absorption in the visible wavelength, which is pointing to the fact that all the samples are colorless [21]. In addition, the increase in the values of the refractive index after exposure to UV radiation for 24 hours could be attributed to localized density increased arising from photoinduced cross linking [22]. Moreover, Figure 6 shows that the increase of refractive index ( $n$ ) for the samples after exposure to UV radiation was more obvious than that after exposure to filtered radiation due to the effect of UV.

## 4. Conclusions

Blend films of PMMA and PVAc with different concentrations have been prepared by casting method, and they were exposed to UV and filtered radiation for 24 hours. The films were characterized spectroscopically using FTIR which illustrated that the decrease of the intensity of transmission spectra of (50/50 PMMA/PVAc) blend after exposure to UV radiation for 24 hours was lower than that of PMMA and PVAc. Consequently, (50/50 PMMA/PVAc) blend has improved the degradation of its homopolymer. Furthermore,

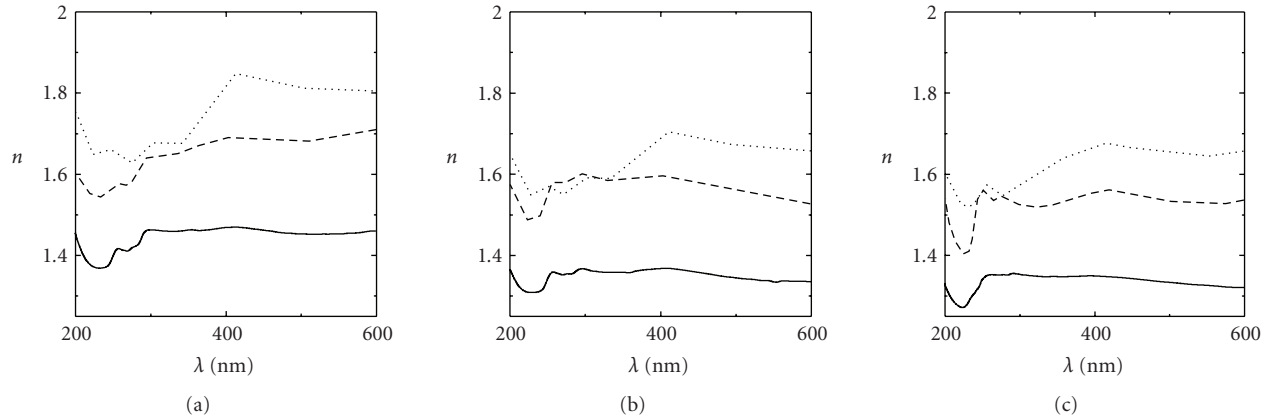


FIGURE 6: Spectral distribution of refractive index ( $n$ ) for (a) pure PMMA, (b) a blend of (50/50 PMMA/PVAc), and (c) pure PVAc before (—) and after exposure to filtered (- -) and UV radiation (...) for 24 hours.

the calculated values of the optical parameters illustrated that there was a reduction in  $E_g$  values of the films by increasing the concentration of PMMA in the blend and also after exposure to UV radiation. Moreover, the refractive index values have been calculated from a combination of reflectance and absorbance measurements at normal incidence for all films which illustrated that there was an increase of these values by increasing the concentration of PMMA in the blend and also after exposure to UV radiation for 24 hours. In conclusion, from all the previous results, it could be concluded that (50/50 PMMA/PVAc) blend has modified the optical properties of its homopolymers and also it may be suggested to be a good matrix for the dyes used in fluorescent solar collectors.

## References

- [1] H. Kaczmarek, R. Drag, M. Swiatek, and D. Oldak, "The influence of UV-irradiation on poly (vinyl chloride) modified by poly (vinyl acetate)," *Surface Science*, vol. 507–510, no. 1–3, pp. 887–882, 2002.
- [2] M. Peesan, P. Supaphol, and R. Rujiravanit, "Effect of casting solvent on characteristics of hexanoyl chitosan/poly lactide blend films," *Journal of Applied Polymer Science*, vol. 105, no. 4, pp. 1844–1852, 2007.
- [3] C. Wochnowski, S. Metev, and G. Sepold, "UV—laser-assisted modification of the optical properties of polymethylmethacrylate," *Applied Surface Science*, vol. 154–155, pp. 706–711, 2000.
- [4] A. K. Baker and P. E. Dyer, "Refractive-index modification of polymethylmethacrylate (PMMA) thin films by KrF-laser irradiation," *Applied Physics A*, vol. 57, no. 6, pp. 543–544, 1993.
- [5] T. Kardinahl and H. Franke, "Photoinduced refractive-index changes in fulgide-doped PMMA films," *Applied Physics A*, vol. 61, no. 1, pp. 23–27, 1995.
- [6] A. Kamińska and M. Świątek, "Thermal and photochemical stability of poly(methyl methacrylate) and its blends with poly(vinyl acetate)," *Journal of Thermal Analysis*, vol. 46, no. 5, pp. 1383–1390, 1996.
- [7] W. Ki-Lee and C. S. Ha, *Korea Polymer Journal*, vol. 8, no. 6, pp. 934–941, 1994.
- [8] M. G. El Shaarawy, A. F. Mansour, S. M. El-Bashir, M. K. El-Mansy, and M. Hammam, "Electrical conduction and dielectric properties of poly(methyl methacrylate)/perylene solar concentrators," *Journal of Applied Polymer Science*, vol. 88, no. 3, pp. 793–805, 2003.
- [9] H. Kaczmarek and H. Chaberska, "The influence of UV-irradiation and support type on surface properties of poly(methyl methacrylate) thin films," *Applied Surface Science*, vol. 252, no. 23, pp. 8185–8195, 2006.
- [10] H. J. Heller and H. R. Blattman, "Some aspects of stabilization of polymers against light," *Journal of Pure and Applied Chemistry*, vol. 36, no. 1–2, p. 141, 1973.
- [11] R. M. Ahmed, *Characteristics of some transparent polymer films and its application in solar energy conversion*, M.S. thesis, Zagazig University, Zagazig, Egypt, March 2004.
- [12] E. A. Davis and N. F. Mott, "Conduction in non-crystalline systems V. Conductivity, optical absorption and photoconductivity in amorphous semiconductors," *Philosophical Magazine*, vol. 22, no. 179, pp. 903–922, 1970.
- [13] C. M. Joseph and C. S. Menon, "Electrical conductivity, optical absorption and structural studies in AgInSe<sub>2</sub> thin films," *Semiconductor Science & Technology*, vol. 11, no. 11, pp. 1668–1671, 1996.
- [14] R. Swanepoel, "Determination of surface roughness and optical constants of inhomogeneous amorphous silicon films," *Journal of Physics E*, vol. 17, no. 10, pp. 896–903, 1984.
- [15] M. F. Kotkata, H. T. El Shair, M. A. Afifi, and M. M. Abdel Aziz, "Effect of thallium on the optical properties of amorphous GeSe<sub>2</sub> and GeSe<sub>4</sub> films," *Journal of Physics D*, vol. 27, no. 3, pp. 623–627, 1994.
- [16] R. M. Ahmed, *Studies on fluorescent dye doped in transparent solid matrix and its application in solar energy collection*, Ph.D. thesis, Zagazig University, Zagazig, Egypt, June, 2007.
- [17] A. F. Mansour, "Photostability and optical parameters of copolymer styrene/MMA as a matrix for the dyes used in fluorescent solar collectors," *Polymer Testing*, vol. 23, no. 3, pp. 247–252, 2004.
- [18] S. K. J. Al-Ani, Y. Al-Ramadin, M. S. Ahmad, et al., "The optical properties of polymethylmethacrylate polymer dispersed liquid crystals," *Polymer Testing*, vol. 18, no. 8, pp. 611–619, 1999.
- [19] M. Fox, *Optical Properties of Solids*, Oxford University Press, New York, NY, USA, 2001.

- [20] T. Kada, A. Obara, T. Watanabe, et al., "Fabrication of refractive index distributions in polymer using a photochemical reaction," *Journal of Applied Physics*, vol. 87, no. 2, pp. 638–642, 2000.
- [21] N. A. Bakr, A. F. Mansour, and M. Hammam, "Optical and thermal spectroscopic studies of luminescent dye doped poly(methyl methacrylate) as solar concentrator," *Journal of Applied Polymer Science*, vol. 74, no. 14, pp. 3316–3323, 1999.
- [22] W. J. Tomlinson, I. P. Kaminow, E. A. Chandross, R. L. Fork, and W. T. Silfvast, "Photo induced refractive index increase in poly(methylmethacrylate) and its applications," *Applied Physics Letters*, vol. 16, no. 12, pp. 486–489, 1970.

## Research Article

# Optical, XPS and XRD Studies of Semiconducting Copper Sulfide Layers on a Polyamide Film

Valentina Krylova<sup>1</sup> and Mindaugas Andrulevičius<sup>2</sup>

<sup>1</sup>Department of Inorganic Chemistry, Kaunas University of Technology, Radvilėnų street. 19, LT-50254 Kaunas, Lithuania

<sup>2</sup>Institute of Physical Electronics, Kaunas University of Technology, Savanorių avenue 271, 50131 Kaunas, Lithuania

Correspondence should be addressed to Valentina Krylova, valentina.krylova@ktu.lt

Received 15 April 2009; Revised 7 July 2009; Accepted 2 September 2009

Recommended by Mohamed Sabry Abdel-Mottaleb

Copper sulfide layers were formed on polyamide PA 6 surface using the sorption-diffusion method. Polymer samples were immersed for 4 and 5 h in  $0.15 \text{ mol} \cdot \text{dm}^{-3}$   $\text{K}_2\text{S}_5\text{O}_6$  solutions and acidified with HCl ( $0.1 \text{ mol} \cdot \text{dm}^{-3}$ ) at  $20^\circ\text{C}$ . After washing and drying, the samples were treated with Cu(I) salt solution. The samples were studied by UV/VIS, X-ray diffraction (XRD) and X-ray photoelectron spectroscopy (XPS) methods. All methods confirmed that on the surface of the polyamide film a layer of copper sulfide was formed. The copper sulfide layers are indirect band-gap semiconductors. The values of  $E_{\text{bg}}$  are 1.25 and 1.3 eV for 4 h and 5 h sulfured PA 6 respectively. Copper XPS spectra analyses showed Cu(I) bonds only in deeper layers of the formed film, while in sulfur XPS S 2p spectra dominating sulfide bonds were found after cleaning the surface with  $\text{Ar}^+$  ions. It has been established by the XRD method that, beside  $\text{Cu}_2\text{S}$ , the layer contains  $\text{Cu}_{1.9375}\text{S}$  as well. For PA 6 initially sulfured 4 h, grain size for *chalcocite*,  $\text{Cu}_2\text{S}$ , was  $\sim 35.60 \text{ nm}$  and for *djurleite*,  $\text{Cu}_{1.9375}\text{S}$ , it was  $54.17 \text{ nm}$ . The sheet resistance of the obtained layer varies from  $6300 \text{ } \Omega/\text{cm}^2$ .

Copyright © 2009 V. Krylova and M. Andrulevičius. This is an open access article distributed under the Creative Commons Attribution License, which permits unrestricted use, distribution, and reproduction in any medium, provided the original work is properly cited.

## 1. Introduction

Modification of polymers physical properties by formation on their surfaces of thin layers of inorganic compounds allows obtaining composites with desirable properties. The last few decades saw an increasing interest in semiconducting copper sulfide thin films, because of their applications in various fields of science and technology. Copper sulfide thin films have a number of applications in various devices such as: solar cells, superionic conductors, semiconductors, photodetectors, photothermal conversion devices, electroconductive electrodes, microwave shielding coating [1–4], gas sensors functioning at temperatures tending to room temperature [4], as polarizers of infrared radiation [5], and active absorbents of radio waves [6].

Numerous studies are devoted to the production of  $\text{Cu}_x\text{S}$  layers in the polymer matrix by chemical methods [7, 8]. Application of these copper sulfide layers depends on their properties, such as chemical composition, structure, and electrical conductivity. The properties of the obtained layers

depend on the conditions of synthesis, the precursor of sulfur and their composition [9, 10]. Compositions of these layers have been studied by XRD [11, 12], FTIR [13], potentiometry [14], however, to our knowledge, investigations by XPS are lacking.

The aim of this work was to study the phase composition of  $\text{Cu}_x\text{S}$  layers obtained by the sorption-diffusion method in a polyamide matrix by means of UV/VIS, XPS, and XRD.

## 2. Experimental Details

Potassium pentathionate,  $\text{K}_2\text{S}_5\text{O}_6 \cdot 1.5\text{H}_2\text{O}$ , was prepared from  $\text{As}_2\text{O}_3$  and potassium thiosulfate, and was chemically analysed according to published procedures [15]. The purity of the obtained potassium pentathionate was 99.3%. Salt was stored in the desiccators over sulfuric acid.

The solutions of freshly prepared  $\text{K}_2\text{S}_5\text{O}_6 \cdot 1.5\text{H}_2\text{O}$  in  $0.1 \text{ mol} \cdot \text{dm}^{-3}$  HCl at a concentration of  $0.15 \text{ mol} \cdot \text{dm}^{-3}$  and a temperature of  $20^\circ\text{C}$  was used for the diffusion of sulfur(II) containing anionic particles into PA samples.

The polyamide PA 6 tape 70  $\mu\text{m}$  thick (specification TY 6-05-1775-76, grade PK-4, Russia) were used for experiments. This film is close to a nonporous material, because the pores of PA 6 are much less than 1.5 nm. The porosity was measured by the BET method [16] using a Quantasorb sorption system (USA). Film density was checked by the flotation method. It was found, that the density of PA is equal to  $1.13 \text{ g} \cdot \text{cm}^{-3}$ .

Prior to the experiments, samples of the PA 6 film 15 mm  $\times$  70 mm in size, were boiled in distilled water for two hours to remove the remainder of the monomer, then dried with filter paper and in a desiccators over  $\text{CaCl}_2$  for 24 hours.

PA 6 films were sulfured in a thermostatic vessel using a continually stirred acidified ( $0.1 \text{ mol} \cdot \text{dm}^{-3} \text{ HCl}$ , pH  $\sim$  1.5)  $0.15 \text{ mol} \cdot \text{dm}^{-3} \text{ K}_2\text{S}_5\text{O}_6$  solutions at a temperature of  $20^\circ\text{C}$ . Preliminary experiments had shown that sorption from the solutions of a lower concentration was too slow and insufficient. At temperatures higher than  $30^\circ\text{C}$ , the stability of pentathionate solution was insufficient, and gradual spontaneous decomposition of polythionate with the liberation of elemental sulfur occurred [7].

After 4 and 5 hours of pretreatment in  $\text{K}_2\text{S}_5\text{O}_6$  solution, the PA 6 film samples were removed, rinsed with distilled water, dried with filtration paper, kept over  $\text{CaCl}_2$  for 24 hours, and then used in further experiments and analysis.

Sulfur concentrations in PA 6 film samples were determined potentiometrically [17]. Firstly, the sample of a sulfured PA 6 film was thermally treated in  $10\text{--}15 \text{ cm}^3$  of  $10 \text{ mol} \cdot \text{dm}^{-3} \text{ KOH}$  diluted with the same amount of distilled water. Standard calomel and platinum electrodes were used for the potentiometric titration of the solution obtained in  $\text{KOH}$  with  $0.05 \text{ mol} \cdot \text{dm}^{-3}$  solution of iodine under stirring. For the potentiometric measurements the pH-meter—pH-673 M voltmeter was used.

A solution of Cu(I) salt was produced from the solution of  $0.4 \text{ mol} \cdot \text{dm}^{-3} \text{ CuSO}_4$  with addition of  $3.4 \text{ mol} \cdot \text{dm}^{-3} \text{ NH}_3 \cdot \text{H}_2\text{O}$  and  $0.36 \text{ mol} \cdot \text{dm}^{-3}$  of a reducing agent, hydroxylamine sulfate, by the method presented in [18]. The pH of the solution was 9.73. All ions of divalent copper turn into ions of univalent copper in this mixture independently of the temperature. After pretreatment in  $\text{K}_2\text{S}_5\text{O}_6$  solution, the PA 6 sample was treated for 20 minutes at a temperature of  $35^\circ\text{C}$  with a Cu(I) solution, then rinsed with distilled water, dried over  $\text{CaCl}_2$  and used in further experiments.

The amount of copper in the sulfide film was determined with a Perkin-Elmer atomic absorption spectrometer ( $\lambda = 325 \text{ nm}$ ) [19] after fusing the film in concentrated nitric acid. The content of copper and sulfur was expressed as  $\mu\text{mol} \cdot \text{cm}^{-2}$ .

The sheet resistance of  $\text{Cu}_x\text{S}$  layers of different composition was measured at the constant current using the E7–8 digital multimeter (Russia) with custom design electrodes. The measurements were carried out with  $1 \text{ cm}^2$  square electrodes, therefore the resistance is shown in  $\Omega/\text{cm}^2$ .

The UV/VIS spectra (from 200 to 800 nm) were recorded on a Spectronic Genesys 8 UV/Visible spectrophotometer with compensation of PA 6 absorption.

The composition and chemical state of the elements in the copper sulfide film surface were studied using X-

ray Photoelectron Spectroscopy (XPS) on a KRATOS ANALYTICAL XSAM800 spectrometer. The energy scale of the spectrometer was calibrated using Au  $4f_{7/2}$ , Cu  $2p_{3/2}$ , and Ag  $3d_{5/2}$  peak positions [20]. The X-ray source was operating in aluminium anode mode (Al  $K\alpha$  photon energy of 1486.6 eV). The hemispherical energy analyser with the pass energy of 20 eV and the fixed analyser transmission (FAT) mode were used. The main core level photoemission spectra (with 0.1 eV energy increment) of Cu, O, C, and S were taken. The X-ray excited Auger spectra of copper (Cu  $L_3M_{45}M_{45}$ ) were collected with a 0.25 eV energy increment. For all spectra, the charge shift was compensated according to C 1s peak position. The relative atomic concentrations of copper, oxygen, carbon, and sulfur were calculated from an appropriate peak area with respect to the sensitivity factors, using original KRATOS software. Shirley background subtraction was used for atomic concentrations calculation. Surface cleaning with  $\text{Ar}^+$  ions ( $3 \text{ KeV}$ ,  $18 \mu\text{A}/\text{cm}^2$ ) was used to remove atmospheric contaminants from the surface of samples.

X-ray diffractometry was carried out under a Bragg-Brentano circuit on a Dron-6 diffractometer (Russia) using Cu  $K\alpha$  ( $\lambda = 0.154178 \text{ nm}$ ) radiation, 30 kV voltages, and 30  $\mu\text{A}$  current. The scanning range was  $\theta = 28\text{--}60^\circ$ , and the scanning speed was  $1 \text{ min}^{-1}$ . Results were registered in the in situ mode with a computer, and X-ray diffractograms of PA 6 samples with  $\text{Cu}_x\text{S}$  layers were treated using the Sarch Match, Xfit, ConvX, Dplot95, and Photo Styler programs to eliminate the PA 6 maxima.

### 3. Results and Discussion

**3.1. Chemical Analysis of Thin  $\text{Cu}_x\text{S}$  Film Layers.** As mentioned before, the method of preparation influences the composition and characteristics of sulfide layers. Therefore, the initial stage of the work was aimed to establish the chemical composition of  $\text{Cu}_x\text{S}/\text{PA}$ .

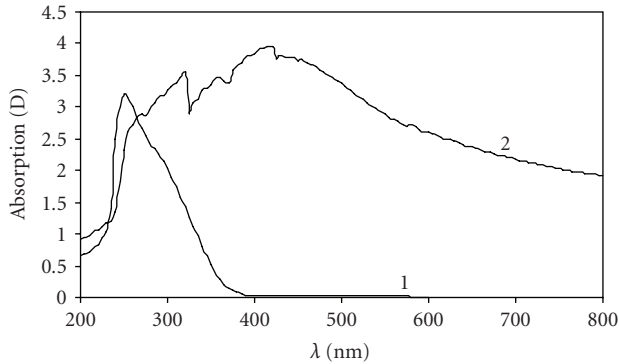
The chemical composition of copper sulfide films obtained in different conditions is presented in Table 1. The molar ratios of copper and sulfur found in sulfide films show that nonstoichiometric copper sulfide and nonsulfide sulfur can coexist.

**3.2. Optical Studies of Thin  $\text{Cu}_x\text{S}$  Film Layers.** The typical UV/VIS absorption spectra of PA 6 samples sulfured for 5 hours in a solution of  $\text{K}_2\text{S}_5\text{O}_6$  at  $20^\circ\text{C}$  are presented in Figure 1, curve 1, where the spectrum of PA substrate is subtracted. Two absorption peaks are observed in these spectra: at 250 nm as a peak, and as a less intense and shallower band at  $\lambda = 295 \text{ nm}$ . Thus, the UV/VIS absorption spectra confirm that the sulfur is sorbed by PA 6 films in the form of pentathionate ions [21, 22]. The intensity of absorption maxima in the spectra increases with increasing exposure time of polymer treatment with potassium pentathionate solution.

After interaction of copper ions with polyamide in the presence of sulfur, a number of new peaks appear in the interval of 295–465 nm for PA sulfured in the potassium pentathionate solution, and a change tendency was observed

TABLE 1: Chemical composition of  $\text{Cu}_x\text{S}$  layers formed in PA matrices, depending on the duration of film pretreatment time.

Parameter	Duration time of treating the PA films in $\text{K}_2\text{S}_5\text{O}_6$ solution, h	
	4	5
Sulfur concentration $c_s, \mu\text{mol} \cdot \text{cm}^{-2}$	3.10	3.26
Copper concentration $c_{\text{Cu}}, \mu\text{mol} \cdot \text{cm}^{-2}$	2.04	2.24
Cu/S molar ratio	1 : 1.52	1 : 1.45

FIGURE 1: Typical UV/VIS absorption spectra: (1) of the layers of PA 6 sulfured for 5 hours in  $0.15 \text{ mol} \cdot \text{dm}^{-3} \text{ K}_2\text{S}_5\text{O}_6$  at  $20^\circ\text{C}$ , (2) of the layers then treated with Cu(I) salt.

in comparison with that before the interaction with copper. Three obvious absorption peaks at 320 nm, 360 nm, and abroad absorption peak at 465 nm appeared on the surface of PA (see Figure 1, curve 2). All these peaks are higher than relevant peaks of PA before the interaction with copper indicating that they are copper sulfides species. These data in Figure 1 are consistent with the number and intensity of copper sulfides phases detected according to our XRD measurements (see Figure 5, curve 2).

The variation of the optical absorption coefficient near the absorption edge follows the power law [23] in the form of

$$\alpha = \frac{B(E - E_{\text{bg}})^n}{E}, \quad (1)$$

where  $E$  is the photon energy- $h\nu$ ;  $E_{\text{bg}}$  is the band-gap energy of the system;  $B$  is the function of density of states near the conduction and valence band edges. The value of  $n$  is 2 for direct transition and  $(1/2)$  for indirect transition.

The optical absorption coefficient is found to have a value of  $1.48 \cdot 10^4 - 1.52 \cdot 10^4 \text{ cm}^{-1}$ .

Transition copper sulfides are usually indirect band-gap semiconductors [24, 25]. The values of  $E_{\text{bg}}$  obtained from the intercepts of the straight line portion of the curves with the  $h\nu$  axis for the zero absorption are 1.25 and 1.3 eV for 4 hours and 5 hours sulfured PA 6, respectively.

The observed  $E_{\text{bg}}$  differences could be connected either with the structural changes of different thickness of layers or different exposure time in potassium pentathionate solution. Therefore, the influence of layers composition on the  $E_{\text{bg}}$  value can be regarded as dominant in our experiment.

**3.3. XPS Analysis of Thin  $\text{Cu}_x\text{S}$  Film Layers.**  $\text{Cu}_x\text{S}$  films deposited on PA 6 surface were examined by XPS measurements. The core levels S 2p, Cu 2p, O 1s, C 1s spectra and the Cu Auger spectrum were measured. During formation of the  $\text{Cu}_x\text{S}$  layer on the surface of polycapromamide, all processes proceed in an open medium; therefore, it is not possible to avoid ambient effects. Since the surface of this layer is active, it adsorbs oxygen, water, and other contaminants [26–28]. The layer of sulfide on the surface of the polymer is distributed in the form of islands enabling an easy contact of the atmospheric oxygen with copper and sulfur ions. Therefore the surface of the  $\text{Cu}_x\text{S}$  layer can differ from the macrostructure and chemical composition of the entire layer. It is necessary to emphasize that the XPS method investigates very thin (up to few nm) surface layers, whereas the grains size in the film determined by optical microscopy [29] is approximately  $30 \mu\text{m}$ , that is, can reach several tens of microns.

The data of XPS analysis show that the composition of  $\text{Cu}_x\text{S}$  layers formed at different pretreatment time in  $0.15 \text{ mol} \cdot \text{dm}^{-3} \text{ K}_2\text{S}_5\text{O}_6$  solutions is rather similar. They consist of copper, sulfur, carbon, and oxygen in various combinations. Oxygen on the surface of the copper sulfide layer was established by other methods, for example, during precipitation of thin  $\text{Cu}_2\text{S}$  films from solutions [30]. The amount of oxygen significantly reduces when the surface of the sulfide layer is cleaned with  $\text{Ar}^+$  ions.

The XPS Cu 2p spectra of PA 6 sample sulfured for 5 hours and afterwards treated in Cu(I) salt solution are shown in Figure 2. In the spectra taken before sputtering (see Figure 2, curve 1), the “shake-up” satellite at 944 eV position and a low intensity peak at 935.5 eV are clearly visible. The “shake-up” satellite is an evidence of Cu(II) ions [26], while the peak at 935.5 eV coincides with the known  $\text{CuSO}_4$  peak position at 935.4 eV [31]. A high-intensity peak at 932.8 eV (FWHM = 1.85 eV) is close to reported peak positions of  $\text{Cu}_2\text{S}$  (932.5 eV),  $\text{Cu}_2\text{O}$  (932.5 eV) [31], and Cu–Cu (932.63 eV) [20]. However, this peak is shifted by 0.6 eV from the known CuS peak (932.2 eV) [31], and by 0.8 eV from the CuO peak (933.6 eV) [31]. A more clear distinction between the mentioned Cu(I) and Cu(II) bonds is described afterwards using copper Auger peaks. After  $\text{Ar}^+$  sputtering (see Figure 2, curve 2) the “shake-up” satellite and the peak at 935.5 eV disappear, while the high intensity peak at 932.8 eV becomes more intense and narrow (FWHM = 1.6 eV), its position being unchanged. It is known that evaporation of volatile sulfur oxides takes place due to bombardment by  $\text{Ar}^+$  ions of the oxidized sulfide surface [32]. Therefore, the sample surface before sputtering can be described as  $\text{Cu}_2\text{S}$

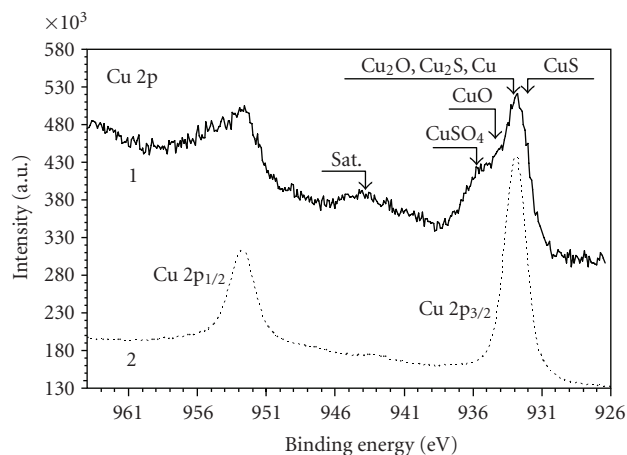


FIGURE 2: Copper XPS Cu 2p spectra of PA 6 sulfured for 5 hours and treated with Cu(I) salt: (1) before and (2) after  $\text{Ar}^+$  cleaning. Arrows show possible positions of copper peaks as described in the text.

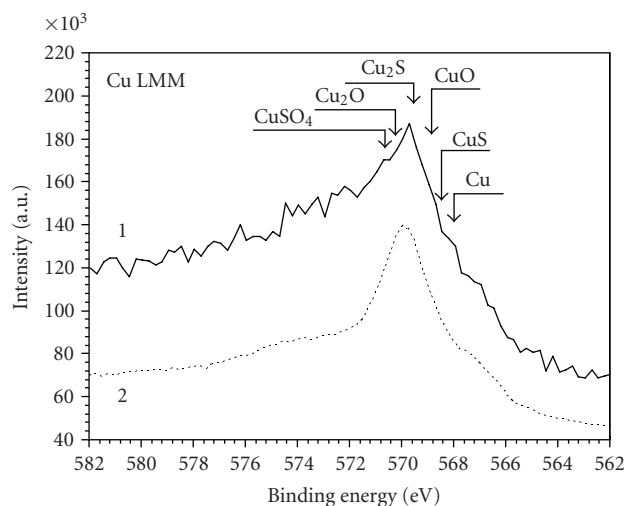


FIGURE 3: Copper Auger spectra of PA 6 sulfured for 5 hours and treated with Cu(I) salt: (1) before and (2) after  $\text{Ar}^+$  cleaning. Arrows show possible positions of copper peaks as described in the text.

copper sulfide with oxidized upper layers. The sample surface after  $\text{Ar}^+$  cleaning can be described as  $\text{Cu}_2\text{S}$  sulfide with removed volatile sulfur oxides if the identification of  $\text{Cu}_2\text{S}$  sulfide is reasonable.

For a clearer picture of Cu bonds, the copper Auger spectra excited with X-rays are shown in Figure 2. It is difficult to distinguish  $\text{Cu}_2\text{S}$ ,  $\text{Cu}_2\text{O}$ , and Cu–Cu bonds from Cu 2p peak positions (see Figure 2), but the Cu  $L_3M_{45}M_{45}$  peak positions for  $\text{Cu}_2\text{S}$ ,  $\text{Cu}_2\text{O}$ ,  $\text{CuSO}_4$ ,  $\text{CuO}$ ,  $\text{CuS}$ , and Cu–Cu bonds are more isolated – 569.5 eV, 569.9 eV, 570.5, 568.7 eV, 568.5 eV [31], and 567.93 eV, respectively [20]. Before  $\text{Ar}^+$  ions bombardment the Cu  $L_3M_{45}M_{45}$  peak position (569.7 eV, Figure 3, curve 1) coincides with known  $\text{Cu}_2\text{S}$ ,  $\text{Cu}_2\text{O}$  positions (569.5 eV, 569.9 eV, respectively) [31]. After surface bombardment, the peak becomes more intense and its position is shifted (569.8 eV). This implies that there

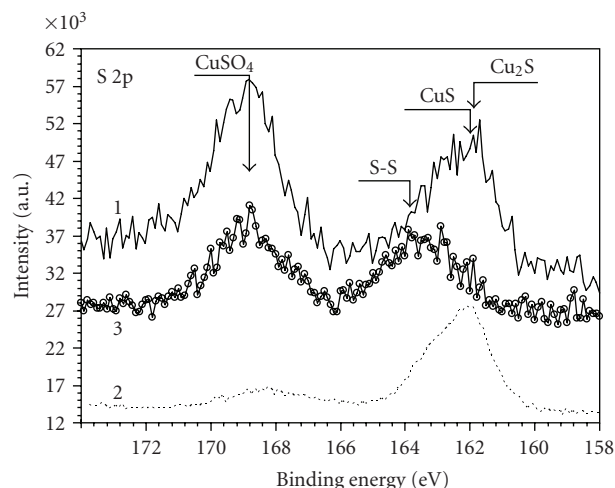


FIGURE 4: Sulfur XPS S 2p spectra of PA 6 sulfured for 5 hours and treated with Cu(I) salt: (1) before and (2) after  $\text{Ar}^+$  cleaning, (3) sulfured PA 6 (for 4 hours at  $20^\circ\text{C}$ ) before Cu(I) salt treatment. Arrows show possible positions of sulfur peaks as described in the text.

are no CuS, CuO, or Cu–Cu bonds, and the dominating phase of copper sulfide is  $\text{Cu}_2\text{S}$ . However, now the peak position is closer to the  $\text{Cu}_2\text{O}$  position and is slightly shifted from the known  $\text{Cu}_2\text{S}$  position.

In the XPS S 2p spectra, different sulfur bonds for Cu(I) salt treated PA 6 (see Figure 4, curve 1) and PA 6 sulfured for 4 hours (see Figure 4, curve 3) were found. For both samples, the higher energy peak position (168.9 eV) coincides with the known  $\text{CuSO}_4$  position (168.8 eV) [31]. This peak for both samples corresponds to sulfur  $\text{SO}_4^{2-}$  bonds in  $\text{CuSO}_4$  in case of the oxidized surface for Cu(I) salt treated PA 6 (see Figure 4, curve 1) and to sulfur  $\text{S}_2\text{O}_3^{2-}$  bonds PA 6 sulfured in pentathionate for 4 hours (see Figure 4, curve 3). The lower energy peak position (161.8 eV) for Cu(I) salt treated PA 6 is in good agreement with known  $\text{Cu}_2\text{S}$  and CuS positions (161.92 eV and 162.1 eV, respectively) [31]. For sulfured PA 6, the lower energy peak position (163.7 eV) is almost the same as the known S–S peak position (163.9 eV) [31], therefore we assign this peak to  $\text{S}^{2-}$ – $\text{S}^{2+}$  bonds in pentathionate or possible elemental sulfur. For Cu(I) salt treated PA 6, oxidized sulfur states are formed on the outermost surface of the  $\text{Cu}_2\text{S}$ ; most likely due to an atmospheric influence. After  $\text{Ar}^+$  ions bombardment (see Figure 4, curve 2), the higher energy peak disappears from S 2p spectra. This confirms removal of volatile sulfur oxides from the copper sulfide surface as was shown in Cu 2p spectra (see Figure 2, curve 2).

Copper and sulfur XPS spectra were almost identical for PA 6 sulfured for 4 hours and treated with Cu(I) salt (not shown here).

Surface atomic concentration after sample treatments is presented in Table 2. The first column (sample description) corresponds to an appropriate PA 6 treatment: “Pure PA 6”—polyamide surface before pentathionate treatment; “Sulf. 4 hours PA 6”—PA 6 treated for 4 hours at  $20^\circ\text{C}$  in

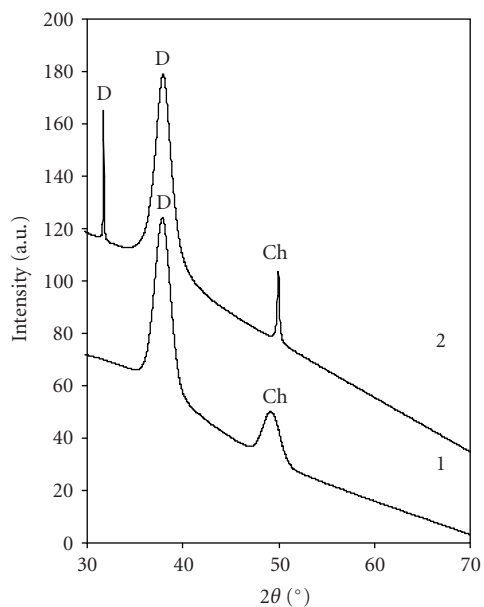


FIGURE 5: X-ray diffraction patterns of  $\text{Cu}_x\text{S}$  layers on PA 6 (peaks of *djurleite*—D, *chalcocite*—Ch). PA 6 initially pretreated for different time and then treated with Cu(I) salt solution for 20 minutes at 35°C. Pretreatment time: 1—4 hours, 2—5 hours.

pentathionate solution; “Sulf. 4 hours PA 6  $\text{Ar}^+$ ”—PA 6 treated for 4 hours at 20°C in pentathionate solution after surface bombardment with  $\text{Ar}^+$  ions for 30 seconds; “Sulf. 4 hours PA 6 Cu(I)”—PA 6 treated for 4 hours at 20°C in pentathionate solution and afterwards in Cu(I) salt solution; “Sulf. 5 hours PA 6 Cu(I)”—PA 6 treated for 5 hours at 20°C in pentathionate solution and afterwards in Cu(I) salt solution.

Surface atomic concentration shows that prolonged (5 hours) PA 6 treatment in pentathionate solution provides increased Cu and S concentrations on PA 6 surface after treatment in Cu(I) salt. In pentathionate-treated PA 6, sulfur atomic concentration decreases after surface cleaning with  $\text{Ar}^+$  ions. The same (4 hours) sample surface treated with Cu(I) salt shows a twice higher sulfur atom concentration even before bombardment with  $\text{Ar}^+$  ions. After surface cleaning, the Cu/S atomic ratio in PA 6 sulfured for 5 hours and treated in Cu(I) salt solution is 1 : 1.4. After  $\text{Ar}^+$  surface cleaning, in this sample the oxygen atomic concentration (22.7%) was approximately three times as high if compared to PA 6 sulfured for 4 hours and cleaned with  $\text{Ar}^+$  (7.7%).

A summarizing analysis of XPS spectra in Cu 2p spectra has shown that the detected position of the peak (932.8 eV) is difficult to distinguish between  $\text{Cu}_2\text{O}$ ,  $\text{Cu}_2\text{S}$ , and Cu—Cu bond positions, but it is fairly separated from the known CuS and CuO bond positions, implying the absence of detectable Cu(II) ions in CuS or CuO bonds after  $\text{Ar}^+$  surface cleaning. This is confirmed by disappearance of low intensity of the “shake-up” satellite which disappears after surface cleaning with  $\text{Ar}^+$  ions. The Cu  $\text{L}_3\text{M}_{45}\text{M}_{45}$  peak position excludes Cu—Cu bonds and confirms existence of only Cu(I) bonds in the obtained film, though possible  $\text{Cu}_2\text{O}$  bonds cannot

be excluded. The sulfur S 2p spectrum for sulfured PA 6 shows sulfur bonds in pentathionate and possible elemental sulfur. For Cu(I) treated PA 6 samples, only sulfide bonds are found in S 2p spectra after surface cleaning with  $\text{Ar}^+$  ions. The oxygen atomic concentration and CuLMM peak shift towards  $\text{Cu}_2\text{O}$  position after  $\text{Ar}^+$  bombardment suggest a certain amount of oxidized Cu(I) in the deeper layers. The chemical bonds of  $\text{Cu}_2\text{S}$  layers initially sulfured for 4 hours and 5 hours are similar, while the atomic concentration of elements in the layers differs. Nevertheless, the Cu/S ratio for both  $\text{Cu}_2\text{S}$  layers is almost the same after  $\text{Ar}^+$  surface cleaning: 1.3 for 4 hours and 1.4 for 5 hours sulfured samples. The XPS data show that the formation of  $\text{Cu}_2\text{S}$  takes place in the bulk of deposits, but it cannot be excluded that the films contain some  $\text{Cu}_x\text{S}$  sites; then  $x$  is close to 2. Due to very close (or overlapping) peak positions in spectra, accurate determination of the  $x$  values in  $\text{Cu}_x\text{S}$  layers from XPS data is impossible.

Another aim of the work was evaluation of the influence of sample treatment on the electrical conductivity of the obtained layers. Sheet resistance for PA 6 treated by Cu(I) salt solution was found to range from 6300 to 102  $\Omega/\text{cm}^2$  and is shown in the second column of Table 2. Sheet resistance variation indicates that the longer pentathionate treatment of PA 6 leads to a better electrical conductivity of produced copper sulfide films. The lowest sheet resistances of 102  $\Omega/\text{cm}^2$  suggest formation of copper sulfide layers with the Cu/S molar ratio 1.45.

**3.4. X-Ray Diffraction Analysis of Thin  $\text{Cu}_x\text{S}$  Film Layers.** The phase composition of the deposited film was investigated by comparing the obtained XRD spectra with those of known minerals [33]. Structural studies of  $\text{Cu}_x\text{S}$  layers deposited by the sorption-diffusion method are limited by the polycrystallinity of the layers obtained, as well as by the existence of  $\text{Cu}_x\text{S}$  phases of various compositions and structure and by the crystallinity of the PA 6 film itself. The intensity of PA 6 peaks at  $\theta < 13^\circ$  exceeds the intensity of copper sulfide peaks several times. Therefore, the area of  $2\theta \geq 26.0^\circ$  was investigated in more detail.

The X-ray diffraction patterns of the layers showed that peaks of various copper sulfide phases are present in the XRD diagram (see Figure 5).

Analysis of the XRD spectra shows that the hexagonal *chalcocite*  $\text{Cu}_2\text{S}$  (PDF 84–209) maximum  $2\theta = 49.28^\circ$  and monoclinic *djurleite*  $\text{Cu}_{1.9375}\text{S}$  (PDF 42–564) maximum  $2\theta = 38.1^\circ$  prevailed in the composition of the sulfide film for PA 6 sulfured for 4 hours and 5 hours (see Figure 5, curve 1, 2).

When the time of pretreatment in the pentathionate solution is prolonged until 5 hours, changes in film composition occur; the intensity of the peaks of *djurleite* slightly decreases, and the intensity of the *chalcocite* peaks increases. This phase predominates in the composition of the sulfide film (see Figure 5, curve 2). After a longer period of sulfuration in  $\text{K}_2\text{S}_5\text{O}_6$  solution, one more *djurleite* (PDF 42–564) maximum  $2\theta = 31.72^\circ$  peak appears (see Figure 5, curve 2), and the intensity of copper sulfide peaks increases.

TABLE 2: The sheet resistance and surface atomic concentration calculation results.

Sample description	Sheet resistance, $\Omega/\text{cm}^2$	Surface atomic concentration, %			
		Cu 2p	O 1s	C 1s	S 2p
Pure PA	—	—	15.8	84.2	—
Sulf. 4hours PA	—	—	18.1	80.6	1.3
Sulf. 4hours PA Ar <sup>+</sup> (30s)	—	—	7.7	91.2	1.1
Sulf. 4hours PA Cu(I)	6300	1.6	12.8	83.5	2.2
Sulf. 4hours PA Cu(I) Ar <sup>+</sup> (30s)		5.0	10.2	80.8	3.9
Sulf. 5hours PA Cu(I)	102	2.1	31.5	62.8	3.6
Sulf. 5hours PA Cu(I) Ar <sup>+</sup> (30s)		19.7	22.7	43.2	14.4

Consequently, we assume that the concentration of copper sulfide in the obtained film increases.

Crystallite size was determined by Scherer's formula [33]:

$$D = \frac{0.9\lambda}{\beta \cos \theta}, \quad (2)$$

where  $\lambda$  is X-ray wavelength,  $\theta$  is Bragg's angle, and  $\beta$  is the full width of diffraction line at half of the maximum intensity.

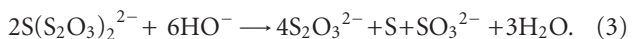
For PA 6 initially pretreated for 4 hours in  $\text{K}_2\text{S}_5\text{O}_6$  solution and then treated with Cu(I) salt solution for 20 minute at 35°C (see Figure 5, curve 1), grain size for *chalcocite*,  $\text{Cu}_2\text{S}$ , was  $\sim 35.60$  nm and for *djurleite*,  $\text{Cu}_{1.9375}\text{S}$ , it was 54.17 nm. For PA 6 initially pretreated for 5 hours in  $\text{K}_2\text{S}_5\text{O}_6$  solution (see Figure 5, curve 2), grain size for *chalcocite*,  $\text{Cu}_2\text{S}$ , was  $\sim 95.56$  nm and for *djurleite*,  $\text{Cu}_{1.9375}\text{S}$ , it was 59.175–90.107 nm.

### 3.5. Mechanism and Kinetics of Copper Sulfide Formation.

The differences of the obtained parameters of thin copper sulfide films on the PA 6 surface permit us to conclude that they may be connected with the peculiarities of their structure and mechanism of reaction following the diffusion of pentathionate across the polycapraamide interface. The mechanism of the heterocatalytic degradation of the pentathionate is still a matter of active investigation.

Pentathionate is, thereby, characterized as sulfur di-(thiosulfate), that is, two thiosulfate groups are bonded to a sulfur atom through the thiosulfur atoms of the thiosulfate groups. The sulfur sulfur bonds in the pentathionate  $^{-2}\text{O}_3\text{S}_2\text{S}^{++}\text{S}_2\text{O}_3^{2-}$  are more ionic than covalent.

With excess alkalis, pentathionate was found to undergo hydrolysis quantitatively as follows [34]:



The stabilizing effect of acids on pentathionate is probably due to the removal of hydroxyl ions. This effect of acids on pentathionate may be also (especially from higher acid concentrations to a small extent) due to the polarizing influence of protons on the oxygen atoms of the terminal sulfuroxy groups. At sufficiently high acid concentrations this polarizing proton effect causes breakdown of pentathionate

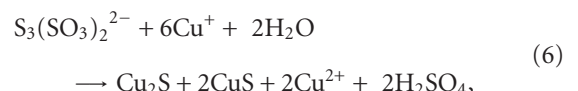
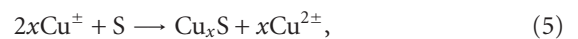
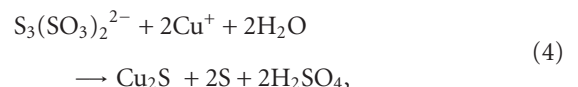
acids with liberation of hydrogen sulfide and elemental sulfur, respectively. The ionisation of thiosulfate ion in monosulfur di-(thiosulfate) in pentathionate is facilitated through the higher electronegativity of sulfur.

Therefore, a polythionic compound of the pentathionic type should keep its central sulfur more firmly bound to the lower oxidability of the thio anion from which it is built up. Since the pentathionate solutions are unstable, after several hours a degradation of the initial solution starts and new structural units like elemental S, polythionates (namely,  $\text{K}_2\text{S}_3\text{O}_6$ ,  $\text{K}_2\text{S}_4\text{O}_6$ ), sulfite, and sulfate may appear. We expect that the chemical degradation also influences the parameters of the anionic particles containing sulfur atoms diffused into PA 6.

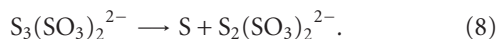
Our data suggest a situation in which previously diffused sulfur particles lead to a modification of PA 6 surface, which favours the further sorption of copper ions.

The results of sorption were interpreted in terms of the semiquantitative estimates of the sorption mechanism. A variety of new effects become important as far as the interactions of inorganic sorbates with PA 6 surface are concerned, for example, the electrostatic interaction of sorbate ions, namely  $\text{S}_3(\text{SO}_3)_2^{2-}$  with charged sites of the sorbent, such as the ionised polycapraamide functional groups  $-\text{CO}-\text{NH}-$  and  $-\text{NH}_2$ , and exchange reactions of these ions with ligands previously bonded to the polymer surface or their ionised functional groups. The charge of these particles becomes dependent on the degree of ionisation and consequently on the pH of the medium [22].

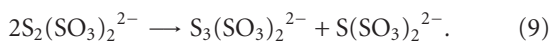
The UV/VIS, XPS and XRD data analyses (Figures 1, 2, 3, 4 and 5) allow us to assume a reaction scheme in which copper sulfide layers on PA 6 are formed by the sorption-diffusion method via heterogeneous chemical reactions [35]:



As mentioned before, pentathionate solutions are unstable; therefore we should expect also the products of chemical degradation to diffuse into PA 6 [36]:



The formed ions can also decompose:



The presence of  $\text{SO}_4^{2-}$  ions in the  $\text{Cu}_x\text{S}$  layers formed on PA 6 can be explained by reaction (6) or the decomposition of adsorbed  $\text{S}_3(\text{SO}_3)_2^{2-}$  by the reaction [36]



$\text{Cu}_2\text{O}$  are conveniently prepared by the reduction of  $\text{CuSO}_4$  using a hydroxylaminosulfate in alkaline ( $\text{NH}_3 \cdot \text{H}_2\text{O}$ ) solution. However, these compounds are rather unstable thermally and tend to be oxidised in air [37]:



The mentioned regularities enable copper sulfide films of desired conductivity to be obtained on PA 6 surface.

#### 4. Conclusions

(1) Layers of copper sulfide of various composition are formed on the surface of polycapromamide if a sulfurized polymer is treated with the water solution of Cu(I) salt: the anionic particles containing sulfur atoms of low oxidation state react with copper ions. The  $\text{Cu}_x\text{S}/\text{PA}$  layers are indirect band-gap semiconductors. Obtained values of  $E_{\text{bg}}$  were 1.25 and 1.3 eV for 4 hours and 5 hours sulfured PA 6, respectively.

(2) Copper XPS spectra analyses showed the existence of only Cu(I) bonds in the deeper layers of the formed  $\text{Cu}_2\text{S}$  film, although possible bonds of  $\text{Cu}_2\text{O}$  were not excluded. In sulfur XPS spectra for sulfured PA 6, sulfur bonds in pentathionate and possible elemental sulfur were found. For Cu(I) treated PA 6 samples, sulfide bonds are found only in S 2p spectra after cleaning the surface with  $\text{Ar}^+$ . Surface atomic concentration calculations show that prolonged PA 6 treatment in pentathionate solution results increased Cu and S concentrations on the formed film surface.

(3) Results of X-ray diffraction analysis confirmed formation of  $\text{Cu}_x\text{S}$  layers of various phases. Comprising in itself mainly phases of hexagonal *chalcocite*  $\text{Cu}_2\text{S}$  ( $84 - 209 : 2\theta = 49.28^\circ$ ) and monoclinic *djurleite*  $\text{Cu}_{1.9375}\text{S}$  ( $42 - 564 : 2\theta = 38.1^\circ$ ) prevails in the composition of  $\text{Cu}_x\text{S}$  film, if PA 6 is sulfured for 4 hours in  $\text{K}_2\text{S}_5\text{O}_6$  solution, but when the period of sulfuration is prolonged (5 hours), the peaks of *chalcocite* and *djurleite* increase. After a longer period of sulfuration, a peak of *djurleite*  $\text{Cu}_{1.9375}\text{S}$  ( $42 - 564 : 2\theta = 31.72^\circ$ ) appears. Consequently, we assume that the concentration of copper sulfide in the obtained film increases.

(4) It was found that grain size for *chalcocite*,  $\text{Cu}_2\text{S}$ , was  $\sim 35.60$  nm, for *djurleite*,  $\text{Cu}_{1.9375}\text{S}$ , it was 54.17 nm for PA 6 initially pretreated for 4 hours in  $\text{K}_2\text{S}_5\text{O}_6$  solution and then treated with Cu(I) salt solution for 20 minutes at  $35^\circ\text{C}$ . For

PA 6 initially pretreated for 5 h in  $\text{K}_2\text{S}_5\text{O}_6$  solution, grain size for *chalcocite*,  $\text{Cu}_2\text{S}$ , was  $\sim 95.56$  nm and for *djurleite*,  $\text{Cu}_{1.9375}\text{S}$ , was 59.175 – 90.107 nm.

(5) The electrical conductivity of the  $\text{Cu}_x\text{S}/\text{PA}$  films at the constant current depends on the layer phase composition. The lowest sheet resistance of  $102 \Omega/\text{cm}^2$  suggests formation of copper sulfide layers with the Cu/S molar ratio of 1 : 1.45.

(6) On the basis of our experiments, the mechanisms of pentathionate reactions in sulfuration medium during its diffusion into PA 6 surface have been considered. Polythionic compounds in their reactions were found to behave as derivatives of divalent electropositive sulfur  $\text{S}^{2+}$  and to undergo hydrolysis and degradation as indicated in the provided reaction formula.

#### Acknowledgments

The authors are gratefully thankful to Dr. N. Dukštienė from Kaunas University of Technology for overall support and help with UV/VIS analysis. They also are gratefully thankful to Dr. R. Ivanauskas from Kaunas University of Technology for helping with XRD analysis.

#### References

- [1] A. Žebrauskas, "Formation of copper sulfide coatings," *Chemical Technology*, vol. 1, p. 39, 1996 (Lithuanian).
- [2] M. A. Korzhuev, "Dufour effect in superionic copper selenide," *Physics of the Solid State*, vol. 40, no. 2, pp. 217–219, 1998.
- [3] T. Yamamoto, K. Tanaka, E. Kubota, and K. Osakada, "Deposition of copper sulfide on the surface of poly(ethylene terephthalate) and poly(vinyl alcohol) films in the aqueous solution to give electrically conductive films," *Chemistry of Materials*, vol. 5, no. 9, pp. 1352–1357, 1993.
- [4] A. Galdikas, A. Mironas, V. Strazdienė, A. Šetkus, I. Ancutienė, and V. Janickis, "Room-temperature-functioning ammonia sensor based on solid-state  $\text{Cu}_x\text{S}$  films," *Sensors and Actuators B*, vol. 67, no. 1, pp. 76–83, 2000.
- [5] M. T. S. Nair and P. K. Nair, "SnS– $\text{Cu}_x\text{S}$  thin-film combination: a desirable solar control coating for architectural and automobile glazings," *Journal of Physics D*, vol. 24, no. 3, pp. 450–453, 1991.
- [6] I. Grozdanov, "Electroconductive copper selenide films on transparent polyester sheets," *Synthetic Metals*, vol. 63, no. 3, pp. 213–216, 1994.
- [7] Lithuanian patent LT no. 4402 B, 1998.
- [8] V. Krylova, R. Ivanauskas, and V. Janickis, "Formation of  $\text{Cu}_x\text{S}$  Layers on Polyamide (PA) Films by use of Potassium Pentathionate ( $\text{K}_2\text{S}_5\text{O}_6$ )," *Chemical Technology*, vol. 4, p. 56, 2002 (Lithuanian).
- [9] V. Janickis, R. Maciulevičius, R. Ivanauskas, and I. Ancutienė, "Chemical deposition of copper sulfide films in the surface of polyamide by the use of higher polythionic acids," *Colloid and Polymer Science*, vol. 281, no. 1, pp. 84–89, 2003.
- [10] I. Ancutienė, V. Janickis, and R. Giesa, "Formation of copper sulfide layers on the surface of polyethylene films of various density by the use of polythionic acids," *Polish Journal of Chemistry*, vol. 78, no. 3, pp. 349–360, 2004.
- [11] V. Janickis, R. Maciulevičius, R. Ivanauskas, and I. Ancutienė, "Study of copper sulfide layers on a polyamide film formed by the use of higher polythionic acids," *Materials Science*, vol. 23, no. 3, pp. 715–727, 2005.

- [12] I. Ancutienė, V. Janickis, and R. Ivanauskas, "Formation and characterization of conductive thin layers of copper sulfide ( $\text{Cu}_x\text{S}$ ) on the surface of polyethylene and polyamide by the use of higher polythionic acids," *Applied Surface Science*, vol. 252, no. 12, pp. 4218–4225, 2006.
- [13] V. Krylova and N. Dukštienė, "Measurements of electrode potentials of the  $\text{Cu}_x\text{S}$  layers obtained on a polycapraamide from  $\text{K}_2\text{S}_5\text{O}_6$  solutions," *Chemical Technology*, vol. 2, p. 91, 2005 (Lithuanian).
- [14] V. Krylova and N. Dukštienė, "Characterization of  $\text{Cu}_x\text{S}$  layers obtained by adsorption-diffusion method on polycapraamide from  $\text{K}_2\text{S}_5\text{O}_6$  solutions," *Polish Journal of Chemistry*, vol. 80, no. 9, pp. 1435–1447, 2006.
- [15] A. I. Brodskij and R. K. Jeriomenko, *Report of the USSR Academy of Sciences*, vol. 101, pp. 487–493, 1955 (Russian).
- [16] S. J. Gregg and K. S. W. Sing, *Adsorption Surface Area and Porosity*, Academic Press, New York, NY, USA, 1969.
- [17] V. I. Aleksejev, *Quantitative Analysis*, Khimya, Russia, Moscow, 1972.
- [18] A. Žebrauskas, "Deposition of copper sulfide coatings on polymeric materials by diffusion method," *Chemistry*, vol. 2, p. 112, 1992 (Russian).
- [19] Perkin-Elmer, "Analytical methods for atomic absorption spectrometry," Perkin-Elmer 503, Perkin-Elmer, 1973.
- [20] ISO 15472:2001, "Surface chemical analysis—X-ray photoelectron spectrometers—Calibration of energy scales".
- [21] R. M. Golding, "Ultraviolet and structural studies of polythionates," *The Journal of Chemical Physics*, vol. 23, no. 6, pp. 1666–1668, 1960.
- [22] V. J. Šukyte, R. Ivanauskas, and V. Janickis, "Preparation and some properties of Cu-Te-S thin films on the polyamide (PA) surface," *Polish Journal of Chemistry*, vol. 79, no. 4, pp. 759–771, 2005.
- [23] M. P. Deshpande, S. K. Gupta, A. Agarwal, and M. K. Agarwal, "Transport and optical property measurements in indium intercalated molybdenum diselenide single crystals grown by DVT technique," *Synthetic Metals*, vol. 123, no. 1, pp. 73–81, 2001.
- [24] P. K. Khanna, "Reduction of transition metal salts by SFS: synthesis of copper and silver sulphides," *Synthesis and Reactivity in Inorganic, Metal-Organic and Nano-Metal Chemistry*, vol. 37, no. 10, pp. 805–808, 2007.
- [25] G. Hodes, *Chemical Solution Deposition of Semiconductor Films*, CRC Press, Baton Rouge, La, USA, 2002.
- [26] C. D. Wagner, W. M. Riggs, L. E. Davis, and J. F. Moulder, *Handbook of X-Ray Photoelectron Spectroscopy*, Perkin-Elmer, Waltham, Mass, USA, 1978.
- [27] I. Možginskienė, *The formation and modification of non-stoichiometrical copper sulfide layers*, Ph.D. thesis, Vilnius University, Vilnius, Lithuania, 1997.
- [28] J. Vinkevičius, I. Možginskienė, and V. Jasulaitienė, "Investigations of the interaction between  $\text{Cu}_{2-x}\text{S}$  coating and  $\text{Ag(I)}$  ions using cyclic voltammetry and X-ray photoelectron spectroscopy," *Journal of Electroanalytical Chemistry*, vol. 442, no. 1-2, pp. 73–82, 1998.
- [29] K. J. Kurzydowski and B. Ralph, *Quantitative Description of the Microstructure of Materials*, CRC Press, Baton Rouge, La, USA, 1995.
- [30] D. Lippkow and H.-H. Strehblow, "Structural investigations of thin films of copper-selenide electrodeposited at elevated temperatures," *Electrochimica Acta*, vol. 43, no. 14-15, pp. 2131–2140, 1998.
- [31] Ch. D. Wagner, A. V. Naumkin, A. Kraut-Vass, J. W. Allison, C. J. Powell, and J. R. Rumble Jr., NIST Standard Reference Database 20, Version 3.4.
- [32] N. M. D. Brown, N. Cui, and A. McKinley, "An XPS study of the surface modification of natural  $\text{MoS}_2$  following treatment in an RF-oxygen plasma," *Applied Surface Science*, vol. 134, no. 1–4, pp. 11–21, 1998.
- [33] T. P. Gujar, V. R. Shinde, and C. D. Lokhande, "The influence of oxidation temperature on structural, optical and electrical properties of thermally oxidized bismuth oxide films," *Applied Surface Science*, vol. 254, no. 13, pp. 4186–4190, 2008.
- [34] O. Foss, "Structures of compounds containing chains of sulfur atoms," in *Advances in Inorganic Chemistry and Radiochemistry*, H. J. Emeleus and A. G. Sharpe, Eds., Academic Press, New York, NY, USA, 1960.
- [35] V. Krylova, "IR absorption spectra of  $\text{Cu}_x\text{S}$  layers on polycapraamide surface formed using potassium pentathionate," *Chemical Technology*, vol. 3, p. 10, 2006 (Lithuanian).
- [36] G. Brauer, Ed., *Handbook Preparative Inorganic Chemistry 1*, Ferdinand Enke, Stuttgart, Germany, 1975.
- [37] N. N. Greenwood and A. Earnshaw, *Chemistry of the Elements*, Pergamon Press, Oxford, UK, 1984.

## Research Article

# Photoluminescence Spectroscopy of CdTe/ZnTe Self-Assembled Quantum Dots

Nebojša Romčević,<sup>1</sup> Maja Romčević,<sup>1</sup> Radmila Kostić,<sup>1</sup> Dušanka Stojanović,<sup>1</sup>  
Aleksandra Milutinović,<sup>1</sup> Jelena Trajić,<sup>1</sup> Grzegorz Karczewski,<sup>2</sup> and Robert Galazka<sup>2</sup>

<sup>1</sup>*Institute of Physics, 11080 Belgrade, Serbia*

<sup>2</sup>*Institute of Physics, Polish Academy of Science, 02-668 Warsaw, Poland*

Correspondence should be addressed to Nebojša Romčević, romcevi@phy.bg.ac.rs

Received 26 June 2009; Revised 27 October 2009; Accepted 9 November 2009

Recommended by Mohamed Sabry Abdel-Mottaleb

We present photoluminescence (PL) measurements of two different, 3 monolayers and 12 monolayers (ml), CdTe self-assembled quantum dot (SAQD) samples. The spectra were recorded in the temperature range 20 K–300 K, with photoexcitation over the ZnTe barrier layer. PL spectra displayed two main emission bands. High-energy PL emission ( $E_1$ ) is ZnTe LO like phonon- ( $\omega_{LO} = 204.2 \text{ cm}^{-1}$  (3 ml),  $\omega_{LO} = 207.3 \text{ cm}^{-1}$  (12 ml)) assisted deexcitation. Dominant low-energy band ( $E_2$ ) presents the direct deexcitation to ground state of the CdTe quantum dots.

Copyright © 2009 Nebojša Romčević et al. This is an open access article distributed under the Creative Commons Attribution License, which permits unrestricted use, distribution, and reproduction in any medium, provided the original work is properly cited.

## 1. Introduction

Great interest has been observed recently in studying the properties of layers of semiconductor materials with a mismatch between their lattice parameters. Favourable conditions for the formation of self-assembled quantum dots are created in such layers [1]. The wide band-gap CdTe/ZnTe system is current interest because of its potential applications in short-wavelength optoelectronic devices, but the large lattice mismatch (6.4%) makes it very difficult to grow CdTe/ZnTe structure of high quality [2].

In the majority of experiments reported so far, dots with sizes larger than the exciton Bohr radius have been studied [3–5]. For instance, the typical size of II-VI CdSe QD's, where the exciton Bohr radius is equal to 3 nm, ranges from slightly larger than this value [3] to even 15 nm in diameter [4]. In these cases then, leakage of the exciton wave function into the barriers is not expected to change significantly for QD size distributions within an ensemble. Consequently, for large QDs no size dependence of the exciton-LO phonon coupling is observed.

Detailed measurements of PL, photoluminescence excitation (PLE), and resonant PL spectroscopy on similar systems are performed in literature [1, 5]. To study the carrier

excitation processes in CdTe/ZnTe SAQD excitations below energy of ZnTe gap were used to identify major carrier excitation mechanisms in CdTe QD's [5].

In our earlier papers we using far-infrared spectroscopy [6], Raman spectroscopy [7], and resonant Raman spectroscopy [8] to investigate structural and phonon properties of CdTe/ZnTe SAQD. By extending this study to photoluminescence spectroscopy we expect to obtain electronic structure and get complete picture of optical properties of these samples.

## 2. Samples and Characterization

Investigated samples were grown by molecular beam epitaxy on GaAs substrate. CdTe buffer layer, 4  $\mu\text{m}$  thick, was deposited on the substrate. After a 0.6  $\mu\text{m}$  thick ZnTe layer, 3 or 12 monolayers (ml) of CdTe were deposited to form a random distribution of quantum dots. The dot layer was covered by 0.1  $\mu\text{m}$  ZnTe capping layer, which is schematic presented in Figure 1. High mismatch of lattice parameters of CdTe (6.482 Å) and ZnTe (6.104 Å) provokes gathering of CdTe molecules and forming of quantum dots. Further details of the samples growth can be found in

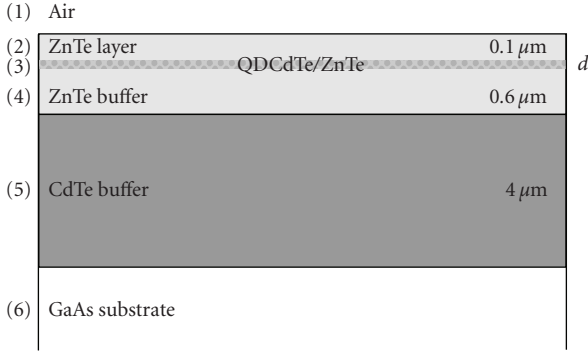


FIGURE 1: A schematic presentation of a six-layer structure.

[1]. It is important to note that the chosen sample set enables us to study quantum dots (QD) with different lateral sizes. Namely, CdTe QDs are very small, and, as estimated by transmission electron microscopy and magnetophotoluminescence measurements, their lateral size is of the order of 2–4 nm in diameter in sample with 3 ml. In second sample (12 ml) there are no CdTe islands; that is, there is a layer with CdTe regions surrounded by alloyed material. This work is focussed to emphasize different properties of these two cases.

Photoluminescence spectra (PL) were excited by several lines of Ar-laser line (514.5 nm, 501.7 nm, 496.5 nm, 488 nm) and Kr-laser line (647.5 nm), measured using a Jobin Yvon model U-1000 monochromator, with a conventional photo-counting system. All Ar-laser lines excite excitons over the ZnTe barrier layer.

### 3. Results and Discussion

The electronic band structure was characterized by a PL spectrum. PL spectra depend on energy excitation. In the case of argon laser excitations the PL spectra displayed two main emission peaks. Typical PL spectra are presented in Figures 2 and 3. Registered bands are separated and no additional analysis was needed to follow the temperature dependence of the energies corresponding to the maximum emission of these bands. Results of all measurements are presented in Figure 4.

We emphasize peaks positions for temperatures at the end of measurement interval. In the case of 3 ml; we have 2.26 eV ( $E_1$ ) and 1.84 eV ( $E_2$ ) at  $T = 300$  K, and 2.346 eV ( $E_1$ ) and 2.17 eV ( $E_2$ ) at  $T = 20$  K. Change in  $E_1$  energy is about 85 meV and change in  $E_2$  is about 330 meV. Red-shift of the high-energy peak  $E_1$  with increasing temperature is the same order of the shift that one would expect from the temperature-induced shrinking of the ZnTe band gap. This peak is registered even at room temperature. Red-shift of the low-energy peak  $E_2$  with increasing temperature is much larger than the shift that one would expect from the temperature-induced shrinking of the CdTe band gap. In the case of 12 mL; we have 2.307 eV ( $E_1$ ) and 2.11 eV ( $E_2$ ) at  $T = 200$  K, and 2.337 eV ( $E_1$ ) and 2.13 eV ( $E_2$ ) at  $T = 20$  K. Change in  $E_1$  energy is about 30 meV and change in

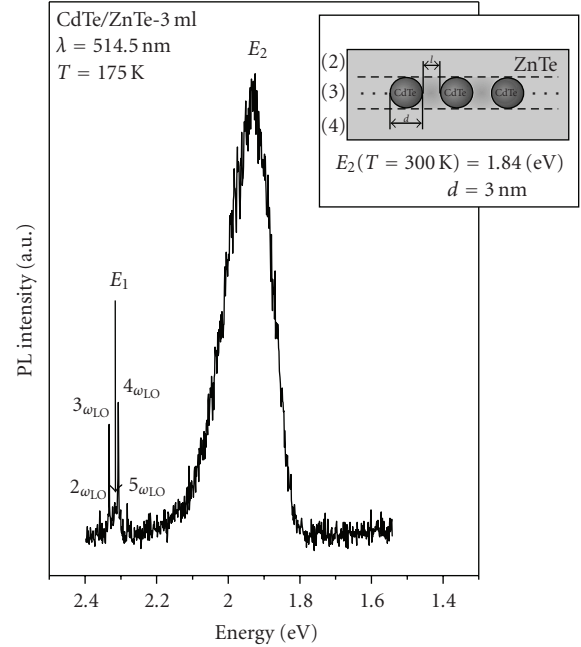


FIGURE 2: Typical PL spectra of sample with 3 ml of CdTe in the finishing layer; PL spectra are excited by  $\lambda = 514.5$  nm Ar-laser line and recorded at 175 K. *Insert*: schematic presentation of the structure of SAQD.

$E_2$  is about 20 meV. Red-shift of both bands with increasing temperature is below values one would expect from the temperature-induced shrinking of the ZnTe and CdTe band gap.

Band energies vary almost linearly with temperature, as presented in Figure 4. The high-energy peak,  $E_1$ , is related to the band gap of the ZnTe barrier [9]. The low-frequency band,  $E_2$ , is related to the recombination in the CdTe quantum dots [5]. MP resonant processes are registered at temperature below 200 K. This process is dominant for QDs with high emission energy, that is, presumably with smaller size [5].

Energies of localized states in QDs, experimentally registered by PL emission characteristics of the QDs, can be reasonably well described by the effective-mass approximation (EMA) with parabolic energy bands. Calculation of electronic transitions is done in EMA [10]. Parameters of CdTe and ZnTe, effective masses, and conduction and valence offsets are transferred from literature [11]. If we assume spherical symmetry of a particle, that is, that single sphere of CdTe is surrounded by ZnTe, calculated value of QD diameter is 3 nm in case of 3 ml matches experimental  $E_2$  value.

When adding a large quantity of CdTe between two layers of ZnTe, it is expected to find larger QDs. As a consequence the energy  $E_2$  would be lower. This expectation was not fulfilled for the 12 ml sample; see Figure 4. To explain experimental results in 12 ml case, we use model core/shell type nanostructures where QD is of gradient composition. CdTe core of radius  $r_C$  is surrounded by concentric spherical

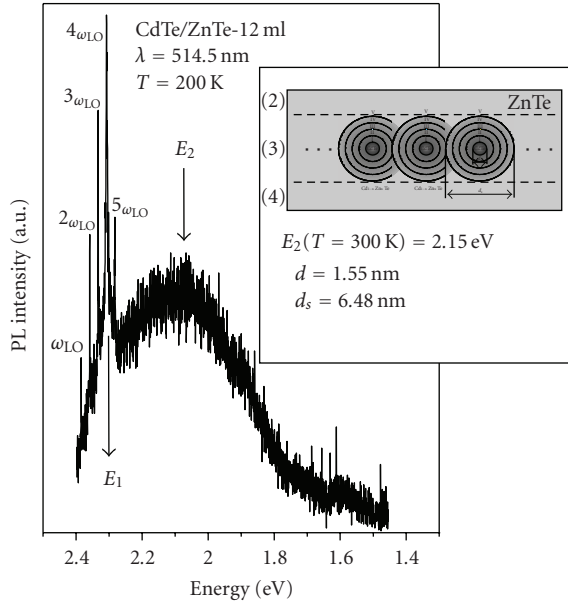


FIGURE 3: Typical PL spectra of sample with 12 ml of CdTe in the finishing layer; PL spectra are excited by  $\lambda = 514.5$  nm Ar-laser line and recorded at 200 K. *Insert*: schematic presentation of the structure of SAQD.

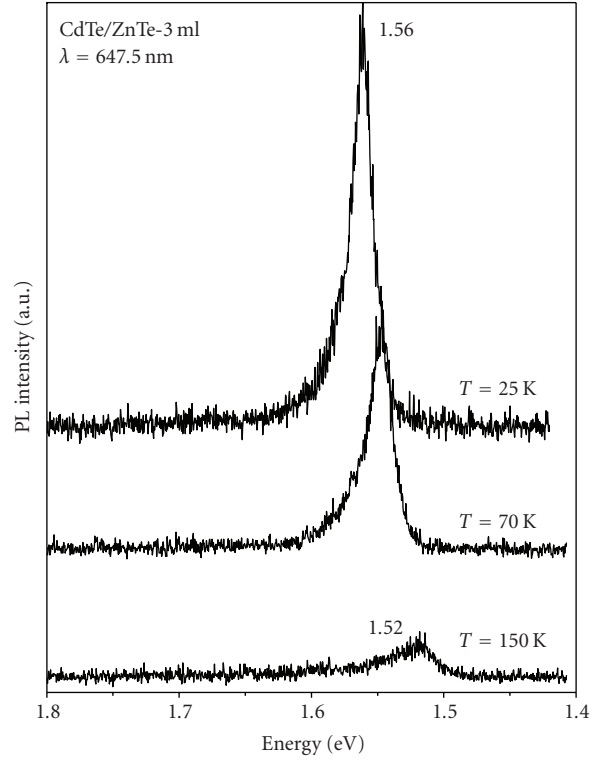


FIGURE 5: Typical PL spectra of sample with 3 ml of CdTe in the finishing layer; PL spectra are excited by  $\lambda = 647.5$  nm Kr-laser line and recorded at different temperature.

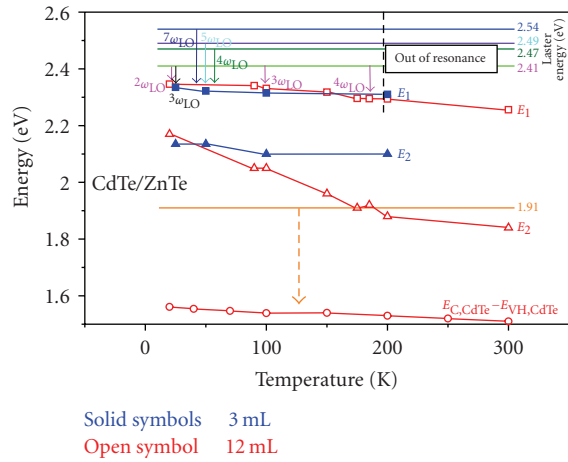


FIGURE 4: Temperature dependences of PL emission peaks and schematic presentation of multiphonon (MP) resonance. Results for 3 ml sample are presented as open symbols, and for 12 ml sample as solid symbols.

layers each of  $\text{Cd}_x\text{Zn}_{1-x}\text{Te}$  composition ( $x$  is proportional to the layer distance from the center) and finally from radius  $r_S$  by  $\text{Cd}_{0.1}\text{Zn}_{0.9}\text{Te}$ . We suppose that electrons and holes from QD are in spherical step-like energy well. Cd concentration in the surrounding  $\text{Cd}_x\text{Zn}_{1-x}\text{Te}$  gradually decreases to 10% ( $x = 0.1$ ), step by step. We assumed that effective masses and conduction and valence offsets change proportionally to  $x$ . The existence of these intermediate layers, as a model of graded composition, influences rapidly electron, hole, and excitons spectra. For measured  $E_2$  the diameter of the core is 1.55 nm and the diameter of outer sphere is 6.48 nm.

In case of 3 ml there is red-shift of the low-energy peak ( $E_2$ ) with increase of temperature, which is much larger than the shift one would expect from the temperature-induced shrinking of the CdTe band gap. In our opinion, even in the case of 3 ml, due to interdiffusion there are fluctuations of QD chemical composition and QD size distribution. So, we deal with the ensemble of QDs of different depths of the corresponding potentials. Thermally induced redistribution of carriers within the dot ensemble causes observed energy shift of photoluminescence energy. Opposed to that in the 12 ml CdTe sample all transitions are preserved due to relatively homogeneous thickness of the layer.

When the sample is excited by  $\lambda = 647.5$  nm Kr-laser line, PL takes place only in the buffer layer of CdTe which is clearly seen in Figures 4 and 5. The temperature dependences of PL emissions peaks and their intensities are identical to the dependences registered for the CdTe bulk crystal.

In principle, registered MP resonant process (see Figures 2 and 3.) can be described by the following equation:  $E_{\text{in}} - K\hbar\omega = E$ ;  $E_{\text{in}}$  and  $E$  are the incident photon energy and electron transition energy, respectively [9],  $\hbar\omega$  is the phonon energy, and  $K$  is the MP order.

MP emission is not registered at  $T = 300$  K. MP emission processes are registered at temperature below  $T = 200$  K (for 2.41 eV laser energy,  $K = 4$ ). The equation means that when the energy of the scattered photon approached the energy  $E_1$ , the Raman line becomes strongly enhanced. This is schematically presented by arrows on the top in Figure 4.

#### 4. Conclusion

Structural and optical properties of CdTe/ZnTe self-assembled quantum dots (SAQDs) growth by molecular beam epitaxy are investigated in this paper. Photoluminescence spectra consist of two main emission peaks: high-energy band connected to barrier band gap and low-energy band concerned to CdTe QD electron-hole recombination. Two mechanisms of relaxation are present in this system: relaxation directly to the CdTe quantum dot exciton ground state and optical phonon-assisted deexcitation. It seems that CdTe quantum dots when embedded in ZnTe barrier layers are very efficient carrier receivers. CdTe/Cd<sub>x</sub>Zn<sub>1-x</sub>Te heterostructures inhomogeneity modelled by gradual composition influence drastically basic transition energy. The present observations can help improve understanding of the optical and the microstructural properties in the CdTe/ZnTe self-assembled quantum dots. The registered multiphonon emission processes depend on temperature. When the energy of the scattered photon approached the energy  $E_1$ , the corresponding phonon line becomes strongly enhanced.

#### Acknowledgments

This work was supported under the Agreement of Scientific Collaboration between the Polish Academy of Science and the Serbian Academy of Sciences and Arts. The work in Serbia was supported by the Serbian Ministry of Science (Project 141028).

#### References

- [1] S. Mackowski, "CdTe/ZnTe quantum dots—growth and optical properties," *Thin Solid Films*, vol. 412, no. 1-2, pp. 96–106, 2002.
- [2] S. Mackowski, G. Karczewski, T. Wojtowicz, et al., "Structural and optical evidence of island correlation in CdTe/ZnTe superlattices," *Applied Physics Letters*, vol. 78, no. 24, pp. 3884–3886, 2001.
- [3] C. S. Kim, M. Kim, S. Lee, et al., "Evidence for 2D precursors and interdiffusion in the evolution of self-assembled CdSe quantum dots on ZnSe," *Physical Review Letters*, vol. 85, no. 5, pp. 1124–1127, 2000.
- [4] H. Kirmse, R. Schneider, M. Rabe, W. Neumann, and F. Henneberger, "Transmission electron microscopy investigation of structural properties of self-assembled CdSe/ZnSe quantum dots," *Applied Physics Letters*, vol. 72, no. 11, pp. 1329–1331, 1998.
- [5] T. A. Nguyen, S. Mackowski, H. E. Jackson, et al., "Resonant spectroscopy of 2–6 self-assembled quantum dots: excited states and exciton-longitudinal optical phonon coupling," *Physical Review B*, vol. 70, no. 12, Article ID 125306, 8 pages, 2004.
- [6] N. Romčević, M. Romčević, R. Kostić, et al., "Far-infrared spectroscopy of CdTe/ZnTe self-assembled quantum dots," *Journal of Alloys and Compounds*, vol. 481, no. 1-2, pp. 6–9, 2009.
- [7] N. Romčević, M. Romčević, R. Kostić, et al., "Resonant Raman spectra of CdTe/ZnTe self assembled quantum dots," *Acta Physica Polonica A*, vol. 116, no. 1, pp. 88–90, 2009.
- [8] N. Romčević, M. Romčević, R. Kostić, D. Stojanović, G. Karczewski, and R. Galazka, "Raman spectra of CdTe/ZnTe self-assembled quantum dots," *Microelectronics Journal*, vol. 40, no. 4-5, pp. 830–831, 2009.
- [9] S. L. Zhang, Y. T. Hou, M. Y. Shen, J. Li, and S. X. Yuan, "Multiphonon Raman scattering resonant with two kinds of excitons in a (CdTe)<sub>2</sub>(ZnTe)<sub>4</sub>/ZnTe short-period-superlattice multiple quantum well," *Physical Review B*, vol. 47, no. 19, pp. 12937–12940, 1993.
- [10] M. Tkach, V. Holovatsky, O. Voitsekhivska, and M. Mikhalyova, "Exciton-photon interaction in the spherical nanoheterosystem CdS/B-," *Physica Status Solidi B*, vol. 203, no. 2, pp. 373–386, 1997.
- [11] T. A. Nguyen, *Investigation of electronic structure and optical properties of 2–6 self-assembled quantum dots*, M.S. thesis, University of Cincinnati, Cincinnati, Ohio, USA, 2006.

## Research Article

# Growth of GaN@InGaN Core-Shell and Au-GaN Hybrid Nanostructures for Energy Applications

**Tevye Kuykendall,<sup>1</sup> Shaul Aloni,<sup>1</sup> Ilan Jen-La Plante,<sup>2</sup> and Taleb Mokari<sup>1</sup>**

<sup>1</sup>The Molecular Foundry, Materials Science Division, Lawrence Berkeley National Laboratory, 1-Cyclotron Road, Berkeley, CA 94720, USA

<sup>2</sup>Department of Chemistry, University of California at Berkeley, 1-Cyclotron Road, Berkeley, CA 94720, USA

Correspondence should be addressed to Taleb Mokari, tmokari@lbl.gov

Received 2 April 2009; Accepted 25 May 2009

Recommended by Mohamed Sabry Abdel-Mottaleb

We demonstrated a method to control the bandgap energy of GaN nanowires by forming GaN@InGaN core-shell hybrid structures using metal organic chemical vapor deposition (MOCVD). Furthermore, we show the growth of Au nanoparticles on the surface of GaN nanowires in solution at room temperature. The work shown here is a first step toward engineering properties that are crucial for the rational design and synthesis of a new class of photocatalytic materials. The hybrid structures were characterized by various techniques, including photoluminescence (PL), energy dispersive x-ray spectroscopy (EDS), transmission and scanning electron microscopy (TEM and SEM), and x-ray diffraction (XRD).

Copyright © 2009 Tevye Kuykendall et al. This is an open access article distributed under the Creative Commons Attribution License, which permits unrestricted use, distribution, and reproduction in any medium, provided the original work is properly cited.

## 1. Introduction

The optical, electrical, and chemical properties of semiconductor nanostructures have been studied intensively in the last two decades. Semiconductor nanostructures have been shown to have unique properties compared to the bulk. Due to their large surface to volume ratio, effects at the surfaces, and/or interfaces in multicomponent nanomaterials, have been shown to strongly influence the properties of the materials. By controlling the size, shape, and composition of these materials, the energy levels within the materials can be altered in a way that may offer better control over exciton creation, charge separation, recombination, and transport. With the increasing push to find clean energy alternatives to fossil fuels, many recent studies have been exploring the potential use of nanomaterials for energy conversion. Solar energy is possibly one of the cleanest and most abundant sources of renewable energy. Photocatalysis has been shown to be one of the most promising areas of solar energy conversion and is the focus of this research.

Many semiconductors that fulfill the requirements of being a good substrate for photocatalytic reactions possess bandgaps that are too large for solar applications. For

example: GaN has been intensively used for water splitting and other photocatalysis reactions but possesses a wide bandgap (3.4 eV), which is not capable of absorbing light over the majority of the solar spectrum. The need to increase the absorption efficiency of photocatalytic materials in the visible portion of the solar spectrum is one of the major challenges to be addressed.

New “engineered” nanomaterials may offer unique solutions critical for the harvesting of solar radiation and conversion to electrical and chemical energy. The assembly of two or more nanostructured components with precise control over the size, shape, composition, and spatial orientation is desirable not only for the combination of different functionalities, but also for advanced properties that can arise independent of the single-component materials. Engineering hybrid multi component nanostructures draws on the vast array of synthetic techniques now at our disposal to assemble nanocrystals with very different properties; a semiconductor nanocrystal can be combined with a metal in such a way that the hybrid structure can be tailored to a specific application.

$\text{In}_x\text{Ga}_{1-x}\text{N}$  has been shown to be a good candidate for solar energy conversion since the material forms a solid solution with a bandgap that can be tuned from 3.4 eV to

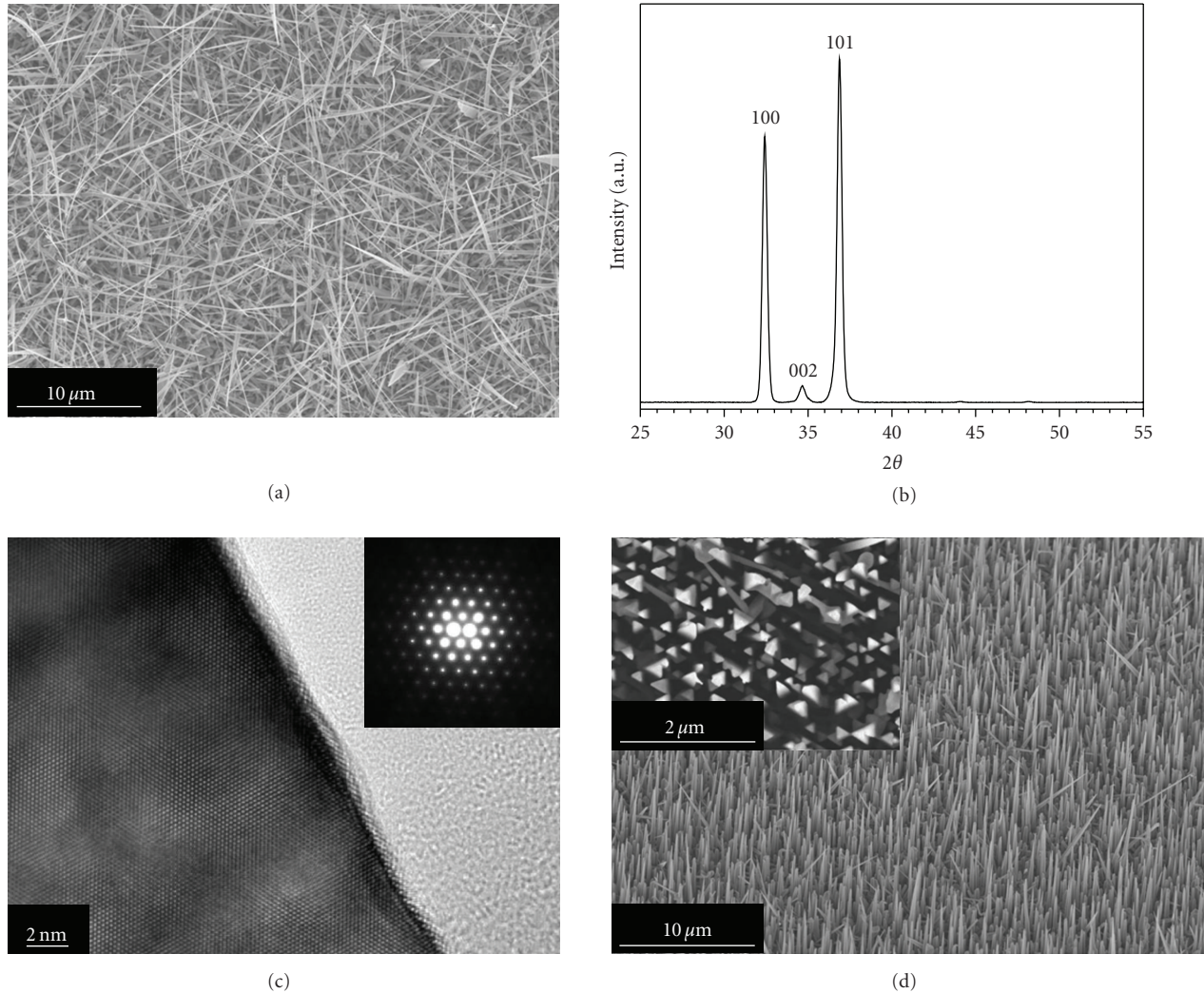


FIGURE 1: (a) SEM image of GaN nanowires grown with  $\text{NiNO}_3$  catalyst on  $c\text{-Al}_2\text{O}_3$  substrate. The wires have random orientation with diameters from 50 to 500 nm, and lengths on the order of 10 to 20  $\mu\text{m}$ . (b) XRD of the GaN nanowires indicates that it has the wurtzite crystal structure. The peaks shown correspond to the (100), (002), and (101) planes from left to right. (c) TEM phase contrast image of a single GaN nanowire oriented along the [001] zone axis. The wires length extends along the [210] direction. The inset shows the electron diffraction pattern, indicating that the wires are single crystalline. (d) SEM showing vertically aligned GaN nanowires on  $a\text{-LiAlO}_2$  tilted  $30^\circ$ . The inset shows the triangular cross-section of the nanowires from the top-down view.

0.9 eV by altering the alloy composition from  $x = 0$  to 1 [1]. There has been considerable difficulty, however, in producing high-quality InGaN materials with indium concentrations greater than  $x \approx 0.2$  due to a large miscibility gap [2]. At high indium concentrations, alloy decomposition, indium segregation, and strain related cracking are often observed. Metalorganic chemical vapor deposition (MOCVD) is the most widely commercially used technique for growing GaN and InGaN films. While full composition tunability of  $\text{In}_x\text{Ga}_{1-x}\text{N}$  nanowires (with  $x = 0$  to 1) has recently been demonstrated using chloride precursors [3], the direct growth of InGaN nanowires using MOCVD remains elusive. In the chloride approach, relaxation of strain due to the small dimensions of nanowires and low growth temperatures was suggested to be critical in overcoming the miscibility gap. This idea was strengthened by theoretical calculations

that modeled indium incorporation as a function of strain and wire diameter [4]. A similar relaxation of strain may be possible in core-shell geometry by reducing the dimensions of the epitaxial interface and may lead to higher indium content alloys.

Here we show that a GaN@InGaN core-shell morphology can be accomplished using MOCVD and will allow us to tune the bandgap of the nanowires to absorb solar radiation in the visible. To achieve this, single-crystalline gallium nitride GaN nanowire cores were grown [5, 6] and subsequently coated with InGaN shells [7]. Trimethylgallium (TMG), trimethylindium, and ammonia were used as the Ga, In, and N precursors, respectively. The 1 D nanowire growth was achieved using the vapor-liquid-solid (VLS) mechanism [8], with gold or nickel as the catalyst. Using  $\text{Ni}(\text{NO}_3)_2$  as the catalyst's precursor on a  $c$ -plane sapphire substrate yielded

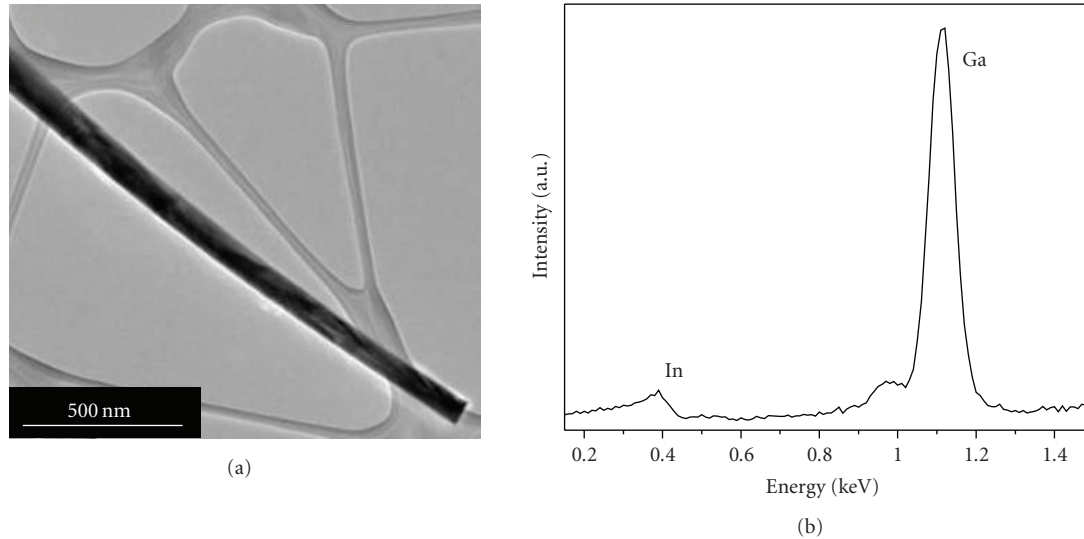


FIGURE 2: (a) TEM image showing the morphology of the GaN@InGaN core-shell nanowires. (b) Energy dispersive X-ray spectroscopy shows peaks from the In shell and the Ga shell indicating the presence of Indium in the shell of the GaN@InGaN core-shell heterostructure.

GaN nanowire arrays with no apparent preferred orientation with respect to the substrate. Scanning electron microscopy (SEM) images of the wires are shown in Figure 1(a). The wires generally have triangular cross-sections with widths from 50 to 500 nm and lengths on the order of 10 to 30  $\mu\text{m}$ . The X-ray diffraction pattern shown in Figure 1(b) confirms that the wires are GaN and have the wurtzite crystal structure with lattice constants  $a = 0.319$  nm and  $c = 0.514$  nm. The transmission electron microscopy (TEM) phase contrast image shown in Figure 1(c), and electron diffraction pattern (inset) confirms that the wires are single crystalline. The images, taken down the [001] zone axis, show that the wire's length extends in the [210] direction. TEM taken for many wires indicates that this is the primary growth direction. The optical properties of the wires will be discussed below.

To improve the orientation and uniformity of the wires we have chosen a substrate that closely matches the preferred wire growth direction [6]. On this substrate the use of gold as the catalyst further improves the wire's uniformity and alignment. The tertiary structure offered by controlling the growth direction and uniformity will provide a better template for later film overgrowth, and particle decoration. An SEM image of GaN wires grown on a-LiAlO<sub>2</sub> is shown in Figure 1(d) with the substrate tilted 30° from normal. The crystallographic orientation along the wires length remained in the [210] direction. However, when LiAlO<sub>2</sub> was used, the wires grew vertically and perpendicular to the substrate. Figure 1(d) (inset) is taken from the top-down view, and it clearly shows the triangular cross-sections of the nanowires.

The core-shell wires were synthesized by first growing GaN nanowires (as discussed previously), followed by thin-film deposition of InGaN at reduced temperatures. TEM images of the nanowires (Figure 2(a)) show that the InGaN shell is a smooth and continuous coating. Energy dispersive X-ray spectroscopy (EDS), shown in Figure 2(b), shows the presence of indium and gallium.

Photoluminescence (PL) spectra were taken for both as-made GaN and core-shell GaN@InGaN nanowires. PL was carried out on individual wires to clearly demonstrate that the emission is from the nanowires and not from a film on the underlying substrate. The PL spectra in Figure 3(a) are of single GaN and GaN@InGaN core-shell nanowires dispersed on glass cover slips. The wires were excited with a 349 nm Q-switched diode laser operating at 6 kHz, focused down to  $\sim 5$   $\mu\text{m}$  spot. The GaN nanowire showed a peak emission at 384 nm (3.2 eV). Importantly, the well-known defect induced yellow emission band is not observed, indicating that the high optical quality of these nanowires. The narrow peak observed at 349 nm is due to the excitation laser. PL spectra of several GaN@InGaN core-shell wires, taken from samples grown at different temperatures, show that the wavelength can be tuned from 380 nm to 550 nm. CCD images collected from the nanowires shown in Figure 3(b) indicate the color and approximate size of the wires. A plot of emission energy versus concentration is shown in Figure 3(c). The wavelengths observed here correspond to approximate indium concentrations of 0, 18, and 25 percent indium. The presence of two peaks on the right-most spectrum (Figure 3(a)) indicates that there may be some spinodal decomposition or phase segregation of the InGaN shell at higher indium concentrations. Further work will hopefully yield even higher indium concentrations.

There has been significant interest in growth of metals on the surface of nanorods and wires to facilitate charge transfer. A number of approaches have been used to grow metals on semiconductors through reduction, physical deposition, or photochemistry to give Au and Ag on ZnO [9, 10], Co and Au on TiO [11, 12], and others [13, 14]. Here, we describe our progress on the development of metal-semiconductor heterojunctions focused on GaN nanowires interfaced with Au nanoparticles as shown in Figure 4. Figure 4(a) presents the GaN nanowires before they were introduced to the gold

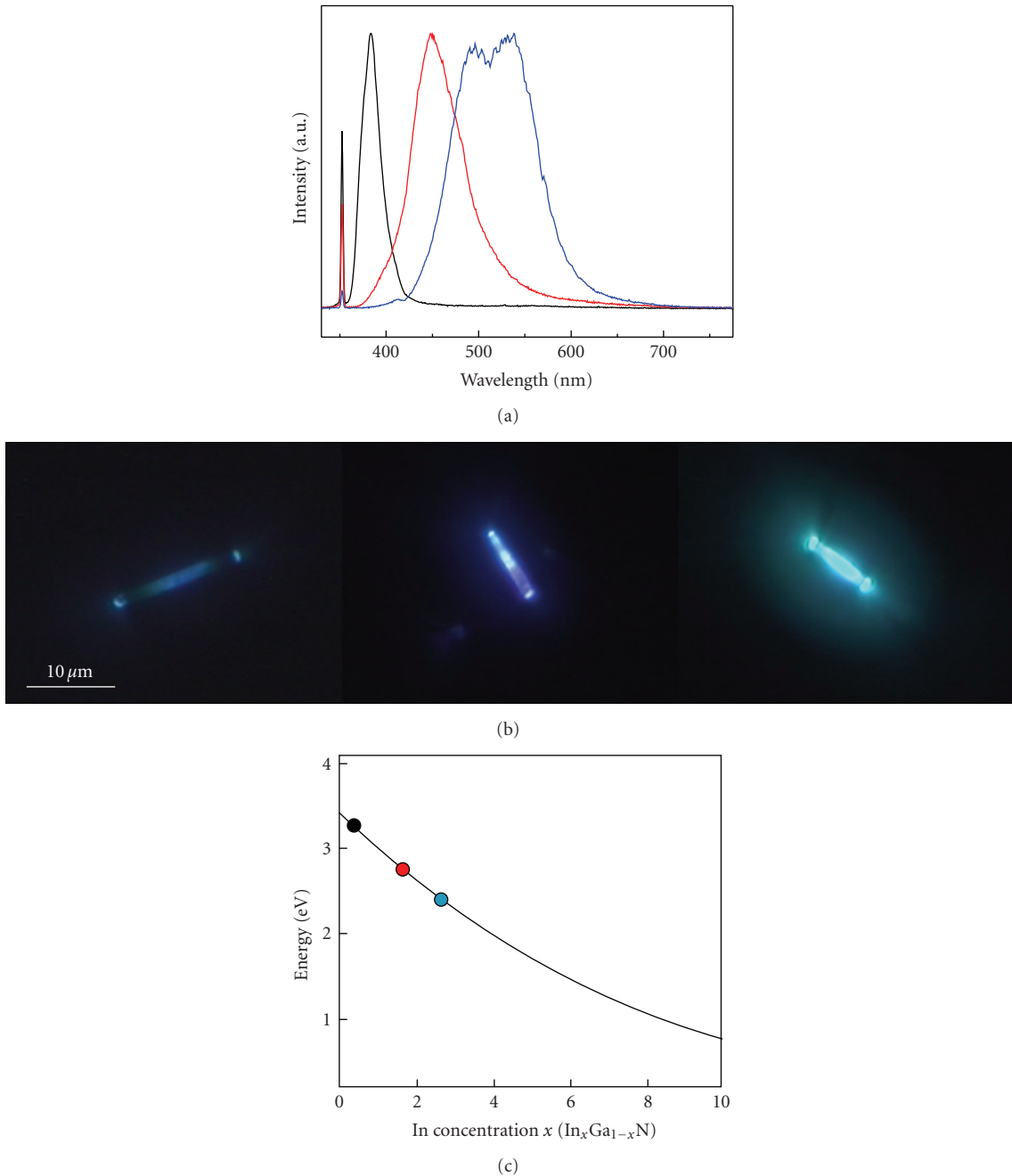


FIGURE 3: Photoluminescence of individual wires are shown. (a) PL spectra from left to right with peaks around 380, 450, and 525 nm. The images in (b) are the corresponding wires from the PL spectra in (a) arranged from left to right. (c) A plot of concentration versus bandgap energy shows the approximate concentration of the wire shells.

solution. A facile method for the growth of Au on the tips of CdSe nanorods was developed by one of the co-authors of this paper based on the reduction of Au by dodecylamine in the presence of didodecylmethylammonium bromide (DDAB) at room temperature. The method was used here to grow gold on the GaN nanowires and is described in the experimental section [15]. The results of the growth are shown in Figure 4(b). The gold particles have an average diameter of  $\sim 30$  nm. The composition of the hybrid wires

(shown in Figure 4(b)) was characterized by EDS and clearly shows a peak that confirms the Au growth.

*Conclusion.* We demonstrated a method to engineer bandgap by growing GaN/InGaN core-shell structures. The bandgap energy was tuned from 380 nm to 550 nm, which could improve the absorption efficiency. Then, we succeeded to grow catalytic metal (Au) on the surface of the GaN nanowires, an important hybrid structure for photocatalysis.

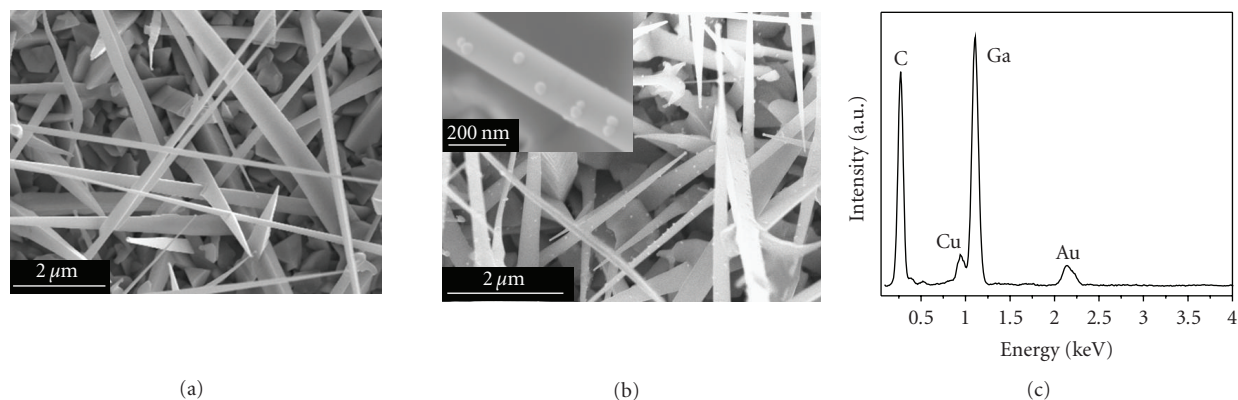


FIGURE 4: SEM images taken (a) before and (b) after growth of gold nanoparticles on GaN nanowires. (b) Gold nanoparticles can clearly be seen to decorate the surfaces of the GaN nanowires, the inset shows a close up of a single wire with multiple particles attached. (c) EDS of the particles taken by TEM confirms that they are gold.

## 2. Experimental

GaN and GaN@InGaN core-shell nanowire growth was carried out in a Thomas Swan, Showerhead  $3 \times 2$  MOCVD cold-wall reactor. The growth substrates were prepared by drop-casting  $40 \mu\text{L}$  of  $0.2 \text{ M}$  solution of  $\text{NiNO}_3$  in ethanol onto  $1 \text{ cm}^2$  c-plane sapphire wafer. For  $\text{LiAlO}_2$  substrates,  $3 \mu\text{L}$  of  $5 : 1$  ratio B. B. International  $10 \text{ nm}$  gold colloid to ethanol was drop-cast onto  $1 \text{ cm}^2$  wafers. Pure GaN nanowires were grown for 10 minutes at  $\sim 825^\circ\text{C}$ . The reactive and carrier gas flows were 600, 41, 200, and 400 sccm for ammonia, TMG, hydrogen, and nitrogen. The TMG bubbler was kept at  $5^\circ\text{C}$ , and the reactor pressure was 140 Torr. For core-shell wires, the same conditions were used for GaN nanowires with a subsequent step for InGaN deposition. The InGaN shells were grown for  $\sim 15$  minutes with temperatures from  $700\text{--}750^\circ\text{C}$ . The reactive and carrier gas flows were 5000, 1, 190, and 1000 sccm for ammonia, TMG, TMI, and nitrogen. The TMI bubbler was kept at  $18^\circ\text{C}$ , and the reactor pressure was 400 Torr.

PL was acquired using a WITec Alpha 300S system equipped with a Crystalaser, 349 nm Q-switched diode laser operating at 6 kHz. The laser spot was focused on the nanowire with a spot-size of  $\sim 5 \mu\text{m}$ . The PL emission was collected through a second objective from an area of  $< 300 \text{ nm}$  and passed through a fiber to an Ocean Optics QE65000 spectrometer.

SEM and EDS were acquired using a Zeiss Gemini Ultra-55 Analytical Scanning Electron Microscope with an acceleration voltage of 5 kV, equipped with an EDAX EDS detector. TEM and EDS were acquired using a JEOL 2100-F 200 kV Field-Emission Analytical Transmission Electron Microscope. XRD was acquired using a Bruker AXS D8 Discover GADDS Diffractometer, with a  $\text{Cu-K}\alpha$  source.

## 3. Growth of Gold Nanoparticles on the GaN Nanowires

A stock solution was prepared with 3 mL toluene, 12 mg gold trichloride, 40 mg didodecyldimethylammonium bromide,

75 mg dodecylamine and was sonicated for about 20 minutes until the solution changed color to yellow. 1 mL of this stock solution was added dropwise to the substrate ( $4 \text{ mm} \times 4 \text{ mm}$ ,  $\text{Al}_2\text{O}_3$ ) with GaN in a vial with 1 mL of toluene. The final solution was stirred in the vial with the substrate bound GaN and allowed to reduce for 72 hours.

## Acknowledgments

Thanks to Adam Schwartzberg for PL spectroscopy. The work at the Molecular Foundry was supported by the Office of Science, Office of Basic Energy Sciences, of the U.S. Department of Energy under Contract no. DE-AC02-05CH11231.

## References

- [1] J. Wu, W. Walukiewicz, K. M. Yu, et al., "Superior radiation resistance of  $\text{In}_{1-x}\text{Ga}_x\text{N}$  alloys: full-solar-spectrum photovoltaic material system," *Journal of Applied Physics*, vol. 94, no. 10, pp. 6477–6482, 2003.
- [2] F. A. Ponce, S. Srinivasan, A. Bell, et al., "Microstructure and electronic properties of InGaN alloys," *Physica Status Solidi B*, vol. 240, no. 2, pp. 273–284, 2003.
- [3] T. Kuykendall, P. Ulrich, S. Aloni, and P. Yang, "Complete composition tunability of InGaN nanowires using a combinatorial approach," *Nature Materials*, vol. 6, no. 12, pp. 951–956, 2007.
- [4] H. J. Xiang, S.-H. Wei, J. L. F. Da Silva, and J. Li, "Strain relaxation and band-gap tunability in ternary  $\text{In}_x\text{Ga}_{1-x}\text{N}$  nanowires," *Physical Review B*, vol. 78, no. 19, Article ID 193301, 4 pages, 2008.
- [5] E. A. Stach, P. J. Pauzauskie, T. Kuykendall, J. Goldberger, R. He, and P. Yang, "Watching GaN nanowires grow," *Nano Letters*, vol. 3, no. 6, pp. 867–869, 2003.
- [6] T. Kuykendall, P. J. Pauzauskie, Y. Zhang, et al., "Crystallographic alignment of high-density gallium nitride nanowire arrays," *Nature Materials*, vol. 3, no. 8, pp. 524–528, 2004.
- [7] F. Qian, S. Gradečak, Y. Li, C.-Y. Wen, and C. M. Lieber, "Core/multishell nanowire heterostructures as multicolor,

- high-efficiency light-emitting diodes,” *Nano Letters*, vol. 5, no. 11, pp. 2287–2291, 2005.
- [8] Y. Wu and P. Yang, “Direct observation of vapor-liquid-solid nanowire growth,” *Journal of the American Chemical Society*, vol. 123, no. 13, pp. 3165–3166, 2001.
- [9] V. Subramanian, E. E. Wolf, and P. V. Kamat, “Green emission to probe photoinduced charging events in ZnO-Au nanoparticles. Charge distribution and Fermi-level equilibration,” *Journal of Physical Chemistry B*, vol. 107, no. 30, pp. 7479–7485, 2003.
- [10] C. Pacholski, A. Kornowski, and H. Weller, “Site-specific photodeposition of silver on ZnO nanorods,” *Angewandte Chemie International Edition*, vol. 43, no. 36, pp. 4774–4777, 2004.
- [11] P. V. Kamat, M. Flumiani, and A. Dawson, “Metal-metal and metal-semiconductor composite nanoclusters,” *Colloids and Surfaces A*, vol. 202, no. 2-3, pp. 269–279, 2002.
- [12] M. Casavola, V. Grillo, E. Carlino, et al., “Topologically controlled growth of magnetic-metal-functionalized semiconductor oxide nanorods,” *Nano Letters*, vol. 7, no. 5, pp. 1386–1395, 2007.
- [13] D. V. Talapin, H. Yu, E. V. Shevchenko, A. Lobo, and C. B. Murray, “Synthesis of colloidal PbSe/PbS core-shell nanowires and PbS/Au nanowire-nanocrystal heterostructures,” *Journal of Physical Chemistry C*, vol. 111, no. 38, pp. 14049–14054, 2007.
- [14] J. Yang, H. I. Elim, Q. Zhang, J. Y. Lee, and W. Ji, “Rational synthesis, self-assembly, and optical properties of PbS-Au heterogeneous nanostructures via preferential deposition,” *Journal of the American Chemical Society*, vol. 128, no. 36, pp. 11921–11926, 2006.
- [15] T. Mokari, E. Rothenberg, I. Popov, R. Costi, and U. Banin, “Selective growth of metal tips onto semiconductor quantum rods and tetrapods,” *Science*, vol. 304, no. 5678, pp. 1787–1790, 2004.